Advances in 4D X-ray microtomography: new experimental tools for hydrothermal processes and materials

Ian B. Butler, Florian Fusseis & Alexis Cartwright-Taylor
School of GeoSciences, University of Edinburgh, UK

Abstract. A novel suite of experimental environments have been developed to explore chemical and physical processes *in-situ* in experiments using 4D X-ray microtomography. These experimental environments are designed to enable investigation of fluid-rock reaction, fluid transport, coupled chemical, mechanical, thermal and hydraulic processes and the evolution of geological samples towards mechanical failure. Four dimensional data acquired in such experiments can provide novel insights into processes of importance to geological and engineering applications. Experimental access to the hydrothermal temperature range, along with the ability to chemically react and to deform samples means these cells are applicable to studies of materials and processes relevant to economic geology, mineralisation and mining.

1 Introduction

The application of non-destructive 3D imaging using X-ray microtomography (µCT) has made a significant impact across the Earth Sciences over the last decade or more. These applications have included studies of ore deposit geology and investigations of mineral processing (e.g. Godel 2013; Kyle and Ketcham, 2015). A particular virtue of µCT imaging is the ability to process the digital image data produced to obtain quantitative information about, *inter alia*, the distribution, size, shape and orientation of materials. The analysis of such data can be considered to be the equivalent of examining multiple 2D thin sections in a non-destructive way. Thus for sparsely distributed minerals, like gold, µCT analysis is advantageous in order to acquire a statistically representative sample of grains for analysis (Kyle and Ketcham 2003). Other recent ore-related applications of µCT have included the observation of the relationship between metasomatic reaction haloes and base metal or PGE-rich sulfides in mantle xenoliths (Hughes et al., 2016) and the optimization of preparation methods for chemical and isotopic analysis of metal sulfide inclusions in diamonds (McDonald et al., 2017).

While 3D analysis of materials can offer new insights not available from conventional 2D techniques, the most exciting and potentially transformative experimental applications of µCT techniques have come from 4D approaches. In 4D microtomography the 4th dimension indicates resolution in time or another progress variable for a reaction or physical change in a sample. Continuous X-ray imaging of progressive change means that a single 4D experiment can be the equivalent of 10s-100s of conventional batch experiments which are analysed post-mortem. While 4D experiments have found considerable application in the context of oil & gas and other reservoir-related studies (e.g. Al-Khulaifi et al., 2017; Andrew 2015) and in some fluid-rock reaction studies (e.g. Zhu et al., 2016; Bedford et al., 2017), there have been few studies which focus upon economic mineralization, although the method has been employed in some mineral process investigations (e.g. Dobson et al., 2017). In 4D experiments an experimental cell provides the pressure, temperature and chemical environment required to promote change in the sample. In part this paucity of studies relating to mineralisation reflects the lack of experimental environments that can operate within a µCT instrument, or a synchrotron beamline and which are capable of providing the conditions of elevated temperature, pressure and reactive fluid access typical of many ore forming environments.

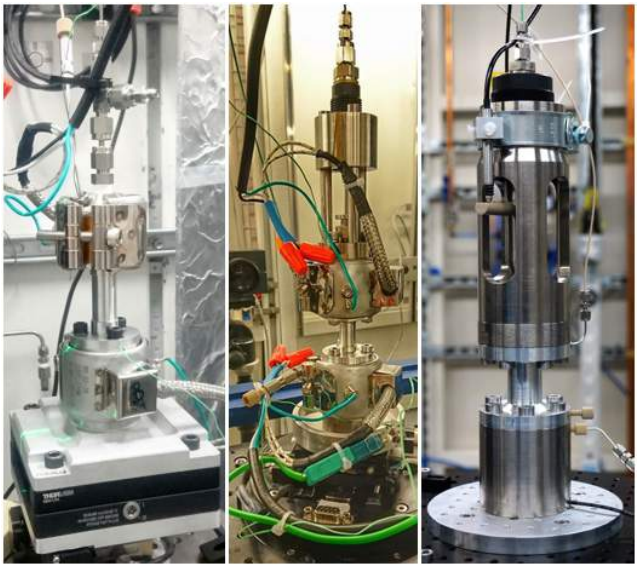

Figure 1. Three experimental environments for 4D synchrotron microtomography experiments in operation on synchrotron beamlines. From left to right, Sleipnir, Mjölnir, and Stór Mjölnir. See text for details of capabilities.

Herein we describe a suite of new experimental environments designed and built at the School of Geosciences, University of Edinburgh which facilitate experiments at elevated temperature and pressure, with differential applied stress and with access for reactive fluids. We illustrate the capability of each cell with example data which have been produced through

studies of fluid rock reaction, coupled processes and dynamic failure of rocks. Our purpose in presenting is to illustrate that tools for experimental studies of processes *in-situ* at elevated pressures and temperatures consistent with subsurface applications and mineralisation have become recently available and to explore, with the mineral deposit, mineral processing and mining engineering community, their potential to be used to obtain new insights to processes and materials of importance to economic geology using µCT methods.

2 Apparatus for 4D X-ray microtomography

The three experimental environments are shown in figure 1. Each environment has different capabilities and has built in modularity for flexibility of use in a range of studies. These experimental environments are designed and optimized for use with synchrotron light sources (Fusseis et al., 2014a) and each has been successfully employed during experimental campaigns the Advanced Photon Source (APS, Chicago, USA), the Diamond Light Source (DLS, Oxfordshire, UK), the Swiss Light Source (SLS, Villagen, Switzerland) and the Soleil synchrotron (Saint-Aubin, France).

2.1 Sleipnir – fluid flow and fluid-rock reaction at elevated P & T.

Sleipnir (Fusseis et al., 2014b & Fig. 1), was developed as a fluid-rock reaction cell and has been used for *in-situ* investigations of carbonate mineral formation during reactions of carbonate-rich fluids with olivine (Zhu et al., 2016), and for investigations of gypsum dehydration at elevated pressure and temperature (Bedford et al., 2017). In addition Sleipnir has been employed for highly time-resolved investigations of multiphase fluid infiltration in porous media (Yang et al., 2018).

Sleipnir can accommodate a 3 mm diameter cylindrical sample up to 20 mm in length, which is located between two static pistons and jacketed with a flexible silicone sleeve. The cell can operate to 230°C and 20 MPa confining pressure for reaction durations of 150 hours. Pressurised fluid can be introduced from either end of the sample. Thus the cell is able to access the lower range of temperatures and pressures associated with the formation and hydrothermal reprocessing of hydrothermal ores. The flexibility of the cell design allows each component of the cell to be replaced subject to the demands of fluid compatibility, or if enhanced x-ray transparency is required.

Experimental results produced by Zhu et al., (2016) using Sleipnir as a fluid-rock reaction cell are shown in Figure 2. In these experiments San Carlos olivine (Fo90) was reacted with a 1.5M bicarbonate solution at 200°C. The reaction product was magnesite. The use of µCT imaging enabled visualization of the volumetric change on magnesite formation and the way that expansion and microfracturing created fresh reactive surface to enable continued reaction progress. Moreover, analysis of crystal size from time resolved tomographic data demonstrates that this technique can provide both spatially distributed and bulk kinetic data for complex reactions in heterogeneous media. Rate data such as this cannot readily be obtained using conventional analytical methods.

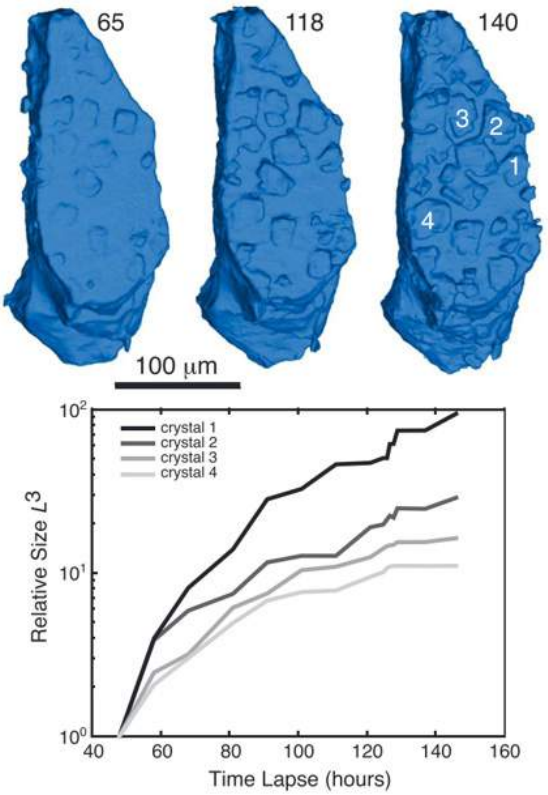

Figure 2. Top: Growth of magnesite crystals on an olivine crystal at 200°C, 13 MPa confining Pressure and 10 MPa pore fluid pressure from 65 to 140 hours reaction. Bottom: Growth curves for discrete magnesite crystals quantified from µCT data. (After Zhu et al., 2016).

2.2 Mjölnir – fluid–rock interaction at elevated T with triaxial stress.

Mjölnir (Butler et al., 2017 & Fig. 1) was designed as a triaxial deformation cell and adapted for multicomponent studies by the addition of fluid access via pistons and sample heating. This has enabled the cell to be used for studies of coupled thermal, hydraulic, chemical and mechanical processes involving geological media.

Mjolnir can accommodate a 3 mm diameter cylindrical sample up to 10mm long, which is located between two pistons and jacketed with a silicone sleeve. The upper piston is driven by a hydraulic actuator and can apply constant or increasing axial load to the sample. The cell is able to confine samples at up to 50 MPa, with applied axial loads of up to 700 MPa in order to perform triaxial rock tests coupled with high resolution imaging of pre- and post-failure processes. Sample temperatures up to 150°C can be attained.

Coupled process data acquired by using Mjölnir at beamline 2-BM of the Advanced Photon Source is shown in Figure 3. A 3mm diameter sample of gypsum was confined at 15 MPa and loaded to 40 MPa differential stress. The sample was heated to 115 °C.

Between 198 minutes and 204 minutes the sample failed along a shear plane, which created a conduit for fluid expulsion. The fluid conduit enabled water from dehydration of gypsum ($CaSO_4.2H_2O$) to basanite ($CaSO_4.½H_2O$) to be transported from the reaction site, facilitating the pervasive conversion of gypsum to basanite seen between 222 minutes and 270 minutes. Progressive healing of the initial shear plane was observed between 270 and 295 minutes. We note that the dehydration of gypsum to bassanite is itself an important industrial process as well as being a source of fluids during thin-skinned tectonic processes.

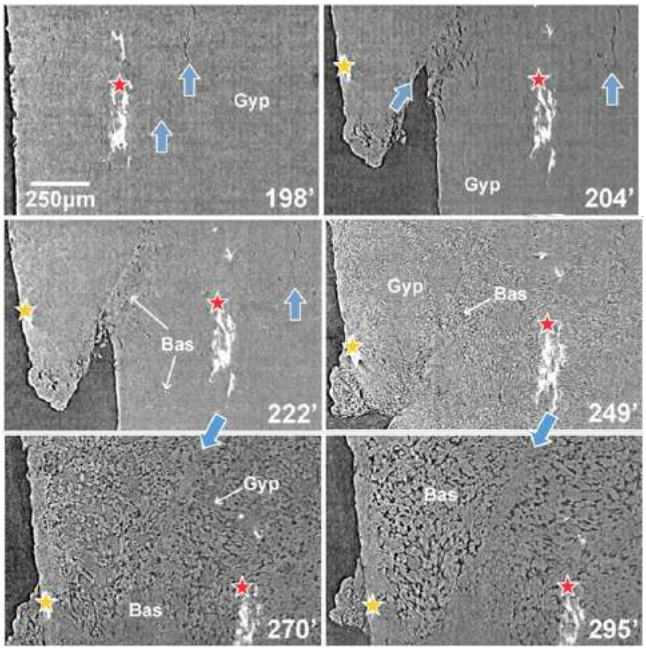

Figure 3. Time sequence of a mineral reaction (dehydration of gypsum to bassnanite, coupled to increasing sample porosity) coupled the to the shear failure of the sample and progressive healing of the failure plane (diagonal blue arrows). The red and yellow stars each mark the position of an equivalent point in the sample as the structure evolves.

2.3 Stór Mjölnir – triaxial deformation with acoustic monitoring.

Stór Mjölnir (Fig. 1) was built in 2018 and is a triaxial deformation cell, akin to a full-size rock deformation apparatus in which the principal stresses are configured as $\sigma_1>(\sigma_2=\sigma_3)$. The sample size is a 10 mm diameter by 25 mm long cylinder, which can be confined at up to 50 MPa (σ_2, σ_3) and axially loaded to 500 MPa (σ_1). Pore fluid pressure can be applied at pressures $<\sigma_2$. The addition of a linear variable displacement transducer enables stroke control of the hydraulic actuator for experiments performed at a constant strain rate. Two acoustic transducers are located axially at either end of the sample in order to be able to measure i) p-wave velocity during deformation and ii) to acquire acoustic waveforms and event rates of seismic signals produced as a consequence of deformation.

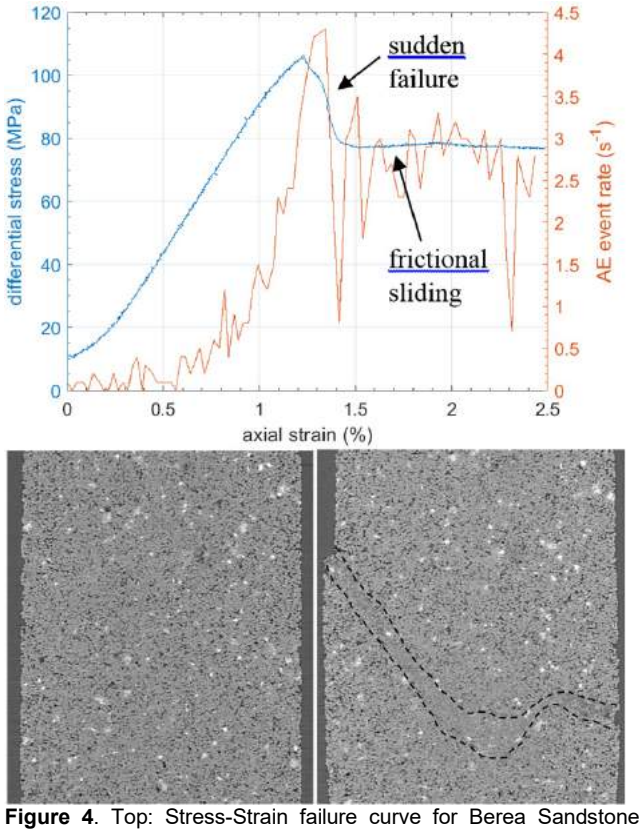

Figure 4. Top: Stress-Strain failure curve for Berea Sandstone (blue) with associated acoustic event rate (orange). Bottom: vertical slices through 3D volumes (sample diameter 10mm) before and after loading and failure illustrating the development of a shear failure.

Data from the triaxial deformation of Berea Sandstone are shown in Figure 4 for a sample confined at 15 MPa with 5 MPa pore fluid pressure and deformed at a strain rate of 10^{-5} s^{-1}. The AE event rate tracks progressive accumulation of stress induced damage with the sample and peaks at the point of failure (~1.25% axial strain) with continual damage generated during frictional sliding of the failure surface. The before and after slices cut vertically through the tomographic image of the core illustrate barreling of the sample and the locus of the shear failure. The time–resolved sequence of tomographic volumes acquired continuously during deformation can be analysed using digital volume correlation methods to establish the localized distribution of volumetric and shear strain as well as localized strain rates. Our aim is to develop improved micromechanical models for the localization of failure.

3 Summary and developments in progress.

The experimental environments described were not developed specifically for application to mineral deposit related research. Nevertheless the studies highlighted illustrate that a combination of fast x-ray synchrotron microtomography with new experimental technology is able to offer unique insights into deformation processes, fluid rock reaction and complex, coupled processes, all of which are relevant to industrial and ore minerals, mineral deposition and mining engineering.

At the present time, our equipment development is focused upon the extension of the operational range for our experimental environments towards 450 °C and 100 MPa, while maintaining capability for axial deformation and the introduction of reactive fluids. These temperature and pressure targets are not technically demanding for conventional experimental vessels, but are restrictive in the context of materials with low x-ray attenuation. These developments will access much of the hydrothermal pressure and temperature range, fully opening the potential for new experimental approaches to understanding hydrothermal mineralisation processes and the properties of geological materials critical to mining and mineral processing.

Acknowledgements

We are indebted to Robert Brown, Alex Hart and Ivan Febbrari of the Mechanical Workshop, School of Geosciences, University of Edinburgh for manufacturing the experimental cells. Thanks to Michael Flynn for technical support. We acknowledge SOLEIL, APS, Diamond and SLS for provision of synchrotron radiation facilities and would like to thank the beamline scientists Dr Andy King (PSICHE, Soleil), Dr Xianghui Xiao (formerly 2-BM, APS), Drs Christian Schlepütz and Federica Marone (TomCAT, SLS) and Drs Oxana Magdysyuk and Nghia Vo (JEEP I12, Diamond) for their help.

References

Al-Khulaifi Y, Lin Q, Blunt MJ, Bijeljic B. (2017), Reaction rates in chemically heterogeneous rock: coupled impact of structure and flow properties studied by X-ray microtomography. Env. Sci. Tech. 51:4108-4116, doi.org/10.1021/acs.est.6b06224

Andrew M, Menke H, Blunt MJ, Bijeljic B. (2015) The imaging of dynamic multiphase fluid flow using synchrotron-based X-ray microtomography at reservoir conditions. Transport Porous Med. 110:1-24. doi.org/10.1007/s11242-015-0553-2

Bedford J, Fusseis F, Leclère H, Wheeler J, Faulkner D (2017), A 4D view on the evolution of metamorphic dehydration reactions Sci. Rep. 7:6881. doi.org/10.1038/s41598-017-07160-5

Butler IB, Flynn M., Fusseis F., Cartwright-Taylor A. (2017) Mjölnir: A novel x-ray transparent triaxial rock deformation apparatus. 3rd International Conference on Tomography of Materials and Structures Lund, Sweden, 26-30 June 2017, ICTMS2017-56

Dobson KJ, Harrison STL, Lin Q, Ní Bhreasail A, Fagan-Endres MA, Neethling SJ, Lee PD, Cilliers JJ (2017) Insights into ferric leaching of low grade metal sulfide-containing ores in an unsaturated ore bed using X-ray computed tomography. Minerals 7:85. doi.org/10.3390/min7050085

Fusseis F, Xiao X, Schrank C, De Carlo F (2014a), A brief guide to synchrotron radiation-based microtomography in (structural) geology and rock mechanics. J. Struct. Geol. 65:1-16. doi.org/10.1016/j.jsg.2014.02.005

Fusseis F, Steeb H, Xiao X, Zhu W, Butler IB, Elphick S, Mäder U (2014b) A low-cost X-ray-transparent experimental cell for synchrotron-based X-ray microtomography studies under geological reservoir conditions. J. Synchrotron Rad. 21:251-253. doi.org/10.1107/S1600577513026969

Godel B. (2013) High-resolution X-ray computed tomography and its application to ore deposits: from data acquisition to quantitative three-dimensional measurements with case studies from Ni-Cu-PGE deposits. Econ. Geol. 108:2005–2019. doi.org/10.2113/econgeo.108.8.2005

Hughes HSR, McDonald I, Loocke M, Butler, IB, Upton, B, Faithfull, JW (2016) Paradoxical co-existing base metal sulphides in the mantle: The multi-event record preserved in Loch Roag peridotite xenoliths, North Atlantic Craton' Lithos 276:103-121. doi.org/10.1016/j.lithos.2016.09.035

Kyle JR., Ketcham RA (2015) Application of high resolution X-ray computed tomography to mineral deposit origin, evaluation, and processing. Ore Geol. Rev 65: 821-839. doi.org/10.1016/j.oregeorev.2014.09.034

Kyle JR, Ketcham RA (2003) In-situ distribution of gold in ores using high resolution x-ray computed microtomography. Econ. Geol. 98:1697–1701. doi.org/10.2113/gsecongeo.98.8.1697

McDonald I, Hughes HSR, Butler IB, Harris JW, Muir D (2017), Homogenisation of sulphide inclusions within diamonds: A new approach to diamond inclusion geochemistry. Geochim. Cosmochim. Acta 216:335-357 doi.org/10.1016/j.gca.2017.04.039

Yang Y, Butler IB, Fusseis F, van Dijke MIJ, Geiger S, Xiao X. (2018) Immiscible fluid displacement and trapping during a drainage-imbibition cycle in porous carbonate rock imaged by synchrotron X-ray micro-tomography. American Geophysical Union, Fall Meeting 2018, abstract #H41E-08. http://adsabs.harvard.edu/abs/2018AGUFM.H41E..08Y

Zhu W, Fusseis F, Lisabeth H, Xing T, Xiao X, De Andrade V, Karato, S (2016) Experimental evidence of reaction-induced fracturing during olivine carbonation. Fracturing during olivine carbonation. Geophys. Res. Lett. 43:9535-9543 doi.org/10.1002/2016GL070834

Carbonatization of the Antimony line in the Murchison reenstone Belt (South Africa): geochemical investigations along two drill cores.

Johannes Mennicke
Martin-Luther-University Halle-Wittenberg, Germany

Marylou Vines , Axel Hofmann
University of Johannesburg, South Africa

Christoph Gauert
University of the Free State; Geological Survey and Mining authority of Saxony-Anhalt, Germany

Abstract. Alteration of the host rock is a common process during ore genesis. Penetrative carbonatization can be observed along the Antimony Line of the Murchison Greenstone Belt (South Africa). The alteration shows zonation from proximal strongly carbonatized and mineralized carbonate-quartz schist in the vicinity of Sb-Au mineralized zones to distal, slightly carbonatized talc-chlorite-quartz schists. It is assumed that the Sb-Au veins played a major role with respect to the formation of the alteration zones. First results show high contents of MgO and Sb in Sb-mineralized zones of the Antimony Line compared to adjacent sections. However, K_2O and Al_2O_3 contents are relatively low. Due to exceptionally high MgO contents, the precursor rock of the alteration zones was presumably an ultramafic, komatiitic rock. Major variations in MgO and Al_2O_3 ratio within the Antimony Line likely indicate compositional variation in volcanic lava flows or sections of intense alteration in which Al is relatively immobile. Higher contents of K_2O in the Antimony Line are likely due to a late-stage potassium metasomatism and gave rise to fuchsite mineralization.

1 Introduction

The antimony (-gold) vein deposit of the Antimony Line in the Murchison Greenstone Belt (MGB) was in the 1970's the largest producing area of antimony in the world (Pearton & Viljoen 1986). In the vicinity of the deposit, the host rock was altered by intense carbonate alteration. Carbonatization is promoted by fluids with high partial pressure of CO_2 (e.g. Fyon et al. 1984). In Archean greenstone belts, carbonatization is often accompanied by silicification due to seafloor alteration (e.g. Hofmann et al. 2017) and/or hypogene hydrothermal magmatic or mantle-derived metamorphic fluids.

With respect to the genesis of the Antimony Line and the related alteration zones, many models have been proposed. An early model of a sedimentary origin of the carbonates (Hall 1912; Mendelssohn 1938; van Eeden et al. 1939) was replaced with current theories of mineralization by epigenetic magmatic derived ore-forming fluids (Boese 1964; Kedda 1992), syngenetic volcanogenic exhalative fluids (Muff 1978) or syngenetic hot spring systems (Minnitt 1975), and syndeformational metamorphic derived fluids (Pearton 1980; Boocock 1984; Pearton & Viljoen 1986).

In the Antimony Line in the MGB, different textures and ore minerals were observed. After Muff (1978) they can be distinguished as stibnite (Sb_2S_3) ore, berthierite ($FeSb_2S_4$) ore and iron-sulphide rich ore. Muff & Saager (1979) described more than 40 ore minerals from the Antimony Line.

Close to mineralized veins the host rock commonly consists of mineralized cherty quartz-carbonate rocks. In more distal parts the rocks change to green fuchsite-quartz-carbonate schists, gray quartz-carbonate schists, talc-carbonate-quartz schists, talc-chlorite-quartz-carbonate schists, and chlorite-quartz-carbonate schists (Pearton 1980). However, due to shearing and multiple veining in the Antimony Line, this zonation is not well pronounced in most areas.

The aim in this project is to provide a reliable mass balance of altered/unaltered rock to establish a geochemical fluid modeling in order to characterize the mineralizing and altering fluid, which should combined with stable isotopic studies (e.g. Jaguin et al. 2014) and thermodynamically fluid modeling (Blaauwbroek 2016) contribute to a holistic view of the fluid system.

This study provides an insight into the geochemical evolution of alteration zones along two drill cores, "Free State Mine drill core" (FS drill core) and "Weigel Shaft drill core" (WS drill core) of the Antimony Line and adjacent sequences. Preliminary analyses were carried out by a portable XRF. The examined rocks are strongly altered by carbonatization. However, different units could be distinguished with different geochemical and mineralogical features.

2 Geological setting

The Antimony Line is situated in the MGB in the north-eastern part of South Africa. The MGB is divided into several tectonostratigraphic domains (Fig. 1)..

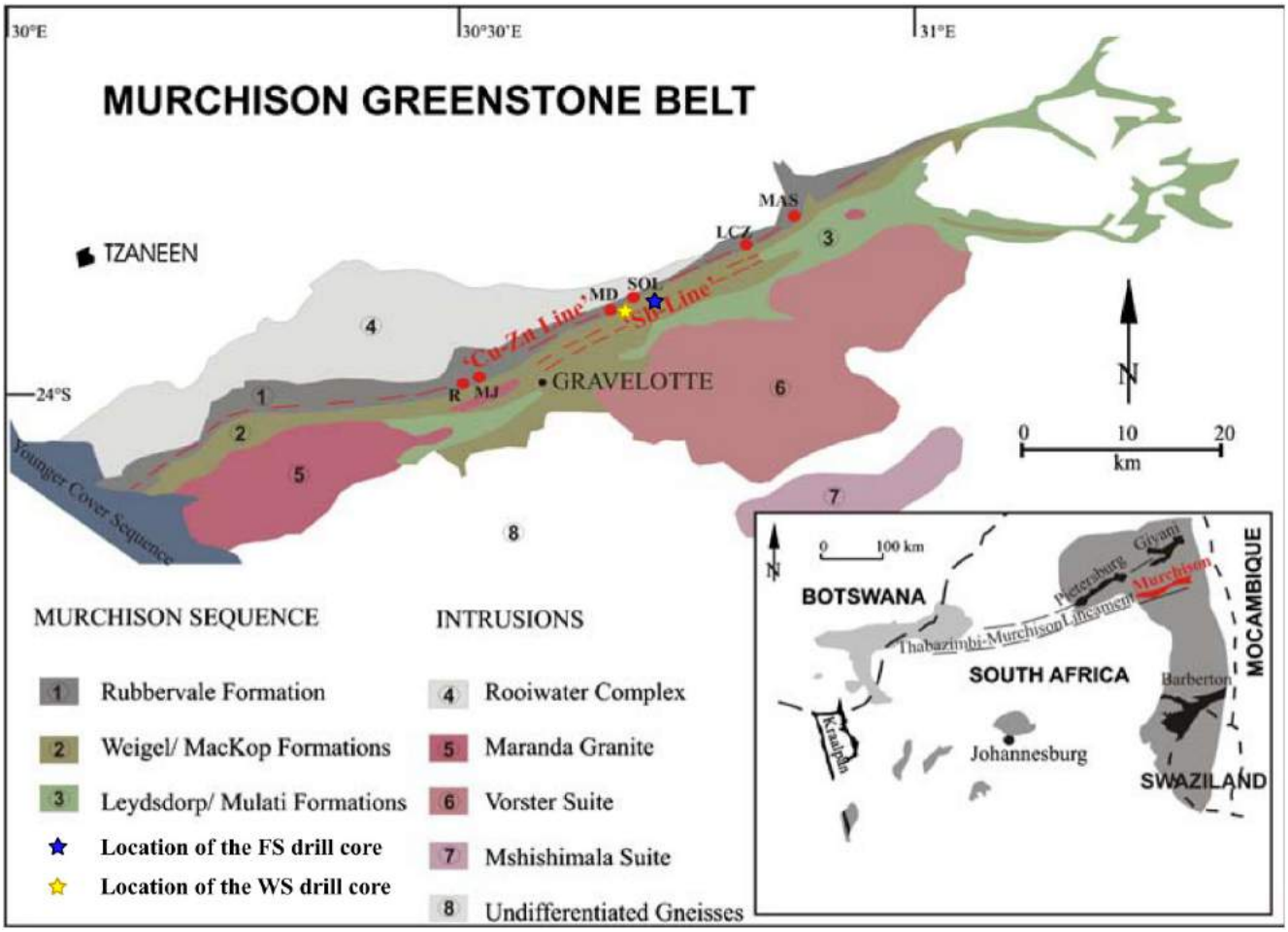

Figure 1. Geological map of the Murchison Greenstone Belt with the location of the FS and WS drill core. The Antimony Line is marked with "Sb-Line" (edited after Schwarz-Schampera et al. 2010, modified from Poujol et al. 1996)

These units were subjected to greenschist- to amphibolite-facies metamorphism (Vearncombe 1988) during the first deformation stage D1, which is considered to be the main deformational event in the MGB (Boocock 1984).

The central portion of the MGB is made of the 3.07 Ga old Weigel Formation, which hosts the Antimony Line. It consists of steeply N-NNW dipping metasediments and carbonatized mafic to ultramafic volcanic and subvolcanic rocks subjected to greenschist facies metamorphism (Vearncombe et al. 1992). Along a 50 km shear zone in the center of the Weigel Formation, the WSW-ENE oriented Antimony Line (Sb-Line) (Fig. 1) exposes several districts of Sb- and Au-enriched ore bodies in massive hydrothermal quartz-carbonate veins.

3 Portable XRF analyses of drill cores of the Antimony Line

XRF analyses were obtained from two drill cores that are representative of rocks of the Antimony Line and adjacent sequences. The obtained data show a geochemical trend of altered rocks and give indications for significant changes of whole rock geochemistry and the possible precursor rock.

The analyzed cores both comprise mineralized zones and characteristic alteration zones can be distinguished. Talc-chlorite-carbonate-quartz-fuchsite (talc-chl.-carb-qtz-fuchs) bearing schists with different compositional and textural features were observed. They were defined as qtz-carb schist, talc-carb (-qtz) schist, talc-chl-qtz-carb schist, fuchs-qtz-carb schist, talc-chl schist and chl-qtz-carb schist with varying modal mineral proportions. MgO, Al_2O_3, K_2O, and Sb were used to represent the significant changes in rock composition. Rocks of the Antimony Line are accompanied by strongly pronounced carbonatization and silicification as well as continuously detectable values of Sb (>38 ppm).

3.1 XRF analyses of the Free State (FS) drill core

The FS drill core was drilled in the Free State mining area of the MGB (Fig. 1) and comprises a profile through the Antimony Line from N to S in this area.

The majority of the rocks (Fig. 2) in the Free State drill core are representative for rocks of the Antimony Line. However, the chl-qtz-carb schists at the base of the drill core exhibit different geochemical features and likely represent a sheared sedimentary unit. The dotted line in figure 2 displays a major change in lithology which is accompanied by a decline of MgO and Sb contents as well as higher contents of Al_2O_3 and K_2O

downhole.

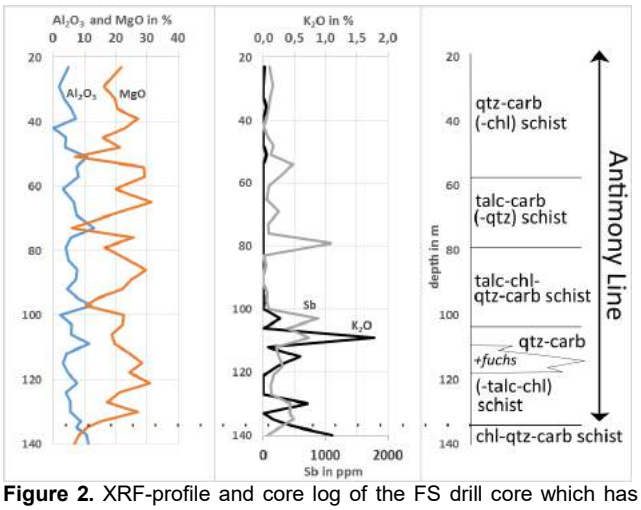

Figure 2. XRF-profile and core log of the FS drill core which has been sampled and analyzed at a 3 m spacing. The left diagram shows the MgO and Al_2O_3, the right diagram shows the K_2O and the Sb distribution. The dotted line signifies a major change in lithology.

The Antimony Line, however, exhibits constantly high MgO values and relatively low Al_2O_3 values. Three analysis at 51 m, 73 m, and 97 m depth in the Antimony Line show slightly higher values of Al_2O_3 compared to MgO. These changes could indicate intraformational variations in lithology or degree of alteration. The K_2O contents are below detection in most of the core. From 100 m to 120 m depth K_2O is enriched. This enrichment is accompanied by a distinct Sb enrichment in the same depth. Sb was detected over the whole range of the Antimony Line up to 1000 ppm. Besides, several stibnite-enriched mineralization zones were observed in different sections of the drill core. These are not displayed in Fig. 2, as the main priority of this study is to explain the formation of the alteration zones.

3.2 XRF analyses of the Weigel Shaft (WS) drill core

The WS drill core was drilled in the Athens-Weigel mining area in the central part of the Antimony Line, approximately 3 km west of the Free State drill core (Fig. 1).

The drill core intersected a variety of schists (Fig. 3). The dotted line in figure 3 divides the rocks into two units. In the upper unit, which consists of qtz-chl-talc-carb schist and talc-chl (-carb) schist, Sb was barely detected. However, the carb-talc-qtz schist and talc-chl-carb-qtz schist in the lower unit are considered to be representative for the Antimony Line due to higher contents of Sb up to 1500 ppm. In the main mineralized zone from 128.5 m to 136 m Sb contents up to 8.83 % were detected (Unpublished data - Consolidated Murchison Ltd.). In the upper unit, the drill core exhibits higher Al_2O_3 values than MgO. After a 20 m transition zone from about 90 m to 110 m depth, where Al_2O_3 and MgO show similar values, the ratio changes in the Antimony Line to concentrations of higher MgO and lower Al_2O_3. K_2O contents are fairly high in the upper unit compared to the K_2O contents in the lower unit, where K_2O was barely detected. However, right below the contact of upper and lower unit in the Antimony Line, a small enrichment peak of K_2O was identified.

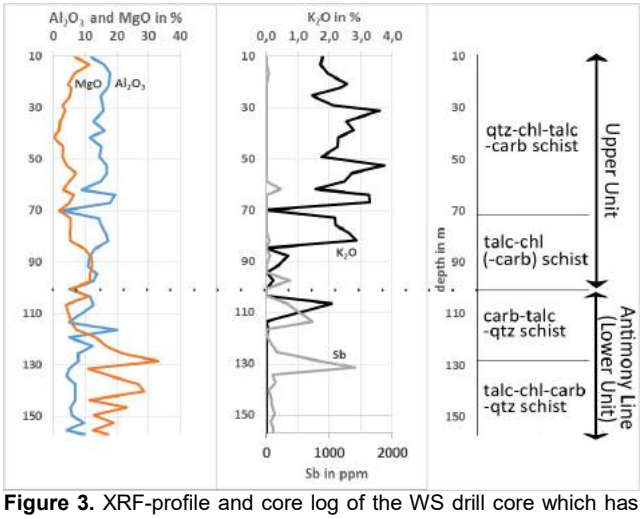

Figure 3. XRF-profile and core log of the WS drill core which has been sampled and analyzed at a 3 m spacing. The left diagram shows the MgO and Al_2O_3, the right diagram shows the K_2O and the Sb distribution. The dotted line signifies a major change in lithology.

4 Discussion

High MgO and low Al_2O_3 contents were observed in the Antimony Line compared to non-Sb-bearing sections. After Pearton (1980) the rocks in the Antimony Line contain 20-36 % of MgO but only 4-6 % of Al_2O_3. This difference is evident in the displayed XRF analyses. Because of high MgO contents, an ultramafic, komatiitic precursor rock is assumed, as previously proposed by several authors (Minnitt 1975; Pearton 1980; Pearton & Viljoen 1986). This assumption is supported by the occurrence of fuchsite indicating high contents of Cr and, therefore, an ultramafic precursor rock.

According to the map of Wilson & Viljoen (1986), the upper unit of the WS drill core should consist of chlorite-quartz schists and phyllites. This study, however, revealed that these sequences are fairly carbonatized and enriched in talc as well.

K_2O was not detected in broad sections of the Antimony Line. Close to the boundary of the sequences both drill cores show a small enrichment of K_2O and Sb which is accompanied by an enrichment of fuchsite in the FS drill core. According to Pearton (1980), a late-stage potassium alteration took place, whereby fuchsite was generated. This indicates that potassium was introduced into the Antimony Line by hydrothermal solutions and would, therefore, have only to a minor extent a primary origin in the host rock.

The variation in MgO and Al_2O_3 contents in three analysis of the FS drill core could indicate a heterogeneous composition of the ultramafic sequence. Komatiitic lava flows exhibit pronounced variation in chemical composition with regards to the position in the lava flow pile (e.g. Arndt 1986). The variation, therefore,

could represent compositional variation in the komatiitic lava flows. It is also possible that mafic to andesitic lava flows are interlayered with the komatiites. The portable XRF data show relative variations of some major and trace elements, but do not provide sufficient accuracy to classify the rocks. Another approach to explain the varying ratio of MgO and Al_2O_3 is intense alteration which led to an enrichment of immobile elements (Al) (MacLean and Kranidiotis 1987).

5 Outlook

The presented data are preliminary results of further quantitative XRF investigations as part of an MSc project. Samples of both drill cores will be analyzed by XRD, ICP-MS, and XRF to obtain reliable data for the zonation in the alteration assemblage. The compositional variation of trace and main elements from proximal to distal alteration zones should contribute to the understanding of the formation of the carbonate alteration in the MGB. Furthermore, petrographic analyses will be conducted in order to examine textural features of the alteration zones and to gather detailed information of mineralogy of the rocks.

Obtained data will be used to set up a mass balance of altered/unaltered rocks and fluid modeling of the mineralizing and altering fluid.

Acknowledgments

Funding by CIMERA at the University of Johannesburg is acknowledged for supporting this project. We also acknowledge support by Vincent Mashoene from Mopani Mine (Stibium Mining South Africa) for access to drill cores and mine sites.

References

Arndt NT (1986) Differentiation of komatiite flows. Journal of Petrology, 27(2):279-301

Blaauwbroek N (2016): Geochemical models of Sb (-As, Au, Ag) mineralization in Archaean and modern hydrothermal settings. PhD thesis, University Bremen

Boocock CN (1984) Ore genesis along the Antimony Line; Murchison Range, North-Eastern Transvaal. M.Sc. thesis, University of the Witwatersrand

Boese R (1964) Die Antimonglanzgänge von Gravelotte in der Murchison Range in Nordost-Transvaal/Südafrika. Dissertation, University Hamburg

Fyon JA, Schwarcz HP, Crocket JH (1984) Carbonatization and gold mineralization in the Timmins area, Abitibi greenstone belt; genetic links with Archean mantle CO 2; degassing and lower crustal granulitization. In Geological Association of Canada Program with Abstracts, Vol. 9, p. 65

Hall AL (1912) The geology of the Murchison Range and District. Mem. Geol. Surv. S. Afr., 6

Hofmann A, Pitcairn I, Wilson A. (2017) Gold mobility during Palaeoarchaean submarine alteration. Earth and Planet. Sci. Lett., 462:47-54

Jaguin J, Boulvais P, Boiron MC, Poujol M, Gapais D, Ruffet G, Briant N (2014) Stable isotopes (O, C) and fluid inclusion study of quartz-carbonate veins from the antimony line, Murchison Greenstone Belt. Amer. Jour. of Sci., 314(7):1140-1170.

Kedda SW (1992) Geochemical and stable isotope studies of gold bearing granitoids in the Murchison Schist Belt, North Eastern Transvaal. Dissertation. University of the Witwatersrand, Johannesburg

MacLean WH, Kranidiotis P (1987) Immobile elements as monitors of mass transfer in hydrothermal alteration; Phelps Dodge massive sulfide deposit, Matagami, Quebec. Econ. Geol., 82(4):951-962

Mendelssohn E (1938) Gold deposits of the Central Murchison Range, Transvaal. Trans. Geol. Soc. S. Afr., 41:249-272

Minnitt RCA (1975) The Geology of the geology of the eastern portion if the Murchison Range between the Quagga camp area and the Kruger National Park. Dissertation, University of the Witwatersrand

Muff, R (1978) The antimony deposits in the Murchison Range of the northeastern Transvaal, Republic of South Africa, 16, Monogr. Ser. on Mine. Depos. Gebrüder Borntraeger, Berlin

Muff R, Saager R (1979) Metallogenic interpretations from a mineragraphic and geostatistic study of antimony ores of the Murchison greenstone belt, South Africa. Special Publication, Geol. Soc. of South Afr., 5:167-179

Pearton TN (1980) The Geochemistry of the Carbonate and Related Rocks of the Antimony Line, Murchison Greenstone Belt: With Particular Reference to Their Genesis and the Origin of Stibnite Mineralization. Dissertation, University of the Witwatersrand

Pearton TN, Viljoen MJ (1986) Antimony mineralization in the Murchison greenstone belt-an overview. Miner. Depos. of Southern Afr., 1:293-320

Poujol M, Robb LJ, Respaut JP, Anhaeusser CR (1996) 3.07-2.97 Ga greenstone belt formation in the northeastern Kaapvaal Craton; implications for the origin of the Witwatersrand Basin. Econ. Geol., 91(8):1455-1461

Schwarz-Schampera U, Terblanche H, Oberthür T (2010) Volcanic-hosted massive sulfide deposits in the Murchison greenstone belt, South Africa. Miner Deposita, 45(2):113-145

Van Eeden OR, Partridge FC, Kent LE, Brandt JW (1939) The mineral deposits of the Murchison Range, east of Leydsdorp. Mem. Geol. Surv. S. Afr., 36

Vearncombe JR (1988) Structure and metamorphism of the Archean Murchison Belt, Kaapvaal Craton, South Africa. Tectonics, Vol. 7(4):761–774

Vearncombe JR, Barton JM, Cheshire PE, De Beer JH, Stettler EH, Brandl G (1992) Geology, geophysics and mineralisation of the Murchison schist belt, Rooiwater Complex and surrounding granitoids (Vol. 81). Dept. of Mineral and Energy Affairs, Geological Survey

Willson C, Viljoen MJ (1986) The Athens Antimony ore body, Murchison Greenstone Belt. In Anhaeusser CR, Maske S, (ed) Mineral Deposits of Southern Africa: Johannesburg, South Africa, Geol. Soc. of South Afr., p. 333–338

Ore mineralogy, trace element distribution and 3D X-ray tomography of the polymetallic sulphide deposits at Mavres Petres and Piavitsa, Greece

Karin Högdahl[1], Erik Jonsson[1,2], Samuel Roško[1], Adam Włodek[3], Thomas Zack[4], Eric Landström[5], Edward P. Lynch[2], Fredrik Sahlström[1], Pavlos Tsitsanis[6], Vaggelis Bacalis
[1]Department of Earth Sciences, Uppsala University, Uppsala, Sweden
[2]Department of Mineral Resources, Geological Survey of Sweden, Uppsala, Sweden
[3]AGH University of Science and Technology, Kraków, Poland
[4]Department of Earth Sciences, University of Gothenburg, Gothenburg, Sweden
[5]Orexplore AB, Kista, Sweden
[6]Hellas Gold, Chaldiki, Greece

Abstract: The Mavres Petres mine, operated by Hellas Gold, and the Piavitsa prospect are both located along the Stratoni fault in the Kassandra mining district, northern Greece. These Tertiary deposits are brecciated, carbonate replacement Pb-Zn-Ag-(Au) mineralisations and the Piavitsa deposit is also associated with Au-rich epithermal veins. Both mineralisations were variably overprinted by later fluids as well as ductile and brittle deformation affecting ore mineralogy and trace element distribution. Galena is the main Ag-carrier, contains significant concentrations of Sb and Bi and is locally associated with a suite of Sb-As-Bi phases. Sphalerite is either massive or occurs as a later cockade-textured type. Both varieties are variably enriched in Mn and can exhibit elevated concentrations of In and Ga. In Piavitsa, alabandite is present as small euhedral crystals or in veins in fractured sphalerite. Pyrite is ubiquitous and is either present as disseminations, massive to skeletal aggregates or as a matrix in breccias. It is often arsenic-bearing and even more so towards the later stages. Arsenopyrite appears to be a late phase and occurs interstitial to pyrite and as euhedral crystals. While both arsenopyrite and arsenian pyrite can be enriched in Au, As-minerals are not necessarily associated with Au.

1 Introduction

The Mavres Petres Pb-Zn-Ag-(Au) deposit and the Au-Ag-Pb-Zn prospect at Piavitsa in the Kassandra mining district in northern Greece are included in the on-going H2020 X-Mine project as pilot-scale demonstrators for testing novel sensor technologies. One of the aims of the X-Mine project is to improve the efficiency and sustainability of mineral exploration and mining operations by applying X-Ray Fluorescence (XRF), X-Ray Transmission (XRT) on-site scanning for better and faster characterisation of the ore. In order to improve and further develop the sensor technology the ore mineral assemblages are being investigated by means of ore and electron microscopy, electron microprobe (EMP) and laser ablation inductive coupled plasma mass spectrometry (LA-ICP-MS) analyses.

2 Geological setting

The mineral deposits in the Kassandra mining district in northern Greece are hosted by the Serbo-Macedonian and Rhodope terranes (Figs. 1 and 2). In this area mining activities date back thousands of years, and both exploration and production of base and precious metals are still on-going (e.g. Voudouris et al. 2017).

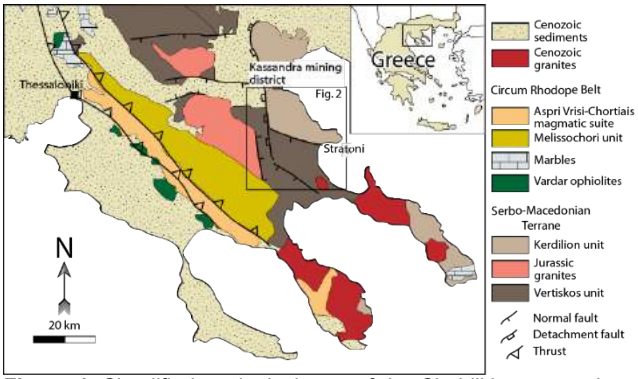

Figure 1. Simplified geological map of the Chaldiki area, northern Greece. The Mavres Petres and Piavitsa deposits are located along the Stratoni fault in the Kassandra mining district (modified after Melfos and Voudouris 2017 and Siron et al. 2018).

The Serbo-Macedonian and Rhodope terranes are continental fragments accreted to the Eurasian margin during the Hellenic orogeny (Pe-Piper and Piper 2006). In the Kassandra mining district (Fig. 2) the mineralisations occur in the Kerdilion and the Vertiskos units within the Serbo-Macedonian Terrane. The Kerdilion unit encompasses a Permo-Carboniferous magmatic arc and Paleotethyan carbonates that are juxtaposed with the Ordovician to Silurian gneisses and leucogranites of the Vertiskos unit (Siron et al. 2018). Accretion of this unit in the Late Cretaceous caused thrust faults and metamorphism that reached greenschist to amphibolite facies (Kydonakis et al. 2016). Amphibolite facies metamorphism in the Kerdilion unit occurred in middle Eocene, later to be overprinted by retrogression into greenschist facies.

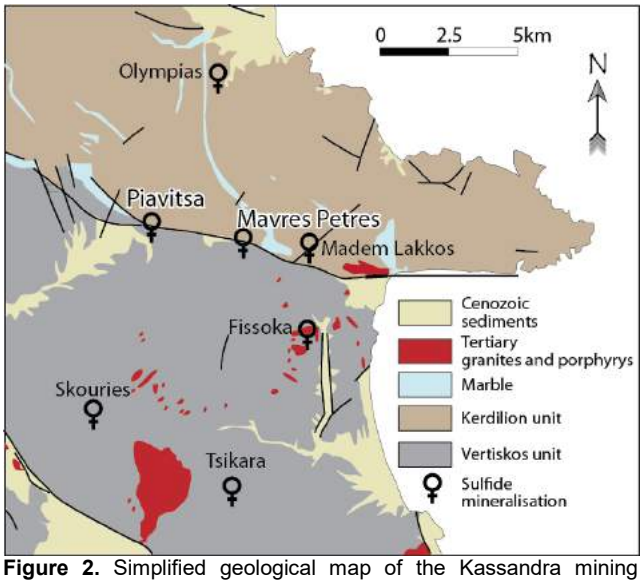

Figure 2. Simplified geological map of the Kassandra mining district. Cu-Au porphyry deposits occur at Skouries, Fissoka and Tsikara, while manto-type carbonate replacement deposits are represented by the Ag-Pb-Zn mineralisations at Mavres Petres, Madem Lakkos, the Au-Ag-Pb-Zn Olympias deposit and the Piavitsa prospect, which is also associated with Au-rich veins.

Mineralisation in both the Vertiskos and the Kerdilion units occur in shear zones and faults and are associated with intrusions that are present along a NE trending corridor (Fig. 2). These intrusions were formed during two pulses of post-collisional magmatism in a back arc extensional setting in the Oligocene and Miocene, respectively (e.g. Siron et al. 2018). The shear zones and faults were either initiated or reactivated during extensional tectonics that commenced in the middle Eocene and continued into the Neogene. Many of the mineralisations are interpreted to be related to shear zones, detachment faults and subsequent magma intrusions (Voudouris et al. 2017). In the Kassandra mining district, the most important mineralisation types include Cu-Au porphyry deposits (Skouries, Fissoka, Tsikara), skarn and manto-type carbonate replacement mineralisations (Mavres Petres, Madem Lakkos, Olympias, Piavitsa) and overprinted epithermal deposits (Piavitsa) (Melfos and Voudouris 2017, and references therein).

2.1 Mavres Petres

The Mavres Petres Pb-Zn-Ag carbonate replacement deposit is located along the southward-dipping Stratoni fault (Fig. 2). The present underground mine is operated by Hellas Gold and contain measured and indicated resources of 0.58 Mt at 161 g/t Ag, 6.2 % Pb and 8.3 % Zn (Eldorado Gold Corporation 2018). The ore body is hosted in a marble lens within the Kerdilia unit at the boundary to the Vertiskos unit. The marble lens is fault-bounded and entrained within a strongly carbonaceous part of the fault (Siron et al. 2018).

The mineralisation was formed during two stages (Melfos and Voudouris 2017). During the first stage hydrothermal fluids utilised a permeable network caused by fault intersection, fault bifurcations and strain variations between imbricated marble lenses (Siron et al. 2018), which resulted in a massive sulphide replacement mineralisation (Melfos and Voudouris 2017). This is dominated by galena and sphalerite with lesser amounts of pyrite and arsenopyrite. During a second stage the mineralisation was sheared and brecciated and overprinted by later fluids that led to, among others, pyrite disseminations. Pyrite also comprises the matrix to brecciated ore and gangue.

2.2 Piavitsa

The Piavitsa prospect is located c. 5 km from Mavres Petres further to the west along the Stratoni Fault (Fig. 2). It is a siliceous-manganese carbonate replacement mineralisation associated with epithermal Au-rich veins (Siron et al. 2016) that was historically explored and mined from the surface for manganese. It has an estimated resource of 10.54 Mt at 57 g/t Ag and 5.7 g/t Au (Eldorado Gold Corporation 2018). Similar to the Mavres Petres deposit, it is largely controlled by the Stratoni Fault and massive sulphide mineralisation is located both within the fault as well as in the footwall, replacing the marble under the overlying hanging wall amphibolite. The mineralisation occurs mainly as brecciated, massive to semi-massive sulphide lenses affected by a later hydrothermal brecciation with clasts of altered marble and sulphide as well as epithermal quartz-kutnahorite/rhodochrosite-gold veins (Siron et al. 2016; Melfos and Voudouris 2017).

3 Mineralogy

The ore mineral assemblages at Mavres Petres and Piavitsa are being investigated by optical reflected light and electron microscopy, EDS and WDS X-ray spectroscopy, LA-ICP-MS and Geocore X10 drill core scanning developed by Orexplore in Kista, Sweden. The characterisation of the ore mineralogy will be used in further development of the GeoCore X10 in addition to assess the critical metal potential of these deposits.

The GeoCore 10X uses a novel technique by combining XRT and XRF measurements, together with automatic weight measurements to scan drill core with a diameter of up to 50.6 mm. The generated 3D-tomographical visualisations display the distribution of minerals with contrasting density in the cores with a resolution of down to 200 μm (Fig. 3). Using Orexplore software the tomography scan can be rotated in three directions whereby various textures and structures can be highlighted. The XRF measurements give concentrations for most elements heavier than S with a resolution of between 10 and 100 ppm.

3.1 Ore mineralogy, textures and trace element distribution at Mavres Petres

At Mavres Petres galena occurs together with sphalerite and pyrite and is mainly present as rather coarse-grained, locally highly strained aggregates. It is also observed as irregular inclusions in the former two

phases. It is variably

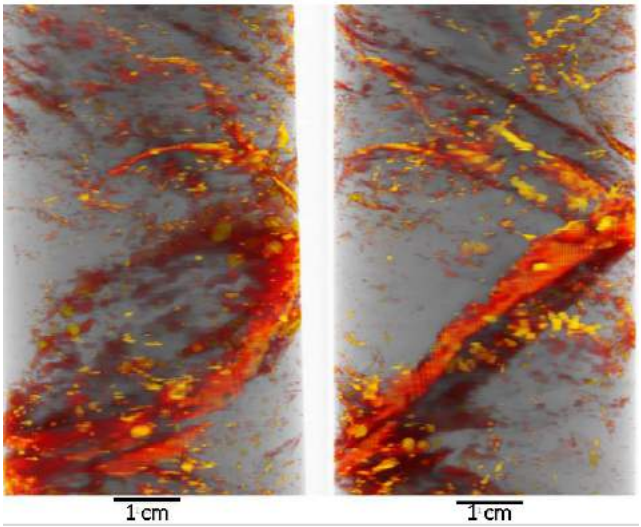

Figure 3. XRT-XRF scans of a drill core section from Mavres Petres imaged by GeoCore X10. Red colours indicate Pb and Zn enrichments corresponding to galena and sphalerite, and yellow colours show Fe enrichments corresponding to pyrite and arsenopyrite. Lead shields the X-rays efficiently from penetrating the core and causes the galena-bearing vein to appear transparent.

Ag-enriched (100-2000 ppm) and the Ag content appears to be higher in outer parts of unstrained crystals. When Bi is present is has a negative correlation with Sb, of which the latter may reach 2000 ppm. Selenium has only been detected in a few of the analysed galenas, featuring concentrations up to 3500 ppm. In some grains the Zn content is rather high (3.5 wt.%) accompanied by increased contents of Cd (up to 640 ppm).

There are at least two generations of sphalerite. The first generation is massive, coarse-grained and occurs together with massive galena and pyrite. These phases are also common as inclusions along with numerous micro-inclusions of chalcopyrite ("chalcopyrite disease"). This sphalerite generation is invariably brecciated and intermittently overgrown by a second generation of euhedral to subhedral crystals exhibiting cockade texture and oscillatory growth zoning (Fig. 4a).

The Fe concentration in both sphalerite generations ranges between 5 and 10 wt.%, they are Mn-bearing (6000-8000 ppm), have Cd contents of c. 3000 ppm and Ga concentrations typically around 20 ppm, reaching 75 ppm locally. Both generations are also variably enriched in In ranging from a few ppm up to 155 ppm even within the same grain.

Pyrite is either massive, present as small inclusions in sphalerite and galena or occurs as disseminated subhedral to euhedral crystals. The massive pyrite is typically less than 1 mm in grain size and occurs in the matrix of brecciated sphalerite and galena and the disseminated pyrite is up to several centimeters in size.Pyrites of both types are characteristically zoned and occur together with the less abundant arsenopyrite. The zoning reflects an increasing As content towards the margins of the grains (Fig. 4b). This As-zoned pyrite is locally overgrowing an earlier stage of As-poor pyrite. It is also common that As-rich, platy-shaped pyrite is succeeded by free-growing, comb textured arsenopyrite.

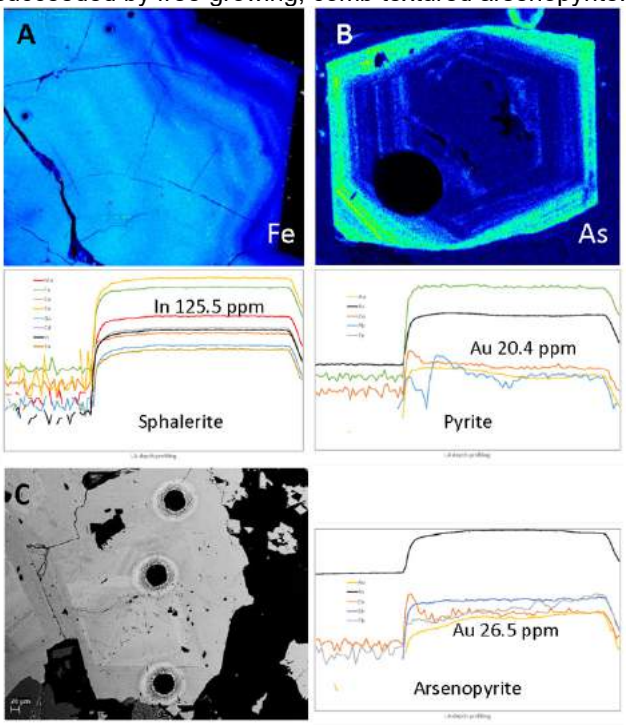

Figure 4. Element maps, BSE image and LA-ICP-MS plots. **a.** Iron map of an oscillatory zoned second generation sphalerite. The LA-ICP-MS depth profile is smooth and shows enrichments in Mn, Cd, In, Cu, Ga and Sn. Indium in this sphalerite reaches 125 ppm. **b.** Arsenic map of an oscillatory zoned pyrite with high As contents at the margin of the crystal. The LA-ICP-MS data displays elevated concentration of Cu, Pb and Au. The Au content is 20 ppm and the smooth depth profile show that it is lattice-bound. **c.** BSE image of a compositionally zoned arsenopyrite. The LA-ICP-MS data shows that the zoning is related to variations in Cu, Sb and Pb contents. The smooth depth profile for Au implies that it is lattice-bound. Dark, round spots in the crystals are the LA-ICP-MS pits.

In the disseminated pyrite, the increase in As covaries with Au, from a few ppm in the cores of the crystals, up to about 20 ppm Au in As-rich rims. However, early-formed slightly As-enriched pyrite appears to be barren in Au.

Arsenopyrite is a late phase that occurs interstitial between pyrite grains, projecting into open cavities, or as euhedral sub-millimeter sized crystals in the host-rock. Gold is heterogeneously distributed in it and in general ranges between 3 and 25 ppm although concentrations of up to 135 ppm Au have been measured. The Sb concentration is between 200-2000 ppm and there are traces of Co (2-15 ppm), Cu (2-40 ppm, Ag (2-35 ppm) and Te (2-18 ppm).

LA-ICP-MS analyses of both pyrite and arsenopyrite typically exhibit smooth down-hole profiles indicating that Au is lattice-bound in both these phases.

In a sphalerite-rich part of the ore, argentian tetrahedrite has been observed as inclusions in galena in addition to various Pb-Sb-Bi-Ag-(As) phases that likely represent solid solutions between galena-stibnite-matildite components (cf. George et al. 2015).

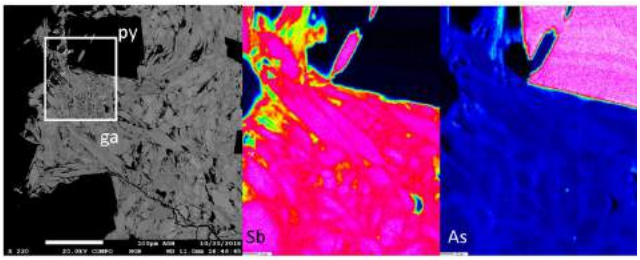

Figure 5. BSE image and element maps of a deformed galena and associated euhedral, compositionally zoned arsenian pyrite. In the galena Sb and As are heterogeneously distributed as shown by the element maps (Sb and As). py – pyrite, ga – galena.

3.2 Ore mineralogy, textures and trace element distribution in the carbonate replacement ore at Piavitsa

The main ore mineral assemblage studied is represented by an assemblage of sphalerite, pyrite, arsenopyrite, galena and alabandite in a matrix dominated by carbonates. Isolated galena grains are corroded, often fractured and rimmed by reaction zones, potentially consisting of cerussite, towards the host carbonates (Fig. 6). Analysed grains have Ag contents of about 2000 ppm and inclusions of Pb-Sb-Ag-As-phases are common. The sphalerite is also corroded and typically contains fractures that are filled with carbonates. Micro-inclusions of chalcopyrite occur sporadically. Pyrite is sub- to euhedral and is often rich in inclusions of galena and sphalerite. Alabandite occurs mainly in the carbonate, often as small, euhedral to subhedral crystals (Fig. 6), and is also present in the sphalerite-hosted fractures. Arsenopyrite is mainly present in late veins, often together with pyrite and galena.

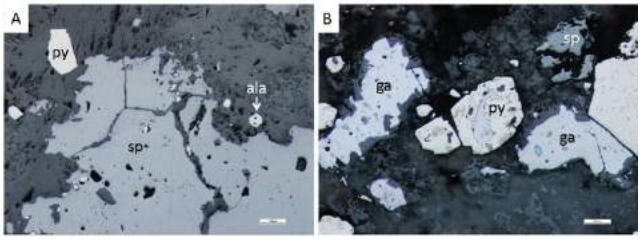

Figure 6. BSE images of the manto-type ore at Piavitsa. **a.** Corroded sphalerite and subhedral pyrite with small euhedral alabandite in a carbonate-silicate matrix. **b.** Corroded galena with a reaction rim (possibly cerussite), euhedral to subhedral pyrite with galena inclusions and corroded sphalerite in a carbonate matrix. py – pyrite, sp – sphalerite, ala – alabandite, ga – galena.

4 Summary

A combination of optical and electron microscopy, EDS and LA-ICP-MS analyses have been used to characterise the ore, and the host and distribution of important trace elements in the Mavres Petres and Piavitsa deposits. The results will be used to further improve the development of the GeoCore X10 technology and its application in mineral exploration.

The present observations show that sphalerite from the Mavres Petres deposit is variably enriched in In, hosted by two generations of sphalerite that are also modestly enriched in Ga. Galena is not only the main Ag-host but also carries Sb and Bi in locally considerable concentrations. These trace elements are heterogeneously distributed and exsolution of sulfosalts is rather common. Gold occurs lattice-bound in arsenopyrite and at the rims of compositionally zoned arsenian pyrite. Early formed pyrite appears to be Au-poor. Gold is always associated with As, but As is not necessarily associated with Au.

Galena and sphalerite in the carbonate replacement ore at Piavitsa prospect are corroded, which is likely to be a result of fluids that formed the later epithermal Au-enriched vein mineralisation. Disseminated, inclusion-rich pyrite and small euhedral alabandite post-date the main ore-forming stage.

Acknowledgement

The X-Mine project is funded by the European Union's Horizon 2020 research and innovation programme under grant agreement No 73027.

References

Eldorado Gold Corporation, 2018. Reserves as of September 30, 2018 www.eldorado-gold.com/assets/resources-and-reserves/

George L, Cook NJ, Ciobanu CL, Wade BP (2015) Trace and minor element in galena: A reconnaissance LA-ICP-MS study. Am. Min. 100:548-569.

Melfos M, Voudouris P (2017) Cenozoic metallogeny of Greece and potential for precious, critical and rare metal exploration. Ore Geol. Rev. 89:1030-1057.

Kydonakis K, Brun JP, Poujol M, Monié P, Chatzitheodoridis, E, (2016) Inferences on the Mesozoic evolution in the North Aegean from the isotopic record of the Chaldiki block. Tectonophysics 682:137-144.

Pe-Piper G, Piper DJW (2006) Unique features of the Cenozoic igneous rocks of Greece. Geol. Soc. Am. Spec. Pap. 409:259-281

Siron CR, Thompson JFH, Baker T, Friedman R, Tsisanis P, Russell SV, Randall SB, Mortensen JK (2016) Magmatic and metallogenetic framework of Au-Cu porphyry and polymetallic carbonate-hosted replacement deposits of the Kassandra mining distric, Northern Greence.Soc. Econ. Geol. Spec. Publ. 19:29-55.

Siron CR, Rhys D, Thompson JFH, Veligrakis T, Camacho A, Dalampiras L (2018) Structural control on porphyry Au-Cu and Au-rich polymetallic carbonated-hosted depositis of the Kassandra mining district, Northern Greece. Econ. Geol. 113:309-345.

Voudouris P, Tarantola A, Melfos V (2017) Field guide to the Tertiary hydrothermal ore deposits of northern Greece, 8-15 April 2017 54 pp.

Diversity of Devonian Lahn-Dill-type iron ores from the Rhenish massif, Germany: evidence from petrography and geochemistry

Leanne Schmitt[1,2], Thomas Kirnbauer[1], Thomas Angerer[3], Sabine Klein[4,2]
[1]Faculty of Geo-Resources and Process Engineering, Department of Economic Geology, TH Georg Agricola, Bochum, Germany
[2]Institute of Geology, Mineralogy and Geophysics, Ruhr-Universität Bochum, Germany
[3]Institute of Mineralogy and Petrography, University of Innsbruck, Austria
[4]German Mining Museum, Bochum, Germany

Abstract. Deposition of the Lahn-Dill-type iron ores took place during the Devonian in a marine environment with mineralisation being related to volcanic and volcaniclastic rocks.

Field work and petrographical studies reveal different depositional environments for Lahn-Dill-type iron ores that took place either in basinal sediments or reef carbonates. Also, modes of mineralization are diverse: Shrinking textures in jasper-like hematite assemblages indicate synsedimentary (or early diagenetic) formation, while replacement textures of carbonates by hematite in limestone are evidence for metasomatic mineralisation.

Geochemical analyses of Lahn-Dill-type iron ores yield a significant volcanogenic component (transition metals, HFSE, Eu anomaly) as well as a (Devonian) seawater REE+Y signature. Few differences between REE+Y of Lahn-Dill ores and youngest iron formation (e.g. Red sea, Neoproterozoic and Cambrian iron ores) is apparent regarding LREE depletion, anomalies in La, Eu and Y and lack of pronounced negative Ce anomaly.

1 Introduction

Stratiform mineralisation in submarine settings represents one of the most important sources for iron (Bekker et al. 2010). These iron ores are widely used as proxies for local to global marine depositional environments, despite the fact that deposits often experienced extensive tectonometamorphic overprint, hydrothermal alteration or weathering (Bekker et al. 2010, and references therein).

Stratiform iron ores of the Lahn-Dill-type sensu stricto are a peculiar deposit type: these ores are exclusively associated with Middle Devonian to Lower Carboniferous submarine basaltic volcanism (Quade 1968), without showing any link to massive sulfide occurrences. Ore layers can reach thicknesses up to several meters and lateral extensions of several hundreds of meters (Lippert and Flick 1998). Typically, siliceous or carbonate-rich, these oxide ores have variable iron grades which in places reach up to 60 wt.% Fe, arguably representing the most enriched iron accumulations in any sedimentary setting (Quade 1976).

In these ores, early (primary or diagenetic) textures are preserved related to a generally low metamorphic overprint reaching only lower greenschist facies (Massonne 1995). Thus, these rocks may provide the possibility to decipher modes of iron oxide (trans-) formation. Understanding these ores will yield insight into precipitation and diagenetic regimes with regard to the interplay of marine, volcanic, microbial and hydrothermal processes in the Devonian and Carboniferous marine basins.

Numerous genetic models for the Lahn-Dill-type iron ores have been proposed during the past 140 years, though, a systematic approach using advanced analytical methods does not exist currently.

Here, we present field, petrographical and geochemical data from hematite ores located within the Lahn-Dill area in western Germany.

2 Geological setting and stratigraphy

Lahn-Dill-type iron ores were deposited within the Rhenohercynian Ocean along the southern shelf of the Old Red Continent (Königshof et al. 2010). Footwall rocks consist of mafic volcanic and volcaniclastic rocks, geochemically corresponding with alkali basalts (Nesbor et al. 1993). These mafic rocks are part of an extensive submarine volcanic event at the Middle to Upper Devonian boundary (Givet-Adorf phase), which occasionally reached sea level facilitating reef development (Nesbor et al. 1993). In basinal settings, clastic sediments were deposited on top of the volcanic and volcaniclastic rocks.

The orebodies are located at four different positions (Position I–IV) within the volcano-sedimentary sequence: (I) concordantly intercalated with Middle Devonian volcanic and volcaniclastic rocks (Lippert 1997); (II) at the top of the volcanic and volcaniclastic rocks with hanging wall rocks either being composed of reef carbonates or clastic sediments (Lippert 1997); (III) as layers within the Upper Devonian clastic sediments (Lippert 1997) or as resediment ores in local subbasins (Rösler 1962); (IV) as layers and lenses overlying tholeiitic volcanic rocks that were emplaced during a Lower Carboniferous volcanic phase (Hein 1998). Because Position II iron ore represents the main mineralisation regarding extent, grade and abundance, it will be the focus of this study.

3 Ore type classification

Field observations, optical microscopy, SEM and XRD analyses reveal that Lahn-Dill-type iron ores are mainly composed of hematite (locally magnetite) that forms assemblages with either quartz (siliceous iron ores "kieselige Roteisenerze") or carbonates including calcite, siderite and ankerite (carbonatic iron ores "Flusseisensteine"). Minor components are pyrite, Fe-Mg chlorite, greenalite and bitumen. According to Quade (1976) dolomite and stilpnomelane occur rarely.

3.1 Siliceous iron ores

Siliceous ores are subdivided into hematite- and jasper-rich ores. These subtypes differ with regard to occurring mineral assemblage and textures.

Jasper-rich ores show nano-scale hematite needles that form dense accumulations appearing as masses. These masses form schlieren and clasts. Nests of hematite blades are also present. Furthermore, a distinct hematite-quartz assemblage is present where nano-scale hematite occurs as homogeneously distributed needles within quartz. The hematite-quartz dispersions range in Fe from 5 to 45 % and form schlieren, spherulites and clasts. Another assemblage is jasper-like quartz with <5 % Fe forming clasts, veinlets and schlieren.

Hematite-rich ores consist dominantly of nano-scale hematite needles that form dense accumulations appearing as masses. Quartz is a minor component.

3.2 Carbonatic iron ores

Carbonatic iron ores are subdivided into carbonate/quartz- and hematite-rich ores. These subtypes differ not only in assemblage and texture, but also in temporal relationship.

Carbonate/quartz-rich ores show microscopic textures where hematite occurs as masses forming schlieren, as blades distributed homogenously across the sample, or locally as radial fibres. In this subtype quartz is present.

In contrast, hematite-rich ores are hosted within limestone, where the ore has replaced reef carbonates metasomatically. In these replacement ores, hematite is present as blades which can form masses, around calcite grains, fills cracks and fissures. Macro- (Fig. 1) and microfossils are completely or partly replaced by hematite.

4 Whole-rock geochemistry

We present unpublished whole rock and trace element analysis of 27 and REE analysis of 16 iron ore samples (by H.D. Nesbor and H. Quade; data from the 1990s). Thirteen samples are from selected exploration drill cores located in the eastern Dill-syncline, and 14 samples from the Fortuna mine (northern Lahn-syncline) representing a vertical profile of an ore layer (8 m thickness).

Figure 1. Brachiopod *Stringocephalus burtini* from Christiane mine (Adorf, Sauerland) replaced by hematite.

4.1 Major elements

Siliceous iron ores show Fe contents of 22 to 62 wt.%, and 1 to 31 wt.% Si. They show average Al content of 1.2 wt.% and 0.5 wt.% Mg, locally reaching up to 4 wt.% Al and 1.3 wt.% Mg implying the occurrence of chlorites from the chamosite-clinochlore series. Titanium averages 0.15 wt.%. Manganese shows an average of 0.7 wt.% as well as a positive correlation with Fe.

Carbonatic iron ores with more than 10 wt.% Ca and 3 – 13 wt.% Si show Fe contents varying from 20 to 39 wt.% Fe. Aluminum and Ti show higher average values than siliceous ores with 2 wt.% and 0.2 wt.%, respectively. Magnesium averages 0.4 wt.% and Mn 0.03 wt.%.

Iron and Ca show a distinct vertical variation within the Fortuna-profile. The Fe/Ca ratio decreases towards the top.

4.2 Trace elements

Lahn-Dill iron ores are rich in trace elements with respect to V, Cr, Ni and Zr compared with various chemical iron formations. Recent iron-rich sediments show a comparable trace element enrichment as the Lahn-Dill ores.

Lahn-Dill-type iron ores show V values that average 256 ppm. Chromium shows average values of 91 ppm, and Ni of 125 ppm which is in good agreement with average values of mined ores (Doutch 1977). Zirconium content can be as low as 7 ppm but reaches up to 240 ppm in samples. Strontium averages 81 ppm.

Within Lahn-Dill ores a negative Si correlation with V, Ni, Zr and Sr is present. Iron shows positive correlations with Sr and Ba.

4.3 Rare earth elements

The Lahn-Dill samples reveal quite uniform REE fractionation patterns (Fig. 2A). They all show minor LREE depletion and rather flat HREE (PAAS-normalized). A number of samples have a positive La, Eu and Y anomaly, and in some samples a weak negative Ce anomaly may be present. Carbonatic and siliceous iron ore both show similar patterns.

REE appear to be largely tied to a detrital or volcanogenic component (positive correlation of ∑REE with Al, Ti, Zr). Additionally, a positive correlation with P is present evidence for a local relation of REE with apatite.

5 Discussion

5.1 Syn- versus epigenetic depositional environment

Deposition of the Lahn-Dill iron ores took place in an open marine setting with a large seafloor relief due to extensive volcanism (Nesbor et al. 1993). In environments where volcanic rises reached sea level and reef development was facilitated, carbonates overly volcanic and volcaniclastic rocks (Königshof et al. 2010). Here, hematite mineralisation occurs heterogeneously within limestone and replacement of calcite by hematite took place indicating metasomatic processes.

Contrastingly, hematite mineralisation also occurs in basinal settings where clastic sediments represent the hanging wall (Lippert 1997). In these ores relative timing of hematite microtextures is ambiguous. Observed shrinking structures in jasper-like textures are indicative of sedimentary or early diagenetic formation. Thus, this hematite and quartz assemblage may have been precipitated from a syngenetic Fe- and Si-rich gel (Cissarz 1924). Furthermore, in hanging wall rocks younger resedimented ores occur and are composed of hematite-rich clasts providing evidence for syngenetic deposition as well.

In both mineralisation settings, however, well crystallised hematite textures may be products of prograde ripening or fluid-aided redistribution during late diagenesis or very low-grade metamorphism.

5.2 Geochemical comparison with other submarine iron ores

Lahn-Dill-type iron ore are rich in trace elements, though showing slightly lower values compared to their footwall rocks (c.f. Doutch 1977).

Lahn-Dill ore samples all show similar REE+Y patterns (Fig. 2A) with fractionation resembling its footwall rocks (Fig. 2B) indicating a strong volcanogenic component. Hanging wall rocks show a HREE depletion not typical for a marine environment.

Positive Eu anomalies in ores are either related to high temperature hydrothermal fluids (Bau and Dulski 1999) or inherited from volcanogenic components.

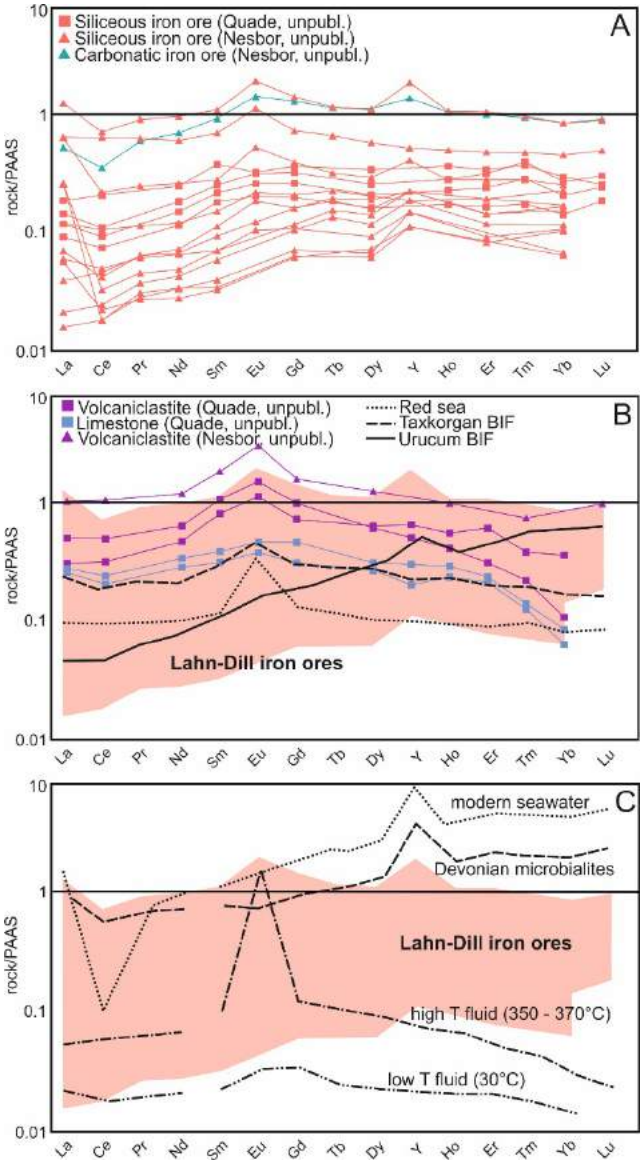

Figure 2. REE+Y PAAS-normalized (McLennan 1989), see a, b and c for legend. a. Lahn-Dill-type siliceous and carbonatic iron ores. b. Comparison of Lahn-Dill ores (pink background) with hanging- and footwall rocks and corresponding data from Red sea sediments (Laurila et al. 2014), Taxkorgan BIF (Li et al. 2018) and Urucum BIF (Angerer et al. 2016). c. Comparison of Lahn-Dill ores (pink background) with corresponding data from modern sea water, Devonian microbialites, high T fluids and low T fluids (Angerer et al. 2016, and references therein). To ease comparison, all normalized fluid data are multiplied to fit into shown data range.

Lahn-Dill ores show a comparable fractionation pattern with Devonian microbialites (LREE depletion, La- and Y anomalies) evidence for a seawater signature (Nothdurft et al. 2004). However, a small negative Ce anomaly within Lahn-Dill ores may indicate a non-oxidized marine environment (c.f. Alibo and Nozaki 1999). Rare earth elements in Lahn-Dill ores show similarities to iron oxide muds from the Red sea (Laurila et al. 2014), to Cambrian “Algoma-type” BIF (Li et al. 2018), and to Neoproterozoic Rapitan-type BIF (Angerer et al. 2016; compare Fig. 2B). Red sea metalliferous deposits are interpreted to have formed due to hydrothermal venting,

a lack of negative Ce anomalies indicating brine composition without seawater mixing (Laurila et al. 2014). Rapitan-type BIF as well as Cambrian "Algoma-type" BIF are assumed to have formed in ferruginous marine subbasins under anoxic conditions (Angerer et al. 2016; Li et al. 2018). These chemical iron sediments are interpreted to have formed under different conditions, nevertheless similarities in their REE+Y fractionation patterns exists.

6 Conclusion

Lahn-Dill-type iron ores represent a peculiar deposit type regarding their depositional environment as well as their geochemical composition.

Two distinct processes are involved in the formation of these iron ores. They show features characteristic for a synsedimentary formation as well as for mineralisation related to metasomatic replacement in reef carbonates, thus being related to epigenetic processes.

Lahn-Dill iron ores show REE+Y patterns indicating a strong volcanogenic component as well as a seawater signature. However, a distinct negative Ce anomaly is absent suggesting a marine environment that may not have been oxidizing. Comparison with recent iron ore deposits, Cambrian and Neoproterozoic BIF show patterns with some resemblances.

A minor heterogeneity between the two sets of data (c.f. Nesbor and Quade data) is present regarding Eu anomalies highlighting the importance of new data.

Acknowledgements

We would like to thank Heinz-Dieter Nesbor (HLNUG, Wiesbaden) and Horst Quade† (TU Clausthal) for providing geochemical data. We would also like to say thank you to Jan Sessing from the Deutsches Bergbau Museum, Bochum, for analytical support.

References

Alibo DS, Nozaki Y (1999) Rare earth elements in seawater: particle association, shale-normalization, and Ce oxidation. Geochim Cosmochim Acta 63:363-372.

Angerer T, Hagemann SG, Walde DHG, Halverson GP, Boyce AJ (2016) Multiple metal sources in the glaciomarine facies of the Neoproterozoic Jacadigo iron formation in the "Santa Cruz deposit", Corumbá, Brazil. Precambrian Res 275:369–393. doi: 10.1016/j.precamres.2016.01.002.

Bau M, Dulski P (1999) Comparing yttrium and rare earths in hydrothermal fluids from the Mid-Atlantic Ridge: implications for Y and REE behavior during near-vent mixing and for the Y/Ho ratio of Proterozoic seawater. Chem Geol 155:77-90.

Bekker A, Slack JF, Planavsky N, Krapez B, Hofmann A, Konhauser KO, Rouxel O J, (2010) Iron Formation: The Sedimentary Product of a Complex Interplay among Mantle, Tectonic, Oceanic, and Biospheric Processes. Econ Geol 105 (3): 467–508. doi: 10.2113/gsecongeo.105.3.467.

Cissarz A (1924) Mineralogisch-mikroskopische Untersuchungen der Erze und Nebengestein des Roteisensteinlagers der Grube Maria bei Braunfels an der Lahn. Mitt Kaiser-Wilhelm-Inst Eisenforsch 5:109–125.

Doutch S (1977) Die Eisenerzlagerstätte Falkenstein, Lahn-Dill-Gebiet. Dissertation, RWTH Aachen University.

Hein, UF (1998) Eisenkiesel des Unterkarbons. In: Kirnbauer T (ed) Geologie und hydrothermale Mineralisationen im rechtsrheinischen Schiefergebirge, 1st edn. Nassau Ver Naturkd, Wiesbaden, pp 129-131.

Königshof P, Nesbor HD, Flick H (2010) Volcanism and reef development in the Devonian: A case study from the Lahn syncline, Rheinisches Schiefergebirge (Germany). Gondwana Res 17 (2-3): 264–280. doi: 10.1016/j.gr.2009.09.006.

Laurila TE, Hannington MD, Peterson S, Garbe-Schönberg D (2014) Early depositional history of metalliferous sediments in the Atlantis II Deep of the Red Sea: Evidence from rare earth element geochemistry. Geochim Cosmochi Acta 126:146-168.

Li ZQ, Zhang LC, Xue CJ, Zheng MT, Zhu MT, Robbins LJ, Slack JF, Planavsky NJ, Konhauser KO (2018) Earth's youngest banded iron formation implies ferruginous conditions in the Early Cambrian ocean. Sci Rep 8:1-10. doi:10.1038/s41598-018-28187-2.

Lippert HJ (1997) Eisenerze. In: Bender P, Lippert HJ, Nesbor HD (ed) Erläuterungen zur Geologischen Karte von Hessen, Blatt Nr. 5216 Oberscheld 1:25000, 2nd edn. Hess L-Amt Bodenforsch, Wiesbaden, pp 236-291.

Lippert HJ, Flick H (1998) Vulkano-sedimentäre Roteisenerze vom Lahn-Dill-Typ. In: Kirnbauer T (ed) Geologie und hydrothermale Mineralisationen im rechtsrheinischen Schiefergebirge, 1st edn. Nassau Ver Naturkd, Wiesbaden, pp 121-128.

Massonne HJ (1995) Metamorphic Evolution. In: Dallmeyer RD, Franke W, Weber K (ed) Pre-Permian Geology of Central and Eastern Europe, 1st edn. Springer, Berlin-Heidelberg, pp 132–137.

McLennan SM (1989) Rare earth elements in sedimentary rocks: influence of provenance and sedimentary processes. In: Lipin BR, McKay GA (ed) Geochemistry and Mineralogy of Rare Earth Elements, 1st edn. Rev of Mineral Geochem 21:169–200.

Nesbor, HD, Buggisch W, Flick H, Horn M, Lippert HJ (1993) Vulkanismus im Devon des Rhenoherzynikums. Fazielle und paläogeographische Entwicklung vulkanisch geprägter mariner Becken am Bespiel des Lahn-Dill-Gebietes. Geol Abh Hessen 98:3-87.

Nothdurft LD, Webb GE, Kamber BS (2004) Rare earth element geochemistry of Late Devonian reefal carbonates, Canning Basin, Western Australia: confirmation of a seawater REE proxy in ancient limestones. Geochim Cosmochim Acta 68:263–283.

Quade H (1968) Die Entwicklung des initialen Geosynklinal magmatismus und die Bildung der exhalativ-sedimentären Eisenerzlagerstätten im mitteleuropäischen Variszikum. Post-doctoral thesis Clausthal University of Technology.

Quade H (1976) Genetic problems and environmental features of volcano-sedimentary iron ore deposits of the Lahn-Dill Type. In: Wolf KH (ed) Handbook of strata-bound and stratiform ore deposits, 1st edn. Elsevier, Amsterdam, pp 255-294.

Rösler HJ (1962) Zur Entstehung der oberdevonischen Eisenerze vom Typ Lahn-Dill in Ostthüringen. Freib Forschungsh C 138:1–79.

Evidence for late Lufilian orogenic mineralizing fluids at the Kamalondo Cu-Co deposit (Tenke Fungurume, Democratic Republic of the Congo)

Pascal Mambwe, Philippe Muchez
KU Leuven, Department of Earth & Environmental Sciences, Belgium

Sébastien Lavoie
Tenke Fungurume Mining S.A., Department of Exploration Geology, Democratic Republic of the Congo

Louis Kipata
University of Lubumbashi, Department of Geology, Democratic Republic of the Congo

Stijn Dewaele
Gent University, Department of Geology, Belgium

Abstract. The Democratic Republic of Congo, part of the Central African Copperbelt, contains numerous Neoproterozoic world-class Cu-Co deposits. The Kamalondo Cu-Co deposit, located in the Tenke Fungurume Mining District, is a mega-fragment of the Mines Subgroup. The Cu-Co mineralization is characterized by a multistage origin, from a diagenetic mineralization, to a syn-orogenic phase (carrollite, chalcocite, chalcopyrite, bornite), and a final supergene enrichment (chrysocolla, heterogenite, malachite). The late Lufilian orogenic Cu-Co mineralization shows carbonate veins (brittle stage 5) crosscutting both carbonate and quartz veins related to brittle stages 1 to 4. The petrography of fluid inclusions reveals the presence of two-phase (liquid and vapor), three-phase, and four-phase inclusions (liquid, vapor and solids, such as anhydride, halite and sylvite). The fluid inclusions microthermometry indicate that the Cu-Co mineralization formed from a fluid with a minimum temperature of 60°C and a salinity ≥26.5 eq. wt.% NaCl. These temperature and salinity data are lower than the values typically recorded from the late diagenetic and syn-orogenic stages (homogenization temperature ≥270°C; salinity between 35-45.5 eq. wt.% NaCl).

1 Introduction

The Neoproterozoic Katanga Supergroup in the Central African Copperbelt (CACB) contains several Cu-Co (U) and Pb-Zn-Cu (Ge) sediment-hosted ore deposits (Cailteux et al., 2005, Dewaele et al., 2006; Schuh et al., 2012; Sillitoe et al., 2017; Twite et al., 2019). These sedimentary rocks are a succession of carbonate and detrital rocks deposited in a paleorift (Batumike et al., 2007; Mambwe et al., 2019). The Kamalondo Cu-Co deposit is located in the Tenke Fungurume Mining District (TFMD) in the CACB. The Cu-Co mineralization is hosted in the Mines Subgroup of the Roan Group. At a local scale, this deposit is part of the alignment forming the southern limb of the larger Dipeta syncline together with the Kansalawile and Mambilima deposits, while the Mwadinkomba and Shadirandzoro deposits occur in the northern limb.

The sediment hosted stratiform Cu-Co deposits in the CACB are generally thought of having a multistage origin (Dewaele et al., 2006; Haest and Muchez, 2011), however, also one mineralization phase has been proposed (Sillitoe et al., 2017). This single phase spans a time period of 50 Ma. Cu-Co mineralization started with diagenetic hydrothermal stages, followed by syn-orogenic (early to late) to post-orogenic stages. The diagenetic phases dated at ~800 Ma (Muchez et al., 2015), caused the precipitation of Cu-Co sulfides during burial of the Roan strata. The Th values of the fluid inclusions range between 115 and 220 °C, with a salinity between 11.3 and 20.9 eq. wt.% NaCl (El Desouky et al. (2009, 2010). The late diagenetic to syn-orogenic fluids have a minimum temperature of 270°C and high salinities (35-45.5 eq. wt.% NaCl).

During the Lufilian orogeny, a remobilization of the stratiform ore deposit occurred, causing the formation of stratabound deposits (Van Wilderode et al., 2015). A mineralization/remobilization phase is proposed to have occurred between ~720 to ~670 Ma by hydrothermal fluid convection during the Nguba proto-oceanic rifting or early stages of the Congo-Kalahari craton convergence (Decrée et al., 2014). The main mineralization/remobilization stage of Cu and U took place between 652 Ma and 530 Ma (Loris et al., 1997) in the Congolese part of the Copperbelt. In the Zambian Copperbelt, remobilization of Cu mineralization has been dated at 583 ±24 Ma (Barra et al., 2004) and at ~550 to ~530 Ma (Eglinger et al., 2013). An event dated at ~510 to ~500 Ma was related to Ca- and Na-rich metamorphic fluid (Eglinger et al., 2014). The 540–490 Ma ages of Cu-Mo mineralization (Sillitoe et al., 2017) are likely related to the syn- to post-orogenic timing of mineralization/remobilization.

The brittle stages 1 and 2 as defined by Kipata et al. (2013) belong to the Kolwezian orogeny-D1 and are characterized by folding and thrusting (Kampunzu and Cailteux, 1999; Kipata et al., 2013). The Monwezian phase-D2 is characterized by transpression, transtension and arc-parallel extension deformation,

which are recorded in respectively brittle stages 3, 4 and 5 (Kipata et al., 2013). These Lufilian phases control the mineralization in the Katanga Supergroup (Haest and Muchez, 2011; Mambwe et al., 2017a; b).

This study aims to characterize the nature and origin of the Cu-Co mineralizing fluids during the late stages of the Lufilian orogeny in the CACB. Using the Kamalondo deposit as an example (fig.1), the results will be compared with previous studies (El Desouky et al., 2009; 2010).

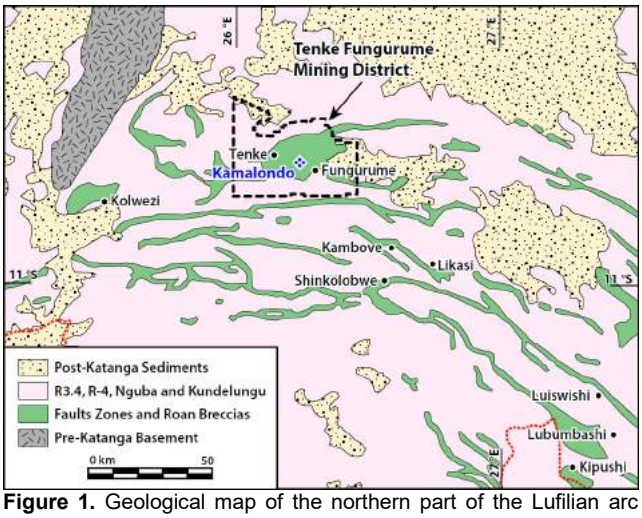

Figure 1. Geological map of the northern part of the Lufilian arc showing the Tenke Fungurume Mining District and Kamalondo Cu-Co deposit.

2 Methodology

Fieldwork, followed by detailed petrography and mineralogy, was completed at the Kamalondo Cu-Co deposit on both outcrops and cores. The characterization of fluid inclusions focused on dolomite veins mineralized with chalcocite, bornite, chalcopyrite and carrollite, hosted in a stratified siliceous dolomite. A representative sample was collected from the KAMA0052 borehole at a depth of 216.5m (Figs. 2, 3). This borehole was drilled in the western part of the deposit. Two doubly polished thick sections were made from the vein with hypogene Cu-Co sulfides.

The petrography of the fluid inclusions was completed on Olympus (BX41 and BX60) microscopes, and the microthermometry was done using an Olympus BX51 microscope equipped with a LINKAM MDS heating-cooling stage coupled to a computer. Calibration of the stage was done using glass standards with fluid inclusions of H_2O-CO_2 ($TmCO_2$ = -56.6°C), H_2O-NaCl (Te = -21.2°C), H_2O-KCl (Te = -10.4°C) and H_2O (Tm = 0.0°C). The detailed petrography and fluid inclusion microthermometry were completed at the Geodynamics and Geofluids Research Group of the KU Leuven.

3 Results

3.1 Cu-Co mineralization

Several generations of Cu-Co mineralization are observable in the Kamalondo deposit. The initial phase is characterized by nodules of dolomite-bearing carrollite or chalcopyrite with minor bornite, and disseminated pyrite, chalcopyrite and carrollite. This phase is followed by multiple generations of dolomite and quartz veins. The formation of the latter veins can be linked to the D1 tectonic phase (cf. Kampunzu and Cailteux, 1999). The mineralized zone is controlled by a strike- slip fault, interpreted to be related to the D2 deformation of the Lufilian orogeny (cf. Kampunzu and Cailteux, 1999).

Mineral zonation of the hypogene ore is recognized. Pyrite and chalcopyrite, with minor/occasional bornite, chalcocite and carrollite, are present in the upper ore body (e.g. SDS, SDB). Chalcocite, carrollite and bornite are more abundant than pyrite and chalcopyrite in the lower ore body (e.g. RSC, RSF, RAT).

Spatial distribution of grades vary from the western part (poorly mineralized), characterized by a NE-SW sinistral strike-slip fault (brittle stage 3), to the eastern part, well mineralized and affected by a NW-SE dextral strike-slip fault (brittle stage 4). Dolomite veins bearing pyrite, chalcopyrite, chalcocite, carrollite and bornite formed during the late Lufilian Cu-Co stages at Kamalondo. These late veins cross-cut all earlier generations of dolomite/quartz veins including drag folds. They are interpreted as recording the late orogenic brittle deformation (stage 5).

Figure 2. Late orogenic Lufilian veins bearing Cu-Co sulfides (chalcocite, chalcopyrite and carrollite ± bornite) in the lower ore body (drill hole KAMA0052, HQ core samples 64 mm wide).

The supergene enrichment zone is developed until a depth of 70m. Spherocobaltite, chrysocolla, chalcocite and malachite replace the Cu-Co sulfides. Usually the spherocobaltite and malachite rim the carrollite and the chalcopyrite and both hypogene and supergene chalcocite are intergrown with dolomite in fractures. The chalcocite has spots of hematite/goethite indicating oxidation. Dolomite/quartz with sulfides (chalcopyrite, chalcocite, carrollite) and supergene ores (malachite, spherocobaltite) occur in fractures. The weathering processes built a leached zone and an oxide zone above the hypogene zone. The thickness of these two zones is generally dependent on the permeability of the rocks (Fig.3).

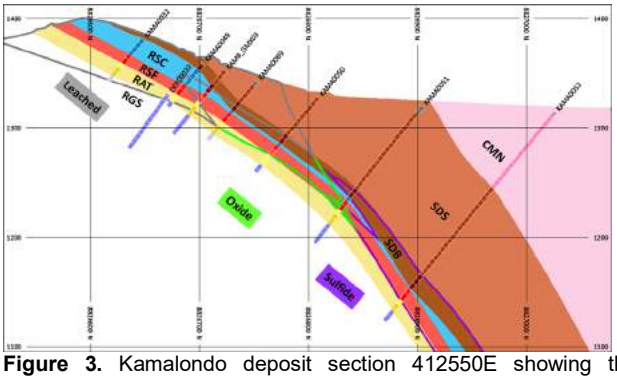

Figure 3. Kamalondo deposit section 412550E showing the lithology and mineral zonation (leaching, oxide and hypogene sulfide). Hole KAMA0052 is located on the right hand side of the section. RAT: Roche Argilo-Talqueuse, RSF: Roche Siliceuse Feuilleté, RSC: Roche Siliceuse Cellulaire, SDB: Shale Dolomitique de Base, SDS: Shale Dolomitique Supérieur, CMN: Calcaire à Minéraux Noir, RGS: Roche Gréseuse Siliceuse.

3.2 Fluid inclusion characteristics

The petrography of the fluid inclusions in the dolomite cement reveals the presence of two-phase aqueous-vapor inclusions or aqueous-gaseous inclusions with several solidst (Fig. 4). The volume of the vapor bubble ranges between 5 and 20%. The solids can have a cubic (halite, sylvite) or rectangular habit (anhydrite). In all cases, the volume of the solids ranges between 5 and 10%.

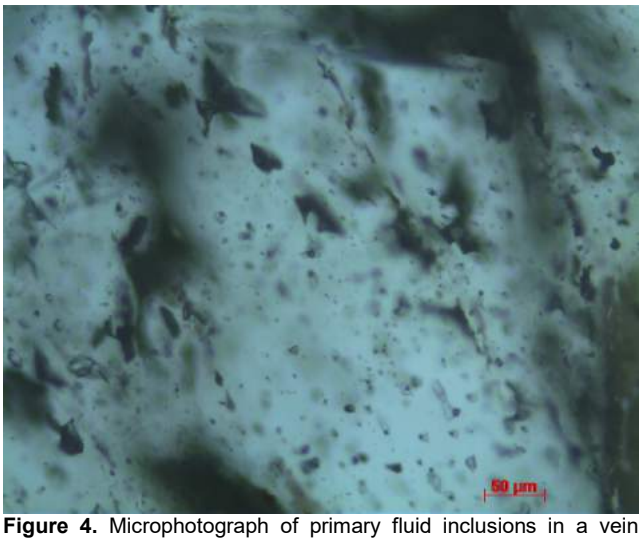

Figure 4. Microphotograph of primary fluid inclusions in a vein dolomite cement at the Kamalondo Cu-Co deposit.

Microthermometry was done only on primary fluid inclusions. The temperatures of homogenization (Th), and dissolution of halite (Ts) were measured. The Th values of the fluid inclusions in the dolomite cement are between 60° and 259°C, and Ts values between 48° and 250°C (Figs 5A, B). The latter corresponds with a salinity range between 26.5 and 35 eq. wt.% NaCl.

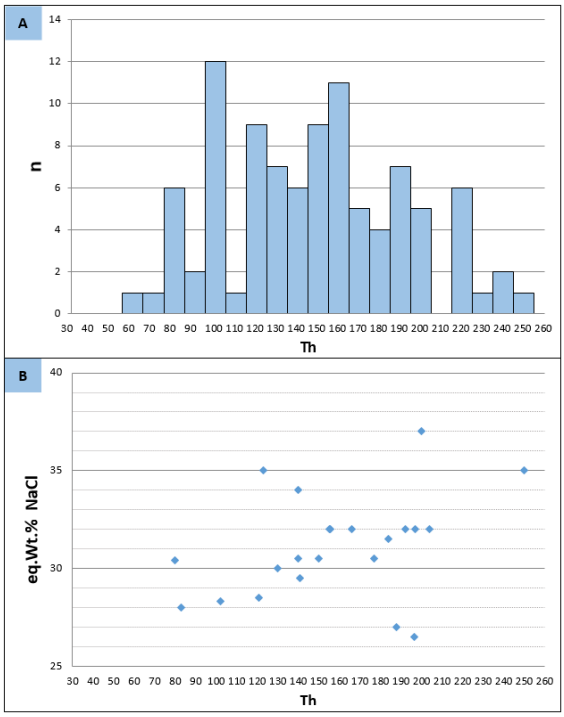

Figure 5. Homogenization temperatures (A) and salinity versus homogenization temperature (B) at the Kamalondo Cu-Co deposit.

4 Discussion and conclusion

The Cu-Co mineralization at the Kamalondo deposit is hosted in the classical lower and upper ore bodies of the CACB. The zonation observed results in a temporal grade distribution of Cu-Co. An abundance of carrollite in the lower ore body resulted in a higher concentration of Co than in the upper ore body. The carrollite formed after the first sulfide mineral phase. The syn to late orogenic phase is interpreted to have caused the formation of the carbonate and quartz veins mineralized in chalcocite, chalcopyrite, carrollite and bornite. The Kamalondo deposit forms a stratiform/stratabound Cu-Co deposit similar to other deposits in the Katanga Supergroup (Schuh et al., 2012).

The large range of Th and Ts values requires some discussion. Although special attention has been paid to avoid analysis of deformed inclusions, it cannot be excluded that the inclusions have been stretched or slightly leaked after entrapment. Stretching results in an increase in Th values, however does not affect could have caused an increase in both the Th and Ts values. Homogenization temperature of 60°C is the minimum temperature of the mineralizing fluid at a minimum salinity of 26.5 eq. wt% NaCl. In order to obtain the actual temperature of the fluid, the homogenization temperature has to be corrected for the pressure during fluid entrapment in the inclusions. Such low minimum temperature of 60°C can also be used to determine the approximate depth during mineralization, since the pressure correction is small. Taking into account a geothermal gradient of 20°C this corresponds to a depth of ~2km. If the fluid has a higher temperature than the surrounding rocks, i.e. a hydrothermal fluid, the depth is lower. This firstly indicates that this stage of

mineralization took place after significant uplift of the area. This is in agreement with the formation of the mineralization during brittle tectonic stage 5 characterized by arc-parallel extension (Kipata et al., 2013). Alternatively, if the higher Th values are not due to stretching or leakage, the temperatures measured reflect the migration of warm fluids from the deep subsurface. The mineralizing fluid with a higher content of Na, K and Ca, as indicated by the solids present in the inclusions, is comparable to the late diagenetic to syn-orogenic mineralizing fluids studied by El Desouky et al. (2009, 2010). However, the salinity and temperature of the inclusions studied in the present study are lower in comparison with those investigated by El Desouky et al. (2009, 2010). The syn-orogenic fluids are interpreted to be related to the Kolwezian phase (brittle stages 1 and 2 of Kipata et al., 2013) and probably to the early stages of the Monwezian phase (brittle stage 3 of Kipata et al., 2013).

These results demonstrate the evolution of a high temperature and high salinity mineralizing fluid (Th ≥ 270°C, salinity: 35-45.5 eq. wt. % NaCl) present during late diagenesis and orogenesis to a late orogenic fluid with much lower temperatures (≥Th 60°) and lower salinities (≥26.5 eq. wt.% NaCl).

Acknowledgements

Ongoing research work by Pascal Mambwe funded by a Ph.D. grant of the Marc Vervenne Fund (KU Leuven). Tenke Fungurume Mining S.A. provided support and permission to publish. Dr. Rudy Swennen and Dr. Olivier Namur are thanked for their constructive suggestions.

References

Barra F, Broughton D, Ruiz J, Hitzman M (2004) Multi-stage mineralization in the Zambian Copperbelt based on Re-Os isotope constraints. The Geological Society of America Abstracts with Program 36. Denver Annual Meeting, 7-10 November 2004.

Batumike MJ, Kampunzu AB, Cailteux JH (2007) Lithostratigraphy, basin development, base metal deposits, and regional correlations of the Neoproterozoic Nguba and Kundelungu rock successions, Central African Copperbelt. Gondwana Research 11:432-447.

Cailteux JLH, Kampunzu AB, Lerouge, Kaputo AK, Milesi JP (2005) Genesis of Sediment-Hosted Stratiform Copper - Cobalt Deposits, Central African Copperbelt. Journal of African Earth Sciences 42 (1–5):134–58.

Decree S, Deloule E, De Putter T, Dewaele S, Mees F, Baele JB, Marignac C (2014) Dating of U-Rich Heterogenite: New Insights into U Deposit Genesis and U Cycling in the Katanga Copperbelt. Precambrian Research 241:17–28.

Dewaele S, Muchez Ph, Vets J, Fernandez-Alonzo M, Tack L (2006) Multiphase origin of the Cu-Co deposits in the western portion of the Lufilian fold and thrust belt, Katanga (Democratic Republic of Congo). Journal of African Earth Sciences 46:455-469.

Eglinger A, André-Mayer AS, Vanderhaeghe O, Mercadier J, Cuney M, Decrée S, Feybesse JL, Milesi JP (2013) Geochemical Signatures of Uranium Oxides in the Lufilian Belt: From Unconformity-Related to Syn-Metamorphic Uranium Deposits during the Pan-African Orogenic Cycle. Ore Geology Reviews 54:197–213.

Eglinger A, Tarantola A, Durand C, Ferraina C, Vanderhaeghe O, André-Mayer AS, Paquette JL, Deloule E (2014) Uranium mobilization by fluids associated with Ca–Na metasomatism: a P–T–t record of fluid–rock interactions during Pan-African metamorphism (Western Zambian Copperbelt). Chemical Geology 386:218–237.

El Desouky HA, Muchez Ph, Cailteux J (2009) Two Cu-Co Sulfide Phases and Contrasting Fluid Systems in the Katanga Copperbelt, Democratic Republic of Congo. Ore Geology Reviews 36 (4):315–32.

El Desouky HA, Muchez Ph, Boyce AJ, Schneider J, Cailteux JLH, Dewaele S, Quadt AV (2010) Genesis of Sediment-Hosted Stratiform Copper-Cobalt Mineralization at Luiswishi and Kamoto, Katanga Copperbelt (Democratic Republic of Congo). Mineralium Deposita 45 (8):735–63.

Haest M, Muchez Ph (2011) Stratiform and Vein-Type Deposits in the Pan-African Orogen in Central and Southern Africa: Evidence for Multiphase Mineralisation. Geologica Belgica 14 (1–2):23–44.

Kampunzu AB, Cailteux J (1999) Tectonic evolution of the Lufilian Arc (Central African Copperbelt) during Neoproterozoic Pan-African orogenesis. Gondwana Research 2:401-421.

Kipata ML, Delvaux D, Sebagenzi MN, Cailteux J, Sintubin M (2013) Brittle and stress field evolution in the Pan-African Lufilian and its foreland (Katanga, DRC): from orogenic compression to extensional collapse, transpressional inversion and transition to rifting. Geologica Belgica 16 :1-17.

Loris NBT, Charlet JM, Pechmann E, Clare C, Chabu M, Quinif Y (1997) Caractéristiques minéralogiques, cristallographiques, physico-chimiques et âges des minéralisations uranifères de Lwiswishi (Shaba, Zaire): International Cornet Symposium, September 5–9, 1994, Mons, Royal Academy Overseas Science, Proceedings: 285–306.

Mambwe P, Kipata ML, Chabu M, Muchez Ph, Lubala R T, Jébrak, M, Delvaux D (2017a) Sedimentology of the Shangoluwe breccias and timing of the Cu mineralization (Katanga Supergroup, D. R. of Congo). Journal of African Earth Sciences 132:1-15.

Mambwe P, Milan L, Batumike J, Lavoie S, Jébrak M, Kipata L, Chabu M, Mulongo S, Lubala RT, Delvaux D, Muchez Ph (2017b). Lithology, petrography and Cu mineralisation of the Neoproterozoic glacial Mwale Formation at the Shanika syncline (Tenke Fungurume, Congo Copperbelt; Democratic Republic of Congo). Journal of African Earth Sciences 129:898–909.

Mambwe MP, Lavoie S, Delvaux D, Batumike J (2019) Soft sediment deformation structures in the Neoproterozoic Kansuki formation (Katanga Supergroup, Democratic Republic of Congo): Evidence for deposition in a tectonically active carbonate platform. Journal of African Earth Sciences 150:86-95.

Muchez Ph, Andre-Mayer AS, El Desouky AH, Reisberg L (2015) Diagenetic origin of the stratiform Cu-Co deposit at Kamoto in the central African Copperbelt. Mineralium Deposita 50:437-447.

Schuh W, Leveille RA, Fay I, North R (2012) Geology of the Tenke-Fungurume sediment-hosted strata-bound copper-cobalt district, Katanga, Democratic Republic of Congo. Society of Economic Geologists Special Publication 16:269-301.

Sillitoe RH, Perelló J, Creaser RA, Wilton J, Wilson AJ, Dawborn T (2017) Age of the Zambian Copperbelt. Mineralium Deposita 52 (8):1245–68.

Twite F, Broughton D, Nex P, Kinnaird J, Gilchrist G, Edwards D (2019) Lithostratigraphic and structural controls on sulphide mineralisation at the Kamoa copper deposit, Democratic Republic of Congo. Journal of African Earth Sciences 151:212-224.

Van Wilderode J, Debruyne D, Torremans K, Elburg MA, Vanhaecke F, Muchez Ph (2015) Metal Sources for the Nkana and Konkola Stratiform Cu-Co Deposits (Zambian Copperbelt): Insights from Sr and Nd Isotope Ratios. Ore Geology Reviews 67:127–38.

Mineralization styles of the Tullacondra Cu-Ag deposit (Cork, Ireland)

Andressa A. Silva[1], Pedro F. O. Cordeiro[1,2], Laisa S. Colaço[1], Anderson M. Santos[1], Leonardo E. Lagoeiro[1], Patrick Meere[3], Richard Unitt[3], Sean C. Johnson[4]
[1]Federal University of Paraná[1]
[2]Pontifical Catholic University of Chile
[3]University College Cork, Irland
[4]Irish Centre for Research in Applied Geosciences

Abstract. The Tullacondra Cu-Ag deposit is located 10 km from Mallow, in Ireland, and contains an unexploited reserve of 3.6 Mt of 0.7% Cu and 27.7 g/t Ag. The deposit is hosted within Carboniferous marls of the Lower Limestone Shale (LLS) and consists of an EW-trending Cu-Ag rich orebody. Although Tullacondra is hosted within the same stratigraphic and structural context as Navan, its relationship with the metallogenic controls of the rest of the province remains poorly known. The purpose of this study is to obtain data from Tullacondra by means of petrographic and chemical analysis to understand its metallogenic controls and to further discussions on its relationship with other Zn-Pb deposits. For this purpose, six styles of mineralization were determined: disseminated chalcocite-bornite-chalcopyrite, chalcopyrite, tennantite-arsenopyrite and pyrite, vein-hosted chalcocite-bornite-chalcopyrite and vein-hosted tennantite-arsenopyrite. Disseminated and vein-hosted chalcocite-bornite-chalcopyrite is hosted through the whole LLS and in the beds with the highest Cu values, while disseminated and vein-hosted tennantite-arsenopyrite is hosted mainly in the base of the LLS, in samples with the highest Ag values. Textural and mineralogical data thus show that Cu-bearing sulfides precipitate before Sb-As-bearing sulfides and that they concentrate in two connected orebodies.

1 Introduction

The Tullacondra deposit is an Irish-type Cu-Ag mineralization located 10 km NNW of Mallow, County Cork, in Ireland, and is hosted within the Irish Midlands (Wilbur and Carter 1986). This province has some of the most important Zn-Pb deposits in the world such as Navan, Lisheen and Silvermines, with about 110 Mt at 8% Zn and 2% Pb, 22 Mt at 11.63 wt % Zn and 1.96 wt % Pb and 17 Mt at 6.4 wt % Zn, 2.5 wt %, and 23 g/t Ag, respectively (Andrew 1986; Convery 2017; Torremans 2018). Tullacondra contains unexploited resources of 3.6 Mt of 0.7% Cu and 27.7 g/t Ag characterized as an EW-trending near-vertical Cu-rich orebody and a stratabound Ag-rich orebody. The deposit is hosted within Lower Carboniferous carbonate rocks of the Lower Limestone Shale, laterally equivalent to the Navan group, at the northern limb of the Variscan Kilmaclenine anticline (Fig. 1 - Wilbur and Royall 1975; Wilbur and Carter 1986). Albeit spatially apart by several tens of kilometres, the Tullacondra deposit is hosted within the same stratigraphic intervals as other Zn-Pb deposits in the province. It is also associated with regional dolomitization and shares similar NE to ENE trending structural controls (Johnston, 1999). These similarities suggest that they are part of the same mineralizing system. However, ore formation processes which allow for the formation of a Cu-Ag deposit instead of a Zn-Pb deposit remain poorly understood.

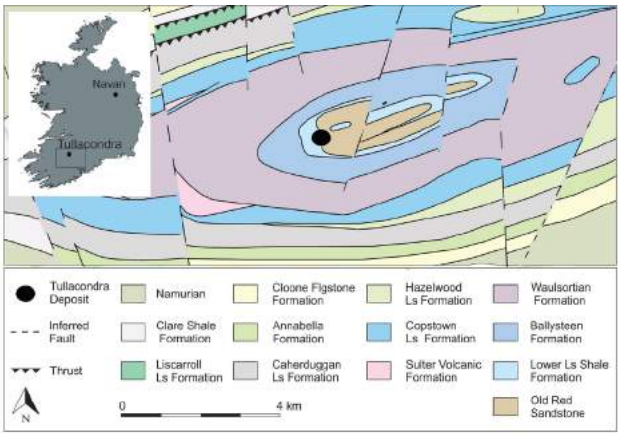

Figure 1. Geological map of the Kilmaclenine anticline in southern Ireland. Tullacondra deposit sits in the central part of the Kilmaclenine anticline. (Adapted from Geological Survey of Ireland - GSI Bedrock Geology 100k Series (1:100,000))

Therefore, the aim of this study is to obtain petrographic and geochemical data of a satellite copper deposit in order to further the discussion on Cu-Ag deposit genesis and their relationship with Zn-Pb deposits. For this purpose, petrography, whole-rock chemistry and SEM-EDS analysis were carried out and interpreted, and the main styles of mineralization, their distribution and a preliminary paragenetic sequence were determined.

2 Samples and methods

The studied samples were collected from three drill holes termed M73-3, M73-11 and M73-19, located in the western, central and eastern Tullacondra orebody, respectively (Fig. 2). Petrography of 41 samples was carried out to characterize the main host rock and sulfide mineralogy. EDS-SEM analysis were performed on 31 samples to allow for determination of poorly identified minerals whereas whole-rock chemistry of 43 samples allowed the determination of the geochemical

footprint and Ag and Cu distribution in host rocks.

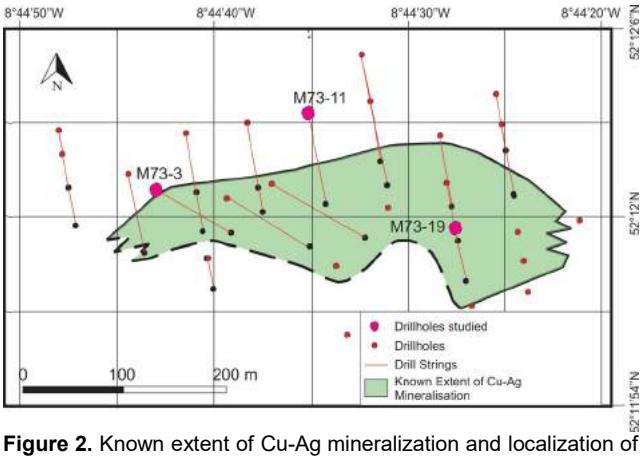

Figure 2. Known extent of Cu-Ag mineralization and localization of studied drill holes M73-3 (western part), M73-11 (central part) and M73-19 (eastern part) (Adapted from Diversified Asset Holdings - Mallow Project 1:4000)

3 Results

3.1 Lithological characterization

The Tullacondra deposit is hosted in the Devonian Old Red Sandstone (ORS) and in Carboniferous rocks (Courceyan age) of the Lower Limestone Shale (LLS), the Ballyvergin Shale and the Tullacondra Limestone (Fig. 3 and 4). At Tullacondra, the ORS is characterized by over 500 m thick siliciclastic and Red Bed rocks, the LLS by ~80 m of oolitic and bioclastic rocks, the Ballyvergin Shale by ~1 m of a fine calcareous limestone and the Tullacondra Limestone by ~35 m of a crinoidal limestone (Wilbur and Carter 1986). Based on the three studied drill holes (M73-3, M73-11, M73-19), these lithological units can be characterized, from base to top, by the followed petrological features:

a) ORS: medium-grained sandstone moderately sorted with quartz, feldspar and muscovite in micritic dolomite and calcite matrix. Red beds are characterized as medium-grained, poorly sorted sandstone containing quartz, feldspar, barite, muscovite, ilmenite and hematite;

b) The LLS is subdivided from base to top in: (I) Lower and (II) Upper Transition Series, (III) Uniform Calcarenite, (IV) Lower Shaly Calcarenite, (V) Oolitic Calcarenite, (VI) Silty Calcarenite and (VII) Upper Shaly Calcarenite (Fig. 3 and 4 - Wilbur and Carter 1986). (I) The Lower Transition Series consists of medium-grained poorly to moderately sorted sandstone with quartz, feldspar and muscovite in micritic calcite and dolomite matrix. Subordinate siltstone is very fine-grained with quartz, micritic calcite and dolomite; (II) The Upper Transition Series consists of medium-grained poorly sorted sandstone containing quartz, and feldspar in a micritic calcite and dolomite matrix; (III) The Uniform Calcarenite sub-unit consists of oolitic and bioclastic calcarenite, also classified as packstone (Dunham, 1962), in micritic dolomite and calcite matrix with trace of fine- to medium-grained quartz and muscovite; (IV) The Lower Shaly Calcarenite sub-unit consists of bioclastic calcarenite, classified as wackestone by Dunham (1962), with medium-grained bioclasts in a micritic calcite and dolomite matrix and traces of medium-grained quartz and muscovite; (V) Oolitic Calcarenite consists of oolitic calcarenite, also classified as packstone by Dunham (1962), containing medium-grained oolite and scattered bioclasts with subordinate medium to fine-grained quartz, feldspar and muscovite. Stylolites cutting through oolites and bioclasts are common; (VI) Silty Calcarenite is not reported in this study; (VII) The Upper Shaly Calcarenite sub-unit is defined by bioclastic calcarenite, or packstone and wackestone, interbedded with shaly beds and laminae, and dolostone in the base of the western orebody (M73-3). Calcarenite hosts calcitic bioclasts, sometimes replaced by chalcedony, disseminated medium-grained quartz and muscovite in micritic and sparitic calcite matrix. Stylolite cuts bioclasts and sometimes concentrates fine- to medium grained quartz along its surface. Additionally, shaly beds and laminae consist of fine-grained quartz, muscovite, micritic calcite and dolomite and show abundant concentration of burial stylolites. Dolostone is also hosted within the base of the Upper Shaly Calcarenite in the western orebody;

c) Ballyvergin Shale consists of fine calcareous shale containing mainly very fine-grained quartz, calcite and muscovite and scattered medium-grained quartz, calcite and muscovite;

d) Tullacondra Limestone consists of bioclastic calcarenite medium- to coarse-grained partially fine-grained near the base, also named as grainstone and packstone according to Dunham (1962) classification. In thin section, Tullacondra limestone contains bioclasts in micritic calcite matrix. Chalcedony replaces several bioclasts and hosted veinlets.

3.2 Ag and Cu chemistry analysis

The whole-rock chemical analysis of drill holes M73-3, M73-11 and M73-19 show that the main Cu values are concentrated along the LLS (Fig. 3). In the western part of the orebody (M73-3), Cu mineralization is hosted in the Ballyvergin Shale, topmost Upper Shaly Calcarenite, through the Lower Shaly Calcarenite, Uniform Calcarenite and Lower Transition Series. In the central part (M73-11), the highest Cu content is hosted in the Upper Shaly Calcarenite, Upper and Lower Transition Series and in eastern (M73-19), in the Oolitic Calcarenite, Lower Shaly Calcarenite and Lower Transition Series. Ag mineralization occurs in the Upper and Lower Transition Series, although not limited to those beds (Fig. 3). Whereas it is lacking in the western part of the orebody, it is hosted in the Upper and Lower Shaly Calcarenite, and Transition Series the in central and eastern part.

3.3 Mineralization styles

Mineralization in Tullacondra is either disseminated or vein-hosted, but the mineral assemblage and textural relationships can vary in different sections of the orebody. Thus, we divided the Tullacondra ores into six

styles based on their cross-cutting relationships and paragenetic sequence, as follows (Fig. 4):

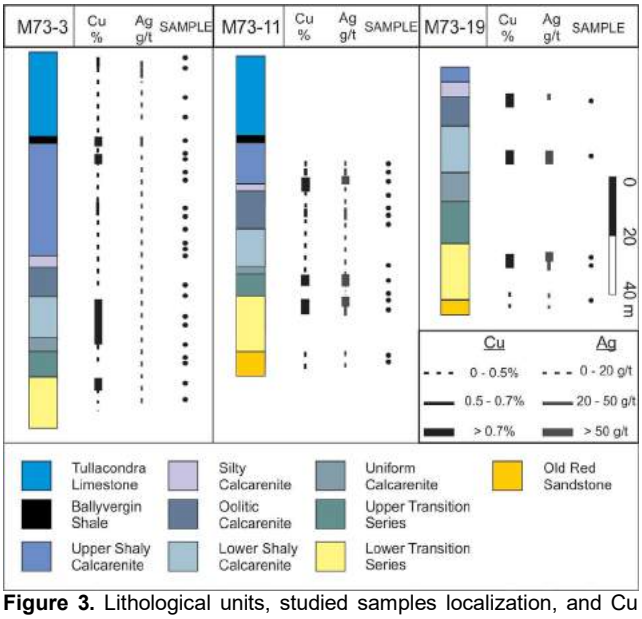

Figure 3. Lithological units, studied samples localization, and Cu (black line) and Ag grade (grey line) from the western (M73-3), central (M73-11) and eastern orebody (M73-19). Based on 30 years worth of drilling and whole-rock chemistry analysis. Note that the Cu-rich samples is hosted along the whole LLS and the Ag-rich samples mainly in the Transition Beds.

1. Disseminated chalcocite-bornite-chalcopyrite: fine- to medium-grained anhedral sulfides hosted in the top of the Tullacondra Limestone and Upper Shally Calcarenite of the western orebody (M73-3) and along of the whole central and eastern orebody (M73-11 and 19). In the fine-grained parts, chalcocite, bornite and chalcopyrite are also elongated parallel and oriented to matrix. In addition, they replace bioclasts, are along stylolites and between the boundaries of other minerals. Bornite are mostly pinkish brown to orange, but also purple when is aggregated with chalcocite. Chalcopyrite is aggregated with chalcocite and bornite, on the border replacing them or as lamellae within bornite;

2. Disseminated Cu-As-Sb (Zn-Ni-Co) sulfide-chalcopyrite-chalcedony: fine- to medium-grained subhedral to euhedral tennantite and arsenopyrite, and traces of freibergite, arsenotennantite, cobaltite and nicolite. They are hosted in the Upper Shaly Calcarenite of the western orebody (M73-3) and along of the whole LLS of the eastern and central orebody (M73-11 and 19). These sulfides overprint chalcocite, bornite and chalcopyrite and are also wrapped with chalcopyrite by chalcedony;

3. Disseminated chalcopyrite: anhedral fine- to medium-grained hosted along of the LLS and ORS. They replace bioclasts and are not associated with another sulfide. This is the main sulfide hosted in dolostone of the western orebody (M73-3);

4. Disseminated pyrite: fine-grained subhedral to euhedral rectangular and squared pyrite. This style occurs in the Tullacondra Limestone of the western orebody (M73-3) and in the top of the Upper Shaly Calcarenite of the central orebody (M73-11);

5. Vein-hosted Cu sulfides: fine to coarse-grained anhedral to subhedral chalcocite, bornite and chalcopyrite within calcite vein. They are hosted in the Tullacondra Limestone of the western orebody (M73-3) and in the LLS of the central and eastern orebodies (M73-11 and 19). This style of mineralization has similar features to the disseminated Cu sulfides consisting of pink to purple bornite with chalcocite, and chalcopyrite replacing them;

6. Vein-hosted Cu-As-Sb sulfides: fine- to coarse-grained subhedral tennantite and arsenopyrite in calcitic and dolomitic vein. They are hosted in the Upper Shaly Calcarenite of the central orebody (M73-11), Upper Transition Series of the eastern orebody (M73-19) and Lower Transition Series in the western orebody (M73-3).

4 Discussion

The lithological characterization from the ORS, the Transition series and the carbonate units shows a progressive transition from a siliciclastic platform towards a carbonatic one with periodic input of siliciclastic material. This transition from siliciclastic to carbonate sequence during the Upper Devonian and Lower Carboniferous has been reported as a marine transgression (e.g. Philips and Sevastopulo 1986).

Based on the styles of mineralization previously defined, we propose that disseminated mineralization is early in the paragenetic sequence and is cut by later stage vein-hosted mineralization. The following general paragenetic sequence is suggested for Tullacondra's disseminated ore:

(1) bornite-chalcocite, (2) chalcopyrite and (3) disseminated tennantite- arsenopyrite. The paragenesis of vein-hosted sulfides and disseminated pyrite will not be covered in this work.

1. Bornite and chalcocite occur earlier than the other copper sulfides in the paragenetic sequence;

2. Chalcopyrite occurs after other copper sulfides in the paragenetic sequence. It might also include more than one generation; either as isolated grains or overprinting bornite and chalcocite. Furthermore, chalcopyrite is the unique sulfide hosted in dolostone, lithology that is described just in the western deposit (M73-3). This chalcopyrite is probably cogenetic or posterior to dolomitization, because it wraps around dolomite grains;

3. Arsenic sulfides are the last disseminated sulfides in the paragenetic sequence as they overprint chalcocite, bornite and chalcopyrite. Besides they are likely coeval or slightly prior to chalcedony, because chalcedony commonly occurs in their rims.

The chemistry and petrological analysis show that there are at least two stages of mineralization, as initially suggested by Wilbur and Carter (1986), a Cu-rich stage consisting of bornite, chalcocite and chalcopyrite, and an Ag-rich stage consisting of tennantite and arsenopyrite (Fig. 4). But in contrast to these authors, the Cu-rich stage is probably the first mineralization followed by Ag-rich stage. Sulfides from the Cu-rich orebody deposited prior to those hosting the Ag-rich

orebody, as per sulfide overprint relationships. These data agree partially with Wilbur and Carter (1986), who designated a Cu-rich vertical orebody along the LLS and an Ag-rich stratabound orebody along the Transition Series (Fig. 3 and 4). Ag-rich mineralization restriction to a stratabound orebody is questionable, because Ag-rich mineralization is not limited to the Transition Series.

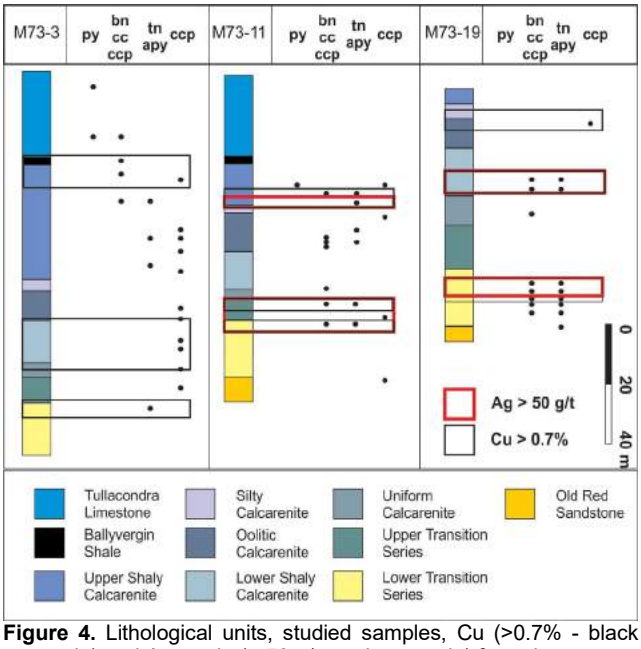

Figure 4. Lithological units, studied samples, Cu (>0.7% - black rectangle) and Ag grade (> 50 g/t - red rectangle) from the western (M73-3), central (M73-11) and eastern orebody (M73-19), and occurrence of the main sulfide phases. Based on 30 years' worth of drilling, whole-rock chemistry and petrological analysis. Note that the Cu-rich samples contain chalcocite, bornite and chalcopyrite and the Ag-rich samples contain tennantite and arsenopyrite. The Cu-rich samples is hosted along the whole LLS and the Ag-rich samples mainly in the Transition Beds.

5 Conclusion

Based on petrography, whole-rock chemistry and SEM-EDS analysis, main features of the lithological units, style of mineralization and Cu and Ag distribution were determined. We conclude that the Tullacondra deposit is comprised of at least six styles of mineralization emplaced within siliciclastic and carbonate rocks from a transgressive sedimentary basin. Chalcocite, bornite and chalcopyrite are the main copper sulfides, and their modal concentration defines the Cu-rich orebody cited by Wilbur and Carter (1986), whilst the concentration of tennantite-arsenopyrite defines the Ag-rich orebody. Additionally, our data shows that Cu-rich mineralization formed before the Ag-rich mineralization.

Future work will involve grain imaging and spot major and trace elements analysis to better characterize chemical variations of sulfides. Isotope analysis (C-O in carbonates and S in sulfides) will be used to determine information about the nature of the fluids.

Acknowledgements

The authors would like to thank the following institutions for helping us with financial, analytical or academic support: Graduate Program in Geology of the Federal University of Paraná, LAMIR (Mineral and Rock Analysis Laboratory), Diversified Asset Holdings Pty, iCrag (Irish Centre for Research in Applied Geosciences) and UCC (University College Cork).

References

Andrew CJ (1986) The tectono-stratigraphic controls to mineralization in the Silvermines area, County Tipperary, Ireland. In: Andrew CJ, Crowe RWA, Finlay S, Pennel WM, Pyne, JF (ed) Geology and genesis of mineral deposits in Ireland. Irish Association for Economic Geology, pp 377-417.

Convery M (2017) Searching for the "next big thing": Examination the potential for new feeder zone mineralization in the western Navan aerea. County Meath, Ireland. Dissertation, University of Glasgow

Dunham RJ (1962) Classification of carbonate rocks according to depositional texture. AAPG Mem. 1:108–121

Johnston JD (1999) Regional fluid flow and the genesis of Irish Carboniferous base metal deposits. Miner Deposita 34: 571-598. doi: 10.1007/s001260050221

Philips WEA, Sevastopulo GDS (1986) The stratigraphic and structural setting of Irish mineral deposits. In: Andrew CJ, Crowe RWA, Finlay S, Penell WM, Pyne JF (ed) Geology and genesis of mineral deposits in Ireland. Irish Association for Economic Geology, pp 1-30

Torremans K, Kyne R, Doyle R, Güven JF, Walsh JJ (2018) Controls on Metal Distributions at the Lisheen and Silvermines Deposits: Insights into Fluid Flow Pathways in Irish-Type Zn-Pb Deposits. Econ Geol 113:1455-1477. doi: 10.5382/econgeo.2018.4598

Wilbur DG, Carte JS (1986) Cu-Ag mineralization at Tullacondra Mallow, Co Cork. In: Andrew CJ, Crowe RWA, Finlay S, Penell WM, Pyne JF (ed) Geology and genesis of mineral deposits in Ireland. Irish Association for Economic Geology, pp 501-508

Wilbur DG, Royall JJ (1975). Discovery of the Mallow copper-silver deposit, County Cork, Ireland. In: Jones MJ (ed) Prospecting in areas of glaciated terrain. Inst Mining Metall, London, pp 60-70

In-situ Cu-isotope systematics of the Copperbelt (DRC, Zambia): variations at different scales

Marion Grosjean*, François Turlin, Anne-Sylvie André-Mayer, Aurélien Eglinger**
GeoRessources, Université de Lorraine, CNRS, CREGU, France
**Now at: Department of Earth Sciences, University of Geneva, Geneva, Switzerland*
***Now at: Université du Québec à Montréal, Département des Sciences de la Terre et de l'Atmosphère, Montréal, Canada*

Etienne Deloule
CRPG, CNRS, Université de Lorraine, France

Philippe Muchez, David Debruyne***
KU Leuven, Geodynamics and Geofluids Research Group, Department of Earth and Environmental Sciences, Leuven, Belgium
**** Now at: Geological Engineering Department, Federal University of Pelotas, Rio Grande do Sul, Brazil*

Panagiotis Voudouris
National and Kapodistrian University of Athens, Faculty of Geology & Geoenvironment, Dept. of Mineralogy and Petrology, Athens, Greece

Olivier Rouxel
IFREMER, Laboratoire Cycles Géochimiques et ressources, Brest, France

Abstract. The internal zone of the Central African Copperbelt (CAC) is characterized by several mineralization stages. Cu isotope signatures from the Lumwana deposit were analyzed by secondary ion microprobe (SIMS). Chalcopyrite and bornite from the two main mineralization stages display both δ^{65}Cu values between -1.37±0.23‰ and +2.95±0.19‰. These results do not allow to determine a specific metal source.

These δ^{65}Cu signatures are compared to Cu-Co deposits of the external zone of the CAC that are characterized by several mineralization stages. The latter stages involve remobilization of an earlier mineralization during the Pan-African orogeny. Copper-sulfides of the CAC present a wide range of more than 6‰ in δ^{65}Cu values. Deposits from the external zone of the CAC have mostly negative δ^{65}Cu values, whereas the internal zone shows ^{65}Cu enrichment. The fractionation at the grain scale can reach up to 3‰. This is significant when compared to the regional scale fractionation. This in-situ method also reveals equilibrium fractionation between the different Cu-phases. Mechanisms for such fractionations remain to be constrained.

1 Introduction

The Lufilian Pan-African orogenic belt hosts the world's largest sediment-hosted stratiform Cu-Co province, namely the Central African Copperbelt (CAC, Fig. 1; Selley et al. 2005), which is divided in two distinct metallogenic zones: the external and internal zone.

The external zone encompasses the Congolese and the Eastern Zambian Copperbelt, where metamorphism reached *P-T* conditions up to greenschists facies (Fig.2; Selley et al. 2005). Deposits of this zone are interpreted as the result of a multiphase mineralization ranging from diagenetic to syn- and post-orogenic (El Desouky et al. 2010; Muchez et al. 2015).

The internal zone is located in the Domes region, and corresponds to the Western Zambian Copperbelt (WZC). It records metamorphic *P-T* conditions up to upper-amphibolite facies (Fig. 2; Eglinger et al. 2014; Turlin et al., 2016). Several mineralization stages have been documented in this internal zone and including pre-, syn- and post-orogenic phases (Bernau et al. 2013; Turlin et al. 2016). However, whether the syn-orogenic Cu was derived from remobilization of a first pre-orogenic phase remains unclear due to the high-grade metamorphic overprint (Turlin et al. 2016). In order to constrain the origin of the Cu, a Cu-isotope study could provide some useful insights. However, the size of the pre-orogenic Cu-sulfide crystals and the common bornite-chalcopyrite intergrowths (e.g. Turlin et al. 2016) do not allow bulk Cu-isotope analyses, but require an *in-situ* method.

The aim of this study is to determine the relationship between the different Cu mineralization stages by analyzing the Cu-isotope signatures of chalcopyrite-bornite assemblages by secondary ion microprobe (SIMS) of both the internal and external zones of the CAC. Copper-Cobalt assemblages are hosted in (i) kyanite-micaschists from the Lower Roan Group or from its pre-Katanga basement (Lumwana deposit, Turlin et al. 2016); (ii) in the siliciclastic Lower Roan Group of the Katanga series (Kambove, Luiswishi, Konkola and

Nkana-Mindola) (Cailteux et al. 2005); and (iii) in the dolomites and sandstones of the Kundelungu Group (Dikulushi) (Haest et al. 2007). These data allow to discuss small and regional scale Cu isotope variation and fractionation, processes that could be due to differences in the source of the metal, temperatures, Eh or pH conditions of the mineralizing fluid.

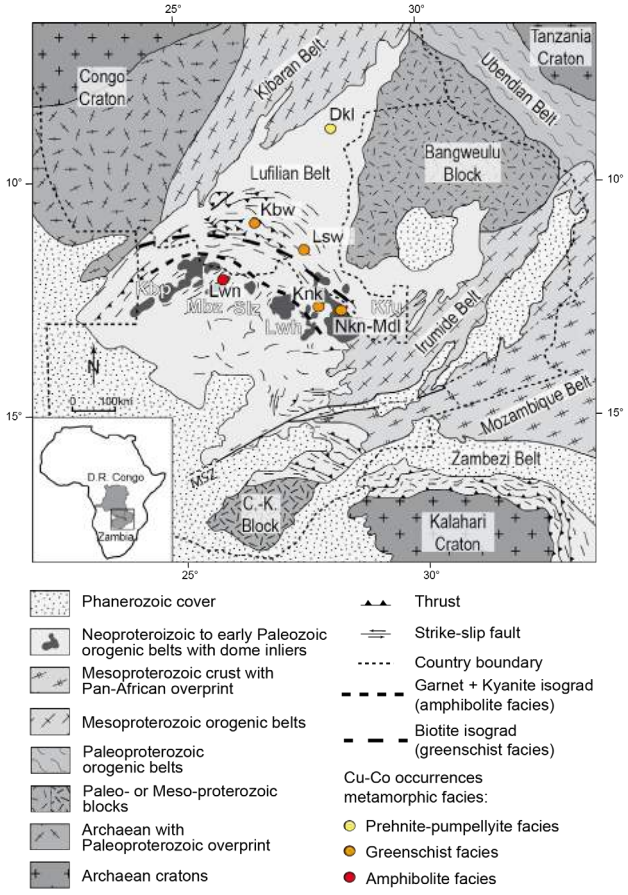

Figure 1. Geological map of the Central African Copperbelt hosting the investigated deposits. *Dkl: Dikulushi, Kbw: Kambowe, Knk: Konkola, Lsw: Luiswishi, Lwn:Lumwana, Mdl: Mindola, Nkn: Nkana*

2 Geological context

The Pan-African orogenic cycle started after intrusion, uplift and erosion of granites, which have been dated at ca. 880 Ma. It forms part of the break-up of the Rodinia supercontinent that initiated the deposition of the Katanga Supergroup in a continental rift (Hanson et al. 1994). A second rifting stage took place between ca. 750 and 720 Ma which led to the formation of an oceanic basin in the Zambezi Belt (Key et al. 2001). An inversion of the tectonic regime is recorded by eclogitic boudins between ca. 660 and 610 Ma (John et al. 2003). Subduction of the Congo craton underneath the Kalahari craton was initiated at ca. 595 Ma (John et al. 2003, 2004). A continental collision that led to the formation of the Lufilian Belt followed this subduction and is characterized by a peak of metamorphism dated at ca. 550 Ma in the internal zone (John et al. 2004; Eglinger et al. 2014b; Turlin et al. 2016). Finally, a post-orogenic exhumation between ca. 510 and 470 Ma led to the exhumation of high-grade metamorphosed rocks (Cosi et al. 1992; John et al. 2004; Eglinger et al. 2014; Turlin et al. 2016).

3 Cu-isotopes analyzed with SIMS

SIMS Cu-isotope analyses were performed for the first time, with a Cameca IMS 1270 E7 and 1280 HR2 at CRPG, Nancy. SIMS analyses were performed by standard bracketing measurements. Chalcopyrite and bornite grains from the Copperbelt were measured by MC-ICP-MS to determine their $\delta^{65}Cu$ values relative to NIST 976 The measured values are $\delta^{65}Cu_{ccp}$=-0.721±0.03‰ and $\delta^{65}Cu_{bn}$=-0.376±0.03‰ respectively. These reference materials were analyzed with SIMS each day prior to any sample analysis.

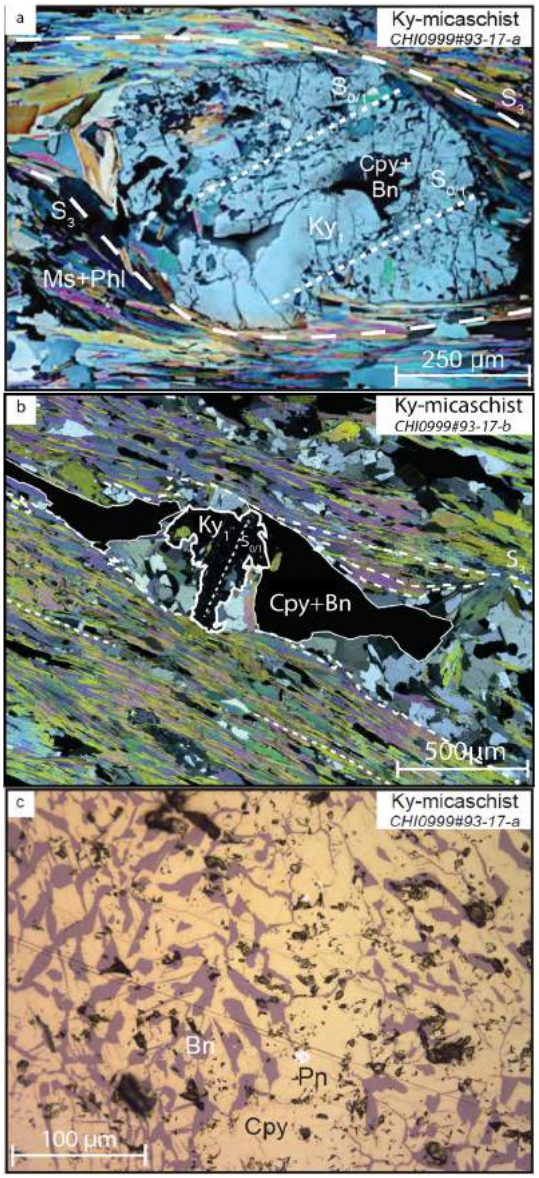

Figure 2. Petrographic assemblage of Cu-sulfides in Ky-micaschists of the Lumwana deposit (WZC). *a*. inclusions of Cu-sulfides in Ky_1=Cu_1. *b*. Cu-sulfides in a pressure shadow around Ky_1=Cu_2. *c*. intergrown bn-cpy characteristic of Cu_2 (after Turlin et al. 2016). Bn: bornite, Cpy: chalcopyrite, Pn: pentlandite.

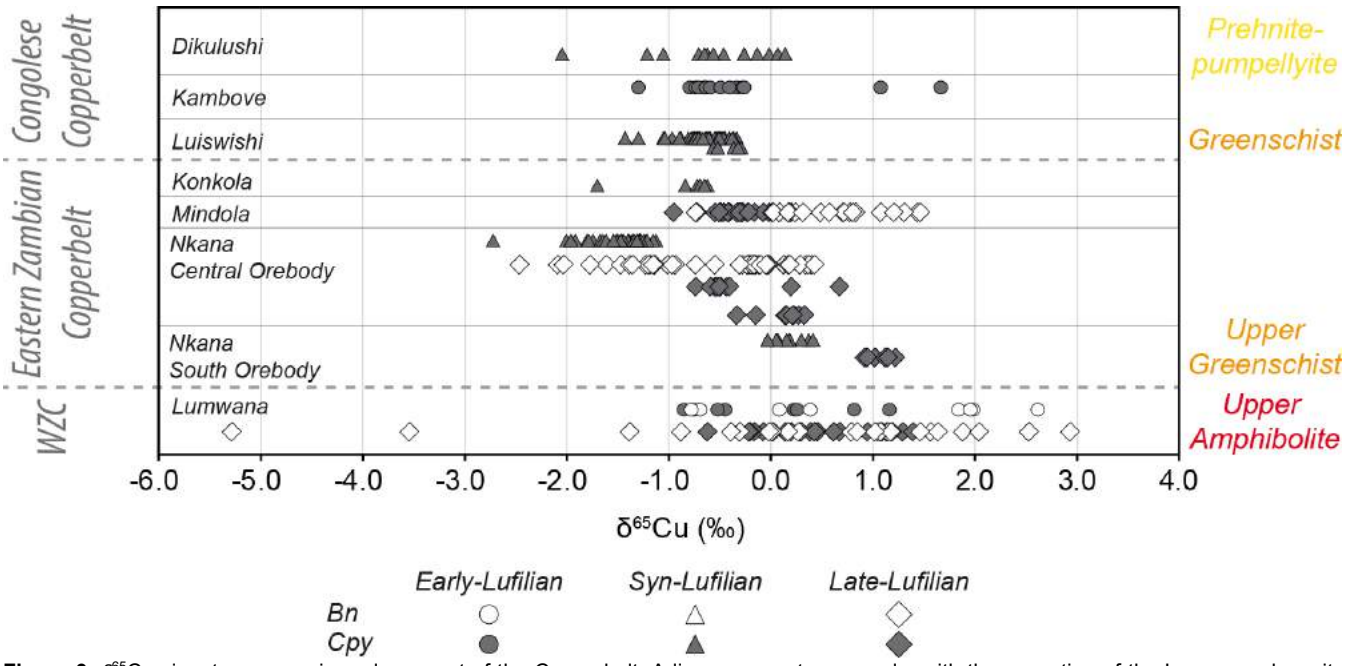

Figure 3. δ^{65}Cu signatures covering a large part of the Copperbelt. A line represents a sample, with the exception of the Lumwana deposit where several samples are combined. Early-Lufilian = late-diagenetic mineralizing stage (ca. 590 Ma); Syn-Lufilian = syn-orogenic mineralizing stage coeval with the regional peak of metamorphism (ca. 580-520 Ma), Late-Lufilian= a late- to post-orogenic stage (ca. 520–490 Ma). See references in the text for details on the sample age.

A primary negative oxygen beam (duoplasmatron) accelerated to 13 keV with an intensty of 10 nA was used for measurments. Secondary ions were measured with a mass resolution (M/ΔM) of 5000 in FC multicollection mode. The measured isotope ratio was converted in delta notation by using the equation:

$$\delta^{65}Cu_{IMF} = [(R_{SIMS}/R_{NIST}) - 1] \times 1000$$

where R_{SIMS} is the $^{65}Cu/^{63}Cu$ ratio measured by SIMS and R_{NIST} is the $^{65}Cu/^{63}Cu$ ratio of NIST976.

The $\delta^{65}Cu_{IMF}$ is then corrected from the instrumental mass fractionation using the equation:

$$\delta^{65}Cu_{sample} = \Delta^{65}Cu_{sample} + (X - \Delta^{65}Cu_{std})$$

where Δ^{65}Cu is equivalent to the $\delta^{65}Cu_{IMF}$ and X is the true δ^{65}Cu of the standard obtain by MC-ICP-MS.

4 Sampling

Samples analyzed with the SIMS come from deposits from the Congolese Copperbelt (Dikulushi, Kambove, and Luiswishi), the Eastern Zambian Copperbelt (Konkola, Mindola and Nkana) and the Western Zambian Copperbelt (Lumwana) (Fig.3). All these samples were taken from previous scientific studies whose ages and mineralization stages were determined based on detailed petrographic and microstructural observations coupled with geochronological analysis. (Haest et al. 2007, 2009a; Brems et al. 2009; El Desouky et al. 2010; Van Langendock et al. 2013; Torremans et al. 2013; Turlin et al., 2016 and references therein) No detailed petrography was carried out in this study.

Statistically, only a few samples from the late diagenetic stage have been analyzed compared to the syn-, late- and post-orogenic stages. The reason why the earliest phases are underrepresented in the samples is due to their lower preservation potential during the Lufilian orogeny.

5 Cu-isotope signatures of the Copperbelt

The pre- and syn-orogenic mineralization stages of the Lumwana deposit present a similar range of Cu isotope values between -1.37±0.23‰ and +2.95±0.19‰, with the exception of a few outliers (Fig. 3).

Deposits from the Congolese and Zambian Copperbelt display δ^{65}Cu values between -2.72±0.10‰ and +2.95±0.19‰ (Fig. 3).

6 Fractionation processes

Based on the similarities in the range of signatures, no distinct metal source could be identified for the multiple mineralization stages of the internal zone of the Copperbelt. The following sections deal with Cu-isotope fractionation processes recorded from grain-scale to regional-scale, as evidenced by the *in-situ* analyses.

6.1 Equilibrium fractionation

In the external zone of the CAC, bornite shows δ^{65}Cu values 1‰ higher than chalcopyrite (e.g. Mindola deposit, Fig. 3). Sample measurements have been standardized to their equivalent standards in order to avoid matrix effects. Accordingly, these differences cannot be attributed to this latter effect.

Such differences are not observed in the Lumwana deposit where analysis of both sulfides yielded similar values (Fig. 3) and where chalcopyrite and bornite show intergrowth textures (Fig. 2c; Turlin et al. 2016). Such

textures are not present in deposits from the external zone where both sulfides coexist. Internal processes associated with these textures need to be investigated to understand how they influence fractionation.

6.2 Grain-scale fractionation

The grain-scale fractionation can be as important as the deposit-scale variation, as shown by a Dikulushi sample where Cu isotopes fractionate up to 2‰, i.e. as much as the deposit-scale variation measured by MC-ICP-MS (cf. Haest et al. 2009). Fractionation up to 3‰ has been recorded by a single mm-sized grain from the Nkana Central Orebody amounting to a significant fraction of the observed regional-scale variation of 6‰ (Fig. 3).

These observations demonstrate that processes that affect fractionation at a large scale could also play a significant role at the grain scale.

7 Conclusion

No specific metal source can be attributed to the different mineralization stages recognized at the Lumwana deposit in the Western Zambian Copperbelt.

The *in-situ* Cu-isotope analyses enable to investigate Cu-isotope fractionation between different phases and at different scales showing that there is as much variation in Cu isotopes within a grain as in a deposit.

Acknowledgements

The author would like to thank OTELo (Observatoire Terre Environnement Lorraine) for its financial support in this multidisciplinary project led between the CRPG and GeoRessources laboratories.

References

Bernau R, Roberts S, Richards M et al. (2013) The geology and geochemistry of the Lumwana Cu (±Co ± U) deposits, NW Zambia. Min Dep 48:137–153.

Brems D, Muchez P, Sikazwe O, Mukumba W (2009) Metallogenesis of the Nkana copper–cobalt South Orebody, Zambia. J Afr Earth Sci 55:185–196.

Cailteux JLH, Kampunzu AB, Lerouge C et al. (2005) Genesis of sediment-hosted stratiform copper–cobalt deposits, central African Copperbelt. J Afr Earth Sci 42:134–158

Cosi M, De Bonis A, Gosso G, et al (1992) Late Proterozoic thrust tectonics, high-pressure metamorphism and uranium mineralization in the Domes Area, Lufilian Arc, Northwestern Zambia. Precambrian Res 58: 215–240

Eglinger A, Tarantola A, Durand C et al. (2014) Uranium mobilization by fluids associated with Ca–Na metasomatism: A P-T-t record of fluid–rock interactions during Pan-African metamorphism (Western Zambian Copperbelt). Chem Geol 386:218–237

El Desouky HA, Muchez P, Boyce AJ et al. (2010) Genesis of sediment-hosted stratiform copper–cobalt mineralization at Luiswishi and Kamoto, Katanga Copperbelt (Democratic Republic of Congo). Miner Deposita 45:735–763.

Haest M, Muchez P, Deweale S, et al (2007) Structural control on the Dikulushi Cu–Ag deposit, Katanga, Democratic Republic of the Congo. Econ Geol 102:1321–1333

Haest M, Muchez P, Petit JCJ, Vanhaecke F (2009) Cu isotope ratio variations in the Dikulushi Cu-Ag deposit, DRC: of primary origin or induced by supergene reworking? Econ Geol 104:1055–1064

Hanson RE, Wilson TJ, Munyanyiwa H (1994) Geologic evolution of the neoproterozoic Zambezi orogenic belt in Zambia. J Afr Earth Sci 18:135–150

John T, Schenk V, Haase K, et al. (2003) Evidence for a Neoproterozoic ocean in south-central Africa from mid-oceanic-ridge–type geochemical signatures and pressure-temperature estimates of Zambian eclogites. Geology 31:243-246

John T, Schenk V, Mezger K et al. (2004) Timing and *PT* Evolution of Whiteschist Metamorphism in the Lufilian Arc–Zambezi Belt Orogen (Zambia): Implications for the Assembly of Gondwana. J Geol 112:71–90

Key RM, Liyungu AK, Njamu FM, et al (2001) The western arm of the Lufilian Arc in NW Zambia and its potential for copper mineralization. J Afr Earth Sci 33:503–528

Muchez P, André-Mayer A-S, El Desouky HA et al. (2015) Diagenetic origin of the stratiform Cu–Co deposit at Kamoto in the Central African Copperbelt. Min Dep 50:437–447

Selley D, Broughton D, Scott R et al. (2005) A new look at the Geology of the Zambian Copperbelt. Soc Econ Geol 100th Anniversary Volume:965–1000

Torremans K, Gauquie J, Boyce AJ, et al (2013) Remobilisation features and structural control on ore grade distribution at the Konkola stratiform Cu–Co ore deposit, Zambia. J Afr Earth Sci 79:10–23

Turlin F, Eglinger A, Vanderhaeghe O, et al. (2016) Synmetamorphic Cu remobilization during the Pan-African orogeny: Microstructural, petrological and geochronological data on the kyanite-micaschists hosting the Cu(–U) Lumwana deposit in the Western Zambian Copperbelt of the Lufilian belt. Ore Geol Rev 75:52–75

Van Langendonck S, Muchez P, Deweale S, et al (2013) Petrographic and mineralogical study of the sediment-hosted Cu-Co ore deposit at Kambove West in the central part of the Katanga Copperbelt (DRC). Geol. Belg 16/1-2:91–104

Anomalous metal enrichment of basin brines in the Zambian Copperbelt

James Davey
University of Southampton and Natural History Museum

Stephen Roberts
University of Southampton

Jamie J. Wilkinson
Natural History Museum and Imperial College London

Abstract. The Central African Copperbelt is one of the most well-endowed metallogenic provinces in Africa, and the largest sediment-hosted Cu-Co-(U) district in the world. The origins, composition and relative timing of ore fluid migration in the Central African Copperbelt remain unclear, with physicochemically anomalous ore fluids potentially responsible for the unique scale of mineralization. Here, we report evidence for the passage of two temporally- and chemically-distinct brines in three deposits across the Zambian Copperbelt (Nkana-Mindola, Nchanga and Lumwana). Pre- to syn-kinematic veins in all three deposits host anomalously high temperature-salinity (>250°C, >35 wt % NaCl + KCl equiv) brines with unusually potassic compositions (K/Na ≥1) and concomitant enrichments in the principal ore-forming metals (Cu-Co). Later fluids are distinctly lower temperature (<250°C) and salinity NaCl-dominant brines with reduced base metal concentrations. We reconcile fluid compositions and base metal budgets with reported alteration assemblages from across the Central African Copperbelt and conclude that highly evaporated, ultra-potassic bittern brines with prolonged residence times in basal clastic sequences were critical to its unique metal endowment.

1 Introduction

Hydrothermal fluids are the foremost transport agent for base metals in the crustal environment and as such, quantifying base metal concentrations in paleofluids ostensibly linked with world-class sediment-hosted Cu-Co-(U) mineralization is a crucial aspect of our understanding of how these systems form. Although base metal concentrations in hydrothermal fluids have been reported from other deposit types (e.g. Wilkinson et al. 2009), we presently lack an understanding of how fluid P-T-*X* conditions vary between sub-economic or barren basin margin settings and some of the giant mineralized systems of the Central African Copperbelt

Microthermometry, scanning electron microscopy and laser ablation ICP-MS analysis of fluid inclusions hosted in suites of barren and mineralized veins from three major deposits in Zambia are here used to address the hypothesis that the fluids responsible for mineralization in the world's largest repository of sediment-hosted Cu-Co were anomalously base metal enriched.

2 Geologic Setting

The Central African Copperbelt is located towards the southeast of the 900 km-long Lufilian Arc, which formed in response to the collision of the Congo and Kalahari cratons during the Neoproterozoic to earliest Cambrian assembly of Gondwana. The Lufilian Arc comprises Archaean to Mesoproterozoic granitic, metavolcanic and metasedimentary basement inliers, overlain by a thick succession of Neoproterozoic, Katangan Supergroup metasediments. The Katangan sediments host the majority of Cu-Co mineralization in the Zambian Copperbelt and are constrained to a maximum age of 877 ± 11 Ma (Armstrong et al. 1999) by unconformably underlying granites. Katangan sediments were deposited during two main rift phases, with the Lower Roan sediments deposited in predominantly terrestrial and shallow marine environments during the earliest stages of rifting. The basin was inverted and metamorphosed, typically to greenschist facies, during the Lufilian Orogeny which peaked at 545 to 530 Ma (John et al. 2004; Turlin et al. 2016).

The Nkana-Mindola and Nchanga deposits comprise of a series of Lower Roan-hosted orebodies located on the western flank of the Kafue Anticline. Mineralization is primarily hosted by reduced argillaceous units, along with footwall arkosic and arenaceous lithologies, with different orebodies characterized by variable Cu:Co ratios. Lumwana represents an atypical style of Cu-Co-(U) mineralization in the Zambian Copperbelt and is hosted by relatively high metamorphic grade schists (± gneisses) of the Mwombezhi Dome, west of the Kafue Anticline (Bernau et al. 2013). The Chimiwungu and Malundwe orebodies at Lumwana represent a mineralized basement shear zone, stratigraphically below the 'classic' prospective stratigraphy of the Lower Roan.

All three deposits display finely disseminated mineralization as well as a range of temporally distinct vein sets, some of which are mineralized. The abundance of veins spanning the pre-orogenic and Lufilian stages of basin evolution at all three deposits provides an excellent opportunity to assess the compositional and temporal evolution of fluids involved in at least some of the mineralizing events in the CACB.

3 Paleofluids in the Zambian Copperbelt

Based on their kinematics relative to peak orogenesis, we divide the veins into two end-member generations. Approximately bedding-parallel, quartz-carbonate-sulphide veins are present at all three deposits and often host significant mineralization. These veins typically occur as planar, or folded and boudinaged arrays (Fig. 1B), implying formation prior to peak orogenic conditions. Temporally distinct, discordant, massive quartz veins with lesser carbonate and rare sulphides typically cross-cut ore horizons, as well as hangingwall/footwall units and Lufilian fabrics (Fig. 1C), indicating post-orogenic emplacement.

Bulk crush-leach analysis of paleofluids hosted by the two end-member vein sets display markedly different Cl/Br ratios, indicating distinct fluid origins (Fig. 1A) (Nowecki 2014; Selley et al. 2018). Fluids hosted by pre- to syn-kinematic veins show molar Cl/Br values below that of modern day seawater, indicating the presence of highly evolved bittern brines. Post-kinematic veins display distinctly higher Cl/Br ratios, indicative of a seawater-derived brine that has dissolved *in situ* halite.

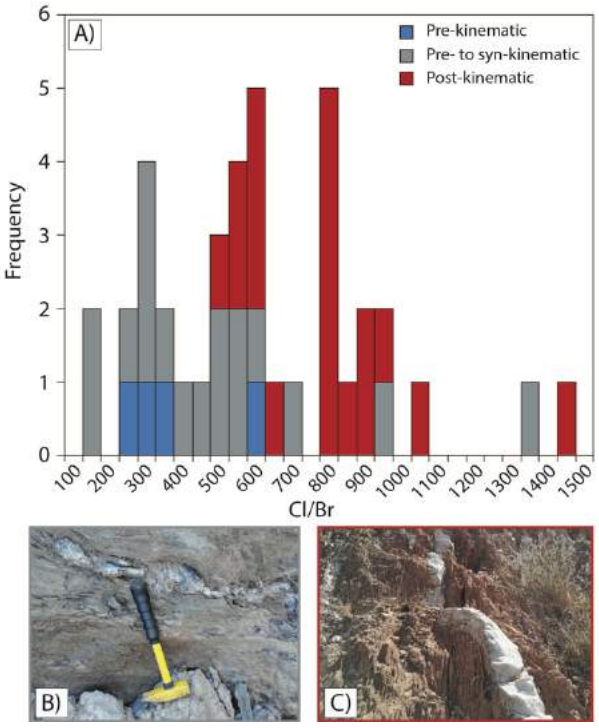

Figure 1. A) Cl/Br ratios of leachates from pre-, pre- to syn- and post-kinematic veins from various Zambian Copperbelt deposits. Data courtesy of J. Nowecki. B) Example of a shale-hosted pre- to syn-kinematic boudinaged quartz-bornite-chalcopyrite vein (Nkana South). C) Arkose-hosted discordant barren quartz vein cross-cutting the Lufilian foliation (Nkana Central).

3.1 Microthermometry

Microthermometric analyses of ~1000 fluid inclusions hosted by pre- to syn-kinematic, or post-kinematic veins from Nkana-Mindola, Nchanga and Lumwana show clear distinctions in total homogenization temperatures (T_{hTOT}) and total salinities (wt % NaCl + KCl equiv.) (Fig. 2). Primary inclusions spatially associated with base metal sulphides and hosted by kinematically early veins represent anomalously high temperature-salinity KCl-enriched brines (>250°C and >35 wt % NaCl + KCl equiv.). Primary inclusions in discordant, post-kinematic veins represent distinctly lower temperature-salinity NaCl-dominant solutions, more typical of fluids recovered from other sedimentary basin environments elsewhere in the world (Fig. 2). These fluids also occur as ubiquitous secondary fluid inclusions in all vein types.

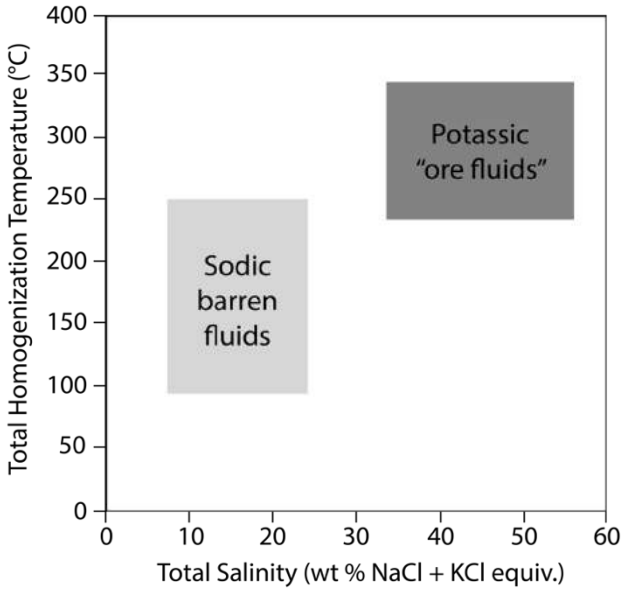

Figure 2. Schematic summary of microthermometric data for approx. 1000 inclusions from pre- to syn-kinematic and post-kinematic veins at the Nkana-Mindola, Nchanga and Lumwana deposits. Inclusions from the two broad fluid populations discussed here form distinct temperature-salinity fields.

3.2 Elemental analysis of fluid inclusions

Laser ablation inductively coupled plasma mass spectrometry (ICP-MS) analysis of individual, texturally-constrained inclusions indicate that pre- to syn-kinematic potassic brines are geochemically distinct from later, lower temperature NaCl-dominant solutions (Fig. 3). Early fluids are characterized by K/Na ≥1 and 1-2 orders-of-magnitude enrichments in the principal ore-forming metals (Cu + Co) relative to later, lower temperature fluids which typically show K/Na <1. Additionally, high-temperature metal-rich potassic brines display distinct enrichments in Fe, Mn, Pb, Zn, Ba and Li.

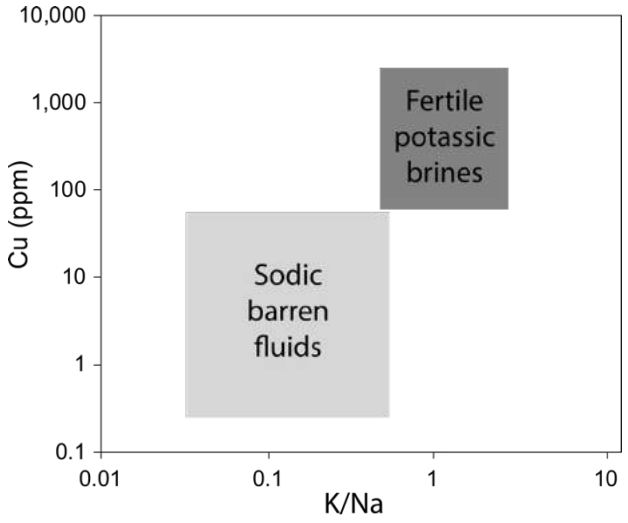

Figure 3. Schematic plot summarizing Cu concentrations and K/Na ratios of anomalously high temperature-salinity primary inclusions in mineralized pre- to syn-kinematic veins ("fertile brines"), and later, lower temperature-salinity barren fluids hosted by post-kinematic veins or as secondary inclusions in all vein types. Fields denote approximate ranges of variables for ~260 fluid inclusions from the Nkana-Mindola, Nchanga and Lumwana deposits.

Scanning electron microscope imaging and net intensity element maps of dried fluid inclusion cavities support this compositional distinction between fluid generations, with early ore fluids commonly hosting unusual intergrowths of halite and sylvite, whereas later, lower temperature, barren solutions typically host only halite as a daughter phase (Fig. 4).

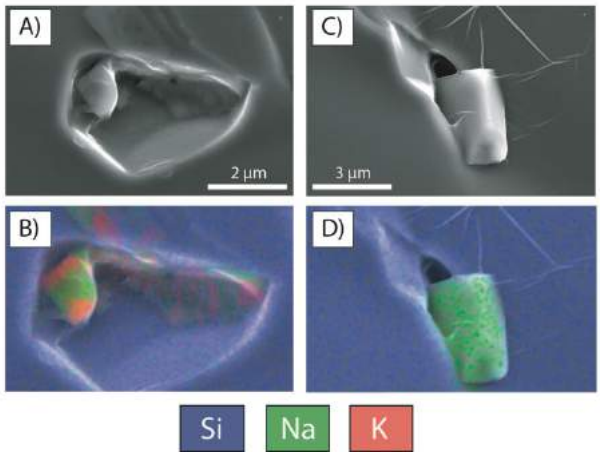

Figure 4. Scanning electron microscope images of dried fluid inclusion cavities at 15.9k magnification. Greyscale secondary electron images show an anhedral salt mass in (A), and a euhedral halite cube in (C). Colored net intensity element maps clearly distinguish intergrown halite and sylvite domains in image (B), a high temperature-salinity 'early' ore fluid inclusion. Image (D) confirms the absence of saturated potassium phases in a lower temperature, barren inclusion hosted by a discordant vein at Lumwana.

4 Discussion

Fluid inclusion phase proportions, homogenization temperatures and major and trace element chemistry indicate a clear compositional distinction between pre- to syn-kinematic fluids associated with mineralization and post-orogenic fluids in mostly barren vein sets. Early ore fluids are confirmed as amongst the most Cu-Co-rich brines recovered from any sedimentary basin environment and across all three deposits studied here, display a unique, ultra-potassic signature (K/Na ≈1).

4.1 Evaporitic ore fluid origins?

Anomalously high-temperature, potassic brines associated with mineralization at Nkana-Mindola, Nchanga and Lumwana correlate with brines shown to possess distinctly low Cl/Br and Na/Br ratios characteristic of highly evaporated bittern brines (Nowecki 2014; Selley et al. 2018). Development of such brines requires extended periods of evaporation in a restricted marine setting, where the conservative nature of K serves to elevate fluid K/Na ratios as NaCl becomes saturated and drops out of solution.

Although estimates of secular variations of Precambrian seawater chemistry, based on a combination of numeric modelling and interpretations of seafloor carbonate precipitate mineralogy, suggest the prevalence of Mg- and SO_4-rich seas during the middle Neoproterozoic (Hardie, 2003), direct measurements of halite-hosted fluid inclusions from the Amadeus and Officer Basins in Australia indicate that during the proposed time period that early, ultra-potassic bittern brines were sourced in the Zambian Basin (*ca.* 800 Ma), marine sulfate concentrations were as low as ~10% of modern seawater values. Both theoretical and observed evaporite crystallization sequences indicate that elevated fluid K/Na ratios can be developed at lower degrees of evaporation from such seawater, where an initially low sulfate budget is largely consumed through gypsum precipitation during the earliest stages of evaporation (Valyashko 1962).

Elevated Ba concentrations measured in ore fluids from all three Zambian deposits, combined with a paucity of $BaSO_4$ daughter phases within brine inclusions supports a sulfate-deficient, Neoproterozoic seawater origin (Kovalevych et al. 2006; Spear et al. 2014).

4.2 Fluid-rock interaction and mineralization

Elevated fluid K/Na ratios of ≥1 likely necessitate further K-enrichment of paleofluids within the Lower Roan clastic sequences of the Katangan Basin. Burial depths of up to 11 km, along with the presence of up to 30% detrital potassium feldspar in these rocks provides a viable source, and mechanism, to further supplement the K(-Ba) contents of fertile ore fluids. Petrographic studies of Lower Roan rocks provide evidence of the pervasive breakdown and replacement of detrital (primary) potassic phases in footwall clastic sequences (Sutton and Maynard 2005; Selley et al. 2005).

Subsequent interaction between fertile ore fluids and reduced argillaceous units is indicated by a strong association between mineralization and secondary potassic alteration assemblages (K-feldspar-phlogopite) (Sutton and Maynard 2005; Selley et al. 2005; Selley et al. 2018).

4.3 Development of halite dissolution fluids

Primary fluid inclusions from largely barren, post-kinematic veins at Nkana-Mindola and Lumwana are characterized by moderate salinities and homogenization temperatures, as well as distinctly low base metal concentrations and K/Na ratios. Similar fluids have been reported from demonstrably post-kinematic deposits such as Kansanshi and Kipushi, ranging in age from ~512 to 451 Ma and appear to have been capable of mobilizing relatively low quantities of Cu ($<10^2$ ppm) (Heijlen et al. 2008; Nowecki 2014; Selley et al. 2018). In all cases, these fluids have returned halogen ratios typical of solutions having undergone a component of halite dissolution. Widespread dissolution breccias in the Upper Roan stratigraphy (Selley et al. 2005, 2018) indicate pervasive breakdown of salt by halite-undersaturated fluids originating at supra-salt levels. The progressive penetration of these fluids into the Lower Roan stratigraphy during, and after Lufilian orogenesis is demonstrated by their presence as primary inclusions in barren, discordant veins, and by structurally-controlled sodic (albite ± scapolite) alteration that commonly overprints stratiform mineralization and earlier potassic alteration assemblages (Sweeney and Binda 1989; Selley et al. 2005).

5 Implications

Quantification of base metal concentrations and major salt chemistries of paleofluids interpreted to be responsible for vein-hosted mineralization at three Cu-Co deposits in the Zambian Copperbelt suggests that ore fluids acquired unique physicochemical characteristics from a series of favorable conditions. Generation of anomalously high temperature-salinity brines was aided by extremely high degrees of evaporation in a restricted marine environment, followed by deep burial within a fertile, hydrologically closed system. Significant degrees of fluid-rock interaction, along with high Cl concentrations in ore fluids promoted the leaching and transport of anomalously elevated base metal concentrations. Few other systems appear to have produced the requisite geologic and physicochemical conditions over sufficient time periods to generate similarly fertile basin brines.

Acknowledgements

This work was supported by the Natural Environmental Research Council (grant number NE/L002531/1), Rio Tinto Group and Mopani Copper Mines plc. Dan Doran and Matt Beverley-Smith are acknowledged for sample preparation. Yannick Buret, Clara Wilkinson and Simon Kocher are thanked for providing assistance with analyses at the NHM.

References

Armstrong RA, Robb LJ, Master S, Kruger FJ, Mumba, PAC (1999) New U-Pb age constraints on the Katangan sequence, Central African Copperbelt [abs]. Journal of African Earth Sciences Special Issue 28:6-7.

Bernau R, Roberts S, Richards M, Nisbet B, Boyce A, Nowecki J (2013) The geology and geochemistry of the Lumwana Cu (± Co ± U) deposits, NW Zambia. Mineralium Deposita 48:137-153.

Hardie LA (2003) Secular variations in Precambrian seawater chemistry and the timing of Precambrian aragonite seas and calcite seas. Geology 31:785-788.

Heijlen W, Banks DA, Muchez P, Stensgard BM, Yardley BWD (2008) The Nature of Mineralizing Fluids of the Kipushi Zn-Cu Deposit, Katanga, Democratic Republic of Congo: Quantitative Fluid Inclusion Analysis using Laser Ablation ICP-MS and Bulk Crush-Leach Methods. Economic Geology 103:1459-1482.

John T, Schenk V, Mezger K, Tembo F (2004) Timing and PT Evolution of Whiteschist Metamorphism in the Lufilian Arc–Zambezi Belt Orogen (Zambia): Implications for the Assembly of Gondwana. The Journal of Geology 112:71-90.

Kovalevych V, Marshall T, Peryt T, Petrychenko O, Zhukova S (2006) Chemical composition of seawater in Neoproterozoic: Results of fluid inclusion study of halite from Salt Range (Pakistan) and Amadeus Basin (Australia). Precambrian Research 144:39-51.

Nowecki J (2014) Tracing seawater evaporation and its role in the formation of sediment-hosted stratiform copper deposits. Unpublished PhD Thesis, University of Southampton.

Sweeney MA, Binda PL (1989) The role of diagenesis in the formation of the Konkola Cu-Co orebody of the Zambian Copperbelt. Geological Association of Canada Special Paper 36:499-518.

Turlin F, Eglinger A, Vanderhaeghe O, André-mayer AS, Poujol M, Mercadier J, Bartlett R (2016) Synmetamorphic Cu remobilization during the Pan-African orogeny: Microstructural, petrological and geochronological data on the kyanite-micaschists hosting the Cu(–U) Lumwana deposit in the Western Zambian Copperbelt of the Lufilian belt. Ore Geology Reviews 75:52-75.

Selley D, Broughton D, Scott R, Hitzman M, Bull S, Large R, McGoldrick P, Croaker M, Pollington N, Barra F (2005) A New Look at the Geology of the Zambian Copperbelt. Economic Geology, 100th Anniversary Volume: 965-1000.

Selley D, Scott R, Emsbo P, Koziy L, Hitzman MW, Bull S, Duffett M, Sebagenzi S, Halpin J, Broughton D (2018) Structural Configuration of the Central African Copperbelt: Roles of Evaporites in Structural Evolution, Basin Hydrology, and Ore Location. SEG Special Publication 21:115-156.

Spear N, Holland HD, Garcia-Veigas J, Lowenstein TK, Giegengack R, Peters, H (2014) Analyses of fluid inclusions in Neoproterozoic marine halite provide oldest measurement of seawater chemistry. Geology 42:103-106.

Sutton SJ, Maynard JB (2005) A fluid mixing model for copper mineralization at Konkola North, Zambian Copperbelt. Journal of African Earth Sciences 42:95-118.

Valyashko MG (1962) Geochemical Rules of the Potassium Salt Deposits Formation [PhD thesis]: Izdatelstvo Moskovskovo Universiteta, 398 p.

Wilkinson JJ, Stoffell B, Wilkinson CC, Jeffries TE and Appold MS (2009) Anomalously metal-rich fluids form hydrothermal ore deposits. Science 323:764-767.

Variability of ore mineralization in the vicinity of fault zones in the Radwanice-Gaworzyce copper-silver deposit (Lubin-Sieroszowice mining district, SW Poland)

Andrzej Chmielewski, Sławomir Oszczepalski, Andrzej Głuszyński
Polish Geological Institute-National Research Institute

Abstract. The characteristics of ore mineralization in the immediate vicinity of fault zones in the Lower Zechstein-related Kupferschiefer deposits are shown. All presented outcomes were obtained on the basis of rock material taken from mining profiles in the Radwanice-Gaworzyce deposit (SW part of the Lubin-Sieroszowice mining district). In all of the analyzed profiles, hematite-enriched Rote Fäule oxidized zone was found, which occurs at various levels of the Kupferschiefer series below the ore-bearing reduced rocks. The redox front cuts across the boundaries of lithostratigraphic units, moving from the Weissliegend to the uppermost parts of the Zechstein Limestone. The primary ore mineralization in the reduced zone is the chalcocite-digenite association with subordinate bornite and covellite. The secondary sulphide mineralization, superimposed on primary ore mineralization and hematitized rocks, is represented by chalcopyrite, bornite, tennantite, tetrahedrite and pyrite. Secondary mineralization is preferentially located in the direct vicinity of fault zones and associated tectonic deformations.

1 Introduction

Previous research conducted on the Fore-Sudetic Monocline revealed a number of regularities in the distribution of the ore mineralization hosted by Lower Zechstein rocks (e.g. Oszczepalski 1999; Speczik 1995), including the mineral zonation pattern in relation to the Rote Fäule oxidized zone (Figs. 1 & 2) and the presence of relict mineralization in profiles with oxidized rocks (Rydzewski 1978; Oszczepalski 1994, 1999; Oszczepalski et al. 2002; Chmielewski, 2014, 2016; Chmielewski et al. 2015; Oszczepalski and Chmielewski 2015) that are locally enriched in gold and PGE (e.g. Oszczepalski 2007). Much less attention has been given to the role of tectonic deformation in the mineralization processes (Salski 1975, 1977; Markiewicz 2007).

Samples of the Kupferschiefer series were collected from underground workings in the G-32 section located in the Polkowice-Sieroszowice mine (Fig. 3), which operates in the westernmost part of the Radwanice-Gaworzyce deposit. The analyzed area is located in the SW part of the Fore-Sudetic Monocline, approximately 5 km north-east of the Middle Odra Fault Zone that separate the Fore-Sudetic Monocline from the Fore-Sudetic Block. As a result of the location close to the border of the Fore-Sudetic Block, this region is characterized by intense tectonic deformations within the deposit series (Salski 1975, 1977; Markiewicz 2007).

Ore and iron oxide minerals were identified under the optical microscope in reflected light and photographic documentation of the examined samples was undertaken. In addition, microprobe examination was carried out for selected samples along with calculations of the chemical composition of ore minerals. During the petrographic research the variability of ore mineralization in the fault zones (normal, reverse and strike-slip faults) as well as other tectonic deformation like thrusts and folds striking NW-SE and NE-SW directions have been studied. The main purpose of the study was to characterize the distribution of ore mineralization and trace the structural and textural relations between ores, iron oxides and rock-forming minerals in the vicinity of fault zones and related tectonic deformation encountered in the studied area (Fig. 4).

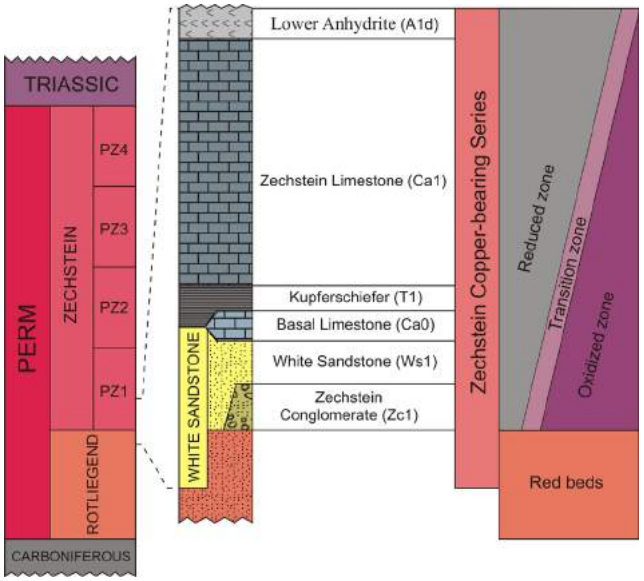

Figure 1. Stratigraphic position of the Kupferschiefer series and the distribution chart of geochemical zones

2 Characteristics of ore mineralization

During studies of the investigated mine profiles, both reduced and oxidized intervals were examined. The following ore minerals have been identified: chalcocite Cu_2S, djurleite $Cu_{1.93-1.95}S$, digenite $Cu_{1.8}S$, roxbyite $Cu_{1.78}S$, anilite $Cu_{1.75}S$, geerite $Cu_{1.6}S$, spionkopite $Cu_{1.4}S$, covellite CuS, bornite Cu_5FeS_4, chalcopyrite $CuFeS_2$, sphalerite ZnS, galena PbS, electrum (Au,Ag), native gold, native silver, silver amalgam Ag_2Hg_3,

stromeyerite AgCuS, naumannite Ag_2Se, tennantite $Cu_6[Cu_4(Fe,Zn)_2]As_4S_{13}$, tetrahedrite $(Cu,Fe)_{12}Sb_4S_{13}$, rammelsbergite $NiAs_2$, gersdorfite NiAsS, clausthalite PbSe, tiemannite HgSe, pyrite FeS_2 and iron oxide minerals: hematite Fe_2O_3 and goethite FeO(OH). Current data on the Kupferschiefer mineralization in SW Poland reveals a number of regularities in spatial distribution patterns of geochemical zones (Figs. 1 & 2).

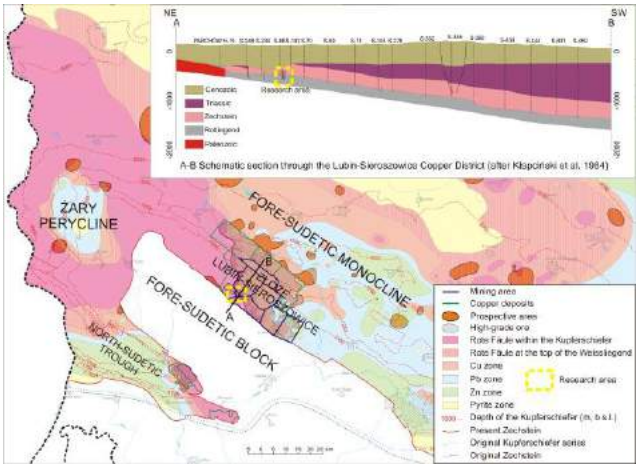

Figure 2. Map showing location of the research area in relation to Rote Fäule areas and metal zoning patterns in the Zechstein copper-bearing series of SW Poland (after Oszczepalski and Chmielewski 2015). A-B Schematic section through the Lubin-Sieroszowice Copper District (after Kłapciński et al. 1984)

The profiles of the Kupferschiefer series within reduced rocks are characterized by the predominance of copper sulphides from the Cu-S group, mainly chalcocite with subordinate digenite and bornite. The richest Cu mineralization is confined to the reduced zone that occurs above the oxidized rocks, transecting lithostratigraphic units. The predominant forms of ore minerals are: disseminations, tiny aggregates, accumulations of microlites and fine crystals (Fig. 5A). Lenses and nests of ore minerals are also common. Individual specimens of the ores usually take on the subhedral and anhedral (Fig. 5B), rarely euhedral textures. Cu sulphides occur primarily as fine-grained crystals dispersed within the rock matrix (Fig. 5C & D). They also occur as replacements of carbonate and detrital minerals by sulphides, chalcocite, digenite, bornite and galena pseudomorphs after pyrite framboids, and the pyrite framboids cemented by chalcocite, bornite or galena. Polymineral aggregates composed of bornite, digenite and chalcocite are also common. Complex intergrowth textures are characteristic and take the form of invasive replacement of bornite by covellite, digenite by bornite or chalcocite by digenite and bornite. Microprobe examination showed elevated concentrations of silver in chalcocite, digenite and bornite. The highest concentrations of silver were found in chalcocite, up to 4% by weight, while the silver substitution in digenite and bornite reaches up to 0.59 wt.% and 1.16 wt.%, respectively. The concentration of silver in the ore minerals decreases towards the top of the mineralized interval. Veinlets and fillings of pores, open spaces and stylolites are sparse.

Oxidized profiles are characterized by the occurrence of iron oxides mainly in the form of hematite. Goethite is rarely found. Iron oxides occur in several forms, as red pigment, clumps, irregular small grains dispersed in the rock background (so-called "hematite dust"), earthy masses with lenticular shapes of brown to red colors. Copper sulphides are rare. Very fine hematite grains often replace carbonate minerals and detrital grains and form inclusions in copper sulphides. Noteworthy are complex hematite intergrowths with covellite, digenite and chalcocite as well as native gold inclusions in ore minerals (Fig. 5E). Particularly important for the interpretation of the origin of ore mineralization are partial or total replacement of covellite, digenite, bornite and chalcopyrite by hematite (Fig. 5F). Sulphide relicts resulting from partial replacement of copper sulphides are most common in the transition zone from oxidized to reduced rocks, which form the highest part of oxidation zone. Evidently, this substitution of copper sulphides by iron oxides and hydroxides often takes on an invasive character, which indicates extensive alteration and leaching of Cu sulphides. In areas where the oxidation front of oxidizing solutions has significantly exceeded the Kupferschiefer horizon, ore mineralization in the Zechstein Limestone is poorer than when the oxidation front has stopped at the boundary of the Kupferschiefer with the Weissliegend.

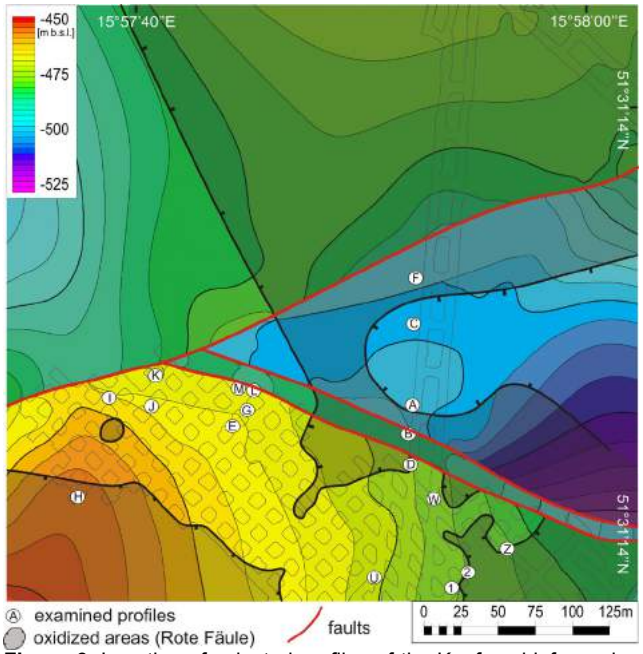

Figure 3. Location of selected profiles of the Kupferschiefer series across the SW part of the Lubin-Sieroszowice deposit (the depth contours are the base of the Kupferschiefer).

An important phenomenon is the presence of secondary sulphide mineralization that includes copper sulphides and sulphosalts, such as: chalcopyrite, bornite, tennantite, tetrahedrite and euhedral pyrite. Secondary mineralization is superimposed on the primary ore mineralization in reduced rocks and

overprinted also hematitized rocks. Occasionally, inclusions of tiemannite and naumannite in chalcopyrite are recorded. Secondary mineralization is strongly associated with fault zones and accompanying tectonic deformations (Fig. 4). This late-stage mineralization occurs in the form of brecciated crystals, irregular nests, fillings of cataclastic fractures in primary ore minerals (Fig. 5G), as well as rims and overgrowths of chalcopyrite (Fig. 5H) and pyrite around hematite accumulations. In addition, replacements and impregnations of Cu-S-type minerals by chalcopyrite, tennantite and bornite are also observed. Very often the faults are partly filled by chalcopyrite and bornite, mainly in the form of encrustations on the fault surfaces. Numerous fractures adjoining to fault zones are commonly filled with irregular sockets and lenses of chalcopyrite and bornite accompanied by tennantite and tetrahedrite with minor pyrite.

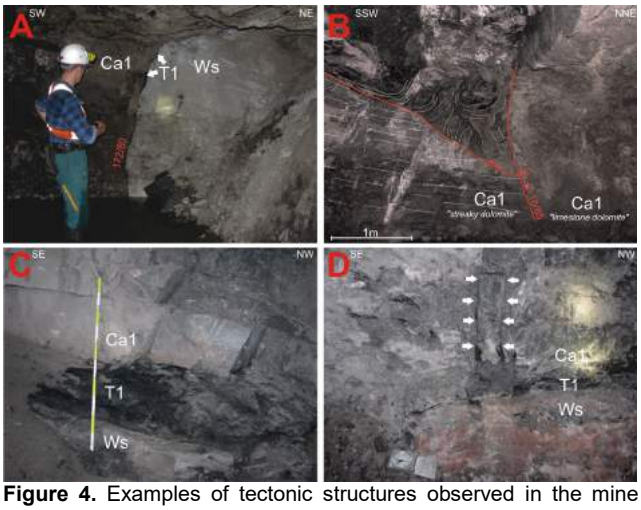

Figure 4. Examples of tectonic structures observed in the mine galleries in the Weissliegend sandstone (Ws), the Kupferschiefer shale (T1) and the Zechstein Limestone (Ca1). **A.** Juxtaposition of the Zechstein Limestone and the Weissliegend sandstone through fault surface, the Kupferschiefer is smeared along the fault plane. **B.** Lower part of the Zechstein Limestone (striped dolomite) juxtaposed with upper part of Ca1 carbonates (calcareous dolomite) through fault zone, near the fault zone the Ca1 carbonates are intensely folded, and the thrust is cutting the vein. **C.** The Kupferschiefer shale tectonically deformed (folded and faulted) **D.** Rock material from the Kupferschiefer shale injected into fractures in the Zechstein Limestone.

Locally, in the uppermost part of the Weissliegend tectonic engagement is visible in the form of extensive and irregular network of veins filled with chalcopyrite, bornite and euhedral pyrite. In some areas, the Kupferschiefer took the form of a pitchy shale, highly deformed and folded, with chalcopyrite and bornite veinlets and irregular nests, both concordant and diagonal relative to lamination (Fig. 5D). In the Zechstein Limestone, small fractures filled with anhydrite, gypsum, bornite, chalcopyrite and tennantite on their surfaces are common. In addition, displacements of thin-skinned-style in the form of slip surfaces and tectonic breccia impregnated and incrustated with chalcopyrite and bornite have been recorded. Furthermore, in some areas a tectonic increase in the thickness of copper-bearing beds was noted due to intraformational thrusting within the Kupferschiefer and the Zechstein Limestone (Fig. 4C). Characteristically, the intensity of the secondary mineralization decreases with distance from the fault zones.

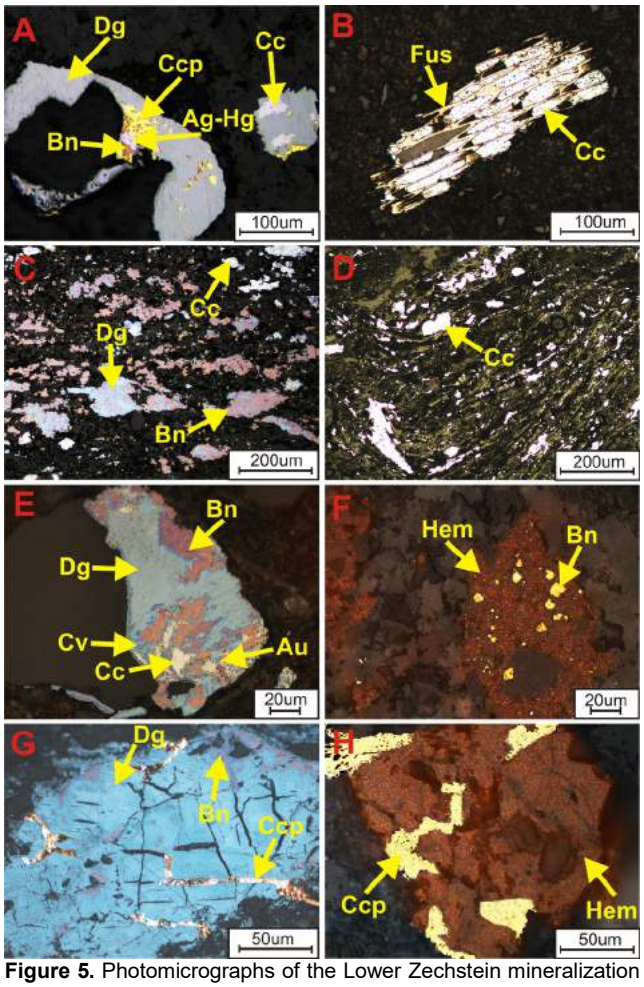

Figure 5. Photomicrographs of the Lower Zechstein mineralization (reflected light; A-D - primary mineralization, E-F - relict mineralization, G-H - secondary mineralization superimposed on primary mineralization) **A.** Digenite (Dg) with tiny inclusions of chalcocite (Cc), bornite (Bn), chalcopyrite (Ccp) and silver amalgam (Ag-Hg), U profile, Zechstein Limestone. **B.** Fusinite (Fus) cells filled with chalcocite (Cc), C profile, Zechstein Limestone. **C.** Rich disseminated bornite (Bn) - digenite (Dg) - chalcocite (Cc) mineralization, K profile, Kupferschiefer. **D.** Chalcocite (Cc) dispersed between folded laminae, with some laminae partly broken by chalcocite crystals, H profile, Kupferschiefer. **E.** Mineral aggregate composed of digenite (Dg), bornite (Bn), chalcocite (Ccp) and covellite (Cv) with native gold (Au), profile 1, Kupferschiefer. **F.** Relicts of bornite (Bn) in replacing hematite (Hem), profile A, Zechstein Limestone. **G.** Cataclastic fractures in digenite (Dg), partly filled by bornite (Bn) and filled with chalcopyrite (Ccp), profile A, Zechstein Limestone. **H.** Hematite (Hem) partly invaded with chalcopyrite (Ccp), profile F, Weissliegend.

3 Discussion

The obtained outcomes of petrographic and tectonic research lead to the conclusion that the change in the mineral composition near the redox zone is a result of

the evolution of ore system, as evidenced by progressive alteration of the earliest formed ore minerals, until their oxidation and replacement by hematite. The components of the reduced intervals underwent advanced alteration, leading to the conversion of ore-enriched reduced rocks into oxidized rocks with relict copper mineralization represented by replacement remnants of sulphides in hematite. The expansion of oxidative alteration is clearly marked by the appearance of red color of the altered rocks and remnants of Cu sulphides. The occurrence of hematite mineralization in the highest parts of the Kupferschiefer series indicates the centers of the most intense activity of ascending hydrothermal solutions. Therefore, it should be considered that the current position of the oxidized zone and sulphide mineralization concentrated in the ore bodies results from preservation of the products of the last phase related to the propagation of flow of mineralizing solutions and their interactions with rocks through which these solutions were moving, consistently with the direction of spreading.

4 Conclusions

The ore mineralization in the reduced zone represents primary mineralization that was transformed by an advancing flow of the same mineralizing fluids which formed the Rote Fäule. Secondary mineralization overprinted primary mineralization and is also present in fault zones and associated tectonic deformations that cut through the mineralization of the first stage. Secondary mineralization in fault zones occurs in the form of microbreccia, impregnations, fillings of cataclastic fractures of the primary ore minerals, irregular nests, lenticular bodies, aggregates and veinlets. Close relationships with tectonic deformation imply that the secondary mineralization is a result of tectonically-controlled late-stage fluid action. Established faults and fractures formed due to extensional stage strain developed in the Permian-Mesozoic basin (presumably during middle Triassic-Lower Cretaceous tectonics), which then were compressively reactivated between Upper Cretaceous and Paleogene during inversion of the basin (Dumicz and Don 1977; Salski 1975, 1977; Jowett 1987; Markiewicz 2007). It is constrained by a tectonic increase in the thickness of the strata in zones of compressional deformations such as thin-skinned thrusts and folds. Following their formation, the ore bodies underwent tectonic deformation and, as a result, became a source of metals for the formation of secondary mineralization, occurring in the immediate vicinity of fault zones and other tectonic structures.

In summary, the distribution of oxidized zones determines the position of the ore body, both vertically and laterally, while the tectonic deformations did not have a significant impact on the formation of primary ore mineralization, but caused its partial remobilization and precipitation in the form of secondary mineral phases. Fluids which mineralized faults and fractures did not carry only remobilized metals from the primary mineralization, but also could carry elements from extrinsic sources, which is indicated by the supply of As and Sb in the form of a tennantite and tetrahedrite enrichments.

Acknowledgements

The main support was provided by PGI-NRI, Grant no. 61.2605.1401.00.0. The authors thank KGHM P.M. S.A. for access to mines and enabling to carried out research.

References

Chmielewski A (2014) Characteristic of relict mineralization in the northern part of Radwanice copper field (SW part of Lubin-Sieroszowice deposit). Biul Państw Inst Geol 458:1–24

Chmielewski A, Oszczepalski S, Speczik S (2015) Relict mineralization in the transition zone, Kupferschiefer series of SW Poland. In: Andre-Mayer A.S et al. (ed.) Mineral resources in a sustainable world. Proceedings 5:1897-1900. GeoRessources, Universite de Lorraine

Chmielewski, A, Oszczepalski S, Głuszyński A, Kuczak A (2018) Variability of ore mineralization in the vicinity of fault zones in the Radwanice-Gaworzyce copper-silver deposit. Petrology in narrow and wide perspective: 25 years of Sessions of the Petrology Group of the Mineralogical Society of Poland. Brunów 2018. Mineralogia – Special Papers 48:39

Dumicz M, Don J (1977) Analysis of the structure of the Fore-Sudetic Monocline in the area of Polkowice.. Acta Univ Wratisl, Prace Geol.-Min 6(378):279–302

Jowett EC (1987) Formation of sulphide-calcite veinlets in the Kupferschiefer Cu-Ag deposits in Poland by natural hydrofracturing during basin subsidence. Jour Geol 95:513-526

Kłapciński J, Konstantynowicz E, Salski W, Kienig E, Preidl M, Dubiński K, Drozdowski S (1984) Atlas obszaru miedzionośnego (monoklina przedsudecka). Wydawnictwo „Śląsk". Katowice

Markiewicz A (2007) Surveying the tectonics of the Lubin-Sieroszowice deposit during its management. Biul Państw Inst Geol 423:151-172

Oszczepalski S (1994) Oxidative alteration of the Kupferschiefer in Poland: oxide-sulphide parageneses and implications for ore-forming models. Geol Quart 38:651–672.

Oszczepalski S (1999) Origin of the Kupferschiefer polymetallic mineralization in Poland. Miner Deposita 34:651–672

Oszczepalski S (2007) Au-Pt-Pd mineralization in the Zechstein Kupferschiefer series on the reserved areas for copper mining. Biul Państw Inst Geol 423:109-124

Oszczepalski S, Chmielewski A (2015) Predicted metallic resources in Poland presented on the prospective maps at scale 1 : 200 000 – copper, silver, gold, platinum and palladium in the Kupferschiefer ore series. Przegl Geol 63:534-545

Oszczepalski S, Nowak G.J, Bechtel A, Žák K (2002) Evidence of oxidation of the Kupferschiefer in the Lubin- Sieroszowice deposit: implications for Cu-Ag and Au-Pt-Pd mineralisation. Geol Quart 46:1–23

Rydzewski A (1978) Oxidated facies of the Zechstein copper-bearing shale in the Fore-Sudetic Monocline. Przeg Geol 26:102–108

Salski W (1975) Tectonics in the Lubin area. Warszawa, Biul Inst Geol 287:61–198

Salski W (1977) Tectonic development in the area between Lubin and Sieroszowice. Kraków, Rocznik Pol Tow Geol 46: 27–48

Speczik S (1995) The Kupferschiefer mineralization of Central Europe: New aspects and major areas of future research. Ore Geol Rev 9:411–426

New gold amalgams from a Kupferschiefer type deposit, Sieroszowice Mine, Poland

Jadwiga Pieczonka, Adam Piestrzyński, Władysław Zygo
AGH-University of Science and Technology, Faculty of Geology, Geophysics and Environmental Protection, Krakow, Poland

Ariel Wojciuszkiewicz
KGHM PM S.A., ZG Polkowice-Sieroszowice, Kazimierzow, Poland

Abstract. Several gold-silver amalgams were identified within the zone characterized by the secondary oxidation profile in sandstone (Weissliegend) and elevated gold concentration. Tetra-auricupride, native gold of high purity, bornite, Se-bearing chalcopyrite and coffinite have been identified in intergrowths with the amalgams. WDS analyses show variable content of major elements in amalgams. The Ag content ranges from 20.79 to 37.90 wt%, gold: from 41.69 to 66.80 wt% and Hg: 10.29 to 19.93wt%. This data does not fit to the described literature phases.

1 Introduction

The Kupferschiefer copper-silver deposit was described in over 600 papers and books (e.g. Kucha and Pawlikowski 1986; Vaughan et al. 1989; Piestrzyński et al. 1996; Piestrzyński 2008; Borg et al. 2012). The mineralogy of this deposit was described in detail by Pieczonka and Piestrzyński, (2000, 2006), Pieczonka et al. (2006, 2007), Pieczonka (2011). In general, sulfide copper mineralization transgresses all sediments close to the Lower-Upper Permian border. The Kupferschiefer organic shale contains the highest metal concentrations, however the Permian Weissliegende sandstone, that overlies Rotliegende sandstone, hosts the biggest Cu-Ag reserves.

The first discovery of gold in the Lubin deposit took place in 1973 (Kucha 1974). Therefore, gold deposit was discovered in 1994 during routine mineralogical study (Piestrzyński et al. 1996, 2002). Ag-amalgams are very common in the ore horizon. Gold amalgams are discovered for the first time in this deposit, and are related to the barren sections.

2 Geological setting

The gold deposit is located in a continuous, thin horizon with an average thickness of 0.22 m (0.05 to 2 m), showing an average content of 2.25 ppm Au, 0.14 ppm Pt and 0.08 ppm Pd and characterized by low copper and organic matter contents (Piestrzyński et al. 2002). Pt and Pd also occur out of the gold horizon.

Gold deposit was found in secondary oxidized sections of the copper deposit (Piestrzyński et al. 1996, 2002; Piestrzyński and Pieczonka 1998; Pieczonka et al. 2008; Speczik et al. 1997). In the literature exists several common opinions about the genesis of the oxidation facies, but only a secondary oxidation system (SOS) is related to the gold deposit. The horizontal shape of the SOS is a paraconformity (Fig. 1) to the sedimentary strata and it was classified as epigenetic (Pieczonka and Piestrzyński 2000, 2008; Piestrzyński et al. 2002; Pieczonka et al. 2008). An average content of gold in the Kupferschiefer horizon is 5.78 ppb only. It is not enough to be a source for the gold deposit.

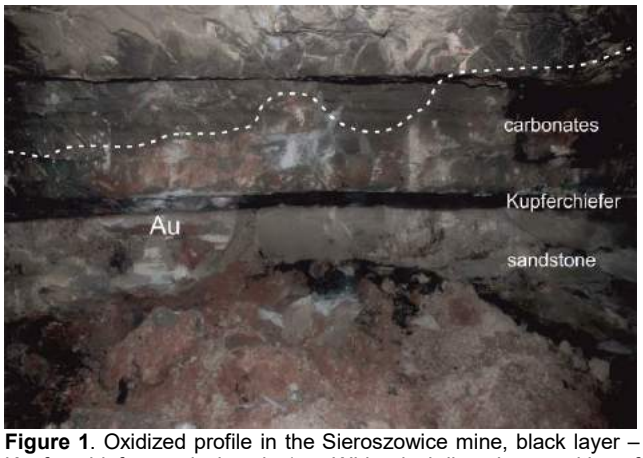

Figure 1. Oxidized profile in the Sieroszowice mine, black layer – Kupferschiefer, vertical scale 1 m. White dash line show position of SOS.

Typical black Kupferschiefer is discolored in the contact with the SOS and becomes a maroon variety. The maroon type of the Kupferschiefer is characterized by a high content of Fe_2O_3 presence of coarse-grained hydrothermal hematite and gold (Piestrzyński et al. 2002),

Two factors control the position of the gold horizon: the redox barrier, which is usually independent of sedimentary textures, and the micro tectonic system (Fig. 2), that is not easy for documentation, especially within the sandstone sections (Pieczonka, Piestrzyński 2011).

The copper mineralization is oxidized and transported away to the more reducing surrounding environment. Copper-enriched zones surround the areas affected with the SOS.

Gold was transported in thiosulphate complexes $\{Au(S_2O_3)_2^{-3}\}$ (Piestrzyński 2008; Piestrzyński and Wodzicki 2000). The system is enriched in trivalent iron. It also suggests that gold was transported in complexes of $(FeAu)(S_2O_3)_2^{-1}$ (Pieczonka et al. 2008).

3 Analytical methods

Quantitative WDS analyses were carried out in the Critical Elements Laboratory of the Faculty of Geology, Geophysics and Environmental Protection, AGH-UST Cracow using a JEOL SQ8200 microprobe (EMP).

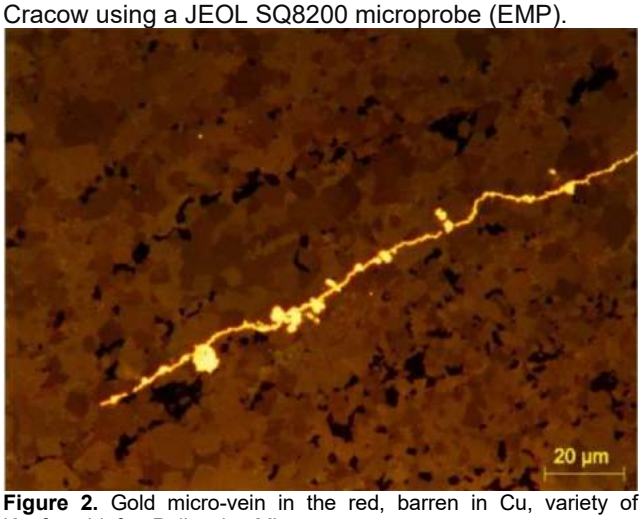

Figure 2. Gold micro-vein in the red, barren in Cu, variety of Kupferschiefer, Polkowice Mine.

The analyses were carried out at an accelerating voltage of 20 kV, and a probe current of 40 nA, with a focused beam diameter of 1 µm. The following standards and measurement lines have been used: SKα, FeKα (Pyrite), AgLα (100 %), CuKα ($CuFeS_2$), SbLα (Sb_2S_3), AuMα (100%), HgMα (HgSe), AsLα (As_2S_3), SeLα (PbSe) Counting times peak/background (in sec.) were as follow 10/5. Original Jeol ZAF procedures were used for a final correction of all measured elements.

4 Gold – mercury mineralogy

Several small grains of amalgams intergrowing with tetra-auricupride (AuCu), native gold of high purity and copper sulphides were identified (Fig. 3). Au-Ag amalgams have been recognized in the uppermost part of Weissliegend sandstone (Fig. 1). Aggregates are up to 100 µm in size and are located in sandstone cement. Au-Ag-Hg alloys formed complicated intergrowths, which can be well recognized on the WDS BSE image (Fig. 4) Major element distributions in amalgams are easily visible in WDS contour maps (Fig. 5, 6, 7, 8, 9, 10). EDS observation revealed also uranium silicate (coffinite) which is occurring in form of thin, around on 3-5 µm thick bands well visible on contour map (Fig. 9). The position of coffinite suggests its early precipitation from the solution containing silica.

WDS composition confirmed presence of tetra-auricupride and mineral phases characterized with different grey colors well visible on Figure 4. Quantitative WDS measurement (Tab. 1) showed variation in chemical composition all analyzed points. Only tetra-auricupride show stoichiometric composition. Within the Au-Ag amalgams at least three different phases can be recognized. Gold varies from 41.69 wt% up to 66.80 wt%. Silver varies from 20.79 wt% up to 37.90 wt%. Finally mercury concentration varies from 7.90 up to 37.90 wt% (Tab. 1). One analytical point shows also 11.00 wt% of copper (Tab. 1). Almost all points reveal small admixtures of iron. Whole investigated area shows also contamination with selenium (Fig. 10). Some visible hot spots on Se map (Fig. 10) belongs to selenides.

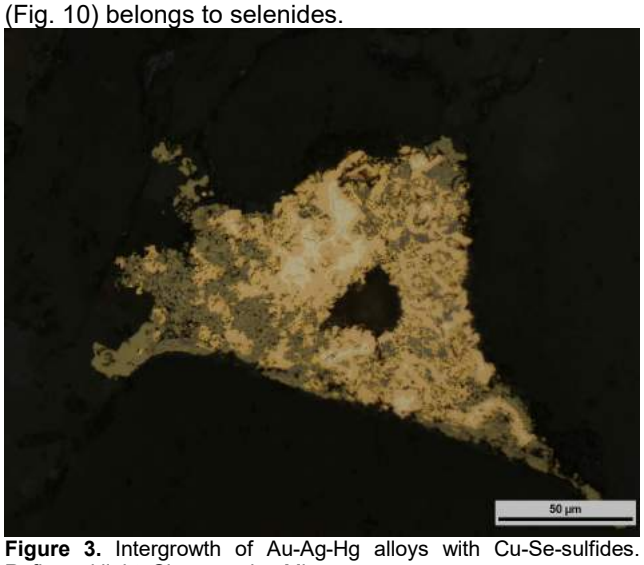

Figure 3. Intergrowth of Au-Ag-Hg alloys with Cu-Se-sulfides. Reflected light, Sieroszowice Mine.

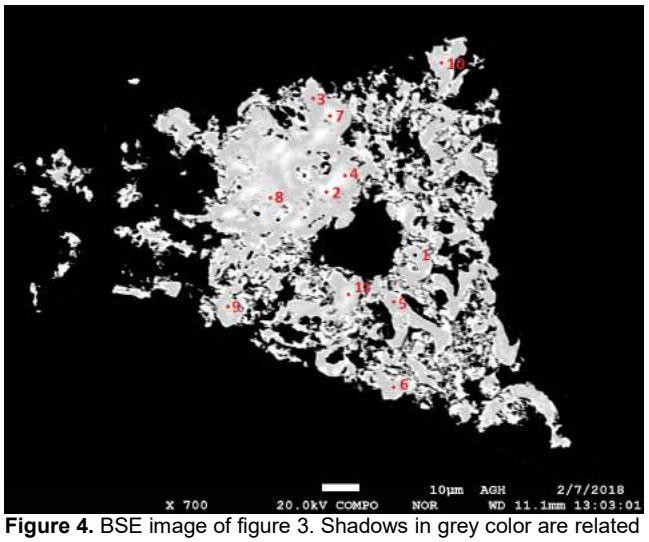

Figure 4. BSE image of figure 3. Shadows in grey color are related to the different concentration of Au, Ag, Hg and Cu. 1-11- point of WDS analyses.

Table 1. WDS composition of amalgams and tetra-auricupride in wt%, analytical points (in red) are mark on figure 4

No.	Ag	Hg	Fe	Au	Cu	Total	Mineral
1	1.01	0.51	0.06	75.63	24.09	101.3	Tetra-auricupride
2	20.79	10.85	0.00	66.80	0.91	99.4	Au-Ag-amalgams
3	0.04	0.26	0.05	76.18	24.33	100.9	Tetra-auricupride
4	34.92	17.68	0.01	46.64	1.15	100.4	Au-Ag-amalgams
5	0.51	0.19	0.07	76.00	24.16	100.9	Tetra-auricupride
6	20.61	7.90	0.06	63.09	11.00	102.7	Au-Ag-Cu-amal.
7	23.51	10.29	0.03	63.25	1.40	98.1	Au-Ag-amalgams
8	33.05	15.63	0.00	49.54	0.96	99.2	Au-Ag-amalgams
9	37.90	19.93	0.02	41.69	1.25	100.8	Au-Ag-amalgams
10	36.18	14.95	0.02	48.73	1.13	101.0	Au-Ag-amalgams
11	27.07	10.72	0.00	61.00	1.62	100.4	Au-Ag-amalgams

Pb, Se- sought but not detected

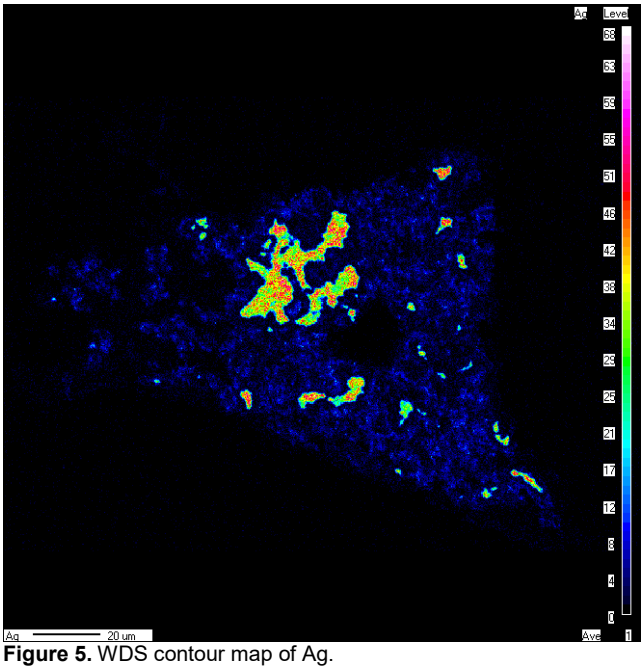

Figure 5. WDS contour map of Ag.

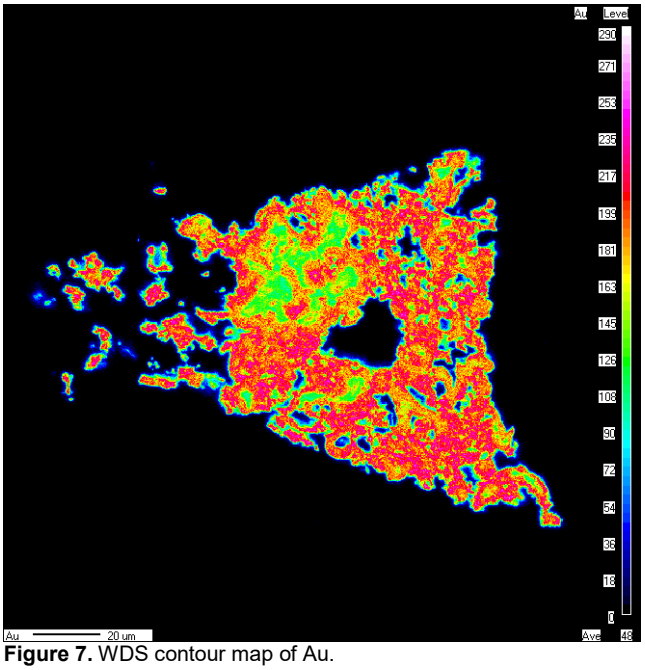

Figure 7. WDS contour map of Au.

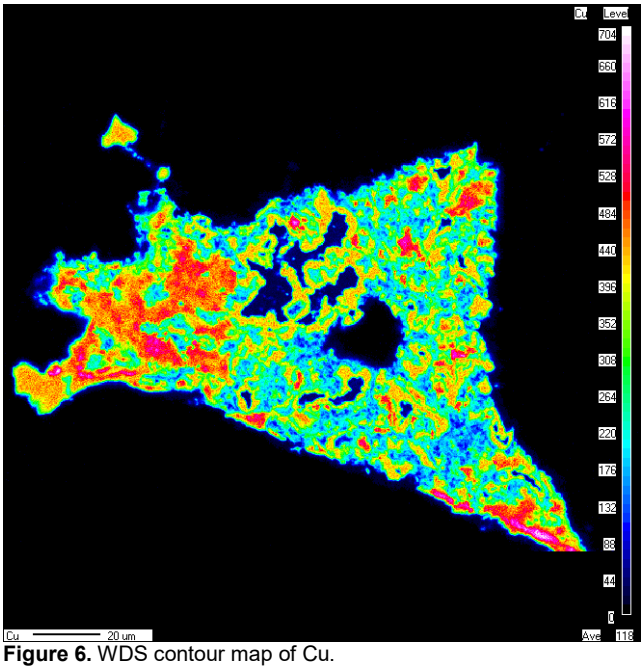

Figure 6. WDS contour map of Cu.

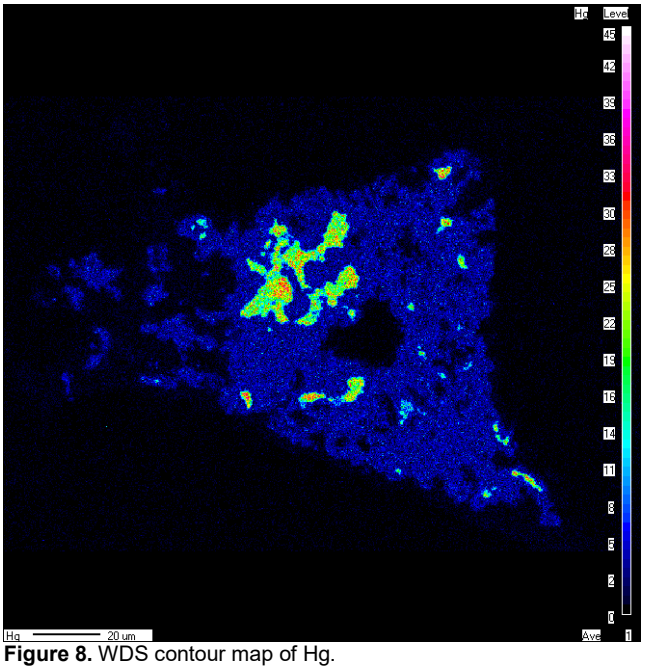

Figure 8. WDS contour map of Hg.

In the zone with Au-Ag amalgams the analyzed sulfides show elevated amounts of selenium, reaching a maximum 10 wt%. This problem, as well as the presence of uranium, requires further investigation.

5 Discussion and conclusions

From the group of amalgams presence of three different alloys can be pointed out. To the first group belongs phases containing low amounts of silver. Their atomic proportions are as follow: $Au_{1.000}Ag_{0.568\text{-}0.810}Cu_{0.042\text{-}0.082}Hg_{0.159\text{-}0.173}$. The next group is representing by a phase containing high amounts of silver: $Au_{1.000}Ag_{1.166\text{-}1.367}Cu_{0.060\text{-}0.093}Hg_{0.301\text{-}0.470}$. Finally one point has high copper content. Its atomic proportions are as follow: $Au_{1.000}(Ag_{0.596}Cu_{0.540})_{1.137}Hg_{0.122}$. Taking into account concentration of major elements and atomic proportions it can be concluded that a new line of Au-Ag-Cu-Hg alloys have been documented. These minerals are related to the secondary oxidation system developed on the redox low temperature barrier. Ag-amalgams are very common in the ore horizon and together with native Ag and silver substitutions in the major copper sulphides give high Ag content in the ore, copper concentrate and SX-EW products. Gold and Au-amalgams are occurring in the foot wall of the economic copper zone, mostly in the uppermost of the secondary oxidized section. During the intensive copper ores production only a small

volume of rocks containing enrichments in gold are mined out together with copper ores. Usually so called transition zone containing low grade copper ore and elevated amounts of gold (Piestrzyński et al. 1996; Piestrzyński and Wodzicki 2000) is extracted. Dilution of the copper ores is on the level of 7 – 15%.

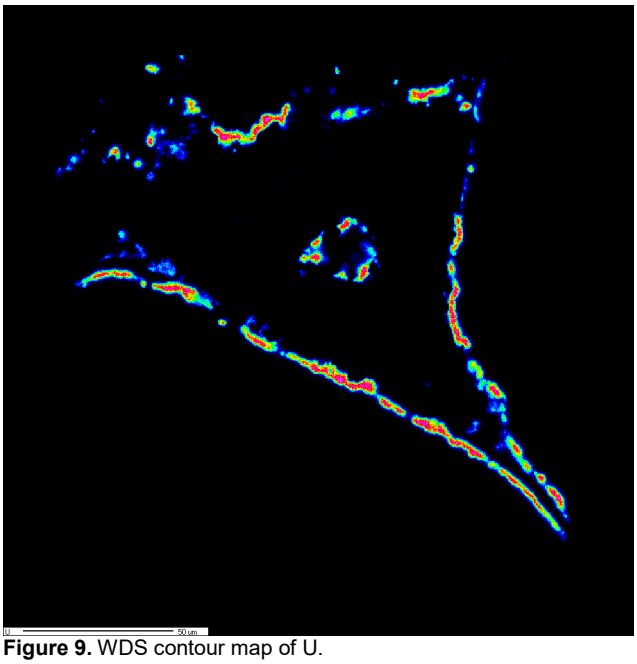

Figure 9. WDS contour map of U.

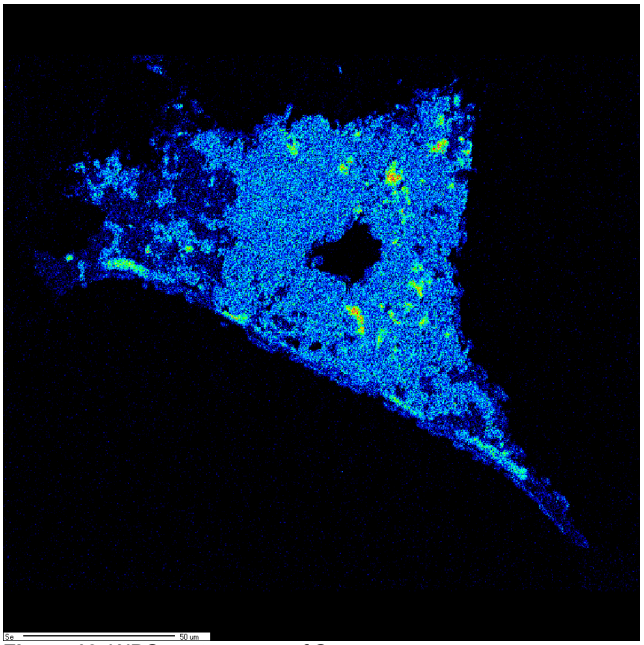

Figure 10. WDS contour map of Se.

Acknowledgements

Authors are thankful for the financial support from AGH-UST grant no. 16.16.140.315 and MSc Eng. Gabriela Budzyń-Kozub for WDS analyses.

References

Borg G, Piestrzyński A, Bachman GH, Puttmann W, Walther S, Fidler M (2012) An overview of the European Kupferschiefer deposits. SEG Special Publication 16:455-486

Kucha H (1974) Native gold in copper deposit on Fore-Sudetic Monocline. Rudy i Metale Nieżelazne. 4: 174-175 (in Polish)

Kucha H, Pawlikowski M (1986) Two-brine model of genesis of strata bound Zechstein deposits (Kupferschiefer- type), Poland. Miner Deposita 21:70–80.

Pieczonka J (2011) Factor controlling distribution of ore minerals within copper deposit, Fore-Sudetic Monocline, SW Poland. Wydawnictwa AGH (in Polish)

Pieczonka J, Piestrzyński A (2000) Genetic model of the gold concentration in the area of copper deposit, Fore-Sudetic Monocline. Mineralogia Polonica, Special Papers 16:55-195 (in Polish)

Pieczonka J, Piestrzyński A (2006) Ore minerals and their significance for genesis of copper deposit, Fore-Sudetic monocline, SW Poland (in Polish). Mineral Resources Management 22, special papers 3:187-202.

Pieczonka J, Piestrzyński A (2008) Mineralogy and geochemistry of ore minerals from secondary oxidized zones. In: Pieczonka et al. 2008: The red-bed-type precious metal deposit in the Sieroszowice-Polkowice copper mining district, SW Poland. Annales Societatis Geologorum Poloniae 78/ 3:195-241

Pieczonka J, Piestrzyński A (2011) Gold and other precious metals in copper deposit, Lubin-Sieroszowice district, SW Poland. In: Gold in Poland, A Kozlowski, S Mikulski eds, Archivum Mineralogiae Mongraph 2:135-152

Piestrzyński A, Pieczonka J, Głuszek A (2002) Redbed-type gold mineralisation, Kupferschiefer, south-west Poland. Miner Deposita 37:512-528.

Pieczonka J, Piestrzyński A, Sawłowicz Z (2007) The sediment-hosted copper-silver deposits in the Lubin-Głogów mining district (Poland). In: Digging Deeper, Proceedings of the ninth Biennial SGA Meeting, Dublin 2007:7-45

Pieczonka J, Więcław D, Kotarba M, Piestrzyński A (2006) Forms of organic matter and mineralization in Kupferschiefer. Lubin-Sieroszowice deposit, SW Poland. In: Understanding the genesis of ore deposits to meet the demands of the 21st century. 12th Quadrennial IAGOD Symposium: 284-287

Pieczonka J, Piestrzyński A, Mucha J, Kotarba M, Głuszek A, Więcław D (2008) The red-bed type precious metals deposit in the Sieroszowice-Polkowice copper mining district, SW Poland. Annale Societatis Geologorum Poloniae 78/3:151-274

Piestrzyński A (2008) Genesis of the deposit. In: Piestrzyński A. (ed.), Monography of KGHM Polska Miedź S.A. Alexim, Wrocław, 228-244 (in Polish)

Piestrzyński A, Pieczonka J (1998) Tetraauricupride from the Kupferschiefer type deposit, SW Poland - the first occurrence. Mineralogia Polonica 29/1:11-18.

Piestrzyński A, Wodzicki A (2000) Origin of the gold deposit in the Polkowice-West Mine, Lubin-Sieroszowice Mining District, Poland. Miner Deposita 35/1:37-47.

Piestrzyński A, Wodzicki A, Banaszak A (1996) Gold in the copper deposit, Fore-Sudetic Monocline. Przegląd Geologiczny 11:1098-1102 (in Polish)

Speczik S, Rydzewski A, Oszczepalski S, Piestrzyński A (1997) Exploration for Cu-Pt-Pd Kupferschiefer type deposits in SW Poland. In: Mineral Deposits: Research and Exploration, Heikki Papunen ed., Turku: 119-122

Vaughan DJ, Sweeney M, Diedle GFR, Harańczyk C (1989) The Kupferschiefer: an overview with an appraisal of the different types of mineralization. Economic Geology 84:1003-1927

New insights into growth history of chimney conduits and local native gold enrichment from a hydrothermal chimney (Manus Basin, PNG)

Si-Yu Hu, Stephen J. Barnes, Anais Pagès, Michael Verrall, Louise Schoneveld, Joanna Parr, Ray Binns
CSIRO Mineral Resources

Zakaria Quadir
John de Laeter Centre, Curtin University

Abstract. Seafloor hydrothermal chimneys from back-arc basins are important hosts for metals, e.g. Cu, Zn, Pb, Ag and Au, and bear potential for deep-sea mining. A solid understanding of the distribution of metals requires an appreciation of detailed mineralogy and chimney growth histories. This study reports the first submicron scale investigation of mineralogy and microstructures of a chalcopyrite-lined conduit wall of a multi-conduit hydrothermal chimney from the PACMANUS hydrothermal field (eastern Manus basin, Papua New Guinea). New observations reveal that the conduits are dominated by thick chalcopyrite walls with bi-directional growth (towards and away from the conduit) which is bounded by a thin layer dominated by fine-grained (< 1 μm) sphalerite. Clustered pyrite grows outwards from the sphalerite substrate. The mineralogy reflects a detailed process of the early growth of chimneys during the initial mixing between hydrothermal fluids and seawater. Late-stage sphalerite and barite then overgrew the conduits at the waning stage. Four types of native gold are observed within the conduit walls, three of which are associated with the sphalerite-rich layer and have not previously been reported. Native gold is interpreted to have precipitated from various mechanisms. This study bears important potential for searching for native gold in fossil hydrothermal chimneys.

1 Introduction

Modern hydrothermal sulfide chimneys, formed due to the rapid mixing between hot hydrothermal fluids and cold seawater (Haymon 1983), have been discovered on the seafloor in various geologic settings, including oceanic spreading ridges in a number of oceanic basins (German and Seyfried 2014). Those from back-arc basins are important hosts for precious metals, such as Au and Ag, as well as other commodities, such as Cu, Zn and Pb (Binns and Scott 1993; Herzig et al. 1993; Herzig and Hannington 1995). The hydrothermal fields in the Manus Basin in particular have attracted interest as potential targets for deep sea mining (Gena 2013). Previous studies have shown that the mineralogy of chimneys at micron-scale is complex; individual minerals within the same zone present various morphologies and were formed under variable physicochemical conditions (Kristall et al. 2011; Berkenbosch et al. 2012). However, so far, there have been relatively few studies investigating the micron to submicron scale mineralogy of sulfide chimneys (e.g. Hu et al. 2019). The characterization of minerals at such small scale is essential to provide detailed information about the microenvironments and a basis for understanding the role of sulfides in controlling the enrichment of precious metals (Kristall et al. 2011).

In this study, we performed the first detailed microstructural investigations of Au-rich chalcopyrite-lined conduits from mm to nm scale to decipher the mineral associations and deposition sequence in the conduits, re-construct the detailed growth processes of conduits and assess their roles in facilitating native gold deposition.

2 Geological setting and studied chimney

The Manus Basin is an extensional back-arc basin, located in the Bismarck Sea, Papua New Guinea (Fig. 1). A series of spreading centers and transform faults are developed in the basin due to the subduction of the Solomon plate under the Bismarck plate along the New Britain Trench. The back-arc extension in the eastern Manus basin (EMB) is developed in the remnant island-arc crust which has formed during the previous subduction along the Manus Trench (Binns and Scott 1993). The volcanic zone in the EMB is located between the Djual and Weitin transform faults, and develops east-west en echelon neovolcanic ridges and domes (Binns et al. 2007). The volcanic edifices are aligned in a northeast direction, normal to the extension direction,

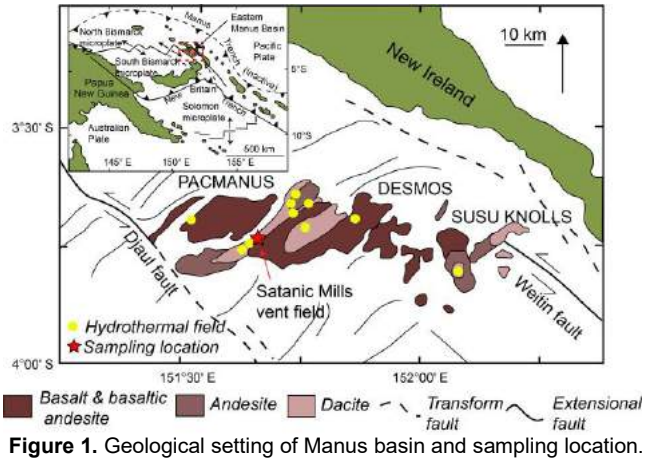

Figure 1. Geological setting of Manus basin and sampling location. Modified from Binns et al. (2007).

and the composition varies from basalt to dacite-rhyodacite. The active volcanic activity has resulted in the occurrence of numerous hydrothermal fields, i.e. PACMANUS (Binns 2014), Desmos (Seewald et al. 2015) and SuSu Knolls (Yeats et al. 2014), and has produced a large number of Cu-Zn-Pb-Ag-Au rich seafloor deposits (Binns and Scott 1993; Yeats et al. 2014).

The analyzed sample is part of a polymetallic chimney fragment with multiple conduits (CSIRO ID: 118584) which has been described in detail by Hu et al. (2019) and in the PACMANUS Memoir (P2+) (Binns et al. 2002). This sample is characterized by multiple sub-parallel chalcopyrite-lined conduits which are surrounded by a chalcopyrite-sphalerite transition zone and further rimmed by a sphalerite-dominated outer zone with variable barite (Fig. 2) (Hu et al. 2019). A cm-scale sub-sample was taken from a part of the chimney containing multiple chalcopyrite-lined channels.

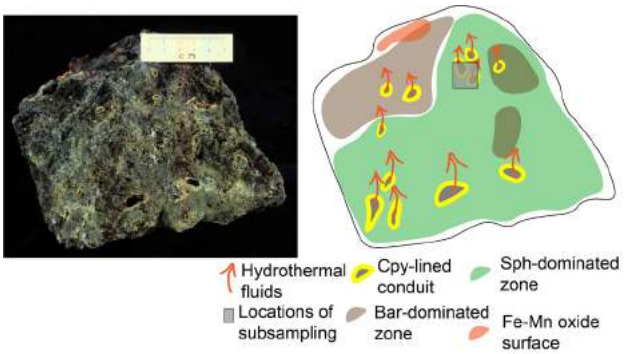

Figure 2. Photograph (left) and sketch diagram (right) of the chimney sample showing the distribution of chalcopyrite (Cpy), sphalerite (Sph), barite (Bar) and Fe-Mn oxide surface. The location of sub-sample is indicated in the sketch diagram with the grey rectangle. Modified from Hu et al. (2019).

3 Mineralogy and paragenesis

This sub-sample includes four small conduits. Each conduit has its wall lined with coarse-grained chalcopyrite, completely or partly overgrown by late-stage coarse-grained sphalerite (as Sp 1). Chalcopyrite can be separated into two groups (Ccp 1 and Ccp 2), which are characterized by inward-directed growth into the conduit, and outward-directed growth in opposite directions, respectively.

Conduit 1 is described in detail as it includes all types of observed native gold and exemplifies the critical features of all other conduits. To better illustrate these features, conduit 1 is further divided into region 1, 2, and 3 based on the various distribution of clustered pyrite and late-stage Sp 1. From higher magnification observations, the conduit can be also divided into four distinguishable zones from the inner to the outer part of the conduit. The detailed associations are illustrated in figure 4 and table 1.

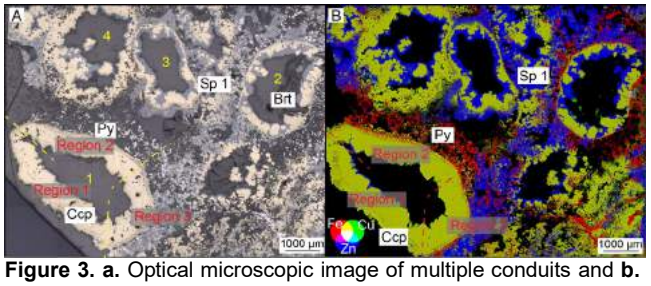

Figure 3. a. Optical microscopic image of multiple conduits and **b.** Corresponding SXFM RGB image showing the distribution of sulfides (chalcopyrite-Ccp), pyrite-Py, and sphalerite-Sp) and barite (Brt).

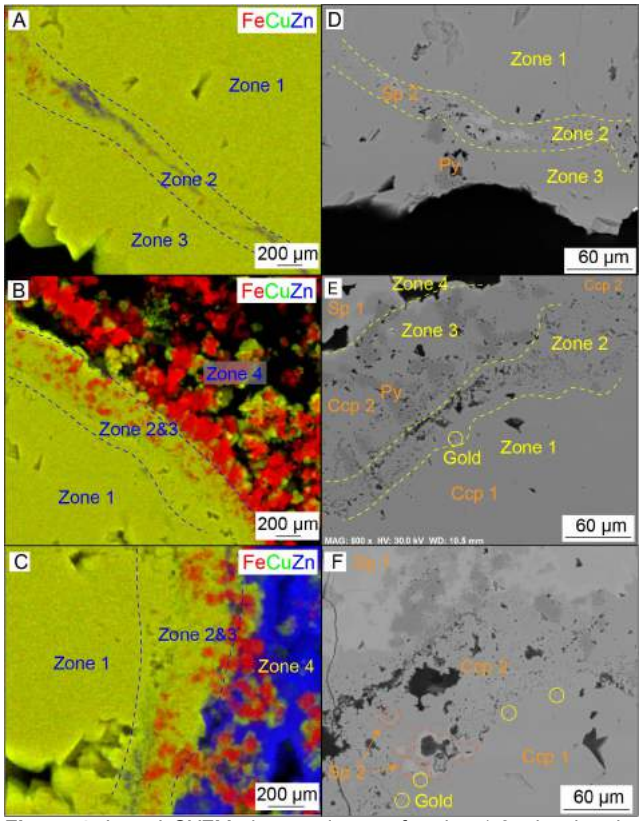

Figure 4. (a., c.) SXFM elemental map of region 1-3, showing the distribution of chalcopyrite (Ccp) in yellow, pyrite (Py) in red and sphalerite (Sp) in blue, in region 1, 2 & 3, respectively. (**d., f.**) SEM-BSE observations of region 1 **(d.)** and 3 (**e., f.).** In region 1, zone 2 includes patches of sphalerite, euhedral pyrite and native gold. In region 3, zone 2 is porous and includes native gold and few sphalerite.

Based on the petrographic observations, the chimney conduits are proposed to grow in four stages (Fig. 5): 1) the development of an initial sphalerite thin wall, then 2) the accumulation of disseminated euhedral pyrite, followed by 3) the bi-directional overgrowth of chalcopyrite and 4) the late-stage precipitation of sphalerite and barite.

Table 1. Mineralogical associations in zones and regions. Ccp: chalcopyrite; Py: pyrite; Sp: sphalerite.

Zone	Mineralogy	Region 1	Region 2	Region 3
Zone 1	Coarse-grained Ccp1			
Zone 2	Sp 2, gold-rich, porous	Large Sp 2 patches; least porous		Almost no Sp 2; most porous
Zone 3	Euhedral Py overgrown by Ccp 2	Thickest		Thinnest
Zone 4	Disseminated Py overgrown by Ccp 2 and Sp 1		Without Sp 1	
Degrees of hydrothermal fluid-seawater mixing		Least	Moderate	Most
Other observations				Dissolution and re-precipitation

4 Native gold

Four types of native gold are observed within the conduit walls, three of which are associated with the sphalerite-rich layer in zone 2. Type 1 gold is associated with tennantite-tetrahedrite solid solution series within chalcopyrite, an association which is likely due to high sulfur activity when hydrothermal fluids mixed with seawater. Type 2 gold occurs at the contacts between early stage sphalerite-chalcopyrite transitions. This enrichment in native gold is attributed to the replacement of Au-rich sphalerite by chalcopyrite. Pyrite is rimmed by type 3 gold, probably resulting from the temperature decreasing during hydrothermal fluid-seawater mixing. Type 4 gold occurs in the cavities which are in the vicinity of dissolution-re-precipitation boundaries of chalcopyrite and is proposed to have re-precipitated from the dissolution of Au-bearing sphalerite.

5 Comparison to fossil chimney conduits

A similar chimney conduit has been found in the Silurian volcanic-host massive sulfide deposit, reported by Maslennikov et al. (2009). It is a well preserved fossil conduit, dominated by chalcopyrite and pyrite. From the inner to outer zone, the conduit includes coarse-grained Ccp 2, drusy chalcopyrite with sphalerite inclusions, and euhedral pyrite cemented by Ccp 1 (see Maslennikov et al. 2009), which are thought to correspond to zone 1, 2 and 3 in this study, respectively. Native gold was not observed by Maslennikov et al. (2009), and this might be due to the optical observations being conducted at ~ 100 microns scale. However, LA-ICP-MS data in that study has shown that the sphalerite layer includes high Au contents, an association which was interpreted to result from a fast precipitation of Au with sulfides directly from hydrothermal fluids. Due to the striking similarity in sulfide distributions between the fossil chimney and the

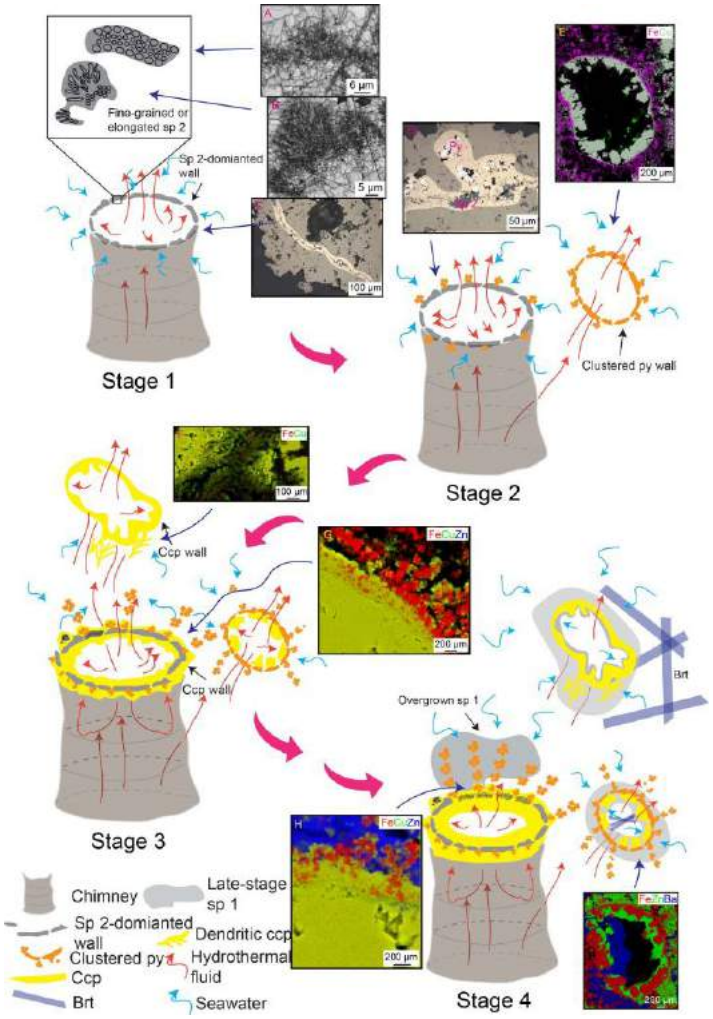

Figure 5. The four stages of formation of chimney conduits. Ccp: chalcopyrite; Py: pyrite; Sp: sphalerite; Brt: barite.

studied modern chimney, we propose that the high content of Au associated with sphalerite could be attributed to the occurrence of native Au nanoparticles, and either due to the high sulfur activity of hydrothermal fluids or the temperature decrease during hydrothermal fluid-seawater mixing, or dissolution and re-precipitation. Therefore, the comparison between similar conduits in fossil and modern chimneys provides new insights into the deposition mechanism of gold in sea-floor chimneys.

Acknowledgements

The authors would like to acknowledge the support for SXFM work, which was undertaken on the X-ray fluorescence microscopy beamline at the Australian Synchrotron (Proposal 12589), part of Australia's Nuclear Science and Technology Organization (ANSTO). Dr Chris Ryan and Dr David Paterson are acknowledged for the assistance during data collection. S.H. and S.B. acknowledges the Research-plus postdoctoral fellowship funded by the Commonwealth Science and Industry Research Organization (CSIRO).

References

Berkenbosch HA, De Ronde CEJ, Gemmell JB, McNeill AW, Goemann K (2012) Mineralogy and formation of black smoker chimneys from brothers submarine volcano, Kermadec Arc. Econ Geol 107:1613–1633.

Binns RA (2014) Bikpela: A large siliceous chimney from the PACMANUS hydrothermal field, Manus basin, Papua New Guinea. Econ Geol 109:2243–2259.

Binns RA, Barriga FJ, Miller DJ (2007) Leg 193 Synthesis: Anatomy of an active felsic-hosted hydrothermal system, Eastern Manus Basin, Papua New Guinea. Proc Ocean Drill Program, Sci Results 193:1–71.

Binns RA, Scott SD (1993) Actively forming polymetallic sulfide deposits associated with felsic volcanic rocks in the Eastern Manus Back-Arc Basin, Papua New Guinea. Econ Geol 88:2226–2236.

Gena K (2013) Deep Sea Mining of Submarine Hydrothermal Deposits and its Possible Environmental Impact in Manus Basin, Papua New Guinea. Procedia Earth Planet Sci 6:226–233.

German CR, Seyfried WE (2014) Hydrothermal Processes. 2nd ed., Elsevier Ltd.

Haymon RM (1983) Growth history of hydrothermal black smoker chimneys. Nature 301:695–698.

Herzig PM, Hannington MD (1995) Polymetallic massive sulfides at the modern seafloor, a review. Ore Geol Rev 10:95–115.

Herzig PM, Hannington MD, Fouquet Y, Von Stackelberg U, Petersen S. (1993) Gold-rich polymetallic sulfides from the lau back arc and implications for the geochemistry of gold in sea-floor hydrothermal systems of the Southwest Pacific. Econ Geol 88:2182–2209.

Hu SY, Barnes SJ, Glenn AM, Pagès A, Parr J, MacRae C, Binns R (2019) Growth History of Sphalerite in a Modern Sea Floor Hydrothermal Chimney Revealed by Electron Backscattered Diffraction. Econ Geol 114:165–176.

Kristall B, Nielsen D, Hannington MD, Kelley DS, Delaney JR (2011) Chemical microenvironments within sulfide structures from the Mothra Hydrothermal Field: Evidence from high-resolution zoning of trace elements. Chem Geol 290:12–30.

Maslennikov V, Maslennikova S, Large RR and Danyushevsky LV (2009) Study of trace element zonation in vent chimneys from the Silurian Yaman-Kasy volcanic-hosted massive sulfide deposits (the southern Urals, Russia) using laser ablation inductively coupled plasma mass spectrometry (LA-ICP MS). Econ Geol 104:1111–1141.

Seewald JS, Reeves EP, Bach W, Saccocia PJ, Craddock PR, Shanks WC, Sylva SP, Pichler T, Rosner M, Walsh E (2015) Submarine venting of magmatic volatiles in the Eastern Manus Basin, Papua New Guinea. Geochim Cosmochim Acta 163:178–199.

Yeats CJ, Parr JM, Binns RA, Gemmell JB, Scott SD (2014) The SuSu Knolls hydrothermal field, Eastern Manus Basin, Papua New Guinea: An actively forming submarine high sulfidation copper-gold system. Econ Geol 109:2207–2226.

Accumulation of uranium in fossil and modern Fe-oxyhydroxide sediments of massive sulfide deposits

Nuriya R. Ayupova, Irina Yu. Melekestseva, Valeriy V. Maslennikov, Alexander S. Tselyiko, Elena V. Belogub
Institute of Mineralogy SU FRC MG UB RAS, South Ural University, Miass, Russia

Abstract. The ferruginous gossanites of the Yubileynoe VHMS deposit (South Urals) and Fe-oxyhydroxide gossans of the Ashadze-2 hydrothermal sulfide field (Mid-Atlantic Ridge) have high U contents (up to 73 ppm and 352 ppm, respectively). In gossanites, small (1–2 μm in size) round inclusions of uraninite, which locally coalesce to large grains up to 5 μm in size, are observed in authigenic chalcopyrite, as well as numerous fine uraninite particles (<2 μm in size) associated with apatite, V-rich Mg-chlorite and micronodules of pyrite and galena in a hematite–carbonate–quartz matrix. In gossans, isometric anhedral zonal uraninite grains (up to 2 μm in size) associated with pyrite, isocubanite, chalcopyrite, atacamite, and galena occur in Fe-hydroxides and sepiolite and are characterized by outer P-rich rim. It is suggested that similar processes of accumulation of uranium in ancient and modern Fe-rich sediments are caused by fixation of seawater-derived U during oxidation of sulfide minerals. Uraninite in gossanites was mostly deposited from pore diagenetic fluids, which circulated in hyaloclast–carbonate–sulfide sediments during Fe-oxide evolution and formation of authigenic sulfide mineralization via oxidation–reduction reactions.

1 Introduction

Despite a wealth of research on modern hydrothermal seafloor massive sulfide deposits and their ancient equivalents (volcanic-hosted massive sulfide/VHMS deposits), little attention has been paid to radioactive elements such as uranium. It is considered that hydrothermal fluids venting at the seafloor are depleted in U and consequently sulfides derived from these fluids are also U-poor (Hegner and Tatsumoto, 1987; Butler, Nesbitt, 1999; German et al., 2002). However Fe-oxyhydroxide sediments from modern massive sulfide hydrothermal field (gossans, cf. Hannington et al., 1988) are characterized by higher U concentrations (up to 20–30 ppm) (Hrischeva and Scott, 2007; Mills et al., 2004). The enrichment of U in these sediments has therefore been attributed to the fixation of seawater derived U during the oxidation of iron sulfides, possibly through microbially mediated reactions (Mills et al., 1994).

The high U concentration (up to 9.08 ppm) are revealed in the Fe-oxide products of submarine oxidation of sulfide ores (gossanites, cf. Maslennikov et al., 2012) in the Uralian VHMS deposits (Maslennikov et al., 2012) and this enrichment is related to the U-bearing (up to 22.59 ppm) pseudomorphic hematite after sulfide clasts and tube microfossils (Ayupova et al., 2017). In this paper, we describe the anomaly contents of U and find of uranium minerals in gossanites in the well preserved Yubileynoe VMS deposit from the South Urals and in gossans (precursor of ancient gossanites) of the Ashadze-2 hydrothermal field of the Mid-Atlantic Ridge. We have revealed the source of U for these rocks and the reasons for U enrichment and track its evolution from seawater to precipitation as a solid phase and further remobilization during postsedimentation processes.

The samples of gossanites and gossans were studied on an Olympus BX51 optical microscope and a VegaTescan SEM equipped with an EDAX (a 1-micron electron beam, 15 nA beam current, 20 kV accelerating voltage, and a counting time of 120 s for peak). The contents of elements were analyzed with classical chemical methods (major oxides) and on an Agilent HP4500 quadrupole ICP MS (trace elements).

2 Geological background

2.1 The Yubileynoe VMS deposit

The Yubileynoe VHMS deposit is situated in the Buribai VHMS region of the West Magnitogorsk zone, which is interpreted as a fore-arc region of incipient oceanic island arc (Herrington et al., 2005) (Fig. 1a). The host rocks are related to the basalt-boninite basement of bimodal mafic Baimak-Buribai succession. It hosts six ore bodies (Fig. 1b), which interpreted as a strongly eroded sulfide mounds (Maslennikov et al., 2013). The ores of the deposit contain 1.5 % Cu, 1 % Zn, and 44 % S. Total ore resources are more than 106 Mt.

Samples of gossanites were collected from the top of the ore body no. 2, which is being exploited by an open pit (Fig. 1c). In the lower part of the mound core, massive pyrite and disseminated chalcopyrite are major minerals. Locally, colloform pyrite ores with carbonates contain numerous fragments of pyritized tube worms. The pyrite-chalcopyrite-sphalerite- and pyrite-chalcopyrite clastic ores (coarse breccias cemented by carbonates and quartz and sulfide turbidites with fragments of paleohydrothermal smoker chimneys) occur at the top and flanks of the ore body (Maslennikov et al., 2013). Gossanites (hematite–carbonate–quartz rocks developed after clastic sulfides) form a discontinuous layer (up to 2–5 cm) at the top of clastic ores. Usually, there is a rhythmic alternation of gossanite with sulfide breccias and fine clastic pyrite-chalcopyrite layers exhibiting asymmetric load casts typical of gravitational mass flows. The gossanites show high contents (ppm, up to) of Cu (9666), Zn (1165), Pb (285), V (120), Ti (487), Se (40), and Te (146). The U

contents are 0.04–0.64 ppm in black smoker chimneys, 1.03–3.18 ppm in sulfide turbidites, and extremely variable from very low (1.77–7.28 ppm) to high (up to 73 ppm) contents in gossanites.

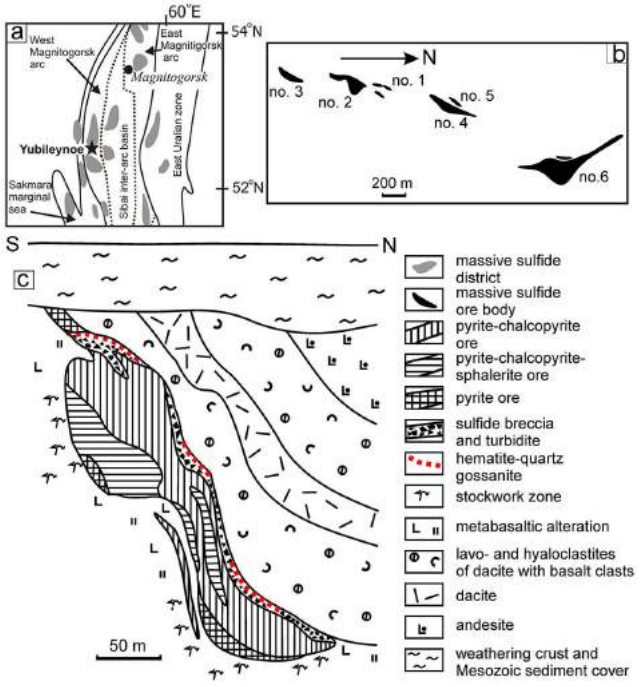

Figure 1. Location of the Yubileynoe VHMS deposit in paleotectonic zone of the South Urals (a), schematic position of ore bodies (b), and geological cross-section of the sulfide ore body no. 2 (c).

2.2 The Achadze-2 hydrothermal sulfide field

The Ashadze-2 hydrothermal field (12°99′ N, 44°91′ W) of the Mid-Atlantic Ridge is part of the Ashadze hydrothermal cluster, which consists of four hydrothermal fields located between the Fifteen Twenty and Marathon fracture zones (Fig. 2a). The Ashadze-2 hydrothermal field (discovered in 2003 by the Polar Marine Geosurvey Expedition, St. Petersburg, Russia) is located in the western wall of a rift valley, at a depth of 3100–3350 m (unpublished report of PGME, 2007; Cherkashev et al., 2013) and is associated with gabbros and ultramafic rocks (Beltenev et al., 2003). A high resolution (up to 30 cm) topographic survey in the Ashadze-2 field revealed a chain of hydrothermal mounds and a crater shaped structure 20–25 m in diameter and 1–3 m deep (Fouquet et al., 2008). Subsequent visual observations revealed black smokers on the crater bottom, indicating recent hydrothermal activity.

Five massive sulfide bodies were found within the Ashadze-2 hydrothermal field (Fig. 2b), most of which is covered by sediments (unpublished report of PMGE, 2007). The largest orebody (number I) is approximately 125 by 335 m in size. Massive sulfide bodies in the south (numbers III and IV) are mostly composed of Fe-sulfides (pyrite and marcasite), whereas those in the centre and far north (numbers I, II, and V) contain significant amounts of Cu and Zn sulfides.

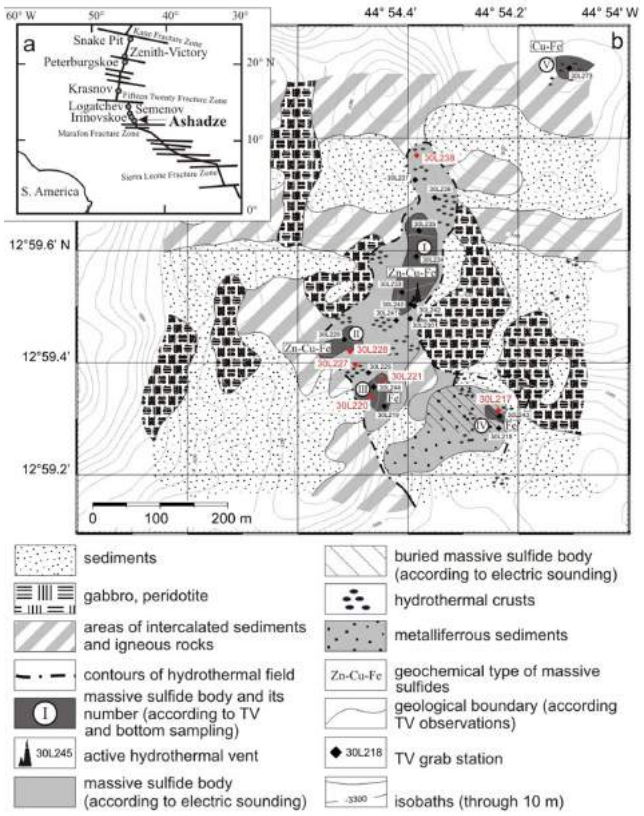

Figure 2. Location of the Ashadze hydrothermal cluster in the Central Atlantic (Mid Atlantic Ridge (a) and the schematic structure of the Ashadze-2 hydrothermal field (b), simplified after an unpublished report by PMGE (2007) (b).

3 Results

3.1 The Yubileynoe deposit

Samples of ferruginous gossanites (Fe_2O_3 12.31–34.23 wt. %) from the Yubileynoe deposit consist of partly or fully oxidized sulfides, which are mixed with carbonates and detrital hyaloclastic material (Fig. 3a). In addition to oxidized sulfides, gossanites host abundant authigenic chalcopyrite (after pyrite) and sphalerite and minor amounts of radial micronodules (10–15 μm across) of pyrite and galena (Fig. 3b). The microinclusions of galena, Ag-rich native gold, cervelleite, altaite, hessite, tellurobismuthite, cobaltite, acanthite, apatite and V-rich (up to 1.2 wt. %) Mg-chlorite are present in authigenic chalcopyrite and hematite–carbonate–quartz matrix (Ayupova et al., 2018; Maslennikov et al., 2019).

Numerous finest uraninite particles (<2 μm in size) were found in hematite–quartz–carbonate matrix (Fig. 3c). Small (1–2 μm in size) round inclusions of uraninite, which locally coalesce to larger grains up to 5 μm in size, are observed in authigenic chalcopyrite with inclusions of galena–hessite intergrowths (Fig. 3d). In some cases, the ED spectra of the uraninite particles (except of U and O peaks) demonstrate peaks of V and P.

3.2 The Ashadze-2 hydrothermal field

Samples of gossans (Fe_2O_3 14.28–73.64 wt.%) from the Ashadze-2 hydrothermal field are composed of amorphous iron hydroxides, crystalline goethite, sepiolite, atacamite, halite, calcite, quartz, and sulfide minerals (Ayupova et al., 2018). The Cu–Fe sulfides sulfides are partly to completely pseudomorphed by Fe-hydroxides (Fig. 3e). The Fe-rich samples are mostly composed of ochreous to reddish brown cryptocrystalline Fe-oxyhydroxides, which completely replace primary sulfide clasts mixed with sepiolite, which makes a cement for oxidized sulfide clasts. Pyrite occurs as euhedral crystals 2–3 μm in size in sepiolite and at the contacts between sepiolite and Fe–oxyhydroxides.

Fe-hydroxides host numerous uraninite particles (2–3 μm) and small particles of Cu–Fe sulfides (isocubanite and chalcopyrite), pyrite, galena, and apatite (Fig. 3f). Isometric anhedral zonal uraninite grains (up to 2 μm in size) occur in sepiolite, are intergrown with pyrite, and are characterized by outer P-rich rim (Fig. 3g and Fig. 3h). ED spectra containing U and O are characteristic of uraninite. Some grains of uraninite are surrounded by fine (<1 μm) rims, which are characterized by much lower brightness in BSE images (Fig. 4h) and peaks of P and Ca (possibly a P- and Ca-rich uraninite), and replaces uraninite.

In spite of extremely low Th contents (max 1.59 ppm) in gossans, Fe-hydroxides locally contain microinclusions of Th–Zr-bearing minerals 1.5 μm in size.

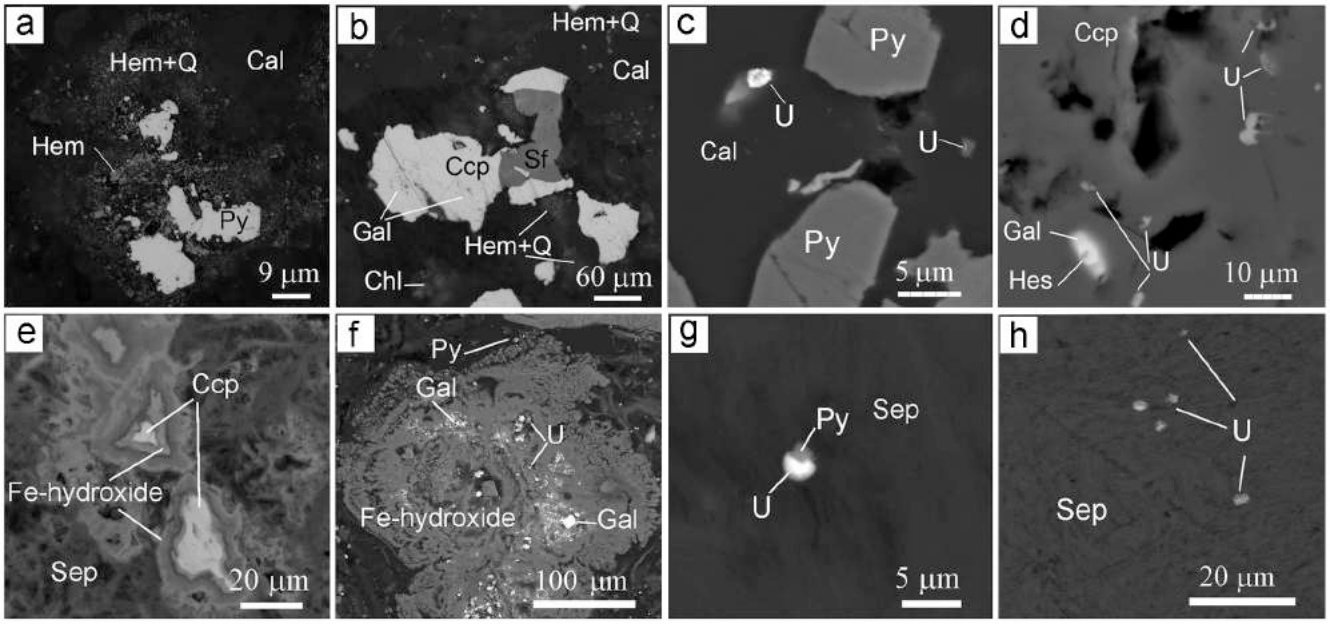

Figure 3. Mineral assemblages of gossanites from the Yubileynoe VHMS deposit (a–d) and gossans of the Ashadze-2 hydrothermal field (e–h): a – authigenic pyrite in assemblage with crystalline hematite inside pseudomorphic fine hematite–quartz aggregate after sulfide clast, b – authigenic chalcopyrite and sphalerite in hematite–quartz-calcite matrix; c – uraninite grains in calcite, d – uraninite, galena, and hessite within authigenic chalcopyrite, e – replacement of chalcopyrite by colloform zonal Fe-oxyhydroxides, f – assemblages of uraninite, galena, and pyrite within colloform zonal Fe-oxyhydroxides, g – intergrowth of pyrite and uraninite with P- and Ca-rich outer rim (light gray) in sepiolite, h – uraninite grains (white) replaced by P- and Ca-rich uraninite (gray) in sepiolite. SEM-photo. Py – pyrite, Ccp – chalcopyrite, Sf – sphalerite, Gal – galena, Hes – hessite, Hem – hematite, Hem+Q – hematite-quartz aggregate, Cal – calcite, U – uraninite, Sep – sepiolite, Chl – chlorite.

4 Discussion

In oxidizing environments, uranium is most soluble and mobile in the hexavalent oxidation state (Langmuir, 1978). U has been shown to be elevated on the surface of altered hydrothermal sulfide minerals (Mills et al., 1994) and in sulfidic plume particles (German et al., 2002), reflecting efficient U reduction and removal onto Fe-sulfide particles in modern Fe-oxyhydroxide sediments. The presence of discrete (smaller 100 nm in diameter) U minerals with P association were found here (e.g., Mills et al., 1994). The average Th/U ratio of the Ashadze-2 gossans and Yubileynoe gossanites is 0.009 and 0.003, respectively, similar to the average Th/U ratio of seawater (0.003) indicated the major source of U for these sediments is related to seawater. The high contents of “hydrogenic” V (up to 458 ppm) and Mo (up to 54) in Fe-oxyhydroxide sediments, as well as U, are due to extraction from seawater during to redox mechanism (Emerson and Huested, 1991; Butler and Nesbitt, 1999). The association of P and U suggests the presence of P–U complex compounds (Langmuir, 1978).

The U distribution in gossans from the Ashadze-2 hydrothermal field and gossanites from the Yubileynoe deposit is extremely heterogeneous. Recently, it was found that U in low-U (<10 ppm) gossanites is hosted in pseudomorphic hematite after sulfide clasts and tube

worms (Ayupova et al., 2017). It is known that U(VI) is co-precipitated or adsorbed onto ferrihydrite may be reduced during the transformation of the iron oxyhydroxide to goethite or hematite, which incorporates reduced U into its mineral structure, where it is readily preserved (Boland et al., 2011). However, unstable sulfide-derived sediments in oxidizing seawater may undergo oxidation after burial. It is suggested that uraninite was deposited predominantly from pore diagenetic fluids, which circulated in hyaloclast–carbonate–sulfide sediments during Fe-oxide evolution and formation of authigenic sulfide mineralization via oxidation–reduction reactions.

Uraninite in gossanites from the Yubileynoe deposit, as well as in gossans of the Ashadze-2 hydrothermal field, is associated with galena, V-rich Mg-chlorite (sepiolite in gossans), and apatite. In addition to Fe-oxyhydroxides, U may also be absorbed by smectite from seawater (a product derived from the decomposition of hyaloclastic material). High U sorption by clay minerals (e.g., montmorillonite, sepiolite) has also been documented (Donat, 2009). During late diagenesis, clay minerals may be transformed to chlorite, which also bears U. Up to 50 ppm U was noted by Ayupova et al. (2017) in chloritized hyaloclasts of gossanites of some VHMS deposits of the South Urals, and hyaloclastites mixed with sulfide clasts could be additional source of U in our case, whereas abundant carbonates provided HCO3–rich conditions favorable for active migration of U(VI). Postdiagenetic processes resulted in loss of sorption ability of Fe-oxides and formation of uraninite. Our comparison of Fe-oxyhydroxide sulfide-derived sediments of oceanic hydrothermal sulfide fields and continental VHMS deposits indicates common processes of U mineral formation.

Acknowledgements

The authors thank Victor Ivanov and Victor Beltenev (PMGE, St-Petersburg, Russia) for the possibility of participation in the 30th cruise of *R/V Professor Logachev* and sulfide sampling. This research was supported by State Contract of the Institute of Mineralogy SU FRC MG UB RAS (project for 2019-2021).

References

Ayupova NR, Maslennikov VV, Tessalina SG, Shilovsky OP, Sadykov SA, Hollis SP, Danyushevsky LV, Safina NP, Statsenko EO (2017) Tube fossils from gossanites of the Urals VHMS deposits, Russia: authigenic mineral assemblages and trace element distributions. Ore Geol Rev 85:107–130.

Ayupova NR, Melekestseva IYu, Maslennikov VV, Tseluyko AS, Blinov IA, Beltenev VE (2018) Uranium accumulation in modern and ancient Fe-oxide sediments: examples from the Ashadze-2 hydrothermal sulfide field (Mid-Atlantic Ridge) and Yubileynoe massive sulfide deposit (South Urals, Russia). Sed Geol 367:164–174.

Beltenev V, Nescheretov A., Shilov V, Ivanov V, Shagin A, Stepanova T, Cherkashev G, Batuev B, Samovarov M, Rozhdestvenskaya I, Andreeva I, Fedorov I, Davydov M, Romanova L, Zaharov V, Luneva N, Artemceva O, Rumyantsev A (2003) New discoveries at 12°58′ N, 44°52′ W, MAR: Professor Logatchev-22 cruise, initial results. InterRidge News 12:13–14.

Boland DD, Collins RN, Payne TE, Waite TD (2011) Effect of amorphous Fe(III) oxide transformation on the Fe(II)-mediated reduction of U(VI). Environ Sci Technol 45:1327–1333.

Butler IB, Nesbitt RV (1999) Trace element distribution in the chalcopyrite wall of a black smoker chimney: Insights from laser ablation inductively coupled plasma mass spectrometry (LA-ICP-MS). Earth Planet Sci Lett 167:335–345.

Cherkashev GA, Ivanov VN, Bel'tenev VI, Lazareva LI, Rozhdestvenskaya II, Samovarov ML, Poroshina IM, Sergeev MB, Stepanova TV, Dobretsova IG, Kuznetsov VYu (2013) Massive Sulfide Ores of the Northern Equatorial Mid-Atlantic Ridge. Oceanology 53(5):607–619.

Fouquet Y, Chercashov G, Charlou JL, Ondréas H, Birot D, Cannat M, Bortnikov N, Silantyev S, Sudarikov S, Cambon-Bonavita MA, Desbruyères D., Fabri MC, Querellou J, Hourdez S, Gebruk A, Sokolova T, Hoisé E, Mercier E, Kohn C, Donval JP, Etoubleau J, Normand A, Stephan M, Briand P, Crozon J, Fernagu P, Buffier E (2008). Serpentine cruise–ultramafic hosted hydrothermal deposits on the Mid-Atlantic Ridge: First submersible studies on Ashadze 1 and 2, Logatchev 2 and Krasnov vent fields. Inter Ridge News 17:15–19.

German CR, Colley S, Palmer MR, Khripounoff A, Klinkhamme GP (2002) Hydrothermal plume-particle fluxes at 13°N on the East Pacific Rise. Deep-Sea Res I Oceanogr Res Pap 49:1921–1940.

Hannington MD, Thompson G, Rona PA, Scott SD (1988) Gold and native copper in supergene sulphides from the Mid-Atlantic Ridge. Nature 333:64–66.

Hegner E, Tatsumoto M (1987) Pb, Sr and Nd isotopes in basalts and sulfides from the Juan de Fuca ridge. J Geophys Res 92:11380–11386.

Herrington R, Zaykov V, Maslennikov V, Brown D, Puchkov V (2005) Mineral deposits of the Urals and links to geodynamic evolution. Econ Geol One Hundredth Anniversary Volume: 1069–1095.

Hrischeva E, Scott SD (2007) Geochemistry and morphology of metalliferous sediments and oxyhydroxides from the Endeavour segment, Juan de Fuca Ridge. Geochim Cosmochim Acta 71:3476–3497.

Langmuir D (1978) Uranium solution-mineral equilibra at low temperatures with application to sedimentary ore deposits. Geochim Cosmochim Acta 42:547–569.

Maslennikov VV, Ayupova NR, Herrington RJ, Danyushevskiy LV, Large RR (2012) Ferruginous and manganiferous haloes around massive sulphide deposits of the Urals. Ore Geol Rev 47:5–41.

Maslennikov VV, Ayupova NR, Maslennikova SP, Tseluyko AS, Large RR, Danyushevsky LV, Lein AYu., Bogdanov YuA (2013) Mineral and chemical peculiarities of vent chimneys from the Yubileynoye VMS deposit at the Early Devonian basalt-boninite basement of West Magnitogorsk arc, the Southern Urals, Russia. Proceedings of the 12th SGA Biennial Meeting "Mineral Deposit Research for a High-Tech World".Uppsala, 2013, 4:1512–1515.

Maslennikov VV, Ayupova NR, Safina NP, Tseluyko AS, Melekestseva IYu, Large RR, Herrington RJ, Kotlyarov VA, Blinov IA, Maslennikova SP, Tessalina SG (2019) Mineralogical Features of Ore Diagenites in the Urals Massive Sulfide Deposits, Russia. Minerals 9:150. doi:10.3390/min9030150.

Mills RA, Thomson J, Elderfield H, Hinton R W, Hyslop E (1994) Uranium enichment in metalliferous sediments from the Mid-Atlantic Ridge. Earth Planet Sc Lett 124(1):35–47.

Accessory diagenetic minerals in clastic ores of the Novy Shemur massive sulfide deposit, North Urals

Nataliya P. Safina[1,2], Nuriya R. Ayupova[1,2], Valery V. Maslennikov[1,2], Aleksandr S. Tseluyko[1,2], Irina Yu. Melekestseva[1], Kseniya A. Filippova[1], Dmitry A. Artemyev[1,2]
[1] *Institute of Mineralogy, Urals Branch, Russian Academy of Sciences, Miass, Russia*
[2] *National Research South Urals State University, Chelyabinsk, Russia*

Abstract. The features of mineral composition are considered for clastic ores composing the main part of rich Cu–Zn ores of the Novy Shemur massive sulfide deposit. Most abundant ore types include sulfide breccias, which are composed of pyrite and sphalerite clasts, enclosed in chalcopyrite–sphalerite–pyrite matrix, and sulfide turbidites with rhythmic alternation of sphalerite and pyrite layers. The amount of newly formed pyrite, sphalerite and magnetite increases and the amount of clasts of primary ores decreases in a range from breccias to sandstones. In the same direction, the Zn, Cd, Ag, Pb and Ga contents increase, while the Cu, Au, As, Co, and Mn contents decrease. The indicative accessory minerals of sulfide breccias include electrum, utenbogaardite, tennantite (up to 3.52 wt. % Ag), Ag- and Se-galena (up to 1.7 wt. % Se) and enargite. The sulfide turbidites contain Ag-rich galena, magnetite, arsenopyrite, tetrahedrite, and cassiterite hosted by newly formed sulfides. The matrix of clastic ores contains Ga-bearing chlorite, mica, epidote and albite (1.24–4.88 wt. % Ga_2O_3).

1 Introduction

As a result of ore facial mapping of the Novy Shemur massive sulfide deposit it was found that the deposit is composed of rich clastic Cu–Zn ores. Among them, the most common are sulfide breccias with fragments of pyrite and sphalerite, enclosed in chalcopyrite–sphalerite–pyrite matrix, and sulfide silty sandstones, which represent a rhythmic alternation of sphalerite and pyrite layers with a thickness of few centimeters.

Unlike breccias, the pyrite–sphalerite silty sandstones contain extremely high contents of Zn (up to 40 %) and Ga (up to 604 ppm), elevated average contents of Pb (0.4%), Cd (0.3%), and Ag (64 g/t) and low contents of Cu (0.46%) and Au (0.2 g/t). The presence of sulfide chimneys fragments enriched in chalcopyrite and sphalerite in clastic ores is responsible for specific position of rich Cu–Zn ores and strongly variable Cu and Zn contents of ores. Therefore, a detailed study of mineral composition of various granulometric clastic ores is necessary to enhance the extraction of useful components from ores minimizing the cost of Cu and Zn concentrates.The identification of higher Ga contents is relevant because of the growing use of Ga in high-tech economic areas and its classification as a critical material (Erdmann and Graedel 2011).

2 Geological background

The Novy Shemur massive sulfide deposit is located in the North Urals within the northern part of the Tagil rift-paleoisland arc system (Prokin et al. 1988). It is confined to the central part of the Shemur tectonic-volcanic structure, filled with Ordovician-Silurian rhyolite-basaltic rocks (Kuskov 1983; Prokin et al. 1988; Kontar 2013) (Fig. 1).

A lenticular ore body 1050x500 m in size extends in longitudinal direction and dips to the west at an angle of 40–50°. Numerous post-ore dikes of diabases and plagioclase rhyolites divide the deposit into small fragments and ore layers are characterized by sharp flanks. The "core" of the deposit is dominated by massive pyrite ores. The upper horizons and flanks of northern, southwestern and southeastern directions are composed of rich Cu, Cu–Zn clastic ores, dominated by sulfide breccias and layered and banded pyrite–sphalerite ores (Fig. 2). The various clastic ores are frequently intercalated at the deposit.

The ore samples were studied macroscopically at the Institute of Mineralogy (IMin UB RAS), Miass (Russia). The chemical composition of ores was analyzed using ICP MS analysis on a Agilent 7700X mass spectrometer at the IMin UB RAS (analyst K.A. Filippova).The chemical composition of minerals was analyzed on a Tescan Vega 3sbu SEM equipped with an Oxford Link EDS (IMin UB RAS, analyst I.A. Blinov) and on an Agilent 7700X mass spectrometer equipped with a LA-ICP-MS device (IMin UB RAS, analyst D.A. Artemyev).

3 Results

In sulfide breccias of the Novy Shemur deposit, the high Zn (up to 10%) and Cu (up to 6%) contents are typical of ores with chalcopyrite–sphalerite and sphalerite chimney fragments, as well as with authigenic sphalerite, which occurs in small-clastic matrix (up to 20%). The higher contents of Co (827 ppm), Mn (153 ppm) and As (401 ppm) are characteristic of breccias with dominant pyrite fragments. In contrast to breccias, sulfide turbidites contain extremely high contents of Zn (up to 40%) and Ga (up to 604 ppm), elevated average contents of Pb (0.4%), Cd (0.3%), and Ag (64 g/t) and low contents of Cu (0.46%) and Au (0.2 g/t).
Indicative accessory minerals of sulfide breccias are electrum, utenbogaardite, tennantite (up to 3.52 wt %

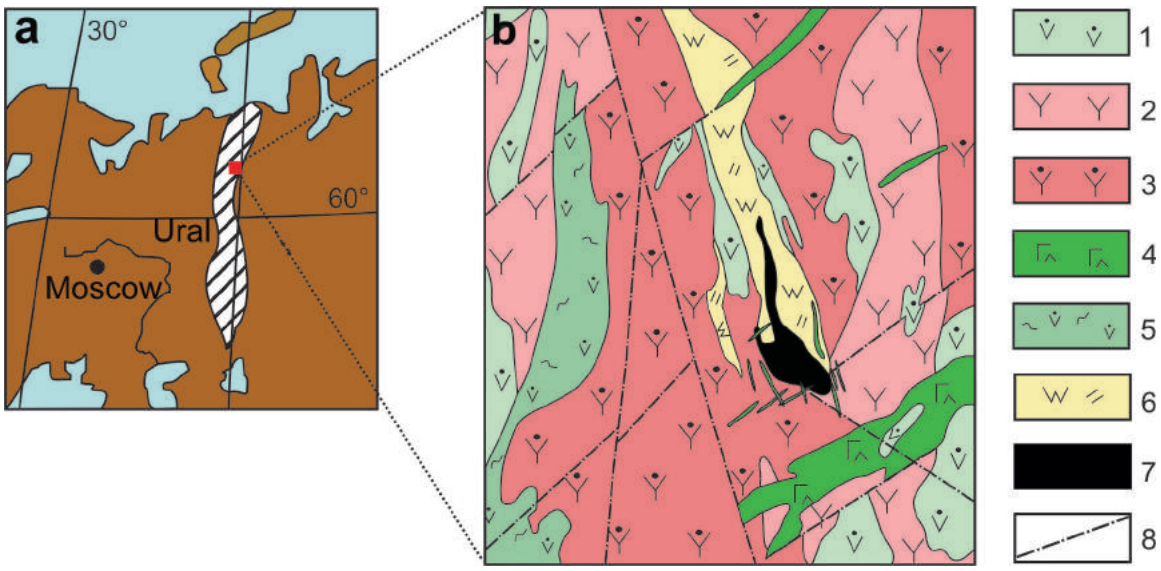

Figure 1. Geographical (a) and geological (b) setting of the Novy Shemur massive sulfide deposit (Figure b is based on unpublished materials of the Severnaya copper-zinc mine). 1 – basaltic andesites and basalts; 2 – plagiodacites and dacitic andesites; 3 – plagiorhyodacites; 4 – diabases, gabbrodiabase; 5 – volcaniclastic basaltic andesites and basalts; 6 – sericite-chlorite-quartz metasomatites; 7 – ore body; 8 – faults.

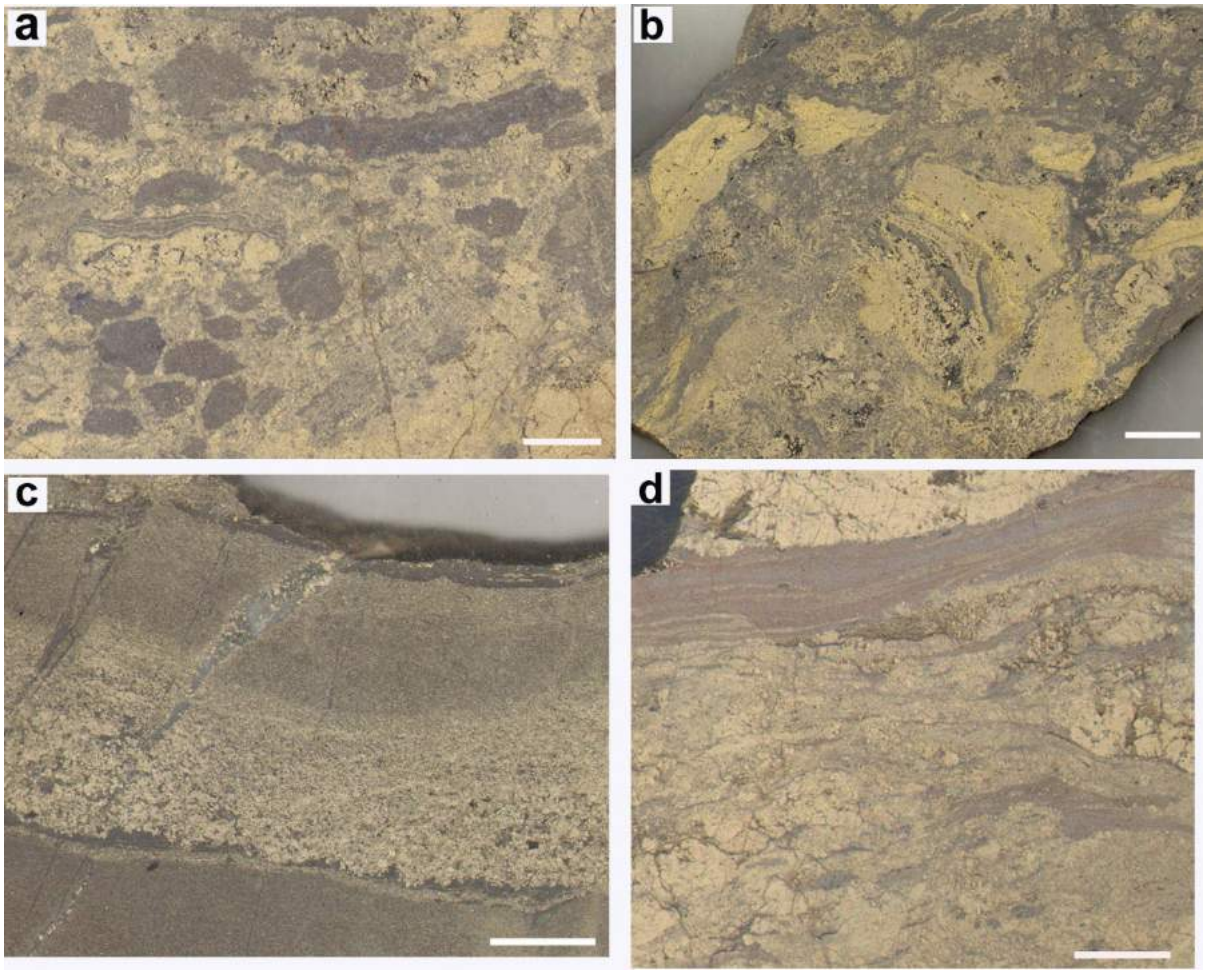

Figure 2. Sulfide breccias (a, b) and sulfide turbidites (c, d) of the Novy Shemur massive sulfide deposit: a. sphalerite and pyrite clasts enclosed in pyrite–sphalerite cement; b. chalcopyrite–pyrite clasts enclosed in pyrite–sphalerite cement; c. gradational layering of fine-clastic sulfide turbidite; d. layers of thin-bedded pyrite–sphalerite ores in coarse-clastic breccias. Scale bar is 1 cm.

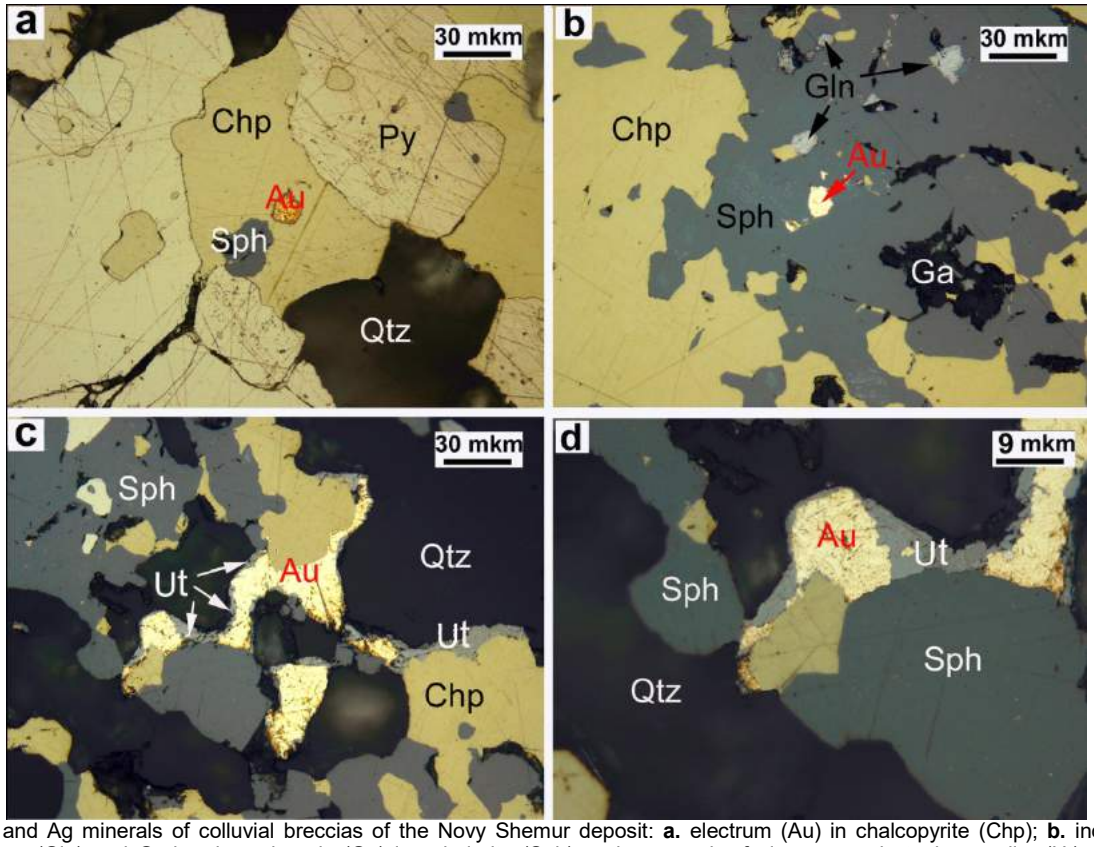

Figure 3. Au and Ag minerals of colluvial breccias of the Novy Shemur deposit: **a.** electrum (Au) in chalcopyrite (Chp); **b.** inclusions of electrum, galena (Gln) and Ga-bearing minerals (Ga) in sphalerite (Sph); **c.** intergrowth of electrum and utenbogaardite (Ut) with quartz (Qtz), chalcopyrite and sphalerite; **d.** electrum and utenbogaardite at the contact of sulfides and quartz. Reflected light.

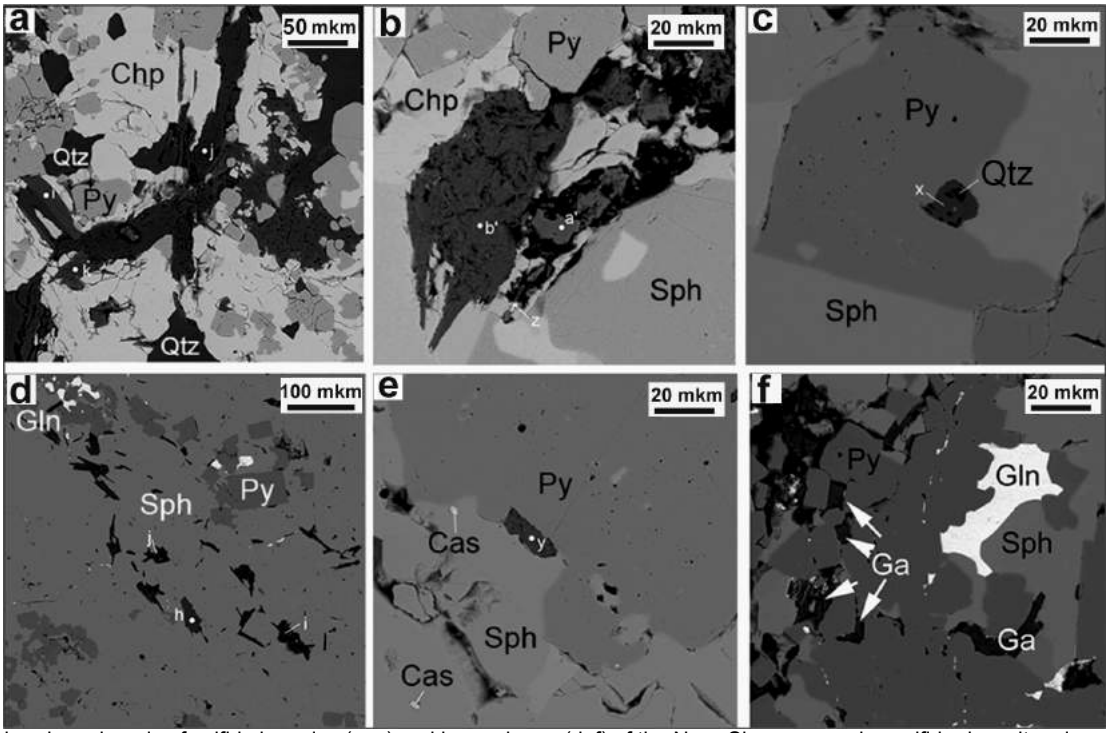

Figure 4. Ga-bearing minerals of sulfide breccias (a–c) and layered ores (d–f) of the Novy Shemur massive sulfide deposit: **a.** lamellar aggregates of Ga-bearing chlorite (j), quartz (Qtz) and fractured pyrite (Py) crystals in chalcopyrite (Chp); **b.** Ga-bearing chlorite (point b) and Ga-bearing epidote (a) in sulfides (gray); **c.** Ga-bearing epidote (x) with inclusions of quartz (Qu) at the contact of pyrite and sphalerite grains; **d**. inclusions of Ga-bearing mica (j, i), Ga-bearing chlorite (h) and galena (Gln) in sphalerite; **e.** inclusion of Ga-bearing chlorite (y) at the contact of pyrite and sphalerite, inclusions of Ta-bearing cassiterite (Cas) in sphalerite; **f.** inclusions of Ga-bearing mica (Ga) and galena

Ag), Ag- and Se-bearing galena (Se up to 1.7 wt %), and enargite (Fig. 3). Sulfide turbidites host Ag-galena, magnetite, arsenopyrite, tetrahedrite and Ta-bearing cassiterite (0.51–1.03 wt % Ta_2O_5) as inclusions in newly formed sulfides. The presence of these accessory minerals has resulted in higher contents of Au, Ag, As, Pb, Sb, and other elements of ores. These elements derived from fragments of hydrothermal ores, e.g., sulfide chimneys. According to LA-ICP-MS data, in fragments of pyrite–sphalerite–chalcopyrite chimneys, pyrite is enriched in (mean, ppm) Co (567), As (1360), Ag (316), Te (170), Pb (up to 1%) and Bi (182); chalcopyrite has higher contents of Co (16), Ga (30), As (up to 70), Sb (up to 210), Pb (up to 80) and Bi (up to 20); and sphalerite has higher contents of Mn (185), Co (22), Se (130) and Hg (145) and high contents of Ga (up to 500).

In contrast to Cu–Zn ores of other massive sulfide deposits of the Urals, the Cu–Zn ores of the Novy Shemur deposit are characterized by high contents of Ga and the presence of Ga-bearing minerals (Fig. 4). The high contents of Ga, along with Zn, Cd, In, and Sb, are characteristic of breccias, whereas banded pyrite–sphalerite ores exhibit extremely high Ga contents (up to 600 ppm).

It is suggested that the decomposition of sulfide chimneys fragments, enriched in Ga, during the formation of fine-clastic sulfide ores, has released this element leading to its accumulation in sphalerite, chalcopyrite and other minerals. Gallium was also absorbed by primary clay material, which cemented the ore clasts and which were later transformed into Ga-bearing chlorites (1.24–2.89 wt % Ga_2O_3) and mica (1.56 wt % Ga_2O_3). Albite and epidote also host Ga: 0.45–1.52 and 1.11–4.88 wt % Ga_2O_3, respectively.

The higher Ga content of newly formed sphalerite (33–364 ppm) and chalcopyrite (67–363 ppm), as well as of mica (up to 13 wt % Ga_2O_3), chlorite (to 14 wt % Ga_2O_3) and magnetite (5–7 wt % Ga_2O_3), is also typical of chalcopyrite and sphalerite of sulfide breccias of the Shemur massive sulfide deposit (Safina et al, 2018), located in 15 km from the deposit studied.

4 Conclusions

Thus, the variable contents of Cu, Zn and other elements of rich Cu–Zn ores of the Novy Shemur deposit are related to the variable mineral composition of clastic ores. Various granulometric types of clastic ores are characterized by specific textural, structural, mineralogical and geochemical features. The diagenetic transformation of clasts of primary hydrothermal ores changes the mineral and chemical composition of ores leading to local accumulation of valuable and toxic elements within the sulfide massive deposit. Small- and fine-clastic ores, as a rule, are enriched in most trace elements, including precious and rare metals. These ores occur mainly in the slopes of the sulfide deposits and cannot be mined, because they form thin layers of few tens of centimeters thick (rarely, few meters thick inside the ore bodies). The flanks of many massive sulfide deposits (e.g., Yubileynoe, Yaman Kasy, Molodezhnoe, Valentorskoe, Aleksandrinskoe, Saf'yanovskoe) in the Urals are enriched in trace elements (Au, Ag, Sb, Pb, Te, Bi, Se, In, U) (Maslennikov et al. 2019). The mode of occurrence of these elements and their associations are atypical of primary hydrothermal ores of the deposits. Thus, our results should be taken into account during processing of ores to enhance the efficient use of the deposit.

Acknowledgements

This research was supported by State Contract of Institute of Mineralogy UB RAS.

References

Kuskov VN (1983) Structure of the Shemur ore field (North Urals). In: Geology, prospecting and exploration of mineral deposits. Irkutsk, 76–81 pp. (in Russian)

Longinov VV (1973) Essays on lithodynamics of the ocean. Moscow, Nauka, 243 p. (in Russian)

Maslennikov VV, Ayupova NR, Safina NP, Tseluyko AS, Melekestseva IYu, Large RR, Herrington RJ, Kotlyarov VA, Blinov IA, Maslennikova SP, Tessalina SG (2019) Mineralogical features of ore diagenites in the Urals massive sulfide deposits, Russia. Minerals, 9(3):150.

Prokin VA, Buslaev FP, Ismagilov MI et al. (1988) Massive sulfide deposits of the Urals: Geological structure. Sverdlovsk: UNC, USSR Academy of Sciences, 241 p. (in Russian)

Safina NP, Ayupova NR, Belogub EV, Maslennikov VV, Blinov IA, Zhukov IG, Artem'ev DA (2018) First find of Ga-Bearing minerals in ores of Ural massive sulfide deposits // Doklady Earth Sciences, 480(2):746–749.

Erdmann L, Graedel TE (2011) Criticality of non-fuel minerals: a review of major approaches and analyses. Environmental Science and Technology, 45:7620–7630.

.

Petrographic and mineralogical study of the Kilmacoo gold occurrence, Avoca District, Southeast Ireland

Thomas Riegler, Sean H. McClenaghan, Foteini Drakou
Trinity College Dublin, School of Natural Science, Department of Geology, Museum Building, College Green, Ireland

Helen Thomas, Christina Wanhainen, Glenn Bark, Tobias Bauer
Luleå University of Technology, Department of Civil, Environmental and Natural Resources Engineering, Universitetsområdet, Porsön, Sweden

Abstract. Petrographic investigation of the quartz vein hosted Kilmacoo gold occurrence spatially associated with the copper rich Avoca massive sulphide ore body evidenced a close association between gold and sulphides. Visible electrum grains are frequently observed within chalcopyrite, and more rarely as minute inclusions in both arsenopyrite and pyrite. Mineralogical investigations also revealed complex sulphide paragenetic succession from framboidal pyrite to colloform and idiomorphic cements with overall a low arsenopyrite content. We also documented the presence of hydrothermal phosphates (apatite and monazite) subsequently altered in aluminum phosphate sulphate minerals, as well as a broad diversity of phyllosilicates. These observations as well as the cross cutting relationships tend to indicate a brittle deformation event involving possible remobilization of some of the copper mineralization from the main VMS ore body. At the present time the source of gold is still under investigation to determine the possible contribution from both local and distal sources.

1 Geological context

Background

The Avoca Belt in Co. Wicklow, southeast Ireland has been host to base-metal production for over 300 years (Fig. 1). Volcanogenic massive sulphide (VMS) mineralization at Avoca consists of semi-massive to massive sulphides (Cu-Zn-Pb) exhibiting both epigenetic stockwork and syngenetic exhalative features, and hosted by Middle to Upper Ordovician volcanic and sedimentary rocks of the Duncannon Group (McConnell et al. 1991). Mineralization covers a strike length of approximately 15 km and is punctuated by the Avoca Mine which produced over 16 Mt of chalcopyrite-rich sulphide ore with a grade of 0.6% Cu (Sheppard 1980; Williams et al. 1986; McArdle 1993). The gold-rich Kilmacoo zone at the northeast end of the Avoca Mine property was identified by Mianrai Teoranta in the 1950's, intersecting 19 meters of quartz veined schist with 2.88 g/t Au and 16.6 g/t Ag (Milner and McArdle 1986). The site was the focus of further exploration in the 1980's by Riofinex defining a resource of at least 300,000 tons at 1.5 g/t Au.

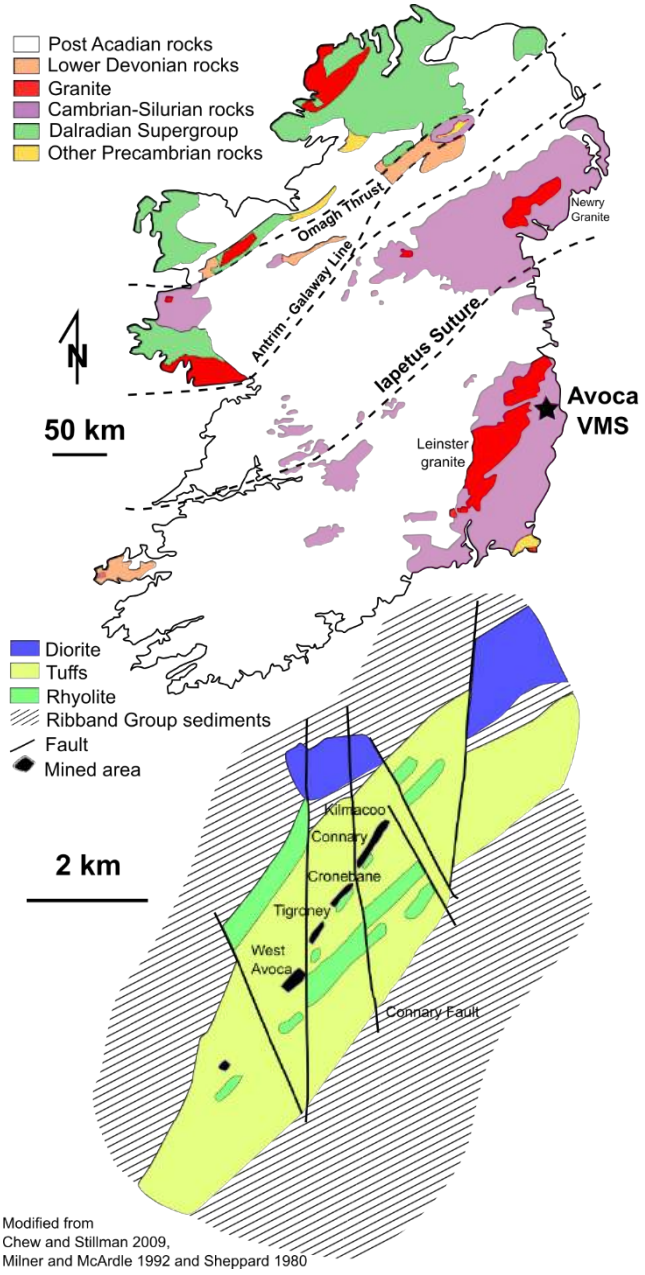

Figure 1. Simplified geological map of Ireland, and of the Avoca area. Modified from Chew and Stillman 2009; Milner and McArdle 1992; Sheppard 1980)

More recently, drilling on the property has been carried

out by IMC Exploration Group and Koza Gold as part of a JV agreement.

1.2 Regional geology

Sulphide mineralization in the Avoca District is hosted by Ordovician volcano-sedimentary rocks of the Duncannon Group. These felsic volcanoclastic rocks were generated in an active continental margin above a southeast facing subduction zone (Iaepetus Ocean), with volcanism initiated during a period of extension within a volcanic arc (Stillman and Williams 1979; McConnell et al. 1991). The volcanic pile sits conformably to unconformably on a continentally-derived turbidite sequence of Cambro-Ordovician carbonaceous (graphitic) sediments (Ribband Group), which were derived from a Peri-Gondwanan margin of Ganderia. Closure of the Iapetus Ocean (Late Ordovician to Late Silurian) and westward-directed subduction resulted in the development of an accretionary wedge, with subsequent obduction onto the continental margin and associated polyphase deformation accompanied by lower to middle-greenschist metamorphism.

1.3 Massive sulphides

Avoca mineralization can be found between two distinct felsic volcanic packages and occurs along a 15 km-long zone (McArdle 1993). Although disseminated sulphide and vein mineralization is common throughout the region, sulphide tonnage is largely concentrated in the Cronebane, East Avoca and West Avoca orebodies. Here, sulphides form vein stockwork replacement and stratiform pyritic lenses that are roughly coeval with their host volcanoclastic and sedimentary rocks. The lenticular shape of the stratiform sulphide zones can, in part be attributed to exhalative processes (i.e., buoyant plumes); however, their aspect ratio has also been affected by post-depositional poly-phase deformation.

Mineralization consists of pyrite, chalcopyrite, sphalerite, and galena, as well as a wide range of trace accessory phases including pyrrhotite, arsenopyrite, native bismuth, bismuthinite, bournonite, tetrahedrite-tennantite, magnetite and hematite. Three hydrothermal facies have been recognized: 1) Stockwork pyrite-chalcopyrite (Siliceous); 2) Sub-massive to massive pyrite-chalcopyrite; and 3) banded pyrite-sphalerite-galena (Platt 1977), consistent with other VMS deposits along the Appalachian-Caledonian Orogen (McClenaghan et al. 2003; 2009).

1.4 Quartz veining and gold mineralization at Kilmacoo

Gold mineralization at Kilmacoo has to-date only been recognized in silicified chloritic sulphide-rich tuffs and one of the main feature of the occurrence is the common quartz veining, as foliation parallel banded veins, foliation-parallel lensoid veins and discordant veins, name respectively QV1, 2, and 3 according to Milner and McArdle (1992). According to these authors, the QV-1 formed of white to grey semi-translucent laminated quartz veins are the main host to the Kilmacoo gold mineralization. According to Milner and McArdle (1992) structural study QV1 are foliation (D_1) parallel and postdate the D_1 cleavage. They are considered to be syn to late D_2 in age. QV2 are foliation parallel lensoid veins associated with chalcopyrite and pyrite. They are similar to the veins miner for copper at Avoca (Platt 1977; Williams et al. 1986). QV3 are sulphide poor and discordant to the main D_1 cleavage.

Petrology and mineralogy

2.1 Sulphides and sulfosalts in gold bearing quartz veins

At Kilmacoo gold occurrences were mostly documented macroscopically in relation to silicified chloritic tuffs with high pyrite, sphalerite and galena content in foliation-parallel banded quartz veins (Milner and McArdle 1991). One of the main results of our new observations of the veins resides in the close spatial relationship between electrum and sulphide, primarily chalcopyrite hosted in quartz veins (Fig. 2).

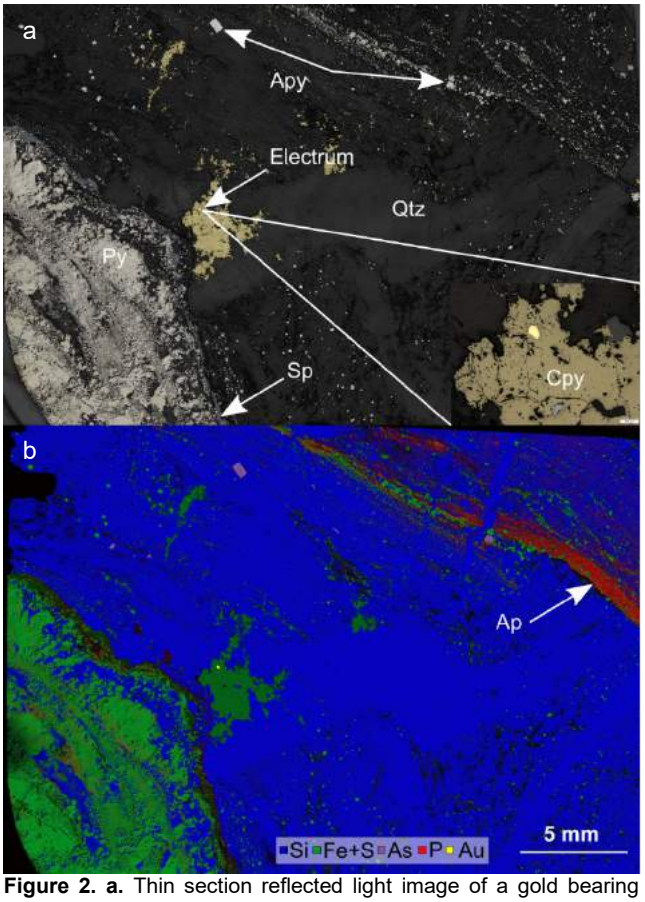

Figure 2. a. Thin section reflected light image of a gold bearing quartz sulphide vein sample from the Kilmacoo occurrence. a cropped image of the electrum grain hosted in chalcopyrite is presented at the bottom right. **b.** coincident scanning electron microscope energy dispersive X-ray spectrometry (SEM-EDS) element map. Abbreviations: Ap (apatite), Apy (arsenopyrite), Cpy (chalcopyrite), Py (pyrite) Qtz (quartz), Sp (sphalerite)

Electrum is commonly present as round anhedral inclusions in chalcopyrite ranging from 10 to 150 microns in diameter. In contrast euhedral pyrite and arsenopyrite hosted electrum is significantly more fine-grained, from small micron-sized rounded inclusions to micro fracture fillings or along the dislocated boundaries of large pyrite porphyroblasts. In places, euhedral crystals of electrum have been found in association with native Bi, Pb-sulfosalts (nuffieldite, $Pb_2Cu(Pb,Bi)Bi_2S_7$) and rare cassiterite; the sulfosalts partially replace chalcopyrite filled fractures. Electrum is also present as a single phase fracture filling in iron sulphides. Irrespective of the type of electrum occurrence and relationship with the host sulphides, electrum has a consistent gold fineness averaging 750‰, (Fig. 3).

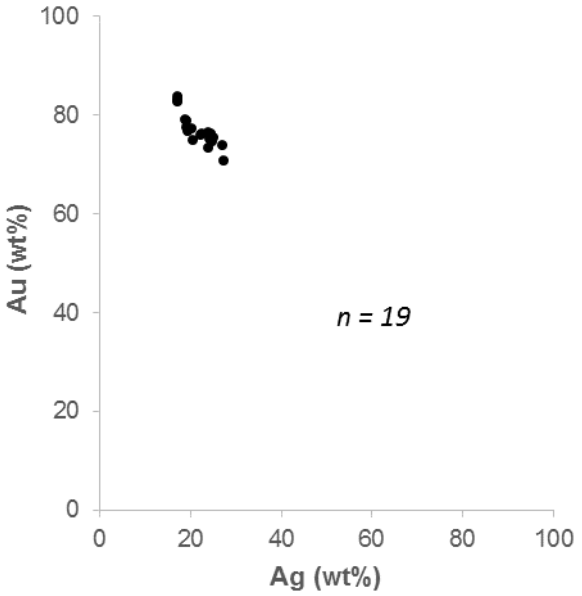

Figure 3. Composition of electrum grains from inclusions hosted in chalcopyrite, arsenopyrite and pyrite from the Kilmacoo gold occurrence.

Pyrite textures allow for the identification of at least six generations: 1) an early framboidal pyrite (Py_1), isolated or occurring in clusters following the main planar fabric (S_1/S_2 penetrative cleavage), 2) colloform pyrite overgrowths radiating from the framboids (Py_2), and 3) euhedral pyrite overgrowth (Py_3) on Py_2. Py_{1-3} occur in relative variable abundance and exhibit the effects of recrystallization forming large porphyroblasts in places (Py_4). Porphyroblast are later partially replaced by a fifth generation of porous pyrite (Py_5). Finally, a late generation of pyrite (Py_6) occurs as euhedral isolated pyrite grains cogenetic with arsenopyrite, in places, both host minute electrum inclusions that postdate the pyrite porphyroblasts.

2.2 Accessory and alteration minerals

A wide range of minerals were identified in samples from Kilmacoo including hydrothermal apatite and monazite associated with the quartz veins (Fig. 2) as well as their alteration to hinsdalite ($PbAl_3(PO_4/SO_4)(OH)_6$) a lead end member of the woodhouseite series of aluminum phosphates sulfates (APS) minerals. Occurrence of such minerals provide important eH/pH constraints on fluid rock interactions during regional metamorphism as well as a possible later phase alteration.

The present work focuses on phyllosilicates associated within rocks hosting gold bearing quartz veins. The most common phyllosilicates are of a Fe-Mg chlorite composition followed by the potassic phyllosilicates. The latter present a broad range of compositions from phengite plotting on the muscovite-celadonite line to illite and interstratified illite/smectite to possible beidellite according to their compositions (Fig. 4). This represents a record of the metamorphic/hydrothermal and late alteration events across the region. Both laths of phengite and chlorite are ubiquitous in the host strata and are well developed in the pressure shadows of pyrite porphyroblasts; these growths most likely coincide with peak metamorphic conditions and define the penetrative S1/S2 Caledonian fabric. Temperature estimates using the ^{VI}Al occupancy of chlorite from Cathelineau (1988) indicates temperatures of c. 400°C, consistent with widespread greenschist conditions. In masses of Fe-Mg chlorite an indicator of the high pressure and low temperature conditions is present in the form of partially dislocated ferrocarpholite $(Fe,Mg)Al_2Si_2O_6(OH)_4$, to our knowledge described for the first time in the Avoca area.

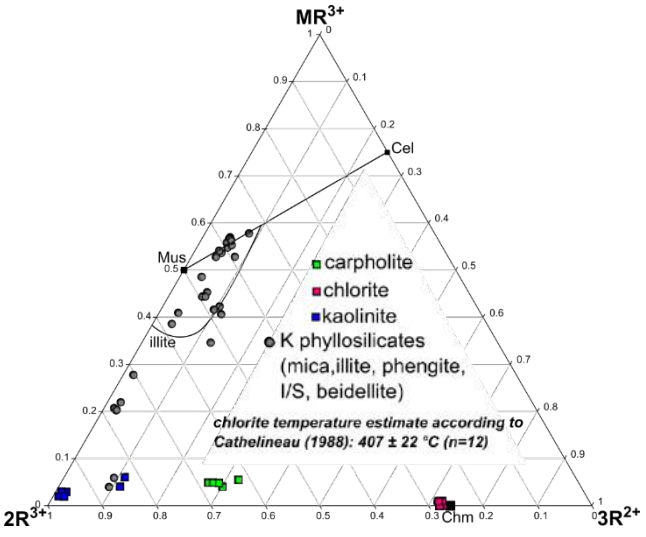

Figure 4. Composition of phyllosilicates from Ribband Group metasediments hosting the Kilmacoo Au occurrence, plotted in the 2R3-3R2-MR3 coordinates. Abbreviations: Chm (chamosite), Cel (celadonite), Mus (muscovite).

Genetic implications for gold occurrence in the Avoca VMS

The new petrographic and mineralogical knowledge gathered on the Kilmacoo gold occurrence reveal a link between brittle fractures developed in sulphide porphyroblasts as well as euhedral pyrite and

arsenopyrite formed during metamorphic/hydrothermal events and the gold deposition. The main host of gold is chalcopyrite in fracture-fills hosting electrum. Previous studies solely focused on the structural setting without detailed paragenetic constrain (Milner and McArdle 1992) nevertheless documented free gold in quartz in the banded quartz units, however such occurrence were not present in the sample set (n=30 thin sections) from the present study.

A cross-cutting relationship between the auriferous banded quartz units and the early penetrative S_1/S_2 Caledonian fabric indicates late gold emplacement in the region, postdating regional prograde metamorphism and associated ductile deformation (Fig.5). Petrographic observations also indicate a late paragenesis for gold at Kilmacoo postdating Py_4.

Figure 5. Photo of core from drill hole KG-10 intersecting auriferous banded quartz vein at the Kilmacoo deposit. The specimen shows a distinct cross-cutting relationship between the banded silica and an early Caledonian penetrative cleavage (S_1/S_2), confirming a late paragenesis for gold at Kilmacoo.

This late event is coincident with growth of Py_4 and arsenopyrite and may be linked to late brittle deformation during the retrograde path as indicated by the chlorite temperature estimate from pyrite porphyroblast pressure shadows. In addition the presence of ferrocarpholite could help to refine the pressure and temperature conditions as the mineral is the marker of LT HP metamorphism (Goffé 1982; Pourteau et al. 2014). This would support that lower greenschist metamorphic condition generally identified for the area would have an affinity toward a low grade blueschist facies.

Acknowledgements

This research is funded by the ERA-NET Cofund on Raw Materials (ERA-MIN 2) through the Geological Survey Ireland and Vinnova for Ireland and Sweden, respectively. First author would like to personally thank Balz Kamber for initiating the project and his decisive contribution to the success of the grant financing this research. We are grateful toward IMC exploration and Liam McGrattan for allowing us to sample material from their exploration projects at Avoca.

References

Cathelineau M (1988) Cation site occupancy in chlorites and illites as a function of temperature. Clay miner 23-4:471-485.

Chew DM and Stillman CJ (2009) Late Caledonian Orogeny and magmatism. In: The Geology of Ireland, 2nd edition (Eds. Holland, C.H. and Sanders, I.S.) Dunedin Academic Press, Edinburgh pp 143-173.

Goffé B (1982) Définition du faciès à Fe Mg carpholite-chloritoïde, un marqueur du métamorphisme de HP-BT dans les métasédiments alumineux. Diss. Université Pierre et Marie Curie-Paris VI.

McConnell B (1991) Geochemistry and mineralogy of volcanic host rocks as indicators of massive sulphide genesis at Avoca, Southeast Ireland. Irish journal of earth science pp 43-52.

McArdle P (1993) Evolution and preservation of volcanogenic sulphides at Avoca, southeast Ireland: Trans Inst Min Metall (Section B) 102:B149-B163.

McClenaghan SH, Goodfellow WD and Lentz DR (2003) Gold in massive sulfide deposits, Bathurst Mining Camp, New Brunswick: Distribution and genesis in, editor(s) Goodfellow, WD, and McCutcheon, SR, Massive sulfide deposits in the Bathurst Mining Camp, New Brunswick and Northern Maine, Littleton, Colorado, The Econ Geol Publishing Company pp 303-326.

McClenaghan SH, Lentz DR, Martin J, and Diegor WG (2009) Gold in the Brunswick No. 12 volcanogenic massive sulfide deposit, Bathurst Mining Camp, Canada: evidence from bulk ore analysis and laser ablation ICP-MS data on sulfide phases, Miner Depos 44:523-557.

Milner AL, and McArdle P (1992) "Gold mineralization in Ordovician volcanic rocks at Kilmacoo, Co. Wicklow: its exploration and geological controls." in Bowden et al. (eds), The Irish Minerals Industry 1980–1990, Dublin. Irish Association for Econ Geol pp 51–63.

Sheppard WA (1980) The ores and host rock geology of the Avoca Mines, Co. Wicklow, Ireland. Norges geologiske Undersokelse 360:269-83.

Williams FM, Sheppard, WA, & McArdle P (1986) Avoca mine, County Wicklow: a review of geological and isotopic studies. Geology and genesis of mineral deposits in Ireland. Irish Association for Econ Geol pp 71-82.

Stillman CJ, and Williams CT (1979) Geochemistry and tectonic setting of some Upper Ordovician volcanic rocks in east and southeast Ireland. Earth Planet Sci Lett 42(2): 288-310.

Platt, J. W. (1977) Volcanogenic mineralization at Avoca, Co. Wicklow, Ireland, and its regional implications. J Geol Soc, London, Special Publications, 7(1):163-170.

Pourteau A, Bousquet R, Vidal O, Plunder A, Duesterhoeft E, Candan O, Oberhänsli R (2014) Multistage growth of Fe–Mg–carpholite and Fe–Mg–chloritoid, from field evidence to thermodynamic modelling. Contrib Mineral Petrol 168(6):1090.

Rare metal mobility in a metamorphosed base metal deposit: the Scheeberg / Monte Neve Zn-Pb-(Ag-Cu) SHMS

Thomas Angerer, Albin Volgger, Peter Tropper, Franz Vavtar
Mineralogical-Petrographical Institute, Innsbruck University, 6020 Innsbruck, Austria

Peter Onuk
Department of Applied Geological Sciences and Geophysics, Montan-University 8700 Leoben, Austria.

Abstract. We present element abundances and evidence for rare metal (Ga, In, Co, Ag) mobility in the metamorphosed sedimentary massive sulphide (SHMS) deposit Schneeberg / Monte Neve, Italy. Within the main stratiform ore body, elements that are predominantly hosted in solid solution within sphalerite include (in order of decreasing median abundances) Fe, Cd, Mn, Cu, Hg, Co (20 - 440 ppm), In (3 - 250 ppm), Ga (1 - 18 ppm), Ag (1 - 10 ppm). Secondary ore lenses caused by intra-metamorphic, hydrothermal sulphide remobilisation, are depleted in Fe, Cu, In, Ga, Co, and enriched in Ag, relative to main ore. During subsequent static recrystallisation Fe and Cu partition into exsolution trails along grain boundaries, without capturing mobile In, Ga, and Co. Late stage shearing form dynamic recrystallised textures and lead to further depletion of In and Co. Low temperature-induced ejection of coupled one-, two, and three-valent cations triggered coeval (fluid-assisted) mobilisation from sphalerite. Evidence for complex mobility of rare metals from sphalerite ore in metamorphic/-hydrothermal modification has significance for ore genetic studies and also for metallurgy.

1 Introduction

Sphalerite, (Zn,Fe)S, occurs as a dominant ore mineral in many types of base metal sulphide deposits. A number of elements can substitute for Zn and Fe and because of this, sphalerite is an economically important carrier of rare metal by-products Ga, Ge, In, Co, Sn, Sb, or Ag (Cook et al. 2009; Sinclair 2014). Metamorphism and deformation as partitioning processes for trace metals in sphalerite are not thoroughly investigated, even though a good understanding of mobility and partitioning of rare metals will advance our knowledge on metal cycling in nature and impact on ore genesis and metallurgy.

We are beginning to understand how metamorphic processes control trace metal concentrations: Lockington et al. (2014) showed that Mn, Fe, Cd, In and Hg in various metamorphosed SEDEX and VHMS ores are not correlated with metamorphic grade, hence primary signatures prevail. On the other hand, Frenzel et al. (2016) revealed a statistical dependence of trace metal concentrations with peak metamorphic grade up to 400 °C. George et al. (2015) showed that Ga, In, and Sn change their preferred host in recrystallised sulphides at high metamorphic grades from sphalerite to chalcopyrite.

Besides these recent advances, there is still a lack of robust models for the mobility of minor and trace metals under (wet) deformation. Here we investigate the significance of element mobility in an amphibolite facies metamorphosed SHMS system, namely the Schneeberg / Monte Neve deposit in the Austroalpine Ötztal-Stubai crystalline (ÖSC) complex. At the microscale we employ laser ablation ICPMS and EMPA to understand the relationship of element budgets with sulphide remobilisation and sulphide deformation.

2 Geological framework

2.1 The Ötztal-Stubai crystalline complex

The polymetallic ore district ÖSC includes numerous occurrences of stratiform sulphide mineralisations hosted mainly in paragneisses and mica schists. There are two regionally distinct metal associations: the northern Cu-Fe domininated with chalcopyrite – pyrite – pyrrhotite ± arsenopyrite ± sphalerite parageneses and the southern Pb-Zn domininated with sphalerite – galena ± chalcopyrite ± pyrite – pyrrhotite parageneses (Vavtar 1988). The overall lithostratigraphic context suggests an Late Neoproterozoic or early Palaeozoic, clastic dominated sedimentary exhalative (CD-SEDEX) genesis of ore.

The ÖSC region experienced a mining boom in the 15th and 16th century with silver-rich galena being a sought-after ore. Emerging Zn production rejuvenated mining in the 19th century, and the Schneeberg-St. Martin mine grew to one of Central Europe's major Pb-Zn producers. In the 1960ies, annular productions reached a climax with ~50,000 t @ ~7 wt.% Pb and ~1.5 wt.% Zn. Mining activity terminated in 1989.

2.2 The Schneeberg deposit

The Schneeberg district in the eastern part of the ÖSC hosts the largest Pb-Zn ore deposit in the ÖSC. Schneeberg is located in an amphibolite facies (kyanite zone) metamorphic zone (Mair et al. 2007, and references therein). Country rocks are mainly paragneisses with minor mica schists and amphibole-garnet schists.

Within the Schneeberg mine, three orebodies were exploited. They are mostly concordant with the moderately steep, NNW dipping lithostratigraphy and metamorphic foliation. Main mineralisation style is massive layers of sphalerite - galena ± pyrrhotite ± chalcopyrite ± sulfosalts with variable quantities of the gangue minerals quartz - calcite - siderite - dolomite - garnet - tremolite/ ferroactinolithe - antophyllite. Distal concordant ore lenses and discordant remobilised ore are present at the meter scale.

2.3 Paragenetic sequence of mineralisation

The framework of the paragenetic sequence follows the established tectonometamorphic evolution of the ÖSC. Primary massive sulphide mineralisation style during basin evolution was most likely a sedimentary exhalative or shallow bedded vein replacement (Vavtar 1988). However, genesis remains ambiguous without primary phases being preserved. The earliest preserved sulphide texture is a coarse grained type, interpreted as peak-metamorphic stage. At the Schneeberg area Variscan and Eoalpidic orogeny caused similar overprint, which makes a clear age determination impossible. However, this texture is preserved in main ore and in distal remobilised ore, thus remobilisation took place prior to, presumably Eoalpidic, peak metamorphism. Two retrograde metamorphic sphalerite types overprinted the coarse peak-metamorphic textures, an earlier annealed recrystallisation textures, and a latter fine grained dynamic shear texture.

3 Petrography

Massive sphalerite - galena - chalcopyrite ± sulfosalts ± (arseno-) pyrite textures are typical for the Schneeberg ore. Gangue is variably present and always interlocked in the massive sulphide matrix, forming a weak layering, concordant with wall rock foliation.

3.1 Sphalerite textural types

Peak-metamorphic sphalerite: Earliest preserved sphalerite is relatively coarse with grain sizes ranging from 180 to 2100 µm. Growth and deformation twinning is common (Figure 1a). Grain boundaries are serrate or bulged without showing annealing textures.

Annealed sphalerite: This sphalerite type is characterised by a foamy, massive, fabric produced by straight boundaries and 120°-triple points. Grain sizes range from 50 to 550 µm. Recrystallisation replaced larger stage 1 grains (Figure 1a). Typical for stage 4 are pyrrhotite and chalcopyrite trails along the straight grain boundaries. Evidence for progressive deformation of annealed stage 4 sphalerite are deformation twinning, flattening of polygons and associated pyrrhotite/ chalcopyrite trails, bulging along polygon-boundaries, subgrain formation and recrystallization to a fine grained sheared sphalerite.

Sheared Sphalerite: Plastic shearing of sphalerite locally produced fines grained shear bands (Figure 1b).

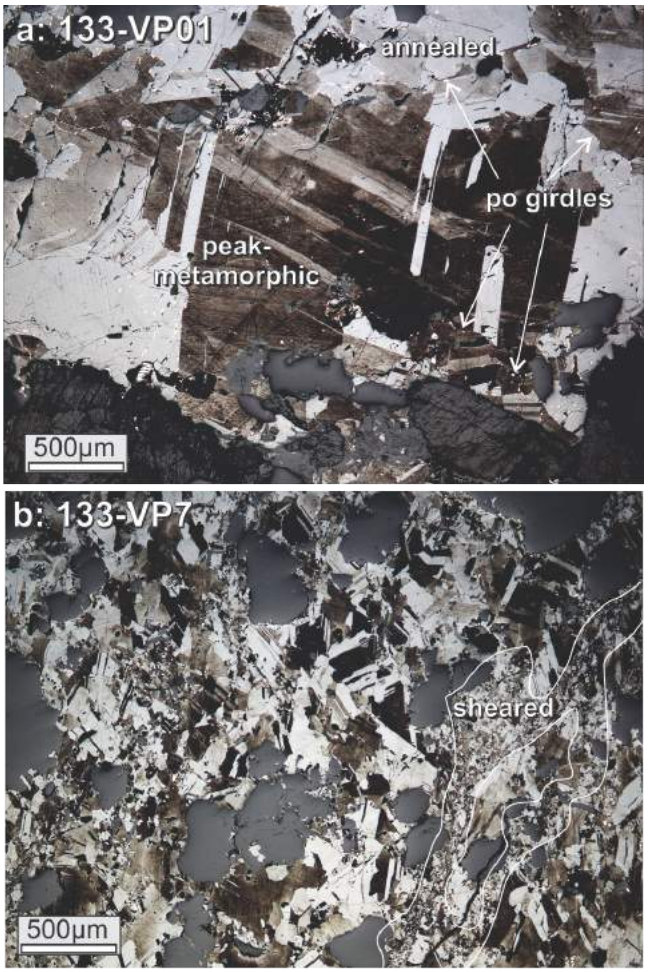

Figure 1. Textural types of sphalerite in Schneeberg ore (H-Iodine etched). (a) peak-metamorphic type, replaced by annealed type with pyrrhotite trails along grain boundaries. (b) A annealed texture, locally replaced by shear bands of dynamic recrystallised sphalerite.

Grain sizes range from 10 to 100 µm. Shearing took place as a progressive deformation within shear zones.

4 Sphalerite mineral chemistry

4.1 Gross element abundances in sphalerite

The following elements are present in sphalerites of the Schneeberg deposit (inclusion-related concentrations being rejected): Fe (7 - 9.6 wt.%), Cd (2800 - 5200 ppm), Mn (155 - 790), Cu (88 - 350), Hg (14 - 420), Co (20 - 440), In (3 - 250), Ga (1 - 18), Ag (1 - 10), Pb (1 - 4), Sn, Sb (<3), As, Ni, Ge, Bi, Cr (< 1).

Fe, Zn, Cd, Hg, In, show smooth and horizontal spectra, suggesting that these elements are hosted in sphalerite solid solution. Inclusions that affect these elements have not been identified in the samples.

Heterogeneous distributed sulphides and sulphosalts affect Pb, Cu, Sb, Ag, As, Ni, Bi, Ge, and Sn. Carbonates and silicates locally change Mn, Ga and Cr abundances. Common chalcopyrite disease shows extreme effects on Cu abundances (up to >>1000 ppm),

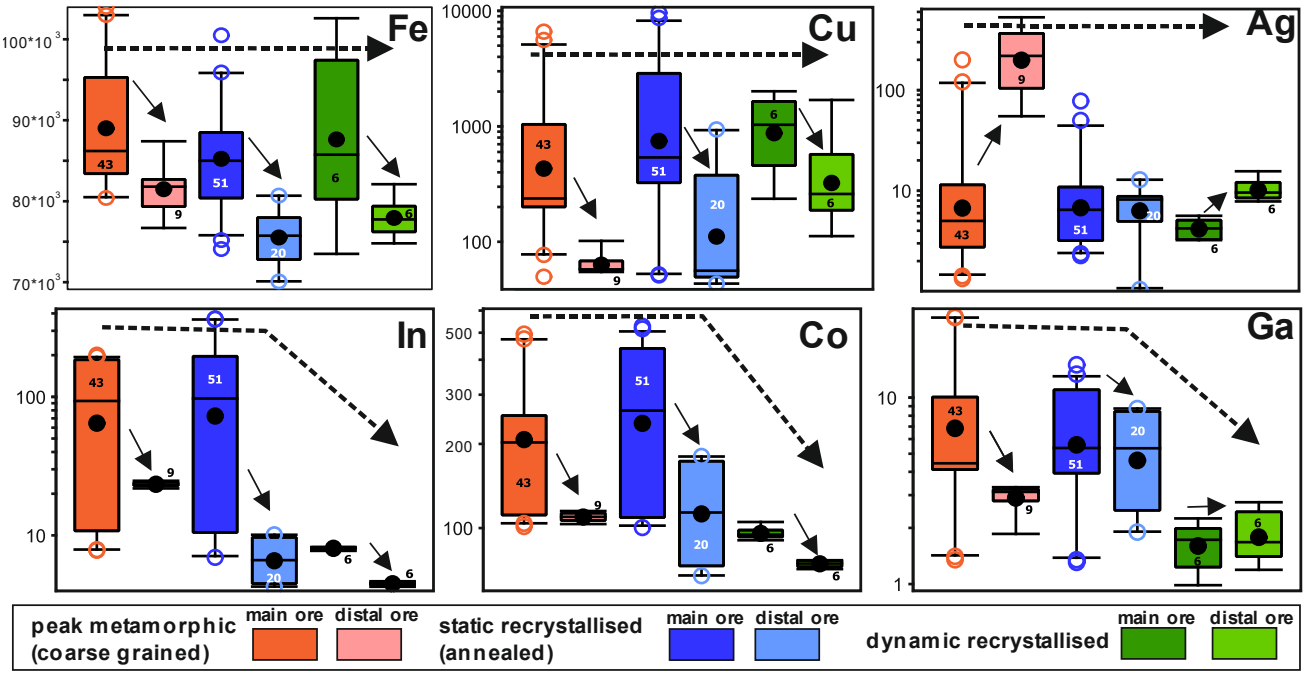

Figure 2. Comparison of element abundances between main ore and remobilised distal ore, and between sphalerite textural types.

while pyrrhotite "diseases" affect Fe to a lesser extent, because of the generally high content in sphalerite.

When comparing main ore with a distal (remobilised) ore, the trace element abundances in sphalerite vary: Fe, Cu, In, Co, and Ga show lower abundances in distal ore (Figure 2). Only Ag shows elevated abundances in distal ore, all other elements do not show clear trends.

A comparison of the three sphalerite types shows that there are some significant variations: While most elements do not show significant differences, the trace metals In, Co, and Ga are depleted in recrystallised sphalerite (Figure 2).

4.2 Spatial distribution in sphalerite types

In EPMA element maps the main elements Fe, Zn, Cu have been mapped. It is shown in various examples that Fe mobility took place at the grain scale in response to deformation: annealed sphalerite has characteristic pyrrhotite trails along the straight grain boundaries, mainly located at 120 triple points. Fe depletion in the vicinity of grain boundaries is shown (Figure 3a). Complete Cu depletion near annealed grain boundaries is revealed, leaving remnant chalcopyrite only in the crystallite cores. Similarly, Cu is depleted in sheared sphalerite (Figure 3b), while disseminated pyrrhotite grains remain in the sheared texture between sphalerite.

5 Discussion and Conclusions

5.1 Controlling mineral hosts

Elements are categorised into three groups with respect to their predominant mineral hosts: (1) *in solid solution* are Zn, Cd, Hg, In, Se. (2) *predominantly in sphalerite solid solution and minor inclusions* are Mn, Co, Ga, Cr, while Fe and Cu are heavily effected by diseases, (3) *predominantly in inclusions and minor presences in solid solution* are Pb, Sb, Ag, As, Ni, Sn, Ge, Bi.

5.2 Processes of element mobilisation

Elements are subject to remobilisation during ore modification at various scales. At the decameter scale inter-metamorphic mobilisation of sulphides is evident by distal, partly discordant vein-type mineralisation. Fe, Cu, In, Ga, Co are depleted in remobilised ore. This depletion may be related to lower fluid temperatures, and/or variations in the travelling distances, thus solubility of elements. Silver is enriched in distal or, indicating highest solubility at the given alteration temperatures.

Pyrrhotite and chalcopyrite diseases are evidence of local Fe and Cu mobilisation during sphalerite annealing. Here no depletion of trace elements is recorded. Pyrrhotite exsolution (Mizuta 1988; Mizuta and Scott 1997) is evident by Fe depletion in the vicinity of grain boundaries. Whether Cu was primarily within the sphalerite structure (c.f., Barton Jr and Bethke 1987) is unlikely, considering that average concentrations of up to 5000 ppm exceed the Cu dissolution capacity in sphalerite (Bortnikov et al. 1991).

Further Cu mobility took place during dynamic recrystallisation. Here, In, Ga and Co are also depleted. A combined mobilisation of mono-valent Cu^{+} and tri-valent In^{3+}, Ga^{3+}, and ($Co^{2+/3+}$) are explained by their coupled presence in and hence ejection from the ZnS structure.

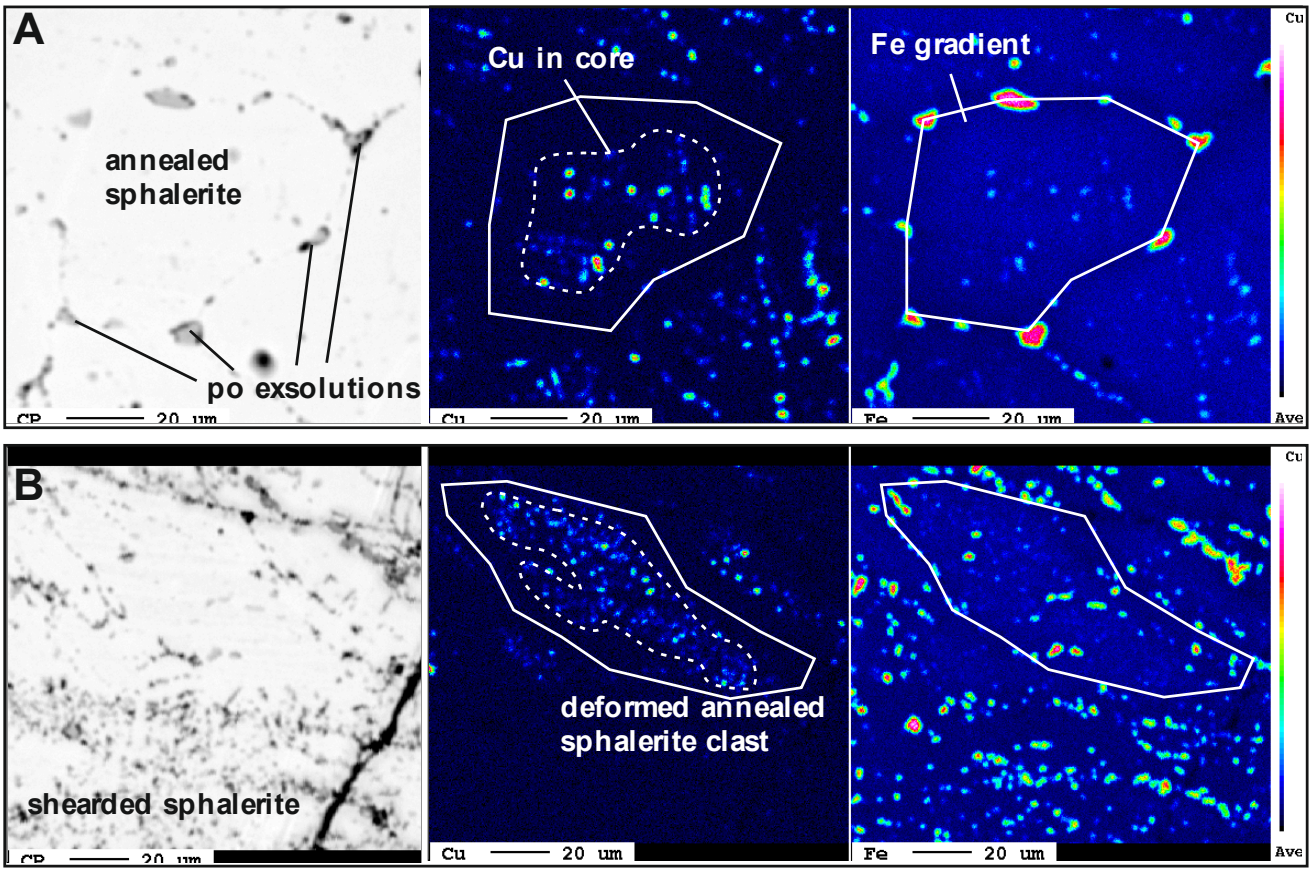

Figure 3. EMPA backscatter, Cu and Fe maps of sphalerite textures. (a) annealed sphalerite polygon with pyrrhotite exsolution trails along grain boundaries and Fe depletion. See the remnants of chalcopyrite (cpy) in the core and absence of cpy close to the grain boundaries. (b) sheared sphalerite matrix showing partial absence of cpy in a clast and complete vanishing within the shear zone.

Dynamic recrystallisation-induced Cu, In, Ga, and Co, mobilisation was at larger scale than Fe, which locally re-precipitated in pyrrhotite. This suggests a fluid-assisted deformation process.

These outcomes indicate a high complexity of modifications of rare metal budgets in metamorphosed stratiform massive sulphide deposits. In future we aim to map trace elements by Nano-SIMS. Implications to metamorphic ore genesis / modification and geometallurgy of high-tech metal are evident.

Acknowledgements

The presented study is part of the project *High-Tech metals in the Ötztal-Stubai crystalline mass*, which is funded by the Austrian Federal Ministry of Education, Science and Research.

References

Barton Jr P, Bethke PM (1987) Chalcopyrite disease in sphalerite: pathology and epidemiology. Am Mineral 72:451-467

Bortnikov N, Genkin A, Dobrovol'Skaya M, Muravitskaya G, Filimonova A (1991) The nature of chalcopyrite inclusions in sphalerite; exsolution, coprecipitation, or" disease"? Econ Geol 86:1070-1082

Cook NJ, Ciobanu CL, Pring A, Skinner W, Shimizu M, Danyushevsky L, Saini-Eidukat B, Melcher F (2009) Trace and minor elements in sphalerite: A LA-ICPMS study. Geochim Cosmochim Ac 73:4761-4791

Frenzel M, Hirsch T, Gutzmer J (2016) Gallium, germanium, indium, and other trace and minor elements in sphalerite as a function of deposit type—A meta-analysis. Ore Geol Rev 76:52-78

George L, Cook NJ, Ciobanu CL (2015) Trace Element Partitioning between Co-Existing Sphalerite, Galena and Chalcopyrite. In: et al, Mineral Resources in a Sustainable World, 13th Biennial SGA Meeting, Nancy, France, Proceedings, pp 737-740

Lockington JA, Cook NJ, Ciobanu CL (2014) Trace and minor elements in sphalerite from metamorphosed sulphide deposits. Miner Petrol 108:873-89

Mair V, Vavtar F, Schölzhorn H, Schölzhorn D (2007) Der Blei-Zink-Erzbergbau am Schneeberg, Südtirol. Mitt Österr Mineral G 153:145-180

Mizuta T (1988) Interdiffusion rate of zinc and iron in natural sphalerite. Econ Geol 83:1205-1220

Mizuta T, Scott SD (1997) Kinetics of iron depletion near pyrrhotite and chalcopyrite inclusions in sphalerite; the sphalerite speedometer. Econ Geol 92:772-783

Sinclair WD (2014) Electronic Metals (In, Ge and Ga): Present and Future Resources. Acta Geol Sinica (English Edition) 88:463-465

Vavtar F (1988) Die Erzanreicherungen im Nordtiroler Stubai-, Ötztal-und Silvrettakristallin. Arch Lagerstforsch Geol B-A 9: 103-153

Stacked VHMS potential at Erayinia in the Eastern Goldfields Superterrane, Western Australia?

Jamie Kelly, Stephen Roberts, Alex Webber
University of Southampton, UK

Steven Hollis,
Geological Survey Ireland & University College Dublin, Ireland

Darryl Podmore, Megan James, Allan Kneeshaw
Black Raven Mining, Western Australia

Abstract. Despite decades of interest, few significant VHMS resources have been delineated in the Archean Yilgarn Craton of Western Australia. At Erayinia in the southern Eastern Goldfields, a small Zn-(Cu) VHMS deposit (King; 2.15Mt at 3.47% Zn) occurs in an overturned and metamorphosed volcanic sequence. Here we present the first results of an exploration target 2.5km to the north, where recent drilling has intercepted zones of Zn-Cu-Au mineralization over a multi-element soil and VTEM anomaly. Combining core logging, detailed petrography of rock chips, SEM imaging, XRD analysis, and high quality fusion lithogeochemistry, the King North stratigraphy has been characterized and correlations made with the King area. Furthermore, hydrothermal signatures have been recognized that are consistent with an overturned VHMS system. The presence of HFSE enriched (FIII-affinity) rhyolites is significant, in addition to a unit of BIF identified higher in the stratigraphy (associated with quartz-sericite-pyrite altered felsic volcanic rocks). The latter suggests there is stacked VHMS potential in the King/King North regional stratigraphy.

1 VHMS mineralization at Erayinia

Volcanic-hosted massive sulfide (VHMS) deposits occur throughout Earth's history and are an important source of base and precious metals (Galley et al. 2007). Despite decades of interest, few significant VHMS resources have been delineated in the Archean Yilgarn Craton of Western Australia. Exploration is hampered by a combination of a paucity of outcrop, deep weathering, and saline groundwater in geologically complex greenstone belts (Hollis et al. 2005).

At Erayinia in the southern Kurnalpi Terrane (Fig. 1), geophysical methods have had limited success in identifying and locating mineral deposits. Geophysical responses from conventional airborne VTEM surveys in the region are strongly affected by conductive sediments, hypersaline groundwater, and units of black shale within the host stratigraphy. Furthermore, relics of an Eocene marine transgression are scattered throughout the region, and several large salt/playa lakes drain the local area. Consequently, the current landscape is characterized by limited outcrop, and bedrock obscured by deep and variable cover.

In the far south of the Edjudina Domain at King, a small base metal deposit has been recognized (~2.15 Mt at 3.47% Zn, non-compliant at 1% cut-off) in a metamorphosed (lower amphibolite), overturned and east-dipping volcanic rock dominated sequence (Hollis et al. 2019). The local stratigraphy is dominated by garnet-amphibolite, intermediate to felsic banded schist, and rare zones of graphitic schist and talc schist (Hollis et al. 2019). Massive sulfide mineralization (1-7m thick) is characterized by stratiform pyrite–pyrrhotite–sphalerite. Locally intense zones of pyrite-(sphalerite) and pyrrhotite–pyrite–(chalcopyrite) veining occurs throughout footwall lithologies, coincident with a feeder zone characterized by quartz-chlorite±magnetite schist, and cordierite-anthophyllite bearing banded schist. The deposit has a confirmed strike length of ~600m, depth of >500m, and remains open in three directions.

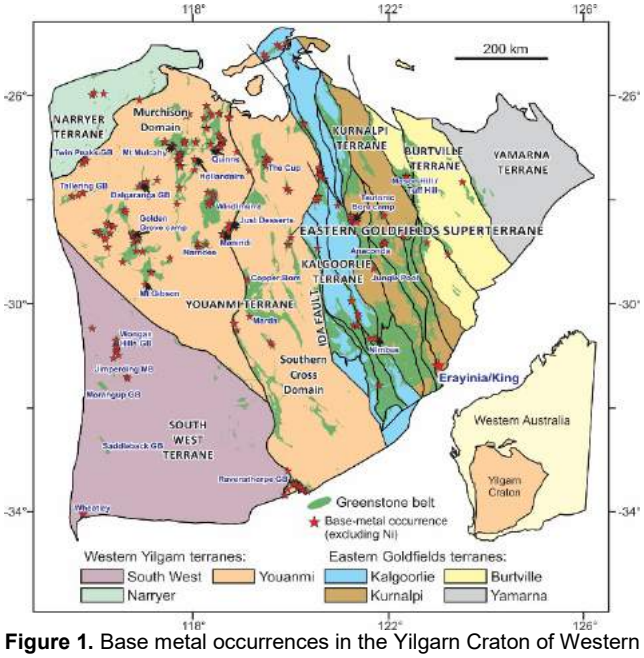

Figure 1. Base metal occurrences in the Yilgarn Craton of Western Australia (modified after Hollis et al. 2015). Significant VHMS deposits and mineral occurrences are labelled.

2 King North

In recent years (2012-2019) Black Raven Mining have

conducted an extensive program of soil and rock-chip geochemistry across the Erayinia area. A heliborne VTEM (Versatile Time Domain EM) geophysical survey was also flown in 2013 identifying 24 targets. In this paper we focus on the King North area, ~2.5km along strike north from the King deposit. A transect of seven west-dipping Reverse Circulation (RC) holes were drilled in 2015-2016 (Fig. 2) over a multi-element soil (Zn-Cu-Pb-Tl-Bi-W-Mo) and VTEM anomaly. An additional RC hole dipping 60°E (EC179) was also drilled in this transect, and in 2018 a diamond extension to RC hole EC173 (from ~125 to 360m). Drilling was in part funded by an Exploration Incentive Scheme grant from the Department of Mines and Petroleum (DMP), Western Australia. Several zones of base and precious metal mineralization have been intersected to date, including:

- EC164: 1m at 4.66% Zn, 2.14% Pb, 0.69g/t Au.
- EC175: 11m at 0.34% Cu, 0.52g/t Au, including 1m at 0.11% Zn and 3.21g/t Au.
- EC179: 13m at 0.2% Cu, 0.16g/t Au.

Through detailed petrography, X-ray Diffraction (XRD), Scanning Electron Microscopy (SEM) analysis of rock chips, extensive lithogeochemistry, and logging of recently drilled diamond core, we have characterized the King North stratigraphy and established clear correlations to units farther south at King. Geochemical signatures are consistent with an overturned VHMS system with the main feeder zone not yet identified.

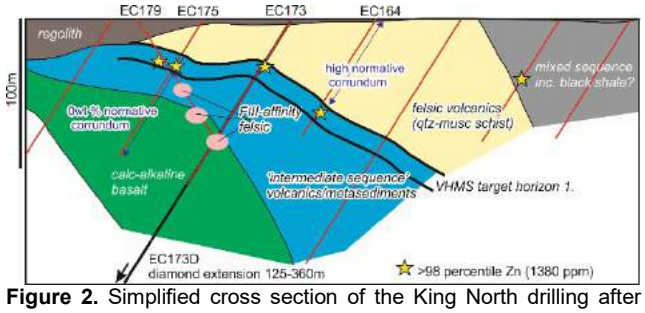

Figure 2. Simplified cross section of the King North drilling after Kelly (2018).

3 Methodology

Rock chips derived from RC drilling were collected from two holes at King North (EC164 and EC175) for detailed petrography and SEM analysis. Four acid digest geochemical data was also supplied by Black Raven Mining for all RC holes along this transect. This was used to correlate identified lithologies between drillholes. From these data, 26 samples were selected for high-quality fusion lithogeochemistry at ALS Laboratories, Ireland. Precision and accuracy for lithogeochemistry was monitored using a suite of laboratory blind standards. X-ray diffraction (XRD) analysis was performed at the University of Southampton on 22 samples to complement the existing lithogeochemical dataset. Samples were chosen based on depth and a variety of geochemical parameters in order to provide a representative analysis of each hole.

4 Stratigraphy

Based on the extensive petrological and geochemical observations, three broad stratigraphic sequences were defined and correlated across the main area of RC drilling (Fig. 2). Logging of the diamond extension EC173D is summarized in Figure 3, with key lithologies shown in Figure 4. Metamorphic grade appears to increase slightly to the east from lower to upper greenschist facies. This is significantly lower than at King (amphibolite facies) which is closer to a large, late-stage granitic pluton.

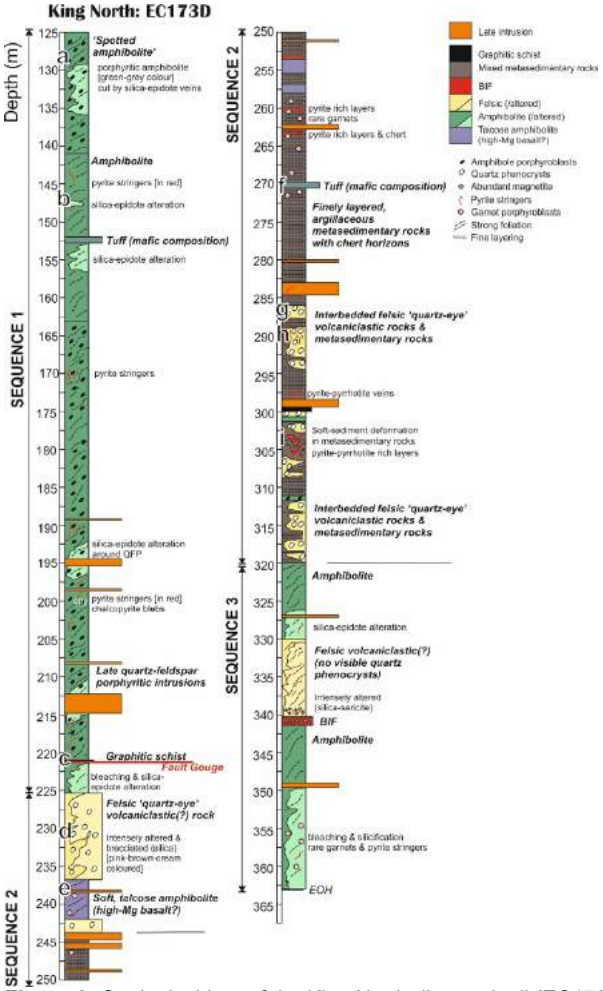

Figure 3. Geological Log of the King North diamond tail (EC173D).

Felsic volcanic and volcaniclastic rocks dominate the upper portions of the RC drillholes. These rocks are dominated by quartz, chlorite and muscovite, with lesser illite, rutile, apatite, zircon and monazite. Immobile element characteristics include high Zr/Ti ratios, FII characteristics (Lesher et al. 1986; Hart et al. 2004) and steeply dipping, LREE-enriched trace element profiles. Pronounced negative Eu anomalies are consistent with plagioclase fractionation at depth. These rocks can be classified as quartz-muscovite±chlorite phyllites or schists.

A relatively thin (~50m thick) package of rocks (of intermediate geochemical composition) occur between

the felsic rocks (near surface) and those of mafic composition at depth. Examined rock chips are either sedimentary or volcaniclastic in origin, and have a highly variable mineralogy (quartz, epidote, amphibole, chlorite, muscovite). Perhaps the most significant finding is the recognition of FIII-affinity (Lesher et al. 1986; Hart et al. 2004) rhyolites at several depths in drillhole EC179 near the top of the 'intermediate sequence' (assuming an overturned stratigraphy – see Section 4). These high field strength element (HFSE) enriched rhyolites have very high Zr/Ti ratios, and Y concentrations exceeding 25ppm. Such rocks are indicative of shallow crustal melting (Lesher et al. 1986; Hart et al. 2004), and are a common host to VHMS mineralization across the Yilgarn and other Archaean cratons (references in Hollis et al. 2015). The base of the 'intermediate sequence' includes the most significant base metal intercepts (VHMS target horizon 1; Fig. 2).

Mafic rocks at depth are dominated by amphibolite, epidote (clinozoisite), chlorite and quartz. Minor muscovite and plagioclase (albite) was noted in the matrix, along with titanite and apatite. These rocks can be classified as amphibolites and actinolite-chlorite schists. Immobile element ratios are subalkaline and samples plot predominantly within the calc-alkaline fields of Pearce (1996) and Hastie et al. (2007). Chondrite normalized REE profiles are typically flat, as at King (Hollis et al. 2019).

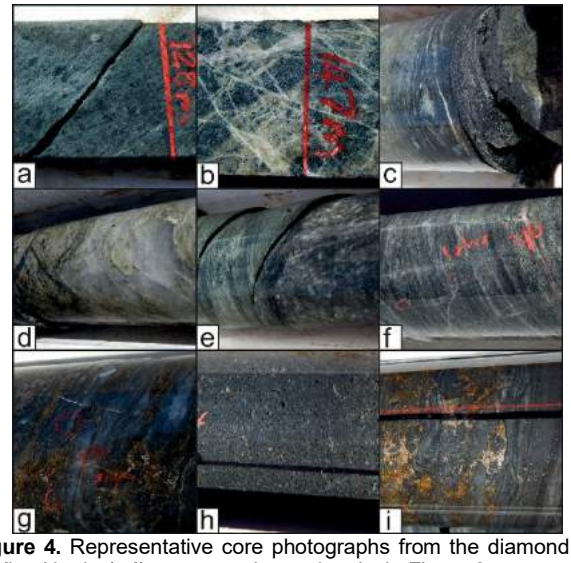

Figure 4. Representative core photographs from the diamond tail at King North. (**a-i**) correspond to rock units in Figure 3.

Rocks logged from the diamond tail of drillhole EC173 (Fig. 3) can be divided into three broad sequences:

1. A thick sequence of silica-epidote altered amphibolite (Fig 3a,b) - a likely continuation of the above mafic stratigraphy. Rare horizons of graphitic schist (Fig. 3c) and mafic tuff also occur. Garnet porphyroblasts are absent, but are abundant in similar rocks from King.

2. A mixed sequence dominated by argillaceous metasedimentary rocks (Fig. 3i). Rare units of altered 'quartz-eye' felsic volcaniclastic rocks (of unknown F-affinity; Fig. 3d,f,g), talcose high-Mg basalt (Fig. 3e), and mafic tuff (Fig. 3h) also occur.

3. A sequence of amphibolite, with a narrow zone of intensely altered (quartz-sericite-pyrite) felsic volcaniclastic rocks and banded iron formation (BIF). The latter resembles a unit from the immediate hanging-wall of the King deposit.

5 Implications for VHMS mineralization

The presence of normative corundum from CIPW calculations is a useful tool for indicating intense alkali leaching in footwall strata associated with VHMS deposits (Grunsky 2013). At King, normative corundum values are highest in the chloritic chalcopyrite-rich feeder zone, and directly below massive sulfides (Hollis et al. 2018). Values are always >0 wt.% in altered footwall rocks due to alkali leaching. By contrast, all hanging-wall units have normative corundum values of 0 wt.% (Hollis et al. 2018).

At King North, samples from holes EC164 yield high values until 73m depth where they drop to zero. A similar situation occurs in EC175 at the shallower depth of 59m (dropping from 6.9-5.5 to 0 wt.%). These depths correlate with the top contact of the felsic rocks assuming an overturned stratigraphy, and corresponds to a zone of highest Zn grades. From this, we infer the stratigraphy is likely inverted (as at King), and that these depths can be inferred to represent the contact between the footwall and hanging-wall to a VHMS target horizon (target horizon 1; Fig. 2). This is also consistent with major element variations (see following), the distribution of pathfinder elements (e.g. Bi, Sb, Ag; Kelly, 2018), and a lack of significant alteration in the mafic sequence.

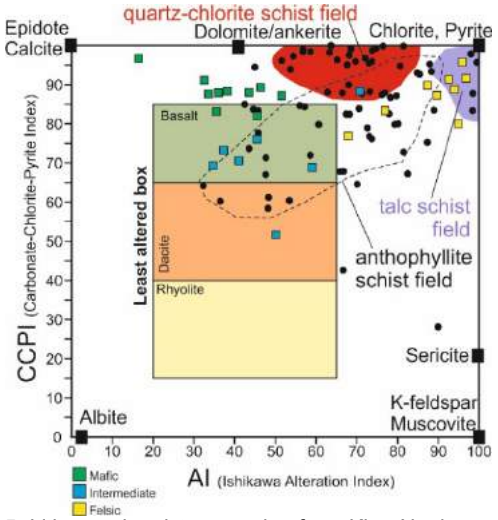

Figure 5. Lithogeochemistry samples from King North on the Box Plot of Large et al. (2001). Data from Hollis et al. (2019; unpublished) from the King deposit (black circles) is shown for comparison.

Felsic rocks from RC drilling at King North are characterized by high SiO_2 (>70 wt.%), generally low Fe_2O_3 (2.35-4.37 wt.%) and low CaO (<1.46 wt.%). Variable Na_2O and K_2O in combination with the above points to intense silicification and sericitic alteration prior to metamorphism. This is consistent with our

petrographic observations of rocks classified as quartz-muscovite±chlorite phyllites/schists. Alteration in the felsic rocks is most intense, plotting towards the chlorite-pyrite node (or 'ore corner') on the Alteration Box Plot of Large et al. (2001; Fig. 5). Mafic and intermediate samples are 'least altered' (Fig. 5). The geochemistry of samples collected from the EC173D diamond tail is in progress.

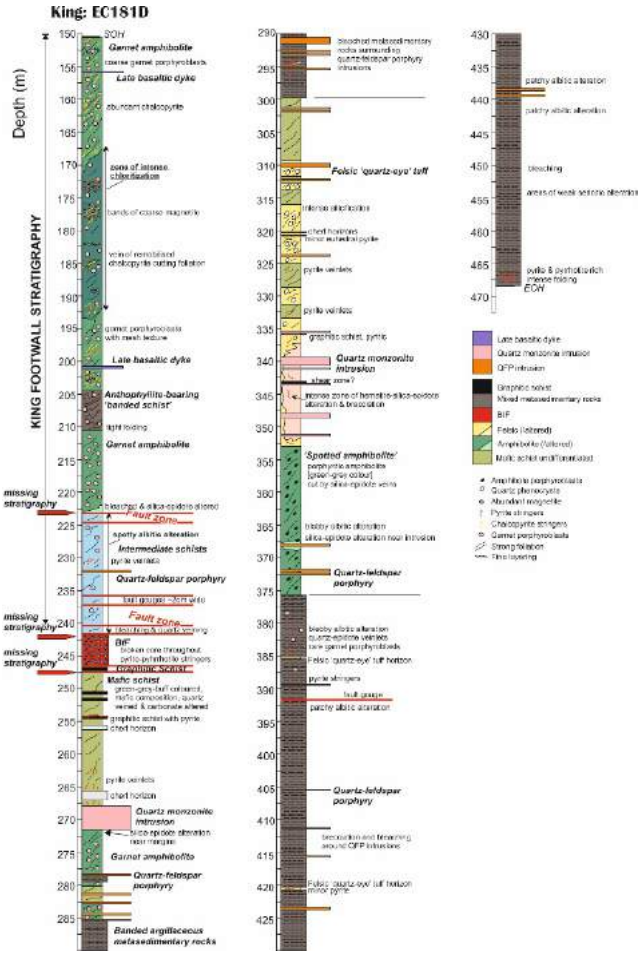

Figure 6. Geological Log of the hanging-wall at King from drillhole EC181D. Note the presence of mafic schists and amphibolite stratigraphically above the BIF (equivalent to King North sequence 1), the return of felsic lithologies (~King North sequence 2) and then a thick sequence of metasedimentary rocks.

6 Stratigraphic correlations

Assuming an overturned stratigraphy, the felsic sequence intercepted in the RC holes at King North is interpreted to broadly correlate with the immediate footwall of the King deposit. The overlying thin 'intermediate sequence' at King North (Fig. 2) may be similar to the immediate hanging-wall at King, which includes BIF, schists of mafic to felsic composition, and graphitic schist (Hollis et al. 2019). This sequence of rocks at King North, which includes FIII rhyolites, represents VHMS target horizon 1 (Fig. 2) for further drill testing. If further investigation was to identify thick units of extrusive FIII affinity rhyolite, this would be significant for exploration.

Diamond drillhole EC181D provides the fullest picture of the hanging-wall stratigraphy at King (Fig. 6), as few other holes were drilled >10m past the ore zone and hanging-wall BIF. Higher in the stratigraphy, above the BIF, a return to more mafic lithologies is evident in EC181D (represented by mafic schist and amphibolite in Fig. 6). This is followed by the return of 'quartz-eye' felsic volcaniclastic rocks, and a thick sequence of finely layered metasedimentary rocks. This sequence can be broadly correlated with lithologies intercepted in drillhole EC173D from King North (sequences 1 and 2 of Fig. 2).

Based on the above correlation, it is anticipated that further into the hanging-wall at King a second BIF horizon will occur. At King North this horizon is associated with hydrothermally altered (and weakly mineralized) felsic rocks. If our correlation is correct, there is the potential for additional VHMS deposits stacked higher (farther west) in the regional King stratigraphy.

Acknowledgements

The authors thank Black Raven Mining for funding this research. Ross Williams and Richard Pearce are also thanked for assistance with XRD and SEM analysis at the University of Southampton. SPH is funded by Geological Survey Ireland/DCCAE Postdoctoral Fellowship Programme, No. 2016-PD-003.

References

Galley AG, Hannington MD, Jonasson IR (2007) Volcanogenic massive sulfide deposits. In Goodfellow WD (ed) A synthesis of major deposit-types, district metallogeny, the evolution of geological provinces, and exploration methods, 141-161.

Hart TR, Gibson HL, Lesher CM (2004) Trace element geochemistry and petrogenesis of felsic volcanic rocks associated with massive Cu-Zn-Pb sulfide deposits. Econ Geol 99:1003-1013.

Hastie AR, Kerr AC, Pearce JA, Mitchell SF (2007) Classification of altered volcanic island arc rocks using immobile trace elements: development of the Th-Co discrimination diagram. Journal Petrol 48: 2341-2357.

Hollis SP, Yeats CJ, Wyche S, Barnes SJ, Ivanic TJ, Belford SM, Davidson GJ, Roach AJ, Wingate MTD (2015) A review of volcanic-hosted massive sulfide (VHMS) mineralization in the Archaean Yilgarn Craton, Western Australia: tectonic, stratigraphic and geochemical associations. Precamb Res 260:113-135.

Hollis SP, Podmore D, James M, Menuge JF, Doran AL, Yeats CJ, Wyche D (2019) VHMS mineralization at Erayinia in the Eastern Goldfields Superterrane: geology and geochemistry of the metamorphosed King Zn deposit. Aus J Earth Sci 66:153-181.

Kelly J (2018) Characterisation of the King North volcanic massive sulfide deposit, Yilgarn Craton, Australia. Unpublished undergraduate thesis, University of Southampton, 50p.

Large RR, Gemmell JB, Paulick H (2001) The Alteration Box Plot: A simple approach to mineralogy and lithogeochemistry associated with volcanic-hosted massive sulfide deposits. Econ Geol 96:957-971.

Lesher CM, Goodwin AM, Campbell IH, Gorton MP (1986) Trace-element geochemistry of ore-associated and barren, felsic metavolcanic rocks in the Superior province, Canada. Can J Earth Sci 23:222-237.

Pearce JA (1996) A user's guide to basalt discrimination diagrams. In Wyman DA (ed). Trace element geochemistry of volcanic rocks: applications for massive sulfide exploration, 79-113.

Mineralogical and geochemical characterisation study of Perkoa Zn mine, Burkina Faso, West Africa

Oliver Parker
Department of Earth Science and Engineering, Imperial College, London, UK

Robin N. Armstrong, Richard J. Herrington
Earth Sciences Department, Natural History Museum, London, UK

Matthew James
Trevali Mining Corporation, Canada

Abstract. This study focuses on the Perkoa Zn deposit, Western Burkina Faso, currently operated by Trevali Mining Corporation. Previous works have not conclusively established the style of mineralization at Perkoa suggesting either VMS or skarn origins. The deposit is located in the Boromo belt of Leo-Man Shield, within the West African Craton. The N-S trending Boromo belt is composed of mafic and intermediate volcanics at its margins, and volcano-sedimentary and sedimentary units in the central portion. This package underwent polyphase deformation during the Eburnean orogeny. The aims of this project are to address the following areas regarding the deposits origin and formation: Determine if the deposit is a VMS or Skarn (debated in the previous study); characterise the lithologies in and around the deposit; propose a formation process for the deposit; and to characterise the alteration geochemistry, developing exploration vectors.

1 Introduction

The Perkoa Zn deposit is located in the Sanguie region of western Burkina Faso. The deposit is hosted within the Boromo Belt of the Birimian Supergroup (Leube et al. 1990), formed during a period of arc-volcanism in the Paleoproterozoic dated to ~2190-2160 Ma (Baratoux et al. 2015). The Birimian Supergroup is comprised of greenstone-granitoid assemblage which are made up of volcano-sedimentary belts separated by extensive tonalite-trondhjemite-granodiorite (TTG) /granitoid provinces or comparatively younger sedimentary basins (Fig. 1).

The Zn mineralisation at Perkoa occurs as a series of stacked, northeast-southwest striking massive sulphide lenses sitting subparallel to foliation. These are hosted within greenschist metamorphosed andesitic tuffs, interpreted as being overturned and dipping at ~70° towards the NW. A granodioritic body (dated 2175 ± 1Ma, U-Pb zircon; Schwartz & Melcher 2003) has intruded the area to the SE and field relationships described, suggest that it post-dates the initial mineralisation. The massive sulphide mineralisation is dominated by coarse sphalerite (30%), pyrite (25%), barite (10%), pyrrhotite (5%), magnetite (5%) and white mica (Schwartz & Melcher 2003). The deposit is a high-grade zinc deposit (averaging 14% Zn) but contains significantly less copper and lead (averaging 60ppm Cu and 0.1% Pb), elements commonly associated with other Zn rich massive sulphide deposits (Torben et al 2018). The remaining measured and indicated resource of 4.85Mt current at a grade of 13.73% Zn with mineralisation still open at depth.

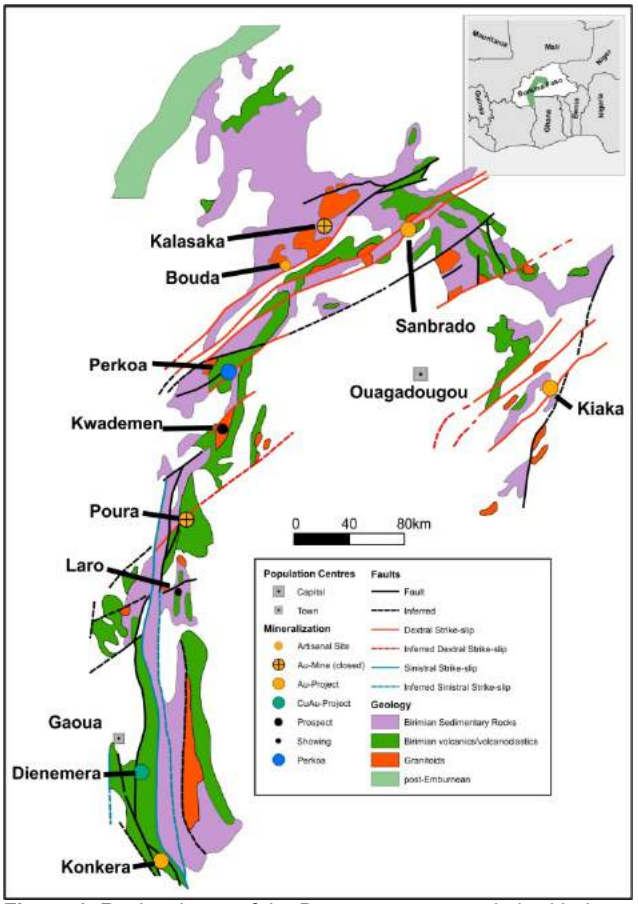

Figure 1. Regional map of the Boromo greenstone belt with the locations of the current mineralization centres and the position of the Perkoa Zn deposit (after Béziat et al 2000). The inset map shows the position of the Boromo greenstone belt with in Burkina Faso.

2 Methodology

A suite of 16 samples were selected from drill core, the open pit and the underground workings representing the key lithologies and mineralization styles. The spatial distribution of the samples reflected distance from the mineralization and the intrusive margin.

Polished sections were prepared for petrological description and mineral chemistry analysis by EDS by analytical-SEM. Whole rock geochemistry was determined at ALS using the propriety Complete Characterisation Package.

3 Results

3.1 Lithological observations

The study represents the first optical petrography description of the Perkoa lithologies. The main litho-types identified are:

An andesitic lapilli tuff, characterised by a predominantly massive fine to medium grained rock with occasional lapilli sized clasts of two feldspar porphyritic material. The mineralogy is dominated by quartz, feldspar, biotite and chlorite and has been metamorphosed to approximately greenschist facies.

An andesitic-volcanoclastic characterised by a strong pervasive foliation and weaker crenulation with a pronounced banding. The bands are formed of quartz + plagioclase + mica + epidote + titanite + ilmenite and chlorite + quartz + epidote. Overall the mineralogy and fabric suggest a metamorphic grade of greenschist facies.

The most felsic volcanic lithology observed is the quartz eye rhyolite, which is characterised by the presence of large quartz phenocrysts in quartz-rich + plagioclase + white mica ground mass. This lithology maybe representative of a cryptodome facies/ subvolcanic intrusion.

The most enigmatic lithology is described at site as a quartz exhalative, in hand specimen is typified by an absence of foliation, however under the microscope the textures and mineralogy suggest a re-worked felsic rock.

The late intrusion, which cross-cuts all the other lithologies, is a coarse grained equigranular leucocratic rock composed of plagioclase + quartz + biotite and Fe-oxides. In places the rock mass is overprinted by a haematitic alteration. This granitoid body shows no obvious deformation features.

The skarn-rocks, are characterised by a high magnetite content and frequent euhedral garnets which have undergone significant alteration to chlorite, possibly as a consequence of retrograde metamorphism.

A key texture observed is the differing fabrics of chlorite. Chlorite is ubiquitous through the more mafic members of the volcanic succession as foliation 'controlled' chlorite (Figure 2A), However, when approaching mineralization chlorite is observed to form a 'parquet-like' texture (Figure 2B). The massive sulphides in the observed intercepts are variable in texture at the macroscopic and microscopic scale. The lenses vary from massive sulphide (sulphide >90%) to a strongly layered sulphide dominated rock, to a clastic semi-massive sulphide containing clasts of host rock. Both lenses are dominated by sphalerite at the stratigraphic top of the lenses with increasing amounts of pyrite and pyrrhotite towards the stratigraphic base of the lenses. Minor chalcopyrite is observed at the base of the lens.

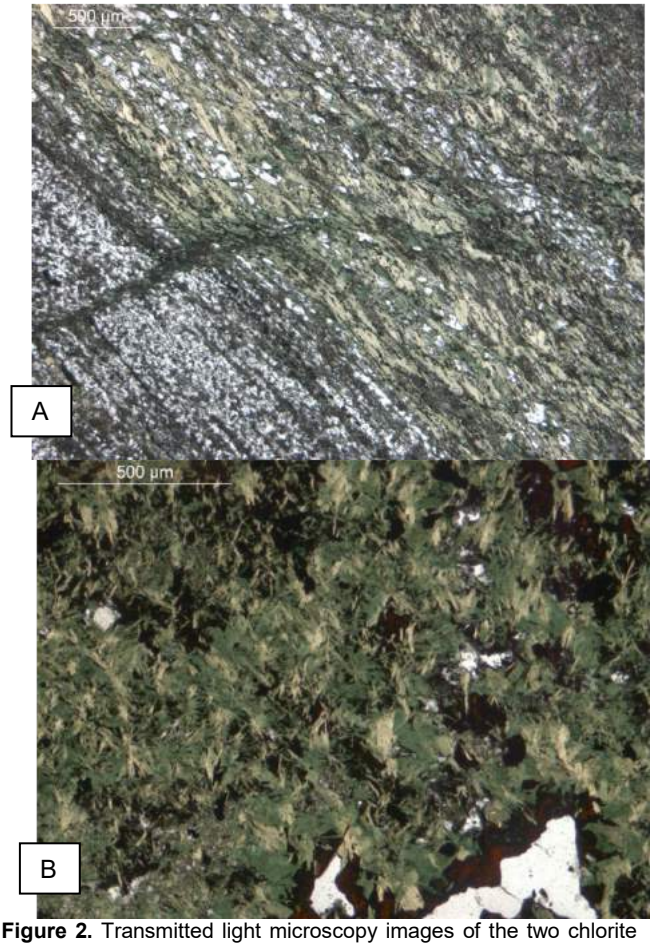

Figure 2. Transmitted light microscopy images of the two chlorite phases seen in the deposit. **A**) Elongate pervasive chlorite aligning with chlorite **B)** Chlorite concentrated into bands displaying a parquet-like appearance and located proximal to ore

3.2 Whole rock geochemistry results

Major element distributions suggest that there has been significant elemental mobilization due to both hydrothermal alteration and metamorphism (regional and contact). However, initial use of conventional major element classification plots, such as TAS (Maitre 1989), R1-R2 (De La Roche et al 1980) and the Jenson Cation plot (Rollinson 1993) show the data to form coherent trends from basaltic andesites to andesites to rhyolites.

Using trace element based classifications diagrams (the Th-Co plot, the modified Winchester-Floyd plot and the $(Zr/TiO_2)/SiO_2$ the samples consistently plotted in the basalt-basaltic andesite fields with the high silica samples plotting as rhyolites. In the Y/Zr plot of MacLean and Barret 1993 the suit of samples show a coherent trend within the calc-alkaline field. Overall the REE patterns when normalized show elevated light REE compared to the heavy REE with a flat to positive Eu

anomaly. This steep LREE, flat HREE pattern is consistent with those expected from a volcanic-to back arc environment.

The effects of hydrothermal alteration were further evaluated using the Alteration Box Plots (Large et al 2001) which showed that where the majority of the samples plotted within the least altered andesite basalt box, some samples, including those rich in sulphide trended towards a chlorite-carbonate-pyrite index (CCPI) = 100. When elements are plotted for the same lithology on the basis of distance to mineralization, some elemental mobility is evident. However, this appears to be largely a consequence of dilution due to increasing sulphide content in the footwall.

3.3 Mineral chemistry results

Chlorite compositional data collected by EDS shows clear variation with distance from ore. As described above chlorite is observed as being related to the metamorphic fabric and as the parquet-like texture related to a hydrothermal event. The chlorites of hydrothermal origin are Fe-rich chamosites whereas the chlorites related to the regional metamorphism are more Mg-rich towards the clinochlore end member (Fig. 3).

EDS analysis of the garnets from the skarn-rocks of the open pit showed that the skarn is typified by Mn-rich garnets close to the spessartine end member; whereas garnets, where present, away from the contact aureole are typically closer to the almandine end member composition.

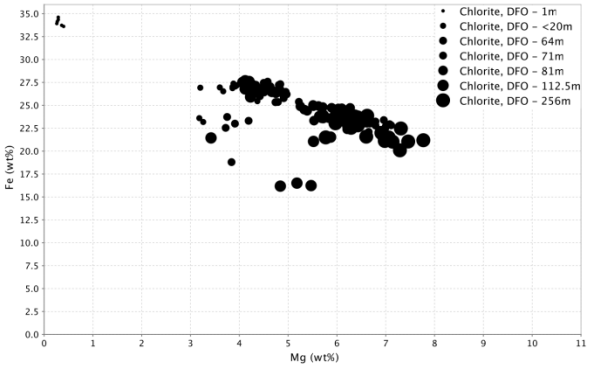

Fig. 3: Plot of iron and magnesium content in individual chlorite crystals from throughout the deposit. Insets: S.E.M spectra for end compositions of the two chlorite phases

4 Discussion

4.1 Ore formation

The following characteristics support a VMS origin for the Perkoa sulphide bodies: Massive to semi-massive sulphide lenses with variable textures, the intimate spatial and temporal relationship of the sulphide lenses with a sea floor deposited rhyolitic to basaltic composition volcanic succession.

The two lenses, although formed by the same hydrothermal system are proposed to have formed in different environments. The stratigraphically lower lens is interpreted as having formed in the paleo-subseafloor, while the stratigraphically higher lens is thought to be exhalative and to have formed on the paleo-seafloor.

Field observations from the open pit suggest that the main conduit to the hydrothermal, with at least two stages of activity causing for the separate lenses and environments. The 'quartz exhalative' lithology, which is located stratigraphically above the lenses, is suggested to have acted as a cap facilitating preservation of the sulphide lenses.

4.2 Implications of skarn formation

Field and geochemical observations suggest that the skarn event, related to the emplacement of the late granite, overprints the altered HW rocks of the deposit, redistributing mobile elements such as manganese which was previously concentrated during the VMS-style mineralizing event. The main effects skarn formation has on the lenses are: The recrystallisation of sphalerite to marmatite; deflection of the lenses to follow the geometry of the intrusion boundary and; the re-mobilisation and recrystallization of the barite and sulphide mineralization in the overprinting skarn facies.

4.3 Alteration

Three main alteration assemblages/products are observed throughout the deposit, varying with distance from ore. These are summarised below in Table 1.

Table 1. Description of the main alteration-types in the footwall and their spatial relationship to ore.

Alteration	Spatial Distribution (footwall)	Description
Chlorite-Quartz-Magnetite	Proximal	Large, interlocking euhedral Quartz crystals with intergranular chlorite and magnetite. Bands of concentrated chlorite observed with a parquet-like texture with minor sulphides and magnetite.
Amphibole-Chlorite-Epidote	Intermediate	Vein controlled alteration with elongate amphiboles seen wrapping round clasts composed of chlorite + epidote + sulphides (minor)
Sericite	Intermediate -Distal	Destruction of plagioclase crystals forming needle-shaped crystal of sericite. Seen intergrowing with chlorite.

These are interpreted as being related to the fluid-rock ratio in different areas of the system. Proximal to mineralisation the fluid-rock ratio is thought to be high causing all elements to be stripped and only quartz being able to crystallise into large interlocking crystals and chamosite from the iron rich fluids. Further from the mineralisation the fluid-rock ratio is assumed to be lower and constrained to fractures within the rock resulting in the formation of iron rich amphibole veins which have incorporated clasts of chlorite and epidote. Classic sericitic alteration is seen and linked to the destruction

of plagioclase, the intensity of sericitization increases as you move further from mineralisation.

5 Implications for ongoing exploration

The below results from this study can be applied in exploration vectoring both at Perkoa and regionally:

- Distinguishing the two different chlorite end members in order to identify the presence of a hydrothermal system. This can be achieved using a combination of analytical field techniques such as XRF, FT-IR-based techniques and "Field portable" XRD.
- The identification of Eu anomalies within the majority of massive sulphide samples and the quartz exhalative sample. This shows Eu anomalies are related to exhalative material so a relative enrichment in Eu could identify exhalative horizons through the succession which ore could have formed on.
- Depletion of elements is a broad scale feature that can act as a vector towards mineralisation. Many major oxides (Na_2O, P_2O_5, TiO_2, CaO) show depletion with increased proximity to ore, allowing for interval core sampling to show relative position in FW alteration and indicate if mineralisation is becoming closer or further downhole.
- LREE in the hydrothermal fluid are slightly mobile and are identified as being depleted with increased proximity to the centre of the system. Therefore the ΣLREE can be used to show proximity to ore.
- An enrichment of Ba and Mn in the HW rocks can be used to identify potential hydrothermal systems from the HW side.

6 Conclusions

The mineralisation is hosted within a bimodal felsic volcanic succession comprised of a coherent volcanic andesite with periodic pyroclastic flows at the base and less coherent andesitic clastic tuffs at the top of the sequence. The majority of the mineralization is hosted by the upper andesitic clastic tuff. mineralisation formed within stratigraphically above.

Post mineralisation, the succession was affected by two metamorphic events. A regional metamorphism occurred first, followed by a contact metamorphic event associated with granotoid intrusion.

Four main hydrothermal alteration features are identified:

1. Proximal to ore: Chlorite + magnetite + quartz
2. Intermediate to ore: Amphibole-rich veins surrounding clasts of chlorite and epidote are observed crosscutting foliation.
3. Intermediate-distal to ore: Destruction of plagioclase to form sericite observed with increasing amounts of sericite seen as distance to mineralisation increases.
4. Throughout succession: replacement of titanite by ilmenite as an accessory phase.

Combining the above results with field observations it is concluded that the Perkoa Zn resource is a regionally metamorphosed bimodal felsic VMS-style deposit which has then been affected by a later contact metamorphic and metasomatic event associated with the intrusion of the cross-cutting granotoid.

Acknowledgements

The authors wish to thank the Trevali Mining Corporation for funding of the fieldwork and their logistical and technical support throughout the project. The IAC team at the Natural History Museum, London are acknowledged for the sample preparation and laboratory assistance

References

Baratoux, L, Metelka, V, Naba, S, Ouiya, P, Siebenaller, L, Jessell, MW, Naré, A, Salvi, S, Béziat, D, Franceschi, G (2015). Tectonic evolution of the Gaoua region, Burkina Faso: Implications for mineralization. *Journal of African Earth Sciences,* 112:419-439.

Béziat, D, Bourges, F, Debat, P, Lompo, M, Martin, F, Tollon, F (2000). A Paleoproterozoic ultramafic-mafic assemblage and associated volcanic rocks of the Boromo greenstone belt: fractionates originating from island-arc volcanic activity in the West African craton. *Precambrian Research,* 101:25-47.

Bonhomme, M (1962). Contribution à l'étude géochronologique de la plate-forme de l'Ouest africain. Imprimerie Louis-Jean.

De La Roche, H, Leterrier, J t, Grandclaude, P, Marchal, M (1980). A classification of volcanic and plutonic rocks using R1R2-diagram and major-element analyses—its relationships with current nomenclature. *Chemical Geology,* 29:183-210.

Large, R, Gemmell, J B, Paulick, H, Huston, D L (2001). The alteration box plot: A simple approach to understanding the relationship between alteration mineralogy and lithogeochemistry associated with volcanic-hosted massive sulfide deposits. *Economic geology,* 96:957-971.

Leube, A, Hirdes, W, Mauer, R, Kesse, G O (1990). The early Proterozoic Birimian Supergroup of Ghana and some aspects of its associated gold mineralization. *Precambrian Research,* 46:139-165.

MacLean, W, Barrett, T (1993). Lithogeochemical techniques using immobile elements. *Journal of Geochemical Exploration,* 48:109-133.

Maitre, L. (1989). A classification of igneous rocks and glossary of terms. *Recommendations of the international union of geological sciences subcommission on the systematics of igneous rocks,* 193.

Metelka, V, Baratoux, L, Naba, S, Jessell, M W (2011). A geophysically constrained litho-structural analysis of the Eburnean greenstone belts and associated granitoid domains, Burkina Faso, West Africa. *Precambrian Research,* 190:48-69.

Rollinson, H (1993). Rock Classification. *In:* Anonymous *Using Geochemical Data.* 63.

Schwartz, M, Melcher, F (2003). The Perkoa zinc deposit, Burkina Faso. *Economic Geology,* 98:1463-1485.

Torben J, Blakely IT, Jacquemin T and Patel AA (2018) Technical Report on the Perkoa Mine, Burkina Faso NI 43-101 Report https://www.trevali.com/operations/perkoa-mine/default.aspx

Rare earth elements in ferriferous crusts of the Semenov modern submarine hydrothermal massive sulfide cluster (13°31´N, Mid-Atlantic Ridge)

Elena E. Amplieva, Nikolay S. Bortnikov
Institute of Geology of Ore Deposits, Petrography, Mineralogy and Geochemistry of Russian Academy of Sciences

Biktor E. Beltenev
Polar Marine Geosurvey Expedition

Abstract. The Semenov modern submarine hydrothermal massive sulfide cluster, associated with peridotites and basalts, was discovered on the 32nd scientific cruise (2009) of the Russian R/V Professor Logachev by the Polar Marine Geosurvey Expedition (PMGE) in collaboration with VNIIOkeangeologia, Saint Petersburg. This work presents the results of mineralogical and chemical investigation of ferriferous crusts of the Semenos-2, -4 and -5 modern submarine sulfide fields (Mid-Atlantic ridge). The total REE content in the ferriferous crusts of the Semenov-2, -4, -5 (ΣРЗЭ – 16.16 – 103.11 ppm) is higher than the total content of REE in sulfides from the hydrothermal fields of the Mid-Atlantic Ridge and lower than in the ferromanganese deposits of Atlantic and Pacific oceans. The ferriferous crusts of the Semenov cluster are similar in the chondrite-normalized REE distribution patterns of sulfides and hydrothermal fluids from modern submarine hydrothermal fields of the MAR (positive Eu anomaly, Eu_{an} – 1.27-15.98), and the ferromanganese deposits of Atlantic and Pacific oceans (negative Ce anomaly, Ce_{an} – 0.18–0.89). The negative Ce anomalies testify to the formation of crusts during the sub-oxidative diagenesis.

1 Introduction

The ferriferous deposits (crusts) associated with modern submarine hydrothermal systems, formed as a result of underwater transformations of sulfide ores, characterized by increased or decreased contents of REE from sulfides and seawater. The study of the chemical composition of ferriferous crusts allows us to characterize the conditions of their formation and to answer the question of what type of sediment they are: hydrothermal, hydrogenic, or is it the oxidation product of sulfide ores. For this purpose, we studied the contents of rare earth elements in the ferriferous crusts of the Semenov-2, -4, -5 at Mid-Atlantic Ridge (MAR).

2 General description

The Semenov sulfide edifice cluster is related to an Oceanic core complex (OCC) at 13°30´N on the Mid-Atlantic Ridge (MAR) (Cherkashev et al. 2013; McLeod et al. 2009). The sulfide cluster (Semenov-1, -2, -3, -4, and -5) are located on the hydrothermally altered (serpentinized and talc-replaced) peridotite and basalt, including fresh pillow lavas with well-preserved quenched glasses, with rare gabbroids, plagiogranite, tonalite, and diorite (Beltenev et al. 2009, Pertsev et al. 2012), composing a rise (OCC massif) with a height of 850 m above the seafloor on the western side of a rift valley at a depth of 2500–2800 m below sea level (bsl). The active Semenov-2 field is associated with the hydrothermally altered basalt at a depth of 2480–2750 m bsl. The Semenov-2 is located along a ridge-parallel fault scarp bounding a local depression. This field shows several hydrothermal mounds, three of which are actively venting (Michaelangelo, Ash Lighthouse, and Yellow Submarine). The Semenov-4 site is located on the eastern slope of the OCC massif at depths from 2560 to 3020 bsl. This field is associated with basalt. The field size is 2700 x 1600 m. The Semenov-5 site is located on the central part of the OCC massifs at depths from 2160 to 2340 m bsl. The field size is 700 x 500 m. The Semenov-5 is associated with serpentinized peridotite and basalt (Escartin et al. 2017).

Chalcopyrite, isocubanite, wurtzite are major sulfides in the edifices of the Semenov-2; sphalerite pyrite, marcasite, and covellite are minor minerals. Galena, pyrrhotite, native gold are rare. Opal, barite, and aragonite were found as well (Melekestseva et al. 2010). Pyrite and marcasite are major sulfides in the edifices of the Semenov-4 and -5 fields; chalcopyrite and hematite are minor minerals. Sphalerite, isocubanite, bornite, and pyrrhotite Barite, quartz, anhydrite, and aragonite were found as well (Bortnikov et al. 2014).

Ferriferous deposits of the Semenov-2, -4 and -5 modern submarine sulfide fields are composed of irregularly porous reddish- or brown-dark, orange-brown, buffy aggregates. Goethite and hematite are major minerals, atacamite, barite, quartz are less abundant. Rhodochrosite, cristobalite, aragonite, siderite, calcite, kaolinite, illite, chlorite nontronite, pyrite, chalcopyrite are rare. Hematite occurs as thin veinlets in crusts. In places, atacamite overlie, as 0.5- to 1-mm layer, ferriferous crust fragments. Atacamite occurs as zonal veinlets as well. An outer zone of these veinlets consists of finely-crystalline atacamite, aggregates of atacamite crystals (1 – 2 mm) occur in an inner zone. Dark-green atacamite crystals (0.5 – 1 mm) line the surface of cavities in porous ferriferous crust.

3 Samples studied

Sample 32L323 was taken from Semenov-2. Samples 32L373/1 and 32L355/3b were taken from Semenov-5. Samples 32L349/2; 32L353/1; 32L354/2; 32L358/1; 32L358/2, 32L359/1 and 32L357/4 were taken from Semenov-4. All samples were collected during the 32nd (2009) cruise of the R/V Professor Logachev.

4 Analytical procedure

Concentrations of rare earth elements were determined by ICP-MS. Measurements were performed at the VIMS (Moscow, Russia) on a Inductively Coupled Plasma Mass Spectrometer ICP Elan-6100 («Perkin-Elmer», USA) with techniques НСАМ № 499-АЭС/МС and НСАМ № 509-МС.

5 Results

The total REE content in the ferriferous crusts of the Semenov-2, -4, -5 is ΣREE = 16.16 – 103.11 ppm. Contents of REE in the ferriferous crusts are presented in the chondrite-normalized REE distribution patterns in figure 1. The maximum concentrations of REE (ΣREE = 103.11 ppm) were established in the ferriferous crusts of Semenov-4. The ferriferous crusts of the Semenov cluster are enriched in LREEs (ΣLREE/ΣHREE = 2.46 – 5.05). The REE content in the ferriferous crusts of the Semenov cluster is higher than in the sulfides of the Broken-Spur, TAG, Rainbow and Irinovskoe hydrothermal fields and lower or closer with the total REE contents in the ferromanganese deposits (FMD) of the Ashadze-1, Logachev- 2 and the Fersman seamount. The REE distribution patterns for all samples from the Semenov cluster show a positive Eu anomalies. Sample 32L323 from the Semenov-2 field demonstrates the smallest Eu anomaly.

The Chondrite normalized REE distribution patterns (Taylor and McLennan 1988) for the sulfides and the hydrothermal fluids of the Broken-Spur, TAG, Rainbow and Irinovskoe hydrothermal fields show a positive Eu anomaly, whereas the Eu anomaly is marked by virtually neutral values in the ferromanganese deposits Atlantic and Pacific oceans (Fig. 1).

Distinctive characteristics of the samples of the Semenov cluster are a low negative Ce anomaly and positive Yb anomaly. It is interesting that the REE distribution patterns for the ferromanganese deposits in the Atlantic and Pacific oceans show a negative Ce anomaly, but positive Yb anomaly was not found in the ferromanganese deposits and sulfides of the hydrothermal fields of the Atlantic Ocean (Davydov et al. 2003, 2007, 2009; Kolesnik et al. 2015; Rimskaya-Korsakova et al. 2003). The total REE content in ferriferous crusts of the Semenov-2, -4, -5 is higher than the total content of REE in sulfides from the hydrothermal fields of the Mid-Atlantic Ridge and lower than in the ferromanganese deposits of Atlantic and Pacific oceans. Chondrite-normalized REE distribution patterns in the ferriferous crusts of the Semenov cluster

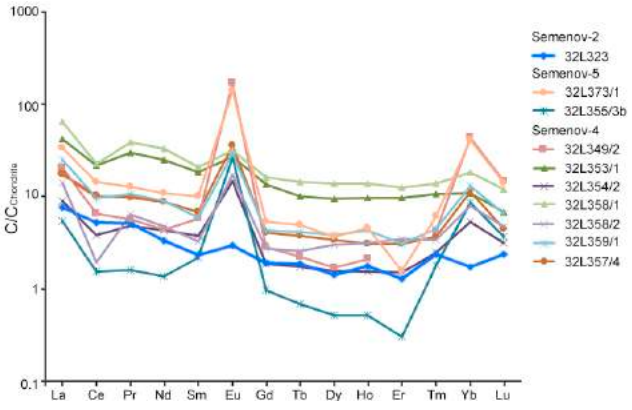

Figure 1. Chondrite-normalized REE distribution patterns in the ferriferous crusts of the Semenov cluster (Taylor and McLennan 1988).

have similar parameters with sulfides and hydrothermal fluids of the Broken-Spur, TAG, Rainbow and Irinovskoe modern submarine hydrothermal fields (positive Eu anomaly, Eu_{an} – 1.27-15.8) and with the ferromanganese deposits of the Ashadze-1, Logachev-2 and the Fersman seamount (negative Ce anomaly, Ce_{an} – 0.18–0.89).

6 Conclusions

The ferriferous crusts of the Semenov cluster are similar in the total REE content and chondrite-normalized REE distribution patterns to sulfides and hydrothermal fluids from modern submarine hydrothermal fields of the MAR, and the ferromanganese deposits of Atlantic and Pacific oceans. The samples of the ferriferous crusts of the Semenov cluster are characterized by more or less prominent negative Ce anomalies. In the case of low total REE content, the above property can testify to the formation of crusts during the sub-oxidative diagenesis (Usui et al. 1997).

Acknowledgements

This work is included in the complex of Scientific-research projects of IGEM RAS. We thank scientific team and the crew of R/V “Professor Logachev”.

References

Beltenev V, Ivanov V, Rozhdestvenskaya I et al (2009) New data about hydrothermal fields on the Mid-Atlantic Ridge between 11° - 14° N: 32nd Cruise of R/V Professor Logatchev. InterRidge News 18:14–18.

Bortnikov NS, Simonov VA, Amplieva EE, Borovikov AA (2014) Anomalously High Concentrations of Metals in Fluid of the Semenov Modern Hydrothermal System (Mid-Atlantic Ridge, 13°31′ N): LA–ICP–MS Study of Fluid Inclusions in Minerals. Dokl Earth Sci 456(Part 2):714–719.

Cherkashev GA, Ivanov VN, Beltenev VE et al (2013) Massive Sulfide Ores of the Northern Equatorial Mid-Atlantic Ridge. Oceanology 53(5):607–619.

Davydov MP, Aleksandrov PA, Perova EN et al (2009) The First Find of Buried Low-Temperature Hydrothermal Deposits in the Mid-Atlantic Ridge Rift Valley. Dok Earth Sic 424(1):1–6.

Davydov MP, Aleksandrov PA, Perova EN, Semkova TA (2007) Ferromanganese Deposits in the Ashadze-1 Hydrothermal Field (Mid-Atlantic Ridge, 12°58´N) Dokl Earth Sci 415A(6):954–960.

Davydov MP, Aleksandrov PA, Goleva RV, et al (2003) Hydrothermal ferromanganese deposits at the Fersman seamount basement, Mid-Atlantic ridge, 12°50′ N. Dokl Earth Sci 390(4):437-477.

Escartın J, Mevel C, Petersen S, Bonnemains D et al (2017) Tectonic structure, evolution, and the nature of oceanic core complexes and their detachment fault zones (13°20´N and 13°30´N, Mid Atlantic Ridge). Geochem Geophys Geosys 18(4):1451–1482.

Kolesnik ON, Kolesnik AN (2015) Rare Earth Element in Ferromanganese Nodules of the Chukchi Sea. Lithol Miner Resour 50(3):181–191.

MacLeod CJ, Searle RC, Murton BJ, Casey JF, Mallows C, Unsworth SC, Achenbach KL, Harris M (2009) Life cycle of oceanic core complexes. Earth Planet Sci Lett 287:333–344.

Melekestseva IYu, Kotlyarov VA, Ivanov VN, et al (2010) Ores of the New Semenov (13°31′ N) Hydrothermal Sulfide Cluster, the Mid-Ocean Ridge. Litosfera 2:47-61.

Pertsev AN, Bortnikov NS, Vlasov EA, Beltenev VE, Dobretsova IG, Ageeva OA (2012) Recent Massive Sulfide Deposits of the Semenov Ore District, Mid-Atlantic Ridge, 13°31' N: Associated Rocks of the Oceanic Core Complex and Their Hydrothermal Alteration. Geol Ore Deposits 54(5):334–346

Rimskaya-Korsakova MN and Dubinin AV (2003) Rare Earth Elements in Sulfides of Submarine Hydrothermal Vents of the Atlantic Ocean. Dokl Earth Sci 389A(3):432–436.

Tailor SR and McLennan SM (1988) The Continental Crust: Its Composition and Evolution. Blackwell, London; Mir, Moscow.

Usui A, Bau M, Yamazaki T (1997) Manganese microchimneys buried in the Central Pacific pelagic sediments: evidence for intraplate water circulation? Marine Geol 141:269–285.

Mineralogical zoning within the Freiberg epithermal Ag-(Au)-Pb-Zn-Cu system, Germany

Laura Swinkels, Constantin Rossberg, Jan Schulz-Isenbeck, Mathias Burisch
TU Bergakademie Freiberg, Division of Economic Geology and Petrology, Germany

Max Frenzel, Jens Gutzmer
Helmholtz Zentrum Dresden-Rossendorf, Helmholtz Institute Freiberg for Resource Technology, Germany

Abstract. The Freiberg epithermal system comprises numerous hydrothermal veins with rich Ag-(Au)-Pb-Zn-Cu mineralisation. Even after more than 800 years of extensive mining, substantial resources remain in the northern sub-districts. This area is subject to recent exploration activity. Preliminary petrographic data of two vertical profiles from the northern part of the district are presented and a new model for the district-scale zoning is proposed. The highest Ag grades occur in Ag-Sb-S-quartz veins and seem to systematically occur above an Ag-Sb-S-Carbonate stage and below Sb-S-quartz mineralisation. This high-grade Ag mineralisation is relatively distal, shallow, and abundant in the northwest sector of the Freiberg district. This, and similar insights may be used to develop new exploration vectors for the Freiberg district.

1 Introduction

The Freiberg district in the eastern part of the Erzgebirge (Germany) hosts one of the largest epithermal Ag-Zn-Pb-Cu-(Au) systems in Europe. In excess of 5600 t of Ag (~180 Moz) were extracted during more than 800 years of active mining. Historical mining focused mainly on the central district (Halsbrücke, Freiberg and Brand-Erbisdorf), while most of the mines in the peripheral sectors (Bräunsdorf, Kleinvoigtsberg, and Siebenlehn) were significantly smaller but richer in Ag (Müller 1901). Mining ceased in 1969 due to political, technological and economic reasons, leaving substantial resources unexploited.

Epithermal veins of the Freiberg district are polystadial with distinct spatial variations within each stage, resulting in an overall increase of Ag at the expense of base metals from the centre to the peripheral sectors. Silver grades reported from veins of the peripheral sectors reach up to 2000 g/t; (Müller 1901; Seifert and Sandmann 2006), and are therefore the prime target of recent exploration. During the last century, only few scientific studies on the Freiberg district were carried out, which is why the genesis of these hydrothermal veins remains poorly understood.

Recent studies (Bauer et al. 2019; Burisch et al. 2019; Ostendorf et al. 2019) on a limited number of samples from the Freiberg district provide valuable insights into the genesis of the epithermal system. However, the processes causing the district-scale variations in mineralogy remain unclear. Understanding these ore-forming processes on the scale of the entire district is key to efficient exploration targeting.

Consequently, this study focuses on the historical mining camps of Kleinvoigtsberg and Reinsberg in the northern sub-district. The silver grades are relatively high (100 to 2000 g/t), and recently, up to 2.27 g/t of gold was reported from a hydrothermal quartz vein near Reinsberg (Globex Mining Enterprises 2018), generating further interest in this particular sub-district.

Petrographic investigation of 25 polished thick sections was carried out to characterize the zonation of the vein mineralisation. This detailed petrographic investigation will be complemented by whole-rock geochemistry, electron microprobe analyses, micro thermometry and LA-ICP-MS analysis in order to understand district-scale spatial and temporal mineralogical and geochemical zonation (vertically and horizontally) of the Freiberg epithermal system.

2 Geological setting

The Erzgebirge extends about 145 km in a NE-SW direction along the Czech-German border and is bound by the Elbe zone in the Northeast, the Gera-Jachymov zone in the Southwest, and the Eger Graben in the southeast. The Erzgebirge formed as part of the Saxo-Thuringian zone during the Variscan orogeny following the collision between Gondwana and Laurussia (Kroner et al. 2007; Kroner and Romer 2013). It is an erosional window exposing a stack of Cadomian and Palaeozoic units, which were metamorphosed during the Variscan orogeny (Romer et al. 2010). Peak metamorphism (c. 340 Ma) was followed by wide-spread late-collisional granitic magmatism (Kroner et al. 2007). Subsequently, the break-up of Pangea led to Permian rifting (c. 310 to 275 Ma) and the intrusion of rhyolite dykes and small granitic intrusions (Förster et al. 2007). The most recent period of exhumation and erosion of the area is related to the Eger Graben rifting (~15-13 Ma; Ziegler and Dèzes 2005; Pälchen and Walter 2011).

The Freiberg district is located in the eastern part of the Erzgebirge and largely consists of a lens-shaped unit of para- and orthogneisses (Fig. 1). In the northwest, the dome is overlain by mica schists and phyllites forming a structurally more complex area (Baumann et al. 2000). The units in the Freiberg district are cross-cut by numerous epithermal veins with a preferred N-S to NE-SW orientation (Baumann et al. 2000).

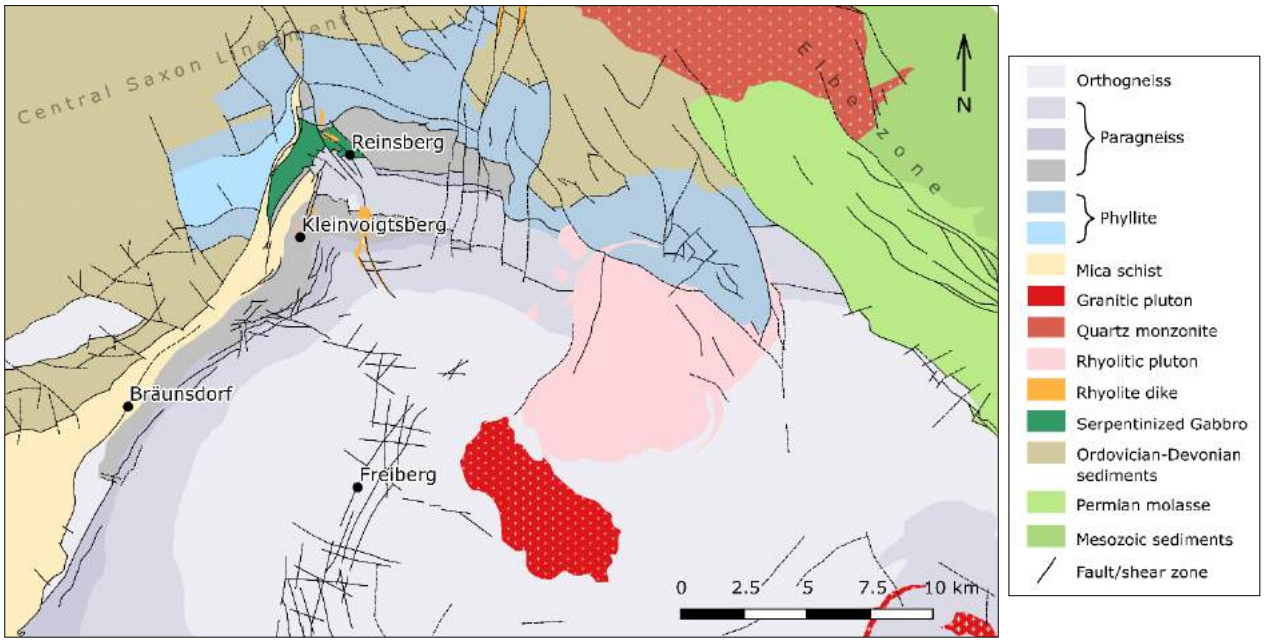

Figure 1. Simplified geological map of the Freiberg district comprising a gneiss dome (in grey) and overlying metamorphic units in the northwest. The dots represent the studied mine sites.

3 Hydrothermal veins of the freiberg district

The epithermal system of the Freiberg district comprises two major stages of vein mineralisation. Stage 1 consists of polymetallic sulphides with quartz. Stage 2 is dominated by Ag-Sb sulphides and sulfosalts accompanied by carbonates and quartz. (Müller 1901; Baumann et al. 2000; Bauer et al. 2019; Burisch et al. 2019).

The veins exhibit a systematic vertical zonation and lateral variability with respect to mineralogy, geochemistry, and fluid inclusion characteristics. In general, stage 1 is most dominant in the deepest parts of the veins and the modal abundance of stage 2 gradually increases upwards (Müller 1901; Bauer et al. 2019; Burisch et al. 2019).

The centre is dominated by stage 1 Fe-Zn-Cu-quartz mineralisation. Fluid inclusion studies of stage 1 yield homogenisation temperatures (T_h) from 300 to 340°C and salinities up to 6 wt.% eq. (NaCl). Heterogeneously trapped fluid inclusions and distinctive quartz textures (bladed calcite, lattice textures) indicate fluid boiling. CO_2 was only detected in the oldest fluid inclusion assemblages with relatively high homogenisation temperatures indicating CO_2 loss in the early stages of mineral precipitation (Bauer et al. 2019).

The peripheral sub-districts are characterized by a significantly higher amount of stage 2, which continues to a greater depth than in the centre (Müller 1901; Baumann et al. 2000). In Bräunsdorf, the abundance of carbonates decreases upwards. Furthermore, in the shallower sections of the veins the amount of Sb-sulphides strongly increases at the expense Ag- and Ag-Sb-sulphides. Fluid inclusion data from the Bräunsdorf sector show that stage 1 formed at ~300°C and stage 2 formed at temperatures from 275 to 180°C. Both stages are associated with low- to intermediate sulphidation, low salinity fluids with 0.6-4.0 wt.% eq. (NaCl). Evidence for boiling is not reported, most likely because initial boiling occurred earlier at deeper levels. The main mineral precipitation mechanism is assumed to be cooling (Burisch et al. 2019).

4 Sampling

60 samples were selected from the scientific collections of the TU Freiberg and from the field. Two veins were studied, 1) Peter Stehender, Kleinvoigtsberg, and 2) Reinsberger Glück Morgengang, Reinsberg, since samples over a large vertical profile were available. A Carl Zeiss Axio Imager M1m light microscope was used to investigate the age relationships between minerals and to characterize textures.

5 Results and discussion

The vertical profiles of Kleinvoigtsberg and Reinsberg are very similar, regarding both textures and mineralogy. The investigated samples include different mineralisation stages which can be classified according to their mineral assemblages: Stage 1 comprises base metal sulphides, including arsenopyrite, pyrite, sphalerite, and galena, with quartz as the main gangue mineral (Fig. 2a). Stage 1 is followed (and partly replaced) by base metal sulphides accompanied by Ag-sulfosalts, carbonate and quartz (Fig. 2b). In several samples containing stage 2, quartz is dominant and carbonate is completely absent or occurs subordinately (Fig. 2c). Well-developed textures like crustiform and lattice bladed quartz can be recognized in various samples (Fig. 2d and e). Ivory-coloured carbonate is often present as cavity infill on flamboyant or euhedral quartz (Fig. 2f). Brecciated vein quartz exhibiting pronounced lattice bladed textures have been

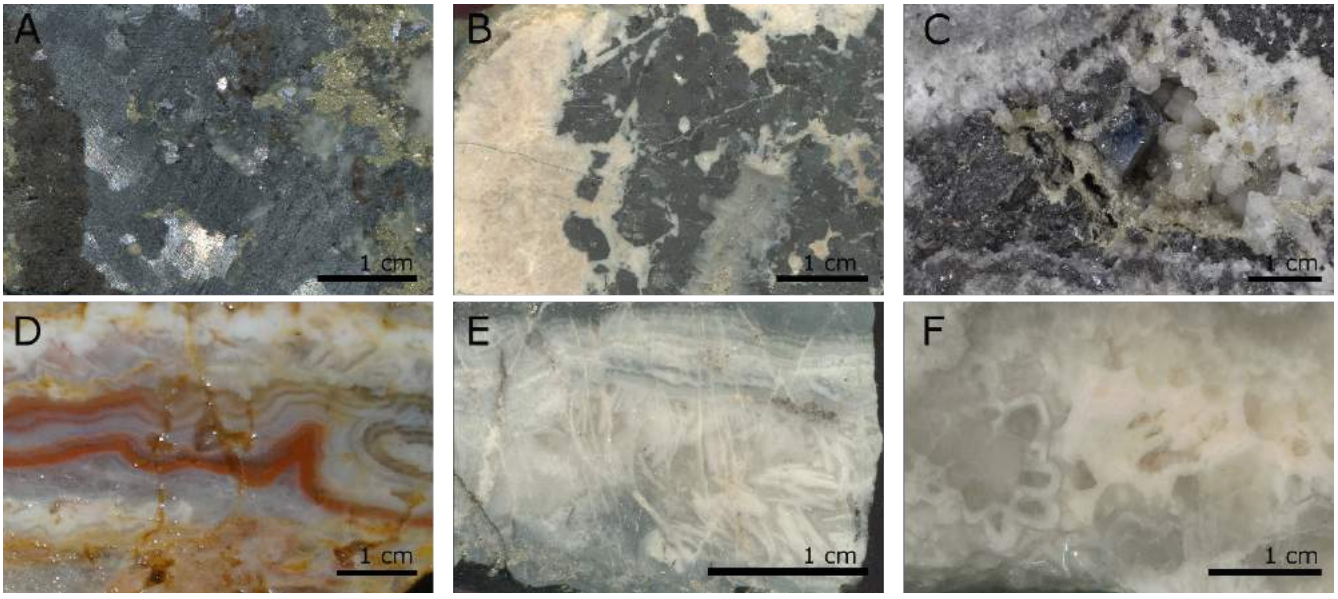

Figure 2. Mineralisation stages: **a.** stage 1 assemblage with pyrite, galena, and sphalerite, **b.** stage 2a with carbonate, quartz, sphalerite, small amounts of pyrite, and Ag-sulphides, and **c.** stage 2b with galena, sphalerite, pyrargyrite, proustite, and quartz. Boiling textures: **d.** Field samples of Reinsberg with colloform quartz, **e.** crustiform and bladed quartz with carbonate from Kleinvoigtsberg, **f.** plumose quartz with carbonate infill.

documented. Sulphide minerals are absent in these samples. This mineralisation style is outcropping near Reinsberg and has not previously been recognised in the Freiberg district. It is interpreted as the latest vein infill.

Both stage 1 and 2 are present at all levels of the sampled profile. Hydrothermal breccias consisting of hydrothermal quartz, altered host-rock and fragments of older vein infill can be observed in the upper levels of the veins.

Based on petrographic observations and data from Burisch et al. (2019), stage 2 can be divided in 4 sub-stages. Stage 2A is the most carbonate-rich and contains high amounts of galena and sphalerite as well as tetrahedrite and freibergite (Fig. 2b). Stage 2B is characterised by Ag-Sb sulfosalts with fine-grained quartz and only minor amounts of carbonate, galena, and sphalerite (Fig. 2c). Besides Ag, stage 2B is also associated with elevated Au contents (up to ~9 g/t; Seifert and Sandmann 2006). Stage 2C is dominated by berthierite and stibnite, accompanied by quartz. Stage 2C has not been identified in Reinsberg and Kleinvoigtsberg. Stage 2D is characterised by late-stage quartz with lattice textures. Preliminary results show that these quartz veins contain up to ~2.5 g/t Au.

5.1 Lateral zonation

The previously introduced paragenetic stages show a distinct and systematic zoning (Fig. 3). Stage 1 with base metal-rich sulphides (Fe, Sn, Cu, Zn) is most prominent in the centre of the district (Müller 1901; Bauer et al. 2019). Shallower and more distal, the modal abundance of stage 2 generally increases. Stage 2A is most prominent in Brand-Erbisdorf near Freiberg (in-between the centre and the peripheral sectors), but also exists in Reinsberg, Kleinvoigtsberg and Bräunsdorf. Subsequently, Ag-sulfosalts with only minor amounts of carbonate prevail (Stage 2B). Even more distal and shallower, the mineralogy of the vein changes to stage 2C dominated by Sb-sulphides (Burisch et al. 2019). The shallowest and most distal part of the epithermal system is marked by Stage 2D.

The formation of the Eger Graben during the Cenozoic resulted in asymmetric uplift and erosion of the Freiberg district (Pälchen and Walter 2011). The zonation pattern at the surface is most likely a direct result of asymmetric erosion caused by increasing uplift towards the southeast combined with the primary mineral zonation. Units exposed at the surface in the centre of the district formed at deeper crustal levels than the units in the northwest. As a consequence, the majority of the shallow mineralisation is preserved in the north and northwest, with the most shallow parts of the epithermal system near Reinsberg (Fig. 3).

5.2 Fluid evolution

Temporal and spatial changes in the mineralogy indicate a distinct physical and chemical evolution of the associated ore fluid. Decreasing T_h in fluid inclusions from the central district to the peripheral sectors, both related to stage 1 indicates an overall spatial cooling trend (Bauer et al. 2019; Burisch et al. 2019). Furthermore, a systematic decrease in T_h from stage1 to stage 2C (290 to 200°C; Burisch et al. 2019) indicates not only a spatial but also a temporal cooling trend. Besides cooling, the presence of CO_2 in pre-boiling and its absence in post-boiling fluid inclusion assemblages (Bauer et al. 2019) as well as the sudden occurrence of carbonates in stage 2A is evidence for CO_2 degassing. CO_2 degassing has a major effect on the ore fluid's pH (White and Hedenquist 1995), and most likely initiated Ag deposition, although highest grades occur more

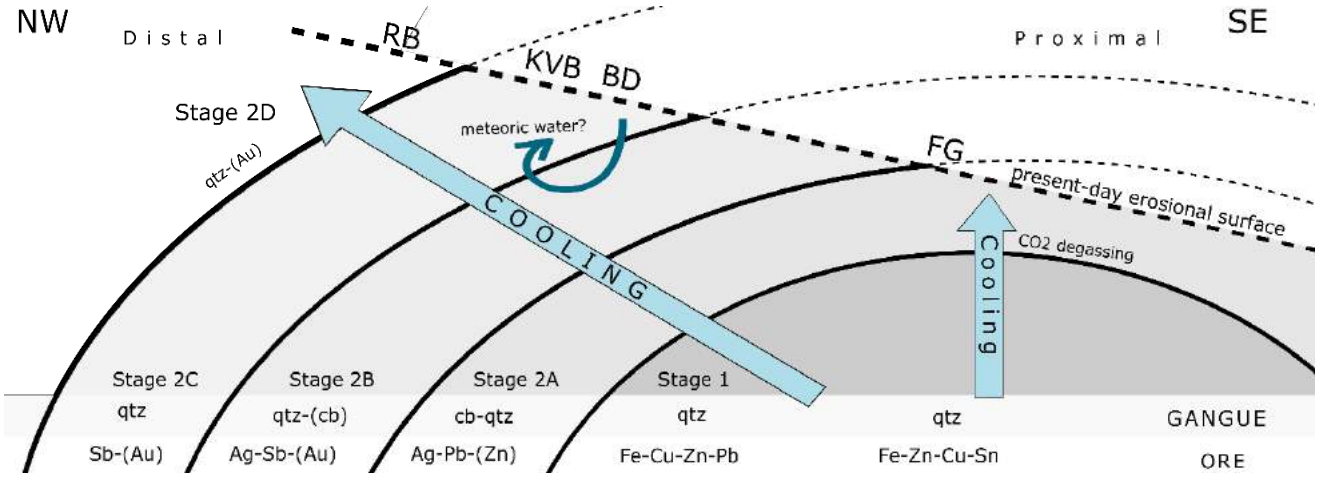

Figure 3. Schematic cross section showing the district-scale zoning and possible mineral precipitation mechanisms. The relative positions of localities are indicated with abbreviations: Freiberg (FG), Bräunsdorf (BD), Kleinvoigtsberg (KVB), and Reinsberg (RB).

distal than the major degassing horizon. In those Ag-rich parts, cooling is most likely the major ore-forming mechanism (Burisch et al. 2019). Gold occurs late and distal in the paragenetic sequence, however the controlling factors for Au precipitation in the Freiberg district are not yet understood.

5.3 Implications for exploration

Understanding processes which cause the distinct mineral zoning facilitates the development of robust exploration vectors by translating the mineral system analysis approach to mappable criteria. From the preliminary data we can assume that the highest silver grades (stage 2B) are spatially confined by the shallow/more distal Sb-sulphide assemblage (stage 2C) and deeper/more proximal Ag-Sb-carbonate assemblages (stage 2A).

6 Conclusion

The Freiberg district represents a large low- to intermediate-sulphidation epithermal system with a resource potential for Ag, Au, and base metals. The mineral zonation exposed in the Freiberg district is a consequence of a physical and chemical evolution of the ore forming fluid and differences in the present-day erosional level.

Acknowledgements

This PhD project is funded by the European social fund (ESF). Analysis and consumables for a MSc thesis were funded by Globex Mining Enterprises Inc. We would like to thank Christin Kehrer (TUBAF) for the support with the sample selection from the scientific collection, and Andreas Bartzsch, Roland Würkert and Michael Stoll (all HIF) for sample preparation.

References

Bauer ME, Burisch M, Ostendorf J, et al (2019) Trace element geochemistry of sphalerite in contrasting hydrothermal fluid systems of the Freiberg district, Germany: insights from LA-ICP-MS analysis, near-infrared light microthermometry of sphalerite-hosted fluid inclusions, and sulfur isotope geochemi. Miner Depos 54:237–262.

Baumann L, Kuschka E, Seifert T (2000) Lagerstätten des Erzgebirges. Enke im Georg Thieme Verlag, Stuttgart, New York

Burisch M, Hartmann A, Bach W, et al (2019) Genesis of hydrothermal silver-antimony-sulfide veins of the Bräunsdorf sector as part of the classic Freiberg silver mining district, Germany. Miner Depos 54:263–280.

Förster H, Gottesmann B, Tischendorf G, et al (2007) Permo-Carboniferous subvolcanic rhyolitic dikes in the western Erzgebirge/Vogtland, Germany: a record of source heterogeneity of post-collisional felsic magmatism. N Jb Miner Abh 183:123–147.

Globex Mining Enterprises (2018) Press Release Bräunsdorf licence area

Kroner U, Hahn T, Romer RL, Linnemann U (2007) The Variscan orogeny in the Saxo-Thuringian zone-Heterogenous overprint of Cadomian/Paleozoic Peri-Gondwana crust. Geol Soc Am Spec Pap 423:153–172.

Kroner U, Romer RL (2013) Two plates — Many subduction zones: The Variscan orogeny reconsidered. Gondwana Res 24:298–329.

Müller C (1901) Die Erzgänge des Freiberger Bergrevieres. Erläuterungen zur Geol Spec des Königreiches Sachsen Verlag W Engelmann, Leipzig, Ger 1–350

Ostendorf J, Henjes-Kunst F, Seifert T, Gutzmer J (2019) Age and genesis of polymetallic veins in the Freiberg district, Erzgebirge, Germany: constraints from radiogenic isotopes. Miner Depos 54:217–236

Pälchen W, Walter H (2011) Geologie von Sachsen. Schweizerbart Stuttgart, Germany

Romer RL, Schneider J, Linnemann U (2010) Post-Variscan deformation and hydrothermal mineralization in Saxo-Thuringia and beyond: a geochronological review. Pre-Mesozoic Geol Saxo-Thuringia–From Cadomian Act Margin to Variscan Orogen Schweizerbart, Stuttgart 347–360

Seifert T, Sandmann D (2006) Mineralogy and geochemistry of indium-bearing polymetallic vein-type deposits: Implications for host minerals from the Freiberg district, Eastern Erzgebirge, Germany. Ore Geol Rev 28:1–31.

White NC, Hedenquist JW (1995) Epithermal Gold Deposits: Styles, Characteristics and Exploration. Publ SEG Newsl 1:9–13.

Ziegler PA, Dèzes P (2005) Neogene uplift of Variscan Massifs in the Alpine foreland: Timing and controlling mechanims. Variscan Massifs 1–24

Genesis of the vein-type Niederschlag fluorite deposit in the Erzgebirge, Germany

Sebastian Haschke, Mathias Burisch
Department of Mineralogy, Technische Universität Bergakademie Freiberg, Freiberg, Germany

Jens Gutzmer
Helmholtz-Zentrum Dresden-Rossendorf, Helmholtz Institute Freiberg for Resource Technology, Freiberg, Germany

Abstract. The Niederschlag fluorite vein deposit in the western part of the Erzgebirge has been actively mined since 2013. In order to approximate constraints on the hydrothermal mineralisation, a comprehensive study on the mineralogy, mineral paragenesis, fluid inclusion compositions and the geochemistry of the two identified hydrothermal fluorite stages was carried out. These two stages constitute the bulk of resources of the Niederschlag deposit. The older fluorite I mineralisation is associated with abundant quartz and forms complex breccia textures. Fluorite II – and closely associated barite and occurs as coarse crystalline and massively-textured or banded open space infill. Microthermometric analyses of fluorite II suggests fluid mixing as the main ore-forming process. Due to obvious similarities to many other fluorite-barite-Pb-Zn-Cu vein deposits in Central and Western Europe we relate the origin of fluorite II to rifting associated with the Mesozoic opening of the northern Atlantic.

1 Introduction

The Erzgebirge/Krušné hory metallogenic province hosts numerous ore deposits, which have been mined since medieval times (Baumann et al. 2000).The fluorite-barite deposit of Niederschlag in the Erzgebirge/ eastern Germany is actively mined for fluorite and barite since 2013 and is operated by Erzgebirgische Fluß- und Schwerspatwerke GmbH (EFS).

The Niederschlag deposit was first discovered during uranium exploration by the SDAG Wismut in 1954 (Kuschka 2002). Despite extensive exploration and active mining, modern geochemical data for this deposit is entirely missing. To fill this gap, we carried out petrographic, microthermometric and geochemical studies on samples from two distinct fluorite stages of the Niederschlag deposit. Both mineralisation stages are economically mined and constitute the bulk of the resources of the mine. Based on this data a preliminary genetic model is proposed.

2 Geological Setting

2.1 Regional Geology

The Niederschlag deposit is hosted by metamorphic Variscan basement units of the western Erzgebirge, which formed at 400-340 Ma due to the collision of Gondwana and Laurussia (Kroner and Romer 2013). The metamorphic basement units of the Erzgebirge were subsequently intruded by post-collisional granitoids (320-280 Ma), as well as rhyolite and lamprophyre dikes (Romer et al. 2010; Seifert 2008).

The host rocks of the Niederschlag fluorite deposit (Fig. 1) comprise gneisses, mica schists and other meta-sedimentary units. Besides the metamorphic units, the F-Li enriched Eibenstock granite (~320 Ma intrusion age) (Förster et al. 1999; Tichomirowa and Leonhardt 2010) is present in the vicinity of the deposit; it has been estimated to also occur ~1000 m below the present-day surface (Kuschka 2002).

Apatite fission track thermochronology suggests a 2-3 km thick marine sedimentary cover was present above the metamorphic host units of the Niederschlag deposit during early Mesozoic times (Wolff et al. 2015).

Uplift and erosion related to the Eger-rift (starting during the Cenozoic) led to a deep excavation of the previously buried basement units (Pälchen and Walter 2012). This event is also associated with the intrusion of phonolite dikes and plugs that crosscut both host rocks and fluorite veins. Intrusions of phonolite dykes at the Niederschlag mine are known to extensively modify hydrothermal vein-type fluorite mineralisation. Relative age relations thus suggest that all fluorite mineralisation postdates peak metamorphism, but predate the intrusion of phonolite dykes.

2.2 Hydrothermal mineralisation

Polystadial hydrothermal mineralisation is bound to the Scheibenberg-Niederschlag-Kovàřskà-fault, an NNW-SSE striking fault system, which extends in strike direction across the German-Czech border.

The thickness of the sub-vertical vein is discontinuous (pinch-and-swell) and varies between 4 and 12 m (Baumann et al. 2000).

The shallow part of the deposit hosts uranium and five-element mineralisation associated with carbon-rich horizons (Guilcher et al. 2019). At greater depths those are absent and the same vein structure comprises multiple generations of fluorite, barite, quartz and minor base metal sulphides. Two distinct fluorite generations are recognised. One is accompanied with quartz (fluorite I), the other one (fluorite II) is associated with barite and sulphides (Kuschka 2002).

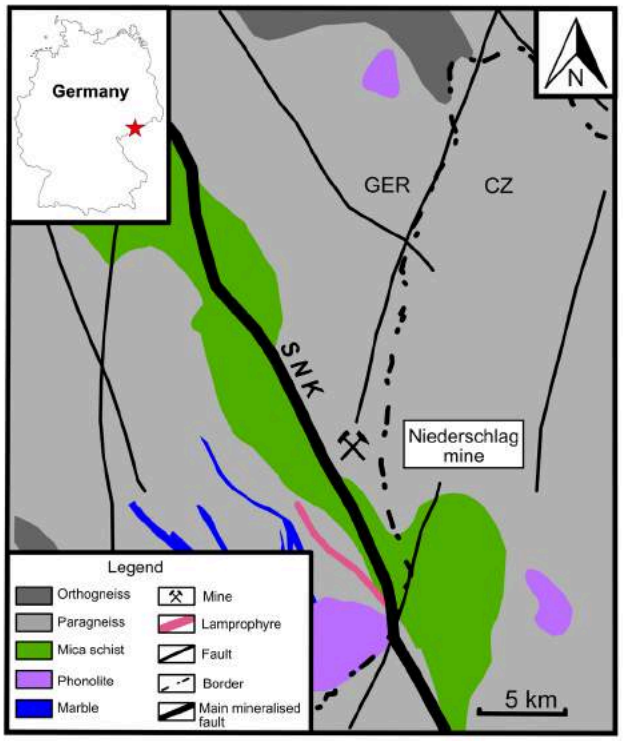

Figure 1. Simplified geological map of the area around of the Niederschlag fluorite-barite mine. Mineralisation occurs mainly on the Scheibenberg-Niederschlag-Kovàřskà-fault zone (SNK) (modified after Baumann et al. 2000).

3 Methodology

Fluorite samples were selected from underground workings (5.1 level south; 650 m a.s.l) and from drill cores of a historical exploration program. Double-polished thick sections (~250 µm) were prepared for fluid inclusion analyses.

Microthermometric analyses were carried out with a Linkam THSMG600 fluid inclusion stage combined with an Olympus BX53 microscope. Synthetic standards of CO_2-H_2O- and H_2O inclusions were used for calibration. Petrographic descriptions are classified as primary, secondary, pseudo secondary or isolated fluid inclusions (van den Kerkhof and Hein 2001). Liquid-vapour ratios were estimated by image analysis. To ensure reproducibility each phase transition of each inclusion was measured three times. Fluid inclusions with signs of post entrapment processes were excluded from the data. Based on the presence of hydrohalite, salinities were calculated according to Steele- MacInnis et al. (2011) for the Na-Ca-Cl-H_2O-System.

4 Results

4.1 Petrographic investigations

Fluorite occurs in two distinct generations (Fig. 2). The older fluorite generation (fluorite I) occurs predominantly along the selvages of the vein structure; it is accompanied by quartz and chalcedony. Besides fluorite and quartz/chalcedony, no other associated minerals were identified. Stage 1 mineralisation (Fig. 3) typically forms multiple sequences of thin, irregularly shaped bands of fluorite and quartz that comprise irregular masses of up to several m thickness. Host rock-brecciation, mostly as cockade breccia (Frenzel and Woodcock 2014), is commonly observed. Fluorite often forms botryoidal or radiating aggregates; prismatic crystal shapes are also observed. Crystal sizes range from very fine-grained to a few cm in size. The bulk of fluorite exhibits green and purple colours, accompanied by subordinate yellow to whitish fluorite.

The second fluorite generation (fluorite II) is developed on the same fault structure where it cross cuts fluorite I and is thus distinctly younger. Fluorite II is accompanied by barite, base metal sulphides and quartz. Barite is often intimately inter-grown with minor amounts of fluorite II and quartz pseudomorphs after barite occur. Chalcopyrite, galena and tetrahedrite are the most abundant sulphides. The fluorite is mostly blue and green in colour and of cubic shape. Vugs and druses abound within the massive fluorite II.

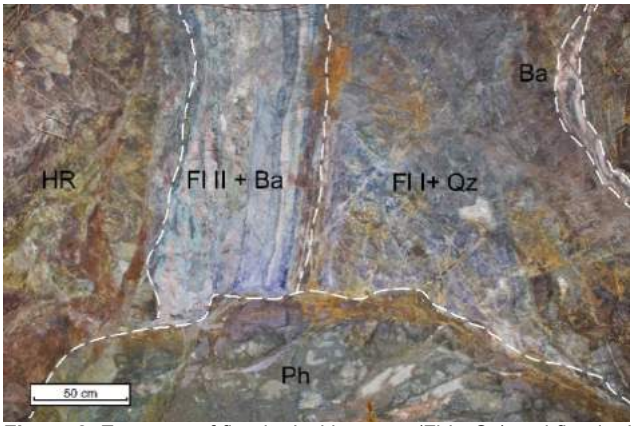

Figure 2. Exposure of fluorite I with quartz (Fl I+ Qz) and fluorite II (Fl II) and barite (Ba) mineralisation, level 6.1 south, Niederschlag mine. Note crosscutting phonolite (Ph) dyke.

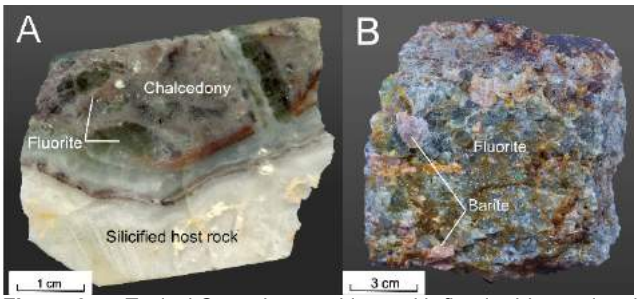

Figure 3. a. Typical Stage I assemblage with fluorite I berecciated and cemented by chalcedony in contact with strongly silicified and altered host rock (SHFB-Nds-01)**. b.** Fluorite II accompanied by barite (SHNds P8).

4.2 Fluid inclusion investigations

Fluorite I and quartz of the first mineralisation stage did not host any fluid inclusions suitable for investigation. Flourite II, in contrast, shows abundant fluid inclusion assemblages; these are of primary, pseudo-secondary and secondary origin with inclusions up to 100 µm in

size. Some inclusions showed evidence for post-entrapment modification; these were excluded from the data set. Two phase liquid-vapour inclusions dominate, but three phase liquid-vapour-solid inclusions are also observed. The solid phase appears greenish with irregular crystals shapes. The phase does not melt upon heating. The fluids show first melting (eutectic) temperatures around -50 °C typical for Na-Ca-Cl dominant fluids. Homogenisation temperatures are between 80 °C and 120 °C with salinities varying greatly between 19 and 27 % eq. w($NaCl+CaCl_2$).

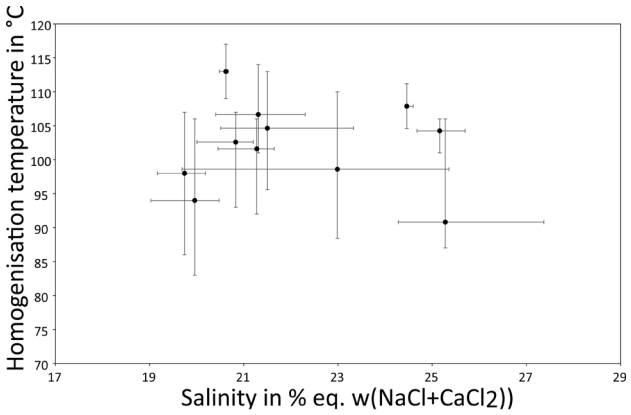

Figure 4. Homogenisation temperature (in °C) versus total salinity (% eq. w($NaCl+CaCl_2$)) including 54 analyses of two-phase inclusions in fluorite II. Data is summarized as fluid inclusion assemblages (FIA). The whiskers indicate the range not the error of the FIAs.

5 Discussion and Conclusions

Preliminary petrographic and microthermometric data suggest that the two different fluorite generations are formed in contrasting fluid regimes.

Fluorite I is not accompanied by any sulphides/sulphates. This indicates that associated fluids were nominally S-free. Furthermore, intense host-rock alteration related to stage I suggests that water-rock interaction could have been an important ore-forming process. Comparable fluorite mineralisation is not reported from other fluorite districts in Europe and the timing and geotectonic framework of stage I remains unclear.

Conversely, fluorite II is only associated with minor host-rock alteration. Variable Na/Ca ratios and salinities of FIAs related to stage II are evidence for fluid mixing of a moderately and a highly saline brine. Fluid inclusion data and the mineralogy of stage II are very similar to other fluorite-barite mineralisation in Europe. Therefore, it is most likely that fluorite II is related to the opening of the northern Atlantic ~140-40 Ma (Golonka and Bocharova 2000); an analogue to other hydrothermal fluorite-barite vein occurrences across Europe (Bauer et al. 2018; Fusswinkel et al. 2013; Munoz et al. 2016).

Acknowledgements

We would like to thank R. Würkert, M. Stoll and A. Bartzsch (Helmholtz-Institute Freiberg) for sample preparation. Furthermore, we would like to thank Henrik Ehle and Martin Zimmermann (both ESF) for giving us access to the underground mine and supporting us with sampling. M. Lapp (Sächsisches Landesamt für Umwelt und Geologie) is thanked for providing access to drill cores and the accompanied documents. This study is funded by the European social fund (ESF) and the Sächsische Aufbaubank (SAB).

References

Bauer ME, Burisch M, Ostendorf J, Krause J, Frenzel M, Seifert T, Gutzmer J (2018) Trace element geochemistry of sphalerite in contrasting hydrothermal fluid systems of the Freiberg district, Germany: insights from LA-ICP-MS analysis, near-infrared light microthermometry of sphalerite-hosted fluid inclusions, and sulfur isotope geochemistry. Miner Deposita 52:651.

Baumann L, Kuschka E, Seifert T (2000) Lagerstätten des Erzgebirges: 13 Tabellen. Enke im Thieme-Verl., Stuttgart

Förster H-J, Tischendorf G, Trumbull RB, Gottesmann B (1999) Late-Collisional Granites in the Variscan Erzgebirge, Germany. Journal of Petrology 40:1613–1645.

Frenzel M, Woodcock NH (2014) Cockade breccia: Product of mineralisation along dilational faults. Journal of Structural Geology 68:194–206.

Fusswinkel T, Wagner T, Wälle M, Wenzel T, Heinrich CA, Markl G (2013) Fluid mixing forms basement-hosted Pb-Zn deposits: Insight from metal and halogen geochemistry of individual fluid inclusions. Geol 41:679–682.

Golonka J, Bocharova NY (2000) Hot spot activity and the break-up of Pangea. Palaeogeography, Palaeoclimatology, Palaeoecology 161:49–69.

Guilcher M, Schmaucks A, Burisch M, Markl G, Gutzmer J. (2019) Ore forming processes and mineral zoning in Ag-Bi-Co-Ni-As ± U (five element veins) of the Erzgebirge, E-Germany: New observations from the Annaberg district. (this issue)

Kroner U, Romer RL (2013) Two plates — Many subduction zones: The Variscan orogeny reconsidered. Gondwana Research 24:298–329.

Kuschka E (2002) Die Uranerz-Baryt-Fluorit-Lagerstätte Niederschlag bei Bärenstein und benachbarte Erzvorkommen. Geoprofil 2002

Munoz M, Baron S, Boucher A, Béziat D, Salvi S (2016) Mesozoic vein-type Pb–Zn mineralization in the Pyrenees: Lead isotopic and fluid inclusion evidence from the Les Argentières and Lacore deposits. Comptes Rendus Geoscience 348:322–332.

Pälchen W, Walter H (2012) Geologie von Sachsen I. Schweizerbart'sche Verlagsbuchhandlung, Stuttgart

Romer RL, Förster H-J, Štemprok M (2010) Age constraints for the late-Variscan magmatism in the Altenberg–Teplice Caldera (Eastern Erzgebirge/Krušné hory). N. Jb. Miner. Abh. 187:289–305.

Seifert T (2008) Metallogeny and petrogenesis of lamprophyres in the Mid-European variscides: Post-collosional magmatism and its relationship to late-variscan ore forming processes in the Erzgebirge (Bohemian Massif). IOS Press Millpress; Gazelle Books Distr, Amsterdam, Hightown

Tichomirowa M, Leonhardt D (2010) New age determinations (Pb/Pb zircon evaporation, Rb/Sr) on the granites from Aue-Schwarzenberg and Eibenstock, Western Erzgebirge, Germany. Zeitung für geologische Wissenschaft:99–123

van den Kerkhof AM, Hein UF (2001) Fluid inclusion petrography. Lithos 55:27–47.

Wolff R, Dunkl I, Lange J-M, Tonk C, Voigt T, Eynatten H von (2015) Superposition of burial and hydrothermal events: post-Variscan thermal evolution of the Erzgebirge, Germany. Terra Nova 27:292–299.

Ore-forming processes and mineral zoning in Ag-Bi-Co-Ni-As±U (five-element) veins of the Erzgebirge, Germany: new observations from the Annaberg district

Marie Guilcher, Anna Schmaucks, Mathias Burisch
Technische Universität Bergakademie Freiberg, Institute of Mineralogy, Freiberg, Germany

Gregor Markl
Universität Tübingen, Faculty of Science, Tübingen, Germany

Jens Gutzmer
Helmholtz-Zentrum Dresden-Rossendorf, Institute Freiberg for Resource Technology, Freiberg, Germany

Abstract. Native metal Ag-Bi-Co-Ni-As±U (five-element) veins in the Erzgebirge host valuable resources of Co, Ni, and Ag. In recent times, these were primarily exploited for U closely associated with Co-Ni-Fe-arsenides. Today, the focus of exploration has shifted to Co, Ni, and Ag. For political and environmental reasons, the identification of Co-, Ni-, and Ag-rich zones with low concentrations of U will be of major importance. High-grade ore shoots in the Annaberg district are restricted to carbon-rich horizons within the gneissic host rock. Furthermore, a distinct vertical zonation is observed along the veins: U-rich mineralisation dominates the shallowest parts of the veins whereas Co-Ni-arsenides prevail below the U-rich zone. With increasing depth, the mineralogy of the veins changes to fluorite, barite, and small amounts of base metal sulphides. These geological observations provide important constraints for the five-element vein system in the Erzgebirge. Complemented by fluid inclusion analyses and thermodynamic computations, they can be used to understand the separation of arsenides and U minerals during ore formation.

1 Introduction

Hydrothermal Ag-Bi-Co-Ni-As±U veins are widespread in the Erzgebirge. Schneeberg, Annaberg, Marienberg, Schlema-Alberoda, Niederschlag, and Hartenstein are some examples of historical mining districts where such mineralisation occurs. In these districts, five-element veins were mined for Bi, Co, Ni, Ag between the 15th and the 20th century.

These so-called “five-element” veins are characterized by the presence of dendritic native Ag, Bi, and/or As followed by a succession of Fe, Co, and Ni arsenides (Burisch et al. 2017; Kissin 1992; Markl et al. 2016). Many five-element vein systems, especially those in the Erzgebirge, are also associated with substantial amounts of U mineralisation.

In the Erzgebirge, five-element veins have been extensively mined for Ag and Co from the 16th to the 19th century and were one of the major sources for U from 1945 to 1991 in the former GDR. Besides Co, Ag, and U, they contain significant amounts of Ni. Co and Ni are increasingly required for renewable energy technologies, in particular for energy storage (rechargeable lithium ion batteries; Crundwell et al. 2011).

The intimate association of Co and U significantly deteriorates the economic potential of five-element veins in the Erzgebirge for obvious environmental reasons. Therefore, exploration would have to target zones of Co-Ni mineralisation with no or negligible U content. In the Annaberg district, a distinct vertical zoning of U minerals and Co-Ni arsenides is observed. It is an example where the five-element association is spatially related to carbon-rich horizons in the host-rock. Understanding this mineral zoning may be used to identify preferred zones in five-element systems, which are rich in Co, Ni, and Ag, but poor in U.

In this study, we present preliminary petrographic observations of samples from the Annaberg district. Petrographic investigations will be complemented by fluid inclusion studies, geochemical analyses and thermodynamic computations. The ultimate goal is to understand how U, Ni, Co, and As fractionate in hydrothermal five-element systems.

2 The Annaberg district

2.1 Geological setting

The Annaberg district is located in the central part of the Erzgebirge. The Erzgebirge is an erosional window which comprises metamorphic and igneous rocks associated with the Variscan Orogeny (Kroner and Romer 2013). The district is situated in the ENE-WSW striking Annaberg-Marienberg anticline (Baumann et al. 2000). The predominant lithology is a muscovite-biotite paragneiss (“Annaberg-Marienberg” gneiss; Tichomirowa et al. 2012). Smaller lenses of orthogneiss (locally referred to as “Rotgneiss”) are present in the NW of the district (Fig. 1). Both gneiss units were intruded by microgranites and Li-F granites occurring in the northwestern and central parts of the district. Tertiary basalts are locally present.

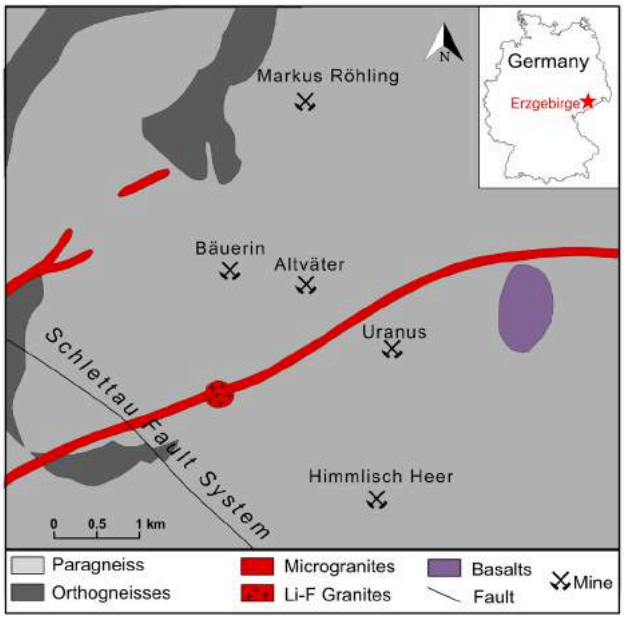

Figure 1. Simplified geological map of the Annaberg district. The mining symbols and names represent the mines from which studied samples originate (modified after Müller (1894); Seifert (1996b) in Baumann et al. 2000).

2.2 Hydrothermal mineralisation

Styles of hydrothermal vein-type mineralisation in the Annaberg district include Sn-quartz, polymetallic-sulphide-quartz, uraninite, fluorite-barite-Pb-Zn and five-element assemblages (Baumann et al. 2000). The past production of Co, Ag and U in the Annaberg district was 8700 t, 350 t, and 496 t respectively (Baumann et al. 2000). Here, we focus only on the younger (post-Variscan) types of mineralisation, which are all predominantly hosted by NW-SE to N-S trending fault systems (parallel to the Schlettau Fault System; Fig. 1). Although relative ages of the mineralisation stages can be inferred from cross-cutting relations, absolute ages of the different mineralisation styles are poorly constrained (Baumann et al. 2000).

The oldest post-Variscan stage of hydrothermal mineralisation (stage 1) comprises carbonate and pitchblende. This stage is preferentially present in the vicinity of carbon-rich horizons (Fig. 2). The timing of the mineralisation is vaguely constrained between 220 and 100 Ma by U-Pb geochronology of pitchblende (Baumann et al. 2000). Examples of major veins with carbonate-pitchblende mineralisation are “Uranus Flacher”, “Sina Flacher”, “Himmlisch Heer Stehender”, and “Merkur Stehender”. Stage 1 is followed by a younger fluorite-quartz stage, typically occurring on the same structures. Hematite, chalcedony, and barite are even younger and mark stage 3. Stage 4 of mineralisation consists of fluorite, barite as well as subordinate quartz and base metal sulphides. “Glück Flacher” and “Gründonnerstag Spathgang” are the major veins that comprise abundant stage 3 and 4 mineralisation (Baumann et al. 2000).

The age and paragenetic position of Ag-Bi-Co-Ni-As-U mineralisation (stage 5) is not entirely clear. It is either younger or of the same age as stage 4. Approximately 160 veins with Ag-Bi-Co-Ni-As-U mineralisation are known in the Annaberg district. Some of the major veins in the district are “Erst Neu Glück", "Heynitz Flacher", “Himmlisch Heer Stehender”, and “Krönung Flacher”. The thickness of the five-element association is highly variable, ranging from 0.1 to 1m (Baumann et al. 2000). These veins are currently difficult to access.

3 Sampling and methodology

Approximately 50 samples were selected from the geoscientific collections of the TU Bergakademie Freiberg. The samples are from the Markus Röhling, Bäuerin, Altväter, Uranus, and Himmlisch Heer mines and cover a vertical profile of about 200m (Fig. 1). This vertical profile includes samples from 346m, 420m, 462m, 485m, 510m and 540m (depth given in meters above sea level). The petrographic description was done based on optical microscopy and scanning electron microscopy (SEM).

4 Vertical zoning

Historical mine records reveal that rich five-element mineralisation occurs in ore shoots where veins intersect carbon-rich horizons (locally referred to as “Schwebende” or “Schwarze Flöze”). These carbon-rich horizons, partly composed of graphite, occur erratically in the paragneisses, but are mostly present in the central and shallow parts of the district (Baumann et al. 2000).

Vein 303 is a well-documented example, which hosts U, Ag-Bi-Co-Ni-As, and fluorite-barite mineralisation and exhibits a distinct vertical mineral zoning. Carbon-rich horizons are restricted to the uppermost part of the vein and are slightly dipping towards SSE (Fig. 2). These carbon-rich horizons are hosting most of the U and five-element associations. In the upper horizon of the vein (around 50m) U minerals dominate with little irregular Co-Ni arsenide mineralisation whereas Co-Ni-arsenides prevail in the lower part of the carbon-rich horizons. Fluorite-barite veins with minor base metal sulphides are present over the entire structure, even below 300m above sea level where five-element mineralisation does not occur.

Uranium mineralisation occurs as veins and stock-work; pitchblende is the most common ore mineral. Ag-Bi-Co-Ni-As mineralisation occurs as veins and forms irregularly-shaped lenses and ore shoots in the vicinity of the carbon-rich horizons.

Very similar observations have been made at the Marienberg and the Niederschlag districts, located farther to the north-east and to the south of the Annaberg district, respectively (Baumann et al. 2000 and references therein).

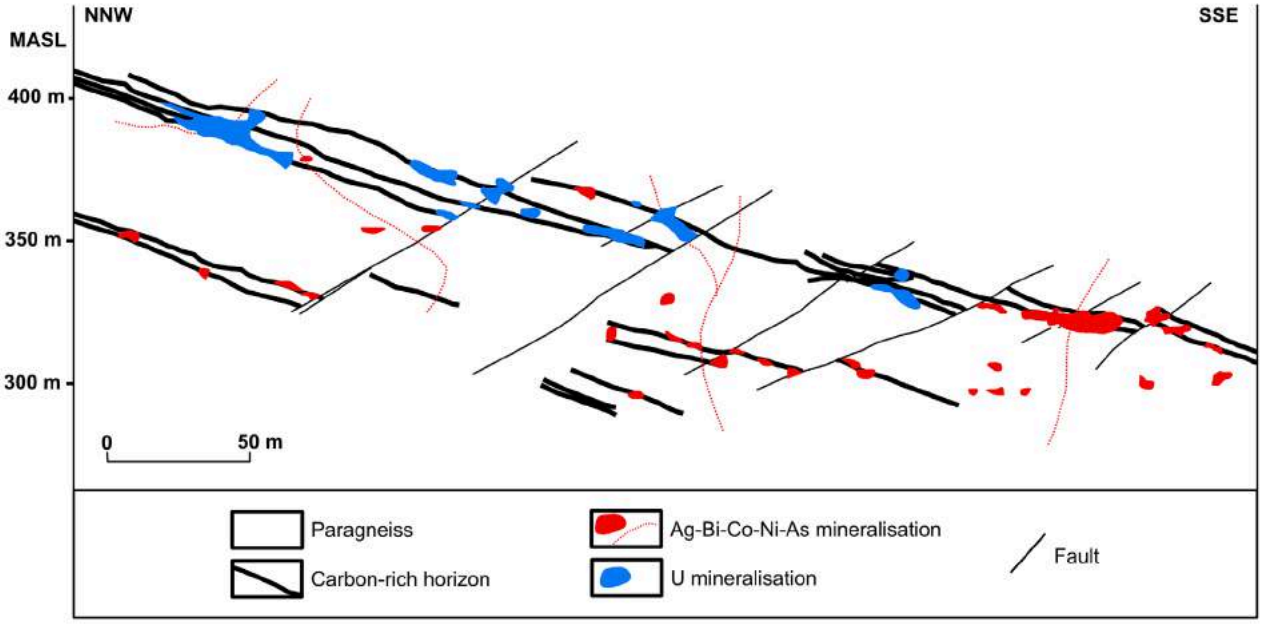

Figure 2. Schematic NNW-SSE cross-section of vein 303 showing the distribution of the U and Ag-Bi-Co-Ni-As mineralisation in the Annaberg district. The vein is hosted by the paragneiss. Abbreviation: MASL for "Meters above sea level". Annaberg's altitude is approximately 600 MASL (modified after Schönherr (1958) in Hösel et al. 1997).

5 Results – Petrographic observations

Ag-Bi-Co-Ni-As associations occur late in the paragenetic sequence of the Annaberg district (stage 5). In the studied samples, the mineralisation consists of native Bi, Ag, As associated with Ni-Co-Fe arsenides, base metal sulphides, and Ag-bearing sulphides (Fig. 3). Gangue minerals are quartz and carbonates (mostly dolomite and calcite) as well as occasional fluorite.

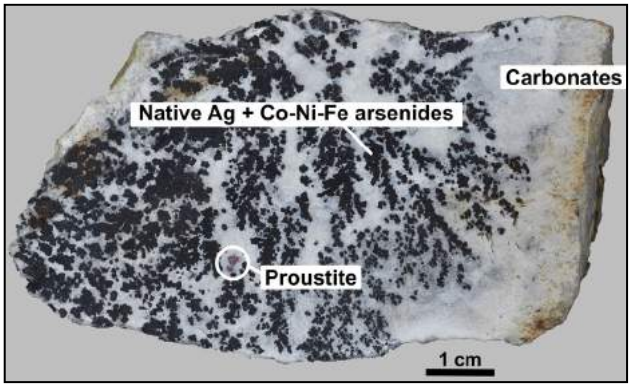

Figure 3. Example of one of the samples studied in the Annaberg district.

Native metals (Ag and Bi) typically form dendritic textures, which are encapsulated by different types of arsenides (Fig. 4A). In most cases, earliest arsenide minerals consist of nickeline, rammelsbergite, and skutterudite (Fig. 4B and 5), which are followed by safflorite, loellingite, and gersdorffite. The arsenide stage is followed by sulphides namely proustite, pearceite, acanthite, sphalerite, chalcopyrite, and pyrite (Fig. 4C and 5). Late stage sulphides often replace native metals or overgrow the arsenides. U-bearing minerals (coffinite and uraninite) occur only subordinately and are coeval with loellingite and late stage sulphides (Fig. 4D and 5). Coeval gangue minerals are quartz and carbonates.

These observations are in agreement with petrographic observations of previous studies in well-documented districts such as Schlema-Alberoda, Niederschlag and Schneeberg where five-element veins occur (Hiller et al. 2008; Kuschka et al. 2002; Lipp 2003).

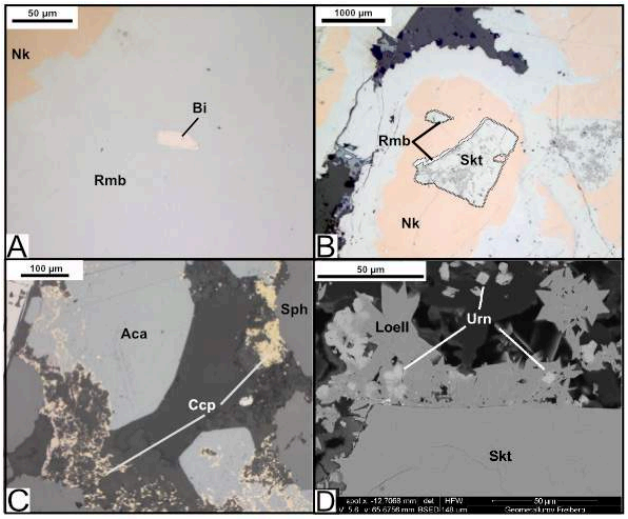

Figure 4. Photomicrographs of Ag-Bi-Co-Ni-As mineralisation thick sections under the microscope (A, B, C; reflected light) and SEM (D; BSE image) from the Annaberg district. A) Native Bi encapsuled by rammelsbergite; B) Co-Ni arsenides; C) Base metal sulphides, and Ag-bearing sulphide; D) Uraninite associated with loellingite. Abbreviations: Aca = acanthite; Bi = native Bi; Ccp = chalcopyrite; Loell = loellingite; Nk = nickeline; Rmb = rammelsbergite; Skt = skutterudite; Sph = sphalerite; Urn = uraninite.

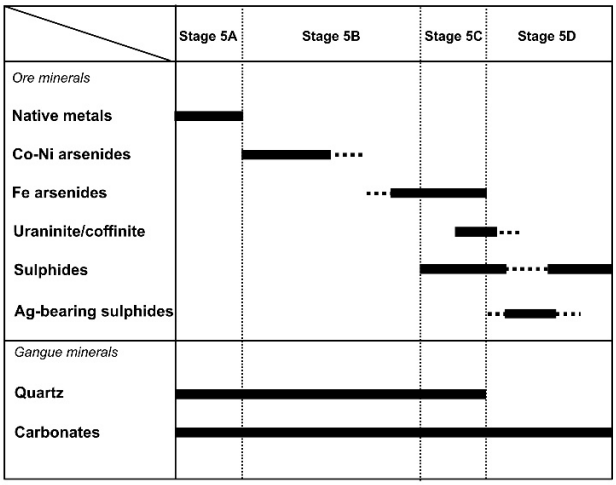

Figure 5. Paragenetic sequence of ore and gangue minerals observed in the samples of the Annaberg district.

6 Discussion and conclusions

As and U are both redox-sensitive elements (Markl et al. 2016). This is the apparent reason for the close spatial link between the carbon-rich horizons, that acted as redox barriers, and the U, and five-element mineralisation (Hösel et al. 1997). Although both elements are highly redox-sensitive, U- and arsenide-minerals seem to precipitate at different fO_2 – they fractionate – thus resulting in the observed spatial separation of U-dominated and As-dominated five-element-vein assemblages. A profound geochemical understanding of this fractionation process is key to the identification of Co-rich and U-poor zones within a given vein system.

Major questions that still remain unclear are: 1.) Is the trend from deeper arsenides to shallower U minerals a result of increasing or decreasing fO_2? 2.) Is the mineral zoning a consequence of a temperature gradient or the implication of different types of fluid? 3.) Is the ore fluid related to the U- and arsenide-minerals the same fluid that formed fluorite- and barite-rich assemblages at depth? 4.) Is the reducing agent actually graphite or methane hosted by the carbon-rich horizons?

We are planning to solve these questions with further petrographic studies, careful fluid inclusion work, and geochemical analyses (on Ag-Bi-Co-Ni-As mineralisation, and samples from the carbon-rich horizons) as well as thermodynamic computations.

Acknowledgements

This study is funded by European Social Fund and the Federal State of Saxony. We thank C. Kehrer for access to the geoscientific collections of the TU Bergakademie Freiberg. R. Würkert, A. Bartzsch and M. Stoll are thanked for sample preparation.

References

Baumann L, Kuschka E, Seifert T (2000) Lagerstätten des Erzgebirges. Enke im Thieme Verlag, Stuttgart, New York

Burisch M, Gerdes A, Walter BF, Neumann U, Fettel M, Markl G (2017) Methane and the origin of five-element veins: Mineralogy, age, fluid inclusion chemistry and ore forming processes in the Odenwald, SW Germany. Ore Geology Reviews 81:42–61. doi: 10.1016/j.oregeorev.2016.10.033

Crundwell FK, Moats MS, Ramachandran V, Robinson TG, Davenport WG (2011) Cobalt – Occurrence, Production, Use and Price. Extractive Metallurgy of Nickel, Cobalt and Platinum Group Metal:357–363. doi: 10.1016/B978-0-08-096809-4.10028-0

Hiller A, Schuppan W, Krejny I (2008) Geologie und Uranbergbau im Revier Schlema-Alberoda. Bergbau in Sachsen Band 14

Hösel G, Tischendorf G, Wasternack J, Breiter K, Kuschka E, Pälchen W, Rank G, Štemprok M (1997) Erläuterungen zur Karte "Mineralische Rohstoffe Erzgebirge-Vogtland/Krušné hory 1 :100 000, Karte 2: Metalle, Fluorit/Baryt - Verbreitung und Auswirkungen auf die Umwelt". Bergbau in Sachsen Band 3

Kissin SA (1992) Five-element (Ni-Co-As-Ag-Bi) Veins. Geoscience Canada Volume 19:113–124

Kroner U, Romer RL (2013) Two plates — Many subduction zones: The Variscan orogeny reconsidered. Gondwana Research 24:298–329. doi: 10.1016/j.gr.2013.03.001

Kuschka E, Leonhardt D, Hiller A (2002) Erläuterungen zur Karte "Mineralische Rohstoffe Erzgebirge-Vogtland/Krušné hory 1 :100 000", Karte 2: Metalle, Fluorit/Baryt - Verbreitung und Auswirkungen auf die Umwelt. Bergbau in Sachsen Band 6

Lipp U (2003) Wismut-, Kobalt-, Nickel- und Silbererze im Nordteil des Schneeberger Lagerstättenbezirkes: Die Mineralisation des Untersuchungsgebietes. Bergbau in Sachsen Band 10

Markl G, Burisch M, Neumann U (2016) Natural fracking and the genesis of five-element veins. Miner Deposita 51:703–712. doi: 10.1007/s00126-016-0662-z

Tichomirowa M, Sergeev S, Berger H-J, Leonhardt D (2012) Inferring protoliths of high-grade metamorphic gneisses of the Erzgebirge using zirconology, geochemistry and comparison with lower-grade rocks from Lusatia (Saxothuringia, Germany). Contrib Mineral Petrol 164:375–396. doi: 10.1007/s00410-012-0742-8

Micas $^{40}Ar/^{39}Ar$ dating of hydrothermal events related with the post-orogenic W (±Sn), (Cu, Mo) mineralization from Borralha, Northern Portugal

Iuliu Bobos, Ana Marta Gonçalves, Luís Lima, Fernando Noronha
Institute of Earth Sciences-Porto Pole, Faculty of Sciences, University of Porto, Porto, Portugal

Masafumi Sudo
Universitäaet Potsdam, Institut für Geowissenschaften, Germany

Abstract. Secondary mica minerals collected from the Santa Helena (W- (Cu) mineralization) and Venise (W-Mo mineralization) endogenic breccia structures were $^{40}Ar/^{39}Ar$ dated. The muscovite $^{40}Ar/^{39}Ar$ data yielded 286.8 ± 1.2 (±1σ) Ma (samples 6Ha and 11Ha) which reflect the age of secondary muscovite formation probably from magmatic biotite or feldspar alteration. Sericite $^{40}Ar/^{39}Ar$ data yielded 280.9 ± 1.2 (±1σ) Ma to 279.0 ± 1.1 (±1σ) Ma (samples 6Hb and 11Hb) reflecting the age of greisen alteration (T~300ºC) where the W-disseminated mineralization occurs. The muscovite $^{40}Ar/^{39}Ar$ data of 277.3 ±1.3 (±1σ) Ma and 281.3 ± 1.2 (±1σ) Ma (samples 5 and 6) also reflect the age of muscovite (selvage) crystallized adjacent to molybdenite veins within the Venise breccia. Geochronological data obtained confirmed that the W mineralization at Santa Helena breccia is older than Mo-mineralization at Venise breccia. Also, the timing of hydrothermal circulation and the cooling history for the W-stage deposition was no longer than 7 Ma and 4 Ma for Mo-deposition.

1 Introduction

The W ± Sn ore deposits in Europe are spatially associated to granites emplaced during syn-orogenic compression and post-orogenic extension of the European Variscan belt (EVC). The timing of W-mineralization geochronology across the EVC evolution is still poorly constrained due to the presence of multiple fluids with distinct origins and to a lack of integrated data combining mineralogical, chemical and isotope geochemistry either on tungstate or silicate neoformation from the hydrothermal alteration.

The main aim of this work is the $^{40}Ar/^{39}Ar$ dating of mica specimens collected from the different locations and hydrothermal stages related to W- and Mo-mineralizations from the Borralha ore deposit, in order to estimate the age of alteration-mineralization event and the time of breccia structure formation.

2 Geology

The Variscan orogeny in the Iberian Peninsula was explained by an obduction–collision orogenic model (Ribeiro et al. 1990, 2007; Matte 1991). The final stages of the continental collision process occurred during the D3 deformation phase (316-310 Ma), where most of the granite intrusions and the associated thermal metamorphic peak are coeval with the D3 phase in the Central Iberian zone (*e.g.* Ferreira et al. 1987; Dias and Ribeiro 1995; Ribeiro et al. 2007). The magmatic activity generated voluminous granitoid batholiths, where the emplacement was, in most cases, controlled by major Variscan structures.

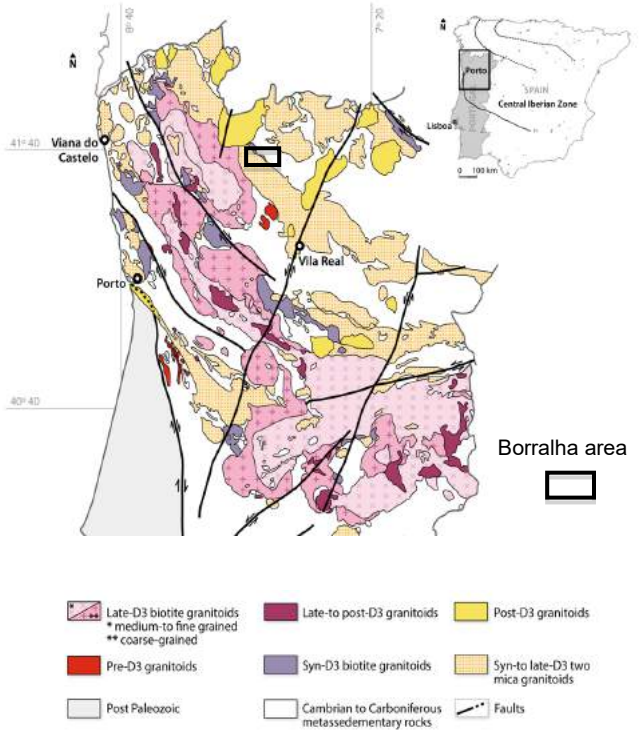

Figure 1. Geological map of the northern part of Portugal (Ferreira et al. 1987) and location of the W (± Sn), (Cu, Mo) ore deposit of Borralha, Gerês Mountains

The W (± Sn) (Cu, Mo) deposit of Borralha is located at the Northwest of the Iberian Peninsula near to the boundary between the Central Iberian Zone and Galicia Trás-os-Montes Zone, where different syn-orogenic Variscan granite-types intruding Paleozoic metasedimentary rocks were assigned: two-mica peraluminous (syn-D3) granites and biotite-rich (syn-D3) granites.

The ore deposit occurs at the contact between

metasedimentary formations and the syn-D3 porphyritic biotite granite (~ 315 Ma) known as the Borralha granite, and syn-D3 two-mica granites (~310 Ma) (Fig. 1).

Four evolving metallogenic stages associated with a magmatic - hydrothermal evolution of the post-D3 Gerês granite were recognized (Noronha 1988): (i) Mo, (W) at Bouzadrago (Galicia-Spain); (ii) W, Sn (Cu,Mo,Bi) at Las Sombras (Galicia-Spain), Carris and Borrageiro; (iii) W, (Cu,Mo,Bi,Sn) at Penedos; and (iv) W (± Sn), (Cu,Mo,Bi) at Borralha.

Assumed to be related to the concealed Gerês granite, the Borralha ore deposit is the second most important W deposit of Portugal after Panasqueira. The ore was exploited from 1903 to 1985 for wolframite, scheelite, and argentiferous chalcopyrite. The mineralization occurs in quartz veins and also in the two breccia pipe structures of Santa Helena (SHB) and Venise (VB).

The mineral ore assemblage in quartz veins consists of tungstates (wolframite and scheelite), sulfide minerals (chalcopyrite + molybdenite and pyrite, pyrrhotite, sphalerite, galena, bismuthinite, marcasite), Pb-Bi-Ag sulfosalts, and native bismuth. Fluid inclusion studies carried out on quartz veins identified aqueous-carbonic fluids (300 ºC < T < 400 ºC and 50 MPa < P < 100 MPa) related to the W mineralization and aqueous fluids (250 ºC < T < 300 ºC and 30 MPa < P < 50 MPa) with sulfide mineralization (Noronha 1984; Noronha et al. 1999). The discrimination of different mineralization events in the magmatic-hydrothermal system of Borralha was discussed on the basis of textural relationships, crystal chemistry and stable isotopic data obtained between chlorite minerals and the W, (Cu, Mo) mineralization (Bobos et al. 2018; Gonçalves et al. 2017), such as: i) early tungsten stage: formation of scheelite (I) and Fe,Mn-chlorite at temperatures from 400 to 500°C; ii) tungsten - sulfide stage II: formation of Mn-rich wolframite + scheelite (II) + sulfide (chalcopyrite), and Fe-chlorite and secondary muscovite at 250 – 350°C; iii) sulfide stage III: formation of molybdenite (+bismuthinite) and Fe,Mg-chlorite at ≤ 250°C.

3 Materials and analytic techniques

Secondary mica (muscovite and sericite) samples from different alteration episodes related to W- and Mo-mineralization were preliminary analyzed by electron microprobe analysis (backscatter), X-ray diffraction and infrared spectroscopy in order to select fresh samples devoid of mineral inclusions or alteration. Handpicked mica samples with grain sizes smaller than 0.15 mm were selected. The samples 6Ha, 6Hb, 11Ha and 11Hb were collected from SBH and the samples 5 and 6 from VB. Preparation of single- or multi-grain mica for $^{40}Ar/^{39}Ar$ dating by the stepwise heating or total fusion technique followed the guidelines of $^{40}Ar/^{39}Ar$ lab in Univ. of Potsdam. Samples were irradiated for 4 hours at the CLICIT facility in the OSTR Reactor, U.S.A. Sanidine age standard, FC3, prepared from the Fish Canyon Tuff by Geological Survey of Japan (GSJ) was used as the neutron fluence monitor with a reference age of 27.5 Ma obtained by GSJ (Uto et al. 1997; Ishizuka 1998). Measured isotopic ratios were corrected for mass discrimination, atmospheric Ar component blanks and irradiation–induced mass interferences. The decay constant was δ = 5.543 x 10-10 year-1 (Steiger and Jäger 1977).

4 Results

Mica samples were collected from the tungstate stage related to the SHB [wolframite, secondary muscovite and sericite (T = 250 – 350ºC)] and from the sulfide stage related to VB [molybdenite ± bismuthinite, secondary muscovite, sericite, and Fe,Mg-chlorite (Tº(C) ≤ 250)] The mica $^{40}Ar/^{39}Ar$ data incorporated apparent age spectra, atmospheric argon, and Ca/K ratios for each step. The ages (±1σ) are plotted against the cumulative released ^{39}Ar fraction for the age spectra (Figs. 2 and 3, inset).

4.1 Tungstate stage

Sample 6Ha (muscovite) has a plateau age of 286.8 ± 1.2 Ma (±1σ) calculated from steps 4 to 7, which represent 62.5% of the total ^{39}Ar released. The inverse isochron age of 288 ± 4 Ma (±1σ) from the plateau steps overlap the plateau age (Fig. 2a), so we prefer the plateau age with its smaller error.

Sample 6Hb (sericite) has a plateau age of 280.9 ± 1.2 Ma (±1σ) from steps 4 to 7, which represent 64.7 % of total ^{39}Ar. The inverse isochron age of 280 ± 4 Ma (±1σ) from plateau steps overlap the plateau age (Fig. 2b), so we prefer the plateau age with its smaller error.

Sample 11Ha (muscovite) does not yield a plateau age, but the total gas age is 286.6 ± 1.4 Ma (±1σ). The inverse isochron age of 288 ± 3 Ma (±1σ) overlap the total gas age (Fig. 2c), therefore we prefer the total gas age with its smaller error.

Sample 11Hb (sericite) does not yield a plateau age, but the total gas age is 279.0 ± 1.1 Ma (±1σ). The inverse isochron age of 279 ± 4 Ma (±1σ) with all plots overlap the total gas age within error, then we prefer the total gas age with its smaller error (Fig. 2d).

4.2 Sulfide stage

Sample 5 (muscovite) does not yield a plateau age, but the total gas age is 277.3 ± 1.3 Ma (±1σ). The inverse isochron age of 284 ± 7 Ma (±1σ) with all plots overlap the total gas age within error, therefore we prefer the total gas age with its smaller error (Fig. 3a).

Sample 6 (muscovite) does not yield a plateau age, but the total gas age is 281.3 ± 1.2 Ma (±1σ). The inverse isochron age of 285 ± 4 Ma (±1σ) with all plots overlap the total gas age within error, then we prefer the total gas age with its smaller error (Fig. 3b).

5 Discussion

A key factor in controlling the W (± Sn), (Cu, Mo)

mineralizing system of Borralha could be the time of post-magmatic activity and cooling history, in addition to magma source and differentiation.

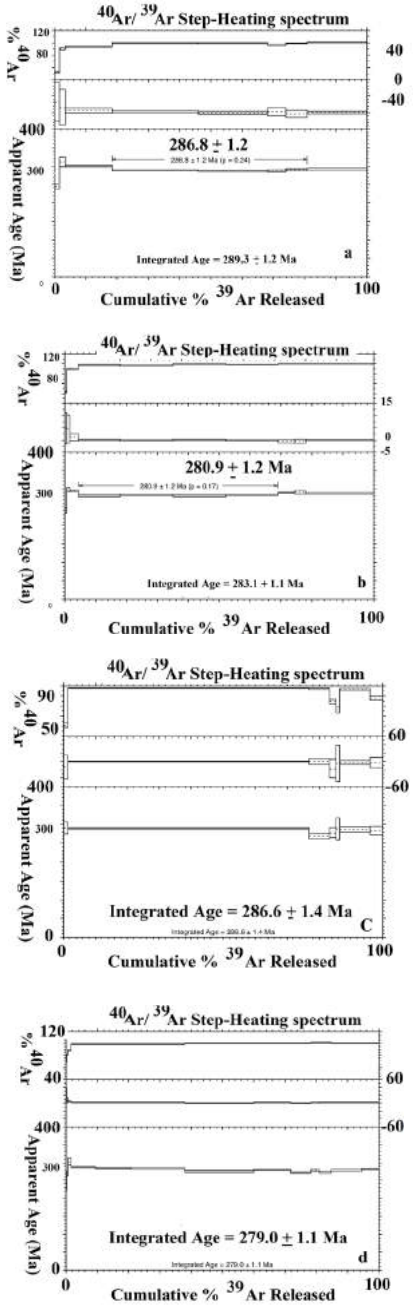

Figure 2. The plateau age of samples 6Ha (286.8 ± 1.2 Ma) (a) and 6Hb (280.9 ± 1.2 Ma) (b) corresponding to muscovite and sericite from tungstate stage. Total gas ages of sample 11Ha (286.8 ± 1.4 Ma) (c) and 11Hb (279.0 ± 1.1 Ma) (b) corresponding to muscovite and sericite from tungstate stage.

The muscovite $^{40}Ar/^{39}Ar$ data yielded 286.8 ± 1.2 (±1σ) Ma to 286.6 ± 1.4 (±1σ) Ma (samples 6Ha and 11Ha) reflect the age of secondary muscovite formation probably from magmatic biotite or feldspar alteration. Sericite $^{40}Ar/^{39}Ar$ data yielded 280.9 ± 1.2 (±1σ) Ma to 279.0 ± 1.1 (±1σ) Ma (samples 6Hb and 11Hb) reflecting the age of greisen alteration (T = 300 ºC) where the W precipitated as disseminated mineralization during greisenisation. The muscovite $^{40}Ar/^{39}Ar$ data of 277.3 ±1.3 (±1σ) Ma and 281.3 ± 1.2 (±1σ) Ma (samples 5 and 6) reflect also the age of secondary muscovite (selvage) crystallized adjacent to molybdenite veins.

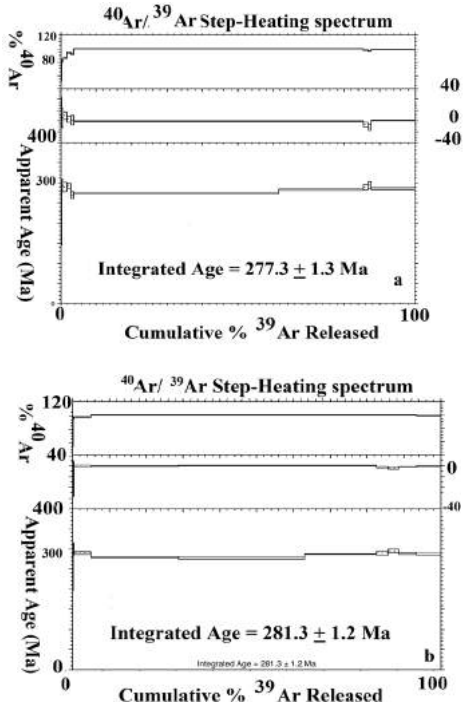

Figure 3. Total gas ages of samples 5 (277.3 ± 1.3 Ma) and 6 (281.3 ± 1.2 Ma) corresponding to mica from sulfide stage.

The same Mo-metallogenic event in the time window between 279 ± 1.2 Ma and 280.3 ± 1.2 Ma was found for the Mo ore-forming stage related with late to post-orogenic granite of Carris (Moura et al. 2014). Also, a younger K-Ar age of 273 ± 1.1 Ma was obtained on feldspar from epysienitic rocks of Carris facies from Gerês granite (Jaques et al. 2016).

Lifespans of tungstate and sulfide mineralizations using secondary mica $^{40}Ar/^{39}Ar$ geochronometers confirm a multi-stage alteration and mineralization where the timing of hydrothermal circulation and the cooling history for the W-stage deposition was no longer than 7 Ma and 4 Ma for Mo-deposition. The $^{40}Ar/^{39}Ar$ ages obtained provide evidence for an exceptionally prolonged and multi-stage alteration-mineralization widely assumed for a giant deposit.

Timing of magmatic and hydrothermal episodes measured on mica ($^{40}Ar/^{39}Ar$) and wolframite (U-Pb) from the French Central Massif, France (Puy-les-Vignes, Limousin) yielded ages around of 320 ± 5.4 Ma (mica) and 322 ± 10 Ma (wolframite) (Cuney et al. 2002; Harlaux et al. 2018). This could be interpreted as a weak expression of post- orogenic Variscan magmatism at French Central Massive contrarily to Central Iberian Zone, Portugal, where an important post-orogenic W-hydrothermal event followed after Sn-deposition event (estimated at about 331 ± 5.6 Ma to 301 ± 4.2 Ma, (Zhang et al. this volume) related to syn- and late-

orogenic magmatism.

Acknowledgements

This work was developed in the frame of ESMIMET project (Ref. 0284_ESMIMET_3_E) co-financed by the European Regional Development Fund (ERDF) through the Interreg Program V-A Spain-Portugal (POCTEP). Thanks also to MINERALIA Lda. for logistic support and permission to access of ore samples. We thank Dr. Martin Smith (Brighton University) for constructive review.

References

Bobos I., Noronha F., Mateus A (2018) Fe-, Fe,Mn- and Fe,Mg-chlorite: A genetic linkage to W, (Cu,Mo) - mineralization in the magmatic-hydrothermal system of Borralha, Northern Portugal. Miner. Magazine, 82:S259-S279

Cuney M, Alexandrov P, Le Carlier de Veslud C, Cheilletz, A, Raimbault L, Ruffet G, Scaillet S (2002) The timing of W-Sn rare metals mineral deposit formation in the Western Variscan chain in their orogenic setting: the case of Limousine area (Massif Central, France). In: Blundel DJ, Neubauer F and A. von Quadt. (ed) The timing and location of major ore deposits in an evolving orogeny, Geol. Soc. London Spec. Publ. 204:213-228

Gonçalves A., Lima L., Mota A, Ramos V, Barros J, Noronha F. (2017) The Santa Helena Breccia Pipe (Borralha – North Portugal). A new type of W ore deposit in the Iberian Tin-Tungsten Metallogenic Province. Com. Geol. 104:55-60.

Dias R, Ribeiro A (1995) The Ibero-Armorican Arc: a collision effect against an irregular continent? *Tectonophysics*, 246:113–128.

Ferreira N, Iglesias M, Noronha F, Pereira E, Ribeiro A, Ribeiro ML (1987) Granitoides da Zona Centro Ibérica e seu enquadramento geodinâmico.. In: Bea F, Carnicero A, Gonzalo J, Lopez Plaza M, Rodriguez Alonso M (ed) Geologia de los granitoides y rocas asociadas del Macizo Hesperico, Editorial Rueda, Madrid (Libro de Homenaje a García de Figuerola LC). pp 37–51

Harlaux M, Romer R.L, Mercadier J, Morlot C, Marignac C, Cuney M (2018) 40 Ma of hydrothermal mineralization during Variscan orogenic evolution of the French Massif Central revealed by U-Pb dating of wolframite. Miner Deposita, 53:21-51

Ishizuka O (1998) Vertical and horizontal variations of the fast neutron flux in a single irradiation capsule and their significance in the laser-heating $^{40}Ar/^{39}Ar$ analysis: Case study for the hydraulic rabbit facility of the JMTR reactor, Japan. Geochem. J., 32:243-252.

Jaques L, Noronha F, Liewig N, Bobos I (2016) Paleofluids circulation associated with the Gerês late-orogenic granitic massif, northern Portugal. Chem. der Erde, 76:659-676.

Matte P (1991) Accretionary history and crustal evolution of the Variscan Belt in Western Europe. *Tectonophysics,* 196:309–337.

Moura A, Dória A, Neiva AMR, Leal Gomes C, Creaser RA (2014) Metallogenesis at the Carris W-Mo-Sn deposit (Gerês, Portugal): Constraints from fluid inclusions, mineral geochemistry, Re-Os and He-Ar isotopes. Ore Geol. Rev., 56:73–93.

Noronha F (1984) Caractéristiques physico-chimiques des fluides associés à la génese du gisement de tungsten de Borralha (Nord Portugal). Bull. Mineral., 107:273–284.

Noronha F (1988). Mineralizações. Geonovas (Lisboa), 10:37-57.

Noronha F, Vindel E, López JA, Dória A, García E, Boiron MC, Cathelineau M (1999) Fluids related to tungsten ore deposits in Northern Portugal and Spanish Central system: a comparative study. Rev. Soc. Geol. España, 12:397-403.

Ribeiro A, Munhá J, Dias R, Mateus A, Peirera E, Ribeiro L, Fonseca P, Araújo A, Oliveira T, Romão J, Chaminé H, Coke C, Pedro J, (2007) Geodynamic evolution of the SW Europe Variscides. Tectonics, 26:1-24.

Ribeiro A, Pereira E, Dias R (1990) Structure in the Iberian Peninsula.. In: Dallmeyer RD, Martinez G (ed) Pre-Mesozoic Geology of Iberia. Springer-Verlag, Berlin pp 220-236

Steiger RH, Jäger E (1977) Subcommission on geochronology convention on the use of decay contants in geo- and cosmochronology. Earth Planet. Sci. Lett. 36:359-362.

Uto K, Ishizuka O, Matsumoto A, Kamioka H, Togashi S (1997) Laser-heating $^{40}Ar/^{39}Ar$ dating system of the Geological Survey of Japan: System Outline and Preliminary Results. Bull. Geol. Surv. Japaŋ, 48:23-46.

Zhang R, Ramos V, Leal S, Noronha F (2019) U-Pb geochronology of cassiterites from primary Sn mineralizations in Sn-W Variscan Metallogenetic Province, Portugal (this volume)

U-Pb geochronology of cassiterites from primary Sn mineralizations in Sn-W Variscan Metallogenic Province, Portugal

Rongqing Zhang
State Key Laboratory for Mineral Deposits Research Nanjing University, China

Violeta Ramos, Sara Leal, Fernando Noronha
Institute of Earth Sciences-Porto Pole, Faculty of Sciences, University of Porto, Portugal

Filipe Pinto
Beralt Tin & Wolfram S.A., Geology Department, Panasqueira, Portugal

Abstract. The Iberian Sn-W Metallogenic Province is one of the main sources of Sn and W in Europe. It is spatially related to syn-collisional and to post-collisional Variscan granites. With this study, different types of Sn mineralization can be distinguished and a sequence of different mineralization episodes can be considered based on the cassiterite U-Pb ages. The first episode, yielding 331 ± 5.6 Ma, corresponds to Sn-quartz veins hosted by a deformed muscovite-rich granite; the second episode, 318.8 ± 5.6 Ma, also consists of Sn-quartz veins in the exocontact of two-mica granites (mus>bi); a third episode, 310 ± 6 Ma, corresponds to Sn-pegmatite veins in the exocontact of biotite granites (bi>mus); and a fourth episode, in Panasqueira W-Sn deposit in the exocontact of a greisen cupola, which yielded 303 ± 3.3 Ma and 301 ± 4.2 Ma. A cycle of about 30 Ma can be considered as responsible for different episodes of Sn mineralization, with a first episode, contemporaneous of the orogenic metamorphism and a last one related to the beginning of the first mineralizing stage at Panasqueira. A later cycle is related to post-collisional magmatism and W (Cu, Mo, Sn) mineralizations.

1 Introduction

Portugal is currently a very minor Sn producer. However, Portugal has an important tungsten production. The only active mine producing cassiterite concentrates is Panasqueira with 105 t Sn and 1132 t WO_3 in 2017.

The Sn and W deposits are found in a zone stretching from Galicia (NW Spain) over Northern and Central Portugal (Fig. 1) and Castilla-Leon, Central-Western Spain, in the SW branch of the European Variscan Belt.

The Variscan belt, originated by the convergence, obduction, subduction and collision of Laurussia and the Gondwana continents, is characterized by several, geotectonic zones with specific and peculiar paleogeographic, tectonic, metamorphic and magmatic characteristics (Ribeiro et al. 1990). The Central Iberian Zone (CIZ) and the Galiza Trás-os-Montes Zone (GTMZ) correspond to the most internal zones of the Iberian Variscan Orogeny (Julivert et al. 1974). Most of the rocks outcropping in these zones are Variscan granites and metasediments with ages from the Upper Precambrian to Lower Cambrian to Devonian.

The number, the age and the relative importance of the folding events in the Iberian Belt have been for a long time, in debate between geologists studying the Geology of Iberia. Ribeiro et al. (1990) considered, not only based on field work, but also on geochronological data in granites from Northern Portugal and NW Spain, that the CIZ and the GTMZ owe their structural deformation to a sequence of three deformation phases corresponding to the third phase (D3) early-late Carboniferous (former Westphalian), D3 being the last Variscan ductile deformation phase. Simultaneously to D3 folding, vertical ductile shear zones can occur. In the late- and post-D3 periods, ductile-brittle and brittle deformation occurred along NNE-SSW and NNW-SSE fractures.

Since the 70's, it is recognized that granite plutonism took place in various episodes during the Variscan orogeny from Upper Devonian, ca. 380 Ma, to Permian, ca. 280 Ma, subsequently confirmed by radiometric dating (Pinto et al. 1987, Dias et al. 1998). More recently, Pereira et al. (2018) and references therein, considering the U-Pb ages in zircons, distinguish two groups of granites: a group of S type granites related to the Gondwana-Laurussia collision with 336 to 306 Ma with three sub-groups 331-321 Ma, 317-315 Ma and 311-310 Ma, of mesocrustal origin related to orogenic metamorphism (335-315 Ma); and a second group of I type granites unrelated to the Gondwana-Laurussia collision with ages of 306 to 287 Ma.

The age of W-Sn mineralization is still a subject of debate. The data concerning the age of mineralization events are very scarce and, sometimes, of difficult interpretation considering the usual influence of late hydrothermal events and alteration. This work was carried out to confirm the possibility of a sequence of different Variscan Sn mineralization episodes with the determination of cassiterite U-Pb ages from hydrothermal Sn deposits, rare metal pegmatites and in W-Sn hydrothermal deposits.

2 Geological settings

Tin deposits in Portugal may be grouped into two types

as follows: 1) cassiterite-rich aplite-pegmatites with little or no W; and 2) quartz-cassiterite veins (and/or with stockworks): 2a. cassiterite veins with little or no W; 2b. wolframite-cassiterite-quartz veins; and 2c. wolframite veins with little or no cassiterite.

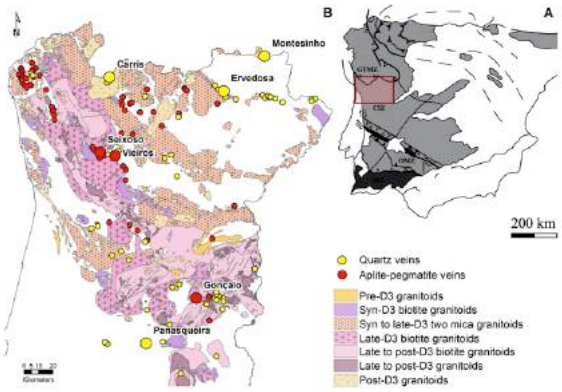

Figure 1. A - Map of the Iberian Massif showing the major tectonic units and structures. B - Distribution of Sn-W mineralization and granitic rocks (based on the classification of Ferreira et al. 1987).

Cassiterite-rich aplite-pegmatites have in the past been mined extensively for cassiterite and columbite-tantalite, but the grade is generally low. The pegmatite field of the Vieiros-Seixoso area in Northern Portugal is a good example and has been described by Lima et al. (2013). The mineralized pegmatite veins are hosted in schists with andalusite in the exocontact of biotite granites. In the Vieiros deposit aplite-pegmatite veins with cassiterite and columbo-tantalite were widely exploited. The veins have a preferred direction N25ºE to 55ºNW and are sub-horizontal. There are also intersecting veins that have preferred N-S direction. The average grade is of the order of 5 kg/t of cassiterite. In addition to Sn-Ta mineralization, the mineralogical study showed a sulphide mineralization. This sulphide mineralization presents a great variety of minerals characterized by the association Ni, Co, As, Ag, Bi and U, that is an evidence of a late hydrothermal episode controlled by fracturing. At the Seixoso pegmatite, the mineralization is predominantly of cassiterite, but with associated columbo-tantalite, which occurs disseminated in the veins, quite weathered to the surface, but hard at depth. The mineralized veins have variable direction and slope, but the main ones have N-S direction, dipping from 0^0 to 45^0 and vertical. The mineralogical study revealed a complex mineral association with well-expressed late sulphide stages with arsenopyrite, galena, sphalerite, pyrite, chalcopyrite and a carbonate stage.

The Gonçalo deposit corresponds to a lepidolite-rich pegmatite hosted in a porphyritic coarse-grained biotite granite. The vein field outcrops are determined by the sub-horizontal dipping and by late NNE-SSW to NE-SW and NW-SE sub-vertical faults that divide the vein field in several sectors. In a more detailed view, it is verifiable that there are sectors where only stanniferous sills outcrop, namely in lower topographic levels, and others with lithiniferous ones in the highest levels. The veins are composed by pegmatite and aplite and the main minerals are quartz, albite, K-feldspar, muscovite, Li-rich muscovite, topaz, apatite, beryl, tourmaline, Mn-oxides and zircon. The major ore mineral is Li-rich mica, but other Li minerals are present like petalite and amblygonite-montebrasite. Cassiterite and columbite-tantalite are also present. In the contact of pegmatite sills with the granite host rock the zinwalditization of biotite is observed (Ramos 2007).

Quartz veins, only with cassiterite, or with predominant cassiterite are not very frequent. Cassiterite is often dispersed in quartz and usually shows a small particle size. In other cases, it concentrates near the host rock in muscovite selvages. Of the known occurrences, the examples of the Montesinho and Ervedosa deposits deserve a special mention. At Montesinho, most of the mineralized veins are hosted in Ordovician wall rocks, and a small part in the Montesinho deformed two-mica granite. The veins have a variable thickness from a few centimeters to more than 2 m, averaging 0.60 m. They are essentially quartz veins, with muscovite, cassiterite, beryl, arsenopyrite and iron oxides. Cassiterite is fairly coarse, brown to light-brown in colour, and preferably associated to muscovite selvages.

The Ervedosa deposit is located in the contact of a fine-grained muscovite granite (327 ± 9 Ma), intrusive in schists, lower Silurian in age, with a schistosity N70ºW, (Gomes and Neiva 2001). The exploitation was made along a quartz vein with direction N40ºW and dipping 70º to 80ºNE to sub-vertical. This vein is poor, but it is associated with a network of veinlets with irregular shape, constituting a stockwork type deposit. The mineralization is located essentially in the veinlets cutting the two-mica granite that in the contact is intensely muscovitized. The veins contain quartz, muscovite, cassiterite, arsenopyrite, pyrrhotite, rutile, apatite, bismuth, pyrite, sphalerite, chalcopyrite, stannite, fluorite and inclusions of bismuthinite and matildite in arsenopyrite.

The wolframite-cassiterite quartz veins are the most important and are well represented by the Panasqueira deposit, which consists of a dense swarm of sub-horizontal wolframite-cassiterite-sulphide-bearing quartz veins. The mineralized area lies in Upper Precambrian schists, largely within a zone of spotted schists. This contact metamorphism is due to a buried granite whose roof was intersected by boreholes. A greisen cupula, recognized in underground works, rises above the irregular roof of a much larger granite massif. The greisen preceded the vein-type W-Sn mineralization. The mineral assemblage reveals a series of mineralizing stages separated in time by brecciation episodes (Kelly and Rye 1979, Pinto et al. 2015). Cassiterite is one of the first minerals and is, generally, contemporaneous with quartz, muscovite and topaz that represent the earliest mineral association; wolframite comes after cassiterite and is the main oxide of the “oxide silicate stage”. Economically, this first stage is by far the most important. This is followed by a second main stage "the main sulphide stage" with arsenopyrite, pyrite, pyrrhotite, sphalerite, chalcopyrite, stannite and by the

"pyrrhotite alteration stage" with pyrite, marcassite chalcopyrite, galena, Pb-Bi-Ag sulphosalts and siderite. A late stage is characterized by a widespread carbonate, dolomite and calcite deposition.

3 Sampling and analytical methods

3.1 Selection of the samples

The Sn-W mines in Portugal were very abundant and several cassiterite crystals were selected for this study from: a) the Panasqueira W-Sn mine that currently produces Sn concentrates; b) the Gonçalo Li-rich pegmatite deposit that is exploited for the ceramic industry and where fresh rocks were sampled from the quarries; and c) the mineralogical collection of the LNEG Museum at S. Mamede Infesta, Portugal, and belonging to the deposits of Montesinho, Vieiros, Seixoso and Ervedosa.

3.2 Analytical methods

U-Pb isotopic and trace elemental analysis of cassiterite was carried out using a LA-ICPMS system at the CAS Key Laboratory of Mineralogy and Metallogeny, GIG-CAS, Guangzhou, China. The system consists of an Agilent 7900 ICP-MS coupled with a Resonetics RESOlution S-155 laser. This laser ablation system is large (155 × 105 mm). Cassiterite grains were analyzed using a laser energy density of 4 J/cm^2, a spot size of 74 μm, and a repetition rate of 6 Hz. NIST SRM 610 and an in-house cassiterite standard AY-4 (158.2 ± 0.4 Ma) were used as external elemental and isotopic calibration standards, respectively. Raw data reduction was performed off-line by ICPMSDataCal software. The uncertainty of single population, ratio uncertainty of the AY-4 reference material, and decay constant uncertainties were propagated to the ultimate results of the samples during the process of data reduction by ICPMSDataCal. Data uncertainties for isotopic ratios in the cassiterite samples are 1 σ. Isoplot 4.0 was used to calculate the U–Pb ages and draw concordia plots and weighted $^{206}Pb/^{238}U$ mean age diagrams.

4 Results

4.1 Cassiterite U-Pb ages

The U contents of the analyzed cassiterite grains are variable. The U-Pb ages have a wide span from 331 to 295 Ma. Some samples with low U contents exhibit large analytical errors (2 σ): Gonçalo 295 ± 21 Ma; and Seixoso 316 ±13 Ma. However, there are samples with small analytical errors (2 σ): Panasqueira 303 ± 3.3 Ma and 301 ± 4.2 Ma; Vieiros 310 ± 6 Ma; Ervedosa 318.8 ± 5.6 Ma; and Montesinho 331 ± 5.6 Ma. These ages indicate different periods for Sn mineralization suggesting three periods related to collisional granites.

A first cycle of about 30 m.y. can be considered as responsible for different episodes of Sn mineralization with a last period associated with the richest deposit. A second cycle of Sn mineralization corresponds to the cassiterite present in W (Cu, Mo, Bi, Sn) deposits associated with the mineralizations from the Gerês area related to post-collisional magmatism (Noronha 2017).

5 Discussion

5.1 Timing of tin mineralizations

Studies carried out in Central Portugal indicated a close spatial relationship with Middle Permian granites. However, studies in Northern Portugal indicated also a close spatial relationship in early-late Carboniferous (former Westphalian) (Schermerhorn 1981, Ribeiro and Pereira 1982).

Priem and den Tex 1984, found a Rb-Sr age of 307 ± 3 Ma for a deformed Sn-pegmatite in the Vila Real area in the exocontact of a two-mica granite with 304 ± 2 Ma.

Panasqueira deposit is the only Portuguese W-Sn deposit with isotopic studies for mineralization dating. Clark (1970), dated white micas from the greisen and muscovite selvages from OSS and obtained K-Ar, ages between 295 and 299 ± 10 Ma. Snee et al. (1988) dating fluid circulation using ^{40}Ar-^{39}Ar in muscovites from veins and of greisen, found ages ranging from 296.3 ± 0.8 to 291.6 ± 0.8 Ma. However, the two-mica granite (muscovite dominantly secondary), cut by drilling, gave a whole-rock, Rb-Sr ages of 289 ± 4 Ma (Priem and den Tex 1984).

Lima et al. (2013) determined U-Pb dates of minerals of the columbite-tantalite group in Seixoso-Vieiros pegmatite field and found an age 301 ± 4Ma for Vieiros pegmatite and 316 ± 9 Ma in cores of two grains with low concentrations in U.

The W-Sn-Mo mineralizations from Carris (Gerês area) are later than I type granites emplacement and Re–Os dating of molybdenite from the ore quartz veins and surrounding granite yields ages from 279 ± 1.2 Ma to 280.3 ± 1.2 Ma, respectively (Moura et al. 2014), which are in very good agreement with the previous ID-TIMS U–Pb zircon age of 280 ± 5 Ma for the Carris granite (Dias et al. 1998).

The main types of Sn mineralizations are spatially related to syn-collisional and post-collisional Variscan granites. However, in spite of its importance, the geochronological data mainly concerns granite emplacement.

With the presented new results, it is possible to confirm the existence of different periods of Sn mineralization. Considering that the oldest Sn mineralization has an age of 331 Ma that is contemporaneous with the orogenic metamorphism responsible for crustal anataxis, it is possible to assume the existence of a specialized middle crust responsible by all specialized S type granites.

The youngest cassiterite is represented by Panasqueira hydrothermal quartz veins as result of a rapid crustal uplift that occurred at ca. 300 Ma. Surface heat flow anomalies were developed, enduring at least ca. 280 Ma. This heat flow regime supported a late extensive hydrothermal activity throughout the entire

crust, involving distinct fluid sources in successively lower P-T conditions along a continuum that provided long-lived hydrothermal systems (e.g. Mateus and Noronha 2010, Noronha 2017).

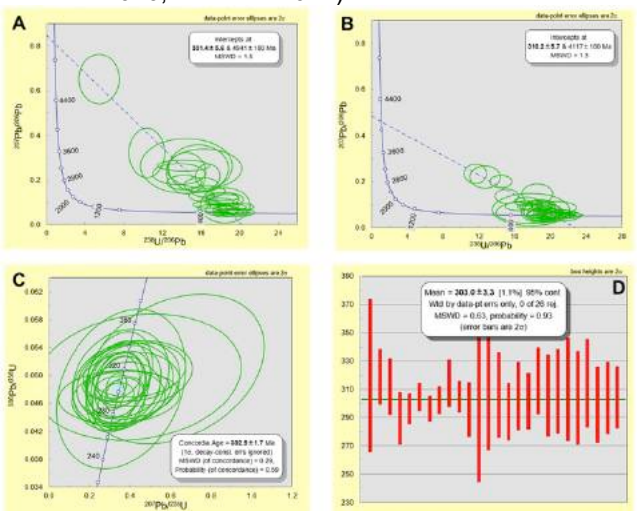

Figure 2. U-Pb concordia plots (error envelopes are 2 sigma) and weighted mean age diagrams for cassiterite grains from Montesinho (A) Vieiros (B) and Panasqueira (C and D).

6 Conclusions

In this work we report the first U-Pb ages of cassiterites from Portuguese Sn-W deposits.

Considering the existing results concerning the age of peraluminous granite magmatism, it is possible to consider that: the age of the first episode of cassiterite mineralization corresponds to Sn-quartz veins hosted by deformed muscovite leucogranites yielding 331 ± 5.6 Ma, that is very close to the age estimated for the Variscan orogenic metamorphism that implied the melting of crustal metasediments and the genesis of the older (331-321 Ma) S-types granites; the Ervedosa cassiterite age (318.8 Ma) is compatible with the age of the D3 peraluminous granites; and Vieiros age (310 Ma) is compatible with the ages of syn- to late-D3 biotite granites. Cassiterites from Panasqueira with 303 ± 3.3 Ma and 301 ± 4.2 Ma are related to a younger event associated with late- to post-D3 biotite (bi>mus) granites.

Acknowledgements

V. Ramos and F. Noronha acknowledge the ESMIMET project (Ref. 0284_ESMIMET_3_E) co-financed by the European Regional Development Fund (ERDF) through the Interreg Program V-A Spain-Portugal (POCTEP).

References

Capdevila R, Corretge LG, Floor P (1973) Les granitoïdes varisques de la Meseta Ibérique. Bull Soc Geol Fr 15:209-228.

Clark AH (1970) Potassium-argon ages and regional relationships of the Panasqueira tintungsten mineralization. Comun Serv Geol Port 54:243-261.

Dias G, Leterrier J, Mendes A, Simões, P, Bertrand JM, 1998 U-Pb zircon and monazite geochronology of syn- to post-tectonic Hercynian granitoids from the central Iberian Zone (northern Portugal). Lithos 45:349–369

Ferreira N, Iglesias M, Noronha F, Pereira E, Ribeiro A, Ribeiro ML (1987) Granitóides da Zona Centro Ibérica e seu enquadramento geodinâmico. In: Geologia de los Granitóides y Rocas asociadas dei Macizo Hespérico. (Bea, et ai. eds) Libro Homenaje a LC Garcia de Figuerola: 37-51.

Gomes MEP, Neiva A (2001) Mineralogical and geochemical characteristics of tinbearing quartz veins, Ervedosa deposit, Northern Portugal. Bol Soc Esp Min, 24:99-116.

Julivert M, Fontbote JM, Ribeiro A, Nabais Conde LE (1972). Mapa Tectónico de la Península Ibérica y Baleares. E: 1:1.000.000, Madrid, IGME: 4 pp.

Kelly WC, Rye RO (1979) Geologic, fluid inclusions and stable isotope studies of the tin-tungsten deposits of Panasqueira, Portugal. Econ Geol 74:1721-1822.

Lima A, Mendes L, Melleton J, Gloaguen E, Frei D (2013) Seixoso-Vieiros Rare Element Pegmatite Field: Dating the Mineralizing Events. PEG 2013: The 6th International Symposium on Granitic Pegmatites, Bartlett, United States. PEG 2013:77-78.

Mateus A, Noronha, F (2010) Sistemas mineralizantes epigenéticos na Zona Centro-Ibérica; expressão da estruturação orogénica Meso- a Tardi-Varisca, In: Cotelo Neiva JM, Ribeiro A, Victor M, Noronha F and Ramalho M (Ed.), Ciências Geológicas: Ensino, Investigação e sua História, Geologia Aplicada, II: 47-61.

Moura A, Dória A, Neiva AMR, Leal Gomes C, Creaser RA (2014) Metallogenesis at the Carris W-Mo-Sn deposit (Gerês, Portugal): Constraints from fluid inclusions, mineral geochemistry, Re-Os and He-Ar isotopes. Ore Geol Rev 56:73-93.

Noronha F (2017) Fluids and Variscan metallogenesis in granite related systems in Portugal. Procedia Earth Planet Sci 17:1-4. https://doi.org/10.1016/j.proeps.2016.12.002

Pereira MF, Díez Fernández R, Gama C, Hofmann M, Gärtner A, Linnemann U (2018) S-type granite generation and emplacement during a regional switch from extensional to contractional deformation (Central Iberian Zone, Iberian autochthonous domain, Variscan Orogeny). Int J Earth Sci (Geol Rundsch) (2018) 107:251-267

Pinto F, Vieira R, Noronha F (2015) Different cassiterite generations at the Panasqueira deposit (Portugal): Implications for the metal zonation model. 13th SGA Biennial Meeting August 2015 Volume: 2, Nancy, France: 3 pp.

Pinto MS, Casquet C, Ibarrola E, Corretge LG, Ferreira MP (1987) Sintese geocronológica dos granitodes do maciço hesperico. In: Geologia de los Granitóides y Rocas asociadas del Macizo Hespérico. (Bea, et ai. eds): 69-86.

Priem H, Den Tex E (1984) Tracing crustal evolution in the NW Iberian Peninsula through the Rb-Sr and U-Pb systematics of Paleozoic granitoids: a review. Phys. Earth Planet Int 35:121-130.

Ramos JMF (2007) Locality no. 5: Seixo Amarelo-Gonçalo Rare Element Aplite-Pegmatite Field. in Alexandre Lima & Encarnación Roda Robles ed (2007) Granitic Pegmatites: the state of the art - Memórias N. º 9, Univ do Porto: 73-86.

Ribeiro R, Pereira E, Dias R (1990) Structure of the Northwest of the Iberian Peninsula. In: R.D. Dallmeyer, E. Martinez Garcia (Eds). Pre-Mesozoic Geology of Iberia, Springer-Verlag: 220-236.

Ribeiro, R, Pereira, E, (1982) Controlos paleogeográficos, petrológicos e estruturais na génese dos jazigos portugueses de estanho e volfrâmio. Geonovas 3: 23-31

Schermerhorn LJ (1981) Framework and evolution of hercynian minerallization in the Iberian meseta. Leidse Geol Med 52(1):23-56.

Snee, LW, Sutter JF, Kelly, WC (1988) Thermochronology of economic mineral deposits: dating the stager of mineralization at Panasqueira, Portugal, by high precious 40Ar/39Ar age spectrum techniques on muscovite. Econ Geol 83:335-354.

Early hydrothermal alteration stages at the giant San Rafael tin deposit, Peru

Stefano Gialli, Matthieu Harlaux, Kalin Kouzmanov, Lluís Fontboté
Department of Earth Sciences, University of Geneva, Switzerland

Alain Chauvet
Géosciences Montpellier, CNRS, France

Oscar Laurent
Institute of Geochemistry and Petrology, ETH Zurich, Switzerland

Andrea Dini
Istituto di Geoscienze e Georisorse, CNR Pisa, Italy

Miroslav Kalinaj
MINSUR S.A., Peru

Abstract. At the giant tin deposit of San Rafael, Peru, the early hydrothermal stages, preceding the economic tin mineralization, include successively: 1) potassic alteration represented by hydrothermal K-feldspar altering magmatic plagioclase; 2) sericite replacing magmatic plagioclase in the ground mass and hydrothermal K-feldspar, with greisen formation in the apical part of the intrusion; 3) widespread albitic alteration, both disseminated and as intense replacement along fractures, overprinting and obliterating the previous stages; 4) quartz-tourmaline veins rimmed by albitic alteration halos. In this contribution, the greisen-style alteration and sodic alteration, are studied in depth. Trace element analysis of hydrothermal albite reveals a marked enrichment in incompatible elements (B, Rb, Cs) compared to magmatic plagioclase, suggesting albitization was triggered by magmatic fluids exsolved from an evolved silicate melt.

1 Introduction

Early alteration taking place during magmatic-hydrothermal transition of granites hosting Sn-W mineralization, has been widely described. A typical feature of Sn-W deposits is the presence of early greisenization and albitization (Černý et al. 2005; Pirajno 2009). In the present contribution we focus on the hydrothermal alteration stages preceding Sn mineralization in the giant San Rafael Sn deposit (Central Andean Tin Belt, Peru; Kontak and Clark 2002; Mlynarczyk et al. 2003; Gialli et al., 2017). We report, in addition to the previously described potassic and sericitic alteration stages, development of greisen-style alteration in the apical part of the main intrusion. We have also found that albitization, already mentioned by Kontak and Clark (2002) is widespread and intense at San Rafael. This alteration feature, albeit commonly associated with many different deposit styles and settings, has received limited attention in the literature (Boulvais et al. 2007 and references therein). Combining optical microscopy, QEMSCAN, optical cathodoluminescence, EPMA and LA-ICP-MS analyses on samples representative of different pre-ore alteration styles, we present here a revised sequence of the early alteration stages at San Rafael and we discuss implications for fluid evolution at the magmatic-hydrothermal transition.

2 Geological setting

The San Rafael mining district is located in the Eastern Cordillera of southern Peru and is the largest and richest underground tin mine in the world, with resources of 11.2 million tons of ore at 1.99% Sn (Minsur corporate presentation 2018). The ore occurs as quartz-cassiterite-sulfide veins mainly hosted by a shallow peraluminous composite granitic intrusion (Kontak and Clark 2002; Mlynarczyk 2005) dated at 24.6±0.2 Ma (U-Pb zircon, Clark et al. 2000) and, subordinate, by surrounding Ordovician slates of the Sandia Formation. Main magmatic facies are biotite-cordierite megacrystic granite, volumetrically less important microgranite, in part as dismembered dikes, and late alkali granite. Lamprophyre dikes crosscut the granitic complex. The vein system formation is controlled by sinistral normal faults striking NNW-SSE and dipping at high angle towards the NE (Gialli et al. 2017; Fig. 1). We distinguish three main alteration and mineralization stages (Fig. 2): i) early pre-ore alteration stage with, from early to late, K-feldspar alteration, sericitic alteration, greisen formation, albitic alteration and tourmaline veining (Tur 2) with albitic halo (Fig. 3); ii) syn-ore stage in veins/breccias including Tur 3 and the main quartz-chlorite-cassiterite ± subsequent sulfide mineralization; and iii) post-ore stage consisting of late quartz ± carbonates ± fluorite ± adularia veins, which cut and overprint the earlier mineralization and alteration stages.

3 Results

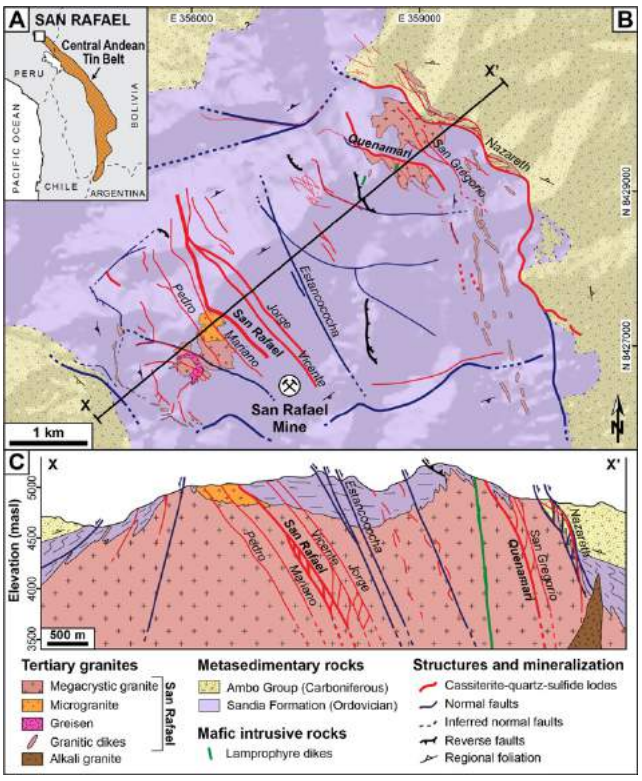

Figure 1. Geological map and cross-section of the San Rafael district, Southeast Peru. **a)** Location of the San Rafael deposit in the Central Andean Tin Belt (modified after Mlynarczyk et al. 2003); **b)** Geological map of the San Rafael district compiled from new mapping campaigns (Gialli et al. 2017, MINSUR S.A. unpublished data) and integrating older data (Arenas 1980, Palma 1981, Kontak and Clark 2002, Corthay 2014); **c)** Longitudinal cross-section of the San Rafael lode system from Gialli et al. 2017; modified after MINSUR S.A. unpublished data.

The early pre-ore hydrothermal stage includes the following four major events (Fig. 2):

A) Potassic alteration. Pervasive potassic alteration is the earliest event of the pre-ore stage and consists of discrete patches of hydrothermal K-feldspar partially replacing magmatic plagioclase in the granitic rocks (Fig. 4A and D). This alteration is volumetrically restricted.

B) Sericitic alteration and greisen formation. Sericite commonly replaces magmatic plagioclase and hydrothermal K-feldspar (Fig. 4D). The intensity of the pervasive sericitic alteration increases progressively towards the upper part of the granitic intrusion where, in patchy areas, least altered granite grades toward intensely sericitized and albitized rocks (Fig. 4E-F). In the apical part of the pluton, cropping out in the south-eastern part of the studied area (Fig. 1B), an elongated area of intense greisenization extending for a few hundred meters in NNW-SSE direction has been recognized for the first time. The greisen mineral composition consists of quartz (~60%), muscovite (~35%), with minor amounts of tourmaline and

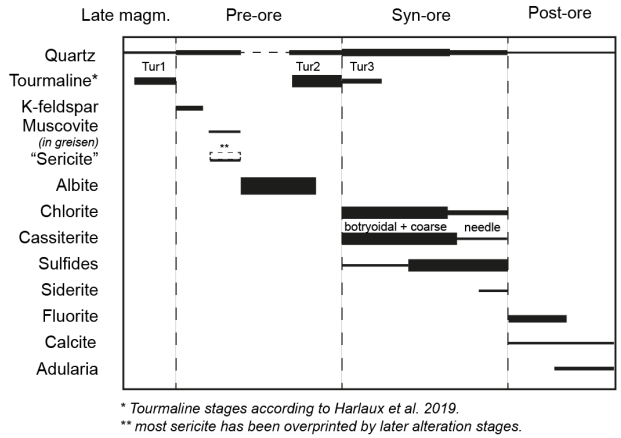

** Tourmaline stages according to Harlaux et al. 2019.*
*** most sericite has been overprinted by later alteration stages.*

Figure 2. Simplified paragenetic sequence of the San Rafael tin deposit detailing the revised paragenesis of the early hydrothermal alteration stages.

dumortierite (<5%) (Fig. 4G).

C) Albitic alteration. Sodic alteration occurs as partial to almost complete replacement of magmatic plagioclase, hydrothermal K-feldspar as well as previous alteration minerals by albite (Fig. 4E). This pre-ore hydrothermal alteration episode is the most widespread and volumetrically important alteration event at San Rafael, affecting the intrusion as a whole, with variable degrees of intensity. Albitic alteration affects most of the samples that should be characterized as "fresh" by naked eye observation, from the bottom level of underground mining operations, till the surface outcrops of the granitic apophyses, with a vertical span of around 1500 meters. Hydrothermal albite occurs disseminated in the whole granitic intrusion, with alteration intensity varying from subtle to intense (Fig. 4E). Mass-balance calculations for albitized granite samples indicate a strong increase in Na and Si, relative increase in Al, and depletion in all other elements, in particular Ba, Y and LREE, leading to LREE-depleted patterns typical of strong albitic alteration (e.g. Boulvais et al. 2007). EPMA followed by LA-ICP-MS analyses were performed on hydrothermal albite and unaltered magmatic plagioclase, ranging in composition from andesine to oligoclase. In Figure 5, where highly incompatible

Figure 3. Intense albitic alteration along a quartz-tourmaline (Tur 2) vein in biotite-cordierite megacrystic granite (sample KK-09).

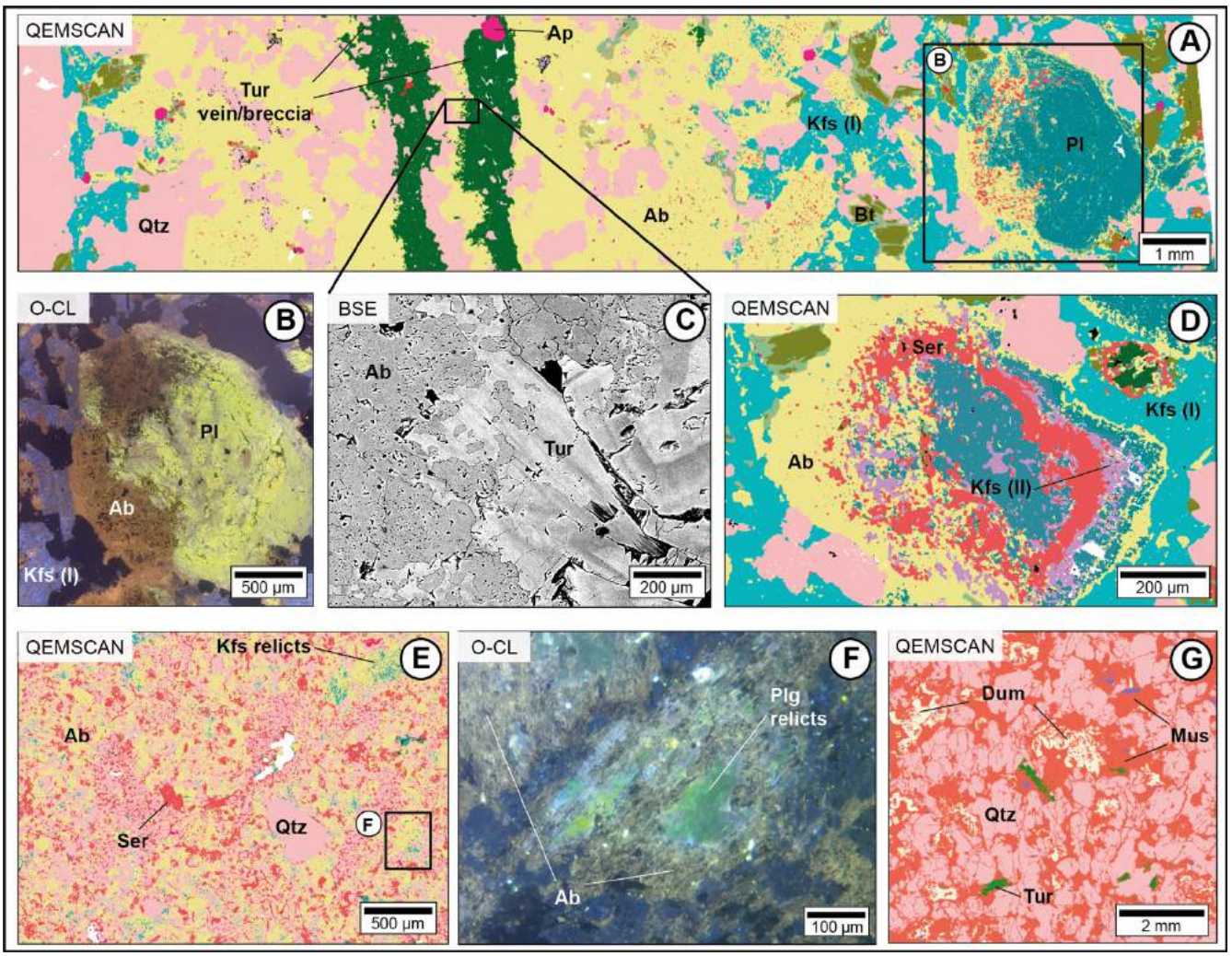

Figure 4. QEMSCAN, back scattered electron (BSE) and optical cathodoluminescence (O-CL) images, illustrating the paragenetic relationships of the early alteration stage at San Rafael. **a)** Megacrystic granite cut by tourmaline vein with albitic halo, overprinting magmatic minerals as well as earlier alteration stages (K-feldspar and sericite) (sample SRG-68); **b)** O-CL detail of magmatic plagioclase partially replaced by albite, which shows a "dusty" texture due to porosity creation during the replacement process (Hövelmann et al. 2010); **c)** BSE image showing hydrothermal albite that is replaced by hydrothermal tourmaline (Tur 2 according the terminology of Harlaux et al. 2019); **d)** Magmatic plagioclase altered to early hydrothermal K-feldspar (Kfs (II), determined by O-CL and QEMSCAN; color changed to violet), in turn replaced by sericite. Hydrothermal albite overprints the whole (sample SRG-68); **e)** Intensely sericitized granite subsequently affected by pervasive albitic alteration (sample SRG-116); **f)** Detail of relictic magmatic plagioclase almost completely replaced by hydrothermal albite; **g)** Greisen consisting mainly of quartz and muscovite with accessory dumortierite and tourmaline (sample SRG-133b). Ab-Albite, Bt-biotite, Dum-dumortierite, Kfs-Kfeldspar, Mus-muscovite, Plg-plagioclase, Qtz-Quartz, Ser-sericite, Tur-

elements (B, Cs, and Rb) are plotted vs. Ca/Na ratio, hydrothermal albite and magmatic plagioclase cluster in clearly different fields. The Ca/Na ratio varies from 0.25 to 0.75 for magmatic plagioclase and from 0.05 to 0.20 for hydrothermal albite. The concentrations of B, Cs and Rb are low in magmatic plagioclase (3.9 to 20.8 ppm, 0.1 to 1.2 ppm and 1.9 to 8.4 ppm respectively). In hydrothermal albite, concentrations range from 10 to 140 ppm B, 0.1 to 25 ppm Cs, and 4 to 207 ppm Rb.

D) Tourmaline veins and breccias. Pre-ore hydrothermal tourmaline (Tur 2) in veins and breccias ranges in composition from dravite to schorl (Harlaux et al. 2019). Tur 2 veins are systematically rimmed by albitic alteration halos (Fig. 3, 4A) and cut the megacrystic granite including the greisen body cropping out at surface.

4 Discussion

After a first alteration stage forming K-feldspar from a near neutral pH hydrothermal fluid exsolving from the crystallizing magma, pervasive sericitic alteration can be interpreted in terms of a fluid becoming more acidic during cooling or by increasing volatile proportion. Concentration of hot and acidic fluids in the apical part of the intrusion would explain the formation of greisen (Černý et al. 2005).

The widespread albitic alteration, followed by tourmalinization (Tur 2), may be the result of a second hydrothermal pulse showing again an evolution path from neutral to acidic conditions.

The high concentrations of B, Cs and Rb in hydrothermal albite suggest a magmatic origin of the

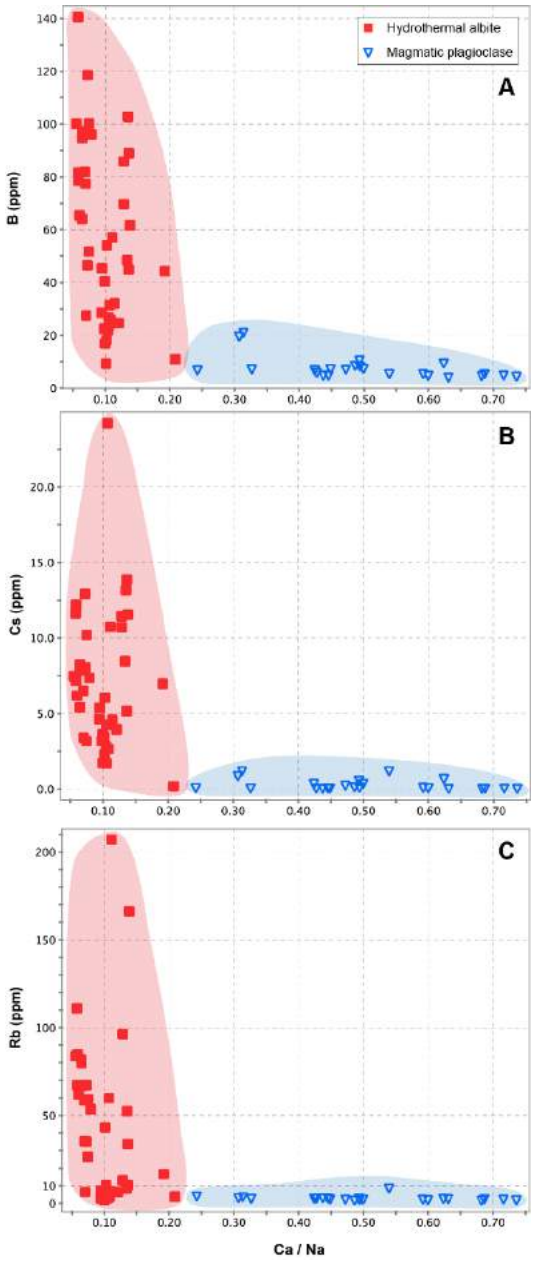

Figure 5. Plots of selected incompatible trace elements vs. Ca/Na ratio for hydrothermal albite (in red) and magmatic plagioclase (in blue). The enrichment in B, Cs, and Rb in the hydrothermal albite is indicative of a precipitation from a fluid of magmatic affinity (Audetat et al. 2000).

fluid responsible for the widespread albitization. This interpretation is also supported by the results of Harlaux et al. (2019), indicating precipitation of Tur 2 at ~500°C, from fluids with magmatic isotopic signature. Our results underline the role of magmatic-dominated fluids at the magmatic-hydrothermal transition during the pre-ore alteration stage at San Rafael.

5 Conclusions

A detailed textural study combining microscopic observations, QEMSCAN, optical cathodoluminescence, and scanning electron microscopy, has been carried out at the San Rafael tin deposit. Focus has been placed on the greisen occurring in the apical part of the composite granitic intrusion and on the importance and volumetric extension of albitic alteration. This has allowed a new interpretation of the sequence of alteration events during the early pre-ore hydrothermal stage at the San Rafael tin deposit. The paragenetic sequence combined with LA-ICP-MS analysis of trace elements in hydrothermal albite strongly support a magmatic origin for the early hydrothermal fluids and suggest the existence of two distinct fluid pulses during the pre-ore hydrothermal stage.

Acknowledgements

This research was supported by the company MINSUR S.A. and the Swiss National Science Foundation (SNSF S19053_169901).

References

Arenas MJ (1980) El distrito minero San Rafael: Estaño en el Perú. B Soc Geol Perú 66:1–11.

Audetat A, Gunther D, Heinrich CA (2000) Magmatic-hydrothermal evolution in a fractionating granite: A microchemical study of the Sn-W-F-mineralized Mole Granite (Australia) Geochim Cosmochim Ac 64:3373-3393.

Boulvais P, Ruffet G, Cornichet J, Mermet M (2007) Cretaceous albitization and dequartzification of Hercynian peraluminous granite in the Salvezines Massif (French Pyrénées) Lithos 93:89-106.

Černý P, Blevin PL, Cuney M, London D (2005) Granite-related ore deposits. Econ Geol 100th Anniversary Volume:337-370.

Clark et al. (2000) Delayed inception of ore deposition in major lithophile-metal vein systems: the San Rafael tin and Pasto Bueno tungsten deposits, Peru. In Proceedings of the GSA 2000 Meeting, Reno, Nevada, 32:A279.

Corthay G (2014) The Quenamari prospect, San Rafael tin District, southern Peru: geology, mineral assemblages, fluid inclusion microthermometry, and stable isotopes. M.Sc. thesis, Switzerland, University of Geneva, 113 p.

Gialli S, Chauvet A, Kouzmanov K, Dini A, Spikings R, Kalinaj M, Fontboté L (2017) Structural control of the world-class Sn district of San Rafael, Peru. In Proceedings of the SEG 2017 Meeting, 17-20 September 2017, Beijing, China.

Harlaux M, Kouzmanov K, Gialli S, Fontboté L, Marger K, Bouvier AS, Baumgartner L, Dini A, Chauvet A, Kalinaj M (2019) Cassiterite deposition triggered by fluid mixing: Evidence from in-situ $\delta^{18}O$-$\delta^{11}B$ analysis of tourmaline from the San Rafael tin deposit, Peru. In Proceedings of the 15th Biennial SGA Meeting, 27-30 August 2019, Glasgow, Scotland (this volume).

Hövelmann J, Putnis A, Geisler T, Schmidt BC, Golla-Schindler U (2010) The replacement of plagioclase feldspars by albite: observations from hydrothermal experiments. Contrib Mineral Petr 159:43-59

Kontak DJ, Clark AH (2002) Genesis of the giant, bonanza San Rafael lode tin deposit, Peru: origin and significance of pervasive alteration. Econ Geol 97:1741-1777.

Minsur SA (2018) Public Corporate Presentation.

Mlynarczyk MS, Sherlock RL, Williams-Jones AE (2003) San Rafael, Peru: geology and structure of the worlds richest tin lode. Miner Deposita 38:555-567.

Mlynarczyk MS (2005) Constraints of the genesis of lode-style tin mineralization: evidence from the San Rafael tin-copper deposit, Peru. PhD Thesis, Canada, McGill University 259 p.

Palma VV (1981) The San Rafael tin-copper deposit, SE Peru. M.Sc. thesis, Kingston, Ontario, Queen's University, 235 p.

Pirajno F (2009) Hydrothermal processes and mineral systems. Springer, 1250 p.

Mineralogical and geochemical aspects of vein-type ores from the Carnon River Mining District, Cornwall

Nicolas Meyer, Gregor Borg, Andreas Kamradt
Institute of Geosciences and Geography, Martin Luther University Halle-Wittenberg, Germany

Abstract. The Carnon River Mining District, part of the Cornubian Ore Field in SW-England, hosts polymetallic and multi-phase tin and base metal vein mineralisation in the cupolae of Variscian granites. Geologically, the study area is composed of Devonian clastic metasedimentary rocks with intercalations of amphibolite, intruded by Late Variscian granites. Multi-phase cross-cutting polymetallic veins were emplaced by late granite-related magmatic-hydrothermal events.

Typical ore minerals are arsenopyrite, marcasite, chalcopyrite, sphalerite, galena, fahlore, cassiterite, and wolframite in different paragenesis at Nangile and Poldice Mine. Stannite, cubanite, and pyrite occur as exsolution either from sphalerite or cassiterite, suggesting high temperature of formation and segregation at lower temperature. The ore minerals are accompanied by quartz, chlorite, and tourmaline, with minor epidote and rutile. Sphalerite is more common at Nangile, arsenopyrite and chalcopyrite is more wide spread at Poldice.

Pulses of tin and tungsten mineralisation as well as mineralisation dominated by copper, lead, and zinc were recognised in thin sections and geochemical analysis. Free gold was not found in thin sections, but geochemical ratios between arsenic and gold suggest that the latter occurs within the lattice of arsenic bearing minerals.

1 Introduction

The Cornubian Ore Field in Cornwall has been exploited from the Bronze Age until the end of the last century. Mining activities were especially extensive during parts of the 18th and into the 19th century, a time span, during which it was one of the most important centres of mining in the world (Dines 1956). Thus, the counties of Cornwall and parts of Devon are characterised by their mining legacies. Although world-renowned for the production of tin, mining in Cornwall has also contributed a substantial portion of the historic copper production as well as other commodities as zinc, arsenic, and minor tungsten and lead (LeBoutillier 2002). Unrecorded quantities of gold were produced in the Carnubian Ore Field, and gold nuggets are kept in the Williams Collection at Caerhays Castle as well as at Royal Cornwall Museum.

2 Regional Geology

The Cornish peninsula is dominated by sub-greenschist facies Devonian and Carboniferous clastic meta-sedimentary rocks and minor metamorphosed limestone. These meta-sedimentary rocks have also been intruded by meta-gabbro and felsic dykes and sills. This lithologically mixed suite has subsequently been intruded by Late Variscian granites (Darbyshire and Shepherd 1985).

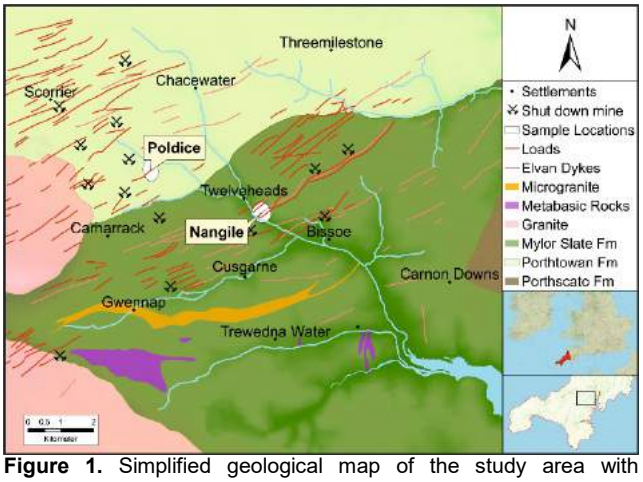

Figure 1. Simplified geological map of the study area with metasedimentary rocks, the Carn Marth Granite (west), the Carnmenellis (south-west) Granite as well as multi-phase, polymetallic (Cu, As, Sn, Pb, Zn, Ag, Au) veins (after British Geological Survey sheet 352 and Dines 1956).

One of these granitic plutons is the relatively small Carn Marth Granite, a satellite stock of the larger Carnmenellis Granite, which intruded into metasedimentary units, locally known as 'killas'. Mineralised quartz-rich porphyritic dykes (Elvan Dykes), and polymetallic veins, called loads; make up the mineralised inventory of the Carnon River Mining District (Fig. 1). The Late Variscian mineralisation is spatially related to mainly ENE-WSW trending faults and fractures in an extensional tectonic setting and is mainly characterised by tin, tungsten, copper, arsenic as well as subordinately by other base metals.

3 Methods

The sampling campaign for this study was carried out in the Carnon River Mining District between St. Day, Chacewater, and Devoran. This district represents an impressive mining heritage site with a post-mining landscape, drainage system, tailing ponds, and mine dumps. Hard rock ore samples have been collected from old mine shaft collars of the Nangile and the Poldice Mine.

All samples have been geochemically analysed by a certificated laboratory (ALS, Ireland). Aqua regia

digestion with ICP-AES finish was used for analysing ore grades of base metals. Lithium metaborate fusion coupled with XRF finish was applied for analyses of the tin and tungsten concentration. Platinum and palladium, was determined by lead oxide collection fire assay and ICP-MS finish.

Imaging and investigation of the mineralogical composition of the ores was carried out with a scanning electron microscope (SEM JEOL JSM 6300), equipped with an EDX-detector XFlash 5010 (Bruker).

The sulphide mineral assemblages of the ore samples were additionally investigated by reflected light microscopy (Carl Zeiss Axiophot).

4 Mineral paragenesis of Poldice Mine

Microscopically, the ore samples show different assemblages of minerals as well as indications for brecciation, cavity fillings, and replacement textures in different stages. Furthermore, typical gangue minerals coupled to different mineralisation stages could be distinguished.

Figure 2. Idiomorphic tourmaline (colourful prism) growing into quartz (white) within subhedral masses of tourmaline, finely intergrown with chlorite. These minerals occur associated with several of the mineralisation stages.

Quartz is a highly abundant gangue mineral occurring in various quantities in all samples forming partly millimetre-sized idiomorphic phenocrysts without deformation features. Scaly to radiating green chlorite is also very common and fills cavities or overgrows epidote and biotite. Some thin sections show euhedral, colourful tourmaline up to a size of more than 300 microns, grown into quartz (Fig. 2) and ore minerals or forming fine-crystalline masses. Remnants of anhedral and mostly elongated mica in wall rock-dominated parts represent muscovite and biotite.

One of the main ore minerals is arsenopyrite, occurring as anhedral to subhedral masses, up to 2 millimetres in size and as arrays of euhedral crystals up to 500 microns in diameter. Almost all of these have characteristics of brittle fracturing and fracture fillings. (Fig. 3).

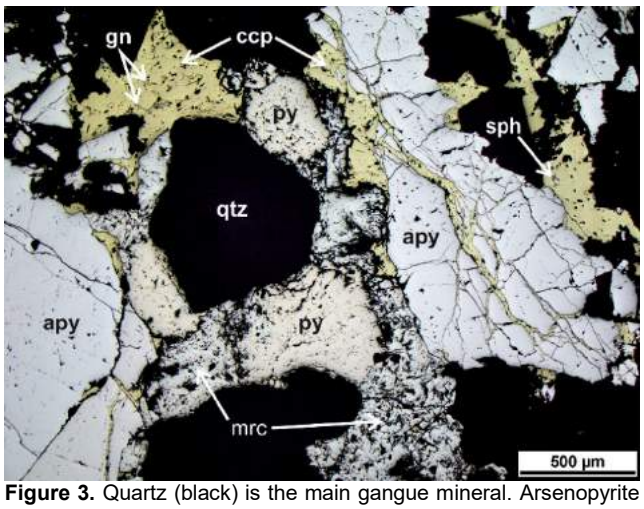

Figure 3. Quartz (black) is the main gangue mineral. Arsenopyrite (bright white) represent the most abundant sulphide in base metal associated ores from Poldice Mine. Both arsenopyrite and quartz are commonly brecciated and crosscut by chalcopyrite veinlets (bright yellow). Sphalerite (medium grey) and galena (white) is also included in the chalcopyrite. Pyrite (pale yellow) and marcasite (greenish white) are common within the samples.

More rarely they have inclusions of galena or cassiterite. Chalcopyrite is also abundant commonly in veinlets crosscutting arsenopyrite or forming anhedral masses. Exsolution blebs of stannite and irregularly scattered, subhedral to euhedral cassiterite occur within chalcopyrite. Additionally, cassiterite can contain exsolutions of chalcopyrite (Fig. 4).

Marcasite shows locally twinning and is abundant within the ores. Fine-crystalline sphalerite and galena occur commonly enclosed in other ore minerals, but locally sphalerite forms also larger crystal aggregates. Pyrite is mostly intergrown with marcasite and pyrrhotite. Furthermore, wolframite occurs embedded in chalcopyrite and as separate crystals. Fahlore and sulfosalts were also observed.

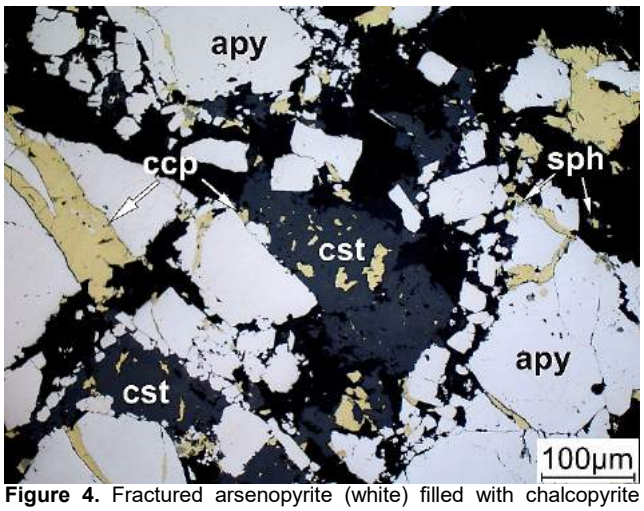

Figure 4. Fractured arsenopyrite (white) filled with chalcopyrite (yellow) and sphalerite (medium grey). Exsolution blebs of chalcopyrite within cassiterite (dark grey) was recognised in several samples.

5 Mineral Paragenesis of Nangile Mine

The main gangue mineral of Nangile Mine is euhedral to subhedral quartz, but also dynamically recrystallized areas of quartz were recognised. Some of them show patchy and undulose extinction suggesting their formation under a deformational regime. Anhedral masses of chlorite are also abundant. They fill cavities between quartz and ore minerals as well as fractures.

Idiomorphic tourmaline, up to 100 microns in size, occurs in some of the thin sections, forming partly clusters of fine-grained masses or growing into quartz and ore minerals. Subordinate amounts of epidote and remnants of biotite as well as muscovite, partly replaced by chlorite, are visible within the sections. Rarely, rutile was recognised as inclusions of quartz and cassiterite.

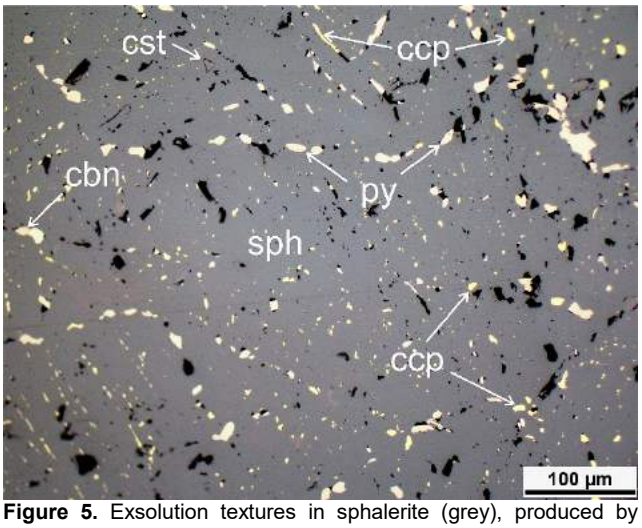

Figure 5. Exsolution textures in sphalerite (grey), produced by chalcopyrite (bright yellow), pyrite (pale yellow), and cubanite (reddish yellow). Cassiterite inclusions (higher relief) are also visible. This is a typical texture of sphalerite within the thin sections.

Sphalerite is one of the main ore minerals and appears in euhedral to subhedral masses up to 5 millimetre in size. Chalcopyrite, cubanite, fahlore, and minor stannite occur as exsolutions in sphalerite (Fig. 5). Deformational characteristics like fracturing or cavity filling were not observed.

Cassiterite occurs also as minute inclusions within sphalerite but also in other mineral phases like arsenopyrite and chalcopyrite or as separate minerals. Chalcopyrite and arsenopyrite occur as euhedral minerals up to 500 microns in size with small inclusions of galena and wolframite. Pyrite and marcasite are common minerals throughout the entire ore mineral assemblage, but they have not been recognised intergrown with sphalerite. More rarely, pyrrhotite and haematite was observed within the section.

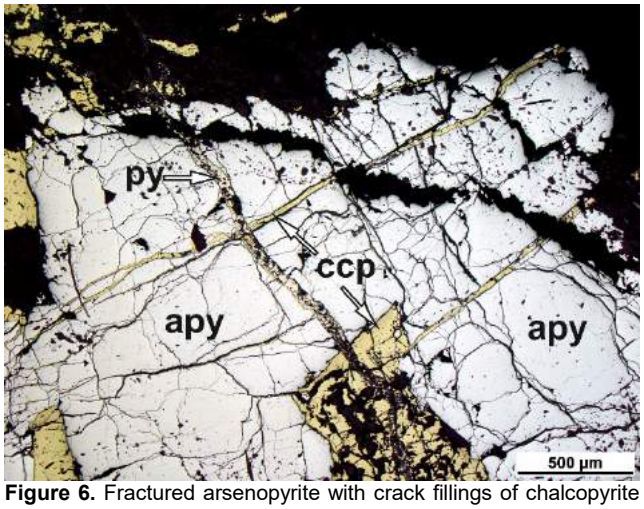

Figure 6. Fractured arsenopyrite with crack fillings of chalcopyrite and pyrite. Arsenopyrite is generally brecciated and partly filled with ore minerals or chlorite and tourmaline, suggesting their chronologically relationship.

Some sections reveal mineralised fractures parallel to foliation getting cross-cut by later mineralised or chlorite veins. Brecciation was recognised mainly within arsenopyrite, followed by filling fissures with chalcopyrite or pyrite (Fig. 6).

6 Geochemistry of ores

Geochemical data for base metals and associated elements of Nangile and Poldice ores reveal differences. Generally, the copper, lead and arsenic as well as silver content of Poldice is higher than in samples from Nangile. In contrast to that, zinc and tungsten values from Nangile are higher. Cobalt, nickel and molybdenum are not enriched in both localities. Gold appears in similar concentrations in both.

Positive correlation between lead and silver were recognized, which most likely reflects the occurrence of silver in galena.

Two correlation paths between gold and arsenic can be distinguished for Nangile Mine and Poldice Mine (Fig. 7). The latter has higher arsenic to gold ratio than Nangile with similar gold content suggesting gold at Poldice preferentially occurs within the lattice of arsenopyrite. This ratio is lower in the ores from Nangile, suggesting gold is substituted in the crystal lattice of other minerals. A higher abundance of tennantite-tetrahedrite group minerals, which were microscopically described, can lead to a lower ratio of arsenic to gold.

Platinum and palladium are measurable in almost all samples from both mines, but show slightly higher concentrations at Poldice.

Some samples from both mines reveal a mineralisation associated with tin and tungsten, with partly elevated copper concentrations. In contrast, copper-lead-zinc mineralisation together with arsenic and high silver content occurs as well.

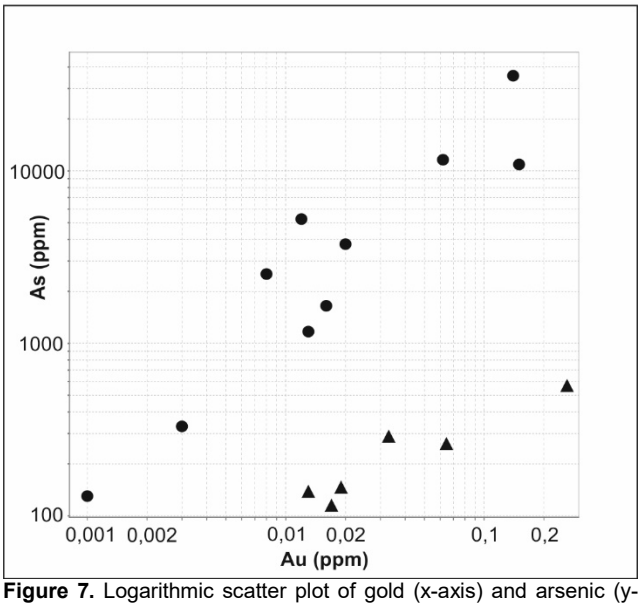

Figure 7. Logarithmic scatter plot of gold (x-axis) and arsenic (y-axis) shows good correlation of Poldice Mine (circles) and Nangile Mine (triangle) ores. Arsenic concentration of Poldice is higher compared to Nangile Mine at similar gold contents.

7 Conclusions

The vein development was influenced by several partly-coupled hypogene hydrothermal processes and supergene enrichment with the development of gossan. Mineralisation events, such as the formation of greisen, are associated with the enrichment of tin and tungsten as well as hydrothermal stages bearing base metal mineralisation. These were described in the literature concerning the study area. They can be partly confirmed by our investigations.

Generally, the mineral associations of Poldice Mine and Nangile Mine are similar, possibly due to their proximity to each other and a similar metallogenetic origin. However, several aspects are different. First of all, sphalerite is more abundant in samples from Nangile Mine than in samples from Poldice Mine, but exsolution fabrics were recognised in both, suggesting eutectic high temperatures of formation with subsequent segregation and exsolution at lower temperature. The same has been described for the formation of stannite in chalcopyrite (Ramdohr 1975). Chalcopyrite and arsenopyrite occur in both mines, but the distribution at Poldice Mine is more widespread than in Nangile. Cubanite is specific for Nangile Mine, although the limited number of samples needs to be taken into account.

Geochemically, the ores from Nangile have higher concentrations of zinc and tungsten and lower concentrations of copper and arsenic compared to Poldice, resulting in the observed respective mineral assemblages. Also, the concentration of lead is increased at Poldice compared to Nangile, leading presumably to more galena and therefore to higher silver concentrations. The occurrence and relationship of platinum and palladium within the system is not clear. Free gold as a phase was not observed in thin section, so far, but geochemical evidence suggests that gold occurs within the lattice of other minerals, for example arsenopyrite.

Results from our investigations of ore samples are similar to the mineral paragenesis described from the neighbouring Mt. Wellington Mine (Kettaneh and Badham 1978). At Mt. Wellington, tin and tungsten as well as base metal mineralisation, associated with quartz, tourmaline, and chlorite were recognized as well.

Acknowledgements

This study is a late result of DFG project FOR550 and has been financially supported by the Landesamt für Denkmalpflege und Archäologie Sachsen-Anhalt in Halle, Germany. We are grateful to the Royal Cornwall Museum, especially Anna Tyacke for support during field work. Simon Camm and Courtenay Smale have helped with their detailed knowledge of the region and its historical mining landscape.

References

Darbyshire, DPF, Shepherd, TJ (1985) Chronology of granite magmatism and associated mineralization, SW England. Journal of Geological Society 142:1159-1177.

Dines HG (1956) The Metalliferous Mining region of South-west England. Vol. 1, Memoirs of the Geological Survey, Great Britain.

Kettaneh YA, Badham JPN (1978) Mineralization and Paragenesis at the Mount Wellington Mine, Cornwall. Economic Geology, 73:486-495.

LeBoutellier NG (2002) The Tectonics of Variscan Magmatism and Mineralisation in South West England - Volume II. Thesis for: PhD Mining Geology. Camborne School of Mines.

Ramdohr P (1975) Die Erzmineralien und ihre Verwachsungen. Akademie Verlag, Berlin.

Epithermal precious metal deposits of the Deseado Massif, Santa Cruz Province, Argentina

Raúl E. de Barrio, Miguel A. Del Blanco, Andrea M. Ramis
Instituto de Recursos Minerales (INREMI), Argentina

Abstract. Epithermal ore deposits of the Deseado Massif, southern Patagonia Argentina, represent a widespread assemblage of gold-silver mineralization. They show a strong spatial relationship with an extensive Jurassic rhyolithic volcanism that covers approximately 30,000 square kilometers. The principal mineralization is the world class Cerro Vanguardia deposit. The main ore deposits and prospects have a marked regional tendency to group in several clusters identified as I, II, III and IV. Most of the epithermal deposits are composed of veins, veinlets, breccias and stockworks with predominant NW and minor NE and E-W strikes. Three main genetic model types of hydrothermal deposits occurred in the Deseado Massif: a) vein type, b) volcano-hosted type, and c) peribatholitic-epithermal type (Pb-Zn-In-Cu-Sn-W-Bi and Ag>Au).

1 Introduction

When Lindgren (1933) characterized the epithermal mineralisation type, he considered that one of the critical aspects for its understanding and classification is the detailed study of the metal association, gangue and alteration assemblages. During the last forty years, many geologists have worked on epithermal deposits in different parts of the world, however, their mineralogical features were not always thoroughly studied. The epithermal precious metal deposits of the Deseado Massif, Patagonia Argentina, are an example of this situation. In fact, their mineralogical and metallogenic knowledge is largely incomplete.

Since the late 1970s, the Deseado Massif has been the subject of numerous studies and investigations searching for gold and silver concentrations. As a result of these explorations many Au-Ag deposits have been discovered, some currently being mined.

This brief contribution aims to provide a broad review of the mineralogical characteristics of the main epithermal deposits of the Deseado Massif, in addition to proposing some general conclusions about their metallogenic models and regional distribution.

2 Regional setting

The Deseado Massif (DM) is a morphostructural region located in the Santa Cruz province, southern Argentina (Fig. 1). The most important geological characteristic of this area is an extensive plateau characterised by a Mid-Upper Jurassic volcanic event composed of intermediate to acid volcanic rocks of the Bahía Laura Complex (BLC). This voluminous volcanism originated during widespread extensional tectonism which extended across Patagonia and Antarctica related to the opening of the Atlantic Ocean (Pankhurst et al. 1998, Giacosa et al. 2010).

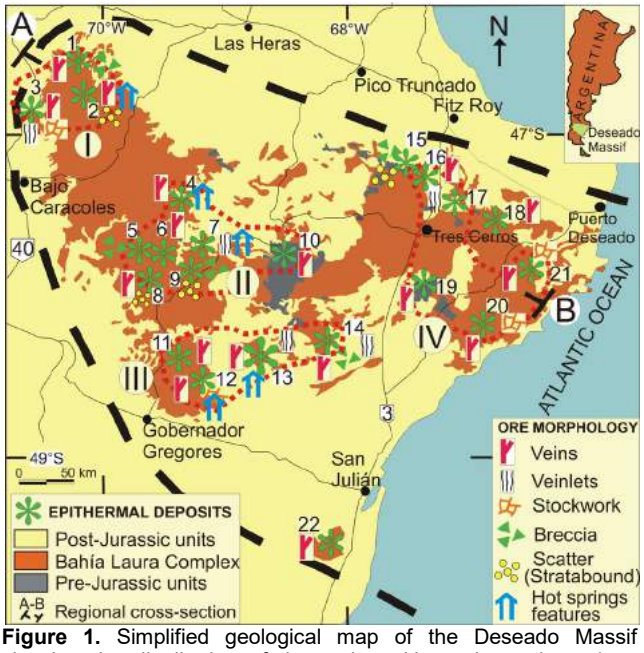

Figure 1. Simplified geological map of the Deseado Massif showing the distribution of the main epithermal metal precious deposits. 1. Huevos Verdes-San José mine, 2. Cerro Negro District (Eureka-La Mariana veins), 3. La Paloma (Lomada de Leiva), 4. Bajo Pobre-Sol de Mayo-El Macanudo, 5. Cap.-Oeste (El Tranquilo prospect), 6. La Esperanza, 7. La Josefina mine, 8. La Manchuria 9. Joaquín, 10. El Piche-Pingüino prospect, 11. Martha mine, 12. Manantial Espejo mine, 13. Cerro Vanguardia mine, 14. El Dorado-Monserrat prospect, 15, Falcon prospect, 16. Las Calandrias, 17. Don Nicolás mine, 18. Bajo de La Leona, 19. Microondas-Martinetas, 20. Chispas, 21. Cerro Moro, 22. Laguna Guadalosa.

The volcanic stratigraphy of the region is complex and has traditionally been subdivided into three formations: Chon Aike Formation, composed by rhyolitic volcanic rocks, commonly ignimbrites and lavas and less frequently agglomerates and tuffs; the La Matilde Formation, integrated by acid tuffs and bedded ash-fall deposits with less frequent ignimbrites; and the Bajo Pobre Formation, which comprises andesitic and subordinate basaltic volcanic rocks forming lava domes, lava flows, agglomerates with minor tuffs and occasional sediments. In addition, widespread and thin Tertiary-Quaternary basaltic lava flows crop out at different altitudes indicating several tectonic events of regional uplift during the Cenozoic era. This makes mining and exploration difficult in the north-western and southern sectors of the Deseado Massif where the covering lava

flows are much more extensive.

3 The epithermal metal precious deposits

3.1 Regional arrangement and general characteristics

Epithermal precious metal deposits of the DM (Fig. 1) comprise an important assemblage of gold-silver mineralization distributed across a large region of about 60,000 square kilometers (Schalamuk et al. 1997, 1999). Although there are many epithermal deposits and occurrences throughout the whole DM, the main ore deposits and prospects show a strong regional tendency to group in several clusters. Consequently, they have been subdivided into four assemblages: I) **Northwestern region**: it comprises San José (Huevos Verdes), Cerro Negro, Eureka and Lomada de Leiva ore deposits, II) **Central region**, with La Josefina and Cap-Oeste mines, and La Esperanza, Bajo Pobre-El Mirasol, Pingüino (El Piche), La Manchuria and Joaquín prospects, III) **Southern region**, comprising Cerro Vanguardia, Manantial Espejo and Martha mines, and El Dorado-Monserrat project (first sector where the gold mining exploration began), and IV) **Eastern region**, with Don Nicolás and Cerro Moro mines, and Bajo de la Leona, Falcon, Las Calandrias, Microondas-Martinetas, and Chispas prospects (Fig. 1 and Table 1). Only the Laguna Guadalosa prospect appears isolated because it is placed in the most southern sector separated from the other deposits by an extensive Quaternary sedimentary cover. This areal arrangement is the result of different geological evolutions. The great majority of the epithermal deposits are hosted by rocks of the Bahía Laura Complex. However, the eastern deposits are placed in much lower stratigraphical portions closely associated to basement rock outcrops which appear in several erosional windows. On the other hand, the NW cluster is placed in areas where the BLC has a large thickness but several drill holes have detected basement rocks at depths of between 50 and 150 m. Other factors consist of the different erosion levels according to the proximity to the great valleys of the Deseado and Chico rivers which limited the DM towards the north and the south, especially in the south and eastern boundaries. There are almost 600 m of difference of altitude between the NW region and the southern and eastern sectors (Fig. 2).

Most of the epithermal deposits (Fig. 2) are composed of veins, veinlets, breccias and stockworks with predominant NW and minor NE and E-W strikes. They show multi-episodic stages with the deposition of silica minerals (quartz, chalcedony and opal), calcite, rhodocrosite, adularia, barite, fluorite and zeolites, among others. Metalliferous minerals are scarce, approximately 1% in volume. They are mainly represented by native gold, electrum, native silver, acantite, Ag-sulfosalts, pyrite, hematite, minor base metal sulfides (sphalerite, galena and chalcopyrite) and some supergene minerals (oxides, hydroxides and Ag halogens).

The most frequent mineral textures are crustiform-banded, colloform, cockade, massive, breccia, climb and pseudomorph replacements.

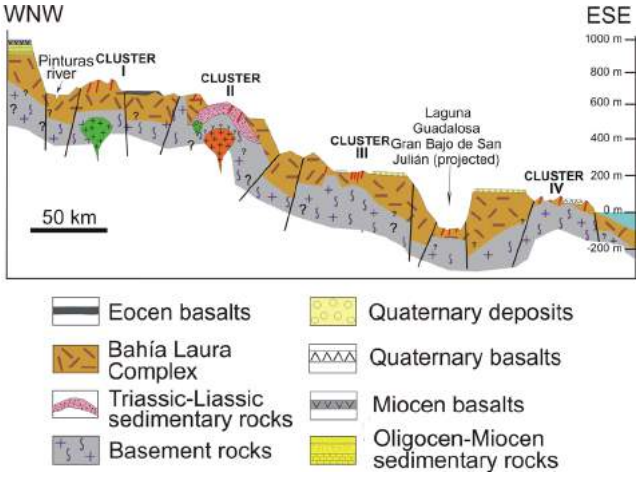

Figure 2. Idealized-schematic regional geological WNW-ESE cross section of the Deseado Massif.

Gold and silver occur together in varying proportions. In virtue of their abundance, the epithermal deposits of the DM are divided into three groups: a) gold deposits with variable amounts of silver (e.g. Cerro Vanguardia mine, among others.), b) silver deposits with minor amounts of gold (e.g. Martha and Manantial Espejo mines), and c) Zn-Pb (Cu-Ag) deposits with minor amounts of gold (e.g. Pingüino prospect).

The most important styles of hydrothermal alteration are silicification, argillization (illite, smectite and kaolinite), sericitization and propylitization. They are poorly developed and are normally restricted to areas in the vicinity of veins. The width varies from a few centimetres up to several tens of metres, depending of the wall rock composition. Argillization may be quite incipient up to very strong (advanced argillization). Silicification is pervasive or displayed in very thin veinlets, randomly arranged.

3.2 Main metalogenic models

At present, there are more than 50 important Au-Ag epithermal projects in diverse exploration stages; also, eight mines are currently active (Cerro Vanguardia, Manantial Espejo, San José, Cerro Negro, Cap-Oeste, La Josefina, Don Nicolás and Cerro Moro). The geochemical signature corresponds to typical epithermal deposits with anomalies in precious metals (Au-Ag), and other elements as As, Sb, Hg, Mo, Ba and Mn with a Au-Ag relation of about 20:1. Only one occurrence belongs to a singular type of polymetallic (Zn, In, Ag) veins related to Early Jurassic magmatism superimposed by a later epithermal system (Pingüino project). The mineralizing fluid composition of the main epithermal deposits is characterised by the presence of H_2O-NaCl (KCl) components, neutral to slightly neutral pH, with salinities from 0.2 to 8.0 wt.% NaCl eq. and variable homogenization temperatures (100°C-320°C).

Table 1. General geological features of the epithermal gold-silver ore deposits and main prospects of the Deseado Massif, Santa Cruz. Alteration abbreviations: adul: adularization, arg: argilization (interm.; intermediate, adv: advanced), chlor: chloritization, oxid: oxidation, prop: propylitization, pyrit; pyritization, ser: sericitization, sil: silicification,. Mineral abbreviations from Whitney & Evans (2010). Texture abbreviations: brx: breccia, collo: colloform, cock: cockade, crust: crustiform, mass: massive, stwk: stockwork.

ORE DEPOSIT/ PROSPECT	LOCATION	MINERAL ASSEMBLAGE		MORPHOLOGY ATTITUDE	TEXTURE	HOST ROCKS	HYDROTHERMAL ALTERATION	OBSERVATIONS
		ORE	GANGUE					
CLUSTER I NORTHWESTERN REGION								
San José-Huevos Verdes	46° 40´ S 70° 18´ W	Ag, Au sulf., Ele, Gal, Sp, Ac	Qz, Chal, Hem, Calc, Py, Mn-oxides	veins, brx NW-SE, NNE-SSW and ONO-ESE	crust, collo, comb	andesitic lava flows, Bajo Pobre Fm.	interm arg, adv arg, sil, chlor	operation
Cerro Negro District Eureka-La Mariana veins)	46° 45´ S 70° 14´ W	Ag, Ele, Au, Ag sulf. and sulfos.	Qz, Chal, Adl, Sme,	veins, WNW brx, disseminated	collo-crust, mass, brx	basalt-andes, Bajo Pobre Fm tuffs-dacitic lavas Chon Aike Fm	adv arg, ser	operation. Mariana vein: blind deposit
La Paloma (Lomada de Leiva and Sofia Breccia)	47° 03´ S 70° 40´ W	Au, Ag	Qz, Chal, Adl	brx, qz network	brx	acid ignimbrites Chon Aike Fm.	arg	closed
CLUSTER II CENTRAL REGION								
Bajo Pobre-El Macanudo-Sol de Mayo	47° 15´ S 69° 14´ W	Au, Ag anomalies	Qz, Chal, Cal	veins N-S, NE-SW	mass, crust, cock	bas. andes. Bajo Pobre Fm	prop, sil	
Cap-Oeste (El Tranquilo)	47° 58´ S 70° 25´W	Au, Ele	Py, Apy, Pyr-Prous, Ttr	brx, NW-SE	brx	acid ignimbrites Chon Aike Fm	arg, ser	operation
La Esperanza	69° 44´ S 47° 40´W	Au	Chal, Qz, Oxid,	veins, replacement N-S	crust	acid ignimbrites Chon Aike Fm	sil, arg	
La Josefina	47° 52´ S 69° 23´ W	Au, Ele	Qz, Chal, Opl, Brt, Hem	veinlets and veins	mass, brx	acid ignimbrites Chon Aike Fm	sil, pyrit, ser, arg	operation
La Manchuria	48° 09´S 69° 54´W	Au, Ele, Ag	Qz, Chal, Py, Gal	Veins, brx	mass, brx	acid ignimbrites Chon Aike Fm	sil, arg, pyrit, oxid	
Joaquín	48° 03´ S 69° 34´ W	Ag, bromargyrite, Ac, stromeyerite, Ttr, Pyr, Steph	Qz, Adl, Py, Gal, Hem	brx, veinlets, stwk	brx	Chon Aike Fm	sil,	blind deposit, stratabound breccia
El Piche-Pingüino	48°01´ S" 68°38´ W"	Sp, Gal, Ccp, Cu-Ag-Sn sulfosalts	Qz, Sd, Rds	sulpfide veins & quartz veins, brx NW-SE	brx, crust	sandstones, tuffs, El Tranquilo and Roca Blanca Frms	arg, pyrit, sil, ser, prop	advanced exploration
CLUSTER III SOUTHERN REGION								
Martha mine	48° 42´ S 69° 43´ W	Pyr, Ac, Ag Py, Sp, Gal	Qz, Adl, Cal, Zeo	veins with silver ore shoots NW-SE, E-W	crust, mass, brx	acid ignimbrites Chon Aike Fm	adul, arg, sil	closed
Manantial Espejo	48° 48´ S 69° 30´ W	Ag, Ele, Au, Ag sulf. Py, Sp, Gal, Ccp, Ttr	Qz, Chal, Opl, Adl, Brt, Cal	veins, stwk WNW-ESE	crust, collo-cock, brx	acid ignimbrites Chon Aike Fm. and andesitic intrusives	sil ser, arg	operation
Cerro Vanguardia	48° 23´S 68° 15´W	Au, Ag, Ele, Ac, Ag sulfosalts	Qz, Chal, Opl, Adl, Py, Apy, Sp, Ccp, Sd-Rds	veins and veinlets WNW-ESE/>70° NW-SE/>70°	crust, brx, mass, comb	acid ignimbrites Chon Aike Fm	arg, ser, sil	operation Grades: 10 g/t Au 100 g/t Ag
El Dorado-Monserrat	48° 25´ S 68° 36´ W	Au, Ele	Qz, Brt, Adl	veins, brx, veinlets	crust, collo, cock, mass	andes. and basalt. Bajo Pobre Fm.	sil, ser, prop, pyrit	
CLUSTER IV EASTERN REGION								
Falcon	47° 35´ S 67°33´ W	Au, Ag	Qz, Chal	brx with silica mineralized halo	brx	acid ignimbrites Chon Aike Fm	sil	blind gold veins?
Las Calandrias	47° 36´S 67°29´ W	Au, Ele	Py, Mrc, Apy Ag sulf	brx, veins	brx	rhyolite domes Chon Aike Fm.	sil, arg	advanced exploration
Bajo de La Leona	48° 05´ S 69° 19´ W	Au anomalies, Cct	Qz, Hem, Mlc	veins WNW-ESE	mass, crust	Dv-Cb leucogranites La mina Fm.	arg, ser	preliminary exploration
Microondas-Martinetas	47° 56´ S 67° 31´ W	Au, Ag	Qz, Chal	veinlets, replacement	mass	tuffs and dacitic dome Bahía Laura Complex	sil, arg	
Don Nicolás	47° 55´ S 67° 23´ W	Au, Ele, Ag	Qz, Adl	sheeted veins	crust, mass	acid tuffs and ignimbrites Bahía Laura Complex	Sil, arg.	operation
Chispas	48° 23´S 66°58´ W	Au	Chal, Qz, Py	veins, stwk NNE-SSW	mass, crust	acid tuffs and ignimbrites Bahía Laura Complex	sil, arg	
Cerro Moro	48° 05´ S 66° 39´ W	Au, Ag, Ag sulf. and sulfos.	Qz	veins, stwk	mass, crust, brx	acid ignimbrites Chon Aike Fm.	sil, arg.	operation
Laguna Guadalosa	49° 29´ S 68° 23´ W	Au anomalies	Qz	veins NE-SW, E-W	crust	acid ignimbrites Chon Aike Fm.	sil, ser, arg	

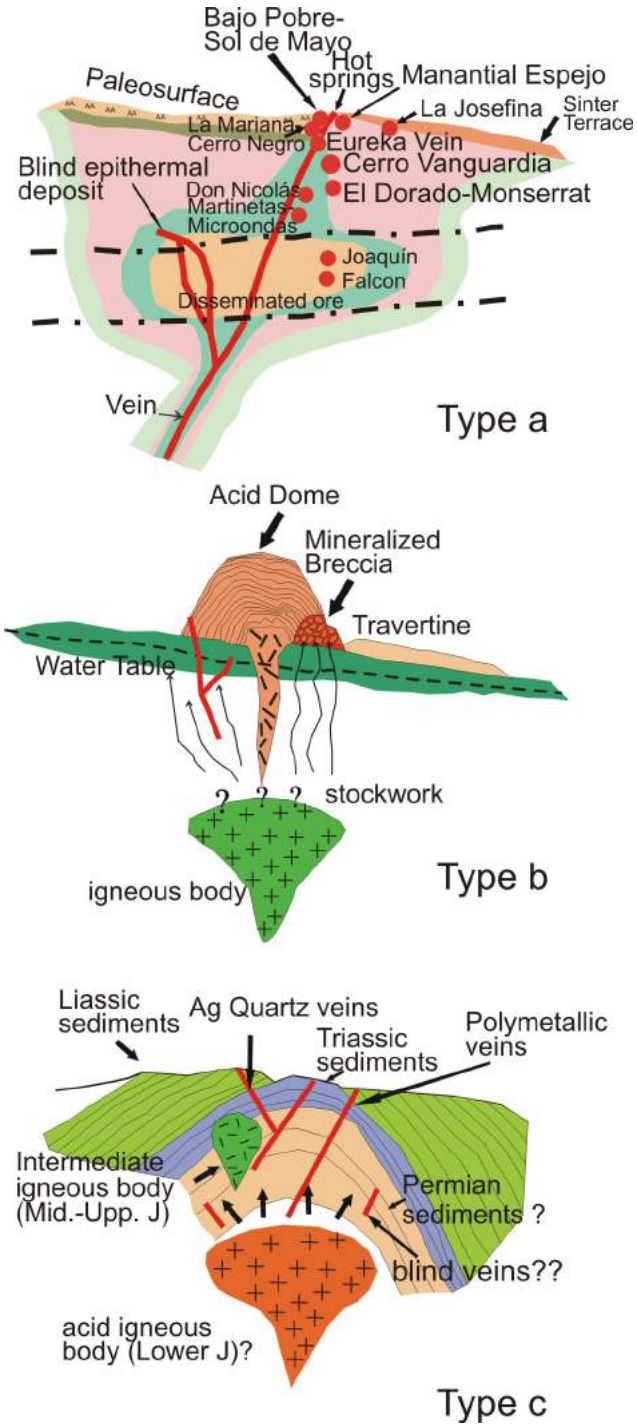

Figure 3. Schematic main genetic model types recognized in hydrothermal deposits of the Deseado Massif. Type a modified from Hedenquist et al. (2000), types b and c modified from Guido et al. (2012).

Fluid stable isotope data ($\delta^{18}O$) preserved in quartz crystals varies between -10 and +6 ‰ suggesting a main meteoric component, while the $\delta^{34}S$ data varies from -2.5 up to 5.0 ‰ revealing a magmatic provenance for sulfur.

Most of the epithermal deposits of the DM corresponds to the low sulfidation type and just a few mineralizations belong to the intermediate sulfidation type (e.g. Martha mine).

Three main genetic model types of hydrothermal deposits were identified in the DM (Fig. 3): a) vein type, b) volcano-hosted type (e.g. Las Calandrias Project, Cap-Oeste), and c) peribatholitic-epithermal type (Pb-Zn-In-Cu-Sn-W-Bi and Ag>Au, e.g. Pingüino Project and Bajo de la Leona prospect). On the other hand, the vein type comprises three subtypes: classic veins (Cerro Vanguardia, among others), veins accompanied with geothermal features (e.g. Cerro Negro, Manantial Espejo, and others), and blind vein deposits (e.g. La Mariana). The most frequent and relevant type deposits are largely the classic quartz veins which usually constitute extended vein fields.

4 Concluding remarks

The main epithermal deposits of the Deseado Massif are grouped in four regions or clusters with different structural and stratigraphical attributes and a diverse geological evolution.

The areal distribution is controlled by lithological, stratigraphical and structural elements. In most cases, there is a marked spatial relationship with the Jurassic acid ignimbritic volcanism of the Chon Aike Formation.

Structural features show a general WNW-ESE orientation in Cluster III, where the world class deposit Cerro Vanguardia presents some veins of more than 10 km in length (e.g. Vanguardia vein). However, the main veins with higher gold values show a NW-SE orientation.

Due to the lack of an integrated watershed and gold occurring as minute particles, rich placers are absent in the Deseado Massif.

References

Giacosa R, Zubia M, Sánchez M, Allard J (2010) Meso-Cenozoic tectonics of the southern Patagonian foreland: structural evolution and implications for Au–Ag veins in the eastern Deseado region (Santa Cruz, Argentina). J South Am Earth Sci 30:134–150

Guido D et al. (2012) Avances en el conocimiento de la geología y mineralizaciones del Macizo del Deseado. Argentina Mining 2012. Dissertation. Salta. www.argentinamining.com/wp-content/uploads/am-presentation/..../16-40guido.pdf

Hedenquist JW, Arribas Jr A, González-Urien E (2000) Exploration for epithermal gold deposits. In Hagemann SG, Brown PE (eds) Gold 2000, SEG Reviews 13:245-277

Lindgren W (1933) Mineral deposits, 4th edition: New York, McGraw-Hill, 930p

Pankhurst RS, Leat P, Sruoga P, Rapela CW, Márquez M, Storey B, Riley T (1998) The Chon Aike province of Patagonia and related rocks in West Antartica: a silicic large igneous province. J Volcanol Geotherm Res 81:113-136

Schalamuk IB, Zubia MA, Genini A, Fernández R (1997) Jurassic epithermal Au-Ag deposits of Patagonia, Argentina. Ore Geol Rev 12 (3):173-186

Schalamuk IB, de Barrio RE, Zubia MA, Genini A, Echeveste HJ (1999) Provincia auroargentífera del Deseado, Santa Cruz. In Zappettini E (ed) Recursos minerales de la República Argentina, Instituto de Geología y Recursos Minerales, SEGEMAR 35:1177-1188. Buenos Aires

Whitney DL, Evans BW (2010) Abbreviations for names of rock-forming minerals. Am Mineral 95:185-187

Timing and P-T conditions of epithermal mineralization in the Bacis and La Cienega Mining districts, Durango, Mexico

Gustavo Adolfo Ramirez-Salamanca
MSc. Student, Centro de Geociencias, Universidad Nacional Autónoma de México, Campus Juriquilla, Mexico

Gilles Levresse
Senior investigator, Centro de Geociencias, Universidad Nacional Autónoma de México, Campus Juriquilla., Mexico

Luca Ferrari
Senior investigator, Centro de Geociencias, Universidad Nacional Autónoma de México, Campus Juriquilla, Mexico

Leonardo Chayogan
Chief exploration, Minas de Bacis SA De CV

Marcelino Rodriguez
Superintendente de Exploración, Minera Mexicana La Ciénega

Abstract. The Bacis and La Cienega districts are Au-Ag hydrothermal deposits located in the Sierra Madre Occidental (SMO) in Mexico. The mineralization in both districts is related to NW-NNW trending structures and exhibits high Au-Ag ratio which become Ag-dominant at deeper levels.

New U-Pb ages from the volcanic host-rock, and K-Ar and $^{40}Ar/^{39}Ar$ ages in adularia and illite from the mineralization assemblages, allow a re-evaluation of the timing of the hydrothermal mineralizing events. In both districts the basement consists of the Lower Triassic and Upper Jurassic metasedimentary successions which are intruded by monzogranitic plutons and overlain by andesitic lavas belong to the Lower Volcanic Complex (LVC). These rocks are in turn covered by an Oligocene ignimbrite succession and rhyolitic domes of the Upper Volcanic Supergroup (UVS). Mineralizing veins affect all the stratigraphic column.

Fluid inclusion microthermometry and decriptometry studies yield comparable temperature ranges in both districts at 210 to 230ºC and 410-430ºC, suggesting the occurrence of a similar mineralizing event. The chemical composition and temperature of formation of chlorite associated with Ag-rich and Au-rich mineralization stages show a bimodal distribution with peaks at 330ºC and 270ºC, respectively.

1 Introduction

The SMO hosts many epithermal deposits of variable age related to a single geodynamic and magmatic event (Camprubí et al. 2003). Montoya et al. (2019) illustrate the importance of the polyphase formation of the hydrothermal mineralization in the large San Dimas district, suggesting that this process may have controlled the genesis of other unconventional deposits in the central part of the SMO.

We chose to study two examples of low sulfidation epithermal deposits to the NNW of San Dimas: the Bacis and La Cienega deposits (Figure 1). The Bacis deposit is describe as a typical Au mineralizing epithermal event (Au/Ag =1/50), whereas La Cienega exhibits a more complex structural and paragenesis assemblage, suggesting a multi event formation (Au/Ag =1/50).

Previous works have proposed a metallogenic framework for these deposits (De la Garza et al., 2001; Camprubí and Albinson 2006). However, the magmatic events associated with mineralization have not been assessed in detail. Also, many of the geologic units are not dated and in the case of the few available K-Ar whole rock ages (Labarthe 1996), significant doubt remains about the extent of possible thermal resetting by later magmatic events.

To better understand these deposits, we re-evaluate the local geologic evolution and hydrothermal mineralization with new petrographic and geochronological studies.

2 Regional geology

The SMO is a major geologic province in western Mexico, which spans 1200 km in length and 400 km in width and extends from the U.S. border to the south up to the Trans-Mexican Volcanic Belt (Ferrari et al., 2007). In the central and southern SMO, volcano-sedimentary basement belonging to the Guerrero terrane is intruded and covered by the igneous rocks of the Laramide continental arc, also known as the Lower Volcanic Complex (McDowell and Keizer 1977). These rocks are covered by a 1 to 1.5 km thick succession of silicic ignimbrites, rhyolitic domes and basalts of late Eocene, Oligocene and early Miocene age, which constitute one of the main silicic large igneous province on Earth (Aranda et al. 2000; Bryan and Ferrari, 2013). These successions are affected by normal fault systems related to lithospheric extension that led to the formation of the Gulf of California rift (Ferrari et al. 2017). The

older sedimentary basement is sporadically exposed on the western side of the SMO. It includes strongly folded metasedimentary and meta-volcanic rocks, granitoids with ages spanning from the Permian to Early Cretaceous (Henry and Fredrikson 1987; Henry et al. 2003) that are locally overlapped by Albian-Cenomanian limestones and shale (Bonneau 1970).

Figure 1. Location of the BACIS and La Cienega Mining District

The Laramide magmatic arc consists of granite, granodiorite and diorite rocks exposed in the coastal areas and along the lower course of the main rivers, with ages progressively younger to the east (from 90 to 40 Ma). These form two main plutonic complexes: The Late Cretaceous to early Paleocene San Ignacio batholith and the Eocene Piaxtla batholith (Henry et al. 2003; Montoya Lopera et al. 2019). Their volcanic counterpart consists of late Cretaceous to Paleocene ignimbrites and andesite lava flows that cover the San Ignacio batholith but are intruded by the Piaxtla batholith (Montoya-Lopera et al. 2019).

The transition between the Laramide magmatic suite and the Oligocene-Miocene volcanism is marked by the deposition of continental conglomerates and sandstones filling small continental basins, and by a ~10 m.y. magmatic hiatus (Montoya Lopera et al. 2019).

The late Eocene-early Miocene volcanism, termed the Upper Volcanic Supergroup (UVS) is composed by a major event of silicic volcanism emplaced in two voluminous episodes of ignimbrite flare up at ~35-29 Ma along the entire SMO, and at ~24-20 Ma in the southern part (Ferrari et al. 2002, 2007; McDowell and McIntosh 2012). Mafic lavas are interspersed within the ignimbrite successions and are often associated with normal faulting (Ferrari et al. 2017).

3 Results

3.1 Geochronology of the lithologies in the Bacis and La Ciénega mining districts

The basement exposed in the two study areas differs in lithology and age. In the Bacis, it consists of greenschist-facies quartz sandstones with lithics fragments. The youngest U-Pb detrital zircon population (LA-ICPMS) indicates a maximum age of deposition of 252 Ma. In La Ciénega the sedimentary basement consists of limestones interlayered with shales with some channels of conglomeratic sandstones. The youngest U-Pb detrital zircon population from the conglomeratic sandstones yielded a maximum deposition age of 150 Ma.

The Laramide continental arc outcrops in Bacis and La Cienega are limited to batholith apophyses dated at ~95 and ~84 Ma respectively. The LVC volcanic units are restricted to andesite lava flows dated at ~86 to 84 Ma (U-Pb, LAICPMS; Figure 2).

In both districts, the UVS consists of ignimbrites with U-Pb LA-ICP-MS ages of ~36 Ma and ~30 Ma respectively. The ignimbrite succession is cut by rhyolitic dikes and domes. The rhyolitic domes range in age from 31 to 29.5 Ma (U-Pb and K-Ar ages respectively). The UVS volcanism is emplaced through fissures associated with a NNW-trending fault corridor.

3.2 Mineralization paragenesis and dating

At Bacis, mineralization occurs along NW- to NNW-trending strike-slip faults, cemented by comb quartz followed by mosaic quartz texture that represents the vein-filling stage and hosts the Au-Ag mineralization. The mineralization stage begins with pyrite + sphalerite ± galena and finishes with acanthite traces and then electrum. Alteration consists of pervasive sericitization and propylitization.

La Cienega deposit exhibits a more complex mineralization distribution and paragenesis. In the UVS the mineralization is characterized by high Au grades, pervasive sericitization and silicification, comb, mosaic, and colloform quartz textures, with the colloform quartz stage corresponding to the waning of the hydrothermal system. The metallic paragenesis is defined by Py+Sph+Gn±Cpy and acanthite traces

In the LVS, mineralization is characterized by increasing Ag grade, adularia rhodochrosite and illite with comb mosaic quartz textures. The metallic paragenesis is composed of trace Sph+Gn±Py+Cpy and acanthite

No phases suitable for geochronology were found in the mineralized assemblages at Bacis. The only constraint is the veins crosscut the ca. 30 Ma Oligocene rhyolitic dome.

At La Cienega, adularia within a pervasive sericite halo in the shallow part of the LVC, and illite in the LVC deepest part of the deposit were selected for geochronology. The illite K-Ar data yield a minimum age of 34 Ma. The adularia $^{40}Ar/^{39}Ar$ dating experiment gave a step heating spectrum that was too disturbed to calculate a plateau age. Single steps range from 34 to 26 Ma, with a cluster of steps at 30 Ma.

3.3 Microthermometric data

Samples of mosaic quartz cement from mineralized structures were collected at different depths in both districts. Only primary fluid inclusions were identified and analyzed (Roedder, 1984; Van den Kerkhof and Ulrich, 2001). Salinities were estimated using the fluid

inclusion melting temperature in the numeric model of Lecumberri–Sanchez et al (2012). At Bacis, the homogenization temperatures range from 165 to 234 °C displaying a unimodal distribution with peak at 210ºC. Salinity estimates range from 0.53 to 9.21 wt% NaCl. At La Cienega, the homogenization temperatures range from 140-240°C, with a bimodal distribution with peaks at 180 and 210ºC. Salinities variation is more restricted than Bacis, from 0.18 to 5.26 wt% NaCl.

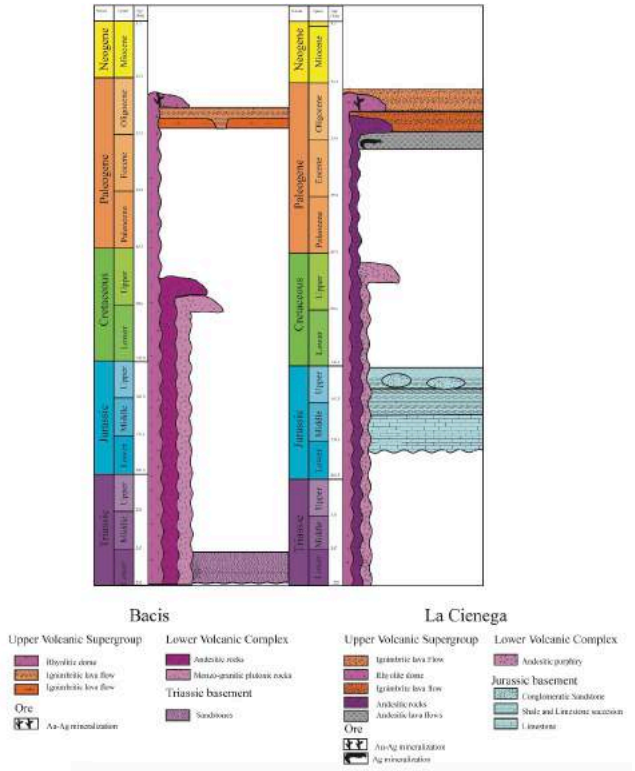

Figure 2. Stratigraphic columns of the Bacis and La Cienega mining districts

3.4 Decreptometry data

The maximum temperatures of the mosaic quartz cement hydrothermal event were estimated by decreptometry using the methodology of Burlinson et al (1983). At the Bacis fluid inclusion decrepitation occurs in a temperature range from 300 to 500°C, with a modal distribution peak at ca. 430°C. At La Cienega, the decrepitation temperature pattern present a wider variation range from 300 to 650ºC with a bimodal distribution. The two maximum peaks are identified at 430 and 550ºC.

3.5 Chlorite geothermometry

Chlorite minerals were sampled in different sites of the districts for representative parts of the mineral paragenesis. The crystallization temperatures were calculated using the Kranidiotis and MacLean (1987) equation. At Bacis the chlorite crystallization temperatures are a very restricted, clustering at ~270±6°C. For the la Cienega deposit, the data obtained exhibit a larger variation ranging from 240 to 372°C with a well-defined bimodal distribution with peaks at 250 and 330 ±10°C

4 Discussion

Dating of Au-Ag mineralization (using both direct and indirect approaches) indicates that the Bacis and La Cienega districts share a common mineralization event at ca. 30 Ma. This age overlaps with Oligocene silicic volcanism in the UVS and in particular within the rhyolitic domes which host some of the veins. In both districts, the mineralization is dominated by gold, pervasive sericitization, silicification, and propylitization. The thermal ranges of this Au mineralization event are also comparable with minimum temperatures from FI homogenization of 230ºC and a maximum temperature from FI decrepitation of 430ºC. Chlorite geothermometers from both deposits indicate comparable crystallization temperatures of 250 and 270±6ºC for La Cienega and Bacis respectively. Taking into account the fluid inclusion salinity (~5%eq NaCl), and the fluid inclusion homogenization and chlorite crystallization temperatures, the maximum depth of ore precipitation is estimated at ca 1000m in Bacis and 1500m in La Cienega.

The deeper part of the La Cienega deposit show particularities compare to the rhyolitic domes mineralizing areas. The deepest parts are characterized by adularia /rhodochrosite cements, the increase of acanthite and molybdenite. The chlorite chemistry, and the homogenization and decriptometry temperatures ranges show bimodal distribution suggesting the occurrence of a second mineralization events.The adularia experiment yielded a spectrum too perturbed to establish a plateau age. The higher temperature step heating ages (~34Ma) are comparable to the K-Ar age of illite and to the emplacement of the LVC andesite (~36Ma). However, both adularia and illite isotopic ages are minimum ages, that were likely reset by Oligocene and Miocene thermal events as illustrated by the adularia step-heating spectra. Illite and adularia have an isotopic closure temperature of ca. 250ºC, which are comparable with the observed chlorite crystallization temperatures and below the decripitation temperatures.

We conclude that the ages of both illite and adularia were partially reset, and that the illite K-Ar age has no geological meaning. The close presence of two districts with Eocene silver mineralization, Topia and San Dimas (Louck et al. 1988; Montoya et al., 2019), suggest that La Cienega deposit could have been affected by an Eocene intrusion associated with a discrete silver and adularia/rhodochrosite Eocene mineralization event. Taking into account the fluid inclusion salinity (~5% eq NaCl), and the fluid inclusion homogenization and chlorite crystallization temperatures, the depth of mineralization precipitation is estimated below 1500m in good agreement with the local stratigraphic column evolution.

5 Conclusion

Our new geological, petrological, geochronological and geothermometric reevaluation of the Bacis and La Cienega mining districts provides new constraints on formation models for both deposits:

Both mining districts have a common mineralization event related to the emplacement of Oligocene rhyolite domes. This Oligocene mineralization event is characterized by high Au/Ag high ratios, the presence of quartz in comb, mosaic, and colloform textures, pervasive sericitic, silica, and propylitic alteration, metallic paragenesis of Py+Sph+Gn with acanthite and then electrum, and a minimum temperature (from FI homogenization) of 180 - 230 ºC and a maximum temperature (from FI decrepitation) of 430ºC, with salinities of 5wt% NaCl, and chlorite crystallization temperatures of 250-270°.

At La Cienega mining district a more complex mineralization model can be envisaged. The K-Ar and $^{40}Ar/^{39}Ar$ data coupled with petrographic evidence imply an Eocene mineralizing event characterized by higher Ag grade, the presence of quartz in comb and mosaic textures, pervasive sericitic and propylitic alteration, metallic paragenesis of Sph+Gn+Py+Cpy traces with acanthite, and a minimum temperature (from FI homogenization) of 240ºC to a maximum temperature (from FI decrepitation) of 550ºC, with salinities of 5% NaCl, and a chlorite crystallization temperatures of 330°C.

Acknowledgements

This research is part of the MSc. project of the first author at Universidad Nacional Autonoma de Mexico (UNAM) Postgraduate Program and was funded by Consejo Nacional de Ciencias y Tecnologia (CONACYT), Mexico, Grant CB 237745-T to L. Ferrari.

We thank Fresnillo and Bacis mining companies for sharing unpublished information and for logistical support. We also thank Carlos Ortega for assistance with U-Pb dating, Gabriela Hernandez for assistance with ^{40}Ar-^{39}Ar dating, Noemi Salazar for assistance with the Electron Probe X-Ray Microanalyzer at the Petrography University Laboratory, Geophysics Institute at UNAM, campus Morelia, Marina Vega for assistance at the Crustal Fluid Laboratory, and Juan Tomás Vazquez for thin sections preparation.

References

Aranda-Gómez JJ, Henry CD, Luhr JF (2000) Evolución tectonomagmática post-paleocénica de la Sierra Madre Occidental y de la porción meridional de la provincia tectónica de Cuencas y Sierras, Mexico. Boletín de la Sociedad Geológica Mexicana UII: 59-71

Bonneau M (1970) una nueva área Cretácica fosilífera en el estado de Sinaloa. Bol Soc Geol Mexic 32:159-167

Burlinson K, Dubessy JC, Hladky G, Wilkins RWT (1983) The use of fluid inclusion decrepitometry to distinguish mineralized and barren quartz veins in the Aberfoyle Tin-Tungsten mine area, Tasmania. Jour Geochemical Exploration 19: 319-333

Bryan S, Ferrari L (2013) Large igneous provinces and silicic large igneous provinces: progress in our understanding over the last 25 years. Geol. Sic. Am. Bull. 125:1053-1078

Camprubí A, Ferrari L, Cosca MA, Cardellach E, Canals A (2003) Ages of epithermal deposits in Mexico: Regional significance and links with the evolution of Tertiary volcanism. Economic Geology 98:1029-1037

Camprubí A, Albinson T (2006) Epithermal deposits in Mexico — Update of current knowledge, and an empirical reclassification. Special Paper of the Geological Society of America. 422:377-415.

De La Garza V, Olavide S, Villasuso R (2001) Geology and ore deposits of the La Ciénega gold district, Durango, Mexico. Soc Eco Geol Spe Pap 8:87-93

Ferrari L, Lopez-Martinez M, Rosas-Elguera J (2002) Ignimbrite flareup and deformation in the southern Sierra Madre Occidental, western Mexico-implications for the late subduction history of the Farallon Plate. Tectonics 21:17-24

Ferrari L, Valencia-Moreno M, Bryan S (2007). Magmatism and tectonics of the Sierra Madre Occidental and its relation with the evolution of the western margin of North America. Geological Society of America Special Papers, 422:1-39.

Ferrari L, Orozco-Esquivel T, Bryan S, Lopez-Martini M, Silva Fragoso, A (2017) Cenozoic extension and magmatism in western Mexico: Linking the Sierra Madre Occidental Silicic Large Igneous Province and the Comondú Group with the Gulf of California rift. Earth-Sci Rev 183:115-152.

Henry D, Fredrikson G (1987) Geology of southern Sinaloa adjacent to the Gulf of California. Geol Soc, Am Map Chart Ser 14

Henry C, McDowell F, Silver L (2003) Geology and geochronology of granitic batholithic complex, Sinaloa, Mexico: implications for Cordilleran magmatism and tectonics. Geol Soc Am Spec pap 374:237-273

Kranidiotis P, MacLean WH (1987) Systematics of chlorite alteration at the Phelps Dodge Massive Sulfide deposit, Matagami, Quebec. Eco Geo 82:1898-1911.

Labarthe-Hernández G, Tristán-González M, Barboza-Gudino JR, Mata-Segura JL (1995) Cartografía geológica 1:10000 del área de la Ciénega y su correlación con otros distritos mineros de la Sierra Madre Occidental en el estado de Durango. Priv Rep Minera Mexicana La Ciénega S.A. de CV Durango, México 87

Lecumberri–Sanchez P, Steele–MacInnis M, Bodnar RJ (2012) A numerical model to estimate trapping conditions of fluid inclusion that homogenize by halite disappearance. Geochimica et cosmochimica Acta 92:14-22.

Loucks RR, Lemish J, Damon PE (1988) Polymetallic epithermal fissure vein mineralization, Topi, Durango, Mexico: Part I. Distric Geology, Geochronology, hydrothermal alteration, and vein mineralogy. Eco Geo 83:1499-1528.

McDowell F, Keizer R (1977) Timing of mid Tertiary volcanism in the Sierra Madre Occidental between Durango City and Mazatlán, Mexico. Geol. S. Am, Bull 88:1479-1487

McDowell F, McIntosh W (2012) Timing of intense magmatic episodes in the northern and central Sierra Madre Occidental, western. Geosphere 8:1505-1526

Montoya-Lopera P, Ferrari L, Levresse G, Abdullin F, Mata L (2019) New insights into the geology and tectonics of the San Dimas mining district, Sierra Madre Occidental, Mexico. Ore Geology Rev 105:273-294

Roedder E (1984) Fluid Inclusions. Min. Soc. Am. Rev, 664

Van den Kerkhof AM, Hein UF (2001) Fluid inclusion petrography. Lithos 55:27-47

Subdivision of wall rock alteration zoning in the Hishikari epithermal gold deposit, southern Kyushu, Japan

Yuji Gonoi, Akira Imai, Kotaro Yonezu, Thomas Tindell, Koichiro Watanabe
Kyushu University

Abstract. Detailed analysis of wall rock alteration seeks to establish discrete hydrothermal alteration zoning around the Hishikari low-sulfidation gold deposit. Samples from four underground cross cuts and five drill holes were collected. As a result of analysis, samples derived from underground cross cuts exhibit a dominant chlorite-smectite interstratified mineral (C/S). Core samples exhibit C/S, but chlorite is also present, which is an index mineral for the exploration of the veins. In the deeper part of the core sample around the Sanjin area, epidote is present which can be used as an index mineral for alteration zoning.

1 Introduction

The Hishikari deposit is an epithermal vein-type gold deposit with high-grade Au (30-40g/t of gold), and is located in Kagoshima prefecture, southern Kyushu, Japan.

Izawa et al. (1990) divided the alteration zoning around the Hishikari deposit into the following four zones: cristobalite–smectite (zone I), quartz–smectite (zone II), interstratified clay minerals (zone III), and chlorite–sericite (zone IV). In the exploration of the veins, zone IV has been used as an index of the proximal host to the mineralized veins. However, even in zone IV there are areas that do not host veins. In addition, some veins occur within zone III. Given these inconsistances, a new alteration zoning proxy that is sensitive to the mineralized veins is under review.

Yasuhara (2004) identified the alteration mineralogy of the host rocks mainly in the Yamada zone, western part of the Hishikari deposit. Yasuhara (2004) conducted XRD analysis on altered host rocks of 230 core samples in 21 bore holes and 50 underground samples. Based on the proportion of chlorite in C/S interstratified clay minerals, zone III was subdivided into 3 subzones as follows: Zone IIIa - chlorite is 0-30%; Zone IIIb - chlorite is 50-60% (corrensite); Zone IIIc - chlorite is 80-100%. By means of the subdivision, two small anomalous zones in the Yamada district were identified. Yasuhara (2004) showed that discrimination of zone III can be useful for exploration.

Therefore, mainly the eastern part of the Hishikari deposit, the Honko-Sanjin zone is studied in this work, with the goal to establish a new alteration index by subdividing the previously established alteration zones.

2 Outline of Hishikari deposit

The basement rock to the Hishikari deposit is the Cretaceous Shimanto-Supergroup, which consists mainly of sandstone and shale. In the mining area, the Shimanto-Supergroup has a Turonian age (88.5 to 90.4 Ma), based on a fossil bivalve identified as *Inoceramus* (*Mytiloides*) *cf. Labiatus* (*Scholotheim*) (Hayasaka 1999). The group is covered by Late Pliocene to Pleistocene volcanic rocks, including the Hishikari Lower Andesites with the age of 0.98 to 1.62 Ma based on K-Ar ages (Izawa et al. 1993).

The mine consists of the following three deposits: the Honko deposit, the Sanjin deposit, and the Yamada deposit. The veins of the Honko and Sanjin deposits are hosted mostly by the Shimanto-Supergroup. In contrast, the veins of the Yamada deposit are hosted by the Hishikari Lower Andesites. The strike of the veins are N30°E-50°E, with dips of 70°NW-90° (Ibaraki and Suzuki 1993).

By means of the K-Ar age-dating, the most economically important mineralization, Hosen, Zuisen and Keisen veins, is considered to have occurred around 0.90 Ma (Sekine et al. 2002). Also, hydrothermal activity is considered to have been active for a longer period for mineralization in the Yamada deposit (from 1.21 to 0.64 Ma) in contrast to the Honko-Sanjin deposits (from 1.01 to 0.88 Ma) (Sanematsu et al. 2005). Fluid inclusion microthermometry has revealed the temperature of mineralization in the Hishikari deposit was 180–250°C (e.g. Izawa et al. 1990; Hayashi et al. 2000; Etoh et al. 2002; Sanematsu et al. 2005, Takahashi et al. 2017; Shimizu et al. 2018).

3 Sampling and methodology

The samples were collected from four underground crosscuts (50W147, 50W163, 70E17, and D70KE) and five drill holes (XV-1, XV-14, SV-4, SV-5, KV-26) from the Hishikari mine (Fig. 1). The core samples were collected at intervals of 15 to 20 m in each crosscut and drill core. The Shimanto Supergroup is considered to have suffered not only hydrothermal alteration but diagenesis and metamorphism, therefore the present study focuses on alteration of volcanic rocks.

Microscopic observation and X-ray diffraction (XRD) were utilized to identified mineral assemblages. Bulk, oriented and ethylene-glycol (EG)-treated samples were analyzed to distinguish smectite or interstratified mineral from other clay minerals such as chlorite or illite.

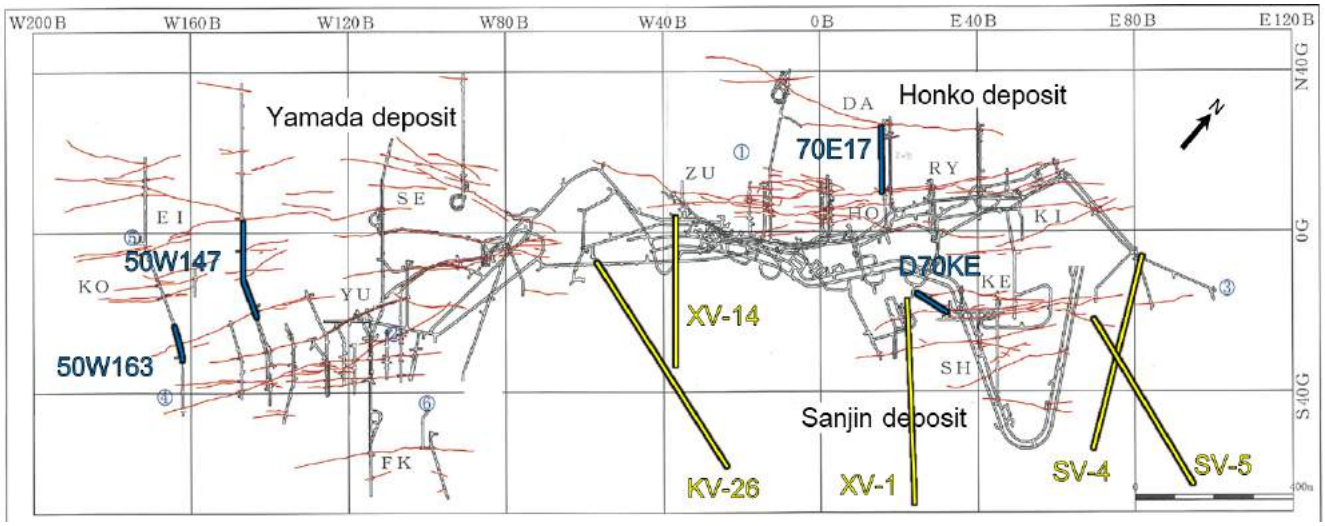

Figure 1. Vein map of the Hishikari mine. Thin red lines show veins. Blue and yellow lines show the underground crosscuts and drill holes, respectively.

4 Results and discussion

4.1 Mineral assemblage

The identified alteration minerals are; chlorite, illite, chlorite-smectite interstratified mineral (C/S), illite-smectite interstratified mineral (I/S), carbonates, quartz, pyrite, epidote; C/S includes corrensite.

Underground, most of samples include the chlorite-smectite interstratified mineral (C/S). The proportion of chlorite in C/S is variable, with the abundance of chlorite very scarce in samples from the four underground cross cuts. Therefore, the alteration zone along the four crosscuts is considered to belong to zone III.

From drill hole SV-4, which is located in the Sanjin area, chlorite occurs around 500m depth. This part belongs to the zone IV. In contrast, in drill hole SV-5 in Sanjin, the proportion of chlorite in C/S tends to decrease, suggesting that the hole is distal from the heat source.

4.2 Presence of epidote

In DDH SV-4, epidote is found in the interval between 480-520m. Epidote is generated at higher temperatures than chlorite and illite in general (Inoue 1995). The presence of epidote in the hydrothermally altered volcanic wall rock in the Hishikari deposit has not been reported in previous studies. Therefore, this mineral may have potential as a new index mineral for the division of alteration zoning.

For the Yamada deposit, previous research has not shown the presence of epidote. This suggests the existence of a higher temperature fluid in the Honko-Sanjin deposits than the Yamada deposit.

5 Future work

In order to subdivide the altered zone, the application of geothermometry on chlorite and/or illite will be conducted. In addition, hydrogen and/or oxygen isotope analysis will be applied to the hydrothermal minerals such as chlorite and illite, in order to understand the isotope halo due to the hydrothermal activity.

Acknowledgements

We are grateful to Sumitomo Metal Mining for providing access to underground workings and drill cores of the Hishikari gold deposit. We thank Mr. Takayuki Seto, the manager of Geology & Exploration Section, Hishikari mine, for his kindness of the permission and suggestion to the publication of the present study. We also thank the staff of Sumitomo Metal Mining, especially Mr. Atsuhiro Kuroda for his various kinds of help and assistance during fieldwork and core sampling.

This work was supported by JSPS Core-to-Core Program, B. Asia-Africa Science Platforms and JSPS KAKENHI Grant Number 18H01927.

References

Etoh J, Izawa E, Taguchi S (2002) A fluid inclusion study on columnar adularia from the Hishikari low-sulfidation epithermal gold deposit, Japan. Resour Geol 52:73–78.

Hayasaka S (1999) Fossil Inoceramus obtained from the Shimanto Group, South Kyusyu. Shizen Aigo 25:2 (in Japanese).

Hayashi K, Maruyama T, Satoh H (2000) Submillimeterscale variation of oxygen isotope of vein quartz at the Hishikari deposit, Japan. Resour Geol 50:141–150.

Ibaraki K, Suzuki R (1993) Gold-silver quartz-adularia veins of the Main, Yamada and Sanjin deposits, Hishikari gold mine. A comparative study of their geology and ore deposits. Resour Geol Spec Issue 14:1–11.

Inoue A (1995) Formation of clay minerals in hydrothermal environments. In Velde, B. (ed.) Origin and Mineralogy of Clays. Springer:269–329.

Izawa E, Urashima Y, Ibaraki K, Suzuki R, Yokoyama T, Kawasaki K, Koga A, Taguchi S (1990) The Hishikari gold deposit: High grade epithermal veins in Quaternary volcanics of southern Kyushu, Japan. Jour Geochem Explor 36:1–56.

Izawa E, Kurihara M, Itaya T (1993) K-Ar ages and initial Ar isotopic ratio of adularia-quartz veins from the Hishikari gold deposit, Japan. Resour Geol Spec Issue 14:63–69.

Murakami H (2008) Variations in chemical compositions of clay minerals and magnetic susceptibility of hydrothermally altered rocks in the Hishikari epithermal gold deposit, SW Kyushu, Japan. Resour Geol 58:1–24.

Sanematsu K, Duncan R A, Imai A, Watanabe K (2005b) Geochronological constraints using ^{40}Ar/ ^{39}Ar dating on the mineralization of the Hishikari epithermal gold deposit, Japan . Resour Geol 55:249–266.

Sekine R, Izawa E, Watanabe K (2002) Timing of fracture formation of mineralization at the Hishikari deposit, southern Kyushu, Japan. Resour Geol 52:395–404.

Shikazono N, Takahashi H (2010) Compositional variation of hydrothermally altered volcanic rocks in Hishikari gold epithermal system: a useful geochemical indicator of gold–silver epithermal mineralization. Resour Geol 60:117–128.

Shimizu T (2018) Fluid inclusion studies of comb quartz and stibnite at the hishikari Au–Ag epithermal deposit, Japan. Resour Geol 68:326–335

Takahashi R, Tagiri R, Blamey N J F, Imai A, Watanabe, Y, Takeuchi A (2017) Characteristics and behavior of hydrothermal fluids for gold mineralization at the Hishikari deposits, Kyushu, Japan. Resour Geol 67:279–299.

Yasuhara S (2004) Zoning of Hydrothermal Alteration in the Hishikari Epithermal Gold Deposit, Southern Kyushu, Japan. The Master Thesis, Kyushu University (unpublished).

Pb-Bi(-Cu) and Pb-Sb sulfosalts from Stan Terg area, Kosovo

Jakub Węgrzynowicz[1], Jaroslav Pršek[1], Sławomir Mederski[1], Burim Asllani[2], Katarzyna Kwiecień[1], Jakub Kanigowski[1]
[1]AGH University of Science and Technology, Kraków
[2]E&E Experts LLC, Prishtina

Abstract. Chemical analysis of lead-bismuth, lead-bismuth-copper and lead-antimony sulfosalts from Mazhiq and Vllahi in Trepça Mineral Belt (northern Kosovo) were performed using electron micro probe analyzer. Bismuthinite, krupkaite, aikinite, cosalite and native bismuth were identified as main Bi-bearing minerals. Presence of Pb-Sb sulfosalts as boulangerite, semseyite and chovanite was confirmed in listwaenite type of mineralization from Vllahi. Cosalite tends to have constant chemical composition, whereas minerals of bismuthinite-aikinite series are characterized by broad degree of aikinite-type of substitution in individual members. Bismuthinite has n_a=0.56 up to n_a=9.69, krupkaite n_a=47.50 up to n_a=58.35 and aikinite n_a=83.92 up to n_a=93.91. Study indicate possible presence of other phases of bismuthinite-aikinite series.

1 Introduction

Stan Terg is the largest Pb-Zn deposit in Trepça Mineral Belt, historically important European district for ore mining (Kołodziejczyk et al. 2015). Several other small deposits and mineral occurrences had been found in this region.

Many previous researches had been describing ore mineralization in Stan Terg region. Some of them reported presence of Pb-Bi(-Cu) and Pb-Sb sulfosalts (Terzić et al. 1974; Kołodziejczyk et al. 2015; 2017). However some specific minerals and mineral groups need further investigation, as authors believe.

The aim of this study is to obtain new data of presence, chemical composition and replacement events of Pb-Bi(-Cu) and Pb-Sb sulfosalts with putting special emphasis on bismuthinite-aikinite series. These could give clues to conditions of ore-forming processes evolution in investigated area (Topa et al. 2002).

2 Geological setting

Stan Terg Pb-Zn deposit is placed in the center of 80-km-long Trepça Mineral Belt in northern Kosovo, within Vardar tectonic zone (Hyseni et al. 2010). Vardar tectonic zone is elongated trending NNW-SSE regional suture between the Serbo-Kosovaro-Macedonian Massif to the east and the Dinarides to the west (Hyseni et al. 2010).

The Stan Terg area contains Triassic sediments, phyllites, volcanoclastic rocks and Upper Triassic carbonates, Jurassic ultrabasic rocks and serpentinites (ophiolite), Cretaceous clastics, serpentinites, volcanics and volcanoclastic rocks of basaltic composition and carbonates and Oligocene-Miocene volcanics (Hyseni et al. 2010). Ore mineralization is linked to Oligocene-Miocene magmatism activity (Kołodziejczyk et al. 2017) of andesite, trachyte and latite composition.

Several types of ore mineralization, such as skarn, hydrothermal replacement, listwaenite-type and faults-controlled vein mineralization had been described (Kołodziejczyk et al. 2017).

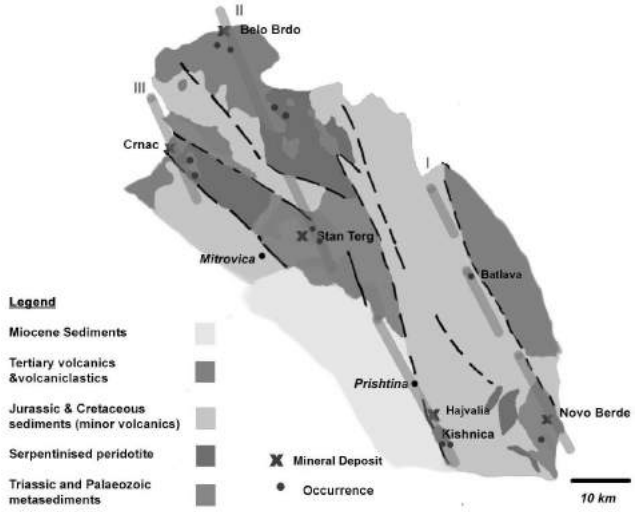

Figure 1. Geological map of Trepça Mineral Belt (from Hyseni et al. 2010).

3 Samples and methods

3.1 Investigated material

Samples containing sulfosalt mineralization were collected from outcrops of altered and weathered ore in three places in Stan Terg region: Vllahi and Mazhiq (two places) villages.

Material from Vllahi is represented by greenish listwaenites, partially brecciated and sillificated. Macroscopically visible galena is disseminated in gangue minerals (mostly quartz). Ore from Mazhiq I contains zones with massive arsenopyrite, pyrite and chalcopyrite in quartz and carbonates. Needles of bismuth sulfosalts up to 2 cm are usually disseminated in quartz or chalcopyrite. Ore from Mazhiq II contain samples with listwaenites and quartz breccia with massive gersdorffite, pyrite and arsenopyrite impregnations. Needle-like crystals of sulfosalts up to few cm are disseminated in carbonates or galena.

3.2 Analytical methods

Chemical analyses were carried out by electron micro probe analyzer (EPMA) using EOL Super Probe JXA-8230 at the Critical Elements Laboratory AGH-KGHM in Kraków, Poland. Operating conditions were an accelerating voltage of 20 kV, a beam current 20 nA, peak time of 20 sec, and a background time of 10 sec, with following standards natural: (pyrite, stibnite, chalcopyrite, galena, arsenopyrite) or synthetic (native silver, native bismuth) and spectral lines: Ag(Lα), Pb(Mα), S(Kα), Sb(Lα), Cu(Kα), Fe(Kα), Bi(Mα), As(Lα) for sulfosalts.

4 Results

4.1 Ore mineralogy

Ore minerals being present in investigated samples from Mazhiq I and Mazhiq II are: chalcopyrite, galena, arsenopyrite, pyrite, sphalerite, cosalite, tennantite-tetrahedrite, bismuthinite-aikinite series minerals, bournonite, native bismuth, pyrrhotite, gersdorffite, marcasite and native gold. These minerals occur in numerous different associations. Bi-sulfosalts are associated with native Bi and Au, in some cases are prior to the last stage of galena and chalcopyrite crystallization.

Mineralogy of Vllahi mineral occurrence is different. Galena and sphalerite are only base metals' sulfides here. Ni mineralization represented by niccolite and gersdorffite (and probably other Ni/Ni-Co sulfides and arsenides) constitute first association in samples from there. It is prior to boulangerite, semseyite and chovanite. Pb-Sb sulfosalts are associated with galena. Tennantite-tetrahedrite, sphalerite, and bournonite are latter.

4.2 Boulangerite, semseyite and chovanite

Pb-Sb sulfosalts occur only in samples from Vllahi. All three phases form zonal crystals from tens up to 500 μm in size (Fig. 3). They are usually euhedral and partially digested. Usually they form intergrowths with galena, where they are overgrowing galena aggregates. Three phases – boulangerite, semseyite and chovanite were identified (Fig. 2).

Calculated average formulas of investigated minerals: boulangerite $Pb_{4.81}(Sb_{4.15}As_{0.03})_{\Sigma 4.18}S_{11.10}$, semseyite $Pb_{8.89}Fe_{0.01}(Sb_{8.03}As_{0.06}Bi_{0.01})_{\Sigma 8.10}S_{21.11}$, chovanite $Pb_{14.62}Fe_{0.01}Cu_{0.01}Ag_{0.01}(Sb_{13.95}As_{0.39}Bi_{0.02})_{\Sigma 14.36}S_{36.21}$.

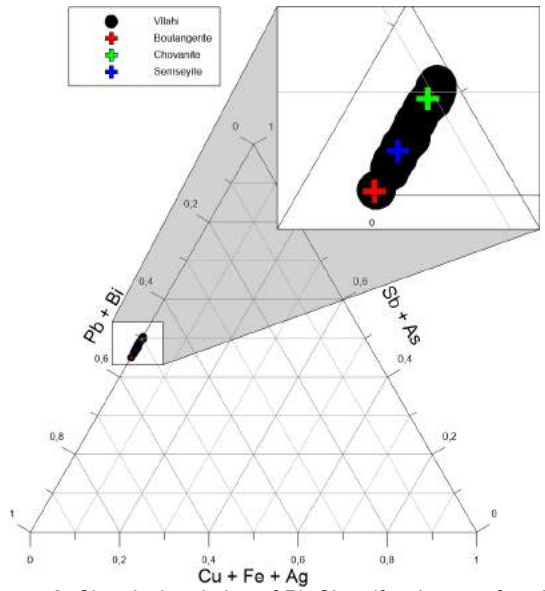

Figure 2. Chemical variation of Pb-Sb sulfosalts as a function of a ternary plot in terms of Sb+As, Cu+Fe+Ag, and Pb+Bi. Black circles – this study, crosses – ideal chemical composition of minerals.

Pb content in boulangerite is 0.19 apfu lower than in standard formula and semseyite 0.11 apfu lower. Investigated Pb-Sb sulfosalts do not have any significant admixtures. As↔Sb substitution level is generally low. Only in chovanite As content has values up to 2.82 wt.% with average 0.49 wt.%.

4.3 Cosalite

Cosalite was found in samples from Mazhiq I and Mazhiq II. It is associated with minerals of bismuthinite – aikinite series and does not occur in sulfosalts aggregates containing native bismuth.

Cosalite occur in form of elongated crystals, sometimes intergrown with bismuthinite. Both phases are later replaced by aikinite or krupkaite. The amount of individual bismuth minerals in the samples is different. Cosalite is dominant mineral in aggregates within chalcopyrite but without presence of native bismuth. Cosalite rarely forms isolated crystals. Mineral occur typically as elongated needle-like crystals up to few centimeters long within chalcopyrite and galena or in massive aggregates filling voids between quartz

Table 1. Average chemical composition of investigated sulfosalts based on EMPA. Number of analyses in brackets. 1 – boulangerite, 2 – semseyite, 3 – chovanite, 4 – cosalite from Mazhiq II, 5 – cosalite from Mazhiq I, 6 – bismuthinite from Mazhiq II, 7 – bismuthinite from Mazhiq I, 8 – krupkaite, 9 – aikinite, na – not analyzed.

	wt% Pb	wt% Fe	wt% Cu	wt% Ag	wt% Bi	wt% Sb	wt.% As	wt% S	total
1(9)	53.75	0.01	0.01	0.00	0.05	27.25	0.13	19.20	100.40
2(22)	52.40	0.01	0.01	0.00	0.06	27.82	0.14	19.26	99.69
3(13)	50.94	0.01	0.01	0.02	0.07	28.56	0.49	19.52	99.62
4(24)	38.46	0.02	0.85	1.25	44.57	0.22	na	16.18	101.54
5(31)	38.68	0.04	1.28	0.87	44.43	0.29	na	16.17	101.77
6(17)	1.30	0.02	0.43	0.00	81.47	0.83	na	18.64	102.70
7(42)	1.68	0.02	0.59	0.03	81.08	0.75	na	18.53	102.68
8(22)	19.73	0.03	6.03	0.00	58.77	0.17	na	17.47	102.20
9(26)	31.68	0.05	9.80	0.01	43.36	0.15	na	16.69	101.74

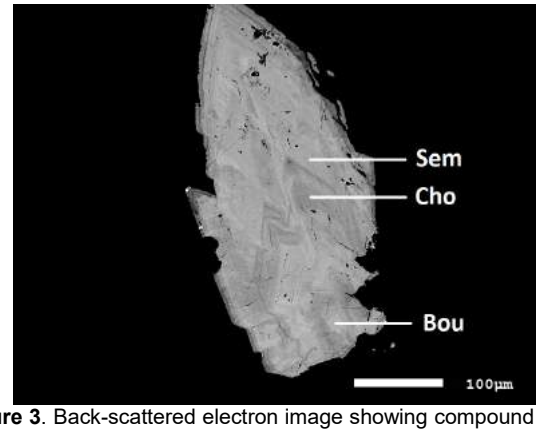

Figure 3. Back-scattered electron image showing compound zonal crystal of Pb-Sb sulfosalts. Bou – boulangerite, Cho – chovanite, Sem – semseyite.

crystals. It appears often also as tens up to 200 µm in size euhedral inclusions within quartz and sulfides.

Chemical analyses of cosalite from Mazhiq I gave average formula as $(Cu_{0.80}Ag_{0.32})_{\Sigma 1.12}(Fe_{0.03}Pb_{7.40})_{\Sigma 7.43}(Bi_{8.43}Sb_{0.10})_{\Sigma 8.53}S_{20}$ calculated on basis of Topa & Makovicky (2010). Cosalite from Mazhiq II has average formula as $(Cu_{0.53}Ag_{0.46})_{\Sigma 0.99}(Fe_{0.01}Pb_{7.36})_{\Sigma 7.37}(Bi_{8.45}Sb_{0.07})_{\Sigma 8.52}S_{20}$. Both of them have significant Ag and Cu substitution. Ag max. content attains 1.02 wt.% in cosalite from Mazhiq I and 1.40 wt.% in samples from Mazhiq II. Max. Cu content is 1.76 wt.% and 1.13 wt.% respectively: Compared with standard chemical composition, investigated cosalite have broader $2(Cu+Ag)\leftrightarrow Pb$ and $Ag+Bi\leftrightarrow 2Pb$ substitutions. Chemical composition of cosalite from this study is substantially stable. Mean chemical composition in Table 1.

4.4 Bismuthinite – aikinite series

Bismuthinite is present in samples from Mazhiq I and Mazhiq II, other minerals of bismuthinite – aikinite series (krupkaite and aikinite) occur only in Mazhiq I. Bismuthinite is the most common phase from the series. Krupkaite and aikinite tend to occur on the boundaries between dominant phases – bismuthinite and cosalite

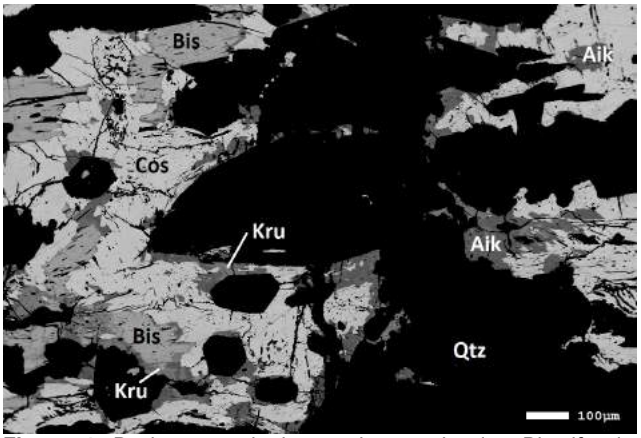

Figure 4. Back-scattered electron image showing Bi-sulfosalts from Mazhiq I. Cos – cosalite, Bis – bismuthinite, Kru – krupkaite, Aik – aikinite, Qtz – quartz.

(Fig. 4), usually replacing these previous minerals.

Bismuthinite often forms elongated needle-like crystals up to few centimeters long, crosscutting carbonates or prior chalcopyrite. It occurs also as aggregates of anhedral crystals in interstices between quartz crystals. This mineral could occur as practically dominant or monomineral Bi-sulfosalt in a sample as well as in association with cosalite, krupkaite and aikinite. It is often associated with native bismuth and rarely with native gold. Its chemical composition is variable. Degree of aikinite-type substitution (on basis of Topa et al. 2002) has values from n_a=0.56 to n_a=9.69 in samples from Mazhiq I and n_a=0.53 to n_a=6.15 in samples from Mazhiq II. Average formula calculated on basis of Topa et al. (2002) is $(Bi_{7.53}Sb_{0.12}Cu_{0.18}Pb_{0.16}Fe_{0.01})_{\Sigma 8.00}S_{11.22}$ for bismuthinite from Mazhiq I and $(Bi_{7.61}Sb_{0.13}Cu_{0.13}Pb_{0.12}Fe_{0.01})_{\Sigma 8.00}S_{11.35}$ for that from Mazhiq II. Bismuthinites from both localities have variable Sb content. In Mazhiq II it varies from 0.24 to 3.38 wt.%, in Mazhiq I from 0.06 to 4.04 wt.%. Fe and Ag content is negligible.

Krupkaite forms thin (usually to 10 µm) fringes on a boundaries of bismuthinite crystals (Fig. 4) or irregular elongated exolutions within bismuthinite. Usually it is product of bismuthinite or cosalite replacement. Its average formula represents as $(Bi_{4.75}Sb_{0.02}Cu_{1.60}Pb_{1.61}Fe_{0.01})_{\Sigma 8.00}S_{9.21}$. Degree of aikinite-type substitution varies from n_a=47.50 to n_a=58.35. Analyses cover practically whole known krupkaite range according to Topa et al. (2002). Average chemical composition of investigated krupkaite is very close to theoretical one.

Aikinite occurs similarly as krupkaite. It forms tens up to 100 µm in size irregular crystals on a boundaries of, or within other Bi-sulfosalts. Also it is a product of bismuthinite, cosalite and krupkaite replacement. Its average formula is $(Bi_{3.21}Sb_{0.02}Cu_{2.39}Pb_{2.37}Fe_{0.01})_{\Sigma 8.00}S_{8.06}$. Degree of aikinite-type substitution varies from n_a=83.92 to n_a=93.91.

5 Discussion

5.1 Cosalite

Cosalite from Stan Terg area was previously reported in Stan Terg deposit (Terzić et al. 1974; Kołodziejczyk et al. 2017) and in Mazhiq I (Mederski et al. 2018). Chemical composition of mineral from this study differs significantly from researches carried out on material from Stan Terg deposit and is similar to data obtained by Mederski et al. (2018).

Kołodziejczyk et al. (2017) described cosalite with strongly variable Sb content up to 13.6 wt. % caused by advanced Sb-Bi substitution. Cosalite from Mazhiq I and Mazhiq II have much lower and very stable Sb content.

Content of Ag and Cu is higher in Mazhiq I and Mazhiq II than in Stan Terg deposit (0.27 – 0.72 apfu of Cu+Ag in Stan Terg. Kołodziejczyk et al. 2017). This is probably a result of more advanced $Ag+Bi\leftrightarrow 2Pb$ and $2(Cu+Ag)\leftrightarrow Pb$ substitutions (Topa & Makovicky 2010), however obtained data does not show such statistical

correlation.

5.2 Bismuthinite – aikinite series

Bismuthinite was previously described as widespread mineral in different ore types from Stan Terg deposit, associated with lillianite, ikunolite and native bismuth, often within galena (Kołodziejczyk et al. 2015). It was also reported in Mazhiq I (Mederski et al. 2018).

This study delivers more data of bismuthinite chemical composition, suggesting higher degree of aikinite-type substitution. Analyses cover nearly entire bismuthinite field, determinated by Topa et al. (2002) and based on aikinite mol.%. Some analyses give results above this field (Fig. 5), but they were excluded from calculations and need further investigation. They show possible broader range for aikinite substitution in bismuthinite. Similar bismuthinite is widespread in the nature and need only crystallographic investigation to prove broad range of aikinite substitution in bismuthinite (Pršek et al. 2008). Analyses which fall between krupkaite and aikinite fields needs more study to prove presence of other phases of bismuthinite-aikinite series in Mazhiq I occurrence. Sb content is highly variable and has values up to 3.78 wt.% in Mazhiq I, which is much more than in previous analyses (up to 1 wt.% in Mederski et al. 2018), but is still low compared to Kutná Hora area in Czech Republic (up to 6.6 wt.%. Pažout et al. 2017) or Brezno-Hviezda occurrence in Slovakia (up to 26 wt.%. Pršek et al. 2008).

Mederski et al. (2018) first reported presence of krupkaite and pekoite as other mineral member of bismuthinite-aikinite series in Stan Terg area. This study confirms occurrence of krupkaite of wider range of krupkaite field (Fig. 4), based on aikinite mol.%. According to obtained data, krupkaite does not have significant admixtures (av. 0.17 wt.% Sb and 0.03 wt.% Fe).

Presence of aikinite in Stan Terg area has not been reported so far. Analyses give results in wide range of aikinite field (Fig. 5). Mineral does not have significant admixtures (av. 0.15 wt.% Sb and 0.05 wt.% Fe).

Occurrence of only these three minerals of bismuthinite – aikinite series indicates low fluid temperature (up to 250˚C) and rather constant crystallization conditions (Topa et al. 2002).

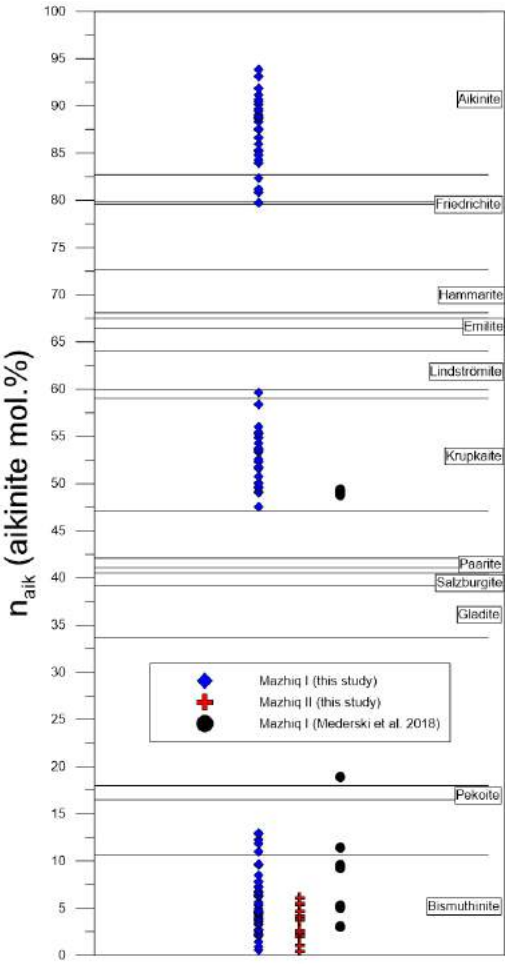

Figure 5. Diagram of appurtenance to minerals of bismuthinite-aikinite series determinated by Topa et al. (2002) and based on aikinite mol.%.

Acknowledgements

Research was founded by AGH-UST Rector Grant assigned to Studenckie Koło Naukowe Geologów. Authors are grateful to Mr. Adam Włodek from Critical Elements Laboratory AGH-KGHM in Kraków for conducting EMPA analyses.

References

Hyseni S, Durmishaj B, Fetahaj B, Shala F, Berisha A, Large D (2010) Trepça Ore Belt and Stan Terg mine – Geological overview and interpretation. Kosovo (SE Europe). Geologija 53:87–92.

Kołodziejczyk J, Pršek J, Melfos V, Voudouris PCh, Maliqi F, Kozub-Budzyń G (2015) Bismuth minerals from the Stan Terg deposit (Trepça, Kosovo). N Jb Miner Abh 192:317–333.

Kołodziejczyk J, Pršek J, Voudouris PCh, Melfos V, (2017) Bi-sulphotellurides associated with Pb–Bi–(Sb±Ag,Cu,Fe) sulphosalts: an example from the Stan Terg deposit in Kosovo. Geol Carpath 68:366–381.

Mederski S, Pršek J, Asllani B, Kozub-Budzyń G (2018) Bi-sulphosalts from the Mazhiq, Stan Terg area, Kosovo. In: Joint 5th Central-European Mineralogical Conference and 7th Mineral Sciences in the Carpathians Conference. Mineralogical Society of Slovakia, Banská Štiavnica, 26 – 30 June, Proceedings 1:74.

Pažout R, Sejkora J, Šrein V (2017) Bismuth and bismuth–antimony sulphosalts from Kutná Hora vein Ag–Pb–Zn ore district, Czech Republic. J Geosci 62:59–76.

Pršek J, Ozdín D, Sejkora J (2008) Eclarite and associated Bi sulfosalts from the Brezno-Hviezda occurrence (Nízke Tatry Mts, Slovak Republic). N Jb Miner Abh 185:117–130.

Terzić SB, Sommerauer J, Harnik AB (1974) Macroscopic cosalite crystals from the Pb-Zn Ore Deposit Trepča (Yugoslavia). Schweiz Mineral Petrogr Mitt 54:209–211.

Topa D, Makovicky E, Paar WH (2002) Composition ranges and exsolution pairs for the members of the bismuthinite-aikinite series from Felbertal, Austria. Can Min 40:849-869.

Topa D, Makovicky E (2010) The crystal chemistry of cosalite based on new electron-microprobe data and single-crystal determinations of the structure. Can Min 48:1081-1107.

Nickel mineralization in hydrothermally altered serpentinites (listwaenites) in the broad area of Stan Terg mine, Vardar Zone, Kosovo

Szczepan Bal[1], Jaroslav Pršek[1], Sławomir Mederski[1], Burim Asllani[2], Adrianna Wojnarowska[1], Adam Cieślak[1]
[1]*AGH University of Science and Technology, Kraków*
[2]*E&E Experts LLC, Prishtina*

Abstract. The presence of various Ni bearing minerals in hydrothermally altered serpentinites from the broad Stan Terg area is documented. Ni minerals occur in the hydrothermally altered serpentinites (Vllahi, Melenica), hydrothermal base metal mineralization in contact with serpentinites (Mazhiq) or in carbonate veins in listwaenites (Selac). Niccolite, millerite, gersdorffite, and maucherite were identified as the main Ni-bearing minerals. They occur in the paragenesis with minerals of the thiospinel (violarite, Co bearing violarite, siegenite, Fe bearing siegenite and polydymite) group and rammelsbergite, gersdorffite-krutovite solid solution, Ni-marcasite and main Zn-Fe-Cu-Pb-Sb sulphides and sulphosalts. This is the first described occurrence of nickel mineralization in the area of Stan Terg mineralizing system.

1 Introduction

Kosovo is characterized by rich occurrences of polymetallic mineralization of economic importance. The most important are hydrothermal Zn-Pb deposits with associated Au-Ag (Cu, Bi, Te, Sb). The presence of Ni mineralization is known only from the listwaenite occurrences close to Crnac deposit in the Rogozna Mountains, Northern Kosovo (Radosavljevic et al. 2015) or from the weathered and hydrothermally altered serpentinites in schists of Veles series in Donje Ljupce (Szczygieł 2017). Minerals such as millerite, bravoite, niccolite, various members of the gersdorffite-ullmannite series in paragenesis with various Cu-Ag-Pb-Sb-Zn-Sn minerals and native elements were indentified in Crnac. Additionally millerite, siegenite, polydymite and pentlandite were identified in Donje Ljupce. In the Stan Terg area, only base-metal mineralization with precious metal epithermal mineralization occurs without any known nickel phases (Kołodziejczyk 2016). The aim of my research is to characterize nickel mineralization in the broad Stan Terg mine area in the Kopaonik Mountains, Vardar Zone, Kosovo.

2 Geological setting

The Vardar Zone is an elongated belt extending from Bosnia through Kosovo, Macedonia and Greece to Turkey in a NNW-SSE trend. It is interpreted to be a transitional zone between the Serbian-Macedonian massif from the east and Dinaric Alps to the west. It was formed during the late Cretaceous closure of Neo-Tethys ocean basin, as a result of the Adria and Eurasia craton collision. The Vardar Zone mainly consists of marine and continental sedimentary rocks which are characterized by different grades of metamorphic and tectonic deformation. Additionally, as a result of continental collision, younger felsic rocks intruded into the sequence. The age of these volcanic rocks is between late Cretaceous and Miocene (Zelic et al. 2010). This structure consists of fragments of Paleozoic crystalline rocks discordantly lying on the Triassic clastic rocks and upper Triassic carbonates. Jurassic rocks mainly consist of an ophiolite sequence. Cretaceous strata is represented by a clastic series. During the Oligocene and Miocene period, voluminous volcanic activity occurred. These rocks were intruded and often exhibit a different chemical composition. In areas where igneous andesite/latite rocks intruded into serpentinites, listwaenite formed (Hyseni et al. 2010). In Kosovo, part of Vardar Zone - the Trepca Mineral Belt is the main metallogenic unit which was recognized. This belt is one of the more important areas for Zn-Pb ores in Europe. His length is above 80 km and start in the northern part of Kosovo (Kolodziejczyk et al. 2016).

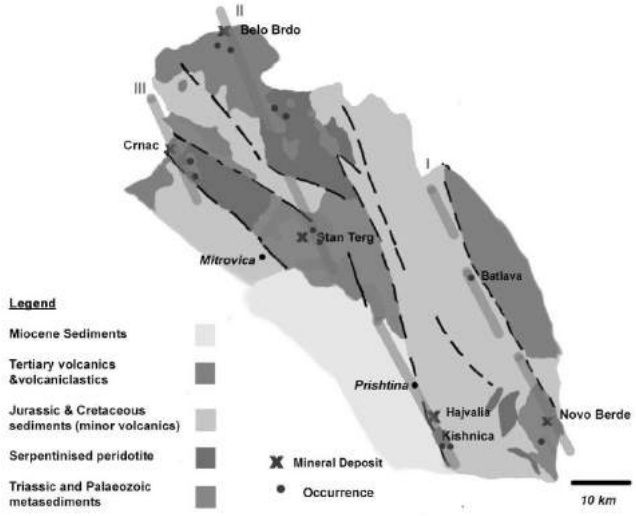

Figure 1. Geological map of Trepça Mineral Belt (from Hyseni et al. 2010).

3 Samples and methods

3.1 Investigated material

Samples with nickel mineralization were collected from

outcrops of altered listwaenites with visible disseminated mineralization (Vllahi, Melenica), from carbonate veins with ore mineralization (Selac) as well as from weathered ore (Mazhiq, Vllahi).

Material from Vllahi is represented either by greenish listwaenites, partially brecciated and sillificated or by massive sulphide ore. Galena is only visible as a disseminated sulphide in listwaenite. Ore from Selac contains massive Fe-Mg-Ca carbonate veins with nests of niccolite and maucherite up to few cm in size. Carbonate veins occur in the tectonic zone with listwaenite occurrences. The Mazhiq samples were collected from the Fe-Mn carbonate blocks in the listwaenite zone. Samples are usually brecciated with quartz, carbonates and sulphides as massive gersdorffite, pyrite impregnations, needle-like crystals of Bi sulfosalts with galena, sphalerite, tetrahedrite and chalcopyrite. Samples from Melenica are represented by greenish listwaenites, partially silicified with galena, sphalerite veinlets and pyrite, millerite and arsenopyrite crystals.

3.2 Analytical methods

Chemical analyses were carried out by electron micro probe analyzer (EPMA) JEOL Super Probe JXA-8230 at the Critical Elements Laboratory AGH-KGHM at AGH-UST University in Kraków, Poland. Operating conditions featured an accelerating voltage of 20 kV, a beam current 20 nA, peak time of 20 sec, and a background time of 10 sec and using the following natural standards (pyrite, stibnite, chalcopyrite, arsenopyrite) and synthetic standards (Bi_2Se_3, pure Co and Ni) and spectral line used Sb (Lα), S (Kα), Fe (Kα), Co (Kα), Ni (Kα), Cu (Kα),Bi (Mα), As (Lα).

4 Results

4.1 Ore mineralogy

Ore minerals which were identified in the Ni mineralization and Ni-bearing samples include: pyrite, galena, chalcopyrite, marcasite, arsenopyrite, sphalerite, Pb-Sb and Bi sulfosalts, hematite, Cr-bearing spinels and quartz, carbonates and Cr-bearing micas. Ni minerals identified in the paragenesis were: niccolite, maucherite, rammelsbergite, krutovite, violarite, siegenite, usually disseminated, but sometimes found as thin sulphide veinlets of polydymite, gersdorffite and millerite. Mineralization is sulphide nests occur. Ore mineralization in listwaenites was formed at least in two stages. The older stage (Ni-bearing stage) is represented by sulphides, sulphoarsenides and arsenides of Fe-Ni-Co: mainly millerite, gersdorffite, niccolite, maucherite, gersdorffite and piryte/marcasite. The younger phase is typical by presence of base-metal mineralization with galena, sphalerite, chalcopyrite, tetrahedrite, pyrite as well as various sulphosalts. Ore minerals usually occur as small individual grains or intergrowths of different size – from 50 up to 500 μm. They rarely could reach few cm in size. The average chemical composition of all identified nickel phases is presented in the Table 1. Chemical variation of Ni mineralization is presented on figure 2.

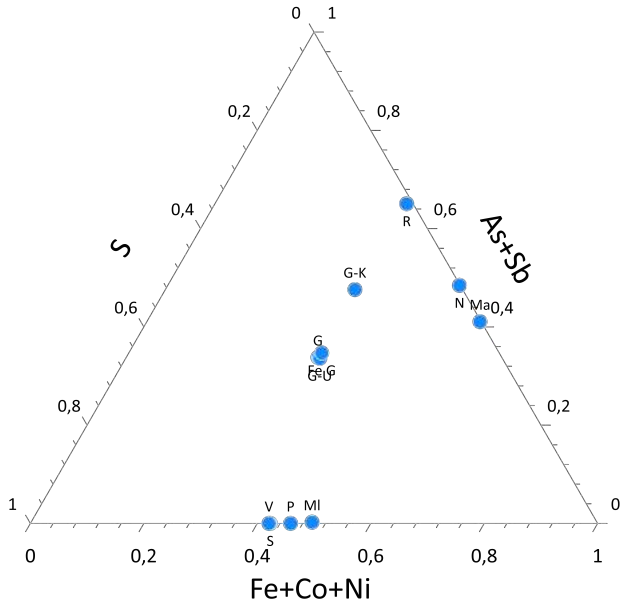

Figure 2. Chemical variation of Ni mineralization in Stan Terg area as a function of a ternary plot in terms of S, As+Sb, Fe+Ni+Co. (R – rammelsbergite (n=20), Ml – millerite (n=17), G – gersdorffite (n=53), N – niccolite (n=30), G-K – gersdorffite-krutovite (n=10), G-U – gersdorffite-ullmannite (n=47), Fe G – Fe bearing gersdorffite (n=13), P – polydymite (n=1), S – siegenite (n=8), V – violarite (n=7), Ma – maucherite (n=57)).

Table 1. Average chemical composition of investigated Ni minerals based on EMPA. Number of analyses in brackets. 1–Millerite (n=17) , 2–Niccolite(n=30), 3–Gersdorffite (n=53), 4–Rammelsbergite (n=20), 5–Maucherite (n=57), 6–Siegenite (n=8), 7–Violarite (n=7), 8–Gersdorffite-Ullmannite (n=47), 9–Gersdorffite-Krutovite (n=10), 10-Fe bearing Gersdorffite (n=13), 11-Polydymite (n=1).

	S (wt.%)	Sb (wt.%)	Fe (wt.%)	Co (wt.%)	Ni (wt.%)	Cu (wt.%)	Bi (wt.%)	As (wt.%)	Total
1	34.94	0.09	0.75	0.14	62.19	0.15	0.05	0.34	98.65
2	0.06	1.00	0.01	0.58	44.48	0.09	0.00	53.58	99.82
3	18.27	3.77	1.46	0.75	32.58	0.06	0.08	42.12	99.10
4	0.53	0.39	0.49	1.76	26.47	0.43	0.00	70.35	100.42
5	0.10	1.28	0.00	0.59	51.72	0.11	0.00	45.89	99.70
6	42.09	0.00	6.30	12.02	37.89	0.11	0.05	0.00	98.45
7	41.99	0.00	13.69	3.46	37.99	0.08	0.06	0.00	97.27
8	17.50	14.75	0.52	0.19	32.92	0.04	0.24	33.15	99.31
9	9.60	4.76	0.19	0.17	30.48	0.04	0.00	53.06	98.30
10	17.65	2.55	4.58	0.29	30.15	0.11	0.08	44.14	99.56
11	38.93	0.01	0.03	6.38	54.01	0.12	0.03	0.00	99.51

4.2 Millerite

Millerite was identified in samples from Melenica, Selac and Vllahi. In Melenica it occurs as small elongated crystals in association with siegenite, Sb-bearing gersdorffite-ullmannite, chalcopyrite, galena and bournonite. Often it is overgrown or replaced by gersdorffite (Fig. 4d). It is a common mineral in the samples. In Vllahi, it is rare, forming elongated crystals up to 100 μm enclosed in galena together with siegenite and gersdorffite, or disseminated needles in carbonates with marcasite and violarite (Fig. 4f). In Selac, it is also rare occurring as needle like crystals with polidymite/siegenite veinlets cutting aggregates of Ni-arsenides. The size of the millerite needles is up to 100 μm. The chemical composition of millerite is close to theoretical with small content of Fe up to 0.94 wt.% and As up to 0.45 wt.%.

4.3 Niccolite, Rammelsbergite and Maucherite

Ni arsenides were found only in samples from Selac; in the Vllahi samples Ni arsenides are rare. They form massive aggregates up to 2 cm in size. Niccolite is intergrown with maucherite, whereas rammelsbergite forms zones in maucherite-niccolite aggregates (Fig. 4b). Niccolite was also identified as small inclusions in galena from Vllahi together with gersdorffite and possible breithauptite. Rammelsbergite from Vllahi was found only in few crystals where it forms small inclusions in galena. Niccolite is slightly enriched in Sb with contents up to 1 wt.%. Similarly, associated maucherite is also enriched in Sb up to 1.28 wt.%. Rammelsbergite has a different chemical composition and it is enriched in S up to 3.28 wt.%, Sb up to 2.16 wt.%, Fe up to 2.70 wt.% (samples from Vllahi) and Co up to 1.81 wt.%. (samples from Selac).

4.4 Gersdorffite

Gersdorffite is the main Ni-bearing phase in the listwaenite type of mineralization. It is present in samples from Mazhiq, Melenica and Vllahi but was not identified in Selac. Usually it forms euhedral crystals, sometimes zone (Fig. 4e), in association with other Ni phases as well as pyrite, galena, tetrahedrite, arsenopyrite and chalcopyrite. The size of the crystals is usually up to 100 μm but sometimes aggregates of gersdorffite crystals can reach 1 cm (Mazhiq). On the basis of chemical analysis we can distinguish several different types of gersdorffite: gersdorffite, Fe bearing gersdorffite (only at Mazhiq), Sb-bearing gersdorffite and gersdorffite-ullmannite solid solution (Vllahi) and gersdorffite-krutovite solid solution (only at Vllahi). Pure, low Fe gersdorffite is the most common phase.

4.5 Thiospinels

Members of thiospinels mineral group are a common mineral in the Ni paragenesis. They were identified in typical listwaenite disseminated mineralization or in the vein type form (Fig. 4c). Usually they form euhedral crystals in association with other Ni minerals like gersdorffite, millerite or Ni arsenides. The size of the crystals is small, usually up to 50 μm. A few different phases were identified: violarite, siegenite, Fe bearing siegenite and polydymite. Siegenite is the most common of the phases, and occurs mainly in association with gersdorffite-ullmannite solid solution. Polydymite was found only in Selac as a thin vein with millerite crystals cutting a niccolite-maucherite aggregate. Violarite is typical for Vllahi polymetallic mineralization, where it forms needle like crystals disseminated in carbonates or as intergrowths with marcasite. Siegenite and intermediate members between siegenite and violarite usually form euhedral crystals in association with millerite and gersdorffite as well as inclusions in galena. Chemical composition of that phases is different. Violarite is enriched in Co up to 4.15 wt.%. Siegenite is usually close to ideal composition whereas siegenite from Melenica is enriched in Fe up to 9.78 wt.%. Polydymite is enriched in Co up to 6.38 wt.%. Chemical variation of thiospinels is presented on figure 3.

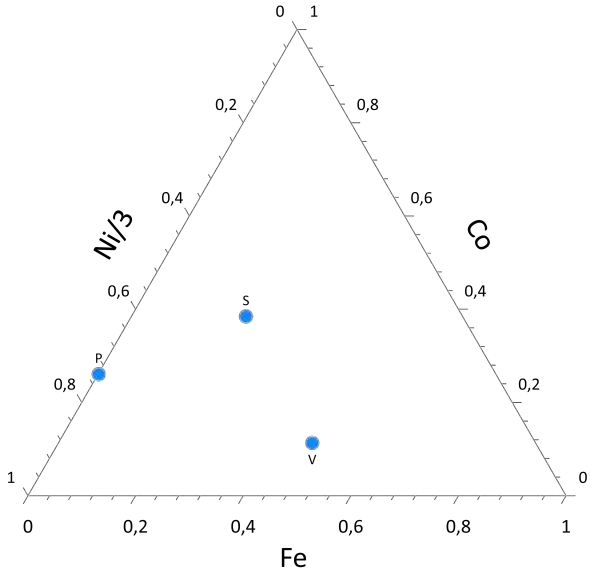

Figure 3. Chemical variation of thiospinels as a function of a ternary plot in terms of Ni/3, Fe, Co. S – Siegenite (n=8), P-Polydymite (n=1), V – Violarite (n=7).

5 Discussion

Ni mineralization in this area is described for the first time. Our research gives information about the composition, structures, textures, relationship between nickel bearing phases and other ore minerals. Nickel mineralization identified in the area has a broad diversity in mineral phases as well as chemical compositions. A similar paragenesis and association were identified in the other part of Kosovo in the same listwaenite type of mineralization (Radosavljević et al. 2015). They described millerite, niccolite, gersdorffite-ullmannite series and bravoite from Crnac, Rogozna Mountains, Northern Kosovo.

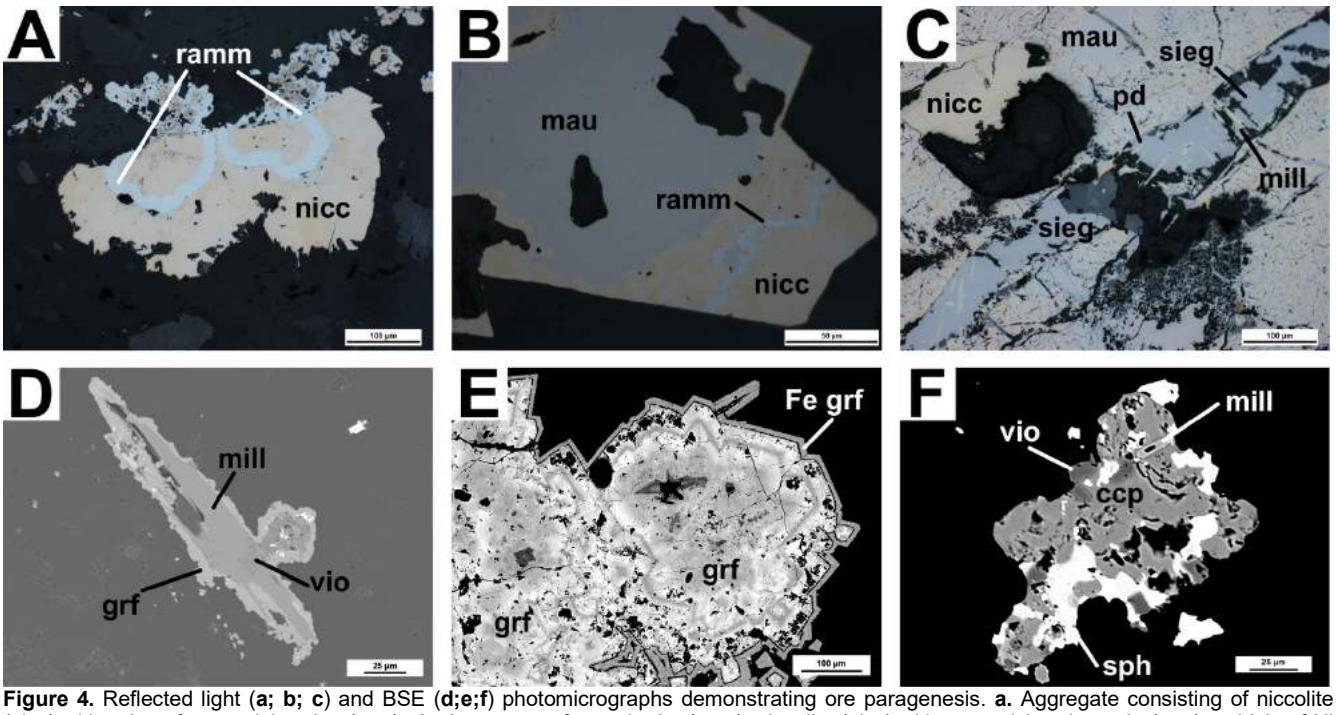

Figure 4. Reflected light (**a; b; c**) and BSE (**d;e;f**) photomicrographs demonstrating ore paragenesis. **a.** Aggregate consisting of niccolite (nicc) with veins of rammelsbergitte (ram). **b.** Aggregate of maucherite (mau), niccolite (nicc) with rammelsbergitte vein (ram). **c.** Vein of Ni sulphides cut Ni arsenides: siegenite (sieg), millerite (mill), polydymite (pd). **d.** .Millerite (mill) needle replaced by gersdorffite (grf) with small inclusion of violarite (viol). **e.** Zonal gersdorffite with zones of Sb bearing gersdorffite (grf) and Fe bearing gersdorffite (Fe grf). **f.** Idiomorphic crystal of millerite (mill) with violarite (viol) chalcopyrite (ccp) and sphalerite (sph) in polimineral aggregate.

Similar Ni mineralization was described for the Kamariza Mining District, Lavrion, Greece. Authors described zoned gersdorffite in association with galena, pyrite and arsenopyrite. The gersdorffite displays oscillatory zoning in terms of Fe, Ni, and As contents, varying from ~1.5 to 9.0 wt.%, ~24 to 32 wt.% and 47 to 60 wt.%, respectively. There is an almost perfect linear correlation between Fe–Ni and As–S in the gersdorffite structure. Additionally gersdorffite from the Clemence deposit contains up to 0.2 wt.% Se, which likely substitutes for sulfur in the structure. At the "km3" locality, gersdorffite contains ~0.5–2 wt.% Fe, 46–48 wt.% As, and ~31–34 wt.% Ni. Millerite (NiS) was found in association with gersdorffite as small inclusions or as euhedral needle-shaped crystals enveloped by galena . As-bearing ullmannite, Ni(Sb,As)S, occurs as inclusions in gersdorffite, whereas vaesite (NiS_2) rims gersdorffite. Cobalt (of up to 0.35 wt.%) substitutes for Ni in vaesite and millerite (Voudouris et al. 2018). Samples from Stan Terg have a similar trend in Fe-Ni-As contents. The main differences between these areas is a lack of vaesite at Stan Terg. From all published data, it is clearly seen that nickel mineralization in the listwaenite rocks is nearly identical with similar trend in chemical composition of main phases.

Acknowledgements

This research was funded by AGH-UST Rector Grant assigned to Studenckie Koło Naukowe Geologów. We are very grateful to Adam Włodek from the Laboratory of Critical Elements at AGH-UST, Faculty of Geology, Geophysics and Environmental Protection for help during EMPA data collection.

References

Hyseni M, Durmishaj B, Fetahaj B, Shala F, Berisha A, Large D (2010) Trepça Ore Belt and Stan Terg mine – Geological overview and interpretation, Kosovo (SE Europe). Geologija 51:87-92.

Kołodziejczyk J (2016) Mineralogical and geochemical diversity within the Stan Terg deposit, Kosovo. PhD thesis. Kraków, 219.

Kołodziejczyk J, Pršek J, Voudouris P, Melfos V, Asllani B (2016) Sn-Bearing Minerals and Associated Sphalerite from Lead-Zinc Deposits, Kosovo: An Electron Microprobe and LA-ICP-MS Study. Minerals 6,42:17.

Radosavljević S, Stojanović J, Vuković N, Radosavljević-Mihajlović A, Kašić V (2015) Low-temperature Ni-As-Sb-S mineralization of the Pb (Ag)-Zn deposits within the Rogozna ore field, Serbo-Macedonian Metallogenic Province: Ore mineralogy, crystal chemistry and paragenetic relationships. Ore Geol Rev 65: 213-227.

Szczygieł A. (2017) Ni mineralization in the Veles Zone (Kosovo). MSc thesis. Kraków, 65.

Voudouris P, Mavrogonatos C, Rieck B, Kolitsch U, Spry P, Scheffer C, Tarantola A, Vanderhaeghe O, Galanos E, Melfos V, Zaimis S, Soukis K, Photiades A (2018) The Gersdorffite-Bismuthinite-Native Gold Association and the Skarn-Porphyry Mineralization in the Kamariza Mining District, Lavrion, Greece

Iron-oxide ores in the Takab region, North Western Iran

Beate Orberger
GEOPS, Université Paris Saclay, France

Christiane Wagner, Omar Boudouma, Colette Derré, Michel Fialin, Nicolas Rividi
Sorbonne Université, CNRS-INSU, Institut des Sciences de la Terre de Paris, France

Johan Villeneuve, Etienne Deloule
Centre de Recherches Pétrographiques et Géochimiques, France.

Ghasem Nabatian
University of Zanjan, Iran

Maryam Honarmand, Iman Monsef, Abdolreza Ghods
Institut of Advanced Studies of Basic Sciences, Zanjan, Iran

Abstract. The siliceous iron ore deposits in the NW part of Iran (Takab region) are hosted within para-metamorphic rocks, and are attributed to a Late Proterozoic age. They comprise massive, banded, nodular and disseminated ore types, which are mainly composed of magnetite. Magnetite contains traces of Al. It is variously hematized. Hematite shows higher Al, Si and Ca contents than the magnetite. The iron oxides contain inclusions of zircon, apatite, uraninite, Mn-carbonate and euhedral monazite. Later hydrothermal solutions precipitated goethite surrounding the magnetite-hematite-maghemite grains and replacing hematite. Barite occurs in fractures of iron oxides, Mn-Ba-Pb oxy-hydroxides and scheelite occur interstitial to iron oxides. The ∂^{56}Fe values observed for magnetite decrease from disseminated to nodular iron ore, averaging +1.3, +0.4 and -0.4 ‰ (± 0.2 ‰), respectively. Iron isotopes of hematite in disseminated and layered ore show higher ∂^{56}Fe values than those of magnetite, in the range of +2 to +4 ‰ (± 0.2 ‰). Volcano sedimentary primary processes are thus superposed by a secondary (magmatic?) hydrothermal process.

1 Introduction

Iran's annual iron ore export reaches about 23.5 million tonnes. Over 90% is exported to China. Projections to 2025, indicates that iron ore production will triple, up to 66.2 MT (Hastorun et al. 2016). Most of the iron deposits are located in the northeastern and central part of Iran, while iron ore deposits of the northwestern part are still unstudied. Here we present results from the Takab Iron ore NW of Zanjan. Our study comprises mineralogy, geochemistry and Fe-isotopic composition.

2 Geological setting

In the Takab region, two types of iron ore deposits occur: (1) related to the Sanandaj-Sirjan Zone: their formation possibly related to the back-arc extension during the Prototethys subduction beneath the Cadomian magmatic arc (Ghorbani 2013; Nabatian et al. 2015). (2) South of Takab: Meso-to Cenozoic: iron oxide–apatite deposits of Kiruna-type are associated with plutonic rocks (Nabatian 2012; Nabatian et al. 2013). The latter present multiple vein deposits <1000 t of iron ore. At present, the Morvarid and Sorkhe-Dizaj deposits (400 000 t) are mined.

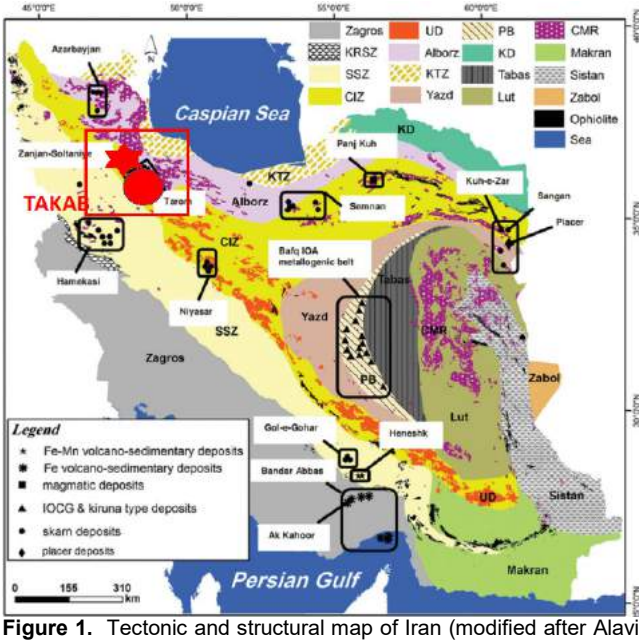

Figure 1. Tectonic and structural map of Iran (modified after Alavi 1991; Aghanabati 1998; 2005). The location of the study area is shown the red square, red star: volcanosedimentary iron ore, red dot: Kiruna type iron ores.

The mineralization forms thin layers and lenses interlayered with quartzite and amphibolites (Nabatian et al. 2015). In the study, the iron oxide mineralogy is essentially described as hematite and goethite, with barite as an accessory mineral. The age of the iron may be Late Proterozoic (Ghorbani et al. 2013).

3 Analytical methods

Optical microscopy in transmitted and reflected light

modes, SEM and electron microprobe analyses were performed on polished thin sections at the Centre Camparis, Sorbonne Université, UPMC Univ Paris 06, Paris, France. X-Ray diffraction was carried out at GEOPS, Université Paris Saclay, Orsay, France. Iron isotope measurements were performed by SIMS at CRPG (Nancy), and elemental geochemistry at SARM, CRPG, Nancy (XRF, ICP-MS).

4 Results

4.1 Petrology and mineralogy

The studied samples are massive, banded and nodular iron ores; disseminated ore is also present (Fig. 2). Massive, banded and nodular ore occurs as decimetric layers within folded mica schist.

The host rocks of the massive magnetite are epidotized, amphibolitized, chloritized fine grained plagioclase-rich rocks, crosscut by veins of magnetite and carbonate. These rocks may represent metavolcanic rocks (basalts). X-ray diffraction on banded and nodular ore samples indicates that all samples contain similar major mineralogy quartz, magnetite, hematite, maghemite, goethite in different proportions. Small peaks are attributed to barite ($BaSO_4$). The magnetite and hematite host traces of Al (< 0.5 wt. %). Goethite hosts variable amounts of Al (up to 0.7 wt. %), Si (up to 1.7 wt. %) and Ca (up to 0.2 wt. %).

The banded ore shows coarse and discontinuous banding with interstitial quartz (Fig. 2A). Magnetite forms individual grains (~50 µm to several hundreds of µm), hosting detrital zircons (sometimes corroded) and droplet-like inclusions of PbS and ZnS. It is partly altered to hematite. Iron oxide veins occur perpendicular to the iron oxide bands. Goethite is abundant around hematized magnetite and in veins, sometimes hosting pyrite relics and P-bearing minerals. In the matrix, apart from quartz, Mn-Ba-oxides and barite (partly replacing Ba-feldspar - hyalophane) and, rare uraninite occur. The matrix quartz grains show undulose extinction, indicating deformation.

The nodular ore is composed of mm-sized iron oxide agglomerates, partly elongated and disrupted in the quartz matrix (Fig. 2B). Other matrix minerals correspond to those in the layered ore. Magnetite is not hematized. It hosts inclusions of phosphates, Mn-and Fe- carbonates and uraninite.

In the disseminated ore, magnetite forms euhedral grains (~400 µm-1.5 mm), which are slightly hematized. The matrix minerals are quartz, minor K-feldspar and phengite. The feldspars host P (U, Th)-bearing phases, zircon and barite. Rutile, phosphates, scheelite, barite also occur interstitial to the matrix grains.

A Banded

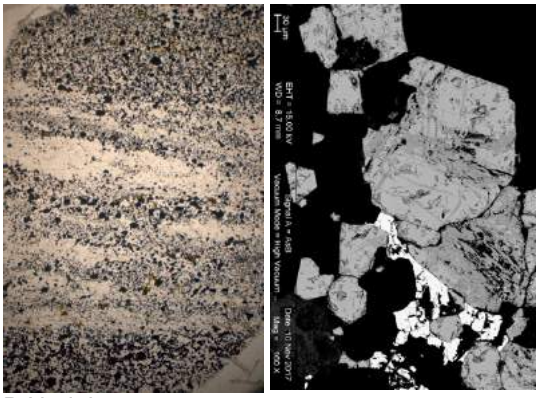

B Nodular

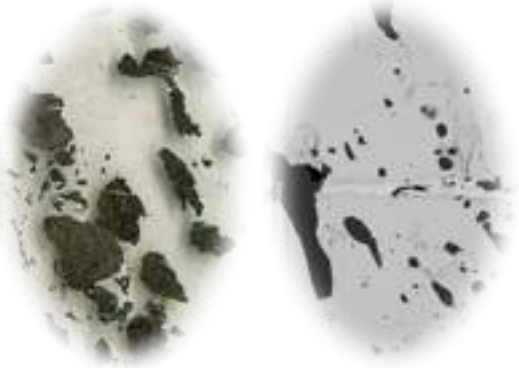

C Disseminated

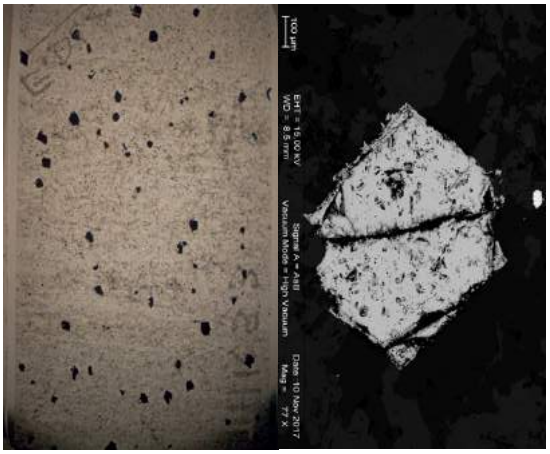

Figure 2. Polished thin section scans. **a.** Banded iron ore: alternating quartz and iron oxide bands and subhedral magnetite grains partly hematized; **b.** Nodular iron ore in quartz matrix**;** magnetite shows minor hematitization; **c.** Disseminated iron ore with euhedral magnetite grains

4.2 Geochemistry

The massive magnetite contains 77 wt.% total iron (Fe_2O_3) of which 22.5 wt.% of FeO. It is silica rich (14 wt.% SiO_2), and contains 1.7 wt.% Al_2O_3, 2,7 wt.% CaO and 0.35 wt.% CO_2. MnO and TiO_2 are low (0.08 wt.% and 0.05 wt.%, respectively). Trace elements comprise

50 ppm Cu, 80 ppm Co, 88 ppm W, 14 ppm V, 25 ppm Sn, 40 ppm Zn and 30 ppm Zr. Arsenic and U are low (7 and 1 ppm respectively). The host rocks of the massive magnetite, the epidotized metabasalts contain about 54 wt.% SiO_2, 10 wt.% Al_2O_3, 9.8 wt.% total iron (Fe_2O_3), with two third FeO (6.6 wt.%), 7.7 wt.% MgO, 8.8 wt.% CaO and 3.2 wt. % Na_2O. TiO_2 reaches 0.5 wt.%. Arsenic and U are as low as in the massive magnetite however, the host rock is richer in Cr (270 ppm), Ni (70 ppm), V (132 ppm), Sc (25 ppm) Sr (170 ppm) and Ba (440 ppm).

The banded ore hosts variable iron contents (13-53 wt.% total Fe_2O_3, 0.56-12 wt.% FeO). Silica (SiO_2) ranges from 44 to 57 wt.%, Al_2O_3 from 0.08 to 0.33 wt.%. CO_2 contents are low, however S reaches up to 4.6 wt.% (barite). Barium is highest in this ore type (3300 ppm to about 15 wt.%). Traces such as As, Mo, V, Zn are also higher than in other ore types (≤80 ppm, ≤ 12 ppm, ≤ 84 ppm, ≤110, respectively).

The nodular ore is high in Fe_2O_3 (60 wt.%) and FeO (11 wt.%) and low in Al_2O_3 (0.1 wt.%). Pb, Zn (1000 ppm) and Cd (60 ppm) are higher than in other ore types. Ba is low (<2000 ppm), As and V similar than the other ore types.

The disseminated ore is rich in SiO_2 (70-79 wt.% SiO_2), Total iron (Fe_2O_3) varies from 6 to 20 wt.% (0.9-4.6 wt.% FeO). Al_2O_3 reaches 14 wt.% in iron poor rocks, and is <0.2 wt.% in iron rich rocks. Arsenic reaches 31 ppm, while U is < 2 ppm. Barium contents range from 900 to 2450 ppm, Rb from 20 to 370 ppm, Zr from 50 to 250 ppm, V from 6 to 39 ppm and W from 38 to 122 ppm.

Rare-Earth-Element + Yttrium composition: PAAS normalized REE+Y patterns of the studied samples are shown in figure 3**.** All samples show a strong positive Y anomaly, and, except for the massive magnetite and calcschist, a positive Eu anomaly. The massive magnetite shows a positive Ce anomaly and a strong enrichment in HREE. The banded ores show variable REE+Y (PAAS normalized) patterns. Most ore samples are characterized by an HREE enrichment and LREE depletion except for one banded ore (23). Banded and nodular ores show both negative and an absence of Ce anomalies. The calcschist has a negative Ce anomaly. The Ba rich layered ore exhibits the lowest LREE. The Y/Ho varies between 23.2 and 40. Highest values are observed in nodular ores (24: 40,4) and calcschist (35), most oscillate around values typical for shales (25-27).

4.3 Iron- and oxygen isotope geochemistry

All ore types were analyzed for ∂^{56}Fe (Fig. 4). In the banded ore, the magnetite is characterized by ∂^{56}Fe (-0.3 to +1 ‰ ± 0.2 ‰) and variable ∂^{18}O (-2 to +2 ‰).

The ∂^{56}Fe values observed for magnetite decrease from disseminated to nodular iron ore averages: +1.3, +0.4 and -0.4 ‰ (± 0.2 ‰), respectively. Iron isotopes of hematite in disseminated and layered ore show higher ∂^{56}Fe values than those of magnetite, in the range of +2 to +4 ‰ (± 0.2 ‰).

In the nodular ore, the magnetite is characterized by ∂^{56}Fe (-1 to +0.5 ‰ ± 0.2 ‰) and ∂^{18}O between +4 to +6 ‰.

In the disseminated ore, the magnetite is characterized by ∂^{56}Fe (+0.7 to +2 ‰ ± 0.2 ‰) and ∂^{18}O between 0.5 ‰ and +4 ‰.

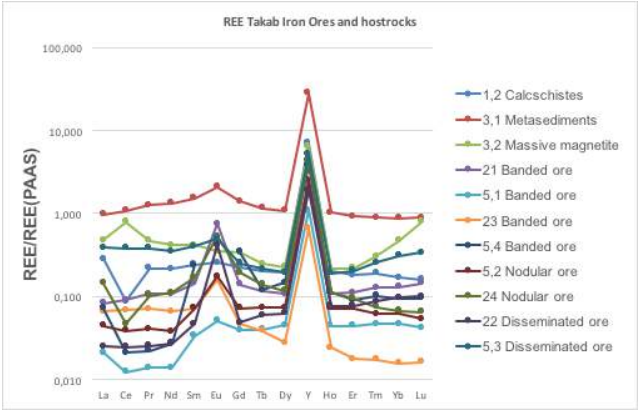

Figure 3. REE+Y PAAS-normalized patterns of the studied samples.

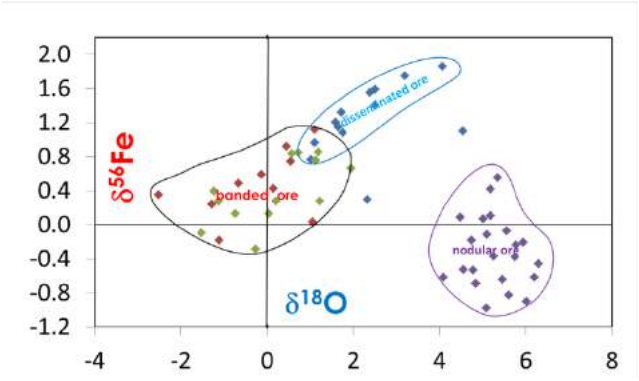

Figure 4: ∂^{56}Fe versus ∂^{18}O (‰) of the studied samples.

5 Discussion and conclusions

Petrological and mineralogical studies (Orberger et al. 2017) showed that primary magnetite ore is banded and crystallized statically from an iron and silica rich solution. Zircon, apatite, Mn-carbonates, uraninite and monazite were included during this step in the initial iron oxide, magnetite. Based on REE + Y compositions it can be concluded that reducing seawater with a contribution from hot hydrothermal solutions is the source of magnetite ores.

Regional deformation is indicated by grain boundary migration during the recrystallization of quartz grains. The nodular ore most likely represents a highly deformed banded iron ore, where magnetite bands were disrupted and recrystallized. Sulphides were present at that state. Oxidizing fluids accompanied this step and transformed the magnetite into maghemite and hematite. (3) Aqueous solutions carrying Mn, Ba, Pb, Ca, W, S,

CO_2 led to the formation of goethite and Mn-Ba-Pb oxy-hydroxides and associated scheelite and barite. This episode is most likely contemporaneous to the W mineralisation in this region (Ghorbani 2013).

This scenario is supported by increasing ∂^{56}Fe and ∂^{18}O with progressive oxidation from banded, nodular to disseminated magnetite reaching highest values in hematite (Orberger et al. 2018). A shift in ∂^{56}Fe towards positive values in oxidizing environments was also observed for example by Rouxel et al. (2008).

Acknowledgements

We thank the Institute of Advanced Sciences of Basic Science and University of Zanjan, Zanjan for logistic support during fieldwork and the stay of BO in Zanjan. Campus France and the French embassy (Gundishapur program 2017-2019) are thanked for financing the stay of BO at IASBS, Zanjan. The UMR7193 ISTeP, UPMC is thanked for financial support of the analyses.

References

Aghanabati A (1998) Major sedimentary and structural units of Iran (map). Geosciences 7:29-30.

Aghanabati A (2005) Geology of Iran. Geological Survey of Iran (Persian book), Teheran, Iran, 538 pp.

Alavi M (1991) Sedimentary and structural characteristics of the Paleo-Tethys remnants in north eastern Iran. Geological Society of America Bulletin 103:983-992.

Hastorun S, Renaud KM, Lederer GW (2016) Recent trends in the nonfuel minerals industry of Iran: U.S. Geological Survey Circular 1421:18.

Ghorbani M (2013) The Economic Geology of Iran: Mineral Deposits and natural ressources. Springer Dordrecht Heidelberg New York, 569 pp.

Nabatian Gh (2012) Geology, geochemistry and evolution of ironoxide-apatite deposits in the Tarom volcano-plutonic belt, western Alborz. Unpublished PhD thesis, Tarbiat Modares University, Tehran, Iran, 375 pp.

Nabatian Gh, Ghaderi M, Dalirian F, Rashidnejad-Omaran, N (2013) Sorkhe-Dizaj iron oxide-apatite ore deposit in the Cenozoic-Azarbaijan magmatic belt, NW Iran. Resource Geology 63:4256.

Nabatian G, Rastad F, Neubauer F, Ghaderi, M (2015) Iron and Fe–Mn mineralisation in Iran: implications for Tethyan metallogeny. Australian Journal of Earth Sciences, 62:2, 211-241.

Orberger B, Wagner C, Boudouma O, Villeneuve J, Deloule E, Fialin M, Nabatian Gh, Honarmand M, Moussef I, Ghods A (2018) Mineralogy and Fe-isotopic composition of iron-oxide ore from the Takab region, North Western Iran. IMA2018-1213.

Rouxel O, Shanks WC, Bach W, Edwards KJ (2008). Integrated Fe-and S isotopes study of seafloor hydrothermal vents at East Pacific Rise 9-10°. Chemical Geology 252:214-227.

Geochemistry of hematite veins in IOA-IOCG deposits of SE Missouri, USA: relation to felsic magmatism and caldera lakes

Corey J. Meighan, Albert H. Hofstra, Erin E. Marsh, Heather A. Lowers, and Alan E. Koenig
U.S. Geological Survey, USA

Abstract. The paragenesis, textures, and chemical compositions of secondary hematite in regional potassic altered rhyolites, four IOA deposits, the sedimentary iron deposit at Pilot Knob and the Boss IOCG deposit in SE Missouri were determined and compared to primary magnetite from the IOA and IOCG deposits. Magnetite is composed of elements characteristics of mafic to intermediate intrusions whereas hematite is enriched in elements characteristic of felsic igneous rocks. These results suggest that magnetite formed from fluids discharged from mafic to intermediate composition intrusions. Hematite precipitated from fluids discharged from felsic intrusions or fluids that evolved in caldera lakes. Hematite in the sedimentary iron deposit at Pilot Knob formed in an evaporative caldera lake with fluid inputs from felsic intrusions.

1 Introduction

The Mesoproterozoic St. Francois Mountains terrane in SE Missouri, USA, contains several iron-oxide-apatite (IOA) ± rare earth element (REE) deposits and one iron-oxide-copper-gold±cobalt (IOCG±Co) deposit. Many of these deposits seem to correspond to the magmatic magnetite-dominated endmember of the IOA-IOCG class, however hematite domains are present locally. In addition, a hematite-dominated sedimentary iron deposit is juxtaposed with a typical magnetite IOA deposit in the Pilot Knob area. The origin of the hematite domains and the sedimentary iron deposit and their genetic relations with IOA-IOCG deposits are poorly defined.

2 Geology

In the St. Francois Mountains terrane, 1.4 Ga igneous rocks are principally subalkaline/ferroan rhyolite ignimbrites and flows, underlain by coeval granite plutons, but also include volumetrically minor tholeiitic basaltic andesite and dacite. Geologic and geochemical relations suggest that these rocks are rift related (Day et al. 2017, and E. du Bray, U.S. Geological Survey, written communication 2018).

The Pea Ridge, Bourbon, and Lower Pilot Knob IOA deposits are all hosted within high-silica rhyolite tuffs or flows (Panno & Hood 1983; Seeger et al. 2001). In contrast, both the Iron Mountain IOA and Boss IOCG deposits are hosted in mafic to intermediate intrusions that are either interlayered with or intrude high-silica rhyolite tuffs (Murphy & Ohle 1968; Seeger 2003). The surficial sedimentary hematite deposit at Upper Pilot Knob is hosted in a coarsening-up sequence of moat sediments, which includes finely laminated siltstones and overlying agglomerates.

Pea Ridge is enclosed and underlain by inferred granitic intrusions surrounded by an annular mafic to intermediate composition intrusion (Day et al. 2016). Bourbon is located near, and partially surrounded and underlain by, the same ring intrusion. Boss, also enclosed and locally cut by inferred granite intrusions, is located ~40 km SW of Pea Ridge and Bourbon. Both Iron Mountain and the two iron deposits in the Pilot Knob area are located along the margins of a caldera ~40 km E of Boss.

IOA deposits consist of magnetite ore bodies that contain lesser amounts of amphibole, apatite, phlogopite, and chlorite. In many cases, these deposits are characterized by magnetite-cemented, amphibole-rich alteration domains adjacent to or enveloped by massive magnetite ore bodies. Silicified and potassically altered zones overprint and surround many of these deposits. Iron Mountain is largely overprinted by hematite alteration and Pea Ridge is altered to hematite near crosscutting REE-enriched breccia pipes. Only minor, hematite infill and/or replacements are observed at Bourbon and the Lower Pilot Knob deposit.

The Boss IOCG deposit is characterized by potassic, propylitic, and phyllic alteration zones. Magnetite-cemented breccias and veins host copper mineralization that is associated with biotite, muscovite, and chlorite (Seeger 2003). Amphibole-rich alteration is rare. Several hematite-cemented breccias occur along the western part of the domical deposit.

3 Samples and methods

Regional potassic altered rhyolite tuffs and flows were sampled in the Ironton (i.e., Grassy Mountain, Lake Kilarney, and Royal Gorge) and Eminence areas (Upper and Lower Coot Mountains and Stegall Mountain). Some of the regional samples are more proximal to known iron deposits than others. Hematite and magnetite samples were collected at the Pea Ridge, Bourbon, Iron Mountain, Boss, and

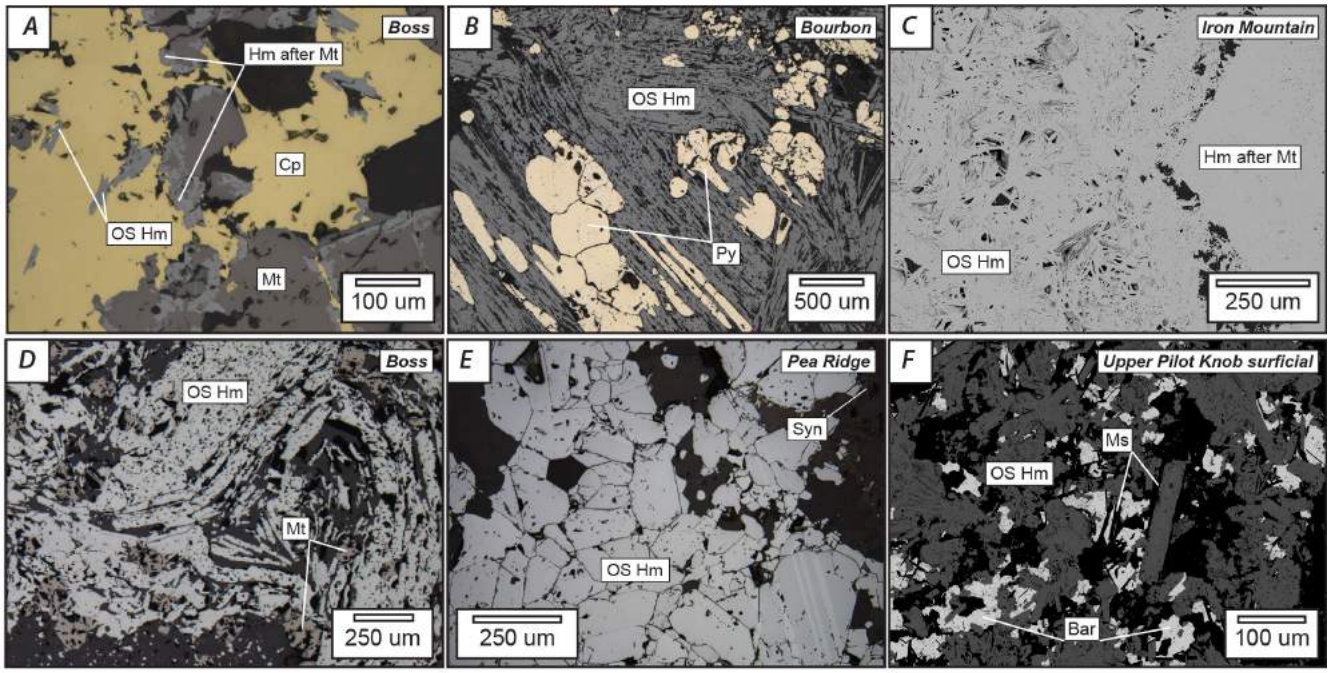

Figure 1. Reflected light and secondary electron microscopy-backscatter electron (SEM-BSE) images showing hematite textures from assemblages 4 and 5. See text for details. Bar=Barite, Cp=Chalcopyrite, Hm=Hematite, Mt=Magnetite, Ms=Muscovite, Py=Pyrite, OS=Open Space, Syn=Synchysite.

Upper and Lower Pilot Knob iron deposits. Hematite and magnetite were identified by reflected light microscopy and analyzed via scanning electron microscopy-backscatter electron (SEM-BSE) imaging, electron microprobe (EMP), and laser ablation-inductively coupled plasma-mass spectrometry (LA-ICP-MS; Longerich et al. 1996). Iron contents from EMP were used as internal standards for LA-ICP-MS analysis. LA-ICP-MS data were reduced to remove the effects of mineral inclusions however some anomalous element enrichments in hematite may reflect mineral inclusions. Both magnetite and hematite were analyzed using the same suite of elements.

Results generated by EMP and LA-ICP-MS analysis were plotted on the Al+Mn vs. Ti+V discrimination diagrams of Nadoll et al. (2014) and multi-element variation diagrams of Dare and Barnes (2014).

4 Petrography of hematite assemblages

In regional rhyolites, either distal or proximal to iron mineralization, magnetite and ilmenite phenocrysts are commonly pseudomorphically replaced by submicron-sized hematite and rutile. In potassically altered rhyolites, the pseudomorphs are recrystallized and grain size and porosity increase. Euhedral 25-500 µm hematite laths and or spongy 2-20 µm hematite aggregates fill some cavities. This generation of hematite is associated with K-feldspar ± hematite-muscovite-quartz and is referred to as assemblage 1 (A1).

In IOA-IOCG deposits, hematite is restricted to assemblage 4 (A4), which consists of hematite-chlorite ± sulfides-muscovite-quartz-fluorite-carbonate-epidote-garnet-amphibole and assemblage 5 (A5), which consists of hematite ± barite-carbonate-K-feldspar-muscovite-chlorite-quartz-REE phosphates. A4 is most likely a combination of propylitic and phyllic alteration, whereas A5 most likely represents hydrolytic alteration. A key distinction is that A4 hematite is associated with sulfides (pyrite ± chalcopyrite) and A5 hematite is associated with barite. A4 typically crosscuts all of primary magnetite-bearing assemblages in the IOA deposits, whereas A5 overprints all of the other stages.

A4 hematite forms 50-750 µm needle-like laths intergrown with sulfides (Fig. 1a, b), locally is zoned, subhedral to anhedral, and forms 25-100 µm crystals intergrown with rutile. These grains are typically recrystallized and or overgrown by coarser grained hematite that is rutile-poor. A5 hematite typically consists of platy laths that fill open spaces; some individual grains are ≥500 µm (Fig. 1d, e). Both A4 and A5 hematite completely or partially replaces preexisting fine- to coarse-grained, euhedral to anhedral, 15-1500 µm magnetite, especially along grain boundaries and/or in inclusion-rich magnetite cores (Fig. 1a, c). Nano- to micrometer mineral inclusions are also present in open space filling A1, A4, and A5 hematite. In laminated and agglomerate iron ore at Upper Pilot Knob, A5 hematite consists of fine-grained, ≤100 µm, aggregates and coarser laths that are often intergrown with barite and muscovite (Fig. 1f).

5 Hematite trace element chemistry

Open space filling (OS) hematite was analyzed to avoid chemical contamination from preexisting magnetite.

On the Al+Mn vs. Ti+V discrimination diagram of Nadoll et al. (2014), compositions of OS hematite from A4 and A5 form two broad arrays. Each array extends

from the magmatic Fe-Ti and V deposit field into the hydrothermal Porphyry, Kiruna, IOCG, Skarn, and BIF fields (Fig. 2). But, A5 hematite generally plots above A4 hematite, which may suggest that hematite formed by multiple fluid inputs and that most hematite formed at low temperature. A5 hematite from Upper Pilot Knob forms another array between A5 and A4, which may imply mixing between fluids that produced the upper and lower arrays. Compositions of A1 and A5 hematite overlap, indicating similar fluid.

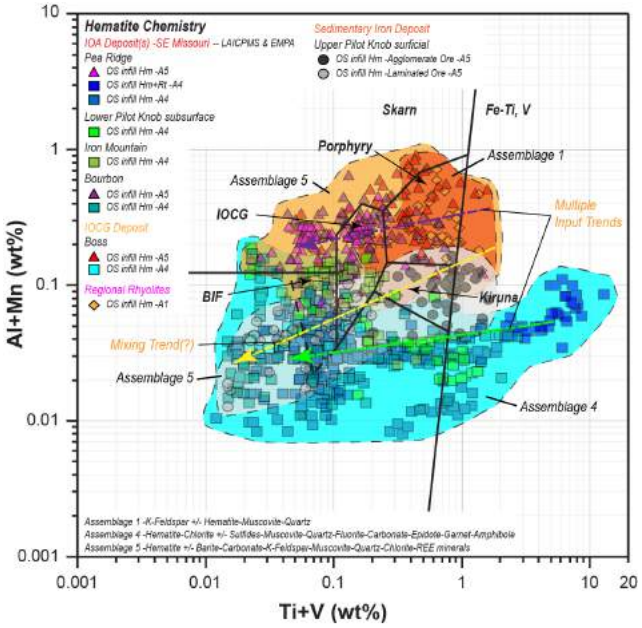

Figure 2. Open space hematite from IOA-IOCG deposits and Upper Pilot Knob in SE Missouri. See text for details. Hm=Hematite, OS=Open Space.

The trace element chemistry of OS hematite is compared to that of primary magnetite on the multi-element variation diagrams of Dare and Barnes (2014) that are normalized to bulk continental crust values from Rudnick and Gao (2003). On these diagrams, A1, A4, and A5 hematite are also compared to one another.

Trace element-normalized patterns of inclusion-poor magnetite from amphibole- and magnetite-dominated alteration zones in IOA-IOCG deposits consist of a similar group of elements, typically V, Mn, Zn, Co, Ga, Ni, Ti, Mg, P, and Al with lesser amounts of Cr, Th, and U (Fig. 3a). Hematite is enriched in a distinctly different group of elements including; Sn, Sb, Mo, Nb, Ta, U, W, Pb, Th, Zr, and Hf, with lesser amounts of La, Ce, Y, Cu, Ba, Sr, K, Cs, Rb, and Si (Fig. 3b, c, d). Many of the elements present in hematite are often below detection limits in magnetite.

A1 hematite, characterized by Mo, Sb, Pb, Th, and Cs with lesser Rb, Ba, and K enrichments and lacking significant Cu, Co, and Ni, is most similar to A5 hematite. In addition to the aforementioned elements in A1, A5 hematite locally contains Ni, lacks Zn and Cs, and contains no significant enrichments in Pb or Th. A4 hematite contains minor Zn, Co, and Cu enrichments, but lacks significant enrichments in Zr, Hf, Mo, Sb, K, Cs, Rb, and Ba. Al is more enriched in A5 than in A4. The element enrichment pattern of laminated and agglomerate A5 hematite from Upper Pilot Knob is similar to A5 hematite from IOA-IOCG deposits, but it is more enriched in U, Mo, and Sb within the laminated ore. Minor differences in trace element enrichments of A1 and A5 hematite compared to A4, including contrasting abundances in Al, may indicate differences in fluid source and/or temperature.

These geochemical signatures suggest that the magnetite in IOA-IOCG deposits precipitated from fluids discharged from mafic to intermediate intrusions. In contrast, A5 hematite precipitated from fluids discharged from felsic intrusions, whereas A4 hematite may have formed from evaporated caldera lake water. Laminated and agglomerate A5 hematite in Upper Pilot Knob formed in an evaporative caldera lake that received inputs of fluid from felsic intrusions.

6 Conclusions

Our results show that hematite has multiple origins distinct from those responsible for magnetite crystallization. Late OS A1 hematite in regional rhyolites is compositionally similar to late A5 hematite in altered rock near REE-enriched breccia pipes at Pea Ridge, hematite-cemented breccias at Boss, and some hematite veins at Bourbon. These hematites all have element enrichments that are consistent with fluids derived from felsic intrusions, including a perhaps more fractionated alkalic intrusion at Pea Ridge (Hofstra et al. 2017). In contrast, A4 hematite alterations at Iron Mountain and locally at Pea Ridge near REE-enriched breccia pipes, along with hematite veins and cavity infill within magnetite ores at Pea Ridge, Boss, Bourbon, and Lower Pilot Knob may be consistent with fluids derived from an evaporative caldera lake. At Upper Pilot Knob, evaporative lake water may have received inputs of fluids associated with felsic intrusions. Most of the iron in hematite was likely remobilized from preexisting IOA-IOCG deposits and or nearby mafic to intermediate intrusions. In summary, the hematite alteration zones in IOA-IOCG deposits and the sedimentary iron deposit at Upper Pilot Knob are related to felsic magmatism and perhaps evaporated caldera lake water, whereas magnetite is associated with mafic to intermediate composition intrusions.

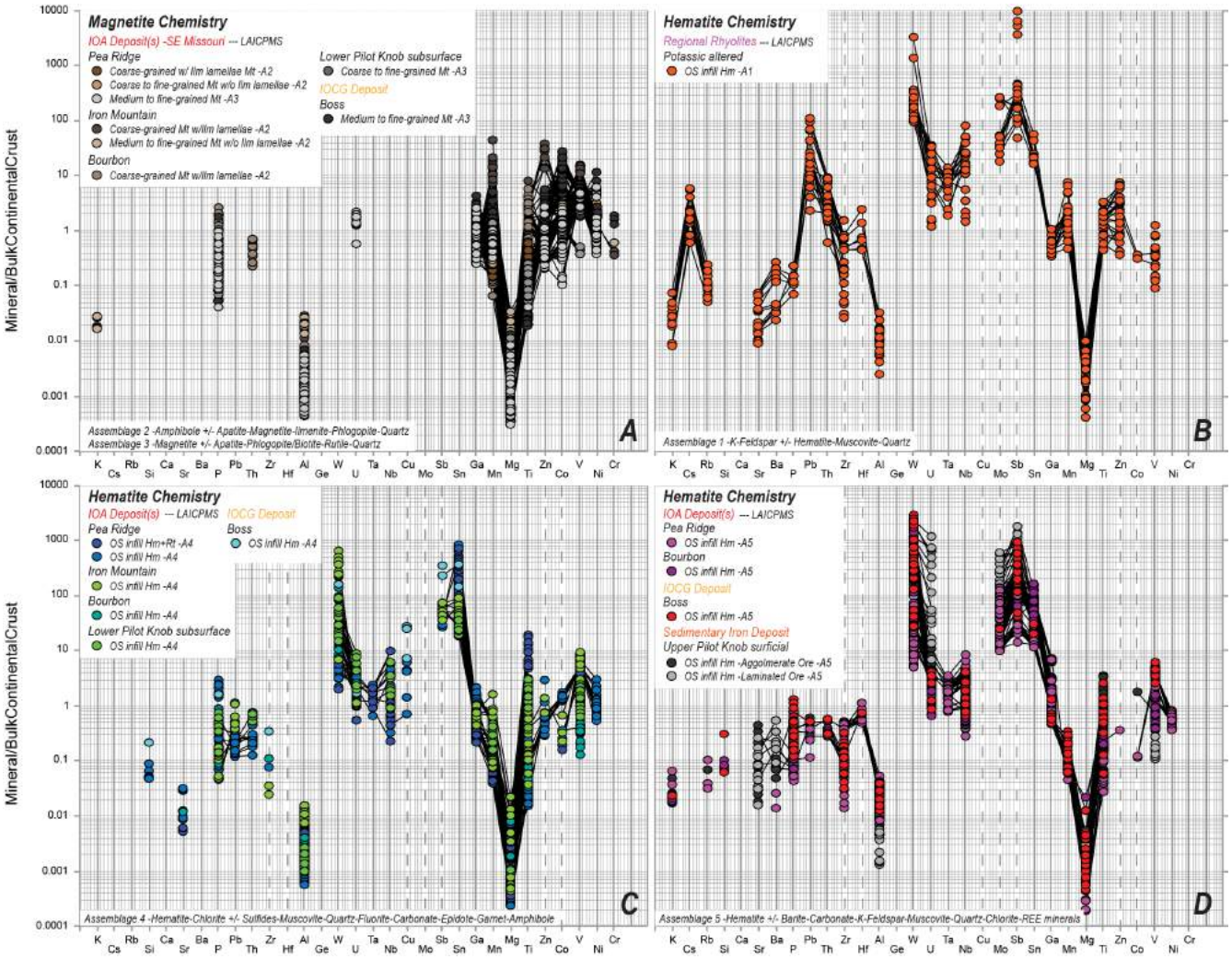

Figure 3. A. Magnetite data from IOA-IOCG deposits **B.** A1 hematite data from regional potassic altered rhyolites **C-D.** A4 and A5 hematite data from IOA-IOCG deposits and Upper Pilot Knob. See text for details. Hm=Hematite, Ilm=Ilmenite, Mt=Magnetite, OS=Open Space.

References

Dare SAS, Barnes S-J, Beaudoin G, Meric J, Boutroy E, Potvin-Doucet C (2014) Trace elements in magnetite as petrogenetic indicators. Mineral Deposita 49:785-796

Day WC, Aleinikoff JN, du Bray E, Ayuso RA, (2017) Constraints on age of magmatism and iron oxide-apatite (IOA) and iron oxide-copper-gold (IOCG) mineral deposit formation in the Mesoproterozoic St. Francois Mountains terrane of southeast Missouri, USA. SGA Conf. Abstract, 3:855-858

Day WC, Slack JF, Ayuso RA, Seeger CM (2016) Regional geologic and petrologic framework for iron oxide ± apatite ± rare earth element and iron oxide copper-gold deposits of the Mesoproterozoic St. Francois Mountains terrane, SE Missouri, USA. Econ Geol 111: 1825-1858

Hofstra AH, Aleinikoff J, Ayuso R, Bennett M, Day W, du Bray E, Johnson C, McCafferty A, Meighan C, Mercer C, Neymark L, Slack R, and Watt K (2017) Magmatic hydrothermal origin of the Mesoproterozoic Pea Ridge IOA-REE deposit, southeast Missouri, USA. SGA Conf. Abstract, 3:863-866

Longerich HP, Jackson SE, Günther D (1996) Laser ablation inductively coupled plasma mass spectrometric transient signal data acquisition and analyte concentration calculation, J Anal At Spectrom 11:899-904

Murphy JE, Ohle EL (1968) The Iron Mountain Mine, Iron Mountain, Missouri. In: Ridge JD, Ore Deposits in the United States 1933/1967 1: 288-302

Nadoll P, Angerer T, Mauk JL, French D Walshe J (2014) The chemistry of hydrothermal magnetite: a review. Ore Geol Rev 61:1-32

Panno SV, Hood WC (1983) Volcanic stratigraphy of the Pilot Knob iron deposits, Iron county, Missouri. Econ Geol 78:972-982

Rudnick RL, Gao S (2003) Composition of the continental crust. Treatise Geochem 3:1-64

Seeger CM, Nuelle LM, Day WC, Sidder GB, Marikos MA, Smith, DC (2001) Geologic maps and cross sections of the Pea Ridge iron mine, Missouri. U.S. Geological Survey Miscellaneous Field Map MF-2353, scale 1:2,400

Seeger CM (2003) Lithology and alteration assemblages of the Boss iron-copper deposit, Iron and Dent counties, Southeast Missouri. PhD Dissertation University of Missouri-Rolla

Absence of magnetite microlites, geochemistry of magnetite veins and replacements in IOA deposits, SE Missouri, USA: relations to intermediate intrusions

Corey J. Meighan, Albert H. Hofstra, David T. Adams, Erin E. Marsh, Heather A. Lowers, and Alan E. Koenig
U.S. Geological Survey, USA

Abstract. The paragenesis, textures, and chemical compositions of magnetite in two mafic to intermediate intrusions and four IOA deposits in SE Missouri were studied to discriminate between igneous and hydrothermal sources. In this study, we found that replacement magnetite with mineral inclusion-rich cores yields erroneously high Ti, Al, Si, Mg, and Mn contents as determined by EMP and LA-ICP-MS due to rutile and silicate inclusions. Thus, identification of high-Ti microlites on the basis of inclusion-rich cores with high Ti contents is an analytical artefact. Since the high-Ti magnetite microlite flotation model is critically dependent on this type of analysis, it may be invalid.

The presence of coarse-grained high-Ti vein magnetite with ilmenite lamellae enveloped by replacement magnetite with inclusion-rich cores in ore zones suggests that the veins were high-temperature conduits for low-temperature replacement ores. The trace element compositions of vein and replacement magnetite suggest that iron was sourced from mafic to intermediate intrusions. These results support a magmatic-hydrothermal origin for IOA systems in SE Missouri.

1 Introduction

The Mesoproterozoic St. Francois Mountains terrane in SE Missouri, USA, contains several iron-oxide-apatite (IOA) ± rare earth element (REE) deposits for which a variety of genetic models have been proposed. Recently, Simon et al. (2018 and references therein) proposed that IOA deposits form from buoyant aqueous emulsions containing high-Ti magnetite microlites derived from underlying intrusions that are overgrown by low-Ti hydrothermal magnetite at the sites of ore formation. This model pertains to microlites identified at Los Colorados in Chile (Knipping et al. 2015a, b) and Pea Ridge and Lower Pilot Knob in SE Missouri (Childress et al. 2016). Although Hofstra et al. (2016) found no evidence of high-Ti microlites at Pea Ridge and Meighan et al. (2017) show that the high-Ti microlites identified by Childress et al. (2016) are actually hematite-rutile intergrowths inherited from the host rocks, Simon et al. (2018) maintain that the model does apply to deposits that lack microlites because, as Simon et al. (2018) suggest, microlites may be destroyed by subsequent dissolution-reprecipitation processes.

To resolve these inconsistencies and further evaluate the applicability of the microlite flotation model to IOA deposits, we documented the paragenesis, textures, and chemical composition of magnetite in igneous rocks and IOA deposits from SE Missouri and compare the results to those for Los Colorados.

2 Geology

The 1.4 Ga igneous rocks in the St. Francois Mountains of SE Missouri consist of subalkaline/ferroan rhyolite ignimbrites and flows underlain by coeval granite plutons. Although tholeiitic basaltic andesite and dacite are volumetrically minor at the surface, geophysical surveys show they are abundant in the subsurface (McCafferty et al. 2018). Geologic and petrologic relations suggest that these rocks are rift related (Day et al. 2017, and E. du Bray, U.S. Geological Survey, written communication 2018).

The Pea Ridge, Bourbon, and Lower Pilot Knob IOA deposits are hosted in a series of high-silica rhyolite tuffs and flows (Panno & Hood 1983; Seeger et al. 2001). In contrast, the Iron Mountain IOA deposit is hosted in mafic to intermediate intrusions that are either interlayered with or intrude a series of high-silica rhyolite tuffs (Murphy & Ohle 1968). Pea Ridge is enclosed and underlain by inferred granitic intrusions that are surrounded by an annular mafic to intermediate composition intrusion (Day et al. 2016). Bourbon is located near, and is partially surrounded and underlain by, the same ring intrusion. Iron Mountain and Pilot Knob are located along the margin of a caldera ~50 km SE of Pea Ridge and Bourbon.

These IOA deposits are composed mainly of magnetite, apatite, and amphibole with lesser amounts of phlogopite and chlorite. In many places, these deposits are characterized by magnetite-cemented amphibole alteration veins adjacent to or enveloped by massive magnetite ore bodies. Iron Mountain is largely overprinted by later hematite alteration and Pea Ridge is altered to hematite near REE-enriched breccia pipes.

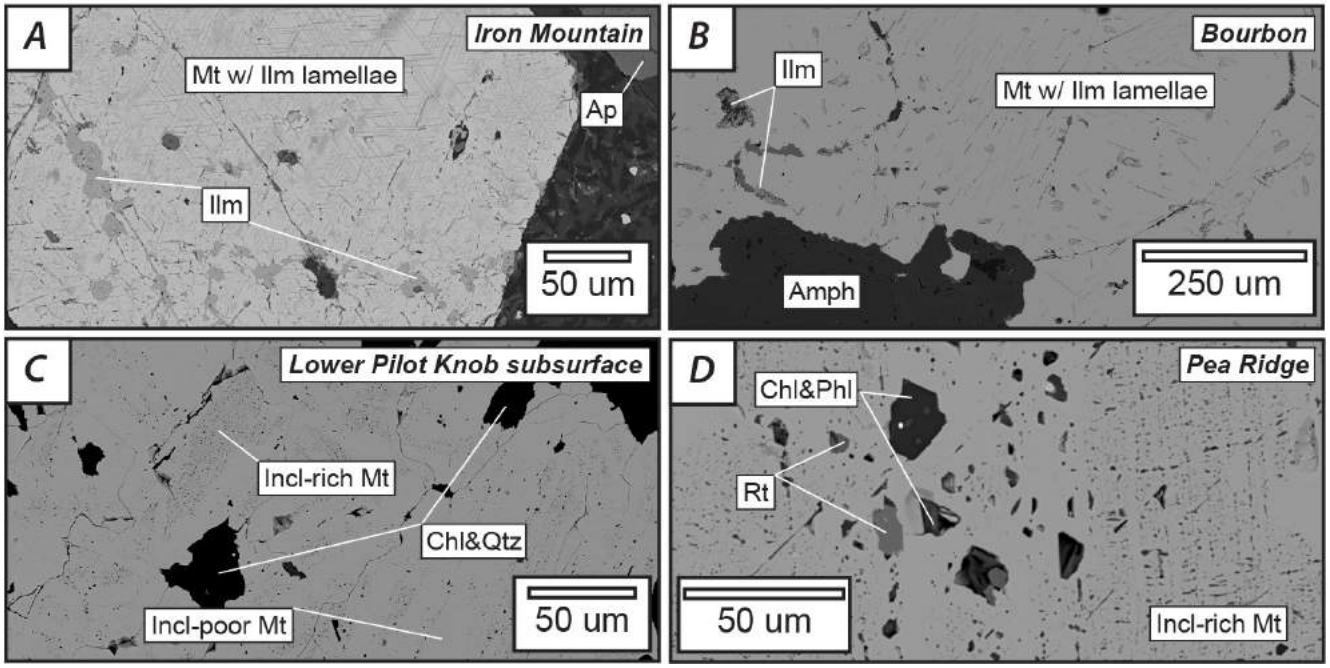

Figure 1. Secondary electron microscopy-backscattered electron (SEM-BSE) images showing magnetite textures from each assemblage. See text for details. Amph=Amphibole, Ap=Apatite, Chl=Chlorite, Ilm=Ilmenite, Mt=Magnetite, Phl=Phlogopite, Qtz=Quartz, Rt=Rutile.

3 Samples, methods, and Monte Carlo simulations

Mafic to intermediate intrusions were sampled at Bourbon and Iron Mountain. Magnetite was collected from Pea Ridge, Bourbon, Iron Mountain, and Lower Pilot Knob. Magnetite was identified using reflected light microscopy and analyzed via scanning electron microscopy-backscattered electron (SEM-BSE) imaging, electron microprobe (EMP), and laser ablation-inductively coupled plasma-mass spectrometry (LA-ICP-MS).

EMP analyses were obtained at 15Kv and 100nA using a spot size of <1 µm. Monte Carlo simulations were used to model the effects of secondary fluorescence as a function of distance from rutile and chlorite inclusions in magnetite (Salvat et al. 2006; Llovet et al. 2012). Iron contents determined by EMP served as the internal standard for LA-ICP-MS analyses; data reduction follows Longerich et al. (1996). Inclusion-rich cores and inclusion-free rims of magnetite were analyzed by LA-ICP-MS using 24 and 32 µm spot sizes. The data from inclusion-rich cores were reduced in two ways: (1) filtered to remove the effects of mineral inclusions and (2) unfiltered to show the effects of mineral inclusions on the results.

Results generated by EMP and LA-ICP-MS analysis were plotted on the Al+Mn vs. Ti+V discrimination diagrams of Nadoll et al. (2014).

4 Petrography of magnetite assemblages

In many places, the mafic to intermediate intrusions surrounding Bourbon and Iron Mountain contain 50-250 µm phenocrysts of tabular ilmenite and equant magnetite ± ilmenite (Fig. 1a). In IOA deposits, magnetite occurs in two assemblages. Assemblage 1 (A1) consists of amphibole ± apatite-magnetite-ilmenite-phlogopite-quartz that fill open spaces. Assemblage 2 (A2) consists of magnetite ± apatite-phlogopite-quartz-rutile-sulfide replacements with lesser pore infillings that often surround A1. Mg-chlorite may also fill remaining pore space in A2.

A1 magnetite consists of coarse subhedral to euhedral 250-1500 µm grains that are frequently intergrown with coarse ilmenite and or contain ilmenite lamellae (Fig. 1b). A2 magnetite consists of finer-grained anhedral to subhedral 15-500 µm grains without ilmenite lamellae. A2 magnetite generally contains mineral inclusions, such as rutile and silicates, and some grains have inclusion-rich cores and inclusion-poor rims (Fig. 1c). Coarser A2 magnetite grains are often observed as overgrowths on A1 magnetite, or in breccias. A1 magnetite is present in deep drill holes at Bourbon, Iron Mountain, and Pea Ridge, but was not identified at Lower Pilot Knob. A2 magnetite is also present at Bourbon, Pea Ridge, and Lower Pilot Knob but was minimal at Iron Mountain.

5 Magnetite compositions and Monte Carlo results

Consistent with an igneous origin, magnetite phenocrysts from mafic to intermediate intrusions plot in two clusters within the magmatic Fe-Ti and V deposit field (Fig. 2). Inclusion-poor A1 magnetite plots in two arrays that extend from igneous magnetite phenocryst endmembers into the hydrothermal Porphyry, Kiruna, IOCG, Skarn, and BIF fields, which suggests high

temperature formation. Most inclusion-poor A2 magnetite plots in the BIF field, though limited data plot in the IOCG and Skarn fields, which suggest low temperature formation.

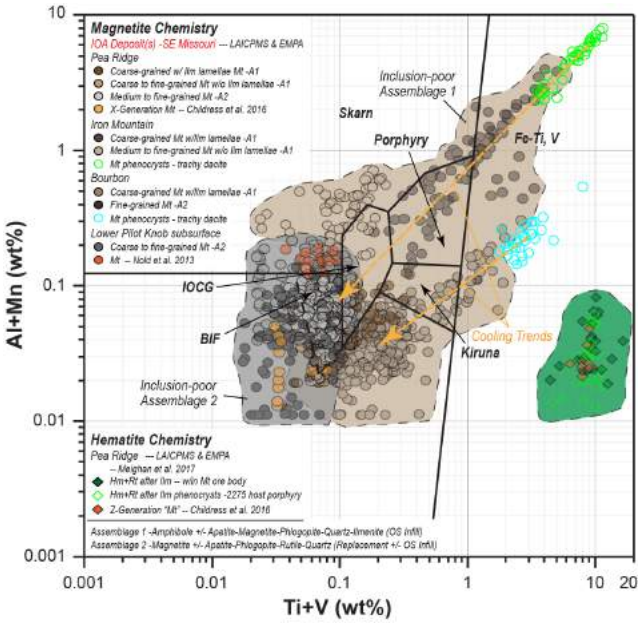

Figure 2. Inclusion-poor magnetite from IOA deposits in SE Missouri. See text for details. Hm=Hematite, Ilm=Ilmenite, Mt=Magnetite, Rt=Rutile.

Magnetite phenocrysts from mafic to intermediate composition intrusions surrounding Bourbon and Iron Mountain contain significant Ti, Mn, V, Cr, Zn, Co, Mg, Al, P, Zr, and Nb, with lesser amounts of Ga, Pb, U, Mo, Y, La, Ce, and Ta. Inclusion-poor A1 and A2 magnetite contain a similar suite of elements, though at lower concentrations, including V, Mn, Zn, Co, Ga, Ni, Ti, Mg, P, and Al with lesser amounts of Cr, Th, and U. These results suggest that A1 and A2 magnetite precipitated from fluids discharged from mafic to intermediate intrusions. Inclusion-rich cores of A2 magnetite contain a similar trace element suite and include higher abundances of incompatible elements such as Si, Ti, Al, Mg, and to a lesser extent Mn that are associated with mineral inclusions.

Monte Carlo simulations exhibit exponential profiles of apparent Ti and Al concentrations in magnetite versus distance from inclusions, such as rutile or chlorite, that are consistent with secondary fluorescence (Fig. 3). Correspondingly, only EMP analysis spots >30 µm from mineral inclusions yield reliable results. The close spacing of mineral inclusions in A2 magnetite cores (Fig. 1c, 1d) suggests that obtaining reliable EMP data from these sorts of materials is essentially impossible. Consequently, concentrations measured in A2 magnetite cores will be erroneously high. To illustrate this phenomenon, EMP analyses of "clean" inclusion-poor rims and "contaminated" inclusion-rich cores are plotted on Al+Mn vs. Ti+V discrimination diagram (Fig. 4a). For comparison, LA-ICP-MS spot analyses are plotted. A shift to higher Ti and/or Al concentrations parallels the compositional shift corresponding to analyses for inclusion-poor versus inclusion-rich magnetite and therefore defines an apparent contamination trend consistent with magnetite contamination by mineral inclusions.

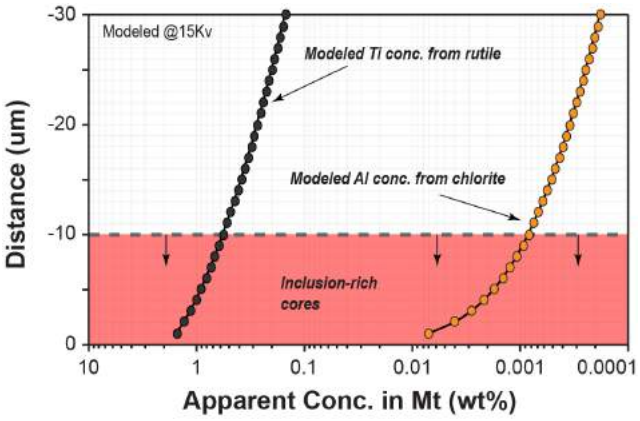

Figure 3. Monte Carlo simulations showing apparent Ti and Al concentrations in magnetite due to secondary fluorescence versus distance from rutile and chlorite inclusions.

Last, the results for Pea Ridge and Pilot Knob were compared to those from Los Colorados (Fig. 4b). Los Colorados magnetite plots in the Porphyry field, which is consistent with its subduction-related magmatic arc setting. The positive shift in Ti and Al concentrations of mineral inclusion-rich magnetite cores is similar to that observed for magnetite cores from Pea Ridge and Pilot Knob. These high core concentrations, which extend into the magmatic field, likely reflect secondary fluorescence associated with inclusions. The interpretation that the inclusion-rich cores are high-Ti magnetite microlites is therefore highly suspect.

6 Conclusions

Mineral inclusions are common in replacement ores of many deposit types. Consequently, the presence of inclusion-rich magnetite among IOA deposits suggests that these deposits formed by replacement processes.

Our data show that the inclusion-rich cores of A2 replacement magnetite from Pea Ridge and Lower Pilot Knob can be misidentified as high-Ti microlites due to rutile and aluminosilicate inclusions. Similarly, high-Ti microlites at Los Colorados may reflect an analytical artefact associated with analysis of inclusion-rich magnetite cores. We infer that no high-Ti magnetite microlites were involved in ore formation

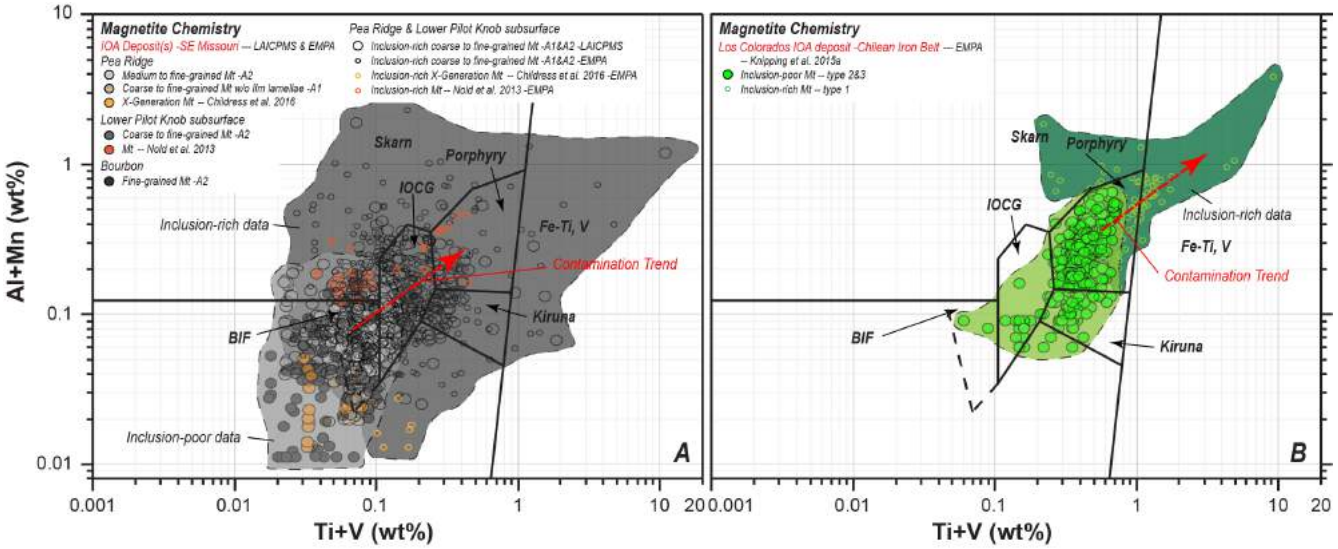

Figure 4. A. Inclusion-poor verses inclusion-rich magnetite from Pea Ridge and Pilot Knob in SE Missouri. **B.** Analogous data from Los Colorados in Chile. See text for further description. Ilm=Ilmenite, Mt=Magnetite.

in SE Missouri IOA deposits. Similarly, high-Ti magnetite microlites may not actually be present at Los Colorados. If so, the magnetite microlite flotation model of Knipping et al. (2015a, b) may be invalid and may instead reflect an analytical artefact.

Since the textures and composition of high-Ti magnetite veins and low-Ti magnetite replacements are preserved, we suggest that the high-temperature veins were conduits for the fluids that generated the low-temperature replacement ores. The suite of trace elements in magnetite suggests that iron was derived from mafic to intermediate intrusions. In summary, our results support a magmatic-hydrothermal origin for IOA deposits in SE Missouri, and perhaps those at Los Colorados.

References

Childress TM, Simon AC, Day WC, Lundstrom CC, Bindeman, IN (2016) Iron and oxygen isotope signatures of the Pea Ridge and Pilot Knob magnetite-apatite deposits, SE Missouri, USA. Econ Geol 111: 2033-2044

Day WC, Aleinikoff JN, du Bray E, Ayuso RA, (2017) Constraints on age of magmatism and iron oxide-apatite (IOA) and iron oxide-copper-gold (IOCG) mineral deposit formation in the Mesoproterozoic St. Francois Mountains terrane of southeast Missouri, USA. SGA Conf. Abstract, 3:855-858

Day WC, Slack JF, Ayuso RA, Seeger CM (2016) Regional geologic and petrologic framework for iron oxide ± apatite ± rare earth element and iron oxide copper-gold deposits of the Mesoproterozoic St. Francois Mountains terrane, SE Missouri, USA. Econ Geol 111: 1825-1858

Hofstra AH, Meighan CJ, Song X, Samson I, Marsh EE, Lowers HA, Emsbo P, Hunt AG (2016) Mineral thermometry and fluid inclusion studies of the Pea Ridge iron oxide-apatite-rare earth element deposit, Mesoproterozoic St. Francois Mountains terrane, SE Missouri, USA. Econ Geol 111:1985-2016

Knipping JL, Bilenker LD, Simon AC, Reich M, Barra F, Deditius AP, Walle M, Heinrich CA, Holtz F, Munizaga R (2015) Trace elements in magnetite from massive iron oxide-apatite deposits indicate a combined formation by igneous and magmatic-hydrothermal processes. Geochim Acta 171:15-38

Knipping JL, Bilenker LD, Simon AC, Reich M, Barra F, Deditius AP, Lundstrom C, Bindeman I, Munizaga R (2015) Giant Kiruna-type deposits form by efficient flotation of magmatic magnetite suspension. Geol 43:491-594

Llovet X, Pinard PT, Donovan JJ, Salvat F (2012) Secondary fluorescence in electron probe microanalysis of material couples. J Phys D: App Phys 45, No. 22

Longerich HP, Jackson SE, Günther D (1996) Laser ablation inductively coupled plasma mass spectrometric transient signal data acquisition and analyte concentration calculation, J Anal At Spectrom 11:899-904

McCafferty AE, Philips JD, Hofstra AH, Day WC (2018) A new geophysical view of the crust and controls on critical mineral systems, southern Midcontinent, USA. SEG Conf. Abstract, Keystone

Meighan CJ, Mercer CN, Hofstra AH, Marsh EE, Lowers HA (2017) Multiple origins of iron oxides in regional rhyolites and the Pea Ridge IOA-REE deposit, SE Missouri, USA. SGA Conf. Abstract, 3:947-950

Murphy JE, Ohle EL (1968) The Iron Mountain mine, Iron Mountain, Missouri. In: Ridge JD, ore deposits in the United States 1933/1967 1: 288-302

Nadoll P, Angerer T, Mauk JL, French D Walshe J (2014) The chemistry of hydrothermal magnetite: A review. Ore Geol Rev 61:1-32

Panno SV, Hood WC (1983) Volcanic stratigraphy of the Pilot Knob iron deposits, Iron county, Missouri. Econ Geol 78:972-982

Salvat F, Fernández-Varea JM, J Sempau J (2006) PENELPE-2006: A code system for Monte Carlo simulation of electron and photon transport. OECD/NEA Issy-les-Moulineaux, France

Seeger CM, Nuelle LM, Day WC, Sidder GB, Marikos MA, Smith, DC (2001) Geologic maps and cross sections of the Pea Ridge iron mine, Missouri. U.S. Geological Survey Miscellaneous Field Map MF-2353, scale 1:2,400

Simon AC, Knipping JL, Reich M, Barra F, Deditius AP, Bilenker L, Childress T (2018) Kiruna-type iron oxide-apatite (IOA) and iron oxide copper-gold (IOCG) deposits form by a combination of igneous and magmatic-hydrothermal processes: evidence from the Chilean iron belt. SEG Special Publication 21:89-114

The Waschleithe W-skarn – a distal relative of skarns in the Schwarzenberg district, western Erzgebirge, Germany?

Nils Reinhardt, Mathias Burisch
Technische Universität Bergakademie Freiberg, Freiberg, Germany

Max Frenzel, Jens Gutzmer
Helmholtz-Zentrum Dresden-Rossendorf, Helmholtz Institute Freiberg for Resource Technology, Freiberg, Germany

Lawrence D. Meinert
Colorado School of Mines, Golden, USA

Axel Gerdes
Goethe-Universität Frankfurt, Frankfurt, Germany

Abstract. The Waschleithe skarn located near Schwarzenberg in eastern Germany hosts sub-economic polymetallic W-Zn-Pb-Cu-Fe mineralisation. Its mineralogy is dominated by prograde clinopyroxene and subordinate garnet. The garnet and pyroxene colours of this skarn as well as low garnet/pyroxene ratios are typical for distal skarn settings. Ore minerals (magnetite, sphalerite, galena, chalcopyrite, pyrite, scheelite) in the prograde skarn do not show a clear association with the weakly developed retrograde overprint consisting mainly of late chlorite and calcite.

1 Introduction

The Erzgebirge/Krušné hory metallogenic province, straddling the border between Germany and the Czech Republic, is host to a broad variety of syn- and post-Variscan hydrothermal ore deposits including greisen, skarn, and vein-type mineralisation. Skarn deposits are known to occur across the entire Erzgebirge and in different stratigraphic positions. Their host lithologies comprise dominantly low-grade metasedimentary units (rarely meta-volcanics). Some skarns contain polymetallic mineralisation (Sn, W, Zn, Pb, Fe, Cu, In) (e.g., Baumann et al. 2000; Hösel 2003; Schuppan and Hiller 2012) and have been mined historically for Fe, Sn, W, Zn and Pb. Despite hosting the majority of Europe´s Sn resources (Bock 2009; ITRI 2016) the understanding of the genesis and resource potential of these deposits is surprisingly poor.

The Schwarzenberg district in the western Erzgebirge comprises numerous skarn bodies that are concentrically distributed around the Schwarzenberg Gneiss Dome (SGD). Although garnet and pyroxene skarns are most common, there is considerable compositional variation related to the degree of retrograde overprint and metal tenor. Their origin and genetic history remain controversial. Some researchers favour a metamorphic provenance for the skarns (e.g., Lefebvre et al. 2018) whereas others present evidence for a magmatic-hydrothermal origin (e.g., Burisch et al. 2019; Kern et al. 2018) affiliated with late-/post-Variscan magmatism. Moreover, the genetic relationships between individual skarn bodies of the Schwarzenberg district are still unknown. The question remains whether this is one skarn system that evolved in time and space or if the different skarn bodies are related to several localized hydrothermal events.

In this study, we focus on the Waschleithe skarn which represents one of the northernmost skarns of the SGD (Fig. 1). This skarn is only poorly documented and modern geochemical data is entirely missing. Due to its distal position relative to the large and well mineralized skarn systems of Hämmerlein-Tellerhäuser and Breitenbrunn, the Waschleithe skarn may provide new insights into ore-forming processes on the district-scale. We use structural and petrographic observations as well as qualitative data on mineral chemistry to better understand the origin of the Waschleithe skarn.

2 Sampling and methodology

Skarn and host rock samples from the upper (USH) and lower (LSH) skarn horizon were collected from seven sampling locations within the historical Herkules-Frisch-Glück underground mine. Of these, a total of 13 polished thin sections as well as 6 double-polished sections for fluid inclusion analyses were produced. Additionally, nine covered thin sections of three drill cores, provided by the Geological Survey of Saxony (LfULG), were also studied. Qualitative SEM-EDX measurements were performed on a JEOL CarryScope JCM-5700 equipped with a Bruker Quantax X-Flash 6/30 EDS detector at an accelerating voltage of 20 kV.

3 Regional geology

The Erzgebirge crystalline complex is a ~145 x 35 km SW-dipping anticlinal structure situated along the N-border of the Bohemian Massif in the Saxothuringian Zone of the European Variscides. Peak regional metamorphism occurred at around 340 Ma (Rötzler and Plessen 2010). The resulting metamorphic units comprise a complex succession of medium- to high-grade rocks including (ultra-) high pressure gneisses

and

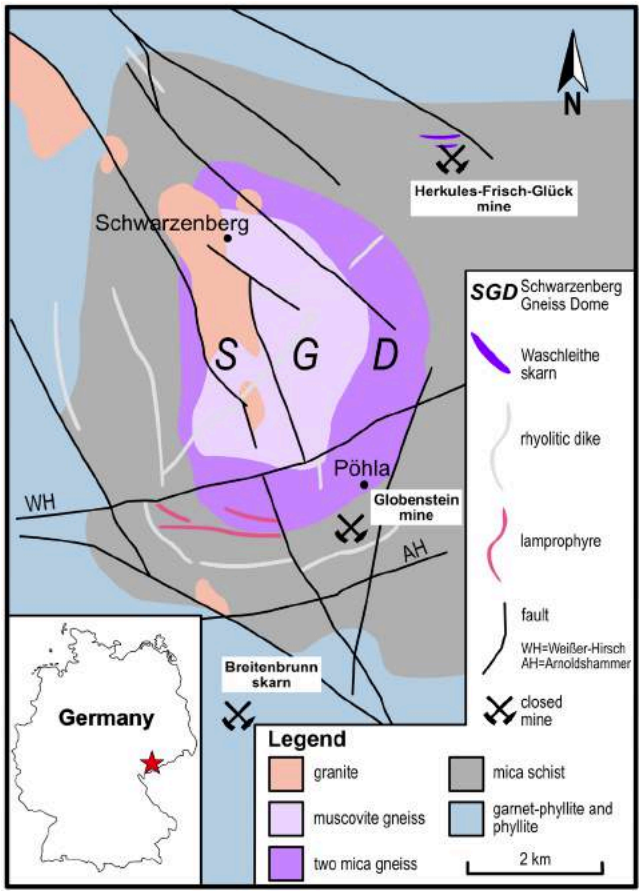

Figure 1. Simplified geological map of the Schwarzenberg district modified after (Baumann et al. 2000; Hösel and Haake 1965). Position of the historical Herkules-Frisch-Glück mine and other skarn occurrences is indicated. Low- to medium-grade meta-sedimentary units are grouped concentrically around the Schwarzenberg Gneiss Dome (SGD). The inset shows position of the SGD (red star) in Germany.

eclogites as well as low- to medium-grade phyllites, meta-carbonates, meta-volcanics, and mica schists. The latter are the host rocks for the skarn mineralisation. The crustal pile was intruded by voluminous post-kinematic plutons as well as subvolcanic dikes, microgranites and lamprophyres between 330-295 Ma (Förster and Romer 2010; Seifert 2008).

4 The Waschleithe skarn

4.1 Local geology

The Waschleithe skarn is situated at the northern margin of the SGD. It is hosted by greenschist facies meta-psammites, mainly mica schists and paragneisses, locally known as the *Obermittweidaer formation* (Baumann et al. 2000; Hösel 1972; Hösel and Haake 1965). In the study area the metasedimentary rocks reach a thickness of more than 900 m and comprise two discrete meta-carbonate horizons. These horizons predominantly consist of relatively pure calcite marble rarely exceeding thicknesses of ~10 m. They host several skarn bodies and have been intersected by core drillings at depths of up to 150 m. Skarn forms stratabound lenses concordant with the metasedimentary sequence dipping at 25 to 35° towards N. Laterally, the thickness of both skarn horizons is highly variable, reaching average thicknesses of 4 m and 6 m for the USH and LSH, respectively (Hösel 1972; Meyer and Röthig 1967). The marbles are typically only partially altered to skarn. A complete alteration of the marbles to skarn is only recognized in zones of intense deformation (Hösel and Haake 1965), clearly overprinting older metamorphic structures. The distance of the Waschleithe skarn to the underlying granites of the Eibenstock and Aue-Schwarzenberg suites is not well constrained but exceeds 1000 m (Hösel 1972). The skarn bodies are accessible at the Herkules-Frisch-Glück underground mine, where both skarn horizons are exposed over a length of ~250 m. Furthermore, four boreholes from the 1960´s and 70´s intersect the skarn bodies.

4.2 Skarn mineralogy

The USH and LSH show similar mineralogy and mineral paragenesis. Consequently, we summarize their petrographic description and highlight only differences.

The marble is dense and appears whitish-grey in colour with very few dark grey, cm-thick *schlieren*. Microscopically, it consists of anhedral calcite with grain sizes of 40 to 600 µm. Calcite exhibits abundant pressure twinning. The marble shows a characteristic granoblastic texture. Locally, fine-grained (100 to 200 µm) subhedral epidote-group minerals and elongated or platy muscovite grains with grain sizes of up to ~500 µm are finely dispersed within the calcite matrix. Veinlets of quartz and fluorite crosscut the marble.

In sharp contrast, the skarn is composed of dense to coarse-grained brownish-green pyroxenes as the major constituent as well as minor amounts of dark green chlorite. Clinopyroxene (most likely diopside-hedenbergite series) shows fan-like intergrowth of cm-sized prismatic crystals as well as fine-grained aggregates. Grain sizes vary between <40 µm to >5 mm. Pale yellowish-green garnet is less abundant than pyroxene and occurs as euhedral zoned crystals (Fig. 2A) with grain sizes between 50 to 600 µm but also as fine-grained anhedral aggregates. Preliminary observations suggest two generations of garnet, one pre-dating and one post-dating pyroxene (Fig. 3). Anhedral ilvaite pervasively replaces pyroxene and is only observed in the LSH. Epidote-group minerals form fine-grained (50 to 100 µm) anhedral crystals that replace clinopyroxene and are associated with quartz and rarely scheelite. Anhedral quartz fills voids within clinopyroxene but also occurs together with fluorite in veinlets post-dating the calc-silicates. Fluorite is colourless and forms subhedral to anhedral aggregates mostly replacing clinopyroxene along fractures. Individual crystals have grain sizes between 50 µm and several mm. Fluorite is mostly associated with sphalerite, galena and quartz and is restricted to the USH where its abundance is highest close to the marble-skarn contact. Elongate, subhedral vesuvianite replaces clinopyroxene. It is restricted to the USH. Milky

hydrothermal calcite occurs as cavity and fracture infill. Calcite is often rimmed by greenish-brown

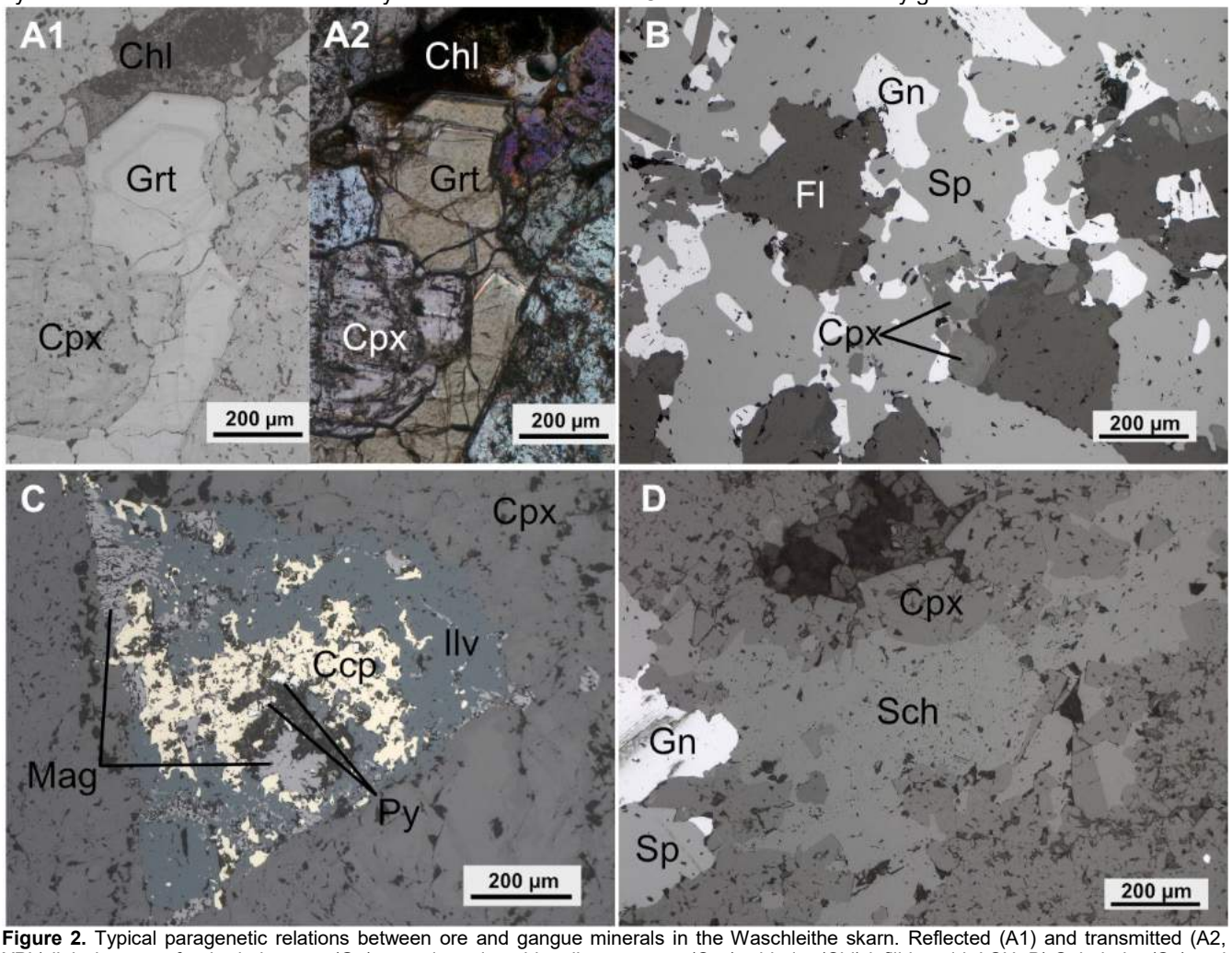

Figure 2. Typical paragenetic relations between ore and gangue minerals in the Waschleithe skarn. Reflected (A1) and transmitted (A2, XPL) light images of euhedral garnet (Grt) crystals replaced by clinopyroxene (Cpx), chlorite (Chl) infill in void, LSH. B) Sphalerite (Sp) and galena (Gn) replaced by fluorite (Fl), USH. C) Complex sulphide-oxide assemblage, early ilvaite (Ilv) replaced by magnetite (Mag) and late chalcopyrite (Ccp)/ pyrite (Py), LSH. D) Galena, sphalerite and scheelite (Sch) replacing clinopyroxene, USH.

chlorite. Chlorite mostly forms fine grained platy aggregates and preferentially replaces clinopyroxene along grain boundaries and fractures. Occasionally, chlorite shows pseudomorphs after clinopyroxene.

The skarn-marble contact is very sharp. Microscopically, a ~5 mm transition zone can be observed. From marble to skarn, a ~1.5 mm thin silicified zone is present, which evolves into a ~3.5 mm thin quartz+fluorite+muscovite+chlorite zone. The latter appears to have overprinted only the primary skarn minerals.

4.3 Ore minerals

Sulphide and oxide minerals are restricted to the skarn and do not occur within the unaltered marble. They are unevenly distributed within the samples and occur in veins, as disseminations, or massive patches. Three distinct assemblages have been observed:

1.) Oxide assemblage: Anhedral magnetite is the dominant oxide in this assemblage. It is closely associated with ilvaite, corroding its grain boundaries and pervasively replacing it from outside to inside (Fig. 2C). Magnetite is only observed in the LSH.

2.) Sulphide assemblage: This comprises mostly of sphalerite, galena, pyrite and chalcopyrite. Sphalerite is the most common sulphide. It occurs as anhedral crystals and aggregates replacing pyroxene and ilvaite. Sphalerite often shows chalcopyrite disease. Anhedral galena mostly occurs with sphalerite but is slightly younger (Fig. 2B). It also occurs disseminated in the skarn where it replaces pyroxene. Sphalerite and galena are often associated with fluorite and quartz. Minor euhedral to anhedral pyrite is strongly associated with sulphides and has never been observed directly replacing skarn minerals. It occurs as fine-grained cubic crystals or massive patches with sphalerite. Anhedral chalcopyrite replaces pyroxene but is mostly associated with older sulphides (Fig. 2C).

3.) Scheelite assemblage: Anhedral scheelite with grain sizes up to 2.2 mm occurs disseminated within the pyroxenes. It is mostly accompanied by sphalerite, galena and quartz (Fig. 2D). It seems to replace pyroxene along fractures indicated by irregular-shaped corroded grain boundaries of pyroxene in contact to

scheelite. Preliminary observations suggest only a weak

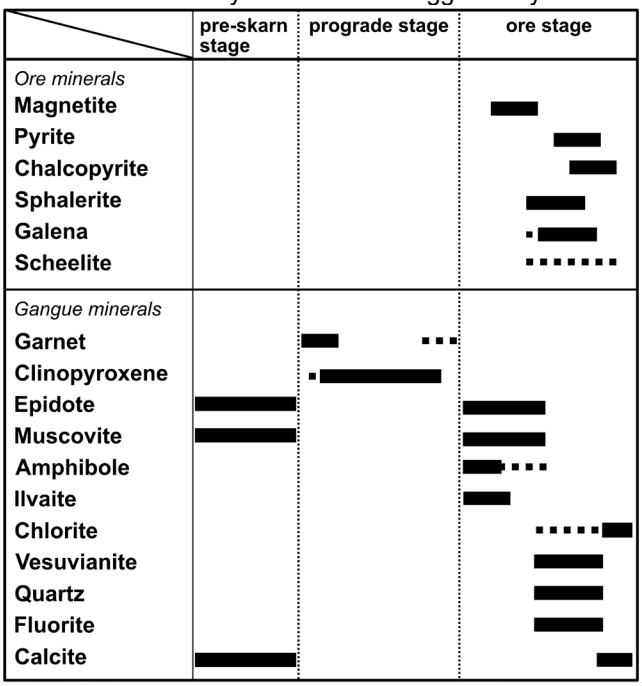

Figure 3. Preliminary paragenetic sequence of the Waschleithe skarn. Dotted lines indicate higher uncertainty.

relationship between sulphides and chlorite.

With respect to their ore mineralogy both the USH and LSH are dominated by disseminated sulphides. However, the USH is more mineralized than the LSH and its ore mineralogy is dominated by Sp+Gn±Ccp, whereas the LSH is dominated by Sp+Ccp±Py(±Mag). Disseminated scheelite mineralisation can be observed in both horizons.

5 Discussion and conclusions

For a given protolith and oxidation state the garnet and pyroxene colour as well as their modal ratio have been recognized to be indicative of the relative distance of skarn mineralisation to its fluid source (Meinert et al. 2005). Pale yellowish-green garnet, dark pyroxenes, the marble front and low garnet/pyroxene ratios of the Waschleithe skarn are typical for distal skarns (Meinert et al. 2005). In contrast, the Hämmerlein-Tellerhäuser and Breitenbrunn skarns (<10 km to the S) contain additional pale brownish-red garnet and have significantly higher garnet/pyroxene ratios, indicating a more proximal position to the fluid source relative to the Waschleithe skarn (Burisch et al. 2019). Taking the enormous lateral extend of the Hämmerlein-Tellerhäuser (~5 km) and Breitenbrunn (~4.4 km) skarns into account, it is likely that the Waschleithe skarn (~7 km to the N) is a distal skarn mineralisation related to the same hydrothermal event/system which also formed the other skarn bodies of the Schwarzenberg district. This hypothesis will be tested with U-Pb geochronology of garnet and carbonates. Furthermore, we are planning to conduct detailed mineralogical and fluid inclusion studies on the local as well as the district scale to better understand the processes that cause the observed mineral zoning within the Schwarzenberg district.

Acknowledgments

M. Riedel (Herkules-Frisch-Glück mine) is thanked for providing mine access and support during sampling. M. Lapp (Geological Survey of Saxony) is thanked for providing access to historical drill cores, thin sections and exploration reports. R. Würkert, M. Stoll and A. Bartzsch (all HIF) are thanked for sample preparation. This PhD project is funded by the European Social Fond (ESF) and the Sächsische Aufbaubank (SAB); project 100339454.

References

Baumann L, Kuschka E, Seifert T (2000) Lagerstätten des Erzgebirges: 13 Tabellen. Enke im Thieme-Verl., Stuttgart

Bock P (2009) Economic Potential of Tin, Fluorspar and Barite occurrences in Saxony. The IMRE Journal 3:22–31

Burisch M, Axel G, Meinert LD, Albert R, Seifert T, Gutzmer J (2019) The essence of time - fertile skarn formation in the Variscan Orogenic Belt. (submitted)

Förster H-J, Romer RL (2010) Carboniferous magmatism. In: Linnemann U, Romer RL (eds) Pre-Mesozoic geology of Saxo-Thuringia: From the Cadomian active margin to the Variscan orogen. Schweizerbart, Stuttgart, pp 287–308

Hösel G (1972) Bemerkungen zum Karbonatgesteins-/Skarnvorkommen der Grube Herkules-Frisch-Glück bei Waschleithe, Kreis Schwarzenberg (Erzgebirge). Wissenschaftliche Zeitschrift der Ernst-Moritz-Arndt-Universität Greifswald. Mathematisch-naturwissenschaftliche Reihe 21:139-142

Hösel G (2003) Die polymetallische Skarnlagerstätte Pöhla-Globenstein, 1. Auflage. Sächsische Druck- und Verlagshaus AG, Dresden

Hösel G, Haake R (1965) Ergebnisbericht Sucharbeiten Skarn Schwarzenberg 1961-1964 (B-Vorhaben). VEB Geologische Erkundung Süd, Freiberg

ITRI (2016) Report on global tin resources and reserves. https://www.internationaltin.org/reports/2016-report-on-global-tin-resources-reserves/. Accessed 23 January 2019

Kern M, Kästner J, Tolosana-Delgado R, Jeske T, Gutzmer J (2018) The inherent link between ore formation and geometallurgy as documented by complex tin mineralization at the Hämmerlein deposit (Erzgebirge, Germany). Min Dep 7:225. doi: 10.1007/s00126-018-0832-2

Lefebvre MG, Romer RL, Glodny J, Kroner U, Roscher M (2018) The Hämmerlein skarn-hosted polymetallic deposit and the Eibenstock granite associated greisen, western Erzgebirge, Germany: two phases of mineralization—two Sn sources. Miner Deposita 21. doi: 10.1007/s00126-018-0830-4

Meinert LD, Dipple GM, Nicolescu S (2005) World Skarn Deposits. In: Hedenquist JW (ed) Economic geology: One hundredth anniversary volume 1905-2005. Society of Economic Geologists Inc, Littleton CO, pp 299–335

Meyer H, Röthig H (1967) Bericht zur Kartierung der Grube "Herkules Frisch Glück" bei Waschleithe (Erzgebirge). VEB Geologische Erkundung Süd, Freiberg

Rötzler K, Plessen B (2010) The Erzgebirge: a pile of ultrahigh- to low-pressure nappes of Early Palaeozoic rocks and theri Cadomian basement. In: Linnemann U, Romer RL (eds) Pre-Mesozoic geology of Saxo-Thuringia: From the Cadomian active margin to the Variscan orogen. Schweizerbart, Stuttgart, pp 253–270

Schuppan W, Hiller A (2012) Die Komplexlagerstätten Tellerhäuser und Hämmerlein, 1. Auflage. Sächsisches Landesamt für Umwelt, Landwirtschaft und Geologie, Freiberg

Seifert T (2008) Metallogeny and petrogenesis of lamprophyres in the Mid-European variscides: Post-collosional magmatism and its relationship to late-variscan ore forming processes in the Erzgebirge (Bohemian Massif). IOS Press Millpress; Gazelle Books Distr, Amsterdam, Hightown

Fertile window of skarn formation in orogenic belts: LA-ICP-MS U-Pb geochronology of skarn-related garnet from the Variscan Erzgebirge, Germany

Mathias Burisch, Thomas Seifert
Division of Economic Geology and Petrology, TU Bergakademie Freiberg, Germany

Axel Gerdes, Richard Albert
Goethe-Universität, Institut für Geowissenschaften, Germany

Lawrence D Meinert
Colorado School of Mines, Department of Geology and Geological Engineering, USA

Jens Gutzmer
Helmholtz Zentrum Dresden-Rossendorf, Helmholtz Institute Freiberg for Resource Technology, Germany

Abstract. Uranium-lead LA-ICP-MS geochronology of garnet from skarns in the Erzgebirge, a classic metallogenic district in the European Variscan belt, constrains the timing and origin of metasomatism and associated Sn, W, Fe, Zn, Cu and In mineralization. Geochronological data of 20 samples from ten skarns distributed across the entire Erzgebirge region, include garnet from three different lithological contexts that yield distinctly different ages. The first group includes sub-calcic garnets with ages between 343 and 331 Ma, the age of peak regional metamorphism in the Erzgebirge. The second group is represented by grandite garnets associated with skarnoid rocks; these yield ages ranging between 325 and 313 Ma and are temporally associated with late-orogenic magmatism. Coarse-grained metasomatic grandite garnets with ages between 308 and 295 Ma define the third group. The latter garnets are related to extensive post-collisional magmatic-hydrothermal processes yielding world-class Sn-Zn-In skarn deposits. Results illustrate that U-Pb geochronology of skarn-related garnet can serve as a sensitive exploration vector to identify fertile skarn environments in complex orogenies.

1 Introduction

Although the majority of skarns are associated with subduction-related magmatism, they also can occur in collisional terrains (e.g. Erzgebirge/Germany, Tien Shan/China or Anatolia/Turkey). In such orogenic zones they typically are polymetallic containing, amongst others, Fe, Zn, Pb, W, Sn and/or Au and contribute significantly to Europe's Sn resources and China's Sn and Au reserves (Chen et al., 2007; Elsner, 2014).
While detailed genetic models for subduction-related skarn systems exist (hundreds documented in Meinert et al., 2005) the precise source of hydrothermal fluids and the timing of fertile skarn formation (skarns with significant metal endowment) in orogenic settings remains poorly constrained. Some of this lack of understanding is related to the scarcity of robust geochronological constraints for most of these mineral systems. Recent applications of LA-ICP-MS U-Pb geochronology to garnet (Deng et al., 2017; Seman et al., 2017; Gevedon et al., 2018; Wafforn et al., 2018) now allows direct age dating of prograde metasomatism in orogenic skarn systems. Results can be used to identify temporal windows of skarn formation within the context of regional geotectonic evolution.

2 Geology of the Erzgebirge

As part of the European Variscides, the Erzgebirge is a ~145 x 35 km SW-NE trending erosional window comprising predominantly metamorphic and igneous basement rocks (Fig. 1). These rock units include high-grade gneisses (E, SE) and low- to medium grade phyllites, marbles, meta-volcanics and mica-schists (W, NW), which experienced peak metamorphic conditions at around 340 Ma (Kröner and Willner, 1998). After rapid uplift, these metamorphic lithologies were subsequently intruded by igneous rocks - predominantly peraluminous leucogranites associated with the late-orogenic phase (325 to 318 Ma (Förster et al., 1999)) of the Variscan collision. Abundant younger (sub-)volcanic rocks record intense post-orogenic magmatic activity from 310 to 290 Ma (Kempe et al., 2004; Seifert, 2008; Hoffmann et al., 2013)

3 Skarns in the Erzgebirge

The Erzgebirge is a classical metallogenic province with a multitude of economically important greisen, skarn and vein-type ore deposits (Baumann et al., 2000). Much of this hydrothermal mineralization is genetically associated with late- to post-orogenic magmatism (Zhang et al., 2017; Burisch et al., 2018; Ostendorf et al., 2018). Skarns are particularly widespread across the Erzgebirge; they vary significantly in size, metal tenor and mineralogy (Hösel, 2003; Schuppan and Hiller, 2013; Hiller and Schuppan, 2016). The majority are hosted by Palaeozoic metamorphic rocks, which comprise alternating sequences of meta-pelites and meta-limestones. A few skarns are associated with

small marble lenses within high-grade gneiss units.

The metal tenor associated with the skarns is variable and may include Sn, W, Fe, Zn, Cu, In and/or Ag. Skarn mineralization is known to include several prograde and retrograde stages but robust age constraints are lacking for all of these in the Erzgebirge skarns. A recent attempt to age date the Hämmerlein skarn was based on Rb-Sr dates of muscovite (~340 Ma; Lefebvre et al., 2018) of a gneiss spatially – but not necessarily genetically - associated with the skarn.

The degree of retrograde overprint of the primary skarn minerals ranges from subordinate to very intense. For the latter, many of the ore minerals are associated with the retrograde alteration (Schuppan and Hiller, 2013). Direct geochronology of the skarn-related minerals has not been successful to date. As a consequence, the origin and the timing of skarn mineralization in the Erzgebirge remains unclear.

4 Sampling and methods

Twenty samples of skarn-related grandite and sub-calcic garnet were selected from the scientific collection of the TU Bergakademie Freiberg and from accessible historic underground mines. Only fresh garnets, which have not been affected by retrograde alteration were selected for analyses.

Samples were screened and analysed *in situ* from polished sections using a RESOLution S-155 (Resonetics) 193 nm ArF Excimer laser (CompexPro 102, Coherent) equipped with a two-volume ablation cell (Laurin Technic, Australia) coupled to a sector field ICP-MS (Element 2, Thermo) at Goethe University, Frankfurt. Ablation was performed in a He atmosphere (0.3 l/min) and mixed in the ablation funnel with 1.0 l/min Ar and 0.06 l/min N. Signal strength at the ICP-MS was tuned for maximum sensitivity while keeping oxide formation below 0.2 % (UO/U) and element fraction low (*e.g.* Th/U = 1). Static ablation used a spot size of 257 µm and a fluence of *c.* 1.5 J/cm^2 at 15 Hz. This yielded for SRM-NIST 614 a depth penetration of *c.* 0.8 µm/s and an average sensitivity of 460000 cps/ppm for ^{238}U. The detection limits (4 x standard deviation of background signal) for ^{206}Pb and ^{238}U were *c.* 0.07 and 0.05 ppb, respectively. Each analysis consists of 20 s background acquisition followed by 20 s of sample ablation and 25 s washout. During 40 s data acquisition, the signal of ^{206}Pb, ^{207}Pb, ^{232}Th and ^{238}U were detected by peak jumping in pulse counting mode with a total integration time of *c.* 0.1 s, resulting in 400 mass scans. Depth penetration was measured with SEM images and 3D photogrammetric reconstruction of an ablation pit and was estimated at *c.* 0.6 µm/s with a total depth of less than 15 µm including a 5 s pre-ablation.

Soda-lime glasses SRM-NIST 614 were used as reference materials together with two garnet standards. Raw data were corrected offline using an in-house Microsoft Excel spreadsheet program (Gerdes and Zeh, 2006; Gerdes and Zeh, 2009). The ^{207}Pb/^{206}Pb ratio was corrected for mass bias (0.08 %) and the ^{206}Pb/^{238}U ratio for inter-element fraction (*c.* 25 %), including drift over the 12 hours of sequence time, using SRM-NIST 614 (n = 26). Additional matrix correction of -14.5 % has been applied on the ^{206}Pb/^{238}U for garnet samples, which was determined using Mali 1 garnet reference material dated by TIMS (202.0±1.2 Ma; Seman et al., 2017), and confirmed by another in-house Mali reference material (called here MaliGUF). Although, Mali 1 and MaliGUF come from the same area, they are distinctly different in composition. Mali 1 is an almost colourless grossular with Ca/Fe of ~7, while MaliGUF is a yellowish-greenish andradite-grossular with Ca/Fe of ~2. Based on the soda-lime glass and the non-common Pb-corrected Mali data the ^{206}Pb/^{238}U fractionation during 20 s depth profiling was non-detectable, thus, no additional correction has been applied. After correcting for drift, mass bias, inter-element fractionation and 14.5 % matrix-offset, the MaliGUF (n = 26) ^{206}Pb/^{238}U ratio of sequence 1 reproduce to 203.0±1.1 Ma (MSWD = 0.6) and that of sequence 2 to 201.3±0.9 Ma (MSWD = 1.3). Common Pb corrections were not applied, due to its high variability, although common Pb content was determined, using the ^{208}Pb signal after subtracting the radiogenic ^{208}Pb (Millonig et al., 2012). According to the analysed standard materials accuracy and repeatability of the method can be assumed to be better than 2 %.

Points of each sample data set derived from a small area (< 1 cm^2) and defining linear arrays in the ^{207}Pb/^{206}Pb vs ^{238}U/^{206}Pb space (TW diagram, Tera and Wasserburg, 1972) interpreted to be a mixture of initial common-Pb and Pb that formed due to *in situ* decay of U since mineralization. The age of formation is defined by the lower intercept with the Concordia curve. Plots and ages were calculated using Isoplot 3.71 (Ludwig, 2007). All uncertainties are reported at the 2σ level.

5 Results

In the following, we summarize the geochronological data (671 analyses) including the lithological context of the analysed samples. According to their lithological context, mineral chemistry and age, garnets associated with skarns in the Erzgebirge can be subdivided into three different types:

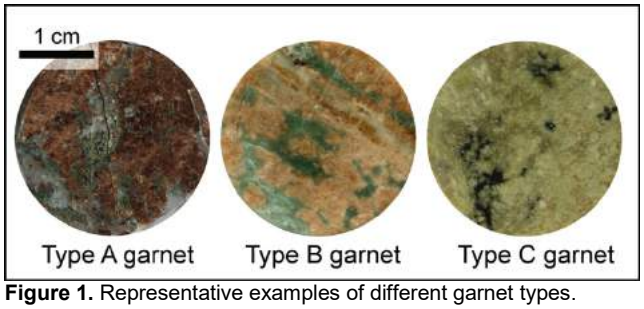

Figure 1. Representative examples of different garnet types.

5.1 Garnet type A (Grt-A)

Grt-A is of sub-calcic composition and forms irregularly shaped dark-red lenses, which may reach up to several cm in size. Individual garnet grains are anhedral and fine-medium grained. Besides pyroxene and magnetite,

abundant quartz accompanies this type of garnet. Lower intercept ages range from 342.9±5.1 to 330.7±10 Ma. Grt-A is locally associated with reaction skarns that occur at interfaces of chemically contrasting lithologies within high grade gneiss units - without any affiliation to intrusions. These skarns do not host significant metal endowment and are therefore not considered to be fertile. Niederschmiedeberg and Boden are examples where this garnet-type occurs.

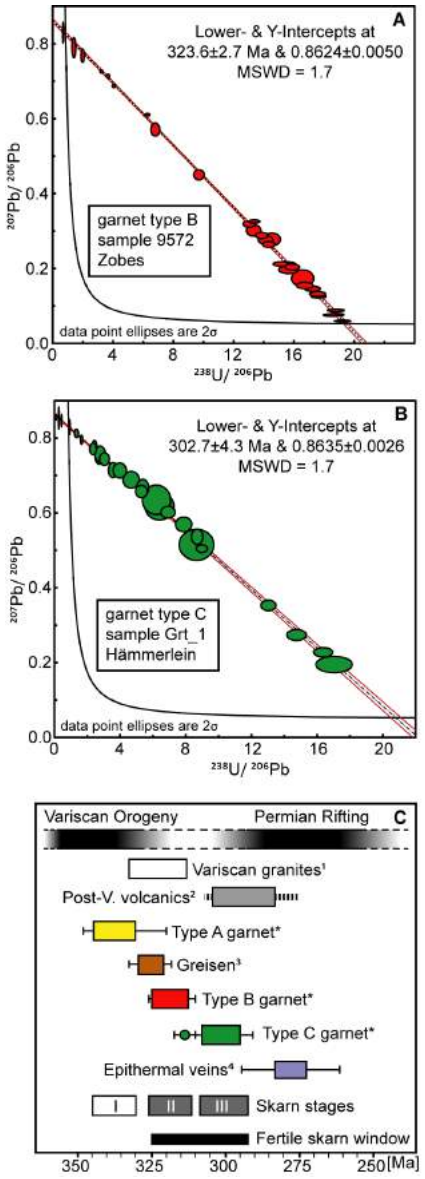

Figure 2. A) Tera-Wasserburg isochron diagram of sample 9572 B) Tera-Wasserburg isochron diagram of sample Grt_1 C) Summary of age data within the geotectonic framework of the Erzgebirge. References cited: [1](Finger et al., 2009; Förster and Romer, 2010; Romer et al., 2010; Tichomirowa and Leonhardt, 2010); [2](Kempe et al., 2004; Romer et al., 2010; Hoffmann et al., 2013); [3](Zhang et al., 2017); [4](Ostendorf et al., 2018); *this study.

5.2 Garnet type B (Grt-B)

Grt-B is a pale to dark red garnet, which typically occurs as alternating layers along with pyroxene, vesuvianite and calcite, which results in a skarnoid texture (intermediate between metamorphic hornfels and metasomatic skarn) parallel to the surrounding lithologies. Individual grandite crystals are fine-grained and subhedral. Primary skarn minerals are often associated with fine-grained scheelite and/or cassiterite. Zinc-Fe-Cu-sulfides occur abundantly, but are often associated with retrograde overprint of the primary skarn mineralogy. These skarns typically host significant quantities of Sn, W, Zn, Cu and Fe - consequently, these are considered as fertile. Dates of Grt-B (Fig. 2A) range from 325.5±2.3 to 312.8±3.4 Ma. Type B garnet is present in skarns that occur in close vicinity (0 to 200 m) to granitoid intrusions (e.g. Zobes). Meta-pelitic hornfelses are often associated with these skarns, which typically contain cordierite and andalusite (Hiller and Schuppan, 2016). Additionally, Grt-B may occur early in the paragenetic sequence of skarns, which also contain abundant type C garnet (e.g. Hämmerlein and Breitenbrunn).

5.3 Garnet type C (Grt-C)

Grt-C is pale brown-green to pale green and forms masses of medium-coarse grained euhedral crystals. This garnet is associated with coeval pyroxene. Primary skarn minerals form an isometric, metasomatic fabric and are accompanied by coeval magnetite, sphalerite and minor amounts of cassiterite (Hösel, 2003). Lower intercept ages range from 308.1±3.6 to 295.5±4.4 Ma (Fig 2B), except one outlier, which has an age of 313.1±4.4 Ma. Skarn bodies with Grt-C (e.g. Hämmerlein, Breitenbrunn and Berggießhübel; Fig. 1) may reach up to several km in lateral extent (Schuppan and Hiller, 2013) and are typically well-mineralized. Investigated garnet grains are from distal skarn environments, hundreds to thousands of m away from known intrusions. Although the majority of cassiterite and sulfides in such skarns are related to the retrograde stage of skarn formation, the occurrence of Grt-C is still regarded as an indicator of skarn fertility.

6 Discussion and conclusion

Economically most important skarns (e.g. Hämmerlein and Breitenbrunn) are not genetically associated with known late-orogenic intrusions. Instead, they are affiliated with a younger, post-orogenic magmatic phase (Fig. 2C) - the actual source intrusion to the largest skarn system (Schwarzenberg District) remains as yet undiscovered. Consequently, distal skarns (hosting Grt-C) may occur anywhere, where hydrothermal fluids encountered receptive lithologies. Undiscovered proximal skarns (with Grt-B) could occur in deeper crustal levels where reactive lithologies are present. Two skarn bodies with exceptionally rich metal endowment - the Hämmerlein and the Breitenbrunn skarns - host two distinctively different garnet generations which are related to different magmatic-hydrothermal events. As a consequence, skarns affected by multiple hydrothermal overprinting seem

generally to be most fertile.

Acknowledgements

We would like to thank C. Kehrer of the geoscientific collection of the TU Bergakademie Freiberg and T. Petermann for support with the sample selection. S. Gilbricht, A. Bartzsch, R. Würkert and M. Stoll are thanked for sample characterization/preparation. This study was partly funded by the BMBF (ResErVar) and the European Social Fund (Grant no. 100339454)

References

Baumann, L., Kuschka, E., and Seifert, T., 2000, Lagerstätten des Erzgebirges: Enke im Thieme-Verlag, Stuttgart.

Burisch, M., Hartmann, A., Bach, W., Krolop, P., Krause, J., and Gutzmer, J., 2018, Genesis of hydrothermal silver-antimony-sulfide veins of the Bräunsdorf sector as part of the classic Freiberg silver mining district, Germany: Mineralium Deposita,, p. 1–18.

Chen, Y.-J., Chen, H.-Y., Zaw, K., Pirajno, F., and Zhang, Z.-J., 2007, Geodynamic settings and tectonic model of skarn gold deposits in China: an overview: Ore geology reviews, 31(1-4):139–169.

Deng, X.-D., Li, J.-W., Luo, T., and Wang, H.-Q., 2017, Dating magmatic and hydrothermal processes using andradite-rich garnet U–Pb geochronometry: Contributions to Mineralogy and Petrology, 172(9):71.

Elsner, H., 2014, Zinn - Angebot und Nachfrage bis 2020: Deutsche Rohstoffagentur (DERA), 68 p.

Finger, F., Gerdes, A., René, M., and Riegler, G., 2009, The Saxo-Danubian Granite Belt: magmatic response to post-collisional delamination of mantle lithosphere below the southwestern sector of the Bohemian Massif (Variscan orogen): Geologica Carpathica, 60(3):205–212.

Förster, H.-J., and Romer, R.L., 2010, Carboniferous magmatism, *in* Linnemann, U. and Romer, R.L. eds., Pre-Mesozoic geology of Saxo-Thuringia: From the Cadomian active margin to the Variscan orogen, Schweizerbart, Stuttgart, p. 287–308.

Förster, H.-J., Tischendorf, G., Trumbull, R.B., and Gottesmann, B., 1999, Late-collisional granites in the Variscan Erzgebirge, Germany: Journal of Petrology, 40(11):1613–1645.

Gerdes, A., and Zeh, A., 2006, Combined U–Pb and Hf isotope LA-(MC-) ICP-MS analyses of detrital zircons: comparison with SHRIMP and new constraints for the provenance and age of an Armorican metasediment in Central Germany: Earth and Planetary Science Letters, 249(1):47–61.

Gerdes, A., and Zeh, A., 2009, Zircon formation versus zircon alteration—new insights from combined U–Pb and Lu–Hf in-situ LA-ICP-MS analyses, and consequences for the interpretation of Archean zircon from the Central Zone of the Limpopo Belt: Chemical Geology, 261(3):230–243.

Gevedon, M., Seman, S., Barnes, J.D., Lackey, J.S., and Stockli, D.F., 2018, Unraveling histories of hydrothermal systems via U–Pb laser ablation dating of skarn garnet: Earth and Planetary Science Letters, 498:237–246.

Hiller, A., and Schuppan, W., 2016, Das Lagerstättengebiet Zobes-Bergen im Vogtland und benachbarte Uranvorkommen im Bereich des Bergener Granitmassivs: Band 18, LfULG, Freiberg.

Hoffmann, U., Breitkreuz, C., Breiter, K., Sergeev, S., Stanek, K., and Tichomirowa, M., 2013, Carboniferous–Permian volcanic evolution in Central Europe—U/Pb ages of volcanic rocks in Saxony (Germany) and northern Bohemia (Czech Republic): International Journal of Earth Sciences, 102(1):73–99.

Hösel, G., 2003, Die polymetallische Skarnlagerstätte Pöhla-Globenstein: Band 8, LfULG, Freiberg.

Kempe, U., Bombach, K., Matukov, D., Schlothauer, T., Hutschenreuter, J., Wolf, D., and Sergeev, S., 2004, Pb/Pb and U/Pb zircon dating of subvolcanic rhyolite as a time marker for Hercynian granite magmatism and Sn mineralisation in the Eibenstock granite, Erzgebirge, Germany: Considering effects of zircon alteration: Mineralium Deposita, 39(5-6):646–669.

Kröner, A., and Willner, A.P., 1998, Time of formation and peak of Variscan HP-HT metamorphism of quartz-feldspar rocks in the central Erzgebirge, Saxony, Germany: Contributions to Mineralogy and Petrology, 132(1):1–20.

Lefebvre, M.G., Romer, R.L., Glodny, J., Kroner, U., and Roscher, M., 2018, The Hämmerlein skarn-hosted polymetallic deposit and the Eibenstock granite associated greisen, western Erzgebirge, Germany: two phases of mineralization—two Sn sources: Mineralium Deposita,, p. 1–24.

Ludwig, K.J., 2007, Isoplot 3.62: Berkeley Geochronology Center Special Publication, 4:70.

Meinert, L.D., Dipple, G.M., and Nicolescu, S., 2005, World Skarn Deposits: Economic Geology, v. 100th Anniversarry Volume, p. 299–336.

Millonig, L.J., Gerdes, A., and Groat, L.A., 2012, U–Th–Pb geochronology of meta-carbonatites and meta-alkaline rocks in the southern Canadian Cordillera: a geodynamic perspective: Lithos, 152:202–217.

Ostendorf, J., Henjes-Kunst, F., Seifert, T., and Gutzmer, J., 2018, Age and genesis of polymetallic vein-type mineralization in the Freiberg ore district, Erzgebirge (Germany): Constraints from radiogenic isotopes: Mineralium Deposita.

Romer, R.L., Förster, H.-J., and Štemprok, M., 2010, Age constraints for the late-Variscan magmatism in the Altenberg–Teplice Caldera (Eastern Erzgebirge/Krušné hory): Neues Jahrbuch für Mineralogie-Abhandlungen: Journal of Mineralogy and Geochemistry, 187(3):289–305.

Schuppan, W., and Hiller, A., 2013, Die Komplexlagerstätten Tellerhäuser und Hämmerlein: Band 17, LfULG, Freiberg.

Seifert, T., 2008, Metallogeny and Petrogenesis of Lamprophyres in the Mid-European Variscides: Post-collisional Magmatism and Its Relationship to Late-Variscan Ore Forming Processes in the Erzgebirge (Bohemian Massif): IOS Press, Rotterdam.

Seman, S., Stockli, D.F., and McLean, N.M., 2017, U-Pb geochronology of grossular-andradite garnet: Chemical Geology, 460:106–116.

Tera, F., and Wasserburg, G.J., 1972, U-Th-Pb systematics in three Apollo 14 basalts and the problem of initial Pb in lunar rocks: Earth and Planetary Science Letters, 14(3):281–304.

Tichomirowa, M., and Leonhardt, D., 2010, New age determinations (Pb/Pb zircon evaporation, Rb/Sr) on the granites from Aue-Schwarzenberg and Eibenstock, western Erzgebirge, Germany: Z geol Wiss, 38(2-3):99–123.

Wafforn, S., Seman, S., Kyle, J.R., Stockli, D., Leys, C., Sonbait, D., and Cloos, M., 2018, Andradite garnet U-Pb geochronology of the Big Gossan skarn, Ertsberg-Grasberg Mining District, Indonesia: Economic Geology, 113(3):769–778.

Zhang, R., Lehmann, B., Seltmann, R., Sun, W., and Li, C., 2017, Cassiterite U-Pb geochronology constrains magmatic-hydrothermal evolution in complex evolved granite systems: The classic Erzgebirge tin province (Saxony and Bohemia): Geology, 45(12):1095–1098.

Chemistry of magnetite in a Mg-skarn iron deposit from the Serranía de Ronda, SW Spain

Antonio J. Moreno-Abril, José María González Jiménez, Fernando Gervilla
Departamento de Mineralogía y Petrología, Universidad de Granada, Facultad de Ciencias, Spain.

Vanessa Colás
Departamento de Procesos Litosféricos, Instituto de Geología, Universidad Nacional Autónoma de México, Ciudad Universitaria, México

Fernando Tornos
Instituto de Geociencias, Consejo Superior de Investigaciones Cientificas-Universidad Complutense de Madrid (CSIC-UCM), Spain.

Isabel Fanlo & Ignacio Subias
Departamento de Ciencias de la Tierra, Universidad de Zaragoza, Spain.

Abstract. This communication provides the first-ever scientific study of the mineralogy and chemistry of magnetite of the Mg-skarn iron deposit of San Manuel, Serranía de Ronda in SW Spain. This iron deposit is hosted in marbles overlying migmatites found forming a tectonic slice along the southern contact of the Ronda ultramafic massif. Prograde and retrograde skarn stages have resulted in zoning of magnetite, characterized by variations in the chemistry and typology of mineral inclusions. Using laser-ablation ICPMS we have measured the contents of trace elements in magnetite, fingerprinting the origin of the mineralizing fluid as related to the migmatites that originated during host emplacement of the upper mantle peridotites in the continental crust.

1 Introduction

Magnetite has been mined intermittently in the Serranía de Ronda, southern Spain since the middle of the IX century till late XIX century. These orebodies share most of the features of magnesial skarns but have the singularity that they are located near the contact between upper mantle ultramafic and metasedimentary rocks, a very rare setting for this type of ore. Despite systematic mining and the abundance of studies dealing with the Ronda Massif, few scientific efforts have focused to understand the genesis of these deposits. In particular, the potential role that the ultramafic rocks played in the formation of the skarns is still unknown.

Within the last few years, the analysis of trace elements in magnetite has been proposed as a tool for understanding the tectonic geodynamic setting and for classification of iron deposits (Dupuis & Beaudoin, 2014; Dare et al., 2014; Nadoll et al., 2014; Hu et al., 2015, 2017; Wang et al., 2018) despite the fact that there is more and more evidence that this approach is not definitive and is unable to distinguish between magmatic and hydrothermal magnetite nor the type of mineralization (Velasco et al., 2016; Broughm et al., 2017). However, trace element geochemistry of magnetite can be useful for distinguishing between different generations of magnetite. This approach relies on the fact that magnetite is an oxide-type mineral that may host variable concentrations of a wide suite of minor (e.g., Mn, Co, Ni, V, Ti, Zn) and trace (e.g., Ga, Ge, Y Zr, Nb, W, Pb, Sb) elements in enough amounts to be measurable using a wide range of techniques for *in-situ* microanalysis such as electron microprobe and LA-ICPMS.

An ever increasing body of work has shown that magnetite in different suites of magmatic-hydrothermal deposits may exhibit complex patterns of zoning (Hu et al., 2014, 2015; Knipping et al., 2015). Zoning is related to single pluses of variation in the composition/nature of the parental magma or hydrothermal fluid, which left its characteristic chemical fingerprint in the magnetite itself. Additionally, a given chemical composition of the magnetite can be related to a specific type of assemblage of nano-to-micron sized mineral inclusions in the given sectors of the magnetite grain (Deditius et al., 2018).

A combination of electron microprobe and laser-ablation microprobe (LAM) coupled to an ICPMS was used for the *in-situ* measurement of minor and trace elements in zoned magnetite from the Mg-skarn iron deposit of San Manuel, Serranía de Ronda, southern Spain. Our preliminary results suggest that during the emplacement of the mantle peridotites in the continental crust, fluids separated during the anatexis of the host crustal rocks could have contributed to the remobilization of iron from metasediments, leading to the precipitation of magnetite ore in the overlying dolomitic marbles.

2 Geological setting of the San Manuel iron deposit

2.1 The Ronda ultramafic massif and its crustal envelope

Three large (> 60 km^2) massifs of ultramafic rocks known as Ronda, Ojen and Carratraca occur widespread in the internal zones of the Betic Cordillera, SW Spain (Fig. 1). These ultramafic massifs correspond to portions of an ancient (1.2-1.8 Ga) subcontinental

lithospheric mantle (SCLM) (Reisberg and Lorand, 1995; Marchesi et al., 2010; González-Jiménez et al., 2013). Among these massifs, Ronda is the largest one. It is thought to be the largest exposure (~300 km^2) of SCLM on Earth. This massif consists of lherzolite and harzburgite with minor amount of dunite as well as different types of pyroxenite. Crustal emplacement of these upper mantle rocks took place during the Late Oligocene/Early Miocene, related to a period of extension that promoted the opening of the Alboran marine basin in the western realm of the Mediterranean Sea. The peridotite was emplaced into the continental crust by means of a thrust-fold structure. Thus, they are overlain by a thick unit of up to 7 km of metapelitic rocks (varying from acid granulite, gneiss and migmatite, to schist, phyllite and locally marble) and underlain by Triassic dolomitic marbles. The emplacement of the peridotite into the crust was still relatively hot, promoting dehydration and subsequent anatexis of the metasediments, and leading to the formation of dikes and migmatite that intruded the peridotite between 22 and 18 Ma.

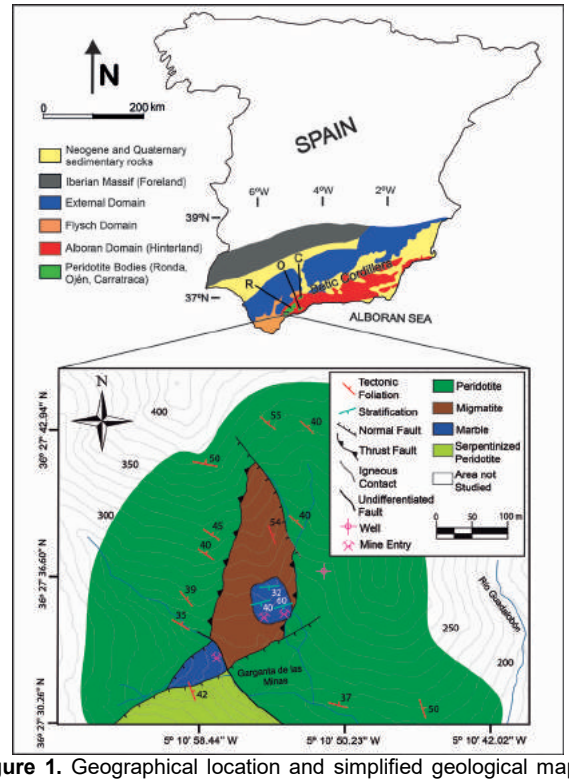

Figure 1. Geographical location and simplified geological map of the ultramafic massifs of the Serranía de Ronda in southern Spain showing the location of the San Manuel Mg-skarn iron deposit.

2.2 Characterization of the Mg-skarn and structure of the iron deposit

The San Manuel iron mineralization is hosted in dolomitic marble overlying migmatite, both forming a tectonic slice imbricated into peridotite along the lower thrust of the southern contact of the Ronda ultramafic massif. An exposed section of ~ 25m of this tectonic slice contains, from the bottom to the top, (1) ~12 m of dolomitic marble completely replaced by a retrograde magnesial skarn (chlorite, serpentine, brucite); (2) a body (1-2.5 m) of massive iron ore; (3) ~ 9 m of prograde magnesial skarn characterized by the presence of olivine, calcite and diopside. Magnetite may be found forming the massive body as well as disseminations along the whole profile. Other metallic minerals include pyrite and chalcopyrite, which are found disseminated in the groundmass of the semi-massive magnetite or in the metasomatized carbonatic rock.

3 Petrography and texture of magnetite

Magnetite at San Manuel includes massive (>85% magnetite) to semi-massive (60-85% magnetite) and disseminated (< 30 % magnetite) textures. In addition, it shows three texturally different types according to the zoning (Fig. 2): (1) ***Type-A zoning*** found in semi-massive samples, which shows cores of Mg-ferrite (Mt-1) hosting inclusions of dolomite. It is surrounded by four distinct rims of magnetite (Mt2, Mt3, Mt4 and Mt5). ***Type-B zoning*** consisting of cores of Mg-ferrite (Mt1) rimmed by porous magnetite (Mt2) in turn enclosed by homogenous magnetite free of inclusions (Mt5). ***Type-C zoning*** consists of cores of magnetite with abundant small inclusions of spinel (Mt3) and hosted by magnetite with inclusions of spinel and chlorite (Mt4) and an external rim of magnetite lacking of inclusions (Mt5).

4 Chemical composition of magnetite

4.1 Major elements

Magnesian ferrite (Mt1) forming cores of Type-1 and Type-2 zoning (Fig. 2) shows $Fe^{3+}/Fe^{2+}+Al^{3+}$ = 0.99-1, $Fe^{2+}/Fe^{2+}+Mg^{2+}$=0.43-0.64 and Mg+Mn =6.8-10.9. Porous magnetite (Mt2) hosting inclusions of dolomite ± chlorite± serpentine surrounds these cores, showing similar $Fe^{3+}/Fe^{2+}+Al^{3+}$ = 0.98-1 and $Fe^{2+}/Fe^{2+}+Mg^{2+}$=0.78-0.1 but lower Mg+Mn <4.11. The third rim of magnetite (Mt3) characterized by the presence of abundant tiny inclusions of spinel show wider $Fe^{3+}/Fe^{2+}+Al^{3+}$ = 0.89-1 and $Fe^{2+}/Fe^{2+}+Mg^{2+}$=0.09-1 and Mg+Mn=0.02-6.08 than Mt1 and Mt2. Magnetite hosting inclusions of spinel and chlorite (Mt4) shows $Fe^{3+}/Fe^{2+}+Al^{3+}$ = 0.96-1 and $Fe^{2+}/Fe^{2+}+Mg^{2+}$=0.63-0.84 and Mg+Mn=2.38-7. Finally, the outermost rim of magnetite free of inclusions (Mt5) exhibits $Fe^{3+}/Fe^{2+}+Al^{3+}$ = 0.99-1 and $Fe^{2+}/Fe^{2+}+Mg^{2+}$=0.96-1 and <0.72. Other elements including Cr_2O_3, CaO, ZnO, NiO, MnO and MgO are below or marginally higher than the detection limit of electron probe at the conditions used for these analyses.

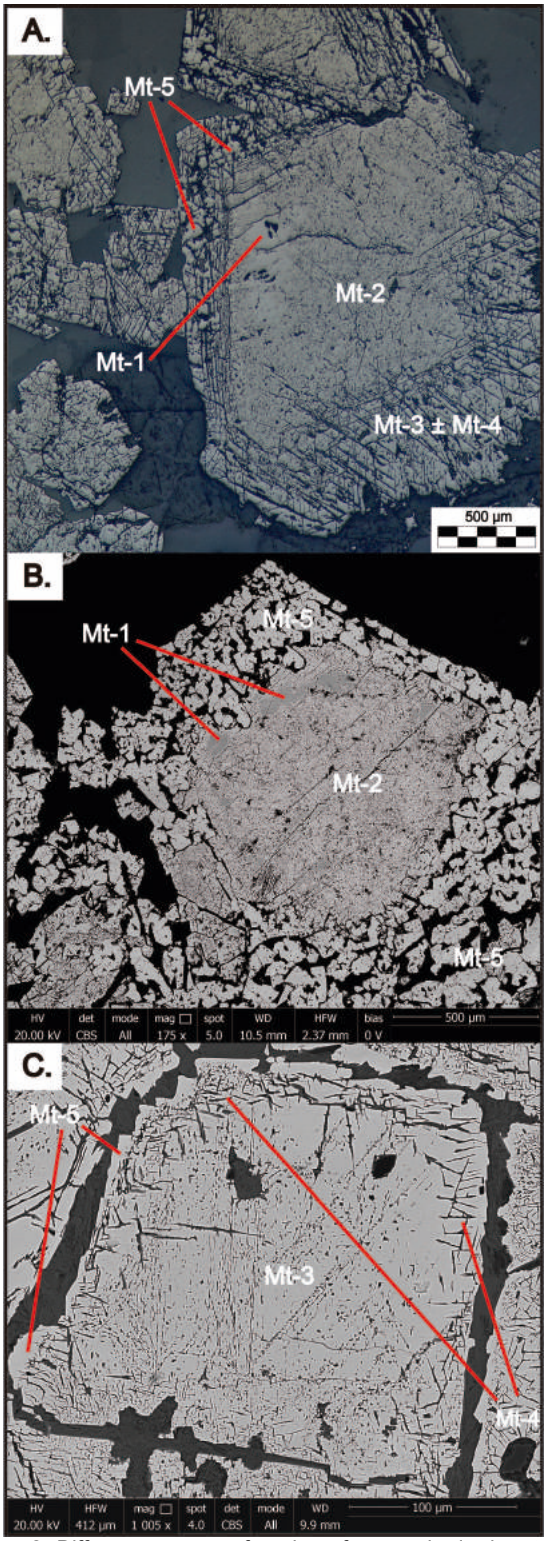

Figure 2. Different patterns of zoning of magnetite in the studied ore. A: Type-A zoning, B: Type -B zoning, C: Type-C zoning.

4.2 Minor and trace elements

The analysis of minor and trace elements of the different magnetite rims using LA-ICPMS show the following ranges of Ti (in ppm): 0.1-325 (Mt1), 0.44-100 (Mt2), 1.33-18200 (Mt3), 38.6-37.5 (Mt4), 5.2-475 (Mt5). The cores of Mg-ferrite have relatively similar contents of Ga (0.66-9.10 ppm) than the rims of Mt2 (0.28-7.5 ppm) and Mt4 (2.8-7 ppm) and Mt5 (0.2-11 ppm) but lower than the rims of Mt3 (0.54-57.55 ppm). Overall, there are core-to-rims trends characterized by a progressive increasing of the Ti/V and Ga/Al contents. In plots Zn+Co+Mn v*s* Ga each magnetite type defines a very distinct group with a progressive increasing of Ga content from Mt1 to Mt2 and Mt3 and Mt4, respectively (Fig. 3).

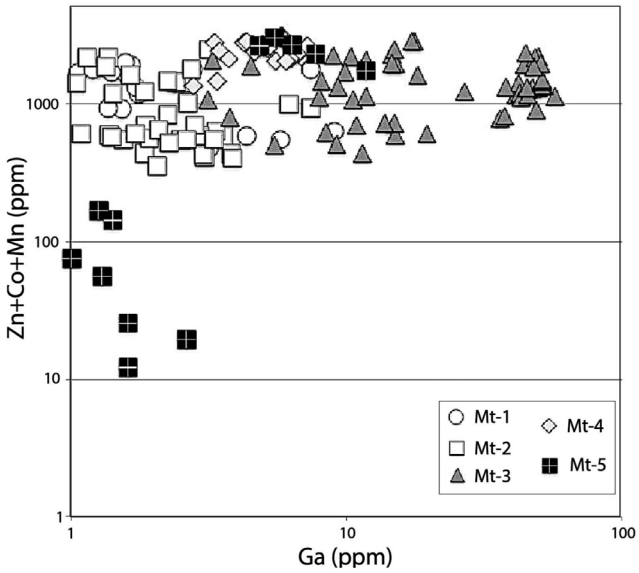

Figure 3. Plot of trace elements Ga vs. Zn+Co+Mn for the difeent types of magnetites identified in the San Manuel magnetite skarn deposit.

Characteristically, Mg-ferrite cores show relatively higher contents of W (2.8-370 ppm) than the rims of Mt2 (0.42-210 ppm) and Mt4 (0.11-2.46 ppm) but lower than Mt3 (<914 ppm) and Mt5 (845 ppm). Similarly, there is a progressive core-to-rim increase of Hg (Mt1 <2500 ppm, Mt2<2300 ppm, Mt3<2710 ppm, Mt4< 3460 ppm, Mt5<3100 ppm) but decreasing of Pb (Mt1 <4.2 ppm, Mt2<2.11 ppm, Mt3<2.87 ppm, Mt4 and Mt5 < 0.74).

5 Discussion

Textural and chemical variation of the studied magnetite from the San Manuel Mg-skarn iron deposit can be related to two distinctively different mineralizing events, which are probably related with the prograde and retrograde evolution of the skarn. Being part of a skarn, this magnetite is thought to have been precipitated from hydrothermal fluids by fluid-rock interaction.

It is worth noting that the relic cores of Mg-ferrite hosting dolomite inclusions are found in grains exhibiting Type-A and Type-B zoning, which are distributed along the entire section of the Mg-skarn including the prograde and retrograde portions. This suggests that the crystallization of Mg-ferrite during the first stage of prograde skarn was very likely from a hydrothermal fluid that supplied Fe and leached Mg during the replacement process. This is consistent with the fact that Type-A zoning predominates the proximities of the major

orebody located between the prograde and the retrograde skarns. In contrast, the formation of a second generation of porous magnetite (Mt2) in these zoned grains is characterized by the presence of inclusions of dolomite ± chlorite± serpentine and similar $Fe^{3+}/Fe^{2+}+Al^{3+}$, $Fe^{2+}/Fe^{2+}+Mg^{2+}$ and lower Mg and Mn, pointing out that the Mt2 is due to the replacement of the Mg-ferrite during the retrograde skarn stage. Moreover, the formation of rims of Mt3 and Mt4 hosting inclusions of spinel and spinel + chlorite indicate further alteration of the pre-existing magnetite by fluids progressively enriched in Al. This later event of alteration may be linked to a stage when the retrograde skarn was more developed, consistently with the fact that the grains of magnetite lacking of Mt1 and Mt2 but consisting of cores of Mt3 surrounded by Mt4 and Mt5 (i.e., Type-C zoning) predominate in the retrograde Mg-skarn.

On the other hand, the analysed magnetite exhibits relatively high contents of W, Hg and Pb. These elements are not typically supplied from hydrothermal fluids derived from upper mantle rocks. Rather, this enrichment is consistent with the hydrothermal fluids being derived from crustal rocks. Indeed, this trace element fingerprint tracks the source of the hydrothermal fluids as related with the dehydration/anatexis of metasediments during the hot emplacement of the peridotites. Variations of these trace elements along the cores and rims of the differently zoned magnetite grains may highlight individual changes in the composition of the parental hydrothermal fluid, each one left behind a characteristic chemical fingerprint in the magnetite itself, similarly to reported zoned magnetite from magmatic-hydrothermal deposits elsewhere (Deditius et al., 2018).

Acknowledgements

Funding for this research was provided by the project CCGL2014-55949-R and the Ramón y Cajal Fellowship RYC-2015-17596 granted by the Spanish “Ministerio de Economía y Competitividad”.

References

Broughm SG, Hanchar JM, Tornos F, Westhues A, Attersley S (2017) Mineral chemistry of magnetite from magnetite-apatite mineralization and their host rocks: examples from Kiruna, Sweden, and El Laco, Chile. Miner Deposita 52:1223-44.

Dare SA, Barnes SJ, Beaudoin G, Méric J, Boutroy E, Potvin-Doucet C (2014) Trace elements in magnetite as petrogenetic indicators. Miner Deposita 49:785-96.

Deditius AP, Reich M, Simon AC, Suvorova A, Knipping J, Roberts MP, Rubanov S, Dodd A, Saunders M (2018) Nanogeochemistry of hydrothermal magnetite. Contrib Mineral Petrol 173:46.

Dupuis C, Beaudoin G (2011) Discriminant diagrams for iron oxide trace element fingerprinting of mineral deposit types. Miner Deposita 46:319-35.

González-Jiménez JM, Marchesi C, Griffin WL, Gutiérrez-Narbona R, Lorand JP, O'Reilly SY, Garrido CJ, Gervilla F, Pearson NJ, Hidas K (2013) Transfer of Os isotopic signatures from peridotite to chromitite in the subcontinental mantle: insights from in situ analysis of platinum-group and base-metal minerals (Ojén peridotite massif, southern Spain). Lithos 164:74-85.

Hu H, Li JW, Lentz D, Ren Z, Zhao XF, Deng XD, Hall D (2014) Dissolution–reprecipitation process of magnetite from the Chengchao iron deposit: insights into ore genesis and implication for in-situ chemical analysis of magnetite. Ore Geol Rev 57:393-405.

Hu H, Lentz D, Li JW, McCarron T, Zhao XF, Hall D (2015) Reequilibration processes in magnetite from iron skarn deposits. Econ Geol 110:1-8.

Hu X, Chen H, Zhao L, Han J, Xia X. Magnetite geochemistry of the Longqiao and Tieshan Fe–(Cu) deposits in the Middle-Lower Yangtze River Belt: Implications for deposit type and ore genesis (2017). Ore Geol Rev 89:822-35.

Knipping JL, Bilenker LD, Simon AC, Reich M, Barra F, Deditius AP, Lundstrom C, Bindeman I, Munizaga R (2015) Giant Kiruna-type deposits form by efficient flotation of magmatic magnetite suspensions. Geology 43:591-4.

Marchesi C, Griffin WL, Garrido CJ, Bodinier JL, O’Reilly SY, Pearson NJ (2010) Persistence of mantle lithospheric Re–Os signature during asthenospherization of the subcontinental lithospheric mantle: insights from in situ isotopic analysis of sulfides from the Ronda peridotite (Southern Spain). Contrib Mineral Petrol 159:315-30.

Nadoll P, Angerer T, Mauk JL, French D, Walshe J (2014) The chemistry of hydrothermal magnetite: A review. Ore Geol Rev 61:1-32.

Reisberg L, Lorand JP (1995) Longevity of sub-continental mantle lithosphere from osmium isotope systematics in orogenic peridotite massifs. Nature 376:159.

Velasco F, Tornos F, Hanchar JM (2016) Immiscible iron-and silica-rich melts and magnetite geochemistry at the El Laco volcano (northern Chile): evidence for a magmatic origin for the magnetite deposits. Ore Geol Rev 79:346-66.

Wang C, Shao Y, Zhang X, Dick J, Liu Z (2018) Trace Element Geochemistry of Magnetite: Implications for Ore Genesis of the Huangganglіang Sn-Fe Deposit, Inner Mongolia, Northeastern China. Minerals 8:195.

Magnetite skarns: precursor and process controls on iron mineralization (Bohemian Massif, central Europe)

Jan Bubal
Museum of the Bohemian Paradise, Czech Republic

Kateřina D. Schlöglová[1,2] and David Dolejš[1]
[1]Institute of Earth and Environmental Sciences, University of Freiburg, Germany
[2]KDS GeoConsult

Abstract. Regional metamorphic complexes in the Bohemian Massif (central Europe) host numerous occurrences of magnetite-mineralized calcic skarns. A well exposed and petrographically variable body near Malešov contains pyroxene, garnet, epidote and magnetite skarn varieties. The pyroxene and magnetite skarns represent products of successive metasomatism of carbonate-rich precursors, whereas the garnet and epidote skarns were produced by replacement of carbonate-siliciclastic precursor. The extent of magnetite mineralization has been controlled by high carbonate reactivity in the appropriate precursor types, coupled with positive feedback of porosity formation during decarbonation reactions. Trace-element distribution in the skarns and in magnetite favors the carbonate replacement hypothesis over the formation by isochemical metamorphism of iron-rich exhalative or sedimentary horizons.

1 Introduction

The Malešov magnetite skarn deposit is located 7 km SW of the town of Kutná Hora, in the central part of the Bohemian Massif, Czech Republic. It is one of the most prominent magnetite skarn deposits in the Bohemian Massif, historically exploited for iron. The origin of magnetite mineralization of skarn type in high-grade metamorphic complexes of the Bohemian Massif has been intensely debated. Accordingly, the magnetite skarns represent (1) metamorphosed ironstones (Zoubek 1946; Vrána 1987; Drahota et al. 2005), (2) metamorphosed iron-rich exhalative-sedimentary horizons (Pertold et al. 2000; Pertoldová et al. 2009), or (3) products of metasomatism of carbonate or marly precursors (Němec 1991; Žáček 1997; 2007). In order to test these competing hypotheses, we have performed detailed mineralogical and geochemical study of the Malešov skarn body, owing to its internal variability, extent of exposure, and accessibility.

Twenty-two hand specimens of skarns and adjacent host rocks were collected in the ground level adit of the mine (Fig. 1) and investigated using optical microscopy, SEM (Tescan Vega, X-max 50; Faculty of Science, Charles University, Prague), EPMA (CAMECA SX100, Faculty of Science, Masaryk University, Brno), and whole-rock geochemistry (Actlabs, Lancaster). Detailed description of the studied samples and analytical conditions can be found in Bubal (2013).

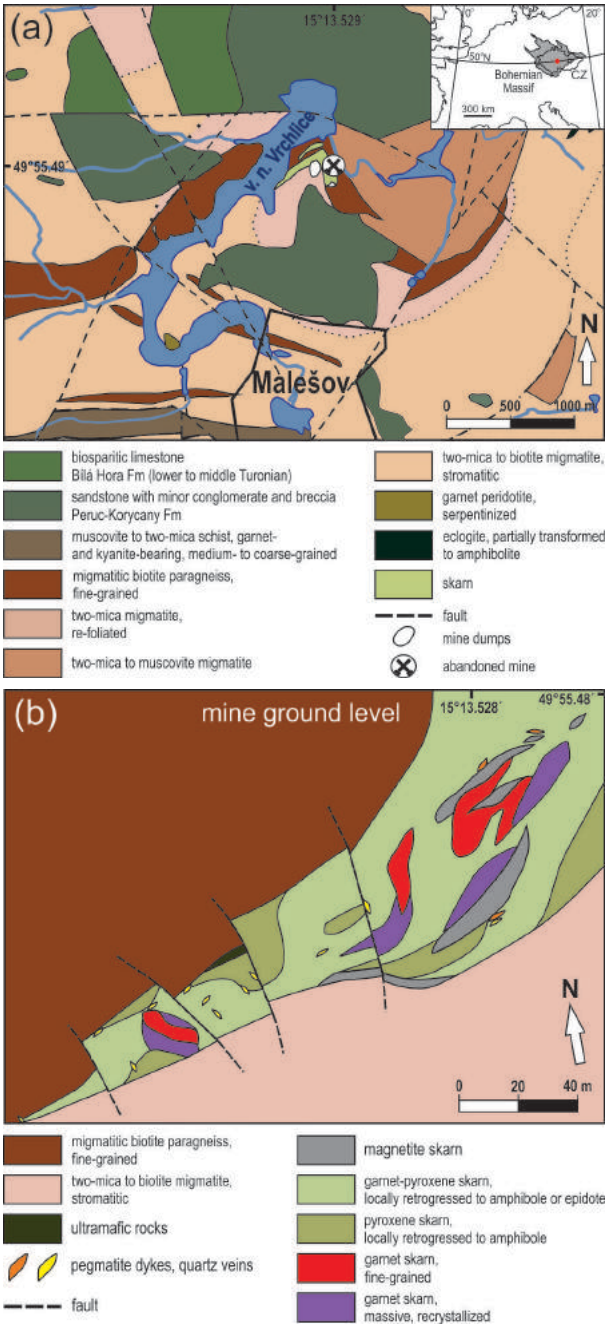

Figure 1. (a) Geological map of the Malešov skarn deposit area, after Štedrá et al. (2011); (b) mine-scale detailed geological map depicting variation in the skarn types at the Malešov skarn deposit.

2 Geological setting

The Malešov magnetite skarn forms an approx. 300 m thick lenticular body, hosted by paragneisses and migmatites of the Kutná Hora Crystalline Complex (Fig. 1a). The dominant calc-silicate minerals are garnet and pyroxene, locally transformed to retrograde hydrous assemblages containing amphibole and/or epidote. Recrystallization of primary skarn assemblages and the formation of hydrous mineral assemblages is associated with Variscan regional metamorphism (Kachlík 1999; Štědrá and Nahodilová 2009) and subsequent emplacement of up to 1 m-thick granite-pegmatite dykes along brittle fractures. Magnetite can be disseminated in pyroxene-dominated skarns or concentrated into massive NE-SW-oriented lenticular bodies (Fig. 1b), typically in anticlinal structures of the folded metamorphic complex. Occasionally, massive magnetite bodies contain traces of younger Fe-sulfides (e.g. pyrrhotite, pyrite).

3 Skarn mineralogy

Eight petrographic and textural varieties of skarns are recognized in the Malešov body (Figs. 2 and 3): (1) fine-grained pyroxene skarn with 80–90 vol% hedenbergite-rich clinopyroxene ($Hd_{60-90}Di_{19-36}$) and minor garnet, amphibole, chlorite, albite and magnetite (e.g. sample ML4); (2) fine-grained garnet skarn with up to 90 vol% optically isotropic andradite-rich garnet ($Adr_{78-88}Grs_{9-19}Alm_{2-4}$) and minor epidote, amphibole and calcite (sample ML18); (3) massive coarse-grained garnet skarn with older grossular-rich garnet cores ($Adr_{13-28}Grs_{31-50}Alm_{29-36}$) and younger andradite-rich rims ($Adr_{28-66}Grs_{21-37}Alm_{12-33}$), with up to 85 vol% garnet in the whole rock (sample ML14); (4) garnet-pyroxene skarn with approx. 60 vol% garnet and 30 vol% clinopyroxene, and minor amphibole, calcite, accessory magnetite, albite, epidote, muscovite, chlorite, titanite and zircon (samples ML3, ML5); (5) fine-grained epidote skarn (more than 70 vol% epidote; sample ML15); (6) garnet-epidote skarn with approx. 70 vol% garnet and 15 vol% epidote, with minor calcite and amphibole and accessory titanite (sample ML11); (7) magnetite skarn containing 50–60 vol% magnetite that replaces pyroxene and minor amounts of secondary amphibole, hematite and leucoxene (samples ML1 and ML17); and (8) partially silicified and amphibole-bearing skarn formed by retrograde overprint associated with emplacement of granite-pegmatite dykes (sample ML2). Amphibole, which formed at the expense of primary pyroxene, is close to hastingsite in composition, while amphibole in cross-cutting albite-calcite-amphibole veinlets evolves from ferrohornblende to actinolite.

Magnetite-rich skarns contain fine-grained, equant to sub-equant magnetite grains that enclose relics of clinopyroxene, and are locally replaced by amphibole. Magnetite has essentially pure endmember composition, and contains very low amounts of minor and trace elements: 0.43–0.76 wt% Al_2O_3, 0.04–0.12 wt% TiO_2, 0.04–0.11 wt% MnO, 0.001–0.006 wt% V_2O_3, 0.003–0.012 wt% Cr_2O_3, and 0.002–0.008 wt% NiO. Low abundances of trace elements, in particular Ni, Cr and V, are characteristic of hydrothermal-metasomatic replacement of carbonate precursor (Dupuis and Beaudoin 2011; Nadoll et al. 2012).

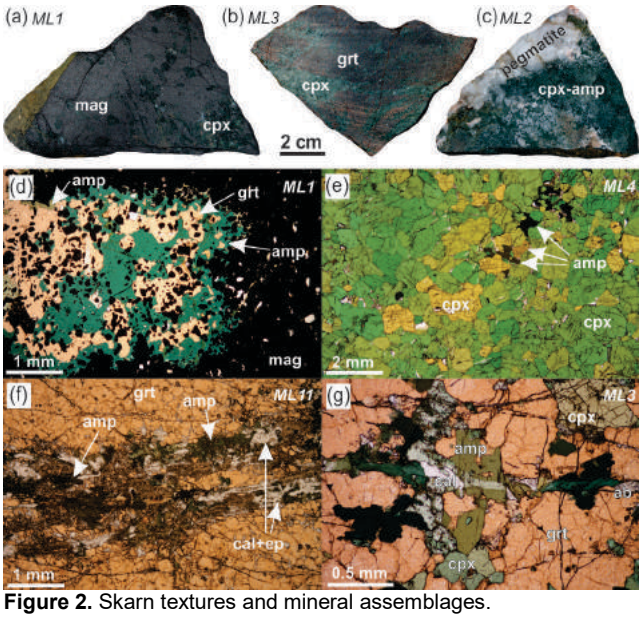

Figure 2. Skarn textures and mineral assemblages.

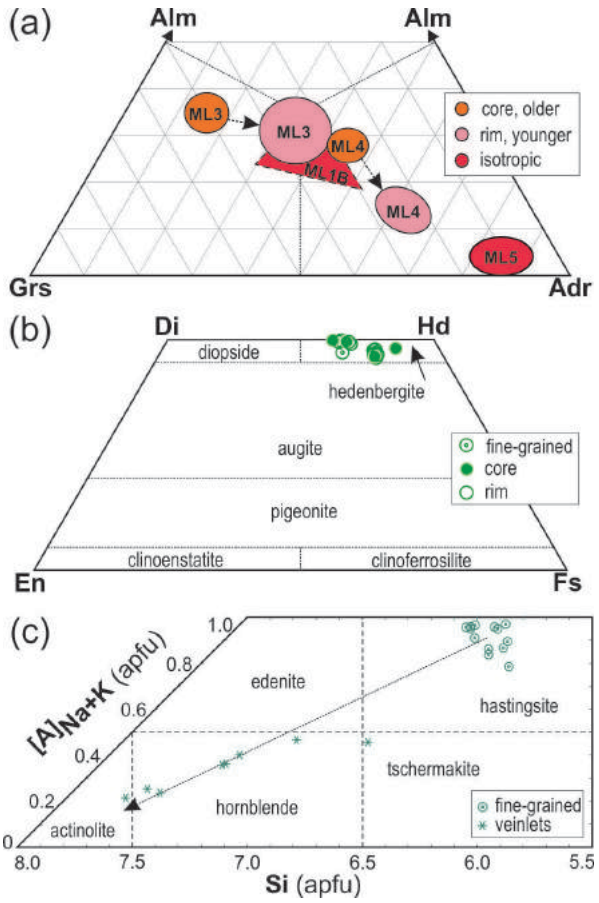

Figure 3. Composition of rock-forming minerals: (a) garnet, (b) pyroxene, and (c) amphibole.

Pressure-temperature conditions of the metamorphic overprint were assessed using univariant equilibria involving solid solutions and thermodynamic modeling. The association garnet-clinopyroxene-magnetite is stable at temperature above 500 °C and pressure of 0.5–1.5 GPa. Univariant exchange equilibria between garnet and clinopyroxene correspond to 670 °C at 1.0 GPa, indicating local Mg-Fe exchange during peak metamorphic conditions. Retrograde amphibole (hastingsite) formed at 550 °C and 0.6 GPa, followed by hornblende and actinolite below 440 °C and 0.4 GPa.

4 Whole-rock geochemistry

Individual skarn varieties are grouped into three categories based on major and trace element composition: (1) magnetite and pyroxene skarns are characterized by very low concentrations of the HFSE, Y, alkalis, and P. They have very low abundances of Al_2O_3 (<1.5 wt%), MnO (<0.2 wt%) and REE (4.4–13.1 ppm). (2) Garnet skarns have higher concentrations of HFSE, Al_2O_3 (5.8–10.4 wt%), and REE (44.1–71.6 ppm), but comparable amounts of alkalis and P_2O_5 (<0.1 wt%). (3) Retrograde epidote skarns generally contain the highest concentrations of Al_2O_3, HFSE and REE.

The chondrite-normalized distribution of REE shows two distinct sample groups (Fig. 4): (1) pyroxene and magnetite skarns with low total REE concentrations, enrichment of LREE as opposed to HREE, and weak positive Ce anomaly; (2) garnet, garnet-epidote and epidote skarns with high REE concentrations and strong positive Eu anomaly. The adjacent paragneiss host rock (sample ML13) shows the same REE enrichment but a prominent negative Eu anomaly. Skarns with coarse-grained, recrystallized andradite-rich garnets are enriched in LREE compared to those with early grossular-rich garnets. This decoupling is due to partitioning of REE between garnet and hydrothermal fluids that facilitated its recrystallization.

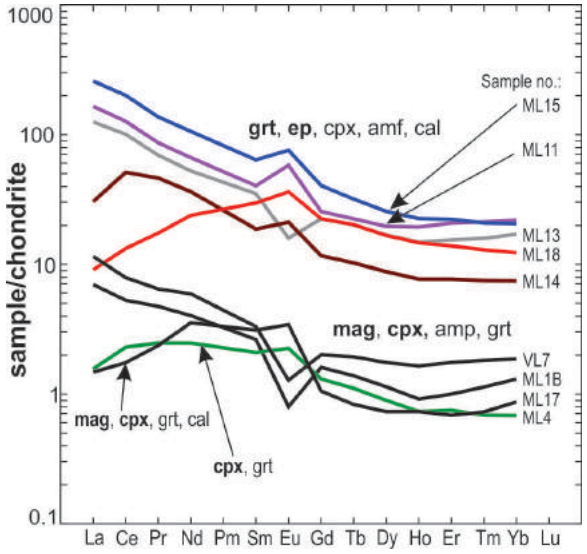

Figure 4. Chondrite-normalized REE patterns of individual skarn types. Dominant mineral assemblage of each skarn type is indicated in bold face.

5 Mass changes

We used isocon diagrams and quantitative evaluation of mass changes in order to assess the plausible range of precursor composition and the magnitude of mass transport during hydrothermal skarn formation. Chemical composition of the precursor has been estimated by mixing of pure carbonate (calcite) with variable amounts of siliciclastic material, approximated by adjacent paragneisses (sample ML13), and assuming negligible mobility of Al_2O_3, TiO_2 and Zr. The low-Al skarn varieties (pyroxene or magnetite skarns) are best reproduced by metasomatism of precursor with 79 % carbonate and 21 % siliciclastic material, whereas the high-Al skarn types (garnet or epidote skarns) require precursor with 46 % carbonate and 54 % siliciclastic component (Fig. 5). Mass balance calculations suggest significant addition of Fe, Mg, Mn, and P in all skarn types, and removal of Ca, LILE and REE during ore-forming metasomatism.

6 Implications and conclusions

Geochemical variation in Al, Ti, Fe, and immobile trace elements (e.g. Zr, Hf, Nb) in skarns, together with low trace element concentrations (e.g., Ti, V, Mn, Cr) in magnetite suggest that the skarn body and its magnetite mineralization formed by hydrothermal-metasomatic replacement of a carbonate-siliciclastic (marly) precursor. The clinopyroxene skarns were formed by metasomatism of relatively pure carbonate precursors (~20 % siliciclastic detrital component), with low concentrations of trace elements including immobile ones, while the garnet and epidote skarns formed by replacement of carbonate rocks with higher amount of siliciclastic detrital component (~45 %). This difference in precursor composition is also supported by the presence of distinct and essentially monomineralic skarn horizons.

Magnetite skarns were formed by advanced metasomatic replacement of the pyroxene skarn horizons. This process has probably been controlled by greater reactivity and more efficient porosity formation in carbonate-rich precursors. By contrast, the garnet skarns have not been mineralized further and only underwent recrystallization from early fine-grained and grossular-dominated to massive, coarse-grained and andradite-dominated types, and partially replaced by epidote.

Skarns together with their host rocks were subjected to Variscan regional metamorphism, leading to formation of compositional layering due to selective partitioning and accommodation of deformation in the mineral assemblages of the skarn bodies. Post-Variscan exhumation of the metamorphic complex led to brittle deformation, dismembering of the skarn bodies and intrusion of pegmatite dykes that caused local silicification and formation of amphibole in anhydrous skarn assemblages.

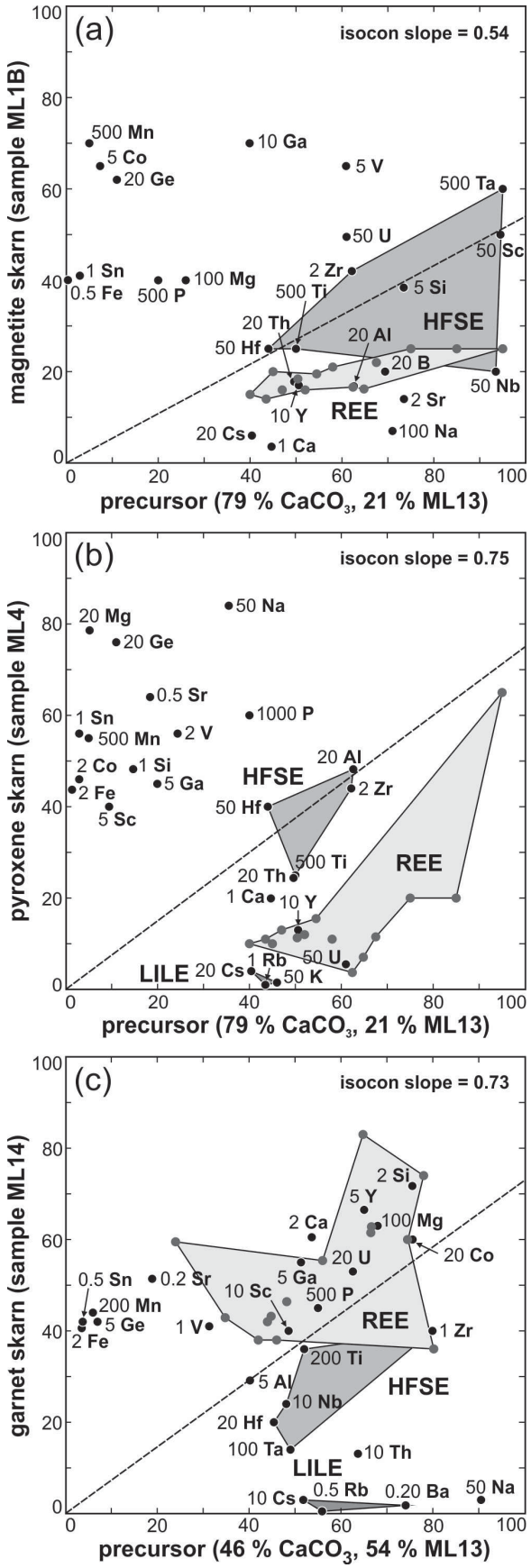

Figure 5. Isocon diagrams for (a) magnetite skarn, (b) pyroxene skarn, and (c) garnet skarn. See text for details.

Acknowledgements

This research has been supported by the Czech Science Foundation Project Nr. P210-12-0986 (DD). We appreciate thoughtful review by Martin Smith.

References

Bubal J (2013) Geochemistry and origin of skarns of the Bohemian Massif. M.Sc. thesis, Charles University, Prague, 147 pages

Drahota P, Pertold Z, Pudilová M (2005) Three types of skarn in the northern part of the Moldanubian Zone, Bohemian Massif – implications for their origin. J Czech Geol Soc 50:19–33

Dupuis C, Beaudoin G (2011) Discriminant diagrams for iron oxide trace element fingerprinting of mineral deposit types. Mineral Deposita 46:319–335

Grant JA (1986) The isocon diagram – a simple solution to Gresens' equation for metasomatic alteration. Econ Geol 81:1976–1982

Kachlík V (1999) Relationship between Moldanubicum, the Kutná Hora Crystalline Unit and Bohemicum (Central Bohemia, Czech Republic): a result of polyphase Variscan nappe tectonics. J Czech Geol Soc 44:201–291

Nadoll P, Mauk JL Haynes TS et al. (2012) Geochemistry of magnetite from hydrothermal ore deposits and host rocks of the Mesoproterozoic belt supergroup, United States. Econ Geol 107:1275–1292

Němec D (1991) Regional typization of the iron skarns of the Bohemian–Moravian Heights (Českomoravská vrchovina). Acta Mus Moraviae Sci Nat 76: 1–82

Pertold Z, Pertoldová J, Pudilová M (2000) Metamorphic history of skarns in the Gföhl Unit, Moldanubicum, Bohemian Massif, and implication for their origin. Acta Univ Carol Geol 41:157–166

Pertoldová J, Týcová P, Verner K, Košuličová M, Pertold Z, Košler J, Konopásek J, Pudilová M (2009) Tectonometamorphic history of skarns, origin and age of their protolith and implications for genetic interpretation; an example from the Svratka Unit, the Moldanubian Zone, and the Kutná Hora Unit, Bohemian Massif. J Geosci 54:101–134

Štědrá V (2011) Geological map of the Czech Republic 1 : 25 000, Sheet 13-324 Kutná Hora. Czech Geological Survey, Prague (in Czech with English summary)

Štědrá V, Nahodilová R (2009) High-pressure metabasic rocks from the Kutná Hora Complex: geological position and petrology of exotic lithologies along the segmented Moldanubian margin, Bohemian Massif. J Geosci 54:135–157

Vrána S (1987) Garnet–fassaitic pyroxene skarn from the granulite complex of southern Bohemia. Věst Ústř Úst Geol 62:193–206

Zoubek V (1946) Notes to the geology of the crystalline complexes of the Bohemian Massif. Sbor Stát Geol Úst 25:339–398

Žáček V (1997) Compositional evolution of garnet in the regionally metamorphosed Moldanubian skarn, Vlastějovice, Bohemia – evidence of the preservation of early stages pre-dating regional metamorphism. Věst Čes Geol Úst 72:37–48

Žáček V (2007) Potassian hastingsite and potassic hastingsite from garnet–hedenbergite skarn at Vlastějovice, Czech Republic. Neu Jb Mineral Abh 184:161–168

Two types of skarn garnets from West Rhodopes, South Bulgaria: LA-ICP-MS U-Pb dating and tracing evidence

Rossitsa D. Vassileva, Irena Peytcheva, Valentin Grozdev
Geological Institute, Bulgarian Academy of Sciences, Bulgaria
Albrecht von Quadt, Marcel Guillong
Institute of Geochemistry and Petrology, ETH-Zurich, Switzerland

Yuliya Plotkina, Ekaterina Salnikova
Institute of Precambrian Geology and Geochronology, RAS, St. Petersburg, Russian Federation

Abstract. The mineralogical and geochemical characteristics of two types of skarn Ca-garnets from the Velingrad area in the West Rhodopes were studied in order to apply U-Pb geochronometry using LA-ICP-MS. The garnets differ by their mineral assemblage, chemical composition, occurrence, trace element signatures, formation processes and timing. Type 1, presented as syntectonic porphyroblasts with grossular composition in close association with diopside, plagioclase, quartz, titanite and pyrite are formed by metasomatic diffusion catalyzed by metamorphic deformation in the host marbles. Type 2 garnets are Fe-rich grossulars, formed by fluid infiltration in marbles on the contact with cross-cutting pegmatite veins. Their mineral assemblage includes epidote, Fe-rich diopside, plagioclase and apatite. Trace element contents in both types show isomorphic substitution into the garnet structure, evidenced by the smooth ablation profiles. The incorporation of V, Cr, Ga, Ge, Y, Zr, Nb, Sn etc. in the contact garnets is one order of magnitude higher compared to porphyroblasts composition. The low U content (1.2-1.7 ppm) in type 1 combined with possible overprinting processes hampers the precise age record, yielding 88±26 Ma. Contact garnets (U content within 1.7-3 ppm) are dated at 42.97±0.66 Ma suggesting genetic link to the 42-37 Ma Cenozoic granites of the Rila-West Rhodope batholith.

1 Introduction

The grossular-andradite (grandite, $Ca_3Al_2Si_3O_{12}$–$Ca_3Fe_2Si_3O_{12}$) garnets are commonly formed by skarnification processes in calcsilicate rocks in contact metamorphic and hydrothermal environments. Being primary skarn minerals, dating their growth directly dates hydrothermal activity. While zircon U-Pb geochronometry provides a high-resolution record of magmatic processes, grandite U-Pb dating has the potential to provide a complementary record for hydrothermal systems (Seman et al. 2017; Salnikova et al. 2017; Wafforn et al. 2018).

This work presents an attempt to apply U-Pb geochronology, using LA-ICPMS analysis, to grossular-andradite garnets from West Rhodope Mts., south Bulgaria. The grandites are observed in close relationship to the composite Rila-West-Rhodopes batholith (RWRB) bearing tungsten and Au-base metal deposits of possibly different age. The mineralogical and geochemical characteristics of Ca-garnets and their mineral association were studied as well in order to better understand the hydrothermal processes that took place in the garnet formation.

2 Geological setting

The studied garnets, outcropping 2-3 km SW of the Velingrad town in West Rhodopes Mts, are formed by skarnification processes in the marble levels of the metamorphic sequence of the Chepinska Unit, composed mainly of amphibolites, calcsilicate rocks, various gneisses and migmatites (Sarov et al. 2009). These rocks act as the metamorphic frame to parts of the RWRB comprising plutonic bodies with different age and tectonic position (Kamenov et al. 1999 and references therein). The Unit 1 granodiorites are interpreted as constituents of an older (~80 Ma) synmetamorphic pluton with calcalkaline affinity and crust-contaminated mantle-derived composition. This pluton outcrops as two bigger bodies that are dated at 67-70 Ma by U-Pb zircon method (Von Quadt and Peytcheva 2005; Peytcheva et al. 2007). The Units 2 and 3 granites (35-40 Ma) are genetically related in between phases of a post-metamorphic pluton with high-K calcalcaline signature (Kamenov et al. 1999; Peytcheva et al. 2007). Crosscutting pegmatite veins and processes of migmatization are assigned to the second and third phases of RWRB and to the Late Alpine metamorphism (43-37 Ma, Cherneva et al. 2006).

3 Analytical procedures

The mineral relationships were studied by optical microscopy and BSE on SEM-EDS. Major elements were determined by EPMA. U-Pb isotope and trace element composition of the garnets were defined at the Institute of Geochemistry and Petrology of ETH Zurich, Switzerland. A Resonetics Resolution 155 laser ablation system coupled to a Thermo Element XR Sector-field ICP-MS was used, equipped with some improvements compared to similar systems previously described. Energy density on sample was ca. 3 J/cm^{-2}, repetition rate was 5, and ablation craters of 40 µm were applied as standard conditions. Mali garnet (Seaman et al. 2017) was used as primary external standard for dating and NIST 612 for trace element analysis. Analytical protocols include the two SRM at the beginning, every

10-15 analyses and at the end. The results were calculated using Iolite combined with Vizual Age to obtain ages and ratios corrected for instrumental drift and down-hole fractionation. The plots were processed using ISOPLOT 3.0 or ISOPLOT 4.15. Iolite or SILLS programs and the SiO_2 content in garnet (as internal standard from EPMA and mineral stoichiometry) were used for calculation of the chemical composition (48 major and trace elements). Additional trace element analysis of the garnets and associating minerals was performed using the New Wave UP193FX laser ablation system attached to Perkin-Elmer Sciex ELAN DRC-e ICP-MS at the Geological Institute, BAS, Sofia, with 75 μm laser craters, 8 Hz repetition rate and ca. 6 J/cm^{-2} energy density on sample.

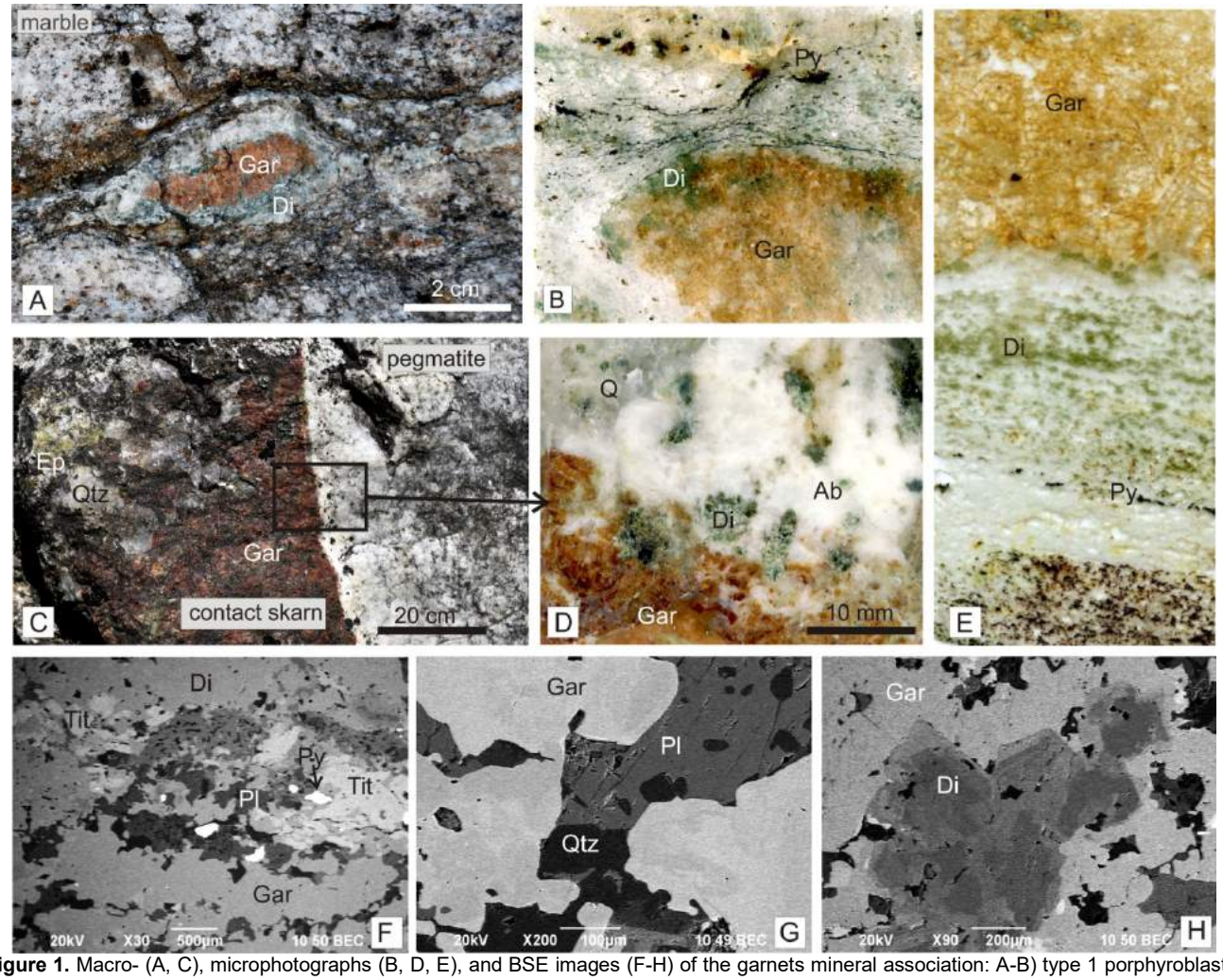

Figure 1. Macro- (A, C), microphotographs (B, D, E), and BSE images (F-H) of the garnets mineral association: A-B) type 1 porphyroblasts, showing garnet-dominated central parts and diopside periphery; C-D) type 2 – massive aggregates of contact garnets formed in the marble along a crosscutting pegmatite vein; D) close view of the skarn-pegmatite sharp contact, showing formation of diopside in the pegmatite part and grossulars in the marble; E) cross section along a porphyroblast, starting from the central garnet parts to the calcsilicate host rock; F) BSE image on the diopside-garnet zones in porphyroblasts, showing formation of titanite and pyrite as accessory minerals; G) inhomogeneous in composition garnet grains with irregular shape; H) well-shaped zonal diopside crystals with Fe-rich cores overgrown by garnet. Abbreviations refer to: Gar-garnet, Di-diopside, Ep-epidote, Pl-plagioclase, Ab-albite, Qtz-quartz. Tit-titanite, Py-pyrite.

4 Results

The studied grandite garnets were formed as a result of marble skarnification by regional or contact metamorphic processes. They are divided in two types according to the mineral assemblage, chemical composition and trace element signatures, temporal and genetic characteristics (Table 1).

4.1 Mineralogy

Type 1 garnets are observed as 1-2 to 5-6 cm porphyroblasts in the marbles (Fig. 1A), wrapped in diopside shells and displaying quartz-plagioclase pressure shadows. Diopside and garnet are intimately intergrown in the central parts of the aggregates (Fig. 1B), while garnet is not observed in the diopside peripheral zone.

Type 2 garnets occur as massive nests in association with epidote and quartz (Fig. 1C) at the marble side separated with sharp contacts from the cross-cutting pegmatite veins. Single diopside crystals formed in the

pegmatite environment in assemblage with albite and quartz (Fig. 1D) and could be interpreted as endoskarns.

Pyrite is very typical for the peripheral parts of the porphyroblasts, forming bands of irregular single grains at the diopside/host rock boundary (Fig. 1E). Scarce pyrite grains are observed in between the diopside and garnet zones, associated with abundant titanite crystals (Fig. 1F). The contact skarns show no evidence of sulphide mineralization. The only accessory mineral here is found to be apatite.

From a compositional standpoint the *type 1* garnets are determined as grossular (Al_2O_3 is ~17-22 wt.%; $Gro_{70-84}And_{14-29}Spess_{0-4}$) with variable Fe^{3+}-content (generally within two ranges 3.3-5.45 wt. % and 11-12 wt. % Fe_2O_3). The BSE images of the irregular garnet grains (Fig. 1G) reveals compositional inhomogeneity due to the changing Al^{3+}/Fe^{3+} ratio (2.4-6.4). TiO_2 incorporation up to 1.12 wt. % is typical. The associated diopside shows variations in Fe^{2+}-content. The rims of the crystals are Fe-enriched (5-6.42 wt. % FeO, 0.07-0.09 apfu) while the cores have ~ 1.6 wt. % FeO (0.02 apfu). The idiomorphic shape of diopside crystals in the garnet matrix suggests formation prior to grossular (Fig. 1H).

The chemical composition of the contact garnets (*type 2*) also reveals grossular-dominated members of the grandite series (14.75-18.83 wt. % Al_2O_3; $Gro_{63}And_{34}Spess_3$), but with significant Fe_2O_3 (9.8-12.20 wt. %). Late, almost pure, grossular (0.06-0.09 Fe^{3+}, 1.90-1.92 apfu Al^{3+}) overgrows Fe-grossular in some places. The type 2 garnet has lower TiO_2 content (up to 0.5 wt. %). The associated diopside (Fig. 1D) is ferroan (0.2 apfu Fe^{2+}) in accordance with the increased iron input in the contact skarns (garnet, epidote).

Apart from the general Al^{3+}/Fe^{3+} substitution in the octahedral site of the grandite structure, the calcium concentration and replacements in the dodecahedral position are important. Ca-incorporation is mainly within the 2.5-2.8 apfu in the studied garnets, utilizing the accommodation of Mn, Mg, REE and U. A significant manganese concentration reaching 2.12 wt. % MnO is typical for both garnet types (0.07-0.14 apfu Mn^{2+}). Some analyses show Mn-content reaching ~ 5 wt. % MnO. These points correspond to the lowest U-content measured. The Mg incorporation remains mainly below 0.3 wt. % MgO in type 1, and ≤0.2 wt. % MgO in the contact type.

4.2 Geochemistry of the grandites

The geochemical patterns of the studied garnets suggest a general trend of trace elements enrichment in the contact garnets compared to the porphyroblactic ones (Table 1). Among the most important traces are V, Cr, Zn, Ga, Ge, Y, Zr, Nb, Sn, incorporated isomorphically in the garnet structure (Grew et al. 2013), evidenced by the smooth ablation profiles. Apart from the Mn and Mg, whose content is in inverse proportion with Ca, only Y is considered to be accommodated in the dodecahedral Ca-position together with REE and U. A trend of positive correlation between the concentrations of V, Cr, Zn, Ga, Ge, Zr, Nb, Sn from one side and Fe^{3+} content from another is observed.

The chondrite-normalized patterns of the REE with low L-REE and higher content of M-HREE (Sm-Lu) are typical in both garnet types. The negative anomalies of Eu and Ce in the contact skarn grossular may be due to the concurrent growth of epidote.

Table 1. Major characteristics of the two distinct garnet types

Garnet characteristics/type	**Type 1** $(Ca_{2.5-2.8}Mn_{0-0.1})(Fe_{0.3-0.7}Al_{1.6-1.76})Si_3O_{12}$	**Type 2** $(Ca_{2.5-2.7}Mn_{0.9-0.14})(Fe_{0.6-0.7}Al_{1.5-1.7})Si_3O_{12}$
Occurrence	lense-like 1-2 to 5-6 cm garnet-diopside porphyroblasts within marbles	massive aggregates in marbles on the contact with pegmatite veins
Mineral association		
main minerals	diopside, plagioclase, carbonates, quartz	epidote, Fe-diopside, quartz, albite
accessories	titanite, pyrite ± scapolite	apatite
Garnet composition	grossular ($Gro_{70-84}And_{14-29}$ $Spess_{0-4}$)	Fe-rich grossular ($Gro_{63}And_{34}Spess_3$)
Selected trace elements, ppm	Ti (~ 1 wt. % TiO_2), Na (23-76), P (6-10), Sc (3-10),V (71-420), Cr (14-104), Zn (13-58), Ga (20-45), Ge (2-8), Y (21-98), Zr (10-66), Nb (1-3), Sn (3-7), U (1.2-1.7)	Ti (up to 0.5 wt. % TiO_2), Na (30-45), P (7-10), Sc (2-14), V (314-914), Cr (15-117), Zn (7-118), Ga (45-70), Ge (40-81), Y (30-172), Zr (7-31), Nb (25-47), Sn (8-57), U (1.7-3.05)
Genesis	metasomatic diffusion catalyzed by tectonic deformation in the metamorphic sequence	contact skarns and infiltration-dominated reactions onto the host marbles
Timing, U-Pb age	88±26 Ma	42.97±0.66 Ma

4.3 U-Pb dating

The low uranium content (up to 1.7 ppm) and relatively high Pb content of the grossulars from type 1 hampers precise LA-ICP-MS U-Pb age dating. The acquired age is 88 ± 26 Ma. However, Late Cretaceous-Paleocene (62–114 Ma, including the 2 sigma uncertainties) tectono-metamorphic events are known in the Rhodopes (Cherneva et al. 2006). Undoubtedly the formation of these garnets is somehow connected with the magmatic processes of the synmetamorphic granodiorites of the Unit 1 of the RWRB which took place at ~ 80 Ma (Kamenov et al. 1999).

Type 2 grossulars from the contact with pegmatite dykes are dated at 42.97±0.66 Ma suggesting a genetic link to the 43-37 Ma Cenozoic granites of the Rila-West Rhodope batholiths (Peytcheva et al. 1998, Kamenov et al. 1999, Cherneva et al. 2006, Von Quadt and Peytcheva 2005).

5 Discussion and concluding remarks

The age results strongly depend on the U-contents in the garnet structure, but also on inclusions of other (Pb-bearing) phases (plagioclase), and probably on overprinting processes that can lead to garnet alteration and new garnet growth. The precise dating record in the garnets is proportional to the U-content, which is considered to replace Ca in the dodecahedral position of the garnet structure. Thus, the concentration of elements which are likely to substitute for Ca (e.g. Mn, Mg, Y) could influence the precise U-Pb garnet dating.

The formation of type 1 garnets is interpreted as syntectonic porphyroblasts, according to their position in the host marble (Fig. 1A). Considering the catalyzing effect of the deformation on the mineral nucleation, these aggregates are product of increased diffusion rate due to the magmotectonic events in the metamorphic sequence. Formation of the contact massive skarn garnets along the pegmatite dykes is strongly influenced by infiltration-driven reactions onto the marble stratum.

Compositionally the mineral association in the contact skarns compared to porphyroblasts reveals increased role of Fe in the garnet and diopside, evidenced also by epidote occurrence. The Ca/Mn substitution is well expressed, showing inverse correlation between their concentrations. Manganese incorporation is typical for both types, together with some Mg. The analysed points with increased Mn are those with the lowest U-incorporation, influencing the dating record. However, the Mn-content show enchanced values in the contact garnet compared to that in porphyroblasts, suggesting that the U-incorporation depends not only on the chemical composition, but also on the possible trace element sources in the system (e.g. the direct contact with pegmatite dykes).

From a geochronometry standpoint the Fe-enriched grossular (type 2) gave better age results, although no direct correlation between Fe-incorporation and U-content is observed. The increased values for Ti, V, Cr, Zn, Ga, Ge, Zr, Nb, Sn do not influence the U-Pb dating accuracy as they are mainly accommodated in the octahedral site of the garnet structure.

The LA-ICP-MS U-Pb dating on grandite distinguishes two separate magmatic-hydrothermal events. We suggest that the deformational processes that type 1 garnets suffered, led to U-depletion, thus the acquired U-Pb age stays tentative. The abundant titanite crystals observed in the mineral assemblage of the porphyroblasts give excellent opportunity for crosschecking the timing of grossular formation. The contact-type skarn garnets (type 2) yield ages with low 2 sigma errors. Despite the unsatisfying age of garnet porphyroblasts they are undoubtedly older than type 1.

Acknowledgements

The study is supported by the DNTS 02/15 bilateral project, financed by the Bulgarian National Science Fund.

References

Cherneva Z, Ovtcharova M, Dimov D, von Quadt A (2006) “Baby-granites” in migmatites from Chepinska river valley,Western Rhodope – geochemistry and U-Pb isotope dating on monazite and zircon. Geosciences-2006:205-208

Grew ES, Locock AJ, Mills SJ, Galuskina IO, Galuskin EV, Halenius U (2013) Nomenclature of the garnet supergroup. Am Miner 98:785–811

Kamenov B, Peytcheva I, Klain L, Arsova K, Kostitsin Y, Salnikova E (1999) Rila-West Rhodope Batholith: Petrological and geochemical constraints for its composite character. Geochem Mineral Petrol 36:3-27

Peytcheva I, Kostitsin Y, Salnikova E, Kamenov B, Klain L (1998) Rb-Sr and U-Pb isotope data for the Rila-Rhodopes batholiths. Geochem Mineral Petrol 35:93-105.

Salnikova E, Stifeevaa MV, Chakhmouradian AR, Glebovitsky V, Reguir E (2018) The U–Pb System in schorlomite from calcite–amphobole–pyroxene pegmatite of the Afrikanda Complex (Kola Peninsula). Dok Earth Sci 478:148–151

Sarov S, Voynova E, Naidenov K, Nikolov D, Georgieva I, Petrov N, Markov N. Marinova R (2009) Geological map of Bulgaria 1:50 000, K-34-72-G (Map sheet Velingrad).

Seman S, Stockli DF, McLean NM (2017) U-Pb geochronology of grossular-andradite garnet. Chem Geol 460:106-116 10.1016/j.chemgeo.2017.04.020

Peytcheva I, Kostitsin Y, Salnikova E, Kamenov B, Klain L (1998) Rb-Sr and U-Pb isotope data for the Rila-Rhodopes batholiths. Geochem Mineral Petrol 35:93-105

Peytcheva I, von Quadt A, Naydenov K, Sarov S, Dimov D, Voinova E (2007) U-Pb zircon-xenotime-monazite dating and Hf-isotope tracing to distinguish Cretaceous and Paleogene granitoids in the Western Rhodopes and Rila Mountain. Geosciences-2007:89-91.

Von Quadt A, Peytcheva I (2005) The southern extension of the Srednogorie type Upper Cretaceous magmatism in Rila-Western Rhodopes: Constraints from isotope-geochronological and geochemical data. Geosciences-2006:113-116

Wafforn S, Seman S, Kyle JR, Stockli D, Leys C, Sonbait D, Cloos M (2018) Andradite garnet U-Pb geochronology of the big Gossan Skarn, Ertsberg-Grasberg mining district, Indonesia. Econ Geol 113(3):769–778 doi.org/10.5382/econgeo.2018.4569

Metamorphosed granite–greisen–skarn assemblage and related tin mineralization in Nedvědice, Bohemian Massif

Ján Kličtinec, Jan Cempírek
Masaryk University, Faculty of Science, Department of Geological Science, Czech Republic

Abstract. The Nedvědice orthogneiss is located in the Svratka Crystalline Complex, eastern part of the Kutná Hora–Svratka Crystalline Unit, Bohemian Massif (Czech Republic). The orthogneiss is surrounded by a varied suite of rock types, such as mica schists, minor marbles, tourmalinites, amphibolites, serpentinites, quartzites and iron skarns. Its southeastern part is characterized by presence of tin mineralization, either associated with metapelites or in calc-silicate skarns, both in vicinity of the tourmaline-rich Nedvědice orthogneiss. Several tourmaline generations (magmatic, hydrothermal, metamorphic) were recorded in the tourmaline from the orthogneiss; together with metamorphic overprint of the tin mineralization in surrounding host rocks, the textures reflect Variscan metamorphic overprint of the Ordovician granite and its autochtonous (meta)sedimetary cover. The protolith of the Nedvědice orthogneiss is highly evolved, leucocratic, prealuminous granite rich in boron and fluorine.

1 Introduction

The Svratka Crystalline Complex of the Bohemian Massif (Fig. 1) consists of a complex and variable assemblage of metapelites, metagranites, skarns, tourmalinites, marbles, serpentinites and quartzites. Its southeastern part is characterized by presence of tin mineralization, either associated with metapelites or in calc-silicate skarns, both in vicinity of the tourmaline-rich Nedvědice orthogneiss. The studied area is located in the southern part of the Svratka Crystalline Complex (SCC), western Moravia, Bohemian massif (Czech Republic). It is bordered by the Moldanubian Zone in the S, by the Moravosilesian Zone in the E, and the Bohemicum in the W and N (Polička Unit).

The radiometric dating of metagranites in SCC revealed three stages of development of these rocks; (i) 1932 ± 7 Ma – indicating the granite protolith was probably derived from the melting of Late Paleoproterozoic basement, (ii) 515 ± 9 Ma – the granite crystallization in Ordovician, and (iii) ~340 Ma, reflecting the Variscan tectonometamorphic overprint (Schulmann et al. 2005; Buriánek et al. 2009). Typical rocks for this area are medium- to coarse-grained mica schist, orthogneiss, two-mica paragneiss, amphibolite, marble, migmatite, skarn, and tourmalinite (Fig. 2; Novák et al. 1998).

2 Skarns of SCC

The most frequent type of skarn is garnet-pyroxene skarn (± magnetite) with transitions to pyroxene skarns,

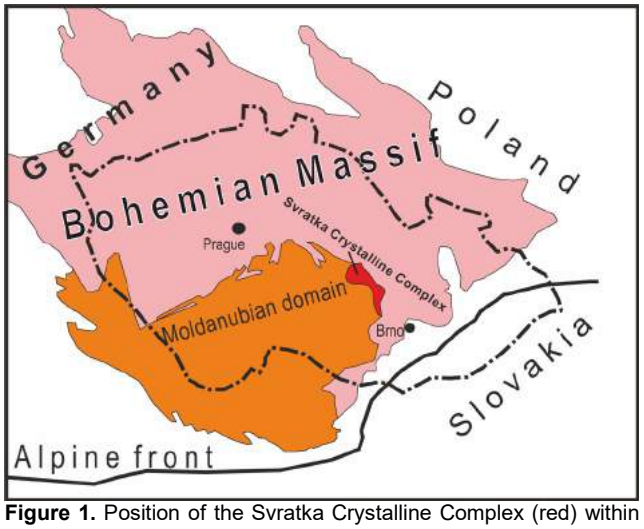

Figure 1. Position of the Svratka Crystalline Complex (red) within the Bohemian Massif

pyroxene skarns with magnetite and garnet-amphibole (Pertoldová et al. 1998). Skarn protoliths were most probably heterogeneous sedimentary rocks with a component of exhalites deposited on the sea floor and endured all the metamorphic events together with the surrounding sedimentary/volcano-sedimentary sequences in the SCC (Pertoldová at al. 2009). Skarn-forming fluids reacting with the carbonates were probably derived from surrounding orthogneiss - former peraluminous granites rich in F, B, Sn, As (Houzar et al. 2006). Contents of Sn in whole rock analyses of Pertoldová et al. (2009) did not exceed 160 ppm.

The main skarn tin-bearing minerals are andradite and accessory malayaite; cassiterite is very rare (Hrazdil et al. 2009). The andradite forms medium- to coarse-grained aggregates with vesuvianite; the garnet contains ca. 1.2-2.4 wt. % SnO_2 (0.038-0.081 apfu Sn) and low F (<0.016 apfu), whereas the vesuvianite is rich in As. Malayaite (tin analogue of titanite) is a typical accessory Sn-mineral, with 54.50 – 56.27 wt.% SnO_2 (Hrazdil et al. 2009).

3 Tin mineralization in metapelites

Significant cassiterite anomalies were found in stream sediments in the region, however cassiterite was never confirmed in the Nedvědice orthogneiss. Placer prospecting revealed elevated contents of cassiterite in some samples (up to 0,75 wt.%) mainly in the vicinity of the orthogneiss and skarns. Other minerals recorded in small amounts were scheelite and zircon (Česneková 1968).

Tin mineralization was subsequently evaluated by the state exploration company Geoindustra (placer prospection, mapping, and drilling; Grym 1969); however, the exploration program did not reveal any significant ore accumulations.

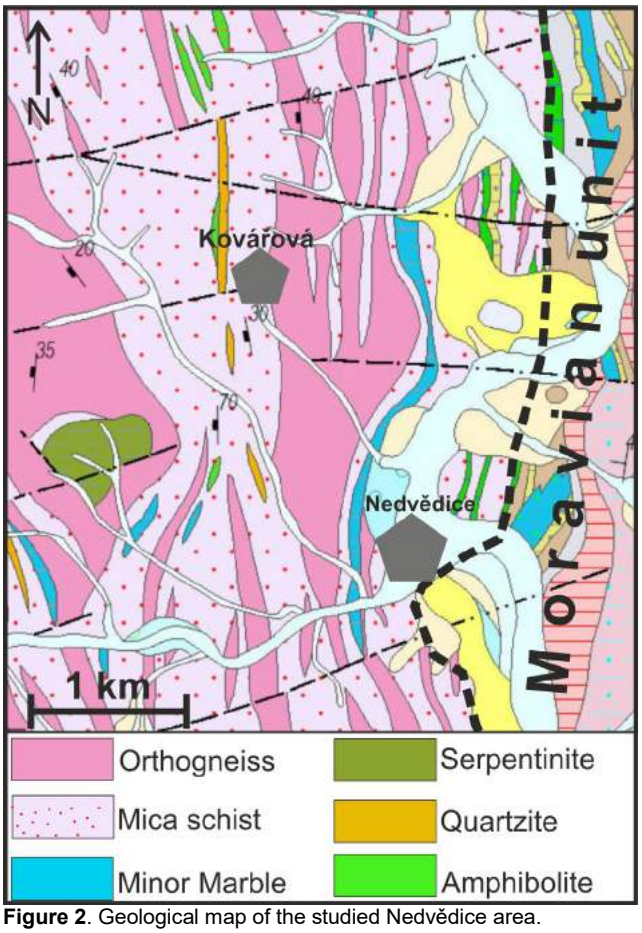

Figure 2. Geological map of the studied Nedvědice area.

4 Nedvědice orthogneiss

Leucocratic orthogneiss at Nedvědice forms a N-S trending elongate body about 100 m thick and up to 1 km long, enclosed in mica schists (Fig. 2). The protolith of the Nedvědice orthogneiss is a highly evolved, leucocratic, peraluminous granite, depleted in Sr, Zr, Cr, and REE but enriched in Rb, B, Ga and F (Novák et al. 1998). The Nedvědice orthogneiss is special by the presence of tourmaline-bearing hydrothermal veins of fluorite which underwent regional metamorphism.

Two types of tourmaline were distinguished at the locality. The first one includes metamorphosed magmatic tourmalines with preserved magmatic cores and younger, recrystallized rims (Fig. 3). This tourmaline contains brecciated primary magmatic cores enriched in Fe, contain high X-site vacancies and variable F-content. The younger rim is enriched in Mg and F caused by probable breakdown of early tourmaline, biotite and plagioclase in the rock. The youngest rim has elevated Ca, Fe and lower F due to fractional crystallization of residual melt. The second type of tourmaline is present in metamorphosed fluorite layers. This coarse-grained tourmaline has patchy zoning where we can distinguish core and rim zones. The core is rich in F, Mg and Na while rim has relatively lower content of F and is enriched in Fe compared to the core. We interpret the core as primary hydrothermal and rim as metamorphic. Similarly to the rims of the magmatic tourmaline, the rims of tourmaline from fluorite layers are rich in Ca and Fe; this may indicate recrystallization under the same metamorphic fluids with elevated Ca and Mg contents.

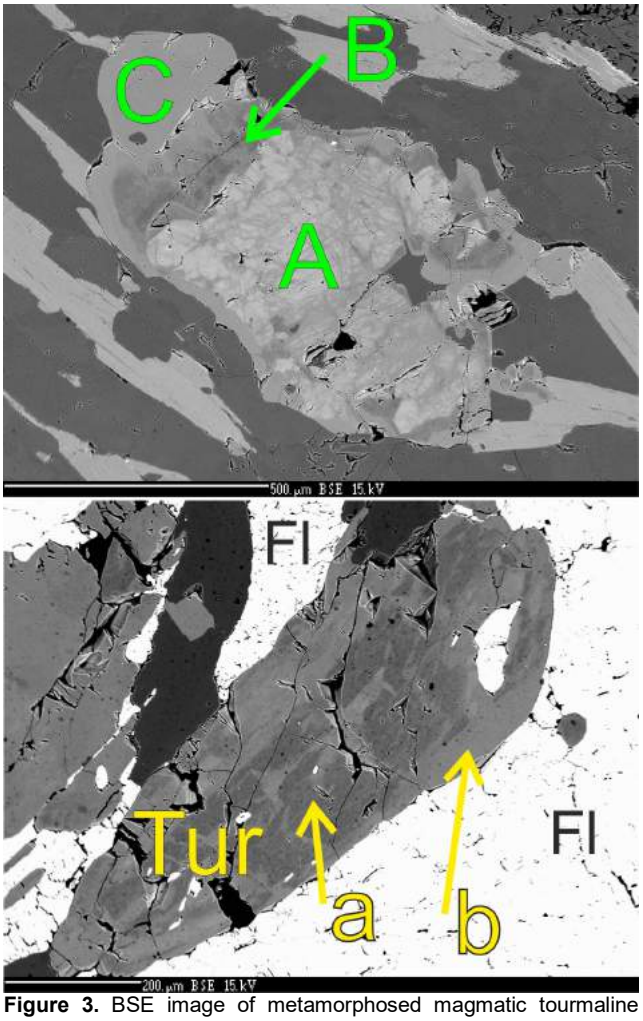

Figure 3. BSE image of metamorphosed magmatic tourmaline (top) and hydrothermal tourmaline in fluorite layer (bottom). Letters in the top image represent: A – preserved brecciated magmatic core, B – metamorphic zone 1, C – metamorphic zone 2. Letters in the bottom image represent: D – primary zone 1, E – metamorphic zone 2.

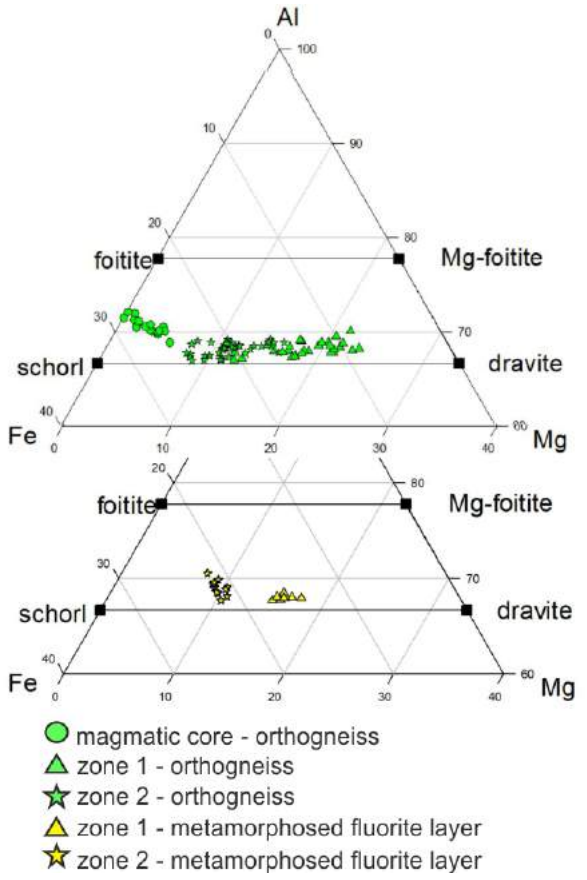

Figure 4. Composition of tourmaline from the Nedvědice orthogneiss (top) and from the fluorite layer (bottom).

5 Metamorphosed greisens in the SCC?

Some of the studied rocks feature elevated contents of rare elements and fluxes (Li, B, F) which suggests they may represent metamorphosed greisens. The topic was earlier studied by Němec (1986) who concluded that the identification of regionally metamorphosed greisens is not a simple task. Granitic rocks are usually homogeneous, and their overprint to orthogneisses does not result in significant mineralogical changes. Sometimes they host "greisen" layers; however, these are also present in surrounding mica schists and could form through greisenization of paraschists (Němec 1986). At the Kovářová locality, Němec (1986) described cassiterite-bearing greisens in mica schist near the Nedvědice orthogneiss and suggested that the original greisens formed by greisenization of para-schists.

Our data from the first type of "greisens" (enclosed in the orthogneiss) support their magmatic-metasomatic origin (Tab. 1), as they contain high F contents of 0.22–1.33 wt. % and show enrichment in Li (73 – 640 ppm). The mica in the "greisens" is unusually F-rich, with up to 3.37 wt. % F; this composition suggest formation from highly evolved acidic fluids.

Table 1. Whole rock analysis of selected samples; 1 and 2 – orthogneiss, 3 and 4 – metamorphosed fluorite layer

sample no.		1	2	3	4
SiO_2	Wt.%	76.06	76.87	64.24	51.97
Al_2O_3	Wt.%	12.65	12.12	18.62	24.10
Fe_2O_3	Wt.%	1.72	1.84	4.51	6.22
MgO	Wt.%	0.16	0.14	1.16	3.90
CaO	Wt.%	0.50	0.53	0.31	0.34
Na_2O	Wt.%	2.57	2.22	1.26	1.99
K_2O	Wt.%	5.04	4.95	5.02	2.66
TiO_2	Wt.%	0.14	0.12	0.54	0.79
P_2O_5	Wt.%	0.25	0.23	0.15	0.12
MnO	Wt.%	0.02	0.03	0.06	0.07
Cr_2O_3	Wt.%	<0.002	<0.002	<0.002	<0.002
Sum	%	99.11	99.05	95.87	92.16
Sn	ppm	11	9	34	20
F	ppm	4300	4800	13300	12600
Li	ppm	255	211	640	250

Acknowledgements

The study was supported from the GA-17-17276S project to JC.

References

Buriánek D, Verner K, Hanžl P, Krumlová H (2009) Ordovician metagranites and migmatites of the Svratka and Orlice-Snežník units, northeastern Bohemian Massif. J Geosci 54:181–200

Česneková M (1968) Težké minerály na území Nedvědic. Dissertation, Charles University

Grym V (1969) Report GF P022753. Geofond, Prague.

Houzar S, Novák M, Doležalová H, Hrazdi, V, Pfeiferová A (2006) Přehled mineralogie, petrografie a geologie nedvědických mramorů, svratecké krystalinikum. Acta Mus Moraviae, Sci geol 91:3–77

Hrazdil V, Houzar S, Škoda R (2009) Zpráva o výzkumu Sn-bohaté minerální asociace s As-vesuvianem v nedvědickém mramoru u Kozlova na západní Moravě, svratecké krystalinikum. GVMS 16:109–113

Němec D (1986) Distinction of regionally metamorphosed greisens from metapelitic mica schists. Geol Rund 75:685–692

Novák M, Selway JB, Houzar S (1998) Potassium-bearing, fluorine-rich tourmaline from metamorphosed fluorite layer in leucocratic orthogneiss at Nedvedice, Svratka Unit, western Moravia. J Geosci 43:37–44.

Pertoldová J, Týcová P, Verner K, Košuličová, M, Pertold Z, Košler J, Konopásek J, Pudilová M (2009) Metamorphic history of skarns, origin of their protolith and implications for genetic interpretation; an example from three units of the Bohemian Massif. J Geosci 54:101–134

Schulmann K, Kröner A, Hegner E, Wendt I, Konopásek J, Lexa, O, Štípská P (2005) Chronological constraints on the pre-orogenic history, burial and exhumation of deep-seated rocks along the eastern margin of the Variscan orogen, Bohemian Massif, Czech Republic. Am J Sci 305:407–448

Mineralogy, geochemistry and U-Pb geochronology of grandite from the Martinovo Fe-skarn deposit, Western Balkanides, Bulgaria

Rossitsa D. Vassileva, Dimitrina Dimitrova, Irena Peytcheva, Valentin Grozdev
Geological Institute, Bulgarian Academy of Sciences, Sofia, Bulgaria

Albrecht von Quadt, Marcel Guillong
Institute of Geochemistry and Petrology, ETH-Zurich, Switzerland

Ekaterina Salnikova, Maria Stifeeva
Institute of Precambrian Geology and Geochronology, RAS, St. Petersburg, Russian Federation

Abstract. Grossular-andradite (grandite) bearing skarns are a favorable environment for deposition of magnetite ore with economic importance in the Martinovo deposit, W Balkanides, NW Bulgaria. Ore mineralization results from hydrothermal activity related to the Carboniferous Sveti Nikola granite emplaced in the Cambrian-Ordovician low grade metamorphics of the Diabase-Phyllitioid complex. Skarns, composed of primary clinopyroxene and garnet, form massive aggregates at the subvertical contacts of schists and calcite/siderite marbles with clear lateral zonality. Distal garnets reveal andraditic composition, while proximal are grossular-dominated. The mineral association includes molybdenite, scheelite and scarce uraninite. Compositionally, the grandites have oscillatory zonation due to the changing Fe/Al ratios. Garnet trace element analyses reveal incorporation of significant amounts of V, Cr, Ga, Ge, As, Mo, Sn, and W. Precise HR LA-ICP-MS U-Pb dating of grandite yields 306.2±1.9 Ma that is in prefect agreement with the ID-TIMS Concordia Age = 306.6 ±1.4 Ma. High U content (10-70 ppm) results in a possibility to apply LA-quadrupole ICP-MS dating that yields a lower intercept age of 303.7±5.2 Ma. The age record does not depend on the major element chemical inhomogeneity of the crystals as the main variation is in the octahedral position, occupied by Fe^{3+} and Al^{3+}.

1 Introduction

Grossular-andradite garnets ($Ca_3Al_2Si_3O_{12}$–$Ca_3Fe_2Si_3O_{12}$), commonly known as grandites, are primary skarn minerals formed by metasomatic processes in carbonate environments. The recent advances in the U-Pb LA-ICP-MS geochronology (Seaman et al. 2017, Salnikova et al. 2017, Wafforn et al. 2018) have shown the ability of the Ca-garnets from the grandite series to record the timing of the hydrothermal processes in ore deposits.

Here we present mineralogical, geochemical and LA-ICP-MS U-Pb dating results of skarn garnets from the Martinovo iron deposit in Western Balkans, NW Bulgaria. We use them to constrain the favorable conditions for timing of iron skarns and discuss the main possible mechanisms for trace element incorporation.

2 Geological background

The Martinovo iron ore deposit is part of the Chiprovtsi ore district, located in the westernmost part of the Balkanides, NW Bulgaria. It is hosted by the Cambrian-Ordovician Diabase-Phyllitoid Complex (DFC; Haydoutov 1991). The DFC is composed of various schists, calsilicate rocks, ophiolite and volcanic materials which suffered low grade metamorphism. Skarn formation processes in the calcite and siderite marbles and economic magnetite ore mineralization is suggested to be genetically related to the intrusion of the Sveti Nikola granite with Late Carboniferous age (313.8 ± 3.5 Ma, Carrigan et al. 2005). The primary skarns are composed by clinopyroxene and garnet, developed on the subvertical schist/marble contacts with the granite. The exoskarns reveal clear mineral and compositional lateral zonality with proximal pyroxene, intermediate garnet-pyroxene and distal garnet zones (Tarassova and Tarassov 1988), due to the bimetasomatic processes in the thermal aureole of the pluton. The magnetite ore, occurring as irregular, columnar, pipe-like bodies is mainly related and hosted by the distal garnet zone, although its formation has also been interpreted as thermometamorphic alteration of siderite (Dragov, 1992).

3 Analytical techniques

The mineral relationships were studied by optical microscopy and BSE on SEM-EDS. Major element garnet compositions were determined by Jeol JSM-6610LV SEM-EDS at the University of Belgrade. Trace element and REE concentrations in garnets and associated minerals were measured by LA-ICP-MS, using the New Wave UP193FX laser ablation system attached to Perkin-Elmer Sciex ELAN DRC-e ICP-MS at the Geological Institute, BAS, Sofia, with 75 μm laser craters, 8 Hz repetition rate and ca. 6 J/cm^2 energy density on sample.

U-Pb isotope and additional trace element composition of the garnets were defined at the Institute of Geochemistry and Petrology of ETH Zurich, Switzerland and the Geological Institute of the Bulgarian

Academy of Sciences. At ETHZ a Resonetics Resolution 155 laser ablation system coupled to a Thermo Element XR Sector-field ICP-MS was used equipped with some improvements compared to similar systems previously described. Energy density on sample was ca. 3 J/cm^2, repetition rate of 5, and ablation craters of 40 µm were applied as standard conditions. Mali garnet (Seaman et al. 2017) was used as primary external standard for dating and NIST 612 for tracing. Analytical protocols include the two SRM in the beginning, every 10-15 analyses and at the end. At GI-BAS UP193FX New Wave LA system and Elan DRCe quadrupole ICP-MS and Dashkesan garnet SRM (Stifeeva et al. 2018) are used for dating, together with NIST 610 as an SRM for tracing. Repetition rate of 8, and ablation craters of 50-75 µm were applied. The results were calculated using Iolite combined with Visual Age to obtain ages and ratios corrected for instrumental drift and down-hole fractionation. The plots were processed using ISOPLOT 3.0 or ISOPLOT 4.15. Iolite and SILLS programs and the SiO_2 content in garnet (as internal standard from EPMA and mineral stoichiometry) were used for calculation of the chemical composition (48 major and trace elements).

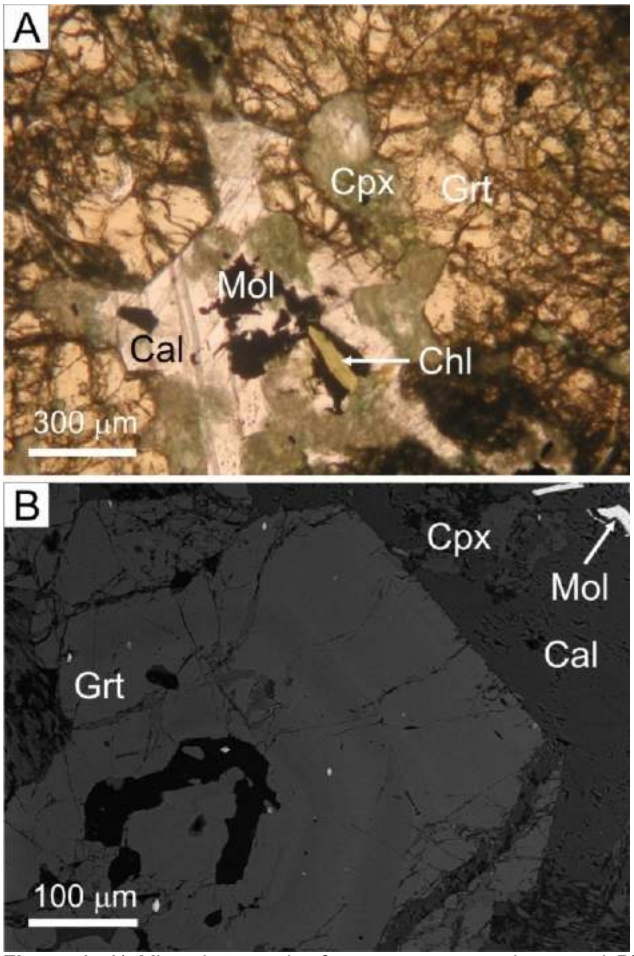

Figure 1. A) Microphotograph of garnet-pyroxene skarn; and B) BSE image of garnet crystal from (A) with oscillatory zonation. Abbreviations refer to: Grt - garnet; Cpx - clinopyroxene; Chl - chlorite; Cal - calcite; Mol - molybdenite.

4 Results

4.1 Mineralogy

Garnet occurs mostly as fine grained, massive aggregates, extensively cracked, intergrown with diopside-hedenbergite in the pyroxene-garnet zone (Fig. 1A). Euhedral garnet crystals are rarely observed. The primary mineral assemblage includes also titanite, plagioclase, K-feldspar, apatite, and allanite. Titanite, apatite, and allanite occur as euhedral to subhedral crystals.

Oscillatory zonation is apparent in the analyzed samples in transmitted light microscopy and in back-scattered SEM images (Fig.1B). It shows variation in Al and Fe content that leans towards intermediate grossular-andradite composition (Al_2O_3 - 8.3-13.0 wt.%, Fe_2O_3 - 15-17 wt.%) of the garnets in the garnet-pyroxene zone; and to andradite composition of the garnets (Al_2O_3 - 0.4-4.0 wt.%, Fe_2O_3 - 15-17 wt.%) in the distal garnet zone. The Mn-content is slightly higher in Al-rich garnets (MnO - 2.5-4.1 wt.%) compared to Fe-rich (MnO - 0.6-1.1 wt. %). The correlation between Mn and Al (0.70) is better than between Mn and Ca, thus suggesting an octahedral incorporation in the structure (Mn^{3+}). Small quantities of Mg (120-1000 ppm) and Ti (10-160 ppm) were detected. The CaO content is within the range 30-35 wt.%.

The skarns underwent retrograde metasomatic alteration with formation of chlorite, amphibole, quartz, calcite, scheelite, molybdenite, uraninite, magnetite, pyrite and other sulfides. The ore mineralization spatially associates with the garnet-pyroxene - garnet zone.

The skarns can be classified as Mo±W according to the abundant molybdenite±scheelite mineralization associated with the garnet (grossular-andradite) – pyroxene skarns (Meinert 1992).

4.2 Geochemistry

Apart from major elements in the grandite, trace element signatures in the studied garnets reveal incorporation of V (44-256), Cr (8-16), Ga (28-32), Ge (23-29), As (5-44), Sr (1-14), Y (up to 4), Mo (1-30), Sn (24-128), La (2-11), Ce (4-13), ^{206}Pb (below 13 ppm). The W-content is significant, reaching more than 2000 ppm in most of the analyzed points (n=24). Among the important trace elements in the garnet structure is U, directly influencing the age record of their formation. All above mentioned elements are presented in the garnet structure as isomorphic substitutions, evidenced by the flat and stable depth ablation profiles.

The ^{238}U incorporation in the studied grandite grains is high, ranging from 10 to 70 ppm. Well expressed positive correlations of U with the following elements are observed: W (0.69), La (0.92), Ce (0.70), As (0.53), and Mo (0.59). Positive correlations exists among these elements as well (Fig. 2). Uranium content correlates positively with total REE (0.75) and LREE (0.76), thus

suggesting incorporation by substitution for divalent cations (Ca^{2+}) in the dodecahedral position (Smith et al. 2004, Gaspar et al. 2008). Correlation with total HREE becomes only positive (0.62) when the analyses with U concentrations below 25 ppm are excluded implying probably late partial extraction of U in some areas of the garnets during retrograde process. This apparently does not affect the U-Pb dating.

The garnets are generally depleted in REE (11.0-48.6 ppm), especially in MREE and HREE, as the latter are hardly detected. The chondrite-normalized patterns of garnet also display LREE enrichment and MREE-HREE depletion, with well expressed positive Eu anomaly (Eu/Eu* =2.5-18.3). This is consistent with the typical chondrite-normalized patterns for andradite garnets outlined by Gaspar et al (2008).

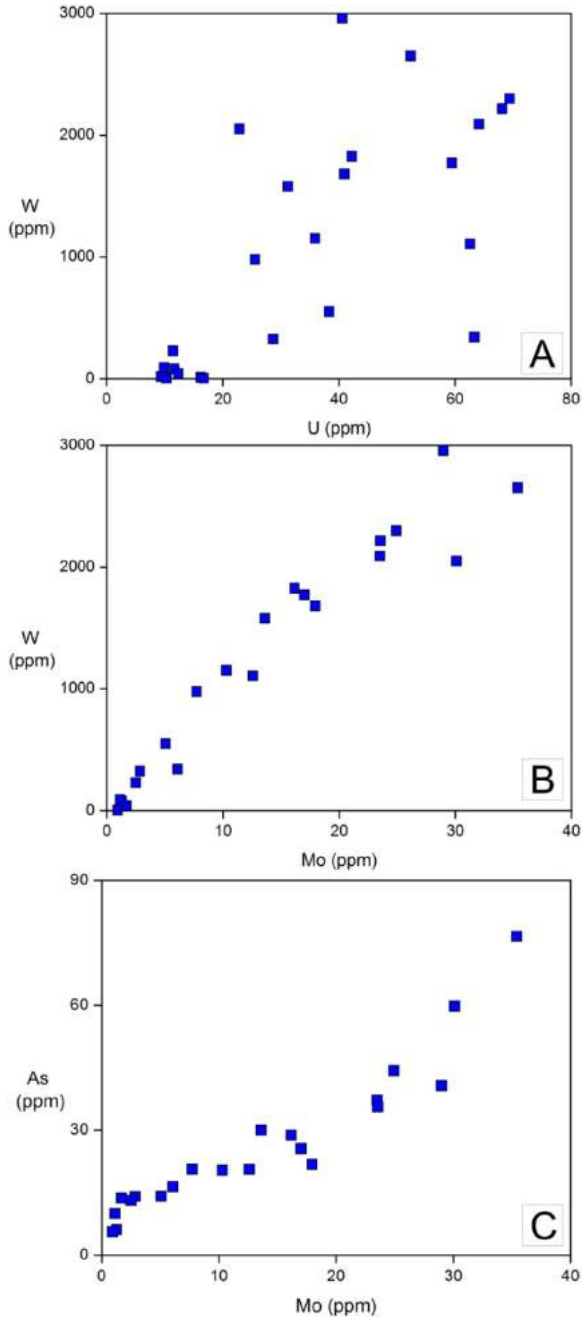

Figure 2. Correlation diagrams: A) W vs. U; B) W vs. Mo; and C) As vs. Mo.

4.3 U-Pb dating

Precise HR LA-ICP-MS U-Pb dating of grandite yields 306.2±1.9 Ma which is in agreement with the ID-TIMS Concordia Age = 306.6 ±1.4 Ma. High U content (10-70 ppm) provides an opportunity to apply LA-quadrupole ICP-MS dating that defines an lower intercept age of 303.7±5.2Ma. All age results support the genetic link to the Sveti Nikola granite intrusion (313.8 ± 3.5 Ma, Carrigan et al. 2005).

5 Discussion

The precision of the HR LA-ICP-MS U-Pb dating of the Martinovo grandites is comparable with the precision of the age obtained by the ID-TIMS techniques. As the skarns are acting as a host environment for the magnetite bodies, their age 306.2±1.9 Ma directly records the hydrothermal activity in the vicinity of the granite and defines the maximum age limit for the economic ore mineralization in Martinovo deposit.

The age record in garnets is directly influenced by the U-content in their structure. The Sveti Nikola granite, as well as some other Carboniferous granites in the Balkans (in Bulgaria and Serbia, Jovanović et al. 2019) are known as enriched in uranium and the latter obviously influences the U-content of the skarn grandites. High U content (10-70 ppm) results in a possibility to apply not only HR LA-ICP-MS dating but also the more common quadrupole-MS technique. Despite the small inclusions of scheelite and molybdenite, we suggest that the garnets from the Martinovo deposit could be used successfully as a standard reference material for garnet dating.

Acknowledgements

The results are part of the bilateral project DNTS 02/15 financed by the Bulgarian National Science Fund.

References

Carrigan CW, Mukasa SB, Haydoutov I, Kolcheva K (2005) Age of Variscan magmatism from the Balkan sector of the orogen, Central Bulgaria. Lithos 82:125-147

Dragov P (1992) Ore-Forming Processes in the Chiprovtsi Ore Zone. DSc Thesis, Geological Institute, BAS, Sofia 179 pp (in Bulgarian)

Gaspar M, Knaack C, Meinert LD, Morretti R (2008) REE in skarn systems: a LA-ICP-MS study of garnets from the Crown Jewel gold deposit. Geochim Cosmochim Acta 72:185-205

Haydoutov I (1991) Origin and Evolution of the Precambrian Balkan-Carpathian Ophiolite Segment. Sofia, BAS, 179 pp (in Bulgarian)

Jovanović D, Cvetković V, Erić S, Kostić B, Peytcheva I, Šarić K (2019) Variscan granitoids of the East Serbian Carpatho-Balkanides: new insight inferred from U–Pb zircon ages and geochemical data. Swiss J Geosci 112:121-142

Meinert LD (1992) Skarns and skarn deposits. Geosci Canada 19:145-162

Salnikova E, Stifeeva MV, Chakhmouradian AR, Glebovitsky V, Reguir E (2018) The U–Pb System in schorlomite from calcite-

amphobole-pyroxene pegmatite of the Afrikanda Complex (Kola Peninsula). Dok Earth Sci 478:148–151
Smith MP, Henderson P, Jeffries T, Long J, Williams CT (2004) The rare earth elements and uranium in garnets from the Beinn an Dubhaich Aureole, Skye, Scotland, UK: constraints on processes in a dynamic hydrothermal system. J Petrol 45:457–484
Stifeeva M., Salnikova E, Plotkina Y, Peytcheva I, Vassileva R (2018) Andradite from Dashkesan iron skarn deposit as a potential standard reference material for U-Pb geochronological studies. "GEOSCIENCES 2018", Abstracts, Review of the Bulgarian Geol Soc 79(3):61-62
Tarassova E, Tarassov M (1988) Horizontal zonality and mineral composition of skarns in the Martinovo deposit. Geochem Mineral Petrol 24:68-76 (in Bulgarian)
Wafforn S, Seman S, Kyle JR, Stockli D, Leys C, Sonbait D, Cloos M (2018) Andradite garnet U-Pb geochronology of the big Gossan Skarn, Ertsberg-Grasberg mining district, Indonesia. Econ Geol 113(3):769–778

Mineral-chemical characterization of the schist-hosted veinlet-style Sn-bearing mineralization of the Pöhla-Hämmerlein skarn deposit, Westerzgebirge, Germany

Tilman J. Jeske, Thomas Seifert, Martin Miehlbradt, Sabine Gilbricht
Institute of Mineralogy, TU Bergakadmie Freiberg (TUBAF), Germany

Abstract. The Pöhla-Hämmerlein Sn-In-polymetallic deposit comprises mainly skarn lithologies (Schuppan et al. 2012). Besides, it features cassiterite-bearing quartz-fluorite-tourmaline veinlets that penetrate the two-mica-schist country-rock. They have been observed at three localities (Hauptstolln, Querschlag 2, Chamber 7543) to occur only below the skarn body where they crosscut the schist in about 15° to the schistosity. The typical mineral association consists of cassiterite, quartz, fluorite, and minor tourmaline. A second occurrence reveals minor amounts of sulfides (arsenopyrite, chalcopyrite, pyrite, pyrrhotite) next to cassiterite. Bulk ore geochemistry reveals grades of up to 3.3 wt.% Sn.

Tin-grades correlate with the frequency of veinlets, and country rock shows only a slight enrichment in Sn, which occurs there as impregnation. Accordingly, possibly economic mineralization is entirely caused by veinlet-style mineralization with cassiterite as the Sn-bearing mineral phase. The mineral assemblage of the veinlets shows homogenization temperatures in the mesothermal range (238–344 °C).

The crosscutting of the late-Variscan country-rock (metamorphose age c. 340 Ma, Kröner and Willner 1998) and the enrichment of incompatible elements are indications for a magmatic influence of the cassiterite-quartz-fluorite-tourmaline veinlets, possibly related to an unidentified granite intrusion stage at the eastern rim of the Eibenstock granite massif.

1 Introduction

The Pöhla-Hämmerlein skarn deposit was discovered in 1969 during uranium exploration in the W-Erzgebirge by the Soviet-German company SDAG Wismut. In the following years, several exploration campaigns were established to bring the deposit into production, however all operations were unsuccessful. New exploration efforts started in 2014, and the whole resource has been estimated to contain ca. 22.1 Mt @ 0.2 wt.% Sn and 15.9 Mt @ ~130 ppm In (Anglo Saxony Minerals Ltd. 2018). In the footwall of the skarn ore bodies, some cassiterite-bearing veinlets occur in the two-mica-schist country rock. These veinlets were firstly described as “Schiefererz” (cf. Schuppan et al. 2012) and present possibly economic Sn-mineralization in stringer zones that are likely associated with the skarn genesis (Fig. 1). This mineralization type has not received intense attendance. With this study, we want to provide new detailed insights into the mineralogy of the veinlets and also deliver new constraints for the genesis.

2 Geological background

The Hämmerlein deposit is hosted by Variscan metamorphic rock units of the western Erzgebirge (cf. Baumann et al. 2000) which belongs to the Saxo-Thuringian zone and is situated at the northern margin of the Bohemian Massif. The metamorphic units consist mainly of schists (greenschist to amphibolite facies), gneisses, and metacarbonates (Rötzler and Plessen 2010). The peak of metamorphic conditions was reached at around 340 Ma (Kröner and Willner 1998).

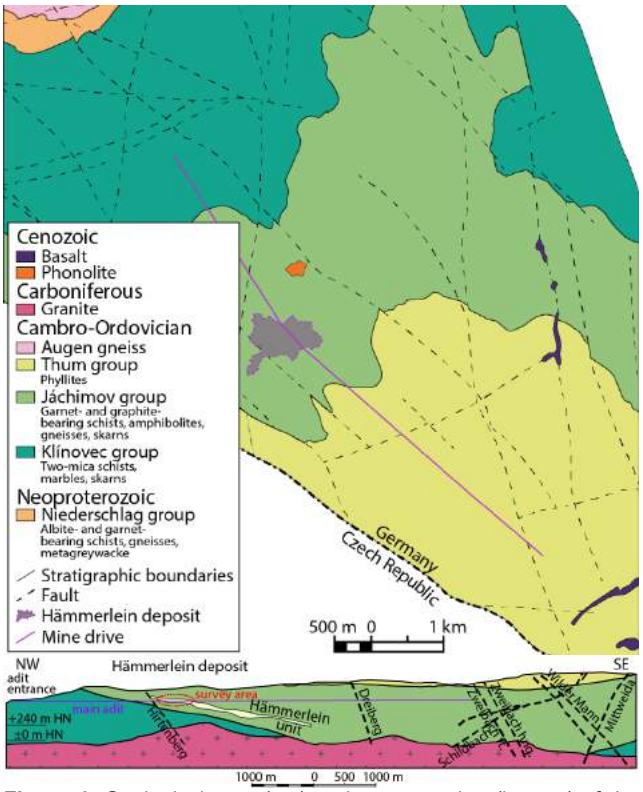

Figure 1. Geological map (top) and cross section (bottom) of the Pöhla-Hämmerlein deposit with the skarn body sandwiched in between two-mica schist country rock. Main adit of the mine as purple line (modified after Schuppan et al. 2012).

The region features several geochemically distinct groups of late-collisional Variscan granites, subvolcanic dikes, and microgranites (cf. Baumann et al. 2000). A further occurrence are lamprophyres that intruded into the metamorphic rocks between 327 and 290 Ma (Seifert 2008). In spatial relation with the magmatism

different types of magmatic-hydrothermal ore deposits like greisen, skarn, and polymetallic veins occur (Baumann et al. 2000). The units are crosscut by networks of local to regional faults, the most prominent being the NW-SE striking Gera-Jáchymov Fault Zone.

The veinlet-hosted "Schiefererz" ore type presents itself as part of a series of two-mica-schist, which is situated below the elongated skarn body of calc-silicates from the Hämmerlein Sn-In-polymetallic skarn. The schist belongs to the Jáchimov group. The whole deposit lies above a granite body of type Eibenstock (Schuppan et al. 2012).

3 Methodology

For this study, underground mapping was performed 2016 and 2017. We gathered a total of 63 samples from the "Hauptstolln", "Querschlag 2", and "Tin Chamber 7543". On these, light microscopy and SEM/MLA (scanning electron microscope/mineral liberation analysis), as well as bulk ore geochemistry (ALS Global), and fluid inclusion analysis (Flinc Lab of the Institute of Mineralogy at TUBAF) was performed.

4 Results

Results provide an overview of the distribution of the Sn-bearing "Schiefererz" ore type and the mineral association of the veinlets. "Schiefererz" was sampled at three locations (Fig. 2). Bulk ore geochemistry outlines enrichment of certain elements related to the veinlets and fluid inclusion microthermometry further shows the formation conditions.

4.1 Mapping

Mapping of two adits shows how veinlets are all crosscutting the two-mica schist host-rock with a slight angle of 10–30° towards N to NE. Furthermore, cassiterite mineralization often disappears at the hanging wall contact to the overlying skarn body. A set of subvertically dipping veinlets occurring NW of "Tin Chamber 7453" shows no cassiterite.

4.2 Petrography

Microscopy revealed that the "Schiefererz"-cassiterite occurs in two major habits: discrete subhedral crystals (c. 50–3,400 µm) or acicular cassiterite (*needle tin*; <100 µm). Discrete crystals reach up to a few mm and are the predominant crystal habit found in the "Hauptstolln" and "Tin Chamber 7453". Cassiterite from "Querschlag 2" consists of *needle tin* and smaller grain-sizes of discrete crystals. Discrete crystals show zoning and twinning, while *needle tin* aggregates only show zoning (Fig. 3).

MLA analyses reveal the association of minerals. Cassiterite predominantly occurs together with quartz, tourmaline, and mica, and minor feldspar, chlorite, fluorite, and rutile. In a second type close to the overlying skarn body, additional sulfides (arsenopyrite, chalcopyrite, pyrrhotite) occur (cf. Fig. 3).

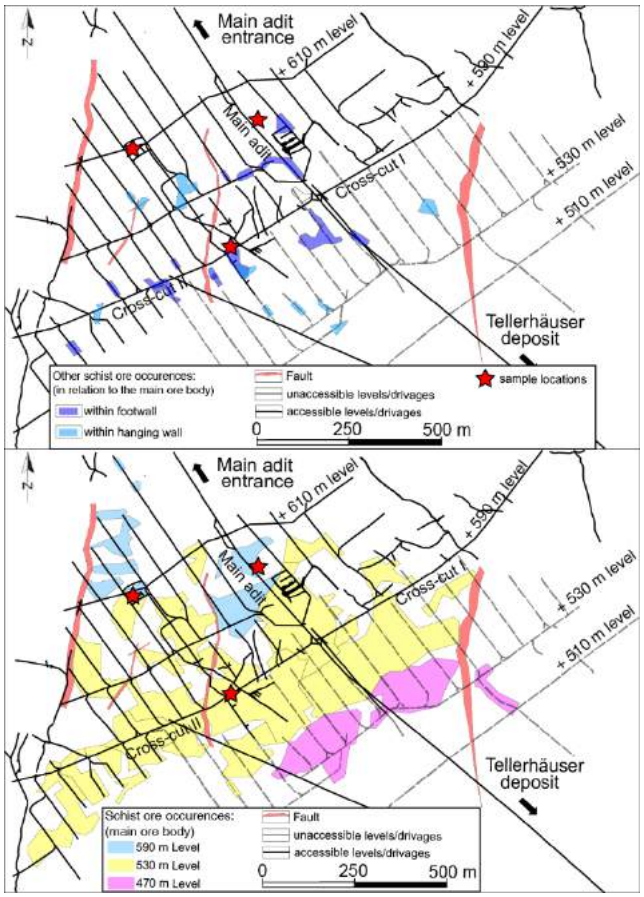

Figure 2 Underground map of the Hämmerlein mine with sample locations (red stars) of "Schiefererz" ore-type. Top: Outcrop locations of "Schiefererz" at the +590 m level. Bottom: General distribution of "Schiefererz" in different mine levels from earlier analyses (modified after Sorokina et al. 1980).

4.3 Fluid inclusion microthermometry

Microthermometry was performed on eight double polished sections (c. 200 µm) using fluid inclusions in cassiterite, fluorite, and quartz (Fig. 4). Homogenization temperatures are 313–344 °C, 238–347 °C, and 263–310 °C, respectively. Salinity is relatively low with 0.6-6.9 equiv. wt.% NaCl, with only some fluid inclusions in fluorite of sample "SOH-2.2" showing 12-19 equiv. wt.% NaCl and a homogenization temperature of 238–274 °C (Fig. 5).

4.4 Bulk ore geochemistry

Bulk ore geochemistry shows an increase of incompatible elements in zones with crosscutting veinlets. Concentrations of Rb, Cs, Li, B, Sn, and W are typically around 3–7-times increased compared to seemingly barren samples (Tab. 1) but can reach up to ~16,000-times enrichment (e.g. for Sn).

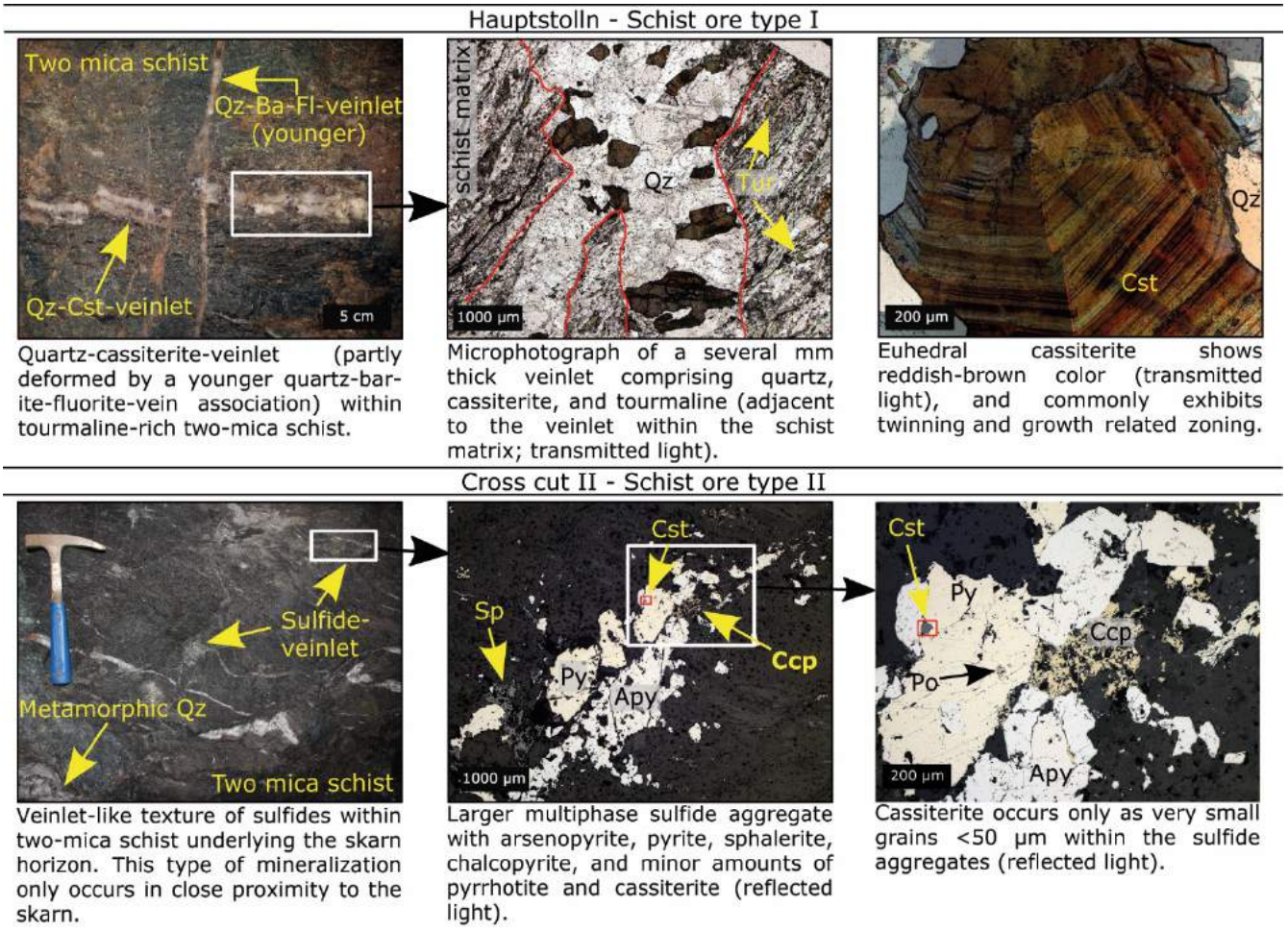

Figure 4 Photos and photomicrographs of the veinlet-style mineralization. Top: Qz-Cst-Tur-mineralization from the Hauptstolln. Bottom: Sulfide-bearing veinlets adjacent to skarn lithologies in Querschlag 2. (Apy=arsenopyrite, Ba=baryte, Ccp=chalcopyrite, Cst=cassiterite, Po=pyrrhotite, Py=pyrite, Qz=quartz, Sp=sphalerite, Tur=tourmaline).

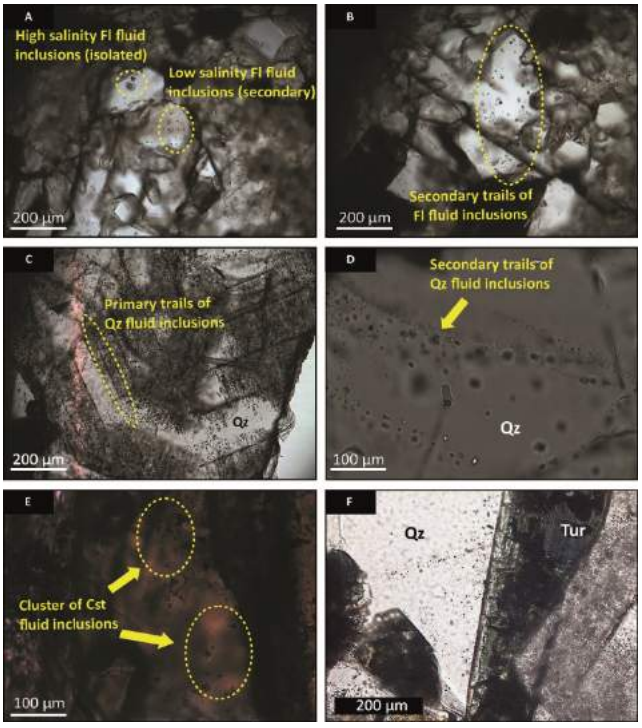

Figure 4 Different types of fluid inclusions in different minerals. (Cst=cassiterite, Fl=fluorite, Qz=quartz, Tur=tourmaline).

5 Discussion

The more or less uniform mineral assemblage and the relatively homogenous values of homogenization temperature and salinity suggest a single event for the formation of the veinlets.

The variation of crystal habits of cassiterite with the occurrence of larger single crystals and needle tin indicates mesothermal formation conditions (Ramdohr 1975). Furthermore, zonations show that the fluid was heterogenic in all areas where “Schiefererz” was observed. This is also supported by variations in homogenization temperatures from 263–347 °C and relatively low salinity (<5 equiv. wt.% NaCl). The slightly enriched salinity in five fluid inclusions in fluorite probably reflects mixing.

The elevated contents of incompatible elements like Rb, Cs, Li, B, F, Sn, and W in samples with mineralized veinlets and homogenization temperatures of up to c. 350 °C support a magmatic origin of the “schist ore” mineralization.

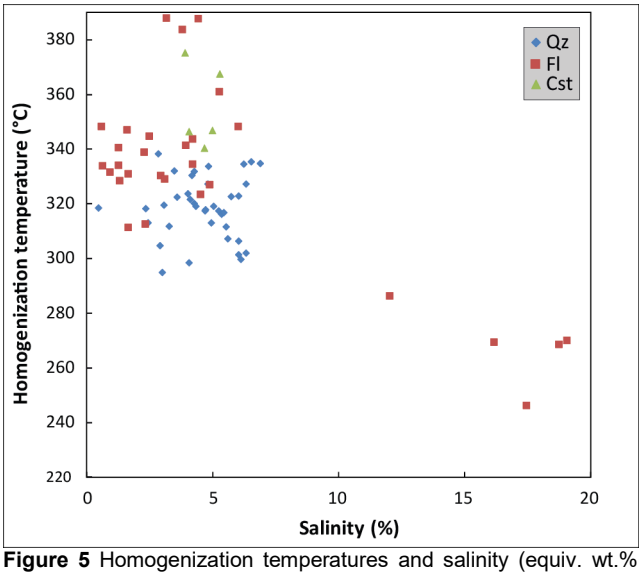

Figure 5 Homogenization temperatures and salinity (equiv. wt.% NaCl) of fluid inclusions in cassiterite (Cst), fluorite (Fl), and quartz (Qz).

Table 1 Bulk ore geochemical composition of unmineralized samples and mineralized samples from Hauptstolln, Querschlag 2, and Tin Chamber 7543.

	unmineralized	Querschlag 2			Hauptstolln			Kammer 7543		
Element (ppm)	mean (n=25)	min	max (n=5)	mean	min	max (n=22)	mean	min	max (n=13)	mean
B	34	54	269	115	109	7660	3316	11	2300	346
Cs	-	159	331	249	17	304	107	8	105	41
F	625	7100	20000	12590	2120	14000	8926	1200	14700	4715
In	-	0	7	5	0	5	1	1	15	5
Li	53	201	364	264	42	367	224	47	210	129
Rb	120	588	1145	891	162	680	435	100	510	310
Sn	4	727	15200	6271	288	63300	13059	200	18700	7208
W	2	8	107	43	4	84	32	2.4	54	21

Acknowledgements

This research is carried out as part of ResErVar project in the national r4 program (grant number 033R129 to TS). The BMBF is gratefully acknowledged for funding. Further gratitude goes to the Sample Preparation Lab at Helmholtz Institute Freiberg for Resource Technology. We highly appreciate the support by Saxore Bergbau GmbH and Zinnkammern Pöhla e.V. during underground mapping and sampling. Final gratitude to Tom Járóka for helping with the manuscript.

References

Anglo Saxony Minerals Ltd. (2018). http://www.anglosaxony.com/. Accessed 17 February 2019

Baumann L, Kuschka E, Seifert T (2000) Lagerstätten des Erzgebirges: 13 Tab. Enke, Stuttgart

Kröner A, Willner AP (1998) Time of formation and peak of Variscan HP-HT metamorphism of quartz-feldspar rocks in the central Erzgebirge, Saxony, Germany. Contrib Mineral Petrol 132:1–20

Ramdohr P (1975) Die Erzminerale und ihre Verwachsungen, 4., bearb. u. erw. Aufl. Akademie-Verlag, Berlin

Rötzler K, Plessen B (2010) The Erzgebirge: a pile of ultrahigh- to low-pressure nappes of Early Palaeozoic rocks and their Cadomian basement. In: Linnemann U, Romer RL (eds) Pre-Mesozoic geology of Saxo-Thuringia: From the Cadomian Active Margin to the Variscan Orogen. Schweizerbart, Stuttgart, pp 253–270

Schuppan W, Hiller A, Krejny I (2012) Die Komplexlagerstätten Tellerhäuser und Hämmerlein: Uranbergbau und Zinnerkundung in der Grube Pöhla der SDAG Wismut. Bergbau in Sachsen, vol 17. Sächsisches Landesamt für Umwelt, Landwirtschaft und Geologie, Freiberg

Seifert T (2008) Metallogeny and petrogenesis of lamprophyres in the Mid-European Variscides: Post-collosional magmatism and its relationship to late-Variscan ore forming processes in the Erzgebirge (Bohemian Massif). IOS Press BV, Amsterdam

Sorokina GP, Müller F, Jefimow WI, Schubert E, Afonin IA, Baumann H (1980) Report DS H1A/5/90. unpublished report, Wismut SDAG

Mineral paragenesis and zoning of the Hashim Abad magnetite-skarn, Isfahan Province, Central Iran

Nico Kropp, Andreas Kamradt, Gregor Borg
Economic Geology & Petrology Research Unit, Institute for Geosciences and Geography, Martin Luther University Halle-Wittenberg, Germany

Hooshang Asadi-Haroni
Department of Mining Engineering, Isfahan University of Technology, Isfahan, Iran

Abstract. The Hashim Abad magnetite-skarn occurrence is situated in the Urumieh-Dokthar-Magmatic -Arc, Central Iran. It is located in a transition zone of Cretaceous, dolomitic limestone and a Miocene, dioritic intrusion along a NW-SE striking fault. A contact metamorphic influence of the wall rock is marked by the formation of green amphiboles in the magmatic rock and the recrystallisation of calcite to marble. The meta-dioritic wall rock is additionally affected by alteration zones, preferentially towards the contact zone. Massive magnetite replaces the marble. Associated with the lens-shaped magnetite load are green calc-silicates. They consist mainly of diopsidic pyroxenes and minor chlorite, actinolite and titanite. Magnetite is locally associated with chalcopyrite and shows an anomalous gold concentration. Several indicators suggest that the Hashim Abad deposit can be assigned to the Fe-Cu-Au-skarn class. Hydrothermal influence is visible by sericitisation of feldspar and due to SWIR analysis indicating the presence of saponite, sepiolite and palygorskite. Furthermore, veins of calcite, ankerite and quartz are present in the whole contact zone, locally associated with epidote. They transect also magnetite and calc-silicate rocks and are themselves influenced by brittle faults.

1 Introduction

The Tethyan belt is a major porphyry-epithermal-skarn related mineralized belt that extends across central and southeast Europe, Turkey, Iran, Pakistan, through the Himalayan region and SE Asia. The less explored Iran, located in the central part of the Tethyan belt, is recognized as hosting world class deposits such as Sar-Cheshmeh porphyry (1.2 Gt @ 0.7% Cu) and Sungun porphyry-skarn (500 Mt at 0.75% Cu). These porphyry and skarn deposits are related to the evolution and closure of the Neo-Tethys Ocean and then the collision of the Afro-Arabian and Eurasian plates. Zagros orogenic belt (ZOB) in Iran, formed as part of these geodynamic processes, is the most important porphyry copper and skarn belt in Iran. The ZOB is part of the central Tethyan belt, which extends about 2000 km in NW-SE direction in Iran, and consists of three parallel NW–SE-trending tectonic segments including Urumieh Dokhtar magmatic arc (UDMA), Sanandaj-Sirjan zone (SSZ) and Zagros fold and thrust belt (Fig. 1).

The Hashim Abad skarn deposit is located in the central part of the UDMA. The occurrence was mined in an open pit with an extent of about 50 m NW-SE and 400 m SW-NE.

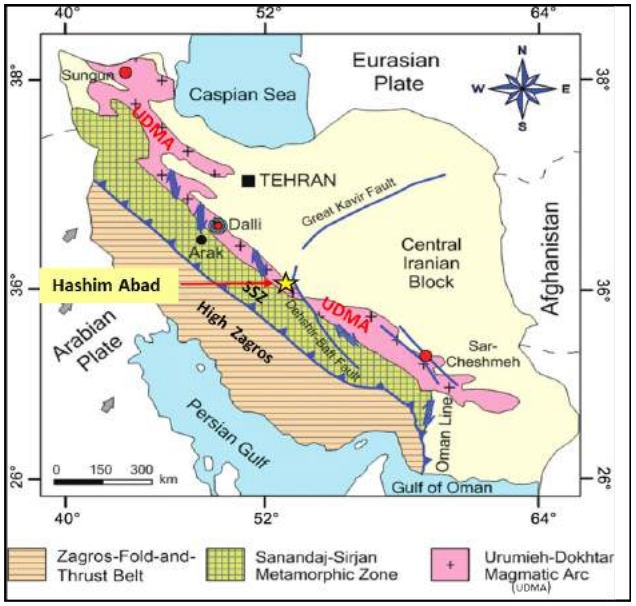

Figure 1. The three geological subdivisions of the ZOB (UDMA, SSZ and Zagros fold and thrust belt) and the location of the Hashim Abad on the central part of the UDMA.

2 Samples & methods

Our study comprised a sampling campaign with geological mapping of an open pit mine and the surrounding area at a magnetite skarn near Hashim Abad, 20 km south of Nain, Isfahan Province.
In the open pit, different levels of the contact zone of the magnetite-body between magmatic rock and a marble unit were sampled along a traverse, perpendicular to the strike of the magnetite-load. The sampling of hard rocks covered the contact zones from magnetite to the different wall rocks in order to trace changes in mineralogy, characteristic mineral textures, as well as ore and rock fabrics.

Optical microscopy on thin and thick sections was carried out for mineral identification and to determine the paragenesis of the different rocks and alteration minerals. Additionally, SEM-imaging and semi-quantitative EDX-analyses were performed to detect mineral compositions more precisely and to identify

geochemical trends of distinct mineral groups (e.g. pyroxene).

For identification of typical alteration minerals (e.g. clay minerals) reflectance spectroscopy in the wavelength range 350 to 2500 nm was conducted on hand specimen, using a TerraSpec spectrometer (ASD Inc.).

3 Geological Framework

The study area is marked by a mountain range with about 2000 m elevation. Lithologically, this area is dominated by Cretaceous limestone, which is associated with dioritic intrusive rocks situated along a major fault.

The wall rock consists of a greenish meta-diorite and a light grey marble. The magmatic rocks show an alteration-zoning towards the magnetite front, indicated by different rock colours (Fig. 2) and mineral assemblages. The contact between the meta-granodiorite and the marble was influenced by tectonic processes, indicated by shear bands, slickensides, and the slight lineation of minerals. Due to field observations, the relative timing of the formation of calc-silicates and magnetite. seems to be syngenetic to the emplacement of the diorite.

The lens-shaped magnetite load follows the marble-meta-diorite-contact. The strike of the contact follows the general strike of the Urumieh-Dokthar-Magmatic-Arc, i.e. NW-SE.

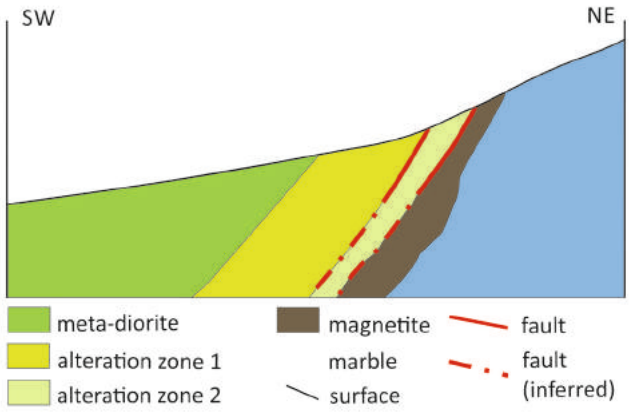

Figure 2. Simplified schematic cross-section across the contact between meta-diorite and marble (not to scale).

4 Results

4.1 Mineralogical characterisation of the wall rocks

The meta-diorite mainly consists of feldspar, amphibole, chlorite, quartz, and subordinate magnetite.

The mineral paragenesis changes continuously towards the marble contact. Distal to the contact, the rocks are green coloured and show a slightly preferred orientation of the amphiboles. These rocks commonly exhibit poikiloblastic growth of amphiboles that contain small quartz inclusions. Chlorite is commonly green-coloured, indicating a high iron content and has replaced pyroxene. Feldspar is the most abundant mineral in the meta-diorite and commonly shows twinning as well as growth zonation. EDX-measurements show that the feldspar is sodium-rich with albitic composition. Fine-crystalline alkali feldspar occurs locally, filling interstitials of albitic feldspar-crystals. The latter show tight lamellae and were internally partly converted to sericite. Interstitial quartz shows indications of recrystallisation. Furthermore, magnetite crystals, as small as tens of µm, display minor martitisation along the crystallographically preferred cleavage. SWIR-spectra of fresh meta-diorite hand specimens are predominantly marked by absorption features of palygorskite with subordinate spectral signatures of chamosite bands.

In an intermediate zone (Fig. 2, alteration zone 1), the meta-diorite tends to be less greenish and is more of white colour. The colour change starts along joints cross-cutting the rock. Microscopic observations revealed that the colour of amphiboles changes from deep green to lighter brown and pale green, respectively. Titanite and epidote occur in small amounts. Euhedral to subhedral feldspars were slightly altered by sericitisation within the centre of the crystals. Additionally, between individual feldspar crystals recrystallised, interstitial quartz represents late fillings. Reflectance spectra of meta-diorite of the intermediate zone contain absorption bands caused by a mixture of SWIR-active minerals comprising mainly palygorskite as well as minor smectite and calcite.

Additionally, small, dark aplitic veins transect the meta-diorite of the intermediate zone and these consist of lath-shaped, green to brown coloured amphiboles, which are embedded in a feldspar-quartz groundmass and are accompanied by fine-crystalline euhedral magnetite. Feldspars are commonly lath-shaped and show slightly growth zoning. TerraSpec-analyses of the aplite veins show a mixture of actinolite and chlorite.

Meta-diorite of the proximal zone (Fig. 2, alteration zone 2) consists of feldspar, quartz, amphiboles, pyroxenes, and in some veins occur epidote in other calcite and quartz. This zone shows shear bands, which transect feldspar and epidote, whereas the quartz seems to be recrystallized. Feldspar crystals are more intensely altered by serisitisation and show a pale brown colour. In some feldspars, small muscovite flakes but also carbonates document advanced alteration in the centre of the feldspar. Recrystallised quartz is partly intimately overgrown by clinopyroxene on crystal boundaries. Reflectance spectroscopy carried out on meta-diorite hand specimens taken proximal to the magnetite ore body revealed characteristic absorption bands of palygorskite and illite/smectite. Veins cross-cutting this zone are spectrally marked by absorption features caused by vermiculite and calcite.

The marble is generally light grey coloured and appears to be tectonically folded. Some areas near magnetite lenses contain subordinate amphibole and chlorite, thus forming locally a calc-silicate marble. SWIR-analyses of marble samples show strong

absorption by calcite and subordinate spectral absorption bands from saponite.

Reflectance spectroscopy on samples from the magnetite ore body showed generally a mixture of absorption features caused by chlorite, actinolite, and minor goethite. Brownish joint coatings within the magnetite contain spectral evidence for the occurrence of sepiolite, a Mg-phyllosilicate, and tilleyite, which represents a characteristic calc-silicate mineral containing additionally a carbonate complex, typical for contact metamorphic zones in the transition from igneous rocks to limestones. SWIR-analyses of samples from the greenish-yellow areas within the magnetite document chlorite-type minerals such as chamosite and sheridanite as well as some chrysotile.

4.2 Mineralogical characterisation of the skarn assemblage

The occurrence of the green rock units is spatially related to magnetite lenses, which are enveloped by a calc-silicate mineral association. The magnetite itself locally contains greenish calc-silicates, which mostly occur as inclusions within the magnetite bodies or at the immediate contact with the marble unit. Generally, magnetite replaced marble and the spatial boundaries are characterized by sharp contacts. Occasionally, larger spherical marble inclusions occur within magnetite lenses. Locally, magnetite contains small, sharp-edged marble clasts, which appear brecciated. Locally, magnetite also replaces marble on a smaller scale along veins within the marble.

Sulphide minerals such as chalcopyrite and pyrite are associated with the magnetite (Fig. 3). Pyrite is partly intergrown with magnetite and chalcopyrite or occurs as individual particles surrounded by carbonates. In some cases, magnetite encloses chalcopyrite completely. It can be assumed, that the sulphide ore minerals occur only on the marble-side of the magnetite lens to marble contact. Chalcopyrite locally occurs together with small amounts of covellite, which might be an indication for a supergene origin of this sulphide mineral. Other green to greenish-blue secondary copper minerals as well as red to brown secondary iron minerals are abundant along joints, supporting the interpretation of a supergene alteration zone near surface. Apatite and titanite occur also intergrown with magnetite.

The magnetite ore lenses show a tectonic overprint and magnetite but also pyrite and chalcopyrite show signs of brecciation, particularly along faults or shear bands. In these areas, the joints are filled with haematite or other secondary iron oxy-hydroxide minerals. Generally, sulphides occur only, where magnetite is closely associated with dark green minerals, which are typically calc-silicates.

The green rocks consist of calc-silicates and the most abundant minerals of these are clinopyroxenes, but also actinolite, titanite and a mixture of carbonates and chlorite. This zone is crosscut by small veinlets of calcite, calcite with quartz, or quartz only. SWIR-spectra of the green calc-silicates display spectral features of actinolite, saponite, and talc. Additionally, on joint coatings, absorption bands caused by sepiolite dominate the reflectance spectra.

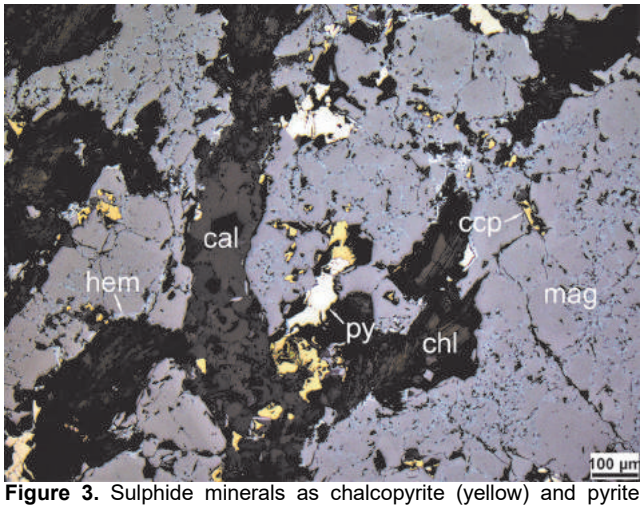

Figure 3. Sulphide minerals as chalcopyrite (yellow) and pyrite (white) are intergrown with magnetite (medium grey). Magnetite shows a slight martitisation along crystallografically preferred cleavage.

4.3 Geochemical trends and skarn formation

The magnetite locally contains small amounts of vanadium. Some pyrites contain small amounts of arsenic, nickel, and cobalt. Analyses revealed that one sample of a hand specimen of magnetite contains an anomalous concentration of 500 ppb gold.

The elemental composition of zoned epidote indicate small amounts of REE were substituted preferentially in outer growth zones.

The clinopyroxenes contain magnesium and iron, but no manganese. Some diopsidic pyroxenes show a slight zonation towards more iron-rich rims. The compositional trend is clearly notable between hedenbergite (Fe-rich clinopyroxene) and diopside (Mg-rich clinopyroxene), but a diopsidic composition is more common. The magnesium content of the measured pyroxenes increases from the magmatic side of the magnetite body to the marble side.

Based on field observations, microscopy, and pyroxene composition it can be assumed that the exoskarn portion exceeds the portion of the endoskarn in this particular system.

4.4 Skarn classification

In order to classify skarn deposits, Einaudi and Burt (1962) and Meinert (1992) created a diagram for clinopyroxenes based on microprobe analyses. In this study, we use EDX-data to delineate the trend of the pyroxene composition typical for the Hashim Abad skarn occurrence (Fig. 4). The data show a trend between diopside and hedenbergite, both commonly associated with Fe-, Cu- and Au-skarns. The occurrence of magnetite, intergrown with some chalcopyrite support this classification.

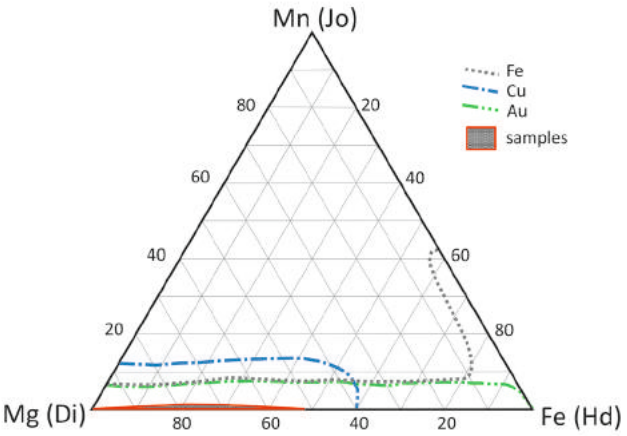

Figure 4. Ternary diagram of clinopyroxene compositions, showing the correlation between composition and skarn-related metal content (after Einaudi and Burt 1962 and Meinert 1992). The EDX-data of samples from Hashim Abad show a trend to magnesium-rich pyroxenes between the endmembers diopside and hedenbergite. The hedenbergitic trend of the pyroxenes can be interpreted as an indicator for a Fe-, Cu- and Au-skarn.

4.5 Hydrothermal alteration

A marked hydrothermal influence is documented by small veins and veinlets throughout the entire contact zone. These veins consist predominantly of carbonates, dominated by calcite with minor ankerite. Some veins are composed of quartz and carbonates or are composed just of quartz. The minerals within the veins are euhedral to subhedral and commonly larger than the surrounding carbonates or quartz crystals. Some vein minerals show typical growth structures from rim to centre. Some of the veins show also brittle deformation with some mm offset by micro-faults.

Saponite and sepiolite/palygorskite can be regarded as alteration minerals formed under hydrothermal conditions by replacement of primary skarn-related magnesium silicates.

Additionally, feldspars show serizitisation, which is also an effect of hydrothermal influence of the wall rock.

5 Conclusions

The formation of skarn deposits and their metal association is strongly controlled by the plate tectonic environment. In case of the Hashim Abad skarn occurrence, the tectonic setting within the subduction-related back-arc of the Urumieh-Dokthar-Magmatic-Arc is a typical situation for copper and gold skarns.

Fault zones are areas of crustal weakness, in which magma can ascend and intrude more easily and can locally form skarn deposits in contact with limestone or marble.

The amphiboles in the meta-diorite are considered to have formed under metamorphic greenschist facies conditions. Therefore, the emplacement of the plutonic rock seems to have occurred before or during the last orogenic events in this region. Additionally, the tectonically induced faulting and associated recrystallisation of limestone to marble accompanied this event.

The ores at Hashim Abad were also affected by shear-bands and faults, indicating a later phase of tectonic activity from transitional ductile to brittle conditions. This event could have been associated with hydrothermal activity as indicated by the occurrence of cross-cutting carbonate veins, locally associated with quartz. The emplacement of veins have been related to extension caused by plutonic crustal uplift and erosion to the recent surface level.

The Hashim Abad exoskarn mainly consists of green, diopsidic pyroxene, which indicates, that magnesium completely derived from dolomitic marble and was incorporate into typical skarn minerals. As a result of the increasing magnesium content of calc-silicates towards the marble front, the reaction front replaces the dolomitic marble and consequently Mg-rich calcsilicatic minerals were formed during prograde skarn formation. In magnesium-rich skarn systems, it is more common to form forsterite than garnets. The only evidence for this could be the presence of talc as supergene alteration product of Mg-rich olivine, particularly along fractures.

The retrograde mineral assemblage of actinolite, epidote, and chlorite replaced magnetite and could have overprinted the initial zoning of the skarn system.

Endoskarn might be present in small amounts where pyroxenes have grown along crystal boundaries in the altered meta-diorite. Depending on the temperature, pH, and Eh conditions, different minerals were formed during that alteration and these are most commonly saponite and sepiolite. More distal to the magnetite body, the fluids altered the meta-diorite as well. Here, the alteration zone 1 was influenced by Mg-bearing fluids, which caused changes in amphibole chemistry and led additionally to the formation of clay minerals.

Alteration zone 2 within the meta-diorite documents a strong fluid-host rock interaction causing the alteration of the wall rock with extensive sericitisation of feldspar phenocrysts.

Acknowledgements

For funding field work we thank the International Office of the Martin Luther University Halle-Wittenberg and PROMOS, a program of the German Academic Exchange Service (DAAD).

References

Einaudi MT, Burt DM (1982) Introduction; terminology, classification, and composition of skarn deposits. Economic geology 77:745-754.

Meinert LD (1992) Skarns and skarn deposits. Geoscience Canada 19:145-162.

EPMA analysis on epidote-group minerals from the LREE-bearing Fe-Polymetallic Skarn-Type Deposit Vesser/ Schmiedefeld, Thuringia, Germany

Steven Zierold, Thomas Seifert, Sabine Gilbricht
Institute of Mineralogy, Technische Universität Bergakademie Freiberg, Germany

Stefan Kiefer
Institute of Geosciences, Friedrich-Schiller-University, Germany

Abstract. The LREE-bearing garnet-magnetite-skarn deposit Vesser/Schmiedefeld is located in southern Thuringia.

Bulk rock analyses from the 'Schwarzer Crux' mine show high contents of light rare earth elements (LREE), e.g. 1025 ppm La and 737 ppm Ce, hosted mainly by epidote group members. The LREE-bearing epidote group minerals from the 'Schwarzer Crux' mine are members of the solid solution system epidote–ferriallanite, respectively ferriallanite-(La). Some of the electron microprobe analysis (EPMA) on epidote group minerals show REE cation levels up to 1.24 atoms per formula unit (apfu) which is more than members of epidote group minerals can regularly incorporate.

However, preliminary results of study show that the LREE enrichment in epidote and the existence of ferriallanite strongly depends on the distance to contact of the granite intrusion. The increasing LREE contents in epidote and the occurrence of ferriallanite in relation to the granite contact as well as elevated F contents and MoS_2 mineralization indicate that the ore bodies in the Vesser/Schmiedefeld area belong to a Fe-polymetallic skarn-type deposit, which show a spatial and temporal relationship to a Variscan granite intrusion.

1 Introduction

The REE-bearing Fe-polymetallic skarn-type deposit Vesser/Schmiedefeld is located in southern Thuringia in the Variscan unit of the Thüringer Wald (Thuringian Forest).

The object of study is the old mining site 'Schwarzer Crux'. It was one of the most important Fe-mines around the town Suhl. From the 19th century it belonged to the mining company 'Vereinigte Cruxzechen', a pit field about one square kilometer in size. The company mined magnetite and hematite as well as secondary pyrite. The mining activities finished in 1924. Today, a part of the 'Schwarzer Crux' mine is opened to the public as visitor mine, but the most of the underground mining work was safely closed, filled or is collapsed today.

The deposit consists of westerly fifty degree dipping and few centimeters to meters thick layers of massive magnetite, which is associated with fluorite (F in bulk ore up to 18.10 wt.%), calcite and barite at different levels (Figs. 1, 2 and 3). The magnetite ore bodies are related to a granite contact and hosted by a garnet skarn. The granite intrusion is probably related to the 'Thuringian main granite' with an intrusion age of 337 ±4 Ma (Zeh et al. 2000).

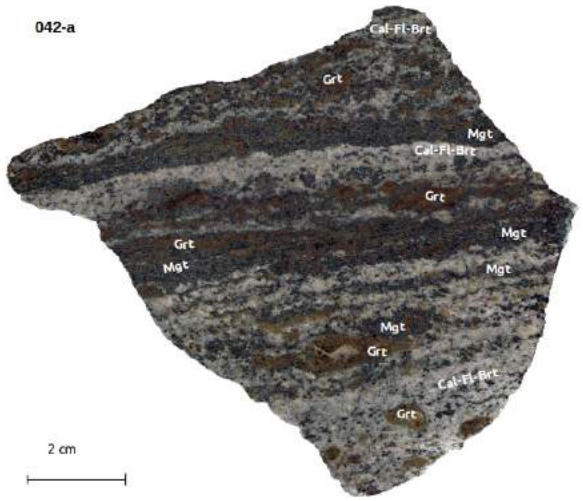

Figure 1. Layered magnetite (Mgt) intergrowing with garnet (Grt) and calcite-fluorite-barite (Cal-Fl-Brt) (sample: 042-a S-heading 'Schwarzer Crux' mine)

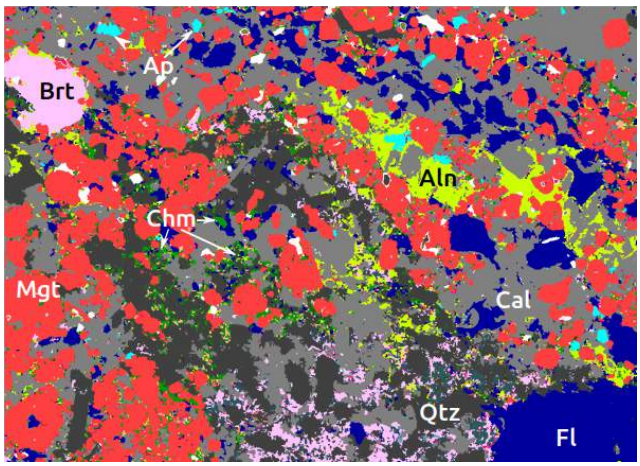

Figure 2. MLA-false colour image (sample: 038-g 'Schwarzer Crux' mine S-heading) Legend: red: magnetite (Mgt); dark-gray: quartz (Qtz); gray: calcite (Cal); blue: fluorite (Fl); pink: barite (Brt); lime green: ferriallanite (Aln); light-blue: apatite (Ap); green: chamosite (Chm); blue green: orthoclase (base of image: 6 mm)

Figure 3. Magnetite ore from 'Schwarzer Crux' mine (S-heading, sample: 038-c)

The main mineral phases are magnetite, calcite (partially enriched in manganese up to 7.83 wt.% MnO), fluorite, barite, rough masses of grossularite-andradite, orthoclase, barite-bearing orthoclase (up to 11.56 wt.% BaO), quartz, chamosite, biotite, stilpnomelane, pyrite, hematite and a great variety of accessory minerals e.g. ferriallanite, epidote, muscovite, ilmenite, chalcopyrite, apatite, monazite, molybdenite, titanite, pyrophanite, zircon and chalcedony.

Bauer (1872) described a two centimeter allanite crystal from the 'Schwarzer Crux' mine. The locality east of the visitor mine is no longer accessible today. But in collected and in archive samples REE-enriched epidote group minerals are very common, with a size up to 3 millimeters (Fig. 2).

2 EPMA analyses on epidote group minerals

The main LREE host minerals are part of the epidote-group. To determine the epidote group and respectively the allanite subgroup by LREE content, we analyzed epidote group minerals by EPMA (Figs. 4 and 5).

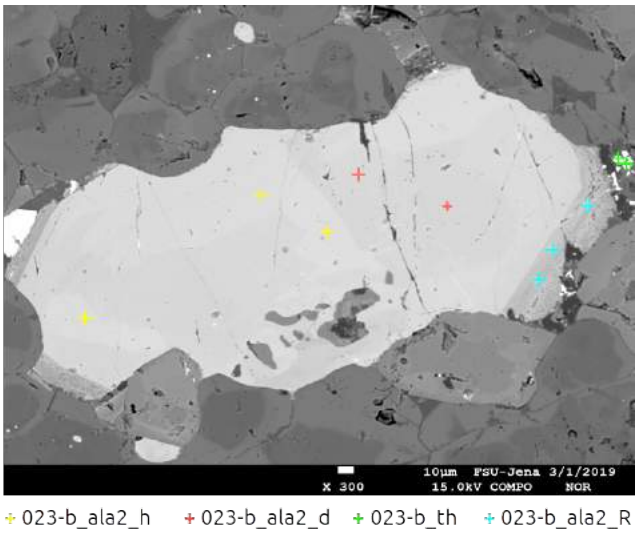

Figure 4. Backscattered electron image with measurement spots on a ferriallanite (023-b: NE-heading, 'Schwarzer Crux' mine)

For best accuracy, we set at least three measurement spots for each mineral and formed the mean. Several measurements were not suitable for stoichiometry and were selected.

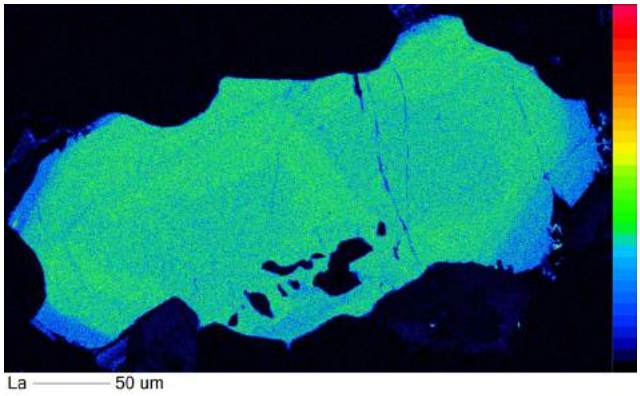

Figure 5. La mapping, LREE zoning and distribution (cf. Fig. 4)

For stoichiometric calculations, the cations where calculated on the basis of 8 cations for 2.97 to 3.03 Si apfu and for 3.03 to 3.05 Si apfu, on a basis of 3 Si apfu respectively (Franz & Liebscher 2004; Armbruster et al. 2006).

Table 1. Exemplary samples of EPMA analyses calculated to numbers of cations (apfu), (023b: NE-heading; 036c and 038g: S-heading; 050-III: S-transverse-heading, 'Schwarzer Crux' mine)

	023-b Epi-1	023-b Ala-2	036-c Ala-3	038-g Ala-4	050-IIIa Ala-5
Si	3.000	3.034	2.979	3.018	3.027
Al	1.959	1.640	1.545	1.088	1.287
Fe^{3+}	0.879	0.131	0.504	0.288	0.308
Ti	0.005	0.030	0.036	0.010	0.003
Mn^{2+}	0.046	0.100	0.088	0.202	0.222
Mg	0.001	0.057	0.025	0.163	0.047
Fe^{2+}	0.016	0.959	0.841	1.203	1.101
Ca	1.827	1.244	1.366	0.997	1.108
ΣREE	0.013	0.798	0.615	1.029	0.893
Y	-	0.001	-	-	0.001
Th	0.001	0.003	-	0.001	-

La is the main LREE. The ratio to Ce is nearly constant for all analyzed LREE hosting minerals (Fig. 6).

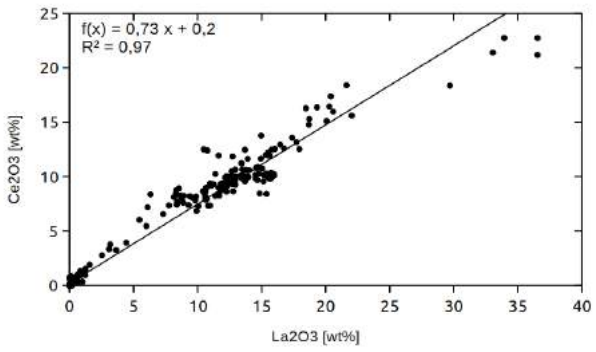

Figure 6. La/Ce ratio of all EPMA analyses

ThO_2 does not correlate with LREE in general. High contents of Th (given as ThO_2 up to 22,5 wt.%) and REE total (given as sum of La_2O_3, Ce_2O_3, Pr_2O_3, Nd_2O_3, Sm_2O_3 and Dy_2O_3 up to 64,9 wt.%) where detected in fractures and grain boundaries as amorphous phases, with anomalous stoichiometry. In most analyses, ThO_2 correlates with Y_2O_3.

3 Stoichiometric calculations

A general formula for epidote is $Ca_2Al_2Fe^{3+}Si_3O_{12}(OH)$. The structural formula for epidote-group minerals is A1A2M1M2M3$(SiO_4)(Si_2O_7)$(O,F)(OH) and simplified $A_2M_3Si_3O_{11}$(O,F)(OH). The A-site position contains divalent cations, e.g. Ca^{2+}, Sr^{2+}, Pb^{2+}, Mn^{2+}, Ba^{2+} but also REE^{3+} and Th^{4+}. The A site where divided into A(1) and A(2), because of different coordination numbers. A(1) is mostly occupied by Ca^{2+}, whereas A(2) site also contains REE^{3+} and Th^{4+} (Fig. 7). M site positions where occupied by trivalent cations M: Al^{3+}, Fe^{3+}, Mn^{3+}, Cr^{3+}, V^{3+} and as charge balance for A site by divalent Fe^{2+}, Mn^{2+} and Mg^{2+}, especially in M(3) site. (Wilson et al. 2013, Armbruster et al. 2006, Franz & Liebscher 2004, Gieré & Sorensen 2004, Dollase 1971).

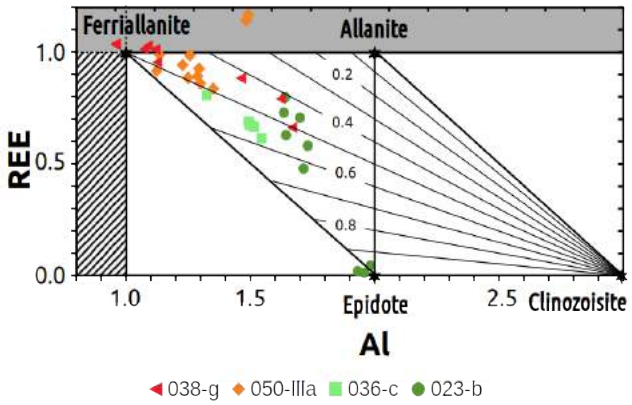

Figure 7. REE vs. Al in apfu (modified after Gieré & Sorensen 2004). The grey field shows LREE cations out of A(2) site. The lines of constant Fe-oxidation state (Fe^{3+}/Fe_{total}) can be used to estimate the ratio between Fe^{2+} and Fe^{3+}. The given samples represent different locations within the deposit with different distances to the granite-contact: red (038-g) few centimeters, orange (050-IIIa) few decimeters, pale-green (036-c) meters, green (023-b) a few tens of meters (cf. Fig. 8).

Preliminary results, show LREE contents up to 1.24 apfu in some minerals (Fig. 7). In this case, the A(2) site is completely occupied by 1 apfu REE^{3+} and probably A(1) site contains the rest. A possible reaction for REE enrichment in epidote group minerals is the substitution of Ca^{2+} and Al^{3+} by REE^{3+} and Fe^{2+} (Gieré & Sorensen 2004).

The analysed samples represent different distances to the granite intrusion contact within the deposit. This sample locations are outcropped in the 'Schwarzer Crux' mine. In vicinity to the granite, Fe is more reduced, for charge-balancing of the increasing REE content. The Fe oxidation state and the REE content determine the epidote group and the appropriate subgroup (Fig. 8).

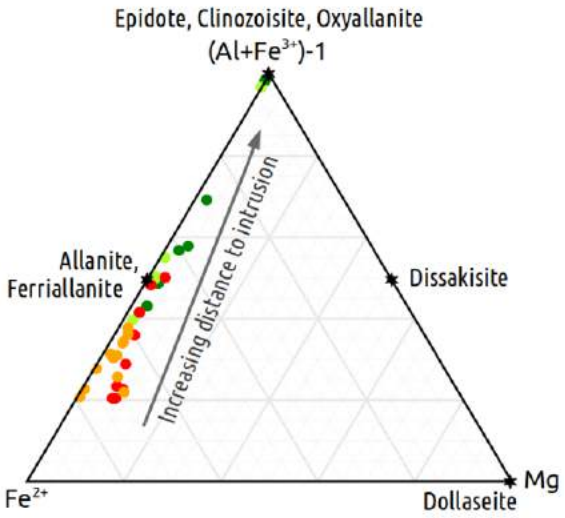

Figure 8. Solid solution in the $Fe^{2+}/Mg^{2+}/(Al+Fe^{3+})$ subsystem depending on the distances to the intrusion contact (modified after Gieré & Sorensen 2004). The given samples represent different locations within the deposit with different distances to the granite-contact: red (038-g) few centimeters, orange (050-IIIa) few decimeters, pale-green (036-c) meters, green (023-b) a few tens of meters (cf. Fig. 7).

4 Preliminary results and further work

LREE bearing epidote group minerals from the 'Schwarzer Crux' mine are part of the solid solution system epidote–ferriallanite, with ferriallanite-(La) as endmember (Figs. 7 and 8). In this study we found a significant relation between the LREE content of the epidote group minerals and the distance to the granite intrusion contact. Probably the LREE enrichment of epidote members are a function of the distance to the granite contact. We plan to confirm these results with additional measurements by EPMA and LA-ICPMS in the future.

Former investigations tried to explain the ore formation as a pre-Variscian VMS deposit formed by black smoker activity in a Cambrian back arc basin, which was later oxidized by a granite intrusion during the Variscan orogeny (Bankwitz and Bau 1997).

The significant dependency of the content of LREE and the Fe^{3+}/Fe^{2+}-ratio to the distance of the granite contact is maybe an indicator that the REE enrichment is associated with the granite intrusion. The increasing REE contents in epidote and the occurrence of ferriallanite in relation to the granite contact as well as elevated F contents and MoS_2 mineralization indicate that the ore bodies in the Vesser/Schmiedefeld area belong to a Fe-polymetallic skarn-type deposit which show indications for a spatial and temporal relationship to the Variscan granite magmatism in the area.

Our new results reinforce the assumption that the Vesser/Schmiedefeld deposit is associated with metasomatic mineralization in calcareous rock units (Schlegel 1902), i.e. as Fe-polymetallic skarn-type mineralization which is possibly related to a granite intrusion.

References

Armbruster, T., Bonazzi, P., Akasaka, M., Bermanec, V., Chopin, C., Gieré, R., Heuss-Assbichler, S., Liebscher, A., Menchetti, S., Pan, Y. & Pasero, M. (2006). Recommended nomenclature of epidote-group minerals. European Journal of Mineralogy, 18(5):551-567.

Bankwitz, P. & Bau, M. (1997). Aufbau und Genese der Magnetitlagerstaette Schwarze Crux bei Schmiedefeld am Rennsteig (Zone von Vesser, Thüringer Wald): Teil einer überregionalen geomagnetischen Anomalie in Mitteleuropa. Zeitschrift für geologische Wissensschaften 25: 341-362.

Bauer, M. (1872). Allanit vom Schwarzen Crux bei Schmiedefeld im Thüringer Walde. Nachrichten von der Königl. Gesellschaft der Wissenschaften und der Georg-Augusts-Universität zu Göttingen, 1872:337-344.

Dollase, W. A. (1971). Refinement of the crystal structures of epidote, allanite and hancockite. American Mineralogist: Journal of Earth and Planetary Materials, 56(3-4_Part_1):447-464.

Franz, G. & Liebscher, A. (2004). Physical and Chemical Properties of the Epidote Minerals–An Introduction–. Reviews in mineralogy and geochemistry, 56(1):1-81

Gieré, R. & Sorensen, S. S. (2004). Allanite and other REE-rich epidote-group minerals. Reviews in Mineralogy and Geochemistry, 56(1):431-493.

Schlegel, K. (1902). Das Magneteisenerzlager vom Schwarzen Krux bei Schmiedefeld im Thüringer Wald. Zeitschrift der Deutschen Geologischen Gesellschaft 54:24-55.

Wilson, M. J., Deer, W. A., Howie, R. A. & Zussman, J. (2013). Rock-Forming Minerals, Volume 3C, Sheet Silicates: Clay Minerals. In Geological Society, London.

Zeh, A., Cosca, M. A., Brätz, H., Okrusch, M. & Tichomirowa, M. (2000). Simultaneous horst-basin formation and magmatism during Late Variscan transtension: evidence from 40Ar/39Ar and 207Pb/206Pb geochronology in the Ruhla Crystalline Complex. International Journal of Earth Sciences, 89(1):52-71.

Zierold, S., Kiefer, S. & Seifert, T. (2018). Mineralogical, geochemical and petrological studies in the old Fe mine 'Schwarzer Crux', Thüringer Wald, Germany-garnet-bearing fluorite-magnetite-skarn mineralization around the Suhl granite. In EGU General Assembly Conference Abstracts, 20:13478.

Mineralization processes of the Carboniferous Malkansu large scale manganese metallogenic belt in Western Kunlun Mountain

Lianchang Zhang, Banglu Zhang, Zhiguo Dong, Zidong Peng
Key Laboratory of Mineral Resources, Institute of Geology and Geophysics, Chinese Academy of Sciences, China

Abstract. The large scale Carboniferous Malkansu manganese carbonate metallogenic belt was a recent discovery newly found in Western Kunlun Mountain. This belt is hosted by a marine sedimentary sequence of the Upper Carboniferous Kalaatehe Formation. Based on trace element and S-C isotopic features of this formation, an oxic-suboxic stratified water system is proposed for the Maerkansu basin. The 1st and the 2nd Member non-mineralized wall rocks display modern seawater-like REEs+Y profiles that are characterized by negative Ce anomalies and HREEs enrichment relative to LREEs in AUCC-normalized diagrams, suggesting an oxic surface water condition. While the absence of a Ce anomaly in non-mineralized rock samples from the 3rd Member argues for relative reducing conditions. Low values of enrichment factors for the redox-sensitive trace elements (U, V, Cr and Mo) in the non-mineralized wall rocks (particularly the 3rd Member) indicate a suboxic rather than an anoxic (precludes euxinic) bottom water conditions. Large fractionation of sulfur isotopes indicates a relatively high sulfate concentration in the water column, and the rate of sulfate replenishment exceeded that of sulfate reduction. Collectively, it is suggested that ore-forming conditions of the Maerkansu manganese metallogenic belt is a relatively open rather than a strictly restricted basin system.

1 Introduction

The large scale Carboniferous Malkansu manganese carbonate metallogenic belt was recently found in the Western Kunlun Mountain of Xinjiang Province (Fig. 1a). The manganese-mineralized beds are stratigraphically continuous, with 60 km in length and high grade (average Mn contents is 35%). It is expected to be a new manganese resource base in China, with defined manganese-carbonate-rich ore reserves (shallower than 300m) up to 45 million tons by the end of 2017 (Gao et al. 2016). Since little work has been done with the manganese belt and its associated rocks, limited information is available for manganese mineralization mechanisms as well as its depositional environment. In this paper, we present petrologic and geochemical results of both manganese ore and the associated rocks, in order to study the depositional environment of the Carboniferous Maerkansu large scale manganese metallogenic belt in West Kunlun Mountain.

2 Geology of manganese metallogenic belt

2.1 Geological setting

As one of the major tectonic units forming the northern boundary of the western Tibetan Plateau, West Kunlun Orogenic Belt (WKOB) underwent long-term crustal assemblage and accretion between early Paleozoic and Mesozoic in response to the evolution of the Proto- to Palaeo-Tethys ocean (Robinson et al. 2016; Zhang et al. 2018), and overprinted by Cenozoic tectonism as well as volcanism accompanying India-Asia convergence (Zhang et al. 2008; Jiang et al. 2013). Tectonically, the Malkansu manganese metallogenic belt is situated at the junction of the western margin of the Tarim block and the western section of the WKOB, belonging to the north Kunlun terrane (Fig. 1a and 1b) (Gao et al. 2016; Zhang et al. 2018). Recent studies suggested that these shallow marine carbonate and clastic rocks are possibly representative of a late Paleozoic to early Mesozoic back-arc basin sequence, which formed in response to the northward subduction of the Paleo-Tethys Ocean in western Kunlun (Zhang et al. 2018).

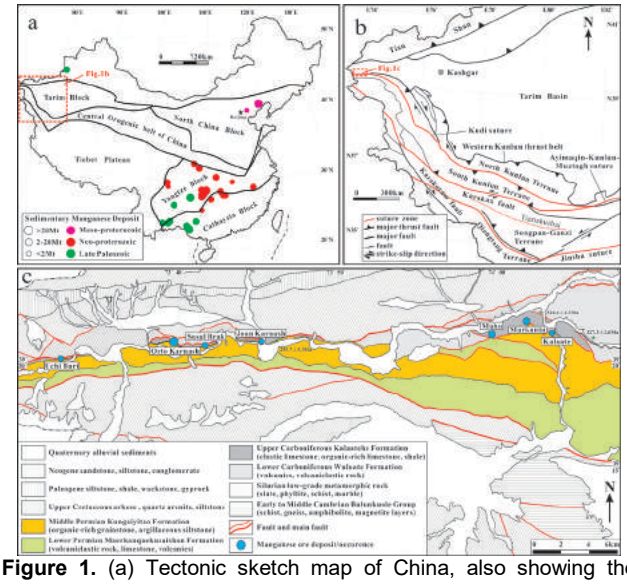

Figure 1. (a) Tectonic sketch map of China, also showing the spatial and temporal distribution of major sedimentary manganese ore deposits. (b) Simplified tectonic units of the West Kunlun Orogenic Belt (modified after Robinson et al. 2004; Zhang et al. 2018). (c) Simplified geological map of the giant Malkansu manganese belt, northwestern portion of the West Kunlun Orogenic Belt (modified after No.2 Geological Bureau, Xinjiang BGMR, 2018).

In addition, geochemistry studies on the Carboniferous volcanic rocks revealed that they display typical characteristics of E-BABB, indicating that the north Kunlun terrane was in a back-arc extensional environment during the early Carboniferous (Yun et al. 2015). Thus, the Carboniferous-Permian sequence in the Malkansu area represents sedimentary occurrences of an extensional back-arc basin.

2.2 Geology of manganese deposits

The Malkansu manganese metallogenic belt is distributed in an approximately west-east orientation, extending more than 60 km (west to east) in length but less than 2 km (north to south) in width (Fig. 1c). Exposed strata include Carboniferous manganese-bearing sedimentary rocks of the Kalaatehe Formation, Permian volcano-sedimentary rocks of the Maerkanque Formation and Cretaceous terrigenous sedimentary rocks of the Kukebai Formation (Fig.1c). The Kalaatehe Formation is subdivided, from bottom to top, into three members (Fig. 2), with the 1st Member (C_2k^1) consisting of sedimentary breccia, the 2nd Member (C_2k^2) of calcarenite, and the 3rd Member (C_2k^3) of organic-rich calcareous mudstone with one or two manganese-mineralized intervals (Gao et al. 2016; Zhang et al. 2018).

Overall, the rock assemblages of the Upper Carboniferous Kalaatehe Formation, from the sedimentary breccia and calcarenite at the bottom to the calcareous mudstone (including manganese ore belt) at the top, and then grade into the calcarenite and micrite at the uppermost, consist a complete transgression-regression cycle. The manganese-mineralized intervals occur in organic-rich calcareous mudstone, together with the black shale nearby the ore zone, suggesting that the occurrence of manganese mineralization occurred during the highstand systems tract.

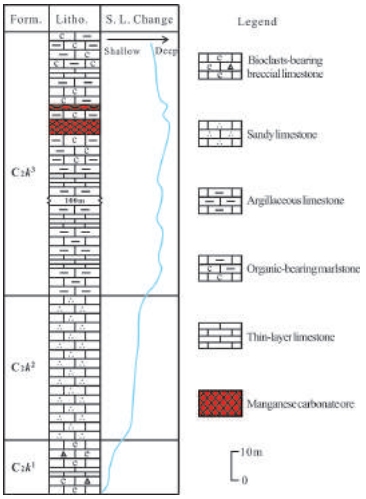

Figure 2. Stratigraphic column of the Kalaatehe Formation.

The presence of dark gray to black well-developed horizontal bedding, organic carbon-rich, and pyritiferous calcareous mudstone indicates that it was deposited in a relatively stable, possibly with minimal hydrodynamic energy environment (Zhang et al. 2018).

Generally, two to three manganese-rich layers occurred in the mining area. The principal ore body, more than 5 km in length, occurs stably and continuously with no branch. However, the thickness varies greatly, ranging from less than 1m to more than 10 m, with an average manganese grade of more than 35% (Gao et al. 2016).

More than ten different minerals are present in the manganese-rich ore and associated host rocks, which can be divided into silicate, carbonate, oxide, sulfide, and graphite and/ or organic materials (Fig. 3). Organic materials, or sometime in the form of graphite, were mostly observed in the calcareous mudstone and the manganese-rich rocks. Besides, minor borates (mainly sussexite), in some cases, are also present in the manganese ore zone based on XRD analysis (Zhang et al. 2018).

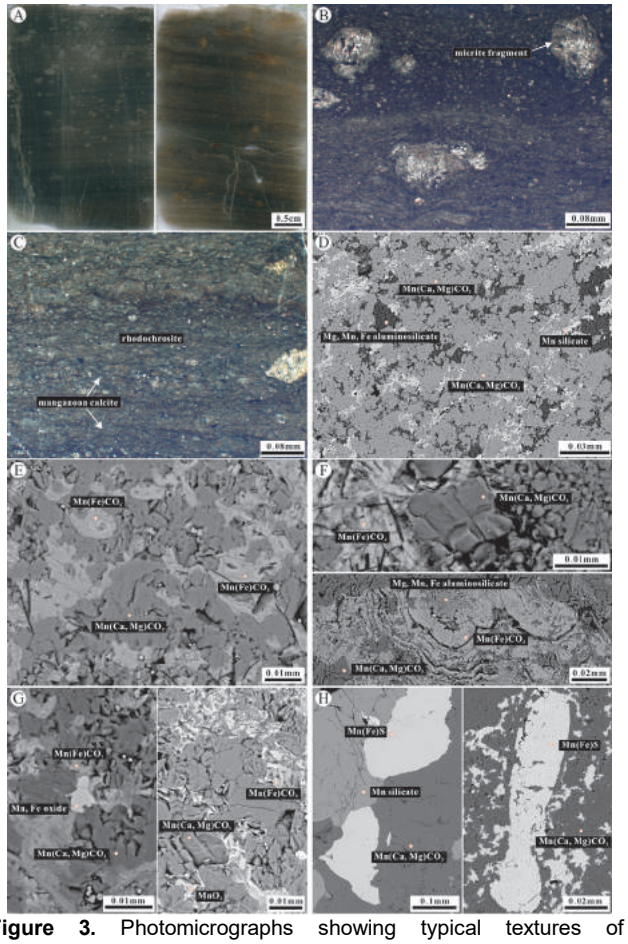

Figure 3. Photomicrographs showing typical textures of manganese carbonate ore. (a) Thin sections of massive manganese carbonate ore, displaying laminated structure. (b) Isolated fragments of micrite showing characteristic of “dropstones” within finer-grained sedimentary rocks (plane-polarized light). (c) Crenulated to wavy laminations in manganese carbonate ore, noting minor manganoan calcite veins also occurred (plane-polarized light). (d) Manganese carbonate (rhodochrosite) is the predominant mineral in the manganese ore, while Mn-rich silicate (friedelite) and Mn-rich aluminosilicate (chlorite) are also common (backscattered electron image). (e) At least two generations of

rhodochrosite occur in the manganese ore with the early one containing minor calcium and magnesium, while the later one incorporating iron (backscattered electron image). (f) Rhombohedral (top) and stromatolitic (bottom) rhodochrosite generally occurred in some cases (backscattered electron image). (g) Minor Mn-Fe oxides (left) are deduced to be the primary precipitates that enter the sediments, while most fibrous manganese oxides (right) are thought to be the results of manganese carbonate surface weathering (backscattered electron image). (h) Alabandite coexisting with rhodochrosite (left) or "floating" on the manganese carbonate (right) is the only sulfide in the manganese ore (backscattered electron image).

3 Geochemistry of the Mn metallogenic belt

The 1st and the 2nd members non-mineralized wall rocks display modern seawater-like REEs+Y profiles that are characterized by negative Ce anomalies and HREEs enrichment relative to LREEs in AUCC-normalized diagrams, suggesting an oxic surface water condition. While slight Ce/Ce^* (close to 1) in the non-mineralized rock samples from the 3rd Member argues for a relative reducing conditions (Zhang et al., 2018).

Despite the variability in the absolute concentration of these redox sensitive elements, however, their enrichment factors show little change through the whole studied profile (Fig.4), which means that there is no obvious enrichment on these elements. For example, the U and the enrichment factor of U (UEF) are constant in all non-ore rocks from the 1st to 3rd Member of the Kalaatehe Formation (0.54-4.01 ppm and 0.26-5.18, respectively). Same regularities were also occurred on the V and VEF (48-243 ppm and 1.19-4.15, respectively), Cr and CrEF (31-484 ppm and 0.82-9.48, respectively) in wall rock samples of all three Members. The low values of enrichment factors of the redox sensitive elements that are observed in the non-mineralized rocks indicate that the enrichment mechanism for these elements mentioned above were not achieved under the depositional conditions of the Kalaatehe Formation, which further argues for a suboxic (unlikely anoxic and cannot be euxinic) conditions during the sedimentation. Intriguingly, it seems that the Mo and the enrichment factor of Mo (MoEF) values increase upward through the studied profile (except for several higher values in the 2nd Member, 0.08-4.30 ppm and 0.08-3.97, respectively) with peak values in the calcareous shale of the 3rd Member (4.42-23.22 ppm and 6.58-21.09, respectively) (Fig. 4), suggesting that the depositional conditions of the first two members and the 3rd Member are somewhat different. Nevertheless, a good relationship between the contents of Mo and the TOC (R^2=0.62) suggests that this Mo enrichment is mainly resulting from the absorption of organic materials.

Additionally, large fractionation of sulfur isotope ($\delta^{34}S$ values from -16.18 to -1.40‰, with an average of -8.36‰) indicates a relative high sulfate concentration in the water column, and the rate of sulfate replenishment exceeded that of sulfate reduction. The ^{13}C-depleted stable carbon isotopes (varying from -6.69 to -22.80‰, with a mean of -24.98‰) in manganese carbonate ores further confirmed that Mn-carbonates are precipitated from the reduction of Mn(IV) oxides precursor by organic matter in the sediments during the diagenesis rather than directly precipitate in the anoxic water column (Zhang et al. 2018).

Based on trace elements, Mo concentration and total organic carbon (TOC) content (ranges from 0.08 to 1.83 wt % with an average of 0.65 wt %), suggests in somewhat a relative open rather than a strictly restricted basin system.

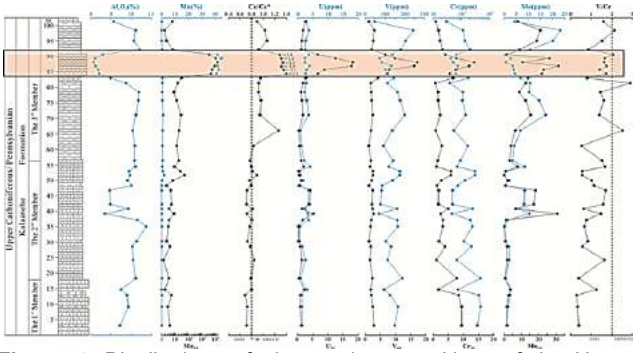

Figure 4. Distributions of elemental compositions of the Upper Carboniferous Kalaatehe Formation. The vertical plots indicate Al_2O_3 which is used for normalization, the cerium anomaly, elemental concentrations of manganese (Mn), uranium (U), vanadium (V), chromium (Cr) and molybdenum (Mo), and their enrichment factors (MnEF, UEF, VEF, CrEF and MoEF, respectively) in each sedimentary horizon. The enrichment factors indicate the enrichment of each element relative to average upper continental crust (Mclennan, 2001). The dotted vertical lines show redox conditions for Ce/Ce* (oxic<0.8 and anoxic>0.8; after Takahashi et al., 2014), for Mo (suboxic<25ppm, anoxic 25–100ppm, and euxinic>100ppm; after Tribovillard et al. 2012), and for V/Cr (oxic<2.0, suboxic 2.04.25, and anoxic>4.25; after Lewan and Maynard 1982; Ross and Bustin 2009).

4 Discussion

4.1 Depositional environment

Petrographic and geochemical studies on the manganese ore reveals that the first precipitates to concentrate manganese in the sediments were Mn(IV)-dominated oxides, and the Mn(II)-bearing carbonates in the Malkansu area have undergone Mn(IV) oxide precursor reduction processes. The consistently large positive Ce anomalies, negative Y anomalies, low Y/Ho ratios, and no obvious fractionation between LREEs and HREEs of the manganese carbonate ores, are features typical of modern marine hydrogenic ferro-manganese oxide precipitates. The ^{13}C-depleted stable carbon isotopes in manganese carbonate ores further confirmed that Mn-carbonates are precipitated from the reduction of precursor Mn(IV) oxides by organic matter in the sediments during diagenesis rather than form as a chemical sediment directly in an anoxic water column.

4.2 Mineralization model of Mn carbonates

Thus, according to the proposed redox-stratified water column (with oxic surface water and suboxic bottom water) for the Malkansu basin, a pool of abundant dissolved manganese (Mn^{2+}) can be envisaged for the

deep suboxic water. During the transgression, upwelling allowed the dissolved manganese to be precipitated in the form of manganese (hydroxide) oxides at or near the oxic-suboxic chemocline where it intersects with the basin substrate. Moreover, this process may also lead to a relative high surface water primary productivity, which ascribes to the nutrients contained in the deep water column been carried to the surface water mass resulting in the thriving of organisms. Manganese (hydroxide) oxide precipitates together with the net productivity (excess organic matter) were rapidly buried due to the continuous transgression. In the sediments, dissimilatory reduction of manganese (hydroxide) oxides in combination with the oxidation of organic matter, resulting in extremely high dissolved manganese (Mn^{2+}) concentration and creating relative high alkalinity condition in pore-waters, which is suitable for the precipitation of manganese carbonates (Fig. 5). The ultimate source of the manganese is uncertain but may have been fluvial-sediment loads of hydrothermal activity associated with the extensional back-arc basin system.

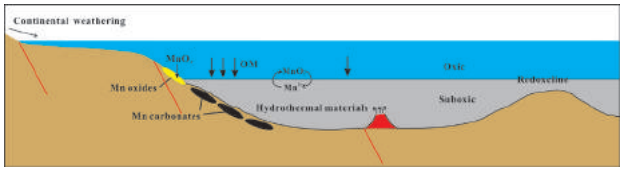

Figure 5. Mineralization model of Malkansu manganese carbonate metallogenic belt.

5 Summary

(1) Based on petrographic and lithologic studies, it is suggested that the Upper Carboniferous Kalaratehe Formation represents sedimentary sequences of an extensional back-arc basin associating with the evolution of the Paleo-Tethys Ocean.
(2) These rock assemblages, from the sedimentary breccia and calcarenite at the bottom to the calcareous mudstone (including manganese ore zone) at the top, and then the calcarenite and micrite at the uppermost, consist a complete transgression-regression cycle, while the manganese precipitation occurred during the highstand systems tract.
(3) Low values of enrichment factors for the redox-sensitive trace elements (U, V, Cr and Mo) in the non-mineralized wall rocks indicate a suboxic rather than an anoxic.
(4) Based on trace elements, S-C isotopes and TOC content, it is suggested that ore-forming condition of the Carboniferous Maerkansu large scale manganese metallogenic belt is a relative open rather than a strictly restricted basin system.

Acknowledgements

This study was financially supported by the National Natural Science Foundation of China (No. U1703242).

References

Armstrong FA (2008) Why did nature choose manganese to make oxygen? Philos. Trans. R. Soc. B: Biol. Sci. 363:1263–1270.
Calvert SE and Pedersen TF (1996) Sedimentary geochemistry of manganese; implications for the environment of formation of manganiferous black shales. Econ. Geol. 91:36–47.
Fan DL and Yang PJ (1999) Introduction to and classification of manganese deposits of China. Ore Geol. Rev. 15: 1–13.
Frakes LA and Bolton BR (1984) Origin of manganese giants: Sea-level change and Anoxic-oxic history. Geology, 12(2):83–86.
Fu Y, Xu Z, Pei Hg, Jiang R (2014) Study on metallogenic regularity of manganese ore deposits in China. Acta Geol. Sin. 88(12):2192–2207 (in Chinese with English abstract).
Gao YB, Teng JX, Chen DH, Sui QL (2016) Geology, Geochemistry and genesis of the Ortokarnash manganese ore deposit. Mineral Deposits, 35(S1):5–6 (in Chinese with English abstract).
Johnson JE, Webb SM, Ma C, and Fischer WW (2016) Manganese mineralogy and diagenesis in the sedimentary rock record. Geochim. Cosmochim. Acta, 173:210–231.
Johnson JE, Webb SM, Thomas K, Ono SH, Kirschvink JL, and Fischer WW (2013) Manganese-oxidizing photosynthesis before the rise of cyanobacteria. Proc. Natl. Acad. Sci. 110:11238–11243.
Lee JH, Kennedy DW, Dohnalkova A, Moore DA, Nachimuthu P, and Reed SB (2011) Manganese sulfide formation via concomitant microbial manganese oxide and thiosulfate reduction. Environ. Microbial. 13:3275–3288.
Maynard JB (2010) The chemistry of manganese ores through time: a signal of increasing diversity of earth-surface environments. Econ. Geol. 105:535–552.
Okita PM (1992) Manganese carbonate mineralization in the Molango District, Mexico. Econ. Geol. 87:1345–1366.
Roy S (2006) Sedimentary manganese metallogenesis in response to the evolution of the Earth system. Earth-Sci. Rev. 77:273–305.
Thamdrup B, Rosselló-Mora R and Amann R (2000) Microbial Manganese and Sulfate Reduction in Black Sea Shelf Sediments. Appl. Environ. Microbial. 66:2888–2897.
Tsikos H, Beukes NJ, Moore JM, and Harris C (2003) Deposition, diagenesis, and secondary enrichment of metals in the Paleoproterozoic hotazel iron formation, Kalahari manganese field, South Africa. Econ. Geol. 98:1449–1462.
Yun J, Gao XF, Xiao PX, Kang L, and Li P (2015) Geochemical characteristics of the Lower Carboniferous volcanic rocks of the Wuluate Formation in the Western Kunlun Mountains and their geological significance. Geol. China, 42(2):587–600 (in Chinese with English abstract).
Zhang CL, Li XH, Li ZX, Lu SN, Ye HM, and Li HM (2007) Neoproterozoic ultramafic-mafic-carbonatite complex and granitoids in Quruqtagh of northeastern Tarim Block, western China: Geochronology, geochemistry and tectonic implications. Precambrian Res. 152:149–169.
Zhang FF, Yan B, Guo YL, Zhu XK, Zhou Q, and Yang DZ (2013) Precipitation form of manganese ore deposits in Gucheng, Hubei Province, and its paleoenvironmental implication. Acta Geol. Sin. 87(2):245–258 (in Chinese with English abstract).
Zhang LC, Dong LH, Zhu MT, Zheng MT, Li ZQ, Hao YH, and Shi YJ (2016) Deposit types, origin and metallogenetic regularity of Taxkorgan iron ore belt in west Kunlun. J. Earth Sci. Environ. 38(4):427–443 (in Chinese with English abstract).
Zhang BL, Zhang LC, Feng J, Xu SQ, Feng CR, Hao YH, Zheng MT, Peng ZD, and Dong ZG (2018) Genesis of the large-scale Ortokarnash manganese Carbonate Deposit in the Malkansu district, western Kunlun: evidence from geological features, Geol. Rev. 64(2):361–377 (in Chinese with English abstract).

Textural evolution of the Lovisa Zn-Pb-(Ag) deposit, Bergslagen, Sweden: insights from microscopy and 3D X-ray tomography

Fredrik Sahlström, Erik Jonsson, Karin Högdahl, Joanna Ghaderidosst
Department of Earth Sciences, Uppsala University, Uppsala, Sweden

Stefan Luth, Edward Lynch
Geological Survey of Sweden, Uppsala, Sweden

Eric Landström
Orexplore AB, Kista, Sweden

Stefan Sädbom
Lovisagruvan AB, Stråssa, Sweden

Abstract. The presently mined Lovisa deposit constitutes a c. 1.9 Ga, stratiform Zn-Pb-(Ag) sulphide mineralisation hosted by rhyolite-dominated meta-volcanic rocks in the Bergslagen ore province, south central Sweden. The mineralised rock sequence at Lovisa has been subjected to polyphase ductile deformation, amphibolite facies regional metamorphism, and late-stage brittle deformation. The combined effects of these processes have produced a diversity of post-genetic ore textures within the sulphide horizons, including metablastic growth, piercements, ductile and brittle sulphide deformation, and durchbewegung and 'ball ore' textures. Here we report on the character and textural evolution of the Lovisa deposit in conjunction with regional metamorphism and deformation, utilising new data from ore- and electron microscopy combined with 3D tomography by means of novel XRT-XRF drill core scanning technique.

1 Introduction

Over the past half-century, there has been an increasing understanding that sulphide ores hosted in orogenic belts exhibit post-genetic textures attributable to mechanical and chemical processes during later metamorphism and deformation (e.g. Ramdohr 1955; Vokes 1969; Marshall and Gilligan 1993; Cook et al. 1993). Such textures have been described from several deposits in the Palaeoproterozoic Bergslagen ore province in south central Sweden (Andersson et al. 2016, and references therein; Fig. 1). A notable example is the case of rotated, rounded silicate clasts occurring within matrices of extensively deformed sulphides; the so-called 'ball ores' (Geijer 1971; Vokes 1973). One of the sulphide deposits in Bergslagen observed to have been significantly affected by metamorphism and deformation is the Lovisa Zn-Pb-(Ag) deposit (Fig. 1). The currently exploited mineralisation at Lovisa comprises stratiform sulphides that occur interbedded with fine-grained, originally rhyolitic rocks, all of which have been overprinted by polyphase ductile deformation, amphibolite facies regional metamorphism, and later stages of brittle deformation. Here we report results from the on-going, EU-funded X-Mine project, on the textural evolution of the Lovisa deposit. This specifically includes the use of 3D tomography by means of novel XRT-XRF drill core scanning technology to provide new insights in such studies, yet also providing input for further method development.

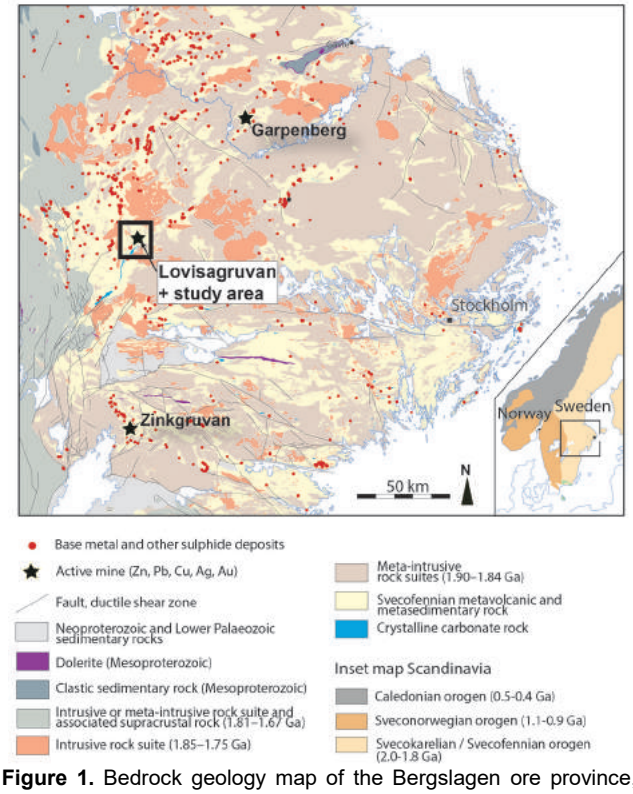

Figure 1. Bedrock geology map of the Bergslagen ore province, showing the location of Lovisagruvan (the Lovisa mine) and other active mines and known mineral occurrences (modified from Stephens et al. 2009). Inset shows location of map in Sweden.

2 Bergslagen and the Lovisa deposit

The extensively mined Bergslagen ore province is situated within the Swedish part of the Fennoscandian Shield and contains a highly diverse array of ore types, of which base metal and iron oxide mineralisation predominate (Fig. 1; e.g. Tegengren 1924; Geijer and Magnusson 1944; Stephens et al. 2009). The main ore-bearing rock sequence in Bergslagen comprises mainly dacitic to rhyolitic, pyroclastic-dominated metavolcanic rocks with local marble interlayers that were originally deposited within an evolving, continental back-arc basin (Allen et al. 1996). This c. 1.90-1.87 Ga metasupra-crustal succession occurs as inliers in intrusive rocks that are penecontemporaneous or younger than the metavolcanic rocks. During the Svecokarelian orogeny, these rocks and their mineralisation were subjected to polyphase ductile deformation and amphibolite-facies regional metamorphism featuring peak conditions between c. 1.87 and 1.80 Ga (e.g. Stephens et al. 2009).

The Lovisa Zn-Pb-(Ag) deposit is located in the northern part of the Guldsmedshyttan syncline in western Bergslagen (Fig. 1). The exploited Zn-Pb mineralisation, as well as a stratigraphically lower, Pb-Ag sulphide-bearing iron formation (Lovisa Iron Formation), are mainly hosted by rhyolitic metavolcaniclastic rocks (Lundström 1983; Carlon and Bleeker 1988). These stratiform sulphide ores have been interpreted to originally have formed syn-genetically in a vent-distal, seafloor exhalative setting in which the Zn-Pb mineralisation was confined to a c. 5-10 m thick stratigraphic interval and concentrated in two distinct ore horizons. The stratigraphically lower 'Sphalerite Ore' (Jansson et al. 2018) comprises fine (generally c. 10-50 mm thick) layers of sphalerite-dominated sulphides that occur interbedded with rhyolitic ash-siltstone and minor chloritic schist. In contrast, the stratigraphically upper 'Main Ore' of Jansson et al. (2018) consists of a tabular body of massive sphalerite-galena, locally up to c. 1 m thick, with minor sulphides also being present in a laminated facies that occurs peripheral to the massive ore.

3 Textural evolution of the Lovisa sulphide mineralisation

The different textures resulting from the metamorphism and deformation of sulphide mineralisation at the Lovisa deposit were investigated using a combination of drill core study, reflected polarised light- and electron microscopy, as well as energy-dispersive X-ray spectrometry (EDS) and wavelength-dispersive X-ray spectrometry (WDS) with a Zeiss Supra 36VP SEM and a JEOL JXA-8530F electron microprobe (Department of Earth Sciences, Uppsala University), respectively, and 3D X-ray drill core scanning in a GeoCore X10 device (Orexplore AB, Kista, Sweden). The GeoCore X10 uses a novel technique; X-ray tomography (XRT) and X-ray fluorescence (XRF) combined measurement together with automatic weight measurement to scan drill cores up to a diameter of 50.6 mm. It produces a 3D tomographical visualisation of the distribution of contrasting minerals in the core with a resolution of down to 200 μm, along with density data as well as concentration data for most major and trace elements (Orexplore, 2019). We here primarily focus on ore textures developed within the two Zn-Pb-rich sulphide horizons (Sphalerite Ore and Main Ore, respectively) and within the Lovisa Iron Formation.

3.1 Primary ore textures

The oldest generation of sulphides at Lovisa is best preserved within the Sphalerite Ore in what is presumed to be relict, essentially syn-genetic sedimentary layering (Figs. 2A-B, 2E-F). The sulphide-enriched layers are dominated by fine-grained, anhedral sphalerite with minor intergrown pyrite and galena. This sphalerite generally carries minute inclusions of chalcopyrite ('chalcopyrite disease'). Such finely-layered sphalerite mineralisation, which is generally difficult to distinguish from the surrounding silicate-rich rock during drill core inspection, can be visualised in great detail using the XRT-XRF scanning data (Figs. 2B, 2F).

3.2 Ore textures related to metablastic growth

Porphyroblastic pyrite is widespread throughout the stratigraphic sequence and has overgrown the primary sulphide assemblages (Fig. 3A). The crystals comprise an early generation of generally anhedral pyrite that contains abundant inclusions of sulphides (sphalerite and galena, locally chalcopyrite and pyrrhotite) and silicates, resulting in a poikilitic texture. Many pyrite porphyroblasts also exhibit a later generation of subhedral to euhedral, inclusion-poor pyrite that form rims around the earlier poikilitic pyrite (Fig. 3A).

Magnetite in the Lovisa Iron Formation generally occurs in aggregates of anhedral crystals. These typically exhibit a poikilitic texture with inclusions of sulphides, suggesting early magnetite blastesis.

3.3 Ore textures related to ductile deformation

Ductile deformation textures visible in the Sphalerite Ore include folding of the primary layering. Metarhyolite interbeds are commonly boudinaged and define Z-symmetric folds (Fig. 2A; Jansson et al. 2018), and related fabrics within the sulphide beds are evident in the XRT-XRF images (Fig. 2B). Locally, sulphide-rich piercement veins protrude from fold hinges (Fig. 2A). The XRT-XRF scanning data show that galena was preferentially remobilised into such veins, while sphalerite has largely remained in the pre-existing layers (Fig. 2B).

The more massive character of sulphides in the Main Ore compared to that in the Sphalerite Ore, and the higher galena:sphalerite ratio, led to partitioning of strain and development of more extreme forms of ductile deformation features (Jansson et al. 2018), such as the distinctive 'ball ore' texture of the Main Ore.

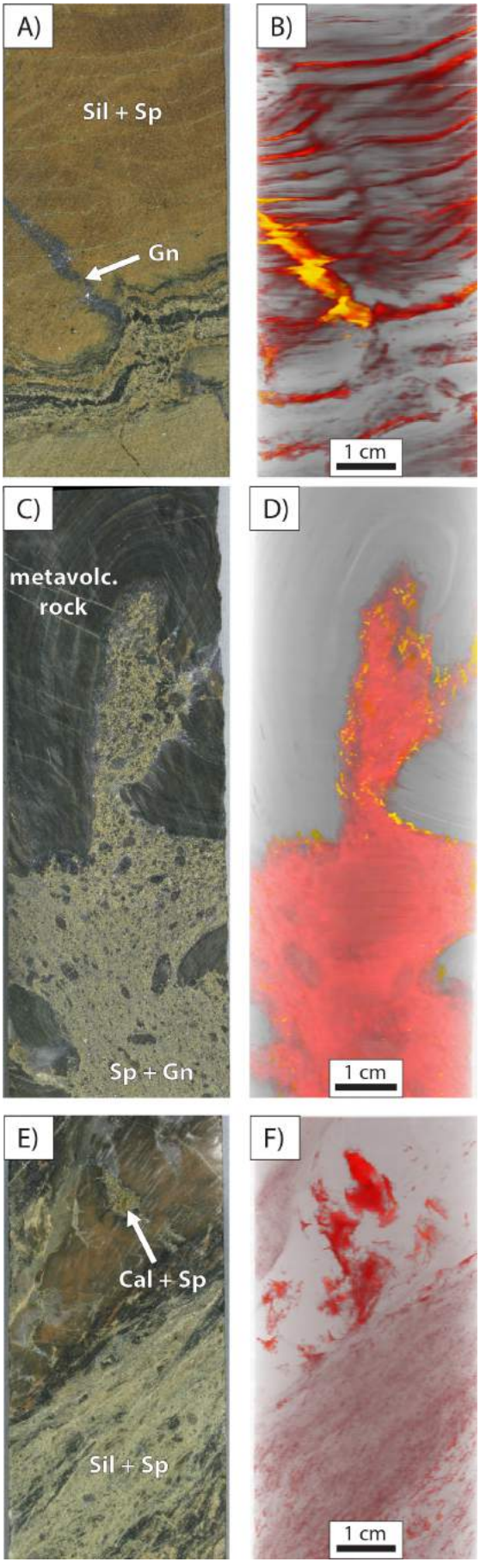

Figure 2. Photographs (left) and XRT-XRF scans (right; composite view from surface to bottom) of cut drill core sections from the Lovisa deposit. Red color indicates Zn enrichment (sphalerite), yellow Pb enrichment (galena). **(A-B)** Folded silicate-sulphide layers with sulphide piercement vein (Sphalerite Ore) **(C-D)** 'Ball ore' texture (Main Ore). **(E-F)** Finely layered sphalerite remobilised into late calcite veins (Sphalerite Ore). Cal – calcite; Ga – galena; Sil – silicate; Sp – sphalerite.

In the ball ore, fragments of silicate-rich rock as well as milky vein quartz and pyrite blasts or clasts occur in a matrix of fine-grained, deformed sulphides dominated by sphalerite and galena. The silicate-rich fragments vary from decimeter-scale, 'detached cores' of folded host rock, to significantly smaller and increasingly rounded clasts (Figs. 2C, 3B). These features reflect the progressive breakup, rotation and 'kneading' of the fragments within the sulphide matrix during deformation (e.g. Vokes 1969, 1973). Rotational fabrics are defined by fine-grained silicates occurring in the sulphide matrix around silicate clasts (Fig. 3B), and locally as curved inclusion trails within porphyroblastic silicates and pyrite. In the sulphide matrix of the 'ball ore', galena mainly occurs in zones of reduced strain, such as within the hinges of detached folds (as revealed by the XRT-XRF image in Figure 2D) or in strain shadows to silicate clasts and pyrite porphyroblasts (Figs. 3A-B), as well as in later veinlets and fractures.

Networks of sulphide veins and fracture fills crosscut the laminated facies peripheral to the Main Ore. The veins are generally dominated by galena over sphalerite and pyrite, and they locally exhibit a minute 'ball ore' texture similar to that observed in the Main Ore. The origin and timing of these veins remains ambiguous. Jansson et al. (2018) argued that they may have formed as piercement veins during shearing of the Main Ore, or by later sulphide remobilisation at the transition to more brittle conditions.

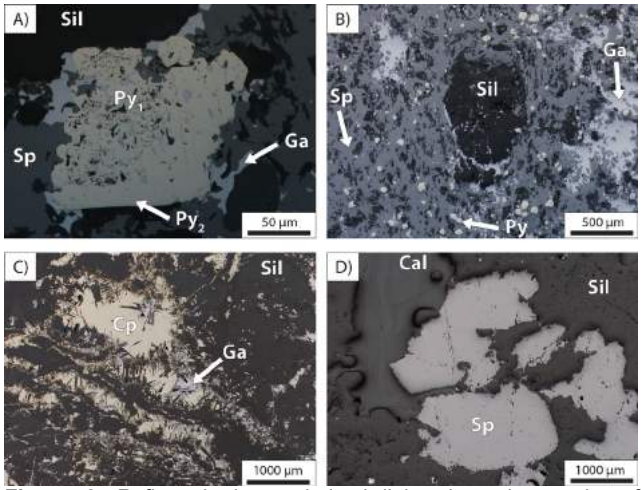

Figure 3. Reflected plane-polarised light photomicrographs of selected ore textures from the Lovisa deposit. **(A)** Pyrite porphyroblast (Main Ore). **(B)** 'Ball ore' texture (Main Ore). **(C)** Galena-chalcopyrite veins intergrown with metamorphic micas (Lovisa Iron Formation). **(D)** Fracture fill made up of extensively twinned calcite and remobilised sphalerite (Sphalerite Ore). Cal – calcite; Cp – chalcopyrite; Ga – galena; Py – pyrite; Sil – silicate; Sp – sphalerite.

3.4 Ore textures related to brittle deformation

Later cataclastic features are superimposed on the early metablastic aggregates at Lovisa. In the case of pyrite porphyroblasts, brittle cataclastic deformation was accompanied by remobilisation of the more ductile galena and sphalerite into microfractures and corroded margins (Fig. 3A), as well as by remobilisation of sulphide inclusions within the pyrite.

Massive sphalerite locally displays some cataclastic fracturing with infilling of galena. This is consistent with galena entering the brittle field after sphalerite during cooling. Late-stage fractures infilled with calcite and local sphalerite are prevalent at the Lovisa deposit (Figs. 2E, 3D). The calcite in such veins exhibits extensive, deformation-related twinning. The XRT-XRF scanning data indicate a close spatial relationship between the late-stage, fracture-filling sphalerite and early, layered sphalerite (Fig. 2F), suggesting that remobilisation of sphalerite also occurred during brittle deformation.

In the Lovisa Iron Formation, abundant galena-dominated veins crosscut the silicate groundmass as well as brittle-deformed magnetite aggregates. The sulphide assemblage locally also contains chalcopyrite, sphalerite, pyrrhotite and rare tetrahedrite, with the chalcopyrite typically having replaced galena. These galena-rich veins exhibit complex intergrowths with metamorphic micas (Fig. 3C), suggesting co-crystallisation during the retrograde stages of regional metamorphism (e.g. Cook et al. 1993). The galena-rich veins are in turn crosscut by later fractures hosting a more complex sulphide-sulphosalt assemblage carrying minerals that are otherwise sparsely occurring or previously unknown in the Lovisa deposit, including chalcopyrite, galena, freibergite, tetrahedrite, pyrite, arsenopyrite, pyrargyrite, and several unidentified Ag-rich phases. These late-stage sulphide-sulphosalt fracture fillings in the Lovisa Iron Formation are in part comparable to remobilised, Pb-Ag-Sb-rich assemblages documented from other metamorphosed sulphide deposits in Bergslagen (e.g. Wagner et al. 2005) and in similar terranes elsewhere (Vokes 1969).

4 Conclusions

The Lovisa Zn-Pb-(Ag) sulphide mineralisation has recorded a diversity of post-genetic ore textures that can be attributed to polyphase ductile deformation, amphibolite facies regional metamorphism, and late-stage brittle deformation, all affecting the original ore deposit and its host rocks. Key examples include multi-stage metablastic growth of pyrite; folding of interlayered sulphide and silicate beds and remobilisation of sulphides into piercement veins; rotation and kneading of silicate-rich fragments in a matrix of extensively deformed, in part durchbewegung-textured sphalerite and galena ('ball ores'); intergrowths of sulphide veins and metamorphic micas; and brittle fracturing with local remobilisation of sulphides. Variations in primary depositional character between the sulphide-bearing horizons, and differences in the proportions of individual, variably competent sulphide minerals (mainly galena to sphalerite ratios) significantly influenced the ore textures that developed during subsequent metamorphism and deformation.

The use of XRT-XRF drill core scanning technology has proven to be a powerful tool in the on-going study of the Lovisa deposit. It allows for detailed 3D tomographic visualisation and chemical characterisation of a wide range of meso- to micro-scale textures related to metamorphism and deformation in both ores and host rocks, as well as – particularly when combined with traditional methods such as ore- and electron microscopy – new insights into the behaviour of specific sulphide minerals during such processes.

Acknowledgements

The X-Mine project is funded by the European Union's Horizon 2020 research and innovation programme under grant agreement No 73027.

References

Allen RL, Lundström I, Ripa M, Simeonov A, Christofferson H (1996) Facies analysis of a 1.9 Ga, continental margin, back-arc, felsic caldera province with diverse Zn-Pb-Ag-(Cu-Au) sulfide and Fe oxide deposits, Bergslagen region, Sweden. Econ Geol 91:979-1008.

Andersson SS, Jonsson E, Högdahl K (2016) Metamorphism and deformation of a Palaeoproterozoic polymetallic sulphide-oxide mineralisation: Hornkullen, Bergslagen, Sweden. GFF 138:410-423.

Carlon CJ, Bleeker W (1988) The geology and structural setting of the Håkansboda Cu-Co-As-Sb-Bi-Au deposit and associated Pb-Zn-Cu-Ag-Sb mineralisation, Bergslagen, central Sweden. Geol Mijnbouw 67:272-292.

Cook NJ, Halls C, Boyle AP (1993) Deformation and metamorphism of massive sulphides at Sulitjelma, Norway. Mineral Mag 57:67-81.

Geijer P (1971) Sulfidic "ball ores" and the pebble dikes. Sver Geol Und C 662, 29 pp.

Geijer P, Magnusson NH (1944) De mellansvenska järnmalmernas geologi. Sver Geol Und Ca 35, 654 pp.

Jansson NF, Sädbom S, Allen RL, Billström K, Spry PG (2018) The Lovisa stratiform Zn-Pb deposit, Bergslagen, Sweden: structure, stratigraphy, and ore genesis. Econ Geol 113:699-739.

Lundström I (1983) Beskrivning till Berggrundskartan. Lindesberg SV. Sver Geol Und Af 126, 140 pp.

Marshall B, Gilligan LB (1993) Remobilization, syn-tectonic processes and massive sulfide deposits. Ore Geol Rev 8:38-64.

Orexplore (2019) GeoCore X10. https://orexplore.com/geocore-x10/. Accessed 30 April 2019.

Ramdohr P (1955) Die Erzmineralien und ihre Verwachsungen. Akademie-Verlag, Berlin, 875 pp.

Stephens MB, Ripa M, Lundström I, Persson L, Bergman T, Ahl M, Wahlgren CH, Persson PO, Wickström L (2009) Synthesis of the bedrock geology in the Bergslagen region, Fennoscandian Shield, south-central Sweden. Sver Geol Und Ba 58, 259 pp.

Tegengren FR (1924) Sveriges ädlare malmer och bergverk. Sver Geol Und Ca 17, 406 pp.

Vokes FM (1969) A review of the metamorphism of sulphide deposits. Earth Sci Rev 5:99-143.

Vokes FM (1973) "Ball texture" in sulphide ores. GFF 95:403-406.

Wagner T, Jonsson E, Boyce AJ (2005) Metamorphic ore remobilization in the Hällefors district, Bergslagen, Sweden: constraints from mineralogical and small-scale sulphur isotope studies. Miner Deposita 40:100-114.

LA-ICP-MS trace element study of sphalerites from the MVT Cracow-Silesia district, Poland

Krzysztof Foltyn[1], Viktor Bertrandsson Erlandsson[2], Frank Melcher[2], Peter Onuk[2], Adam Piestrzyński[1]
[1]AGH University of Science and Technology in Krakow
[2]Montanuniversität Leoben

Abstract. The Cracow-Silesia Zn-Pb district in Poland hosts classic examples of carbonate-hosted MVT deposits. Limited information about the distribution of trace elements in sphalerite has been available for this locality. Results of this LA-ICP-MS study show that trace element concentrations are quite typical for carbonate-hosted MVT deposits. Indium and gallium content is often below the detection limit while the median content of germanium in the dataset is 67 µg/g but varies significantly between samples. In schalenblende samples, a clear difference in Ge and Ga contents between dark and light-colored sphalerite bands has been noticed. This study also demonstrated very high contents of thallium in some samples, up to 3063 µg/g which are some of the highest Tl contents reported for sphalerite. The trace element measurements were used to apply the GGIMFis geothermometer and results are significantly higher than temperatures obtained for fluid inclusion studies of sphalerites from this district.

1 Introduction

Sphalerite in Zn-Pb deposits often contain trace elements at levels that are potentially economic or could pose an environmental threat. Progress in laser ablation inductively-coupled mass spectrometry (LA-ICP-MS) has led to a growing number of studies undertaken to assess differences in the trace element content of sphalerite from different types of Zn-Pb deposits (e.g. Cook et al. 2009; Ye et al. 2011; Mederski et al. 2017). Of special importance is the recent development of the matrix-matched sphalerite reference material MUL-ZnS 1 (Onuk et al. 2017) which improves accuracy and precision of the analyses.

The trace element contents of ore minerals in the Cracow-Silesia Mississippi Valley-type (MVT) district show large variations between different paragenetic stages and vary from mine to mine or even within parts of the same deposit. Compared to other MVT deposits worldwide, the Cracow-Silesian ores contain sphalerites with one of the largest ranges in Ag, Fe and Cd content and early studies identified substantial variations in trace element concentrations in banded sphalerite (Viets et al. 1996, Kucha et al. 2001). To our best knowledge, after early semi-quantitative attempts in the 1990s (Leach and Viets 1992, Mayer and Sass-Gustkiewicz 1998) only limited LA-ICP-MS data for this locality, measured for a single sample, has been available (Ridley et al. 2015). Therefore, the aim of this investigation is to provide trace element data in the main textural types of sphalerites from this classic MVT district. An additional goal is to apply and test the GGIMFis geothermomether proposed by Frenzel et al. (2016), on compositionally zoned banded sphalerites.

2 Geological setting and samples

The Cracow-Silesia ore deposits, located in southern Poland (Fig. 1) are commonly considered a classic example of MVT deposits. Zn-Pb mineralization occurs in the Mesozoic sedimentary cover of the Paleozoic basement of the Central European Platform and is mainly hosted by the epigenetic ore-bearing dolomite of the Muschelkalk Group (Middle Triassic) (Leach et al. 2003). The average content of metals in sulfide ores usually ranges from 2 to 4% Zn and 1 to 2% Pb. The initial total ore resources are estimated to be ca. 700 Mt of Zn+Pb ores at 4 to 6% and are considered one of the richest known MVT Zn-Pb deposits in the world (Leach et al. 2003). After 800 years of continuous mining, current demonstrated resources of zinc and lead ores in Poland are 84.4 Mt of sulfide ores containing 3.63 Mt of Zn and 1.43 Mt of Pb.

The mineralogy is simple: sphalerite, galena, marcasite and pyrite with rarely occurring Fe-Pb and Fe-Pb-As sulphosalts (Mayer and Sass-Gustkiewicz 1998). Gangue minerals include dolomite, barite, calcite and ankerite. Five clusters of mainly stratabound or nest-like karst breccia ore-bodies are present in the region: Olkusz, Chrzanów, Bytom, Zawiercie and Tarnowskie Góry (Fig. 1) with exploitation currently carried out only in the Pomorzany mine. Undeveloped ore deposits are located in the areas of Klucze, Laski and Zawiercie.

Sphalerite samples from the Pomorzany mine, Trzebionka mine and Orzel Bialy mine, representing different textural types, were analysed (Fig. 2). Samples from Pomorzany and Trzebionka are characterized by sulfides replacing host carbonates and commonly mimicking the original host rock fabric. Additionally, they contain colloform and banded ores, consisting of an alternation of colored bands or spherolitic aggregates of colloform sphalerite. Orzel Biały samples are composed of banded sphalerite. Sporadically, sphalerite, galena, and iron sulfides are found in a variety of speleothems (stalactites and stalagmites). Commonly, these features are composed of iron sulfides but in some cases, the dripstone-like forms also contain sphalerite and occasionally galena (sample Röt from the Pomorzany mine).

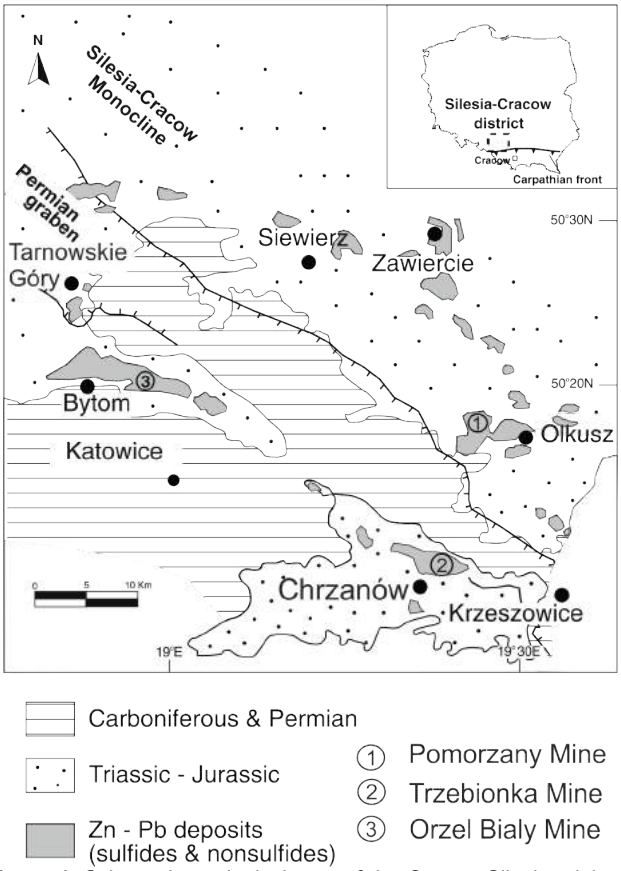

Figure 1. Schematic geological map of the Cracow-Silesia mining district (after Coppola et al. 2009).

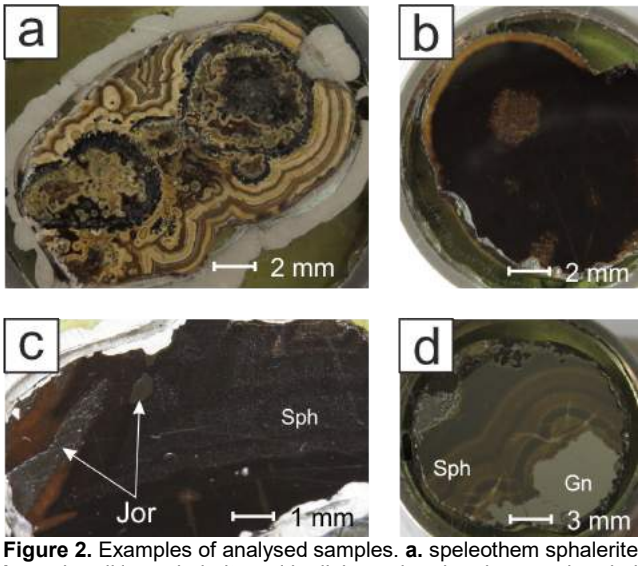

Figure 2. Examples of analysed samples. **a.** speleothem sphalerite **b.** spherolitic sphalerite with light colored edge **c.** banded sphalerite with jordanite (Jor) **d.** typical collomorphic sphalerite.

3 Methodology

Trace element analyses were carried out at the Department of Applied Geosciences and Geophysics, Montanuniversität Leoben, Austria, using an ESI NWR213 Nd:YAG laser ablation system coupled to an Agilent 8800® triple quadrupole ICP-MS. Helium was used as carrier gas with a flow rate of 0.75 L/min. Fluency was set between 2-3 J/cm^2. For sphalerite analyses, the matrix-matched sintered pressed powder pellet reference material MUL-ZnS 1 (Onuk et al. 2017) was used for quantification of the element content and the USGS powder pressed polysulfide reference material MASS-1 (Wilson et al. 2002) was used for quality control of the analyses. Data reduction was done using the Iolite V3.1 software (Paton et al. 2011). The following isotopes have been analyzed: ^{51}V, ^{52}Cr, ^{55}Mn, ^{57}Fe, ^{59}Co, ^{60}Ni, ^{63}Cu, ^{71}Ga, ^{74}Ge, ^{75}As, ^{82}Se, ^{95}Mo, ^{107}Ag, ^{111}Cd, ^{115}In, ^{118}Sn, ^{121}Sb, ^{201}Hg, ^{205}Tl, ^{208}Pb, ^{209}Bi.

4 Results

4.1 Trace elements

Table 1 presents results of LA-ICP-MS analyses for selected elements. The Fe content can be as low as 90 µg/g and as high as 5.6%. Cadmium is usually present at levels of several hundred to several thousand µg/g but some exceptional spots gave values up to 1.2%. Arsenic content varies between a few µg/g and 1.9% while the Pb concentration is between tens of µg/g up to 2.2%. Very high contents of Tl were measured, especially in samples from the Orzel Bialy mine. Some spots yielded as much as 3063 µg/g Tl, ranking among the highest reported in the literature so far. It is important to stress that all elements mentioned earlier seem to be present in the sphalerite structure and do not form micro inclusions of other minerals (Fig. 3). Strong correlations (R^2 = 0,8-0,9) between As and Tl as well as As and Pb were found. Xiong (2007) proposed the substitution of Tl in a low-temperature environment (up to 150°C) in terms of $Tl^{+0.5}As^{3+}{}_{0.5}S$ solid solution; this might explain the observed Tl-As correlation.

Indium, as expected from MVT deposits is very low, usually below detection limit. Gallium content is often below the detection limit and in general does not exceed 12.3 µg/g. The median content of germanium in the whole dataset is 67 µg/g but varies significantly between samples. Measurements of sphalerite from the Trzebionka and the Pomorzany mine has given tens of µg/g of Ge, while in the case of the Orzel Bialy - hundreds of µg/g, up to 384 µg/g. These values are typical for MVT deposits (Frenzel et al. 2016). Belissont et al. (2016) described the coupled substitution $3Zn^{2+} \leftrightarrow Ge^{4+}$ + 2 monovalent cations as the main mechanism of Ge incorporation. This explains correlations observed in some samples between Ge-Mn and Ge-Fe. In some cases, germanium shows also a strong correlation (R^2 > 0,8) with As, Tl, Pb, but this phenomenon is not universal for the whole dataset.

Table 1. The results of LA-ICP-MS measurements in µg/g.

	Mn	Fe	Ga	Ge	As	Ag	Cd	In	Hg	Tl	Pb
Orzel Bialy											
MEDIAN (38)	29	6 172	0.6	66	4 209	0.2	1 672	-	1	552	8 654
MIN	13	2 212	<0.1	14	710	<0.1	415	<0.1	0.6	62	3 348
MAX	65	56 619	1.1	382	19 294	329	12 739	<0.1	1.9	3063	22 747
Trzebionka											
MEDIAN (12)	9.1	4 987	-	14	879	-	763	-	1	77	1 740
MIN	5.4	2 558	<0.1	7.1	457	<0.1	332	<0.1	0.8	39	917
MAX	282	12 321	12	24	2 006	41	2 234	<0.1	2.3	136	3 452
Pomorzany											
MEDIAN(13)	6.9	1 107	0.2	92	261	0.8	1 637	-	2	19	1 110
MIN	<0.1	91	<0.1	1.2	<0.1	<0.1	349	<0.1	1	0.2	20
MAX	141	39 491	2.5	384	5 405	64	6 600	0.1	5.7	485	7 447

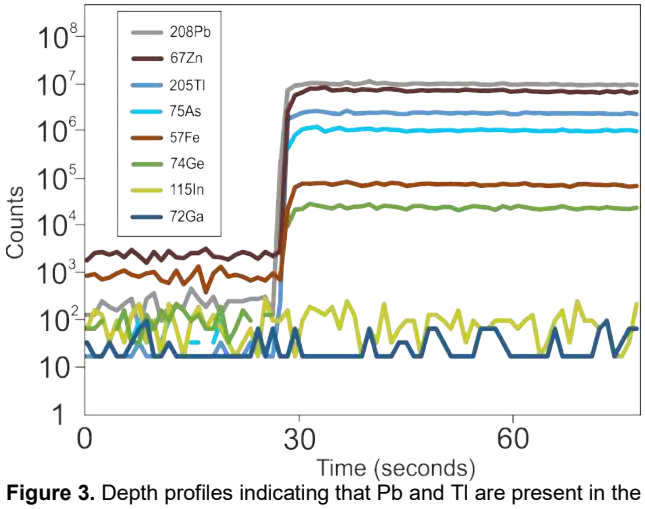

Figure 3. Depth profiles indicating that Pb and Tl are present in the sphalerite and not as a minute inclusions.

In schalenblende samples, a clear difference in Ge and Ga contents between dark and light-colored sphalerite bands have been noticed (Fig. 4). With the exception of the speleothem sample, all light bands have low (max. 12.3 µg/g) but measurable Ga contents, while Ge concentrations remain below 100 µg/g. On the other hand, the dark bands tend to have higher Ge content and usually undetectable Ga concentrations.

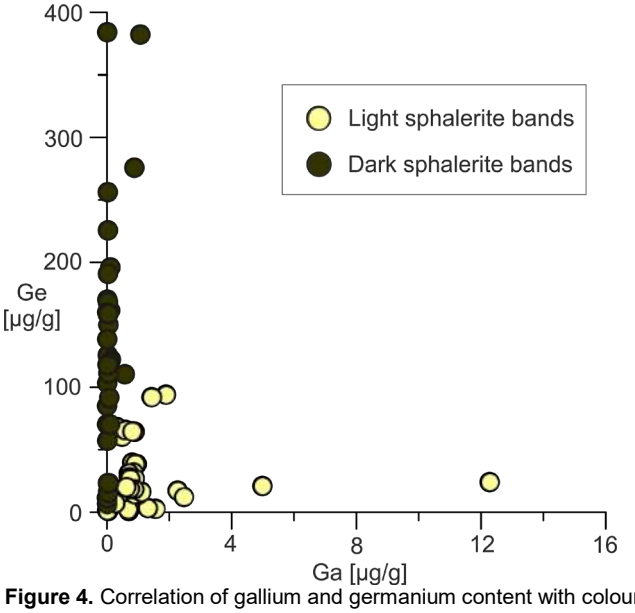

Figure 4. Correlation of gallium and germanium content with colour of the banded sphalerite.

4.2 GGIMFis geothermometer

The trace element measurements were used in an attempt to test the GGIMFis geothermometer proposed by Frenzel et al. (2016). Obtained results (Tab. 2) are significantly higher than temperatures collected by fluid inclusion studies of sphalerites from this district (80 to 158°C, Kozłowski 1995) but they are within a 50–70 °C range in which mean (homogenization) temperature can be predicted by GGIMFis geothermometer (Frenzel et al. 2016). However, it is important to stress that homogenization temperatures should be considered minimum fluid temperatures and previous authors noted the extreme difficulty in investigating fluid inclusions due to their small size and strong internal reflections of the host mineral. Despite these difficulties, it would be

advisable to perform new fluid inclusions studies coupled with trace element determination by LA-ICP-MS in sphalerites, in order to calibrate the GGIMFis and homogenization temperatures in this ore district.

A characteristic feature is a significant change in GGIMFis temperature during the transition from the light to dark bands and vice versa (Tab. 2). It is not surprising given that the band color is mainly connected to the incorporation of different elements and it is believed that often, but not always, darker color is caused by Fe (e.g. Barton and Bethke 1987) which is utilized in the GGIMFis. Minor elements, the presence of organic matter and nano-inclusions of other minerals may also influence sphalerite color. Contents of two other elements of the geothermometer, Ge and Ga, also seems to be "color dependent" (Fig. 4). Although temperature plays an important role in the trace element behavior, it is not the only factor and variations in pH and sulfur activity likely will also have a contribution.

Table 2. Calculated GGIMFis temperatures.

Sample name	GGIMFis temperature range
Orzel Bialy 2 (n=16)	179-217°C
Trzebionka dark band (n=9)	195-240°C
Trzebionka light band (n=3)	100-142°C
Pomorzany (n=12)	113-182°C
Röt (n=28)	34-246°C
Orzel Bialy 1 light bands (n=18)	146-170°C
Orzel Bialy 1 dark bands (n=6)	191-218°C

5 Conclusions

Trace element contents in sphalerites from the Cracow-Silesia district measured by LA-ICP-MS are quite typical for carbonate-hosted MVT deposits. The most interesting result of this study is the extremely high content of thallium in samples from the Orzel Bialy mine. Enrichment in Tl in this ore district has long been known and is illustrated by the presence of rare Pb-As sulphosalts such as gratonite and jordanite that have been found to be enriched in Tl (Paulo et al. 2002). Mayer and Sass-Gustkiewicz (1998) reported that marcasite from the Pomorzany mine may contain up to 1000 µg/g Tl and in Olkusz up to 2300 µg/g. The available literature for Tl content in sphalerites from this district usually lists values up to 100 µg/g but several papers reported higher values (e.g. sphalerites from the Klucze deposit up to 500 µg/g, Górecka 1996).

This study demonstrates values up to 3063 µg/g which are among the highest Tl contents in sphalerite reported in the literature. These results indicate a need for a closer investigation of the effects of sphalerite on thallium environmental hazards in the Cracow-Silesia mining district.

References

Barton PB, Bethke PM (1987) Chalcopyrite disease in sphalerite: pathology and epidemiology. Am Mineral 72:451-467.

Belissont R, Munoz M, Boiron MC, Luais B, Mathon O (2016) Distribution and oxidation state of Ge, Cu and Fe in sphalerite by µ-XRF and K-edge µ-XANES: insights into Ge incorporation, partitioning and isotopic fractionation. Geochim Cosmochim Acta 177:298-314.

Cook NJ, Ciobanu CL, Pring A, Skinner W, Shimizu M, Danyushevsky L, Saini-Eidukat B, Melcher F (2009) Trace and minor elements in sphalerite: A LA-ICPMS study. Geochim Cosmochim Acta 73:4761-4791.

Coppola V, Boni M, Gilg HA, Strzelska-Smakowska B (2009) Nonsulfide zinc deposits in the Silesia–Cracow district, Southern Poland. Miner Dep 44:559-580.

Frenzel M, Hirsch T, Gutzmer J (2016) Gallium, germanium, indium, and other trace and minor elements in sphalerite as a function of deposit type—A meta-analysis. Ore Geol Rev 76:52-78.

Górecka E (1996) Mineral sequence development in the Zn-Pb deposits of the Silesian-Cracow area, Poland. Prace Instytutu Geologicznego 154:25—35.

Kozłowski A (1995) Origin of Zn-Pb ores in the Olkusz and Chrzanów districts: a model based on fluid inclusions. Acta Geol Pol 45:83-142.

Kucha H, Piestrzynski A, Viaene W. (2001). Post-deposition transformation in banded sphalerite, MVT-type deposits, Upper Silesia, Poland. In: Piestrzyński A (ed.). Mineral Deposits at the Beginning of the 21st Century: Proceedings of the Joint 6th Biennial SGA-SEG Meeting - Krakow, 2001, 145-148.

Leach DL, Bechstaedt T, Boni M, Zeeh S (2003) Triassic-hosted MVT Zn-Pb ores of Poland, Austria, Slovenia and Italy. Europe's major base metal deposits: Dublin, Irish Association for Econ Geol, pp. 169-213.

Leach DL, Viets JG (1992) Comparison of the Cracow-Silesian Mississippi Valley-type district, southern Poland, with Mississippi Valley-type districts in North America. USGS Open-File Report No. 92-704

Mayer W, Sass-Gustkiewicz M (1998) Geochemical characteristic of sulfide minerals from Pomorzany and Olkusz lead-zinc deposits based on lasser ablation data, Upper Silesian district, Poland. Mineral Pol 29:87–105.

Mederski S, Kołodziejczyk J, Pršek J (2017) Trace elements in sphalerite from the Stan Terg Pb-Zn deposit, Kosovo. In: Mercier-Langevin P (ed.). Mineral Resources to Discover: 14th SGA biennial meeting proceedings: Québec City - Canada, 2017. Proceedings Volume 4:1563–1566.

Onuk P, Melcher F, Mertz-Kraus R, Gäbler HE, Goldmann S (2017) Development of a matrix-matched sphalerite reference material (MUL-ZnS-1) for calibration of in situ trace element measurements by laser ablation-inductively coupled plasma-mass spectrometry. Geostand Geoanal Res 41:263-272.

Paulo A, Lis J, Pasieczna A (2002) Tal pod koniec XX wieku. Przegl Geol 50:403

Paton C; Hellstrom J; Paul B; Woodhead J; Hergt J. (2011): Iolite. Freeware for the visualisation and processing of mass spectrometric data. J. Anal. At. Spectrom. 26:2508.

Ridley WI, Pribil MJ, Koenig AE, Slack JF (2015) Measurement of in Situ Sulfur Isotopes by Laser Ablation Multi-Collector ICPMS: Opening Pandora's Box. Procedia Earth and Planetary Science 13: 116-119.

Wilson SA, Ridley WI, Koenig AE, (2002): Development of sulfide calibration standards for the laser ablation inductively-coupled plasma mass spectrometry technique. J. Anal. At. Spectrom. 17:406–409.

Magmatic hydrothermal overprinting in the super large Dajiangping S(Pb-Zn) SEDEX deposit, Guangdong Province

Haijie Zhao, Wei Zheng
NLR Key Laboratory of Metallogeny and Mineral Assessment, Institute of Mineral Resources, CAGS, Beijing

Zhangfa Yu
Beijing Research Institute of Uranium Geology

Abstract. The Dajiangping deposit is the largest SEDEX pyrite deposit in South China Block. The pyritic sulphides occur in the Sinian metamorphic rocks as laminated sulphides and massive lenses. Recently, new veins and layered lead-zinc orebodies underlying the pyritic orebodies have been discovered. Sphalerite in Pb-Zn orebodies provided an Rb-Sr icochron age of 88.5±3.9Ma, indicating that it is not contemporaneous with pyrite sulphide bodies. The petrographic and microthermometric analysis of fluid inclusions from the two types of mineralization implies that they have different fluid homogenization temperatures and salinities. Sulfur isotope evidence indicates that the Pb-Zn orebody was formed by magmatic hydrothermal mineralization in the Cretaceous, and the pyrite orebody was probably overprinted by Cretaceous magmatic-hydrothermal activity.

1 Introduction

The Dajiangping deposit in the southwestern Cathaysia Block, is the largest SEDEX-type pyrite deposit in China and contains >200 million tons of pyritic sulphides (Yang et al. 1997). The deposit consists of stratiform orebodies and ubiquitous laminated ores, and recently, Pb-Zn orebodies (prospective reserves Pb+Zn 1.54Mt) were discovered underlying the pyrite orebody (Luo et al. 2004). Although some studies on the genesis and sources of pyrite orebodies from Dajiangping deposit are available (Chen et al. 1998; Zhang et al. 1992; Li et al. 2006; Qiu et al. 2018), the genesis of Pb-Zn orebody and its relationship with the pyrite are still not clear. Sedex deposit is an important source of lead-zinc resources in the world. It accounts for about 50% of the total reserves lead-zinc deposits (Sangster, 2002).whereas, the number of this type pyrite deposits in the world is relatively small, only were reported in the Chinese literature, such as Dongshengmiao from Inner Mongolia.

SEDEX deposits generally have stratabound characteristics, with some developing a "double-layer" structure, in which the upper part consists of layered sulphides, and the lower part is veinlet and vent complex ore-bearing alteration body (Goodfellow et al. 1993; Leach et al. 2005). Regionally, the Dajiangping deposit is located in the core part of Daganshan ore field, which shows clear metal zoning possibly related to hydrothermal (magmatic source) mineralization. However, the role of magmatism is not clear during the formation of the Dajiangping deposit (Song et al. 2011). In this study, we contrast the characteristics of fluids from the lead-zinc orebody with pyrite orebody, Rb-Sr age of Pb-Zn orebody, the sufur isotope composition, in order to discuss the genesis of Pb-Zn orebody and its relationship with pyrite orebody.

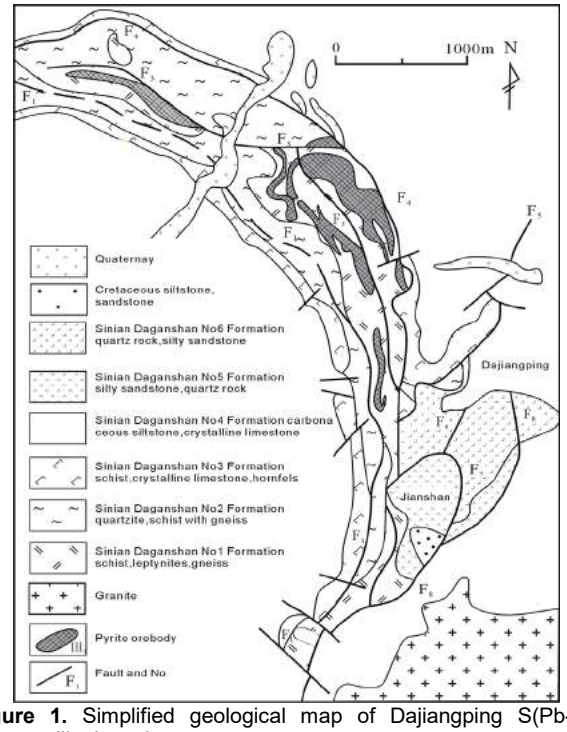

Figure 1. Simplified geological map of Dajiangping S(Pb-Zn) polymetallic deposit

2 Geologic setting

The Dajiangping deposit is located in the northeast margin of the Luoding fault-bounded basins, southwest of Qin-Hang (Qinzhou Bay to Hangzhou) belt, which is a suture zone between the Yangtze and Cathaysia Blocks (Mao et al. 2010, 2011; Yuan et al. 2011, 2015, 2018).

The oldest strata exposed in the Luoding basin is the Proterozoic Shapingwan Formation (Ptsh). The Sinian Daganshan Formation (Zd) including quartz-mica schist,

siliceous rock, crystalline limestone and tuff is the main pyrite-bearing strata. Younger Ordovician and Silurian strata consist of sedimentary flysch deposits. The Devonian and Carboniferous rocks are mainly sedimentary clastics and carbonate rocks. They are key skarn Cu-Pb-Zn orebody bearing strata in this area (Cai et al. 2002). The Triassic conglomerate, sandstone, siltstone and shale are present. The Cretaceous is mainly made of sandstone. The NE-trending structures including Guizihu arc fault and the Wuchuan-Sihui deep fault are developed which was caused by many periods of tectonic movements, and control the develop of rocks and deposits in this area (Yang et al. 2012). The magmatic activity is strongest in Caledonian and Yanshanian, mainly incluiding granite and monzonitic granite (Fu et al. 2010), example is the Dajinshan granite, which has the SHRIMP Zircon U-Pb isotopic age of 84.17±0.34 Ma (Yu et al. 2013).

Luoding basin is a NE-trending Mesozoic fault-bounded basin. A set of Ag-Zn-Pb-Au-Sn deposits are distributed surrounding it, including Xinrong-Lianzhou Au-Ag-Mn ore field in the southern margin (Huang et al. 2002) and Daganshan W-Sn-Ag-Zn-Pb-S ore field in the northern margin. The Daganshan polymetallic ore field is controlled by Daganshan arc or ring structures including folds and faults surrounding the granite zone. It comprises Dajinshan large W-Sn deposit, Dajiangping large S(Pb-Zn), Gaocheng large Ag-Pb-Zn and Jiuquling medium Sn deposit (Qin 2018), Chadong medium Ag-polymetallic deposit and so on. The ore field is not only of a wide variety of mineralized elements, but also has a very clear mineralization element zonation associated with magmatic activities, showing the elements of W/Sn/Bi →Sn→Sn/Pb/Zn/Ag→Ag/Pb/Zn → Au from the granite rock inside to outside.

3 Ore deposit geology

The Dajiangping deposit is mainly exposed in the Sinian Daqishan Formation metamorphic suite. The lithologies consist mainly of metamorphic carbonaceous siltstone, crystalline limestone, quartzite, siltstone and black shales, which are host rocks of pyrite and lead-zinc orebodies. Folds and faults are well developed, especially the NW trending F4 fault, which controls the distribution of pyrite ore bodies (Fig. 1). The magmatic rocks in the mining area are not developed, and only small Yanshanian medium-fine-grained granite was found to the south of the mining area.

The Dajiangping pyrite deposit is composed of five pyrite orebodies, divided into the west and east parts by the F3 fault. The No. Ⅲ stratiform orebody (Fig. 2a) in the west and the No. Ⅳ lens orebody in the east were relatively larger. Stratiform orebodies that are distributed within a 6 × 4 km-wide zone with a thickness of up to 170m, hosted by carbonaceous strata and black shales. The No. Ⅳ lens orebody can reach to 1.59 km in thickness and is 2.15 km in length. The pyrite orebody has conformable boundaries with the host wall rocks. Mineral assemblages consist of pyrite, pyrrhotite, and a small amount of sphalerite, galena and chalcopyrite. Gangue minerals are mainly quartz, calcite, sericite and graphite.

Six newly discovered Pb-Zn orebodies all occur within the Daganshan Formation metamorphic rocks, with the larger No. 2 orebody controlled by a regional arc shape structure. Underlying the stratiform orebodies (Figure 2b), are calcareous siltstone and black shale. The length of Pb-Zn orebody＞1.6km, with average thickness of 4.83 m. The average grade of mineralized elements is Pb: 0.106ppm, Zn: 0.107ppm, Sn: 0.025ppm, Ag: 21.78ppb, Au: 0.40ppb (Luo et al. 2004). Occurrences of part orebodies are consistent with the stratum. The wall rock alterations of V2 orebody composed of silicification, pyritization, sericitization, chloritization and fluorination.

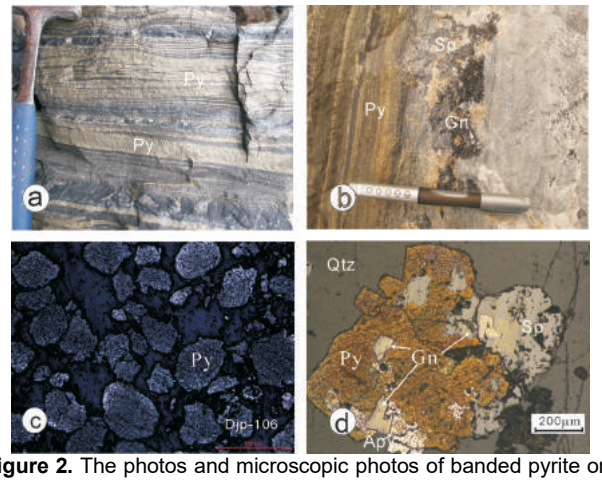

Figure 2. The photos and microscopic photos of banded pyrite ore and vein Pb-Zn ore from Dajiangping S(Pb-Zn) polymetallic deposit. **a.** banded pyrite ore from No Ⅲ stratiform orebody, **b.** vein Pb-Zn ore and it contact relationship with the pyrite, **c.** Round pyrite gains in banded ore, **d.** pyrite overgrowth of with sphalerite and galena

4 Discussion

SEDEX deposits generally develop typical “double layer” structures, upper part is a massive sulfide orebody, and the lower part is vein, disseminated or veinlets, cylindrical sulfide orebody or altered ore-bearing body, which represented submarine hydrothermal replacement (Large et al. 1983; Goodfellow et al. 1993; Leach et al. 2005). Compositionally, the metal elements of the upper layered orebodies and the vein mineralization of the lower sections show the identical evolution regularity from bottom to up (Large et al.1999; Goodfellow et al. 2007). The two parts formed nearly simultaneously in theory. We compared the stratiform pyrite orebody with the vein Pb-Zn orebody in the following aspects.

Lead-zinc ore and pyrite bodies in the Dajiangping deposit have different mineral assemblages and alteration types. Mineral assemblages of the former are relatively diverse, including galena, sphalerite, pyrrhotite, calcite, fluorite, quartz, chlorite, accompanied by sericitization, chloritization, silicification, carbonation and a small amount of epidote. Whereas, the later included only pyrite, pyrrhotite, quartz and calcite, corresponding to silicification and carbonation. The pyrite overgrowths with sphalerite and galena (Fig. 2d),

is bright or light yellow, often medium-coarse grained idiomorphic cubes, with occasional pentagonal dodecahedron crystal forms, and the size of grains ranging between 0.25 mm and 5 mm. Pyrite is white yellow, poor crystallized, irregular or rounded (Fig. 2c) in banded ores, with mostly size of 0.05~0.5 mm. These suggest that the metallogenic environment of lead-zinc ore is different from that of banded ore. The petrographic and micro-thermometric analysis of fluid inclusions from the two types of ores indicate that mineralization-related fluids are both liquid-rich two-phase H_2O-NaCl. The salinities of the fluids ($w(NaCl)_{eqv}$) from vein Pb-Zn ores varies between 1.23% and 12.85%, with an average value of 7.81%, and peak values ranging from 6% to 9%, slightly higher than that of fluid from banded ore, which $w(NaCl)_{eqv}$ are between 3.71% to 9.08%, average and peak values are 5.90% and 4%~7%, respectively. There are various ranges of inclusion homogenization temperatures in vein Pb-Zn ore, varying from 118℃ to 410℃, average is 343℃, but showing two peak intervals of 220~300℃ and 380~400℃ The lower interval is comparative to that in the banded ore, which concentrate on 200~300℃, with an average of 255℃. This indicates that the two ores form in different fluid systems and there is a high-temperature fluid involved in the Pb-Zn mineralization process. Daughter-bearing mineral and melt inclusions were discovered in vein Pb-Zn ore support this.

The sulfur isotope compositions show that the layered orebody has the $\delta^{34}S$ value of (-10.9‰~-25.6‰), which represents bacteria sulfate reduction. The $\delta^{34}S$ value of the lead-zinc orebody is -7.1‰~6.4‰, showing the influx of a deep source of sulfur.

Previous studies have reported a whole-rock Rb-Sr isochron age of 630 Ma for the Dajiangping deposit (Wang et al. 1997). But Qiu et al. (2018) thought the ore-hosting strata were deposited during the mid-late Devonian according to U-Pb ages of detrital zircons from sandstone interlayers within the stratiform orebodies. Sphalerite in Pb-Zn orebodies has a Rb-Sr isochron age of 88.5±3.9Ma (Zhao et al. 2016), implying it formed in various periods of pyrite body formation. The age of Pb-Zn ore vein coincides with the mineralized event in the same Daganshan polymetallic ore field, including Dajinshan W-Sn deposit of Re-Os isochron ages of 80.07±1.19 Ma and Gaocheng Ag-Zn-Pb deposit of Rb-Sr age of 89.7±6.4 Ma.

5 Conclusions

1. The laminated pyrite ore has different inclusion homogenization temperatures and salinities than the vein Pb-Zn ore. These later formed in high-temperature and salinity fluids, indicating that the two ores form in different fluid systems and evolution processes.
2. The age of the lead-zinc orebody has been determined by the Rb-Sr isochron method for sphalerite, yielding a Rb-Sr isochron age of 88.5±3.9 Ma.
3. The sulfur isotope compositions show that the layered orebody has the $\delta^{34}S$ value of (-10.9‰ to -25.6‰), which represents of bacteria sulfate reduction. The $\delta^{34}S$ value of the lead-zinc orebody is -7.1‰ to 6.4‰, showing the characteristics of a magmatic source of sulfur.
4. The newly discovered lead-zinc orebody was formed by magmatic hydrothermal mineralization in Cretaceous, and the SEDEX pyritic sulphides were probably overprinted by the magmatic-hydrothermal activity.

Acknowledgements

This study was financially supported by the National Natural Science Foundation of China (NSFC) (41203036,41773041).

References

Cai MH, Zhan MG, Peng SB, Meng XJ, Liu GQ (2002) Study of Mesozoic metallogenic geological setting and dynamic mechanism in Yunkai area. Miner Deposits 21:254-269 (in Chinese with English abstract).

Chen DF, Cheng GQ, Pan JM, Ma SG, Dong WQ, Gao JY, Chen X P (1998) Characteristics of the hydrothermal sedimentation of the Dajiangping surperlarge pyrite deposit in Yunfu, Guangdong. Geochimica 27: 12-19(in Chinese with English abstract).

Fu LG, Hai T (2010) The study on metallogenic geological environment and prospecting in the surrounding of the Luoding basin, western Guangdong. Gold Science Technology 28:25-28(in Chinese with English abstract).

Goodfellow WD, Lydon JW, Turner RJW (1993) Geology and genesis of stratiform sediment-hosted (SEDEX) zinc-lead-silver sulphide deposits. Geological association of Canada Special Paper 40:01-251.

Goodfellow WD, Lydon JW (2007) Sedimentary-exhalative (SEDEX) deposits: Geological Association of Canada, Miner Deposits division, Special Publication 5:163-183.

Large D, Walcher E (1999) The Rammelsberg massive sulphide Cu-Zn-Pb-Ba-Deposit, Germany: An example of sediment-hosted, massive sulphide mineralization. Miner Deposita 34: 522-538.

Leach DL, Sangster DL, Kelley KD, Large RR, Garven G, Allen CR, Gutzmer J,Walter S (2005) Sediment-hosted lead-zinc deposits: A global perspective. Econ Geol 100th Anniversary volume, 561-607.

Li K, Hu K, Jiang SY, Song SM (2005) Geochemical characteristics of He-Ar and Pb isotopes in the Dajiangping pyrite deposit, western Guangdong, South China. Mineral Deposit Research: Meeting the Global Challenge 7: 773-776

Luo DL (2004) Geological characteristics and origin of Pb-Zn-Ag deposits in Daganshan area of Guangdong Province. Geology and Mineral Resources of South China 2:10-14(in Chinese with English abstract).

Mao JW, Zhang JD, Guo CL (2010) Porphyry Cu, epithermal Ag–Pb–Zn, distal hydrothermal Au deposits: a new model of mineral deposit—taking the Dexing area as an example. J Earth Sci. Environ 32: 1–13 (in Chinese with English abstract).

Mao JW, Zhang JD, Pirajno F, Ishiyama D, Su HM, Guo CL, Chen, YC (2011) Porphyry Cu–Au–Mo–epithermal Ag–Pb–Zn–distal hydrothermal Au deposits in the Dexing area, Jiangxi Province, East China—a linked ore system. Ore Geol Rev 43: 203–216.

Qin J (2018) The ore materials source of Silver deposits from Daganshan and surrounding area in western Guangdong

province, Yunfu Country. West-China Exploration Engineering 2,127-133(in Chinese).
Qiu WHJ, Zhou MF, Liu R (2018) Late Paleozoic SEDEX deposits in South China formed in a carbonate platform at the northern margin of Gondwan. J Asian Earth Sci156:41-58.
Sangster DF (2002) The role of dense brines in the formation of vent-distal sedimentary exhalative (SEDEX) lead-zinc deposits: Field and laboratory evidence. Miner Deposita 37:149-157.
Song SM, Hu K, Wen HJ, Zhang YX, Li K, Fan HF (2011) Molybdenum isotopic composition as a tracer for low medium temperature hydrothermal ore forming systems: A case study on the Dajiangping pyrite deposit, western Guangdong Province, China. Chinese Science Bulletin56:2221-2228(in Chinese with English abstract).
Wang H N, Li H Y, Wang Y X (1997) Rb-Sr isotope dating of silicalite from the Dajiangping massive sulfide ore deposit, Guangdong Province. Chinese Science Bulletin 42: 1983-1985(in Chinese with English abstract).
Yang RY, Cao JJ, Kang XG, Yin ZQ (1997) The geological characteristics and genesis of Yunfu pyrite deposit in Guangdong. Journal of Sun Yatsen University 36:79-84(in Chinese with English abstract).
Yu ZF (2013) Geological characteristics of granites and related mineralization in the Dajinshan tungsten-tin polymetallic deposit, western Guangdong province. Beijing University of Science and Technology. 45 (in Chinese with English abstract).
Yuan SD, Mao JW, Cook NJ, Wang XD, Liu XF, YuanYB (2015) A Late Cretaceous tin metallogenic event in Nanling W-Sn metallogenic province: constraints from U-Pb, Ar-Ar geochronology at the Jiepailing Sn-Be-F deposit, Hunan, China. Ore Geol Rev 65:283–293.
Yuan SD, Peng JT, Hao S, Li H M, Geng JZ, Zhang DL (2011) In situ LA–MC–ICP-MS and ID–TIMS U–Pb geochronology of cassiterite in the giant Furong tin deposit, Hunan Province, South China: new constraints on the timing of tin-polymetallic mineralization. Ore Geol Rev 43:235-242.
Yuan SD, Williams-Jones AE, Mao JW, Zhao PL,Chen Y,Zhang DL (2018) The origin of the Zhangjialong tungsten deposit, South China: Implications for W-Sn mineralization in large granite batholiths. Econ Geol 113: 1193-1208.
Zhang Q, Zhang BG, Pan JY, Chao YB (1992) Silicalite characteristics and rare-earth element model of Dajiangping pyrite deposit in western Guangdong province. Chinese Science Bulletin 37: 1588-1592(in Chinese with English abstract).
Zhao HJ, Yu ZF, Han XQ, Zheng W (2016) Magmatic hydrothermal superimposition in Dajiangping S(Pb-Zn) deposit, Guangdong Province: Rb-Sr isochron age and sulfur isotope evidence. Miner Deposit 35:795-808(in Chinese with English abstract)

Ag-Sb-Pb-Cd mineral paragenesis in the barite veins: Example from the Sowie Mountains, Poland.

Jaroslav Pršek, Sławomir Mederski, Dominik Kowalczyk
AGH University of Science and Technology, Kraków

Abstract. An unusual association of various silver minerals was identified in a barite vein from Bystrzyca Górna, Sowie Mountains, Poland. The ore mineralization is disseminated in a fine-grained dark barite-quartz matrix. The main ore minerals are galena and sphalerite. They are accompanied by various Ag-Sb-Pb-(Cd) minerals. Silver minerals are represented by pyrargyrite, miargyrite, stephanite, argentite, freibergite and Ag-bearing tetrahedrite with AgPbSb sulphosalts as frieslebenite, andorite and zoubekite as well as native antimony, greenockite, dyscrasite, plagionite, boulangerite, bournonite, and two unknown phases. Unknown phase X is chemically close to $(Cu_{3.9}Ag_{0.1})_{4.00}Fe_{2.5}Sb_2Pb_{7.5}S_{16}$ and phase Y is chemically close to $(Cd_{2.43}Ag_{4.46})_{6.89}Sb_{3.06}S_{9.25}$. It is the first occurrence of Ag-Sb-Pb-(Cd) mineralization documented in Poland.

1 Introduction

Silver minerals are the main host of silver in the base metal mineralization in various mineralizing environments, however in barite veins these are not common. In Poland, silver minerals were identified in the LGOM district (Kozub-Budzyń and Piestrzyński 2018), the most common ones include native silver, silver amalgamates, cupropearceite, mackinstryite. Additionally Ag-bearing bornite and chalcocite also occurs. Polymetallic mineralization in the Sudety Mountains, such as Radzimowice, Dziećmorowice, Kowary, Kletno, Miedzianka, contains Ag-Pb-Bi sulposalts and Ag minerals/selenides with native Ag (Siuda 2012; and many others). Silver mineralization in barite veins in Poland has been identified only in the Boguszów deposit (Pršek unpublished). Pyrargyrite, stephanite, polybasite and various members of the tetrahedrite-freibergite solid solution were found there as well. Their occurrence is strongly linked with galena and forms individual crystals up to 0.5 mm, blebs or inclusion. Nearby, in Zagórze Śląskie, argentopentlandite has been identified in barite veins (Piestrzyński and Kowalik 2014). Paragenesis of complex Ag-Pb-Sb sulphosalts with silver minerals (dyscrasite and native silver) as well as Ni-Co minerals is known from Příbram polymetallic veins in Czech Republic (Škácha et al. 2012).

2 Geological background

The Bystrzyca Górna deposit is located in the Sowie Mountains Block, the oldest Precambrian structural element of Middle-Sudetes. The Sowie Mountains Belt is a NW-SE elongated horst composed mostly of Archaic and Proterozoic high grade metamorphosed rocks, including gneisses, migmatites and amphibolites, with a predominance of Late-Proterozoic migmatitic gneiss of sedimentary origin. In the central part of the mountains, non-metamorphosed sediments of the Kulm Group, sit unconformably on the underlying complexes (Gunia 1985). Structurally controlled base-metal mineralization in this region is a result of complicated geological history involving magmatic processes and tectonic rearrangement. The ore mineralization is hydrothermal in origin and occurs in quartz-barite veins. The barite-base metal (±silver) veins were periodically mined over a few centuries, with the most intensive period of mining in the 16th century.

3 Methodology

Ore minerals with Ag mineralization were sampled in the old mine dumps close to Bystrzyca Górna, Sowie Góry Mountains. Silver minerals are disseminated in dark laminated barite. Ore minerals are small in size and macroscopically only galena is visible. Dark laminae, up to 1 cm thick are Ag-bearing but not all contain silver minerals. Silver minerals and sulphosalts were characterized in the Laboratory of Critical Elements at Faculty of Geology Geophysics and Environmental Protection, AGH-UST, Kraków Poland using a JEOL Super Probe 8230. 20 kV of accelerating voltage and beam current 20nA (for sulphosalts) or 10 nA (for silver minerals) were used for measurements with following standards natural: (pyrite, stibnite, chalcopyrite, galena, arsenopyrite, greenockite, cinnabar) or synthetic (native silver, Bi_2Se_3, Sb_2Se_3) and spectral lines: Ag(Lα), Pb(Mα), S(Kα), Sb(Lα), Cu(Kα), Fe(Kα), Bi(Mα), As(Lα) for sulphosalts, Ag (Lα), S(Kα), Sb(Lα), Cu(Kα), Bi(Mα), As(Lα), Se(Lα) for Ag minerals and Ag (Lα), S(Kα), Sb(Lα), Cd(Lα), Cu(Kα), Bi(Mα), Zn(Kα), Fe(Kα), Hg(Mα), As(Lα), Se(Lα) for tetrahedrite and Cd bearing phases.

4 Results

Various silver minerals and silver bearing sulphosalts were identified in the barite veins in Bystrzyca Górna. Ore minerals form individual crystals or intergrowths oriented in quartz veinlets cutting the barite. The main ore minerals are galena and sphalerite with a small amount of chalcopyrite, tetrahedrite, pyrite, bournonite and greenockite. Silver bearing mineralization forms early in the paragenesis, forming thin veinlets up to few hundred microns in size. The main silver minerals are

pyrargyrite and stephanite with minor miargyrite and they are all replaced by younger sulphosalts with native antimony. Various Pb-Sb, Ag-Pb-Sb, Cu(Fe)-Pb-Sb sulphosalts were identified (Fig. 1).

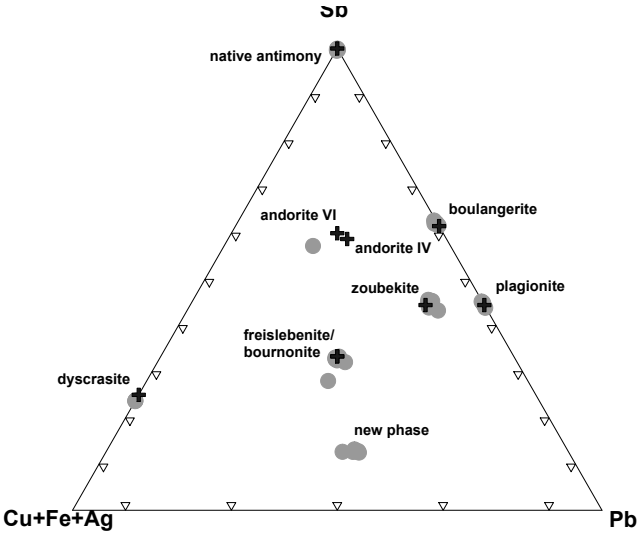

Figure 1. Compositional diagram Pb vs Sb vs Ag+Fe+Cu of sulphosalts and Sb rich phases from Bystrzyca Górna. Ideal phases were marked by cross.

4.1 Early stage – base metal mineralization

Minerals of the tetrahedrite group (TGM) occur as separate crystals in the barite matrix or they form inclusions in galena. They are usually not in connection with any silver minerals and seem to occur irrespective of the silver paragenesis. They are usually found in association with galena, sphalerite and bournonite. BSE imaging shows that crystals of the TGM are zoned (Fig. 2), cores have a lower content of silver while rims are enriched in silver with analyses falling in the field of freibergite (Fig. 3). Probably, the former Ag bearing tetrahedrite was corroded by silver rich fluids of younger paragenesis and freibergite domains were formed. Content of silver in TGM ranges from 8.11 wt.% up to 34.4 wt.% which indicate presence of Ag-bearing tetrahedrite and freibergite. Freibergite also occurs as separate idiomorphic crystals and is enriched in Fe - from 4.4 up to 5.8 wt.% with zinc up to 1.1 wt.% and As up to 0.17 wt.%. Ag-bearing tetrahedrite has more variable chemical composition. Content of Zn vary between 0.4 up to 6.8 wt.% with small content of As up to 0.36 wt.%. Content of Cd is similar for both members and it reaches maximum 0.33 wt.%.

Greenockite is very rare and forms only small crystals up to 50 microns, enclosed and replaced by galena. It exhibits a stoichiometric composition without any other trace impurities.

Bournonite is the only sulphosalt present in early assemblages of the paragenesis. It occurs with TGM and galena as well as sphalerite in the form of small crystals or inclusions in galena. It is stoichiometric without any other admixtures.

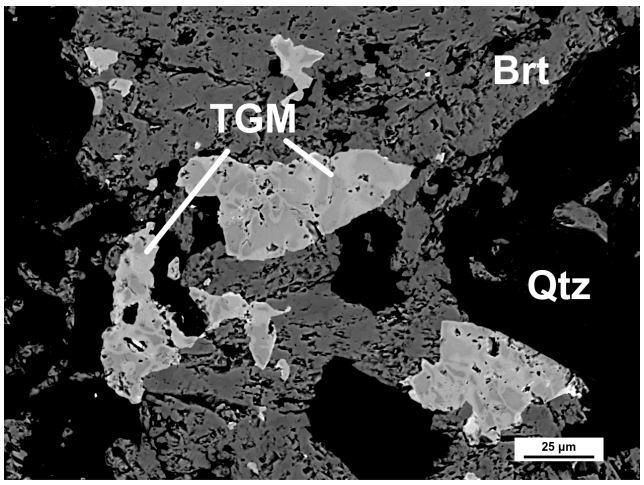

Figure 2. Chemically zoned tetrahedrite group mineral grains (TGM) in barite (Brt) and quartz (Qtz). Zonation is caused by different Ag-Cu ratio. BSE picture.

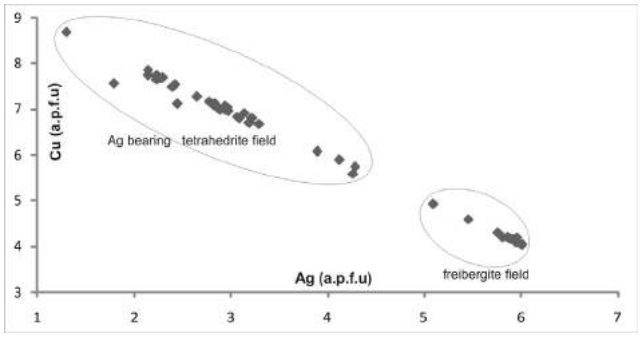

Figure 3. Diagram of the Ag-Cu substitution in TGM from Bystrzyca Górna.

4.2 Ag mineralization associated with Pb-Sb sulphosalts and native antimony

Pyrargyrite, stephanite and miargyrite are the main silver bearing phases in the samples. Acanthite/argentite are rare and occur as separate crystals in the ore bearing veinlets. They are sometimes replaced by Ag-Pb-Sb sulphosalts or they form intergrowths with plagionite, unknown sulphosalts, native antimony or galena. Argentite usually occurs as separate grains filling the vugs in pyrargyrite. It was probably formed during the decomposition of pyrargyrite. The chemical composition of pyrargyrite, stephanite and miargyrite is close to stoichiometric. Some analyses fall in the field between pyrargyrite and stephanite (Fig. 4). Low contents of Cu up to 0.5 wt.% and up to 0.1 wt.% of Bi were detected in pyrargyrite and miargyrite.

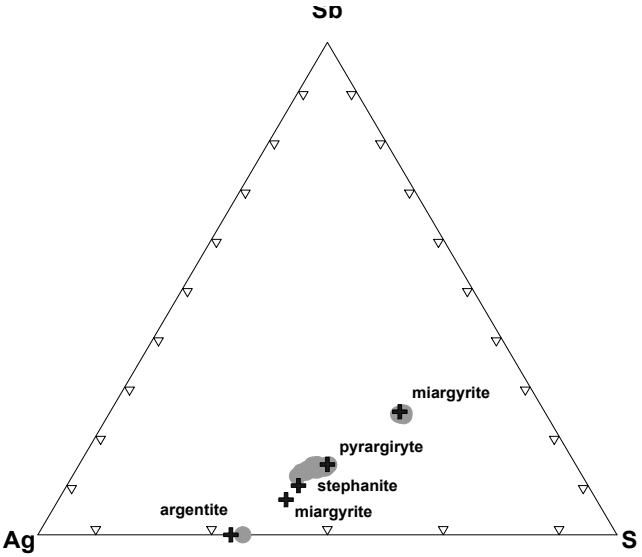

Figure 4. Diagram of the Ag-Sb-S for the Ag bearing phases from Bystrzyca Górna. Ideal phases are marked by cross.

Ag-Pb-Sb sulphosalts are rare, occurring as intergrowths with silver minerals. Sometimes, they form veinlets replacing other minerals in the paragenesis. The size of the crystals is usually up to a few microns, only in the case of the veinlets could they reach up to 100 microns. The main sulphosalt is zoubekite, which occurs only in the form of thin veinlets. Andorite VI and freieslebenite are rare. They have higher contents of Ag in comparison to theoretical ones, which is due to small crystals enclosed by Ag minerals. Andorite VI could be characterized as $^{5.37}L_{97.95}$ which means 97.95 mol.% of AgSb substitution and N=5.37. Zoubekite has a stable chemical composition and the average formula could be written as: $(Ag_{0.68}Cu_{0.09})_{0.77}(Pb_{4.09}Fe_{0.04})_{4.13}(Sb_{4.06}Bi_{0.03})_{4.09}S_{10.59}$.

Pb-Sb sulphosalts are common, forming needle-like crystals or aggregates in association with other minerals for example unknown phase X, bournonite and Ag phases. The size of the aggregates is up to 100 microns. Only two phases were identified: boulangerite and plagionite. Their chemical compositions are nearly stoiciometric.

Native antimony is one of the most common phases in the Ag bearing paragenesis. Usually it replaces silver bearing minerals or sulphosalts and is replaced by galena. It also forms separate crystals disseminated in quartz and barite or intergrowths with dyscrasite which is always in the central part of the crystals. It is chemically pure with only minor arsenic content - up to 0.9 wt.% identified.

Unknown phase X is rare in the overall paragenesis. It occurs in the form of needle like crystals or intergrowths with another minerals (Fig. 5). It is commonly found with plagionite, pyrargyrite, galena and native antimony. The size of the crystals is up to 100 microns and contain on average 0.5 wt.% of Ag, 0.4 wt.% of Bi, 5 wt.% of Fe, 8.7 wt.% of Cu, 9.1 wt.% of Sb, 57.8 wt.% of Pb and 18.76 wt.% of S which give the following formula calculated on the base of 16 cations: $(Cu_{3.74}Ag_{0.12})Fe_{2.44}\ (Sb_{2.04}Bi_{0.05})Pb_{7.61}S_{15.96}$.

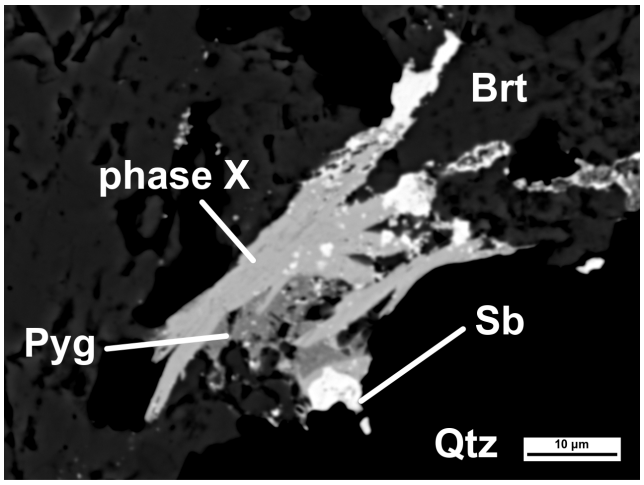

Figure 5. Needle like crystals of unknown phase X in association with pyrargyrite (Pyg) and native antimony (Sb) in quartz (Qtz) - barite (Brt) matrix. BSE picture.

Only two grains of unknown phase Y, up to 50 microns, were identified. It occurs in association with pyrargyrite (up to 3 wt.% of Cd), galena, native antimony, sphalerite (Fig. 6), plagionite and phase X. It contains on average 32.99 wt.% of Ag, 25.61 wt.% of Sb, 20.36 wt.% of S, 0.53 wt.% of Pb, 18.79 wt.% of Cd which gives formula calculated on the base of 10 cations as $(Cd_{2.43}Ag_{4.46})_{6.89}\ Sb_{3.06}S_{9.25}$.

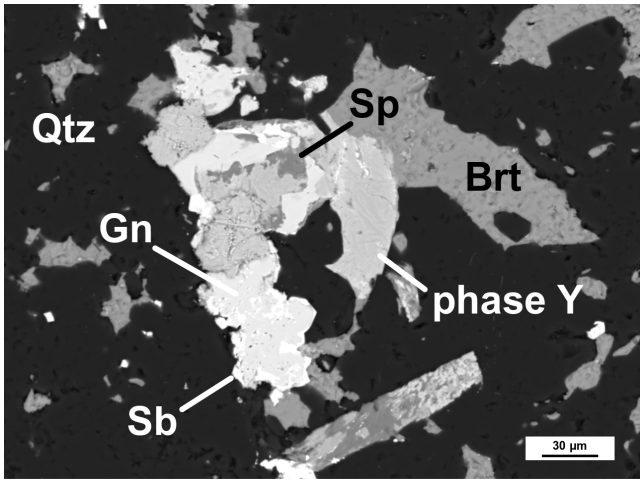

Figure 6. Irregular grain of phase Y (light grey) in association with sphalerite (Sp), native antimony (Sb) and galena (Gn) in barite (Brt) and quartz (Qtz). BSE picture.

5 Summary and discussion

Interesting silver minerals were identified in the barite veins in Bystrzyca Górna. This is the first occurrence of Ag-Sb-Pb-(Cd) mineralization in Poland. The silver-sulphosalt paragenesis is dominated by the Ag minerals and is younger than the main sulphide minerals. During the sulphide crystallization contents of Sb and Ag were increased which lead to the replacement of former

tetrahedrite by freibergite, replacement of previous sulphosalt paragenesis by native antimony and finally by galena. A similar paragenesis with Ag-minerals and various sulphosalts is typical for many barite deposits or base-metal deposits in Poland or in the world (Plumlee et al. 1994; Škácha et al. 2012; Megarskaya et al. 1986; Pršek unpublished and others). The presence of Ag-Pb-Sb, Pb-Sb, Ag-Sb, Ag-Cu-Fe-Pb-Sb sulphosalts with native antimony and dyscrasite together with Ag-Sb-Cd phase and greenockite as well as Ag rich tetrahedrite shows that the ore mineralization in barite veins forms under complex and changing hydrothermal conditions. Similar variability in mineralogy was identified in barite veins in the Apuan Alps (Italy) where many of new Pb-Sb (Tl, O, Cl, Hg, Ag, Cu) sulphosalts were described (Biagioni et al. 2014; Biagioni et al. 2016; Biagioni et al. 2018; and many others). TGM minerals are typical for many hydrothermal veins and mineralization, and they are often the main host of Ag in ores. Substitution of Ag for Cu is typical in base metal Ag bearing mineralization or in Au-Ag mineralization (Grammatikopoulos et al. 2005; Pršek et al. 2006; Gallego-Hernandez and Akasaka 2010; Kołodziejczyk et al. 2016; and many others).

The chemical composition of sulphosalts is usually close to stoichiometric, with only few of variations. The main issue is Ag-Pb-Sb sulphosalts, especially andorite VI and frieslebenite which composition far from the theoretical one are shifted. Zoubekite from the Bystrzyca Górna deposit has lower Ag contents (4.6 wt.%) in comparison with zoubekite from Příbram (5.8 wt.%) (Megarskaya et al. 1986) or from Silver King (6.58 wt.%) (Birch 2017). Contents of Pb, Sb and Cu is similar to the paragenesis for other Ag-Pb-Sb sulphosalts and freibergite. Various combinations of elements in sulphosalts, high Ag and Cd content in the ore could lead to distinguish and discover other Cd-Ag-Pb-Sb-Cu-Fe bearing minerals from the sulphosalt group, similarly how it happend in case of Apuan Alps.

Acknowledgements

Research was founded by AGH grant No. 11.11.140.320. We are grateful to Adam Włodek from Laboratory of Critical Elements at AGH-UST-KGHM, Faculty of Geology, Geophysics and Environmental Protection for help during EMPA data collection. We would like to appreciate group of students from SKNG for the field work and sample collecting.

References

Biagioni C, Orlandi P, Moëlo Y, Bindi L (2014) Lead-antimony sulphosalts from Tuscany (Italy). XVI. Carduciite, $(AgSb)Pb_6(As,Sb)_8S_{20}$, a new Sb-rich derivative of rathite from the Pollone mine, Valdicastello Carducci: occurrence and crystal structure. Miner. Mag. 78:1775-1793.

Biagioni C, Moëlo Y, Orlandi P, Stanley C (2016) Lead-antimony sulphosalts from Tuscany (Italy). XVII. Meerschautite, $(Ag,Cu)_{5.5}Pb_{42.4}(Sb,As)_{45.1}S_{112}O_{0.8}$, a new expanded derivative of owyheeite from the Pollone mine, Valdicastello Carducci: occurrence and crystal structure. Miner. Mag. 80:675-690.

Biagioni C, Moëlo Y, Orlandi P, Paar W (2018) Lead-antimony sulphosalts from Tuscany (Italy). XXIII. Andreadiniite, $CuAg_7HgPb_7Sb_{24}S_{48}$, a new oversubstituted (Cu,Hg)-rich member of the andorite homeotypic series from the Monte Arsiccio mine, Apuan Alps. Eur. J. Mineral., 30:1021-1035.

Birch W D (2017) Mineralogy of the Silver King deposit, Omeo, Victoria. The Royal Society of Victoria 129:41-52.

Gallego-Hernandez A N, Akasaka M (2010) Ag-rich tetrahedrite in the El Zancudo Deposi, Colombia: Occurrence, Chemical composition and Genetic Temperatures. Res. Geol., 60:218-233.

Grammatikopoulos T A, Roth T, Valeyev O (2005) Compositional variation in Hg-Ag rich tetrahedrite from the polymetallic Eskay Creek deposit, British Columbia, Canada. N. Jb. Miner. Abh. 181:281-292.

Gunia T (1985) Geological position of the Sowie Góry block and its influence on the paleography of the Paleozoic of Central Sudetes. Geol. Sudetica, 20:83-119.

Kołodziejczyk J, Pršek J, Asllani B, Maliqi F (2016) The paragenesis of silver minerals in the Pb-Zn Stan Terg deposit, Kosovo: an example of precious metal epithermal mineralization. Geol., Geoph. and Envir. 42:19-29.

Kozub-Budzyń G, Piestrzyński A (2018) The first occurrence of cupropearceite in the Kupferschiefer deposit, Lubin mine, SW Poland. Geol. Quaterly, 62:319-326.

Megarskaya L, Rykl D, Taborsky Z (1986) Zoubekite, $AgPb_4Sb_4S_{IO}$ a new mineral from Pribram, Czechoslovakia. Neues Jahrb. Mineral., Monatsh., 1-7.

Piestrzyński A, Kowalik K (2014) Argentopentlandite from barite vein in Zagórze Sląskie, Lower Silesia, a first occurrence in Poland. Mineralogia 45:13-25.

Plumlee G, Whitehouse-Veaux P (1994) Mineralogy, Paragenesis, and Mineral Zoning of the Bulldog Mountain Vein System, Creede District, Colorado. Econ. Geol. 89:1883-1905.

Pršek J, Chovan M, Ozdín D (2006) Chemical composition of tetrahedrite-tennantite solid solution as the indicator of type of the hydrothermal mineralization: Examples from the Western Carpathians. Miner. Pol. Spec. Paper 28:184-186.

Siuda R (2012) Silver minerals from the Friederike Juliane mine at Ciechanowice (Sudety Mts, Poland). Biul. PIG 448:315-324.

Škácha P, Sejkora J, Knížek F, Slepička F, Litochleb J, Jebavá J (2012) Ag-Sb-Pb mineralization of the vein H14F3, shaft 21, Příbram uranium and base-metal ore district (Czech Republic). Acta Miner. Petrogr., Abstract Series 7:125.

Clastic sediment-hosted Pb-Zn mineralization in the Selwyn Basin, Yukon, Canada and the relationship to alkaline magmatism

Emma J. Scanlan, Matthew Leybourne, Daniel Layton-Matthews, Alex Voinot
Department of Geological Sciences and Geological Engineering, Queen's University, Canada

Suzanne Paradis
Geological Survey of Canada

Nancy van Wagoner
Department of Physical Sciences, Thompson Rivers University, Canada

Abstract. The Selwyn Basin in the Yukon Territory, Canada, is host to several Pb-Zn clastic sedimentary-hosted districts. Two of these districts, Anvil and MacMillan Pass, have alkaline magmatism in the same stratigraphic horizon as Pb-Zn mineralization. We have collected samples from these volcanics and begun to characterise volcanism in the Selwyn Basin. Samples are alkaline basalts and basaltic volcaniclastics produced through within plate magmatism. Samples from the Earn Group in Keno Hill are subalkaline meta-basalts with tholeiitic compositions. Volcanism in MacMillan Pass was more explosive than within the Anvil District, where pillow lavas and lapilli tuffs represent periods of effusive and explosive subaqueous volcanism, respectively. Initial work on the thallium isotopes of volcanic rocks indicates that MacMillan Pass samples have a more negative ε^{205}Tl range (-3.2 ± 1.8 to -14.2 ± 3.2) than those from the Anvil District (-0.9 ± 1.9 to -6.4 ± 1.2). Future work will expand upon initial Tl isotope data, constrain the age relationships between volcanism and mineralization and use Nd, Sr and Pb isotopes to characterise magma sources.

1 Introduction

Our understanding of the formation of Pb-Zn clastic sediment-hosted deposits has evolved over time. Historically, these deposits have been considered as purely hydrothermal, forming through exhalation of metal-rich brines onto the seafloor (Leach et al. 2010; Lydon 1983). However, deposits have been discovered where the ore did not form through exhalation but rather as sub-seafloor replacement (Gadd et al. 2016; Kelley et al. 2004; Magnall et al. 2016). Many deposits have volcanism present in the sedimentary package that hosts the Pb-Zn mineralization but this volcanism has generally been dismissed as unrelated to ore forming processes. The Selwyn Basin provides an ideal location to investigate volcanism in relation to Pb-Zn clastic sediment-hosted deposits. Paleozoic magmatism in the region occurs in spatial and temporal relation to two major Pb-Zn Districts (Goodfellow et al. 1995) (Fig. 1). This project will use a variety of geochemical techniques to characterise magmatism in the region, constrain age relationships and pinpoint linkages between magmatism and mineralization.

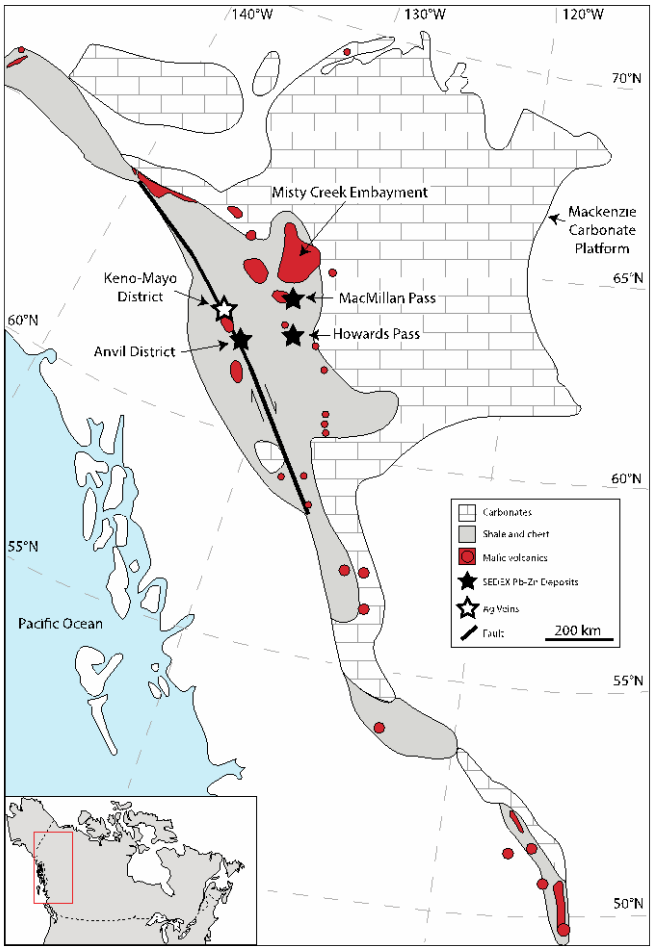

Figure 1. Simplified geologic map of the Selwyn Basin with the distribution of mafic volcanism and relation to Pb-Zn districts. Modified from Goodfellow et al. (1995).

Regional geology

The Selwyn Basin formed on the passive margin of North America from the Late Proterozoic to the Early Carboniferous. Rift-fill and marine facies fill an

extensional sedimentary basin. Interbedded alkaline mafic volcanics from the Cambrian to late Devonian are scattered throughout the region (Goodfellow et al. 1995) (Fig. 1). Volcanic rocks were subdivided by Goodfellow et al. (1995) on the basis of different degrees of partial melting from either a metasomatized lithospheric mantle source or the asthenospheric mantle.

Clastic sedimentary hosted Pb-Zn deposits occur in three major districts within the Selwyn Basin; Howard's Pass, Anvil district and MacMillan Pass (Fig. 1).

2 Methods

A total of 142 samples were sent to ALS Geochemistry in Vancouver, Canada for lithogeochemistry. Whole rock samples were crushed using a low Cr-Mo steel ring. Major elements were measured using inductively coupled plasma-atomic emission spectroscopy (ICP-AES) and trace elements using inductively coupled plasma-mass spectrometry (ICP-MS) as outlined in Leybourne et al. (2018).

Thallium isotopes were measured at the Queen's Facility for Isotope Research. The analytical methods used are outlined in Peter et al. (2018). Isotopes were measured using a Neptune multi-collector ICP-MS.

3 Results & discussion

3.1 Volcanic textures

Samples from the Anvil District were collected from the Menzie Creek Volcanics, which can be subdivided into three lithologies; 1) ash-rich tuffs, lapilli tuffs and volcanic breccias, 2) pillow and basalt flows, 3) gabbroic intrusives. Ash-rich tuffs typically contain no or little lapillus and are often graded. Lapilli tuffs contain relict glass shards with cuspate margins and pumice fragments that range from undeformed to flattened between samples (Fig 2a). Breccia fragments are typically basaltic. Volcaniclastic samples represent pyroclastic flows and fall deposits. Basalt pillows and flows indicate effusive subaqueous eruptions.

MacMillan Pass volcanics are dominantly volcaniclastic. These samples have a distinctive orange alteration in hand specimen. Lapilli tuffs and volcanic breccias are common, with heterolithic clasts. Ash-rich tuffs and a few intrusive samples were also collected. These samples have high carbonate contents. Most of this carbonate is present as coarse crystals comprising the matrix although some carbonate is present as clasts or replacing phenocrysts within clasts. Whereas a large proportion of this carbonate may be alteration, some is likely magmatic in origin. Breccias are poorly sorted and heterolithic, with clasts of basalt, pumice, chert, quartz and rare black shales. Clasts range from sub-mm to tens of cm. Clast boundaries vary from those that are angular and reflect little reworking to sub-rounded clasts. Pumice shows little deformation. Relict glass shards with cuspate margins are present in several lapilli tuffs. The size, sorting and heterolithology of breccias suggests that these samples formed in explosive eruptions and were likely close to the volcanic vent. Ash-rich tuffs are likely ash fall or surge deposits that formed distally from the vent.

Primary features in metavolcanics from the Earn Group in the Keno Hill region have been obscured by regional metamorphism up to the lower greenschist facies. These samples are crosscut by a series of Triassic dikes.

Misty Creek Embayment samples are dominantly basaltic, representing effusive eruptions. Several lapilli tuffs from this region contained mm to cm scale basalt clasts. No pumice or relict glass shards were observed.

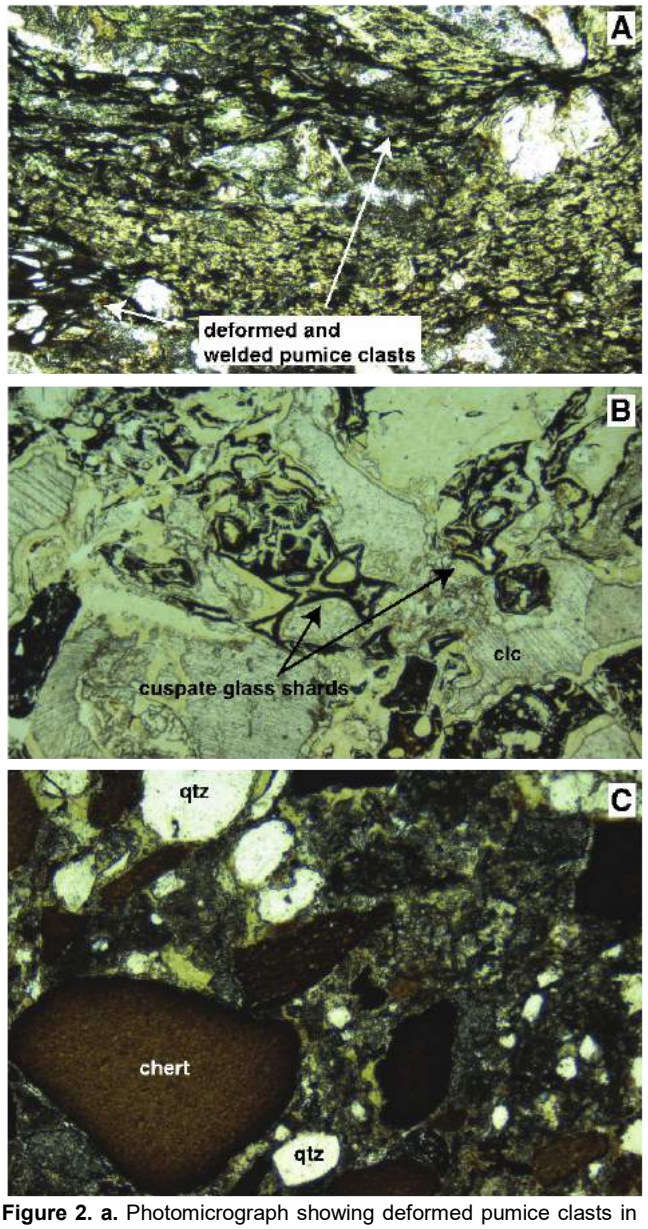

Figure 2. a. Photomicrograph showing deformed pumice clasts in a lapilli breccia from the Anvil District. Field of view (FOV) = 3 mm. **b.** Glass shards with cuspate margins in a lapilli tuff from MacMillan Pass. FOV = 1.5 mm **c.** A poorly sorted heterolithic breccia from MacMillan Pass. FOV = 3 mm. clc = calcite, qtz = quartz.

3.2 Lithogeochemistry

Due to pervasive alteration of volcanic samples, typical sample classification schemes are not useful. A Zr/TiO_2 versus Nb/Y plot indicates that volcanics from the Keno Hill district are subalkaline whereas all other sample suites from the Selwyn Basin are alkali basalts, basanites or trachyandesite (Fig. 3a). Samples from MacMillan Pass, the Anvil District and the Misty Creek Embayment all plot as within plate alkaline basalts on the tectonic discrimination diagram of Wood (1980) (Fig. 3b).

All volcanic samples in the Selwyn Basin show an enrichment in Ba. Thallium shows a positive trend plotted against Ba, which is similar to mineralized samples from the Howard's Pass deposit (Leybourne et al. 2018). Spider diagrams show that all samples have positive peaks in Ba with depletions in K, Sr, Ti, and Rb. Pb is commonly depleted in all samples except for those from Keno Hill.

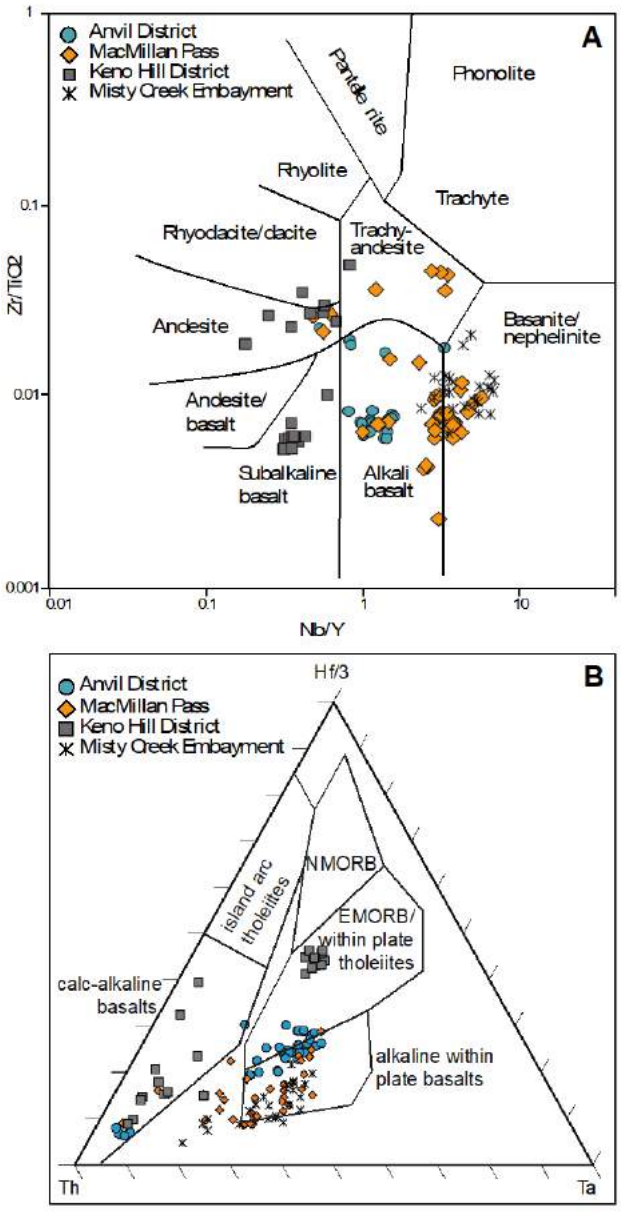

Figure 3. a. Zr/TiO_2 versus Nb/Y identification scheme from Winchester and Floyd (1977). **b.** Tectonic classification scheme of Wood (1980).

3.3 Thallium isotopes

Five volcanic samples from the Anvil District give a $\varepsilon^{205}Tl$ range of -0.9 ± 1.9 to -6.4 ± 1.2. Six samples from MacMillan Pass range from -3.2 ± 1.8 to -14.2 ± 3.2 (Fig. 4). The value of -14.2 has a large error with it and is anomalously low, ~5 units from the second most negative MacMillan Pass sample (-9.5 ± 2.5). There is no clear trend when these results are plotted against Tl concentrations. However, plotted against Ba concentration, Ba concentration increases as $\varepsilon^{205}Tl$ values become more negative (Fig. 4).

MacMillan Pass and Anvil District volcanics both overlap with the Tl isotopic values of the Howard's Pass Pb-Zn deposit (Fig. 5). However, these volcanic samples also overlap with the host rock of the Howard's Pass deposit. When comparing the Tl isotopes to other geological settings, the one outlier from MacMillan Pass only overlaps with altered ocean crust. Tl isotopes from a larger sample suite in the Selwyn Basin will be analysed to investigate the potential of elements such as Ba and Tl in the Pb-Zn deposits to have been sourced from magmas.

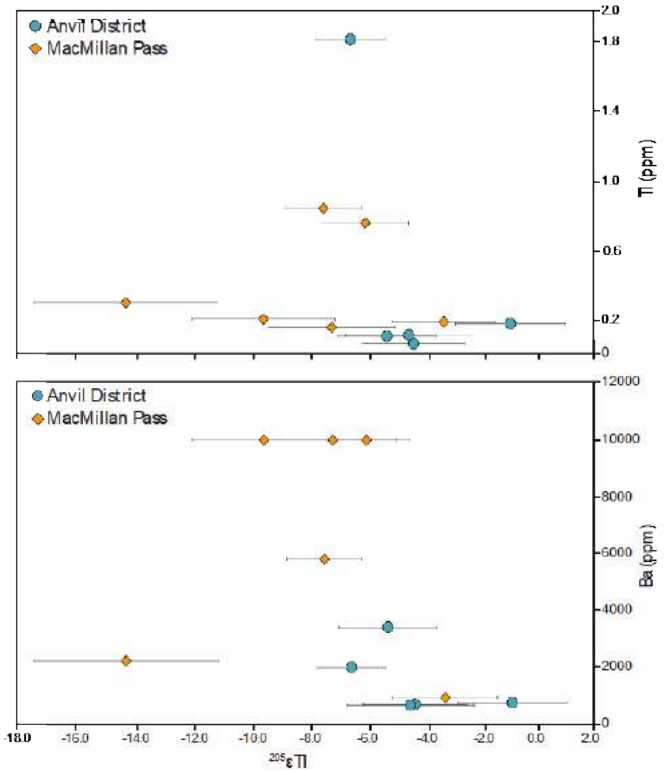

Figure 4. Thallium isotopes ($^{205}\varepsilon Tl$) plotted against Tl and Ba concentrations. One MacMillan Pass sample has an anomalously negative Tl isotopic signature.

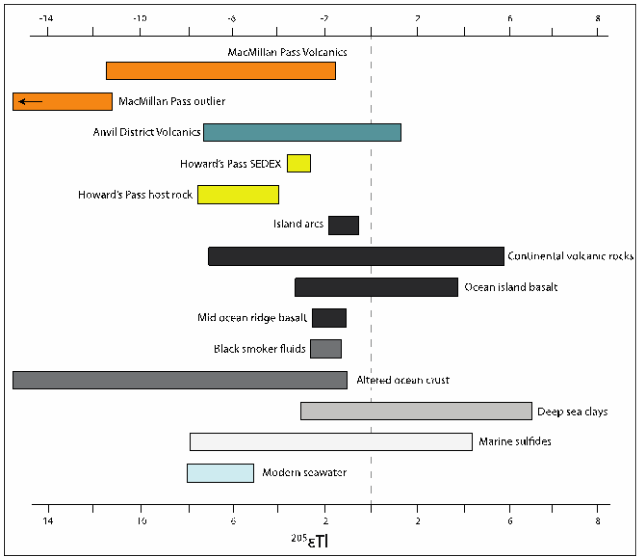

Figure 5. Thallium isotopic ranges for studied samples, Howard's Pass (Peter et al. 2018) and a variety of geologic settings (Kersten et al. 2014 and references therein).

4 Preliminary conclusions

Volcanism within the Selwyn Basin was varied, with different regions within the basin represented by differing eruption styles, geochemistry and alteration styles. Volcanic samples are alkaline in all regions except Keno Hill and were produced through within plate volcanism. Initial Tl isotopes are more negative for MacMillan Pass in comparison to those from the Anvil District and overlap with Tl values from the Howard's Pass Pb-Zn clastic sedimentary-hosted deposits.

Acknowledgements

We would like to acknowledge funding through the Targeted Geoscience Initiative (TGI) scheme to the Geological Survey of Canada that supported fieldwork and analytical costs.

References

Gadd MG, Layton-Matthews D, Peter JM, Paradis SJ (2016) The world-class Howard's Pass SEDEX Zn-Pb district, Selwyn Basin, Yukon. Part I: trace element compositions of pyrite record input of hydrothermal, diagenetic, and metamorphic fluids to mineralization. Miner Deposita 51(3):319-42.

Goodfellow WD, Cecile MP, Leybourne MI (1995) Geochemistry, petrogenesis, and tectonic setting of lower Paleozoic alkalic and potassic volcanic rocks, Northern Canadian Cordilleran Miogeocline. Can J Earth Sci 32(8):1236-54.

Kelley KD, Leach DL, Johnson CA, Clark JL, Fayek M, Slack JF, Anderson VM, Ayuso RA, Ridley WI (2004) Textural, compositional, and sulfur isotope variations of sulfide minerals in the Red Dog Zn-Pb-Ag deposits, Brooks Range, Alaska: Implications for ore formation. Econ Geol 99(7):1509-32.

Kersten M, Xiao T, Kreissig K, Brett A, Coles BJ, Rehkämper M (2014) Tracing anthropogenic thallium in soil using stable isotope compositions. Environ Sci Technol 48(16):9030-9036.

Leach DL, Bradley DC, Huston D, Pisarevsky SA, Taylor RD, Gardoll SJ (2010) Sediment-hosted lead-zinc deposits in Earth history. Econ Geol 105:593-625.

Leybourne MI, Van Wagoner N, Paradis S, Layton-Matthews D, Moertle JA (2018) Selwyn Basin magmatism and relationship to sediment-hosted Zn- Pb deposits. In: Rogers N (ed) Targeted Geoscience Initiative: 2017 report of activities, volume 2, Geological Survey of Canada, Open File 8373, pp 71–92.

Lydon JW (1983) Chemical parameters controlling the origin and deposition of sediment-hosted stratiform lead-zinc deposits. In: Sangster DF (ed) Short course in sediment-hosted stratiform lead-zinc deposits, Mineralogical Association of Canada, pp 175-250.

Magnall JM, Gleeson SA, Blamey NJF, Paradis S, Luo Y (2016) The thermal and chemical evolution of hydrothermal vent fluids in shale hosted massive sulphide (SHMS) systems from the MacMillan Pass district (Yukon, Canada). Geochim Cosmochim Acta 193:251-273.

Peter JM, Gadd MG, Layton-Matthews D, Voinot A (2017) Reconnaissance thallium isotope study of zinc-lead SEDEX mineralization and host rocks in the Howard's Pass district, Selwyn Basin, Yukon: Potential application to paleoredox determinations and fingerprinting of mineralization. In Rogers N (ed) Targeted Geoscience Initiative: 2017 report of activities, volume 1, Geological Survey of Canada, Open File 8358, pp 179–191.

Winchester JA, Floyd PA (1977) Geochemical discrimination of different magma series and their differentiation products using immobile elements. Chem Geol 20:325-343.

Wood DA (1980) The application of a ThHfTa diagram to problems of tectonomagmatic classification and to establishing the nature of crustal contamination of basaltic lavas of the British Tertiary Volcanic Province. Earth Planet Sci Lett 50(1):11-30.

Genetic links between Irish-type Zn-Pb deposits and related geochemical halos

Lola Yesares, Julian F. Menuge
Irish Centre for Research in Applied Geosciences, O'Brien Centre for Science (East), University College Dublin, Ireland.

Drew A. Drummond, Adrian J. Boyce
Scottish Universities Environmental Research Centre, East Kilbride, UK

John H. Ashton, Robert J. Blakeman
Boliden Tara Mines, Exploration Department, Navan, County Meath, Ireland.

Abstract. A broad geochemical dispersion halo has been identified with a direct link to the underlying Tara Deep deposit at Navan, Ireland. In situ laser S isotope analyses have been performed on petrographically well-characterized samples from the halo. Four mineral assemblages have been identified. 1) In black shales, laminated pyrite comprising thin layers of framboidal low-$\delta^{34}S$ pyrite with minor interstitial sphalerite. 2) Pyritized calcarenites are widely distributed and occur chiefly as biodebris replaced by low-$\delta^{34}S$ pyrite. 3) A replacive assemblage occurs as late remobilizations exhibiting both crosscutting and bedding-parallel styles, overprinting the early laminated pyrite. It comprises mostly marcasite, with minor pyrite, sphalerite, chalcopyrite, galena, stibnite, arsenopyrite and pentlandite, with high $\delta^{34}S$ values. 4) Hydrothermal cherts comprise thick microcrystalline quartz bands rimmed by dolomite, associated with marcasite, pyrite, sphalerite, chalcopyrite, galena, Ni-sulfosalts and stibnite with high $\delta^{34}S$ values. These results indicate overlapping diagenetic and multi-phase hydrothermal sulfide mineralization. First, laminated pyrite and pyritized calcarenites suggests a bacterial origin within sediments during early diagenesis. Later, hydrothermal chert and replacive sulfides suggest hydrothermal exhalation during early-mid diagenesis. Similarities in mineralogy and S isotope compositions suggest genetic links between the halo and the underlying Tara Deep deposit.

1 Introduction

Irish-type Zn-Pb deposits are understood to have formed by replacement of Lower Carboniferous limestones. Networks of normal faults acted as pathways for ascending, warm, metal-bearing fluids which had scavenged metal from the underlying Lower Palaeozoic basement, to mix a with cooler, hypersaline brine associated with dissolved bacteriogenic sulphide reduced bacteria (e.g. Ashton et al. 2015).

The Navan deposit is a world-class carbonate-hosted Zn-Pb deposit mined by Boliden Tara Mines DAC and is Europe's largest zinc mine. It exceeds 110 Mt in size, grading 8.0% Zn and 2% Pb prior to mining (Ashton et al. 1986; 2003; 2015; Anderson et al. 1998; Fallick et al. 2001; Blakeman et al. 2002; Gagnevin et al. 2012). Almost all these studies are based on structural, petrologic and geochemical analyses of both the Main Orebody and South West Extension (SWEX). Following an extensive seismic survey in 2012 (Ashton et al. 2018), a new satellite deposit to the Navan orebody was discovered at ~1500m, known as Tara Deep, with an inferred resource of 18.2 Mt grading 7.6% Zn and 1.6% Pb (Ashton et al. 2019).

As discovery depths get deeper, the potential exploration importance of the overlying halos which surround many Irish-type deposits is becoming more important. Halos overlying the Navan deposit present geological features which suggest that here, the hydrothermal fluids that formed Navan replacive ore also reached the seafloor, forming sedimentary-exhalative (SEDEX) mineralisation (Altinok 2005; Yesares et al. 2019). Nevertheless, linkages between these halos and the economic Navan mineralization are poorly understood. Understanding these halos has the potential to significantly enhance mineral exploration strategies for deeply buried ores, and to strengthen genetic models of both replacive and SEDEX mineralization.

Here we focus on the genesis of the alteration halo of the recently discovered Tara Deep orebody associated with the Navan deposit. The geological record suggests that the halo mineralisation was formed close to the seafloor within the Upper Dark Limestone (UDL), linked to the underlying economic Tara Deep replacive ore.

2 Geological setting

The Irish Midlands are dominated by Lower Carboniferous limestones. These rocks were deposited in tropical seas, typically shallow but with sedimentary basins developing in response to crustal extension (Philcox 1984). They represent a marine transgression over clastic sedimentary rocks of late Devonian to Tournaisian age known as the Old Red Sandstone, a terrestrial red bed succession.

Irish-type Zn-Pb deposits consist primarily of stratabound sphalerite, galena and iron sulfides,

accompanied by dolomite, calcite and barite gangue, hosted in Tournasian carbonate sedimentary rocks. They are concentrated near normal faults, which are often associated with development of Upper Palaeozic sedimentary basins. These faults are probably partly inherited from the underlying complex Lower Palaeozoic basement geology that resulted from closure of the Iapetus Suture Zone during Late Caledonian continental collision (Leeder 1982; Murphy et al. 1991).

The Zn-Pb Navan orebody is located in the northern margin of the Dublin Basin and is hosted mainly by the Tournaisian Micrite Unit at the base of Pale Beds, of the Navan Group (Fig. 1).

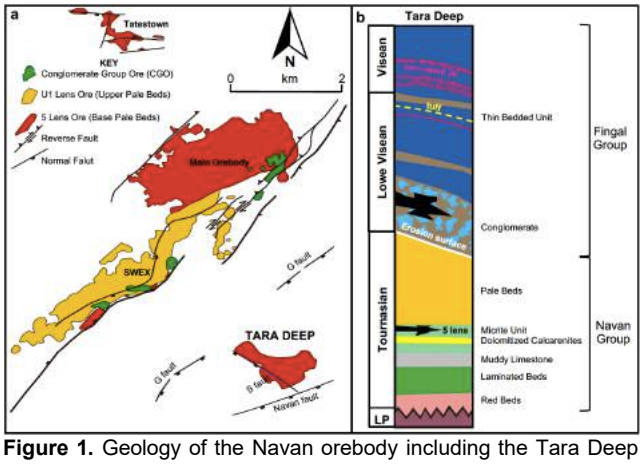

Figure 1. Geology of the Navan orebody including the Tara Deep deposit (a) Map projection of the top surface of the Navan system, including the different deposits and main structural features; (b) Stratigraphic column of the Tara Deep area showing the different ore lenses and hosting rocks. (L.P. = Lower Palaeozoic). Taken from Yesares et al. 2019.

3 Tara Deep deposit and overlying halo

The Tara Deep orebody is located ~3 km SW of the SWEX of the Navan deposit, at a depth of 1.2-1.9 km (Fig. 1a). The current inferred resource, 1.5 x 0.7 km in plan, is mostly hosted by lower Micrite Unit, the Tournaisian basal limestone sequence that hosts most of the Navan Main Orebody (Ashton et al. 2015). The Tara Deep deposit consists of a Zn-Pb semi-massive sulphide body up to 60 m thick. The Pale Beds comprise allochthonous slide units along with melange-like deposits of Shaley Pales, and/or Argillaceous Bioclastic Limestones. This allochthonous package is overlain by a polymict submarine debris-flow, currently considered to be equivalent to the Boulder Conglomerate of the Navan deposit (Fig. 1b).

Tara Deep is located between two major extensional structures. The G Fault forms the northern limit while the southern limit is defined by a larger structure, the ENE striking Navan Fault, which has a displacement of several kilometres. The structural terrace formed by the Navan and G faults is cut by the S fault, a NNW striking, steep westerly dipping structure (Fig. 1a).

As in the main Navan deposit, the majority of mineralization at Tara Deep occurs within a stratigraphic interval analogous to the 5-lens equivalent (lower Pale Beds). It comprises sphalerite and galena (5:1 ratio), with minor pyrite, marcasite, barite, stibnite and chalcopyrite. Tara Deep shows similar mineralogical compositions and textural relationships to the Navan main orebody and SWEX (Ashton et al. 2015).

The Tara Deep deposit is unconformably overlain by a deep marine succession, comprising Lower Visean-Visean basin fill, known as Upper Dark Limestones (UDL) (Fig. 1b; Fingal Group). In the Tara Deep area, the lower UDL includes the Thin-Bedded Unit (TBU) which comprises alternating sequences of black shales, siltstones and calcarenites (Figs 1b and 2). Here, uneconomic seafloor exhalative sulfide mineralization has been identified where the TBU overlies the Tara Deep deposit.

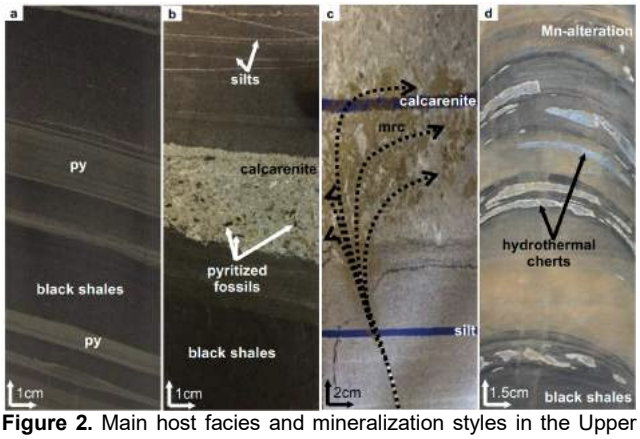

Figure 2. Main host facies and mineralization styles in the Upper Dark Limestone overlying the Tara Deep deposit. (a) Organic matter-rich black shales replaced by ~0.5 to 1.5 cm layers of fine-grained pyrite parallel to bedding; (b) alternating sequences of organic matter-rich black shales, silts and calcarenites including pyritized fossils; (c) Marcasite and pyrite filling fractures and interstices in both silts and calcarenite; and (d) Centimetre-scale hydrothermal cherts, included in black shales which show a reddish Mn alteration.

4 Samples and methods

Samples from the sub-economic mineralization in the Thin Bedded Unit overlying Tara Deep were collected from drill core. Mineralogical, textural and paragenetic analyses were carried out by petrographic microscopy, SEM-EDS and EPMA.

Sulfur isotope analyses were carried out by in-situ laser combustion (Wagner et al 2002) of sulphides on polished blocks.

5 TBU Mineralogy

Petrographic analyses have revealed a texturally complex mineralogy composed mainly of pyrite and marcasite with subordinate sphalerite, galena, chalcopyrite, arsenopyrite, stibnite and undefined Ni-sulfosalts. Four different mineral assemblages have been identified from their mineralogical and textural features:

1) Laminated pyrite: is the major assemblage and is mostly composed of 0.5-15 cm thick bedding-parallel layers of framboidal pyrite and subordinate interstitial sphalerite (Figs 2a and 3a). It is widely distributed in the

TBU, progressively decreasing upwards and is closely associated with black shales.

2) Pyritized fossils: calcarenite layers within the TBU show a high degree of pyritization including bioclast replacement (Figs 2b and 3b). It is widely distributed in the TBU, progressively decreasing upwards and closely associated with the laminated pyrite.

3) Hydrothermal chert: mainly comprises 0.5-2 cm thick microcrystalline quartz bands rimmed by euhedral coarse Mn-rich dolomite associated with bird's eye marcasite, fine euhedral aggregates of pyrite, sphalerite, chalcopyrite, and galena which includes very fine exsolved Ni-sulfosalts and stibnite (Figs 2d, 3c and 3d). It is found systematically at higher stratigraphic levels in the TBU.

4) Replacive assemblage: is pervasively distributed throughout the TBU and occurs mainly in calcarenites. It occurs as late remobilizations both crosscutting, and parallel to, the bedding and overprinting the early laminated pyrite (Fig. 2c). It is formed by marcasite and pyrite, and minor sphalerite, chalcopyrite, galena and siegenite filling of open spaces (Figs 3e and 3f).

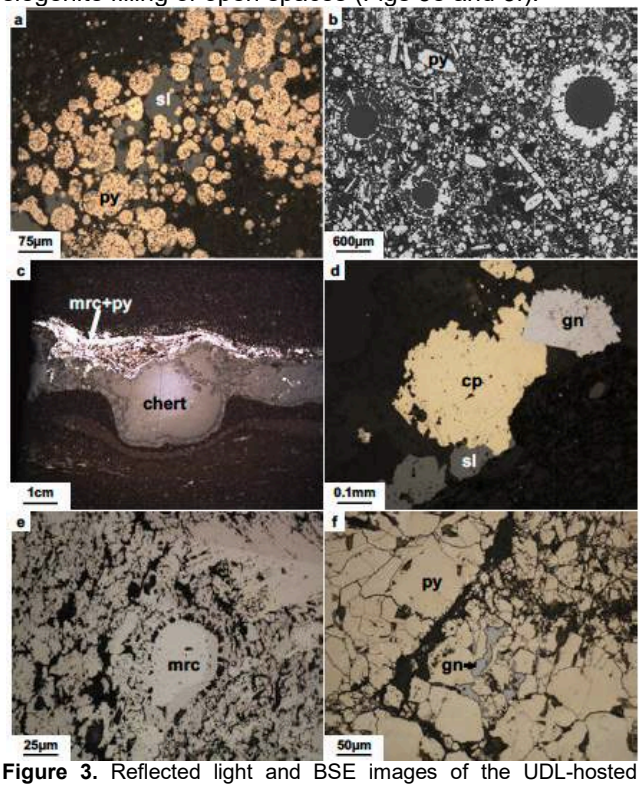

Figure 3. Reflected light and BSE images of the UDL-hosted mineralization overlying Tara Deep. (a) Laminated framboidal pyrite (py) replaced by sphalerite (sl); (b) Pyritized fossils (mainly radiolaria) in a calcarenite layer; (c) Hydrothermal cherts included in black shales showing a sulfide rim formed by marcasite (mrc) and pyrite; (d) Sulfide rim on chert comprising by chalcopyrite (cp), galena (gn) and sphalerite; (e) Skeletal marcasite replacing a calcarenite; (f) Interstitial galena (gn) in pyrite.

6 Sulfur isotope data

Figure 4 shows S isotope analyses on sulfides hosted within the TBU overlying the Tara Deep deposit. The results show a wide range of $\delta^{34}S$ values from -37.4 to +44.2‰.

Framboidal laminated pyrite (Figs 2a, 3a and 3b) shows a wide range of low $\delta^{34}S$ values from -37.4 to 3.3‰ (mean of -24‰) (Fig. 4). The $\delta^{34}S$ for interstitial sphalerite (Figs 2a and 3b) is also low, ranging from -32.8 to 7.1‰ (mean of -20.6‰) (Fig. 4).

Pyritized fossils in calcarenite (Figs 2b and 3c) have a broad range of $\delta^{34}S$ values from -32.2 to 5.6‰ (mean of -13‰) (Fig. 4).

Marcasite associated with hydrothermal cherts (Figs 2d, 3d and 3e) exhibits higher $\delta^{34}S$ values from 5.8 to 44.2‰ (mean of 17.2‰). The $\delta^{34}S$ for sphalerite (Figs 2d and 3f) ranges from 7.0 to 15.2‰ (mean of 10.5‰), while chalcopyrite (Figs 2d and 3f) ranges from 17.5 to 36.8‰ (Fig. 4).

Marcasite included in the replacive assemblage (Figs 2c, 3g, 3h and 3i) shows a wide range of higher $\delta^{34}S$ values from 0 to 24.5‰ (mean of 10.4‰) (Fig. 4)

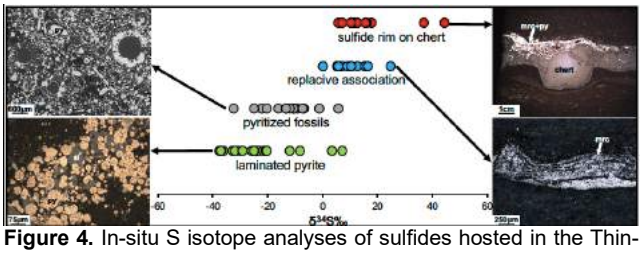

Figure 4. In-situ S isotope analyses of sulfides hosted in the Thin-Bedded Unit overlying the Tara Deep deposit.

7 Discussion and conclusions

Laminated pyrite (Fig. 2a) and pyritized fossils (Fig. 2b) show similar features to other mineral assemblages identified in the lower UDL (Altinok 2005). However, both hydrothermal chert (Fig. 2d) and the replacive assemblage (Fig. 2c) have not been described before.

The geological record (Fig. 2), detailed petrographic analysis (Fig 3) and S isotope compositions (Fig. 4) suggest overlapping of diagenetic and hydrothermal multi-phase sulphide mineralization in the TBU.

The close relationship between organic matter and negative $\delta^{34}S$ values in both laminated pyrite and pyritized calcarenites (Figs 3a, 3b and 4) suggests that mineralization was generated by sulfate-reducing bacteria within soft sediments during early diagenesis, close to the seawater-sediment interface.

Cherts associated with heavy sulfides (Figs 3c, 3d and 4) may also record distal hydrothermal exhalation, via sub-vertical fault pathways, from ascending fluids bearing silica, Zn, Pb, Cu, Ni and Sb during early-mid diagenesis. Whereas replacive heavy sulfide textures (Figs 3e, 3f and 4) suggest the circulation of hydrothermal fluids through the sedimentary pile during early-mid diagenesis, with sulfide deposition controlled by the secondary porosity of calcarenites.

Similarities in mineralogy and S isotope compositions show a clear genetic resonance between the TBU mineralization and Tara Deep deposit (see Drummond et al. in this issue). This strongly suggests that signals in the TBU represent a significant halo to the underlying Tara Deep, with positive consequences for future exploration.

Acknowledgements

This work has emanated from research that is supported in part by a research grant from Science Foundation Ireland (SFI) under grant number 13/RC/2092 and co-funded under the European Regional Development Fund.

References

Altinok (2005) Zn-Pb-Fe mineralization process, evolution of sea wáter oxidation state in a restricted basin, and diagenesis of deep water calcareous sediments: geochemical and geological study of the Navan deposit, Dublin basin, Ireland. Unpublished Ph.D. thesis, Golden, Colorado, Colorado School of Mines, 160 p.

Anderson IK, Ashton JH, Boyce AJ, Fallick AE, Russell MJ (1998) Ore depositional processes in the Navan Zn-Pb deposit, Ireland. Economic Geology. 93:535-563.

Ashton JH, Beach IA, Blakeman RJ, Coller D, Henry P, Lee R, Hitzman M, Hope C, Huleatt-James S, O'Donovan B, Philcox ME. Discovery of the Tara Deep Zn-Pb Mineralization at the Boliden Tara Mine, Navan, Ireland: Success with Modem Seismic Surveys (2018) Society of Economic Geologists, Inc. SEG Special Publications. 21:365-381.

Ashton JH, Blakeman RJ, Geraghty JF, Beach A, Coller D, Philcox ME (2015) The Giant Navan carbonate-hosted Zn-Pb deposit - a review, in Archibald, SM, and Piercey, SJ, eds., Current perspectives on zinc deposits: Dublin, Irish Association for Economic Geology. Special Publication: 85-122.

Ashton JH, Downing DT, Finlay S (1986) The geology of the Navan Zn-Pb orebody. In: Andrew CJ, Crowe RWA, Finlay S, Pennell WM, Pyne JF (eds) Geology and genesis of mineral deposits in Ireland. Irish Association for Economic Geology, Dublin, 243-280.

Ashton JH, Geraghty, JF, Holdstock MP, O'Keeffe WG, Martinez N, Peace W, and Philcox ME (2003) The Navan orebody-discovery and geology of the South West extension, in Fusciardi L, Earls G, Stanley G, Kelly JG, Ashton JH, Boland MB, Andrew CJ, eds., Europe's major base metal deposits: Dublin, Irish Association for Economic Geology, Special Publication: 405-430.

Ashton, J.H., 2019, Boliden Summary Report Resources and Reserves 2018:www.boliden.com/globalassets/operations/exploration/mineral-resources-and-mineral-reserves-pdf/resources-and-reserves-tara-2018-12-31.pdf

Blakeman RJ, Ashton JH, Boyce AJ, Fallick AE, Russell MJ (2002) Timing of interplay between hydrothermal and surface f!uids in the Navan Zn+Pb orebody, Ireland: Evidence from metal distribution trends, mineral textures and $\delta^{34}S$ analyses. Economic Geology. 97: 73-91.

Drummond DA, Boyce AJ, Yesares L, Blakeman RJ, Ashton JH (2019) Preliminary Results: The Tara Deep Zn - Pb Deposit, Navan, Co. Meath, Ireland. SGA 2019 Abstracts.

Fallick AE, Ashton JH, Boyce AJ, Ellam RM, Russell MJ (2001) Bacteria were responsible for the magnitude of the world-class hydrothermal base-metal orebody at Navan, Ireland. Economic Geology. 96: 885–890.

Gagnevin D, Boyce AJ, Barrie CD, Menuge JF, Blakeman RJ (2012) Zn, Fe and S isotope fractionation in a large hydrothermal system. Geochimica et Cosmochimica Acta. 88:183-198.

Kelley SP, Fallick AE (1990) High-precision, spatially resolved analysis of δ34S in sulfides using a laser extraction technique. Geochimica et Cosmochimica Acta. 54:883-888.

Leeder MR (1982). Upper Palaeozoic basins of the British Isles - Caledonide inheritance versus Hercynian plate margin processes. J. geol. Soc London. 139:479-491.

Murphy FC, Anderson TB, Daly JS, Gallagher V, Graham JR, Haroer DAT, Johnston JD, Kennan PS, Kennedy MJ, Long CB, Morris JH, O'Keefe WG, Parkes M, Ryan PD, Sloan RJ, Stillman CJ, Tietzch-Tyler D, Todd SP, Wrafter JP (1991). An appraisal of Caledonian suspect terranes in Ireland. Irish Journal of Earth Sciences. 11:11-41.

Philcox ME (1984) Lower Carboniferous lithostratigraphy of the Irish Midlands. Irish Association for Economic Geology, Dublin, 89 p.

Yesares L, Drummond D, Hollis S, Doran A, Menuge JF, Boyce AJ, Blakeman BJ, Ashton JH (2019) Coupling mineralogy, textures, stable and radiogenic isotopes in identifying ore-forming processes and geochemical vectoring possibilities in Irish-type carbonate hosted Zn-Pb deposits. Submitted to Minerals.